1

|INTRODUCTION |

INTRODUCTION TO BRAIN INFLAMMATION BIOLOGY AND TARGETED IMAGING STRATEGIES USING NANOPARTICLES

The aim of my thesis and this introduction is to provide insight into the molecular changes that occur during brain inflammation and propose a mechanism for the specific binding of carbohydrate Lewis^a (Le^a) binding during brain inflammation using diverse nanoparticle scaffolds and a number of imaging techniques. I sought to explore the efficient binding capacities, studied by molecular resonance imaging (MRI), of Le^a conjugated to magnetic particles of iron-oxide (MPIO) following interleukin-1 beta (IL-1β) induced inflammation, a model of acute brain inflammation in rodents that is not associated with blood-brain barrier (BBB) breakdown. Upstream leukocyte recruitment in neuroinflammatory diseases (e.g. multiple sclerosis (MS)) is known to occur across an intact, but activated, brain endothelium. Brain inflammation at the pre-symptomatic stage is difficult to detect with conventional imaging agents and current (e.g. Gadolinium-based) contrast agents rely on late-stage BBB permeability changes and do not report on the initial upstream pathological events. For many inflammatory brain diseases, BBB breakdown is accompanied by severe clinical signs. Visualization, by MRI, of the activated cerebral endothelium before BBB breakdown could provide a powerful tool for the pre-symptomatic diagnosis and early intervention for neuroinflammatory disease. The molecular changes that are expressed on brain microvascular endothelial cells during acute and chronic brain inflammation allow immune cells to adhere and extravasate though the endothelium. The mechanism by which Le^a-MPIO binds to the activated brain endothelium before BBB breakdown, hitherto, remains to be identified. When this agent was compared to other MPIO-targeted agents to recognise cell adhesion molecules in the same model of CNS inflammation (VCAM-1 antibody or sialylLewis^x (sLex)), it appeared to accumulate more abundantly within the vessel lumen than any of the other agents. Identification techniques such as proteomics and genomics of animal and cell-models of brain inflammation enabled an *in vivo* binding model of Le^a to be developed. The Selectins are a family of carbohydrate binding C-Type lectins that, among other carbohydrates, can bind Lewis-carbohydrates. However, it was unknown whether the *in vivo* binding specificity, observed for Le^a-MPIO (and Le^b-MPIO to a lesser extent), in the models of CNS inflammation would be solely mediated by endothelial (E)-Selectin that was highlighted in the proteomic and genomic screens. *In vitro* sLe^x is reported to be a stronger binder to E-Selectin than Le^a, making the *in vivo* MPIO results all the more surprising. A knowledge of the *in vivo* molecular mechanisms responsible for Le^a binding during the early stages of inflammation is expected to provide cell surface markers to inhibit leukocyte recruitment and enable the selective delivery of drugs or other disease modifying agents *via* Le^a-conjugated delievery systems (liposomes for instance). Furthermore, the strong binding interaction of Lewis^a during brain inflammation allows the development of novel imaging agents for multiplexed imaging of additional inflammatory markers.

INTRODUCTION OVERVIEW

The first part of this introduction describes the unique aspects of central nervous system (CNS) inflammation, cell adhesion molecules, the role of carbohydrates in cell adhesion, and, in particular, the Lewis-antigens and lectins during inflammation. An overview of genomic and proteomic studies on multiple sclerosis and experimentally induced demyelinating diseases are then presented as well as the principles of MRI imaging and other aspects of MS such as vessel-biology. The use of photo affinity labelling using photo-crosslinkers in proteomics is also discussed. Finally, an overview of the use of inorganic nanoparticles for alternative imaging modalities, such as X-ray fluorescence imaging is provided and a description of how these can be applied to study inflammation within the brain in more detail.

1.1 | INFLAMMATION, CELL ADHESION AND CARBOHYDRATES

1.1.1 The blood brain barrier

Brain microvascular endothelial cells are the first barrier (blood–brain barrier (BBB)) between the central nervous system (CNS) and the peripheral circulation. It separates the immune system and the CNS by maintaining an environment to enable optimal neuronal function through actively removing unwanted molecules and by transporting, actively and passively, the essential molecules required for CNS function [1, 2]. The BBB is tightly regulated, however, when inflammatory processes are ongoing in the abluminal parenchymal tissue within the CNS, the endothelial cell surface on the lumen changes and cell adhesion molecule expression is upregulated [3]. These are most early-stage events associated with the development of CNS inflammation. Increased permeability of the BBB is downstream of endothelial cell activation and leukocyte recruitment and typically occurs at much later stages of disease. Not only do endothelial cells regulate the permeability of the BBB, pericytes, astrocytes and microglia control the barrier by secreting factors that act upon on the BBB, but these cells are also capable of expressing chemokines and adhesion molecules [4-6]. Nonetheless, endothelial cells are the separating component between circulating blood and the brain. Identifying and visualising these early-stage inflammation markers on endothelial cells as a surrogate marker for inflammatory processes ongoing in the brain is of great clinical importance. Inflammatory stimuli, induced by cytokines for example, can alter the biochemical composition of the brain microvascular endothelial cells and enables increased leukocyte migration across the BBB before there is loss of barrier function. These transmigration events are mediated by cell adhesion molecules expressed on the cell membrane of brain microvascular endothelial cells [7, 8]. How immune cells interact with the BBB is discussed next.

1.1.1.1 The blood-brain barrier and immune cell infiltration during inflammation

The presence of BBB is a barrier that preserves ionic homeostasis and restricts the passage of polar molecules that might affect neuronal function; however, immune cells are capable of passing through barrier and a limited number are known to extravasate for immunosurveillance of the CNS as part of normal physiology [9, 10]. Although immune cells, typically, do not reside in the brain and there are no tissue lymphatics within the healthy CNS, they can, depending on the

inflammatory stimulus, accumulate behind the BBB and cause CNS inflammation in absence of BBB breakdown [11, 12]. Leukocyte migration can, over time, influence BBB permeability [13]. However, the initial recruitment of potentially damaging leukocytes into the brain before BBB breakdown is difficult to detect with conventional imaging techniques and there is an unmet need to selectively visualise these early stages of CNS inflammation with a suitable imaging agent. A few examples of different brain inflammation models will be given and the effects on the BBB and immune cell recruitment in these models and in MS will be discussed to highlight the dynamics between the BBB and the immune system.

Firstly, Experimental Autoimmune (or Allergic) Encephalomyelitis (EAE), which will be described in greater detail in **section 1.2.5.1**, may be induced by injecting CNS homogenates in an adjuvant into peripheral tissue. An immunological reponse against the CNS antigens develops, and immune tolerance to myelin proteins is disrupted and infiltration of leukocytes into the brain and spinal cord causes encephalomyelitis to develop in the absence of BBB breakdown or manipulation of the CNS. This indicates that immune cells can be primed peripherally and can travel to the CNS [14-16] across an intact BBB. Also, antigen specific T cells can selectively traffic into the brain *via* luminal expression of major histocompatibility complex (MHC) by brain endothelial cells whilst the BBB is intact [17].

Secondly, glutamate receptor agonists such as kainic acid and NMDA (*N*-methyl-D-aspartate) can induce excitotoxicity when injected cerebrally. The effects of these agonists induce different types of brain inflammation, depending on the agonist, time, age and leukocyte recruitment. Most notably, BBB breakage can be induced in the absence of leukocyte recruitment and BBB breakage occurred 4h post NMDA-injection prior to any signs of leucocyte recruitment [18]. Whilst for an IL-1β injection, BBB breakdown is dependent on neutrophils recruited to the inflamed site [19]. In addition, neutrophils, recruited to either the brain or the spinal cord by IL-1β, cause differential chemokine expression patterns in the spinal cord and brain implying CNS compartmentalised immune response towards inflammatory stimuli [20].

Thirdly, the widespread use of gadolinium enhanced Magnetic Resonance Imaging (MRI) allows diagnosing of MS in individuals with CNS-relevant symptoms. However, while gadolinium contrast enhancement detects evidence of BBB breakdown, it is insufficient to detect more subtle changes in the function of the brain endothelium and the presence of inflammation. Inflammation in MS can be associated with transmigration of inflammatory cells through the intact BBB [13] and in diffuse MS lesions axonal loss can be present and polymorphonuclear (PMN) cells can accumulate behind a closed or 'resealed' BBB [21]. These diffuse lesions can occur from either MS-plaques that slowly grow outward, as the focal inflammatory lesion diminishes into a diffuse parenchymal lesion with microglial activation with the BBB no longer open, or they can represent the early

stages of brain inflammation prior to BBB breakdown [22, 23]. In addition, diffuse grey matter cortical lesions may never display BBB breakdown [23]. Diffuse lesions in the brain are characterised by microglial activation and are associated with very little immune cell infiltration or BBB breakdown. However, it is unknown atr what stage the BBB becomes activated by the microglial response [24]. Therefore, it is critical to be able to monitor disease progression and activation status in CNS inflammatory diseases when BBB breakdown is absent in order to establish if inflammation is still ongoing. In this thesis, I have used IL-1β-induced inflammation as a reductionist, but useful, model system to explore the binding of a Le^a-based contrast agent to the brain endothelium. IL-1β is one of the most potent inflammatory stimuli and its biology will be discussed first followed by a discussion on the role of cell adhesion molecules in the brain.

1.1.2 IL-1β: A potent inflammatory cytokine

Interleukin-1 Beta (IL-1β) is part of the cytokine family of proteins that can have both pro- and anti-inflammatory effects in the body. IL-1β is a pro-inflammatory cytokine and pyrogen, and a healthy brain typically only expresses IL-1 constitutively at very low levels [25]. The physiological role of these low levels has not been studied extensively, although some evidence has shown that it may play a role in sleep, core temperature, pain, memory and hypothalamo-pituitary hormones as highlighted in [25-27] and citations therein. Brain inflammatory diseases like MS, stroke, acute brain trauma and other cerebrovascular diseases are typically accompanied by elevated levels of IL-1β [28-30]. Normally IL-1β is only expressed at higher levels during injury or inflammation and is therefore tightly regulated. The roles of IL-1β during inflammation are diverse and an overview of IL-1β transcriptional regulation, protein production and protein regulation will be discussed and how this relates to neuro-inflammation. The closely related IL-1α will be mentioned where necessary, but will not be discussed in detail. In addition, the effects of IL-1β on the periphery and the acute phase response (APR) will be discussed later to complete the systemic contributions of IL-1β to neuro inflammation.

1.1.2.1 IL-1β | Transcriptional regulation

Upon stimulation with pro inflammatory stimuli, like LPS or TNF, the expression of IL-1β occurs typically *via* the transcription factor nuclear factor (NF)-kappaB (NF-κB) pathway [31, 32]. Although at distinct locations on the chromosome, IL-1α transcription occurs though a very similar mechanism that also involve the NF-κB pathway. Multiple cell types have different pathways for transcription initiation and can determine cell type specific expression profiles [25, 29, 32]. Furthermore, additional transcription factors and cytoplasmic signals can increase IL-1β

transcription, see reference [26] for an extensive list. The translated mRNA of IL-1β (and IL-1α) lacks a typical signal sequence for secreted proteins that directs it to the endoplasmic reticulum. Instead, the IL-1β is synthesized in the cytoplasm. Immature mRNA for IL-1β can have suppressors bound to it that can delay, modulate or even prevent its processing into a mature form of mRNA in the absence of inflammatory stimuli. For example LPS stabilizes mRNA of IL-1β and therefore increases its production [33]. IL-1β translation is also amplified by epidermal growth factor, corticotrophin-releasing hormone and ICAM-1. In addition, the half life of mRNA for IL-1β can be prolonged under cell stimulation or stress factors, which is due to the presence of AU-rich sequences (AURE) sequences [26]. mRNAs that contains AURE sequences have a short half-life, however, the half-life is extended upon inflammatory conditions, adding another layer of regulation during stress-conditions [34].

1.1.2.2 IL-1β | Protein production

IL-1β is expressed as pro-IL-1β and in its pro form it is an inactive protein. Caspase-1 or Interleukin-1 converting enzyme (ICE) cleaves pro-IL-1β *via* a proteolytic mechanism into mature active IL-1β and is tightly regulated by a proteolytic cascade involving the inflammasome that will not be discussed here. Some reviews on the processing of IL-1β explain this process in greater detail [35, 36]. Nonetheless, ICE is another major regulator of IL-1β and can contribute to cell death in ischemic and excitotoxic brain injury. ICE is a therapeutic target for brain damage during inflammatory events such as, stroke and neurodegeneration [37]. Mature active IL-1β can be secreted *via* different mechanisms and include release *via* cell lysis, or release by secretory lysosomes and/or release by exosome and/or macrovesicle shedding [25, 35, 36]. However, these release mechanisms are described as 'non-classical' because they differ from the conventional route via the endoplasmic reticulum *and* Golgi secretion as IL-1β does not have a signal sequence and its secretion is not inhibited by agents that block the intracellular transport of other cytokines such as IL-6 or TNF.

1.1.2.2 IL-1β | Protein regulation

Once released, IL-1β can exert its effects *via* multiple routes, and, like the regulation of transcriptional and translational levels, the released IL-1β is highly controlled by the endogenously produced IL-1-receptor antagonist (IL-1RA) and the soluble receptors; soluble type I IL-1 receptor (sIL-1R1), soluble type II IL-1 receptor (sIL-1R2) and soluble IL-1-receptor accessory protein (sIL-1RAcP). The IL-1β receptor for transducing the signal is called the Interleukin-1 receptor (IL-1R), however, the molecules mentioned above can dramatically alter the effects of IL-1β on its

receptor. First, IL-1RA is biology's own antagonist on the receptor and binds to the cell surface IL-1R preventing IL-1β binding to IL-1R and to signal. This is a unique phenomenon and only a few examples of endogenous inhibitors are known. When IL-1RA is administered it affords neuroprotection during IL-1β mediated neuro inflammation [38]. IL-1RA can come from either the periphery or can be produced locally in the brain. IL-1RA is capable of crossing the BBB and can, therefore, be produced in the periphery and modulate CNS IL-1β effects [39]. Upon an inflammatory stimulus, such as LPS administration, IL-1β levels peak at 2h and 1 to 4h later a peak of IL-1RA follows with a 100-fold greater plasma concentration than IL-1β. IL-1RA is mainly produced as an acute phase protein by the liver, which indicates that an initial activation and then dampening of the inflammatory response may be beneficial [40, 41]. When IL-1β is injected into the brain mRNA expression of IL-1RA and the other two ligands, sIL-1R1 and -2, are induced in close proximity to the microvasculature [41]. The soluble sIL-1R1, IL-1R2 and sIL-1RAcP act as competitive inhibitors for IL-1β and are also known as 'decoy receptors', whereas sIL-1RAcP acts as an enhancer by binding to IL-1R2 and increasing the affinity of IL-1R2 for IL-1 β [42, 43]. As highlighted above, IL-1β is regulated at all levels. However, once it activates the CNS a robust inflammatory response occurs, including the expression of molecules that give rise to leukocyte recruitment, which will be discussed next in the sections of this introduction.

1.1.3 Cell adhesion molecules in inflammation

Cell adhesion molecules are rapidly expressed on endothelial cells upon inflammatory stimuli, like IL-1β and these early markers for inflammation are useful for diagnosis using MRI because they can selectively image inflammation whilst the BBB is intact. Within the brain, IL-1β can act on neurons, astrocytes, microglial cells, endothelial cells and invading immune cells. IL-1β classically acts on these cells *via* the NF-κB pathway making these cells produce secondary proinflammatory molecules. However, there are studies that have shown that cell-type-specific signalling pathways may occur, but these are beyond the scope of this thesis and will not be discussed. They are reviewed in [25, 29]. The general effects of IL-1β on endothelial cells will be discussed here and the cell adhesion molecules that are upregulated upon IL-1β exposure. These cells and their cell surface molecules are the principal target for Le^a binding. Endothelial adhesion molecules expressed are listed in the **Table 1.1**. These cell adhesion molecules provide the initial interactions between trafficking leukocytes from the blood stream into the abluminal space behind the endothelial cell layer. Leukocyte extravasation follows after a multistep process where cells tether to the activated endothelium and subsequently roll before sufficient activation allows firm arrest onto the endothelium and extravasation through the endothelial layer [44, 45]. **See Figure 1.1**.

These stages will briefly be described here and the cell adhesion molecules involved will be highlighted. The first leukocytes are attracted to the inflamed endothelium by cytokines expressed by activated endothelial cells. Endothelial cells can become activated by molecules such as IL-1β, Tumor Necrosis Factor alpha (TNF-α) and complement component C5a.

| Table 1.1 | Cell adhesion molecules and their ligands

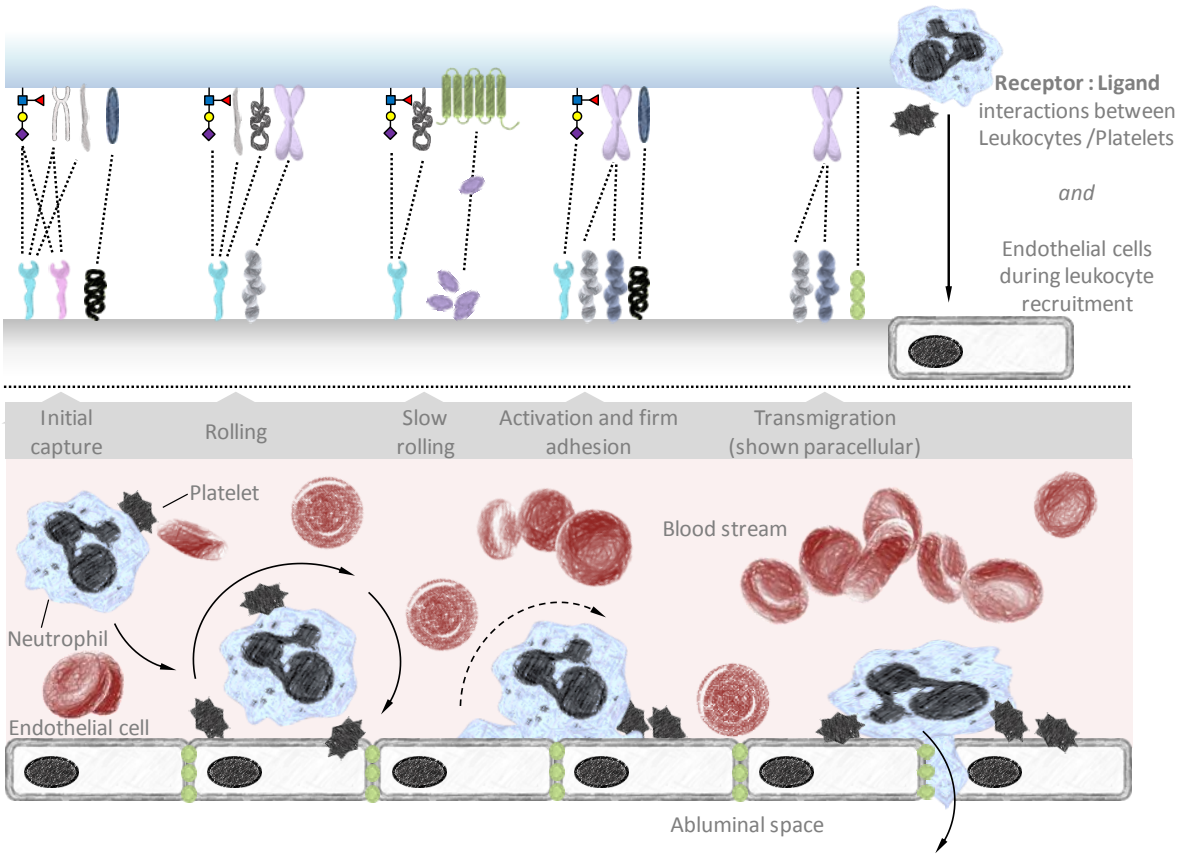
	Abbreviation	Expressed on	Induced by	IL-1β	Ligand or Counter Receptor	Target Cell	Reference
Immunoglobulin gene superfamily							
VCAM-1, CD106	Vascular Cell Adhesion Protein 1	Endothelial Cells	Constitutive (low), upregulated by cytokines	Yes	VLA-4	Monocytes, lymphocytes	[7], [48], [49]
ICAM-1, CD54	Intercellular Adhesion Molecule 1	Endothelial Cells, Leukocytes, Fibroblasts, Epithelial cells	Constitutive (low), upregulated by cytokines	Yes	CD18/11a or LFA-1, CD18/11b or Mac-1	All leukocytes	[7], [49]
ICAM-2, CD102	Intercellular Adhesion Molecule 2	Endothelial Cells, Platelets	Constitutive	?	CD18/11a or LFA-1	All leukocytes	[7]
PECAM-1, CD31	Platelet endothelial cell adhesion molecule	Endothelial Cells, Platelets, Leukocytes	Constitutive	No	PECAM-1, CD31	Endothelial Cells, Platelets, Leukocytes	[7]
β1 (CD29) Integrins							
VLA-4, CD49d/CD29	Very Late Antigen-4	Lymphocytes, Monocytes	Constitutive surface expression and functional after activation	?	VCAM-1	Monocytes, Macrophages, Endothelial Cells, Epithelial Cells	[7]
β2 (CD18) Integrins							
CD18/11a, LFA-1	Lymphocyte function-associated antigen 1	All Leukocytes	Constitutive, function on leukocyte activation	?	ICAM-1, ICAM--2	Endothelial Cells	[7]
CD18/11b, Mac-1	Macrophage-1 antigen	Neutrophils, Monocytes, NK Cells	Constitutive, surface expression increased after activation	?	ICAM-1	Endothelial Cells	[7]
CD18/11c		Neutrophils, Monocytes, NK Cells	Constitutive, surface expression increased after activation	?	Complement		[7]
Selectins							
E-Selectin, CD62E	Endothelial	Endothelial Cells	Cytokines	Yes	sLe^x, Lewis carbohydrates, ESL-1, PSGL-1, CD44	Neutrophils, Monocytes, Lymphocytes	[7], [50], [51], [52], [53], [54], [55], [56], [49]
P-Selectin, CD62P	Platelet	In Weibel-Palade bodies of Platelets and Endothelial Cells	thrombin, histamine and cytokines	Yes	sLe^x, Lewis carbohydrates, PSGL-1	Neutrophils, Monocytes	[7], [52], [54], [57] [58], [56],
L-Selectin, CD62L	Leukocyte	All Leukocytes	Constitutive	No	sLe^x,	Activated Endothelial Cells, Platelets, Eosinophils	[7], [52], [54],

Modified table adapted from [7] and [59], [56]. Additional abbreviations: Sialylated Lewis^x (sLe^x)E-Selectin Ligand-1 (ESL-1), P-Selectin Glycoprotein Ligand-1 (PSGL-1).

Receptor:Ligand Legend

E-Selectin	P-Selectin	VCAM-1	ICAM-1	ICAM-2	Chemokines	GPCR
Lewis antigens (sLe^x)	PSGL-1	ESL-1	CD44	α4 integrins (VLA-4)	B2 integrins	PECAM-1

Multistep process of leukocyte recruitment



| Figure 1.1 | The multistep process of leukocyte recruitment and the receptor:ligand interactions that are involved. The initial capture from the bloodstream is mediated by E- and P-Selectin *via* their ligands (Lewis antigens, PSGL-1 and ESL-1) and VCAM-1. The interactions between the receptor during shear flow conditions in the blood stream results in constant 'making and breaking' contact between the receptors and their ligands. When ICAM-1 and E-Selectin are encountered the rolling slows down and the leukocytes are activated *via* the chemokine receptors (GPCRs). Firm adhesion on the endothelium and the activation of leukocytes results in the activation of integrins that with their counter receptors results in arrest onto the endothelium. Further surface remodelling of both the leukocyte and the endothelium must occur for the transmigration and typically occurs *via* a paracellular manner, breaking the junctional proteins between the endothelial cells, or *via* transcytosis where the leukocyte migrates through the endothelium into the abluminal space. For more details see text, **Table 1.1** and [60].

TNF-α and C5a can elicit the same effects as IL-1β albeit at much higher concentrations. Cell adhesion molecules for immune cell recruitment are rapidly expressed at the endothelial site upon inflammatory stimuli [46, 47]. The initial tethering, rolling stages and adhesion and are mediated by the selectins via PSGL-1 and sLe^x and then by VCAM-1 via VLA-4. Further activation of

the rolling cells is mediated by a conformational change in VLA-4 that strengthens and activates the leukocytes via VCAM-1 interactions [48, 61].Several locally secreted chemokines are envisaged to be presented on the surface of endothelial cells and can then further activate the tethered leukocytes and increase their binding through by the β2 (CD18) integrins on leukocytes and the ICAMs on endothelial cells [44, 45]. Subsequent remodelling of the cell surface of endothelial cells and the extracellular matrix occurs and extravasation of leukocytes *via* PECAM-1 follows [59, 61]. Brain endothelial cells that line the vasculature typically do not express sensible levels of cell adhesion molecules in basal conditions that is believed to protect the neuronal environment in the absence of pathology [62, 63]. However, these cells can rapdly induce cell adhesion expression upon inflammatory stimuli and this is not the cause of the refractory nature of the BBB. Therefore, imaging these cell adhesion molecules can be very informative for disease status confirmation. This has previously been achieved by using MPIOs, as an effective T2*-weighted MRI imaging agent, where

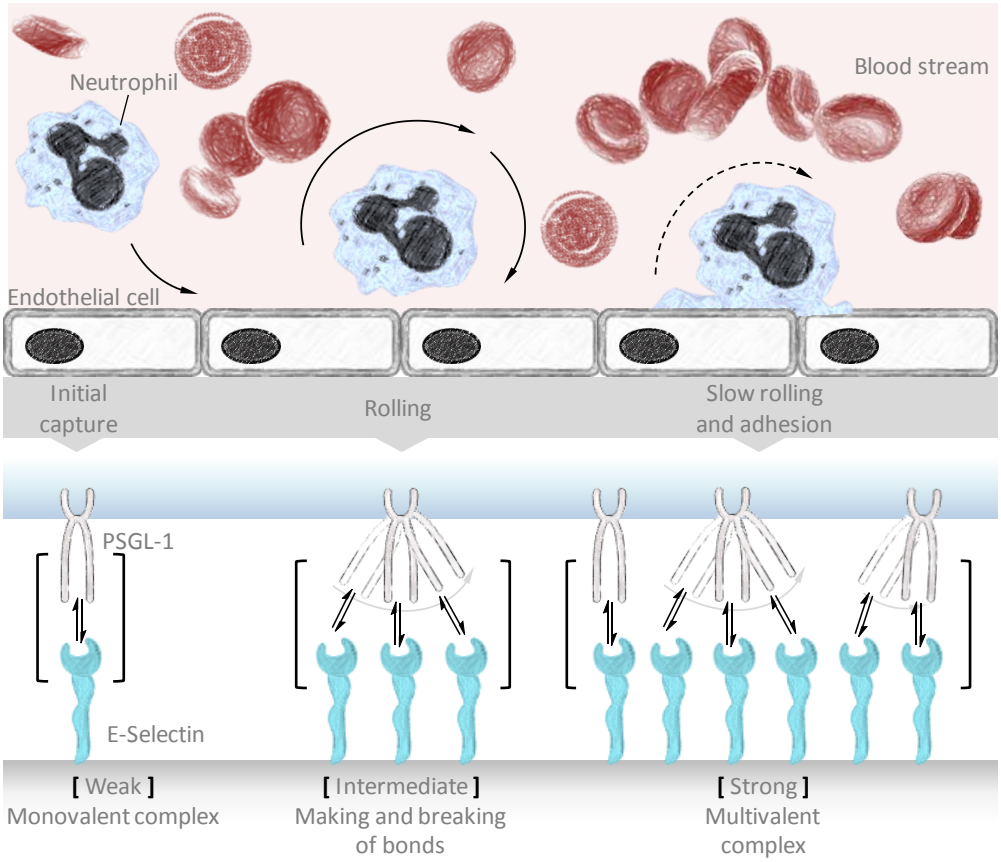
antibodies have been conjugated to the surface of the MPIO that recognise a number of distinct cell adhesion molecules (ICAM-1, VCAM-1, and the selectins). As mentioned above, VCAM-1 is one of the important mediators of leukocyte recruitment and using an anti-VCAM-1 antibody bound to MPIO acute brain inflammation can efficiently be visualized using MRI [64]. The use of sLe^x carbohydrate-functionalized MPIO has also allowed the direct detection of endothelial markers E-/P-selectin in acute brain inflammation using MRI [65].

The selectins are not expressed in the normal brain vasculature and expression levels of E- and P-Selectin are undetectable in non-activated human brain micro vessels [66]. P-Selectin is however constitutively expressed in the choroid plexus and meninges and allows activated memory CD4+ T cells to enter and patrol the subarachnoid space [67]. Therefore, the presence of these molecules on the brain endothelial cells is indicative of inflammatory disease behind the blood brain barrier. In addition, brain endothelial cells, typically, do not have Weibel-Palade bodies that store P-selectin [68]. E-selectin is known to be upregulated in autoimmune diseases like MS, however, when compared to other cell adhesion markers the expression levels are low [5, 49]. In this case, the upregulation of the selectins provides the opportunity to develop selective imaging marker for brain microvascular endothelial cells during inflammation. However the mechanism of action by which selectin interact with immune cell populations *in vivo* in relation to Lewis binding remains to be determined and provides the basis for this thesis. Further subchapters will provide more information on E- and P-Selectin and their ligands, with focus on the Lewis antigens.

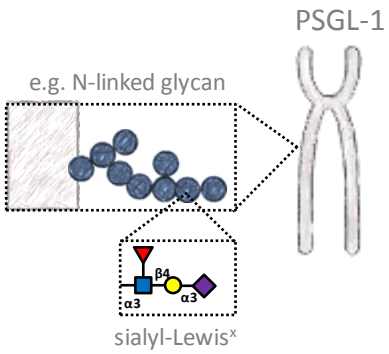
1.1.4 Carbohydrate ligands for lectins and multivalent interactions

Carbohydrates, just like DNA and proteins, are essential for life and through glycoproteins, proteoglycans and glycolipids, these essential functions can be exerted. As briefly mentioned earlier, carbohydrates play an important role in cell adhesion. The immune system as a whole is highly reliant on carbohydrates and glycoproteins; from cellular immunity, antibody stability and function, to cell-cell contact and pathogen detection [69, 70]. Most carbohydrate bearing structures are notoriously difficult to study, as there is no 'code' like DNA to predict how a biological substrate, like a protein or a lipid, is glycosylated due to this dependence on glycosyltransferase enzymes [71]. Approximately 10% of all expressed genes of the human proteome are involved in carbohydrate side chain synthesis and can use numerous protein substrates for glycosylation [70]. Most proteins are heterogeneously glycosylated and a single protein can carry many distinct glycoforms which can alter its structure and function [72]. Recognition of carbohydrate structures and glycoproteins is performed by a protein receptor group called lectins. These receptors are highly specific for carbohydrates and can distinguish different types of glycosidic linkages, mono and/or oligosaccharides and glycoproteins [73, 74]. Some lectins rely on the cluster glycoside effect, a multivalent display of carbohydrates, to effectively engage with its carbohydrate ligands otherwise the bond between a single receptor and its substrate is weak [51, 76, 77]. Most saccharide ligands bind to their protein receptors weakly, but the effective in vivo control of events mediated by protein−carbohydrate binding requires significantly greater affinity. Nature has circumvented the tight binding limitation through multivalency. Multimeric carbohydrates have been prepared and studied as ligands for a wide range of carbohydrate binding proteins, and many exhibit some enhancement in activity compared to the corresponding monovalent ligand on a valence-corrected, basis. It is this phenomenon that is often referred to as the "cluster glycoside effect". Some lectins, especially the selectins on activated endothelial cells, need these multivalent interactions to slow down immune cells in the blood which allows engagement of further receptors that can activate immune cells and allow extravasation. Interestingly, in pilot experiments leading up to this project, it was found that iron oxide particles of approximately 60nm do not bind to activated endothelial cells and the cause of this seemed to be the reduced number of ligands present on the particles. See **Figure 1.2** for a schematic of how multivalent interactions between E-Selectin and PSGL-1 can occur. In order to study and design strong carbohydrate-lectin interactions, a multivalent display of carbohydrates is needed. Nanoparticles and polymeric structures allow the carbohydrates to be presented in a multivalent manner. For example, a 500-fold enhancement of

A



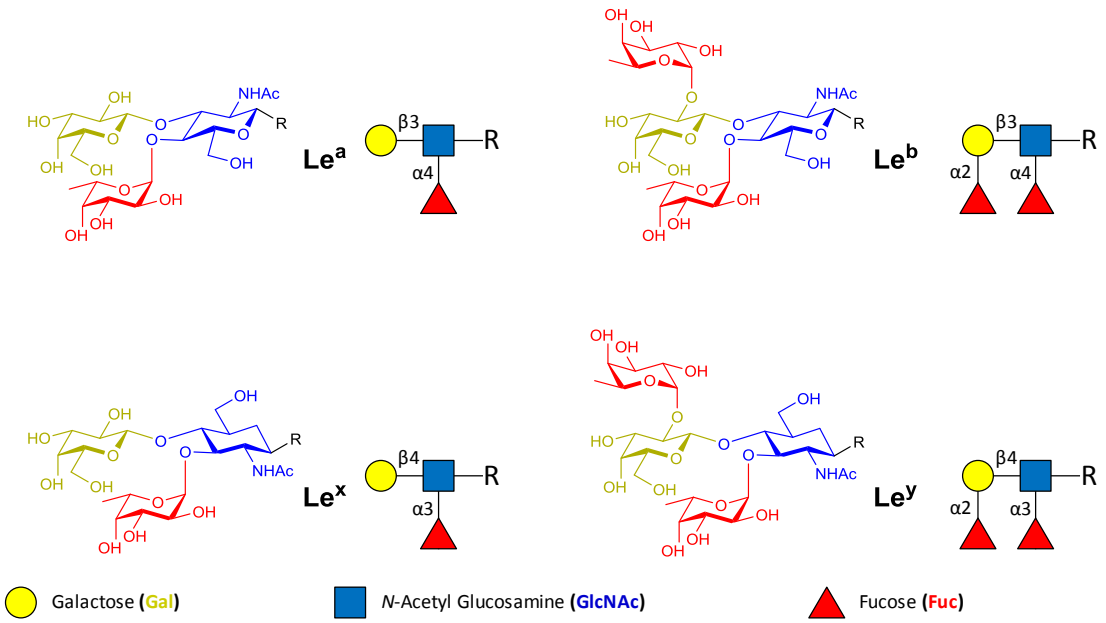
B



| Figure 1.2 | The cluster glycoside effect allows multivalent interactions between PSGL-1 on neutrophils and E-Selectin on endothelial cells **|A|** Immune cells are recruited to the activated endothelium *via* a number of receptors, shown in **Figure 1.1**. This example uses the lectin E-Selectin as an example to explain the cluster glycoside effect observed for multivalent interactions between receptors and their carbohydrate ligands. The initial capture from the bloodstream is mediated by endothelial E-Selectin shown here *via* ligand PSGL-1 on neutrophils, which is heavily glycosylated (see |B|). The initial interactions between a monovalent E-Selectin and a Lewis antigen during shear flow conditions in the blood stream are weak and will not result in the arrest of the cell. Constant making and breaking contact between the receptors and their ligands will eventually slow down the cell and only when multiple carbohydrates presented on PSGL-1 can interact with a display of E-Selectin, the cell is able to slow down enough and strongly adhere. Other receptors can now engage and activate (not shown). **|B|** PSGL-1 is glycosylated and terminal structures contain the Lewis antigen sialyl-Lewis^x [58]

binding of sLe^x presented on liposomes was observed when bound to E-Selectin presented on cells, in comparison to a monovalent sLe^x [75]. Other scaffolds decorated with carbohydrates such as poly-lysine, serum albumin, streptavidin *via* biotinylated carbohydrates, polyacrylamide plates, synthetic dendritic polyglycerol sulphates, dendrimers and serum albumin, all enhance binding to lectins [76-79]. Many of these are have been reviewed elsewhere [80-82] and these texts also discuss the use of an extensive array of nanoparticles. This thesis focusses primarily on the use of

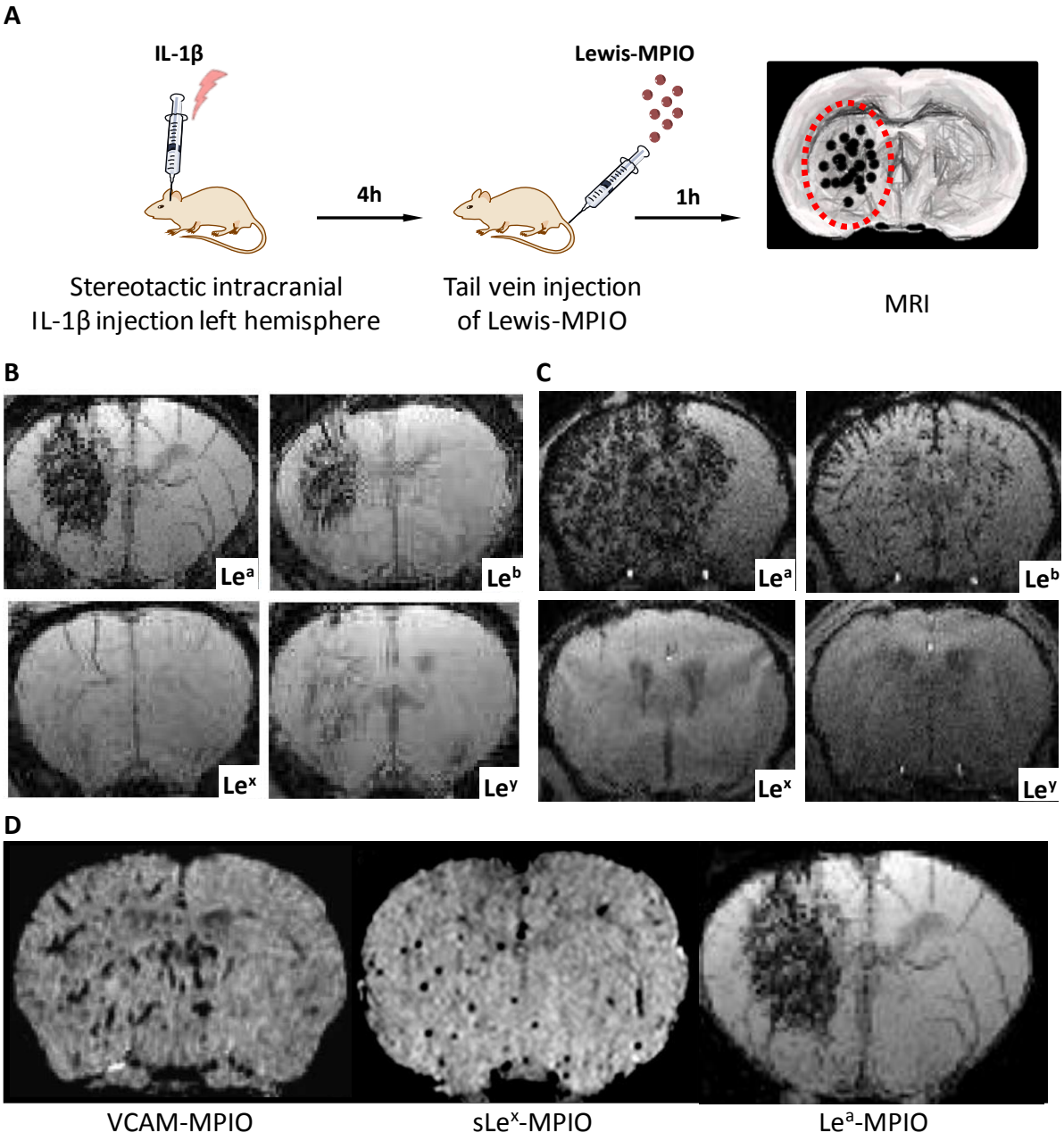
MPIO nanoparticles, but other nanoparticles were also used to display Lewis^a in a multivalent manner. As mentioned earlier, these MPIOs allow carbohydrates to be presented in a multivalent manner. In addition, they possess magnetic properties that allow them to be used as high-contrast MRI agents and in biological pull down experiments. Endothelial adhesion molecules are the targets for brain inflammation. Hence the focus here is primarily on carbohydrates because they are relatively simple to synthesize and characterize than humanized, homogenously glycosylated antibodies against therapeutic targets or other glycosylated ligands, due to the heterogeneity mentioned earlier [83]. Towards the end of this introduction, the properties of these nanoparticles are discussed in more detail, especially in the context of imaging. The next section will discuss the biological synthesis of Lewis antigens and the lectins that interact with them.



| Figure 1.3 | Overview of Type 1 (Lewis^a and Lewis^b) and Type 2 (Lewis^x and Lewis^y) structures used on MPIO in the pilot experiment presented in Figure 1.4. Structural and schematic overview of the Lewis antigens used in the pilot experiment presented in **Figure 1.4**. Lewis antigens were coupled to amine-coated magnetic particles of iron oxide (NH_2-MPIO). This schematic representation of the Lewis antigens highlights the linkages. R= amidine linkage to NH_2-MPIO

1.1.4.1 Lewis antigens in brain inflammation

Sialyl Lewis^x (sLe^x) is a carbohydrate recognized by all Selectins (E- P- and L; endothelial, platelet and leukocyte) [52], however the role of the other Lewis carbohydrates; Type 1 Lewis antigens Lewis^a (Le^a) and Le^b and their Type 2 analogues Le^x and Le^y, during inflammation remain mostly unknown. Given their structural relationship to sLe^x, we sought to discover whether these carbohydrates might also bind to the activated endothelium possibly *via* a Selectin mediated



| Figure 1.4 | Pilot experiment to assess the binding of Lewis antigens Lewis^a, Lewis^b, Lewis^x and Lewis^y during a model of acute brain inflammation in rodents **|A|** Experimental overview. Rats or mice received a well-characterised stereotactic intracranial injection of IL-1β into the left hemisphere (striatum). After 4 hours, the rodents received a tail-vein injection of one of the Lewis-MPIO conjugates. 1-hour after the tail-vein injection of the MPIO, T_2^*-weighted coronal *in vivo* MRI images of the brains were acquired from Bregma AP+2mm to Bregma AP-1mm. The left inflamed (indicated with red dashed circle) hemisphere accumulates, in the case of Lewis^a and to a certain extent Lewis^b, the MPIOs as shown as dark hypo intensities on the left side of the MRI brain images. **|B|** Minimum intensity projections (from Bregma AP+2mm to Bregma AP-1mm) from *in vivo* T_2^*-weighted coronal MRI of MPIO-Le^a, MPIO-Le^b, MPIO-Le^x and MPIO-Le^y after intracerebral injection of IL-1β in the rat left brain hemisphere, right hemisphere control. Representative images of experimental groups (*n=3* (Le^x and Le^y), *n=4* (Le^b) and *n=5* (Le^a). **|C|** Minimum intensity projections (from Bregma AP+2 to Bregma AP-1) from *in vivo* T_2^*-weighted coronal MRI of MPIO-Le^a, MPIO-Le^b, MPIO-Le^x and MPIO-Le^y after intracerebral injection of IL-1β in the mouse left brain hemisphere, right hemisphere control. Representative images of experimental groups (*n=2* (Le^x and Le^y), *n=3* (Le^b) and *n=5* (Le^a). The width of the rat brain is 1.2cm**. *Experiments performed by Daniel Anthony and Guillaume Bort.*** **|D|** Comparison of *in vivo* T_2^*-weighted coronal MRI images of MPIO with an anti-VCAM antibody (left), MPIO with sLe^x (middle) and MPIO with Le^a (right) in a model of acute brain inflammation in rodents (100 ng IL-1β, left hemisphere), [64,65]

manner [65], see **Figure 1.3** for an overview of the structures. A pilot experiment performed by laboratories of Daniel Anthony and Ben Davis showed that the Type 1 Lewis antigens, most prominently Lewis^a, show strong binding *in vivo* during acute brain inflammation and this observation formed the foundation of the work in this thesis, as shown in **Figure 1.4**. A section on the historical discovery, biological synthesis and their role in biology of the Lewis antigens will be discussed next.

1.1.4.2 The historic discovery of Lewis antigens

The haematologist Mourant described the Lewis antigens for the first time when he observed that the blood of two women was able to agglutinate the blood of their new-born babies who were suffering from heamolytic disease. He described this 'agglutinogen' of frequent occurrence to be independent from the previously established blood groups *ABO*, *M N*, *Rh*, *P*, *Lutheran* and *Kell*, which also can cause haemolytic diseases when exposed to sera that is against these antigens [84]. Mourant named the Lewis antigen after the surname of the woman in whom it was discovered in [85]. Subsequently, it was shown by Sneath and Sneath that the red blood cell antigen Lewis can be transformed onto Lewis-negative recipient cells by the plasma of Lewis positive individuals, a unique feature of the Lewis blood group that was not observed for the earlier mentioned blood groups [86]. Later by Marcus and Cass, this transformative property of the Lewis antigens was assigned to plasma glycosphingolipids bearing the Lewis^a and Lewis^b carbohydrate antigens, as it was previously thought to be by glycoproteins [87]. More specifically, the Lewis glycosphingolipids are transported in the blood by lipoprotein particles and vesicles and passively absorbed onto the membranes of red blood cells [73]. Lewis^a and Lewis^b antigens are present on cells other than red blood cells and can either come from passively absorbed glycosphingolipids from plasma or are on glycoproteins [88]. The next section will focus on fucosyltransferases responsible for the synthesis of these Lewis structures and their bio-distribution.

1.1.4.3 Bio-distribution and synthesis of Lewis antigens

The human Lewis histo-blood group system is composed of Type 1 (Galβ1-3GlcNAc) Le^a and Le^b glycosphingolipids. Glycoproteins on red blood cells do not carry any Lewis^a or Lewis^b, and their positivity is solely dependent on glycolipids as mentioned before [84]. The membrane of red blood cells typically carry 12×10^6 glycolipid molecules of which 10^6 are polyglycosylated glycolipids [89]. The glycolipids are synthesized by exocrine epithelial cells (gut, liver, kidney, pancreas) and can be secreted into bodily fluids depending on secretor status [90]. However, the red blood cells

of Lewis negative recipients of a donor liver from a Lewis positive individual will not acquire enough Lewis antigens to be detected by antibodies [91]. The exact function(s) of Le^a and Le^b glycosphingolipids are not known and the Lewis lipids structures are passively absorbed from lipoprotein particles and chylomicrons in blood plasma onto the membranes of erythrocytes, leukocytes and platelets [86],[87]. Human type 1 Lewis antigens, Le^a and Le^b, are produced by the combined action of two fucosyl transferases, FUT3 (Lewis, Le, α1-3/-4FucT) for Le^a and FUT2 (Secretor, Se, α1-2FucT) for Le^b by sequential addition of a fucose monosaccharide onto Type 1 precursor chains, which can be either glycolipids or glycoproteins [90], see **Figure 1.5**. Only one functional copy of the Lewis and/or Secretor gene (Le/Se) is necessary and individuals carrying both a dominant or homozygous Lewis (Le) and Secretor (Se) phenotype will have a $Lewis^b$-positive blood phenotype, with very few $Lewis^a$-glycolipids levels detected in the plasma. Other carbohydrate bearing structures, for example mucins or epithelial cells of the gut, contain both $Lewis^a$ and $Lewis^b$ in these individuals [92]. Individuals having only Lewis (Le), but homozygous for secretor (se), will only produce $Lewis^a$ [84]. Rodents lack the Lewis FUT3 enzyme and therefore cannot synthesize $Lewis^a$ [93-95]. This makes the binding properties described in this thesis all the more surprising. See **Table 1.2**.

| Table 1.2 | Overview of fucosyl transferases and the Lewis antigens

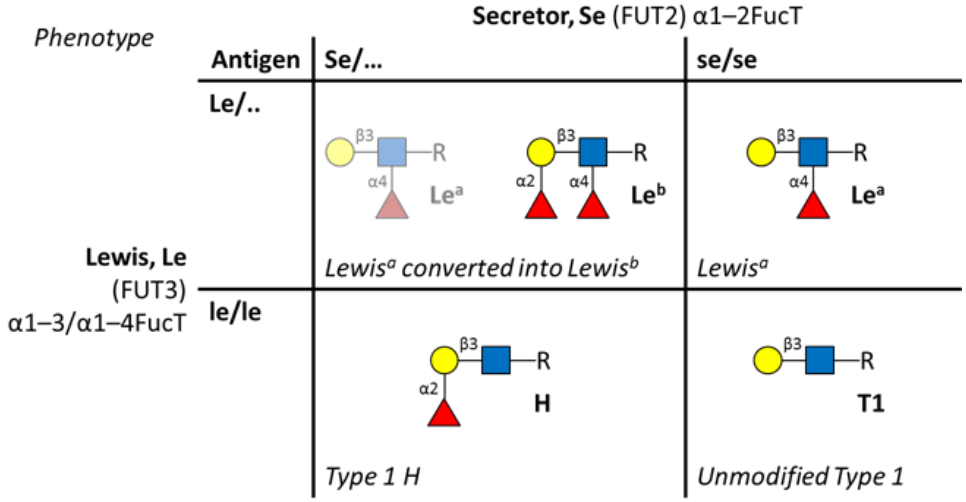
Enzyme	Alias	Linkage	Lewis Antigens	Mouse/Rat homologue
FUT1	H	α1-2	Type 1 and 2 H	rat/mouse
FUT2	Se	α 1-2	Type 1 and 2 H	rat/mouse
FUT3	Le	α 1-3/-4	Le^a, Le^b, sLe^a	(-)
FUT4	Myeloid-type	α 1-3	Le^x, Le^y, sLe^x	rat/mouse
FUT5		α 1-3	Le^x, Le^y, sLe^x	(-)
FUT6	Plasma-type	α 1-3	Le^x, Le^y, sLe^x	(-)
FUT7		α 1-3	Le^x, Le^y, sLe^x	rat/mouse
FUT8		α 1-6	sLe^x	rat/mouse
FUT9		α 1-3	Le^x, Le^y	rat/mouse
FUT10		α 1-3	other	rat/mouse
FUT11		α 1-3	other	rat/mouse

The table shows which FUT can generate which type linkage and which Lewis antigen is generated. Not all FUT enzymes are conserved and the homologue section of the table shows if a rodent FUT is present. *Note:* FUT3 is not expressed in rodents and therefore $Lewis^a$ is not normally expressed in these animals. References used for the table: [90], [93], [96], [97].

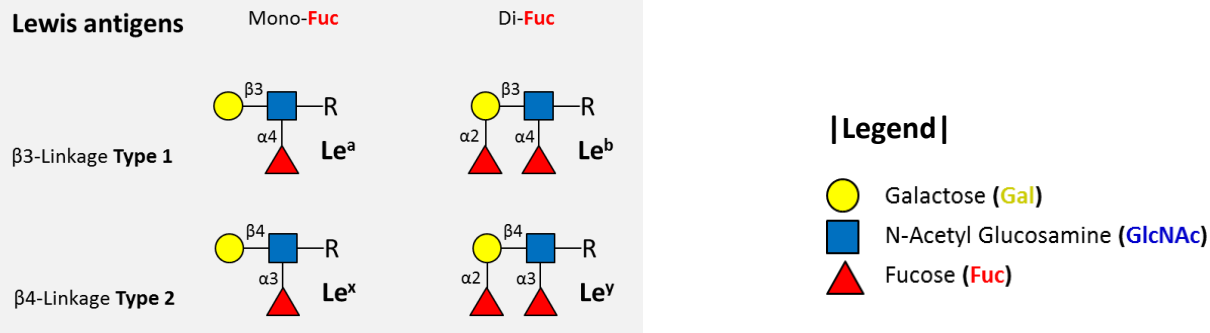
No clear functionality has yet been assigned to $Lewis^a$ glycoproteins, but immune cells bearing Le^a can be recruited to the inflamed intestinal mucosa and blocking of Le^a enhances the transmigration of the polymorphonuclear leukocytes whilst blocking of Le^x blocks their transmigration [98, 99]. Neither the glycoprotein involved nor the receptors that mediate the Le^a

transmigration events were identified. The type 2 (Galβ1-4GlcNAc) Le^x and Le^y are isomers of Le^a and Le^b, synthesized by fucosyl transferases FUT4, FUT5, FUT6, and/or FUT7 and vary in glycoside linkage from the type 1 Lewis histo-blood group antigens. Furthermore, Le^x and Le^y antigens are not part of the histo-blood group antigens because they cannot be detected on erythrocytes. Both can occur as glycoplipids or glycoproteins like the type 1 isomers. Furthermore, Le^x and Le^y are also cancer-associated antigens, as is sLe^a for most gastrointestinal cancers [100-102].

A



B



| Figure 1.5 | Overview of the the fucosyltransferases, linkages and types of carbohydrate present in the Lewis antigens **|A|** Overview of the biological synthesis of Type 1 Lewis antigens using a Mendelian inheritance table or Punnet square. Capitalised gene names (Se or Le) represent dominant genotypes and lowercase gene names (se or le) represent the recessive genes. Lewis negative individuals (le/le) have no Lewis structures and produce unmodified type 1 (T1) structures, if these individuals have the Se gene, they fucosylate T1 to Type 1 H structures. Individuals bearing the Lewis gene, will either make $Lewis^a$ or $Lewis^b$ depending on the presence of the Secretor gene. If present, all $Lewis^a$ is converted into $Lewis^b$. If the se/se genotype is present, $Lewis^a$ is synthesized. **|B|** Overview of the glycosidic linkages in Type 1 and Type 2 Lewis antigens R=remainder of the molecule.

1.1.4.4 E- and P-Selectin in the CNS

As discussed above, E- and P-Selectin are cell adhesion molecules that play an important role in the recruitment of immune cells to the site of inflammation and they do so by binding Lewis antigens. These cell adhesion molecules in the brain vasculature are only expressed when inflammation is present and basal expression levels are undetectable to prevent the brain from 'accidental' infiltration [9]. Multiple studies have looked at both human and rodent Selectin expression levels during brain inflammation and an overview of observations will be given next.

P-selectin and E-selectin are differentially expressed in mouse brain capillary endothelial cells when various methods of inducing inflammation were used [103]. P-selectin (not E-selectin) expression was induced in IL-1β-treated mouse brain capillary endothelial cells, indicating that the type of vessels affects what type of selectins are upregulated [103]. The expression of E- and P-Selectin in the brain microvasculature upon IL-1β activation is considered to play an important role in neutrophil recruitment to the activated endothelium in most tissues in mammals. When P-selectin was blocked following the injection of IL-1β into the brain using the RMP-1 antibody, 85% of the neutrophils recruited to the injection site could be blocked. Thus P-Selectin is sufficient and essential for PMN recruitment to the brain. However, E-selectin blockade using RME-1 antibody had no effect on neutrophil recruitment in rats [104]. This observation suggests either an alternative role of E-selectin in recruiting neutrophils to the brain, requirement of platelets, or that the affinity of the neutrophil ligand for E-Selectin is greater than that of the antibody used. Using a different cytokine and using E- or P-selectin– deficient mice instead of blocking antibodies, TNF-α-mediated neutrophil recruitment to the brain was dependent on endothelial E-selectin and P-selectin as well as for a minor role of P-selectin from platelets [66]. The role of E- and P-selectin in brain microvascular endothelial cells is not straight forward and *in vitro* systems cannot accurately model *in vivo* conditions. The brain expresses less E- and P-Selectin than almost any other organs and human brain micro vessels typically do not have Weibel-Palade bodies which can store P-selectin [66, 68]. However, as mentioned before, P-Selectin is present in the choroid plexus and may play a role in CNS immune cell surveillance [67]. E-selectin is known to be upregulated in autoimmune diseases like MS, however the expression levels are low [49]. In addition, altered P-Selectin expression levels are found on platelets of MS patients, which could carry $Le^{a/b}$ as well, suggesting a dual or a synergistic role of the selectins in the pathogenesis of MS [105]. Even though the selectins are classically considered to be cell adhesion molecules, P-Selectin positive platelets can bind to T-lymphocytes and modulate their inflammatory response. When T-lymphocytes were co-cultured with platelets they produce fewer cytokines and increase the production of the anti-inflammatory cytokine IL-10 and this symbiosis may be of anti-

inflammatory therapeutic value [106]. Besides having undetectable levels of the selectins in the brain during basal conditions, the expression of the selectins during inflammation, albeit low in comparison to other peripheral organs, could be of great importance during inflammatory brain diseases and immune cells recruitment to the inflamed endothelium. Having a contrast agent that can visualize these low levels of expression, yet important Selectins could be of great beneficial value and assessing which selectin mediates this process could provide a more targeted approach to drug design and understanding the underlying mechanism of brain pathologies. Understanding the roles of the type 1 Lewis antigens in immune cell recruitment has not been studied before in detail. Furthermore, E-Selectin provides a promising target for drug delivery and Le^a-decorated nanoparticles that encapsulate a disease modifying drug could potentially be of great therapeutic value [107, 108].

1.1.4.5 Lewis antigens and binding to Selectins is assay dependent

As mentioned before, Sialyl $Lewis^x$ (sLe^x) is the carbohydrate that is recognized by all Selectins (E- P- and L), however the other Lewis antigens all have different levels of affinity for E- and P-Selectin. L-Selectin binds neither $Lewis^a$ nor $Lewis^b$ [109, 110]. The accumulation of $Lewis^a$ and $Lewis^b$ MPIO at the inflamed site, as shown in **Figure 1.4** is more pronounced than sLe^x-MPIO. This is contradictory with the existing literature, as sLe^x is frequently found to be the strongest binder to the selectins. This part of the introduction summarises *in vitro* assays used to assess the binding of Lewis antigens to E- and P-Selectin. Shown in **Table 1.3**, Le^a and Le^b has a moderate binding affinity for E-Selectin when compared to its sialyated Type 1 counterpart sLe^a using E-Selectin expressing cells binding to lipid-linked oligosaccharides chromatographed on silica gel plates as a read-out [51]. Further tests, again using chromatography plate assays and a microwell system showed that Le^a and Le^b have strong affinity for recombinant human E-Selectin from mammalian cells, where Le^x and Le^y only have moderate to trace amounts of affinity for this E-Selectin form as shown in **Table 1.4** [111]. The Lewis antigen binding to P-Selectin has not been extensively studied and a report on binding of both sLe^a and sLe^x to P-Selectin, including the non sialyed Le^a and Le^x, show both binding to this selectin. However, the results are not as clear as for E-Selectin [53], see **Table 1.5.** All these experiments used artificial *in vitro* assays with purified mammalian-derived lectins and neoglyconjugates which do not reflect the binding strength *in vivo* under flow conditions. A step closer to *in vivo* conditions, human colon cell lines were used to test their Lewis antigen binding, Lewis antigen expression and their E- and P-Selectin expression [101]. As shown in **Table 1.6**, $Lewis^a$, when compared to $Lewis^x$ and the sialylated counterparts sLe^a and sLe^x, is the most potent antigen of labelling all the colon cancer cell lines, both *in vitro* and from *in*

| Table 1.3 | Binding of mammalian transfected cells expressing human E-Selectin to Lewis antigens as neoglycolipids run on thin-layer chromatographic plates.

Oligosaccharide	Alternative Designation	E-Selectin Binding Chromatogram	Reference
Le^a	LNFP-II	+	[51]
sLe^a	3'-S-LNFP-II	++	[51]
Le^b	LNDFH-I	+	[51]
Le^x	LNFP-III	+	[51]
sLe^x	3'-S-LNFP-III	++	[51]
Le^y		nd	[51]

(-) none (+) moderate binding (++) strong binding (nd) not determined. Values compared to Le^a (LNFP-II) and Le^x (LNFP-III).

| Table 1.4 | Binding of recombinant human E-Selectin to Lewis antigens as neoglycolipids run on thin-layer chromatographic plates.

Oligosaccharide	Alternative Designation	E-Selectin Binding Microwell	E-Selectin Binding Chromatogram	Reference
Le^a	LNFP-II	+++	+++	[111]
Le^a	Le^a(-sp)	+++	nd	[111]
Le^b	LNDFH-I	+++	+++	[111]
Le^x	LNFP-III	++	±	[111]
Le^x	Le^x(-sp)	-	nd	[111]
Le^y	LNnDFH-I	++	±	[111]

(-) none (±) trace (+) weak (++) moderate (+++) strong (nd) not determined. Values compared to Le^a (LNFP-II). (-sp) is a spacer-biotin.

| Table 1.5 | Binding of recombinant E- and P-Selectin to Lewis antigens immobilized onto bovine serum albumin

Oligosaccharide	E-Selectin IC_{50}	E-Selectin Binding Order	P-Selectin Binding Order	Reference
Le^a	Nd	Low	± Low	[53]
sLe^a	130±20 µM	Highest	± High	[53]
Le^x	Nd	Lowest	± Medium	[53]
sLe^x	380±70 µM	High	±Medium	[53]

Concentration of oligosaccharide that resulted in 50% inhibition of the binding of solution-phase E-selectin-Ig to immobilized BSA-sLe^a, as measured in an ELISA.

| Table 1.6 | Binding of human colon cancer cell lines to biotinylated Lewis antigens

Oligosaccharide	HCT-15 Labelling (%) *in vivo* | *in vitro*	LoVo Labelling (%) *in vivo* | *in vitro*	DLD-1 Labelling (%) *in vivo* | *in vitro*	CoLo-201 Labelling (%) *in vivo* | *in vitro*	Reference
Le^a	~85 % | ~65 %	~70 % | ~40 %	~60 % | ~65 %	~70 % | ~50 %	[101]
sLe^a	~90 % | ~45 %	~40 % | ~30 %	~50 % | ~40 %	~65 % | ~20 %	[101]
Le^x	~65 % | ~10 %	~40 % | ~5 %	~65 % | ~15 %	~50 % | ~30 %	[101]
sLe^x	~50 % | ~15 %	~5 % | ~5 %	~70 % | ~25 %	~75 % | ~15 %	[101]
Lectin	**HCT-15 Labelling (A.U.)**	**LoVo Labelling (A.U.)**	**DLD-1 Labelling (A.U.)**	**CoLo-201 Labelling (A.U.)**	
E-Selectin	~375	~650	~625	~250	[101]
P-Selectin	~350	~360	~240	~300	[101]

Binding of biotinylated Lewis antigens (%) to 4 different human colon cancer cell lines and their respective E- and P-Selectin levels measured by ELISA (A.U.).

vivo xenografts derived from immunocompromised mice injected with the human colon cancer cells. All cell lines express E- and P-Selectin. A possible explanation for the preferred Le^a binding over sLe^a and sLe^x may be that cell-surface derived E-Selectin (and P-Selectin) retained its physiological glycosylation or has a different *in vivo* binding mechanism, which could have an influence on the binding of the Lewis antigens. Most *in vitro* systems use recombinant mammalian derived proteins from monkeys, hamsters and other organisms, which differ in glycosidases, and, therefore, may give rise to different post-translational modification of the glycosylation sites on the selectins that are necessary for physiological binding. This section highlights that the observed Lewis^a-MPIO accumulation is not obvious from *in vitro* literature data and implies that other factors may contribute to the accumulation of Lewis^a-MPIO accumulation during brain inflammation. The next section describes the other known lectins that can bind Lewis^a structures and how they relate to inflammatory diseases.

1.1.4.6 Other Lewis^a-binding lectins

Lectins occur everywhere in the mammalian body. However, for the models used in this thesis, it is highly likely that only blood-derived or vascular endothelial cell lectins could be responsible for the Lewis^a-MPIO binding shown in **Figure 1.4**. As the accumulation of Lewis^a-MPIO in the inflamed brain is larger than previously tested VCAM-1-MPIO and sLe^x-MPIO in the same model, it implies that, potentially, other receptors/lectins may play a role in the retention of the Lewis^a-MPIO. Therefore, this section will briefly describe 2 other known lectins, besides the Selectins, that can bind Lewis^a and that are part of blood components or immune cells.

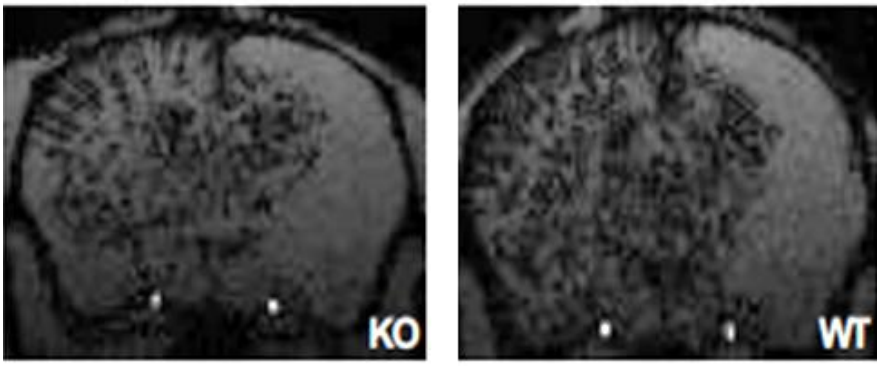
1.1.4.6.1 Mannan Binding Lectin (MBL)

MBL is a blood circulating complement lectin that is expressed in hepatocytes during the Acute Phase Response (APR) reacting to inflammation [112, 113]. It is an oligomeric carbohydrate pattern recognition protein that can activate the lectin pathway of the complement system *via* binding to carbohydrates presented on bacteria or cells [114, 115]. MBL Associated Serine Proteases (MASP) can then activate blood derived C4, by cleaving it into C4a and C4b. C4b can, subsequently, be deposited on the cell surface of the bacterium with an activated form of C2 - C2a. The newly formed C4b:C2a is a convertase that can catalyse the proteolytic cleavage of Complement 3 into C3a and C3b. The process is MASP2 dependent, however there is evidence that MASP1 is able to cleave C3 directly activating the complement pathway [32, 116, 117]. C3 is usually deposited onto pathogens, but it can also interact with the inflamed endothelium and recruit leukocytes [118].There is also evidence that C3 and C4 can be deposited on vascular

collagen and elastin in the vascular wall contributing to vascular stiffness and atherosclerosis, however it is unknown if a similar mechanism might operate in brain microvascular cells [119]. C3 clusters have been found on microglial clusters in chronic but not acute MS [120]. These clusters were also found in stroke lesions and experimental Traumatic Brain Injury (TBI) [121]. In addition MBL has been shown to promote local microvascular thrombosis after TBI in mice [122] and higher levels of MBL and MASP2 are found in the CSF of MS patients [123]. MBL also functions in a cluster glycoside manner. The carbohydrates to which it binds, typically clusters presented on bacterial cells, are displayed in a multivalent fashion. Also, the tetrameric form of MBL is more biologically active than the trimeric and dimeric forms [116]. Given its widespread function in immunology, mostly in recognizing carbohydrate patterns on pathogens, it can also bind a large group of other carbohydrates, including Lewis^{a} and Lewis^{b} [113]. However, it is unknown how the clusters of Lewis^{a} and Lewis^{b} on MPIO could be retained on the vasculature by MBL during inflammation as the resulting activation of the lectin pathway via MBL and deposition of complement is unable to occur onto a synthetic particle [124, 125].

1.1.4.6.2 DC-SIGN (CD209)

Dendritic Cell-Specific Intercellular adhesion molecule-3-Grabbing Non-integrin or DC-SIGN can be found on macrophages and dendritic cells. Just as MBL, it is involved in recognizing carbohydrate patterns on pathogens. Upon binding a pathogen, DC-SIGN can activate phagocytosis, followed by antigen presentation and priming T cells [126]. It also has a high affinity for ICAM-3, which unlike ICAM-1 and ICAM-2 is not expressed on brain endothelial cells, but on leukocytes. Upregulation of these ICAMs is associated with MS [127]. Human dendritic cells with DC-SIGN can attach to the cerebral endothelium *via* a variety of receptors, including *via* sLe^{x} and E-Selectin [126]. However, blocking either sLe^{x} or E-Selectin with monoclonal antibodies has little effect on adhesion, implying other adhesion molecules are responsible for these binding events [128]. DC-SIGN can bind all Lewis antigens, including sulphated and sialylated Lewis^{a} and Lewis^{x}. The murine equivalent of human DC-SIGN, Specific Intercellular adhesion molecule-3-Grabbing Non-integrin Related gene 3 (SIGN-R3) can also bind Lewis antigens, Le^{a}, Le^{b}, Le^{x}, Le^{y} and sLe^{x}, so the carbohydrate binding sites between humans and rodents are comparatively conserved [129-131]. Although dendritic cells can adhere to the inflamed endothelium and bind Lewis^{a}, no difference in Lewis^{a} binding was observed between the wildtype and SIGN-R3 knock out mice in a preliminary study. See **Figure 1.6**. Therefore, either the Selectins, or an unknown lectin may be responsible for the binding observed in the initial pilot experiment shown in **Figure 1.4**.



| Figure 1.6 | Pilot experiment to assess the binding of Le^a-MPIO in SIGN-R3 knock-out mice during a model of acute brain inflammation Minimum intensity projections from *in vivo* T_2^*-weighted coronal MRI of MPIO-Le^a in DC-SIGN (SIGN-R3) knock-out (KO) and wild-type (WT) mice after intracerebral injection of IL-1β in the left brain hemisphere, right hemisphere control. No difference in binding was observed as both left hemispheres appear to have similar levels of Le^a-MPIO accumulation. *N*=5 for both KO and WT.
Experiments performed by Daniel Anthony and Guillaume Bort.

1.2 | MULTIPLE SCLEROSIS

1.2.1 Introduction to MS

Multiple Sclerosis (MS) is an inflammatory autoimmune disease that affects the central nervous system and results in neurological disability. Its aetiology and exact pathogenesis still remain obscure, and, to date, there is no cure for MS and immunomodulatory treatments are only partially effective [132]. MS symptoms include sensory and visual disturbances, pain fatigue, cognitive and motor impairments and symptoms to some extent correlate with the lesions sites within the brain [133]. Immune cell infiltrated lesions and demyelination within the CNS caused by intrusion of these cells across the BBB are a hallmark of MS [134, 135]. However, the ongoing neuronal and axonal destruction by the immune system can occur without lesion formations within the CNS and to date there are no specific or targeted agents that can visualize this early stage of the disease [24, 136-138]. This section of the introduction will first mainly focus on the immune cell infiltration, the vasculature and the BBB breakdown during MS. To finish, it will summarize current imaging strategies for detecting MS, the use of imaging agents and how to visualize ongoing pathology behind a closed BBB.

1.2.2 Immune cell infiltration and the brain vasculature in MS

As mentioned in section 1.1.1 'Blood Brain Barrier', the vasculature in the brain is highly restricted to immune cell filtration and under basal levels no detectable levels of cell adhesion molecules are found [8, 47, 66, 139]. Even though, this 'protective' barrier, in the form of the BBB, is present in the brain and the spinal cord vasculature, immunological surveillance of the CNS occurs as part of normal homeostasis. Immune cells may acquire access to the CNS from the blood *via* three distinct pathways, from the CSF across the choroid plexus, *via* the subarachnoid space or *via* the parenchymal perivascular space into the brain [9, 67]. MS lesions only occur when immune cells accumulate, attack and destruct the myelin sheaths of neurons. The initial stages of the first attack are unknown, the activated immune cells present in the lesion secrete cytokines into the abluminal parenchymal tissue within the CNS, which, in turn, can act on the endothelial cell surface causing luminal changes and upregulation of cell adhesion molecules [139-141]. Autoreactive lymphocytes react to the body's own myelin in an auto-immune fashion and cause the destructive demyelination [142, 143]. Possible explanations of why there are autoreactive immune cells against myelin are the possible dis-regulations during thymic selection and molecular mimicry where antigenic determinants are shared by non-self (infectious agents for

instance) and self-antigens. However, autoreactive T cells against myelin have been found in individuals without MS implying a more complex combination of factors that cause MS [134, 144]. The resulting immune cells that are recruited *via* the BBB can then cause damage to abluminal parenchymal tissue within the CNS resulting in MS.

1.2.2.1 MS | T Cells

Typically, CD4+ T cells reside in perivascular cuffs whilst CD8+ T cells are mainly found within the parenchyma. CD4+ T cells in MS pathology can be reactive against a variety of molecules including: myelin basic protein (MBP), proteolipid protein (PLP) and myelin oligodendrocyte glycoprotein (MOG) [144]. CD4+ T cells react against antigenic peptides presented on class II major histocompatibility complex (MHC) proteins found on the cell surface of antigen presenting cells (APCs). APCs are typically dendritic cells, macrophages and B cells and are not normally resident in the CNS, however microglial cells can express class II MHC proteins [145]. CD8+ T Cells can exert cytotoxicity against the same myelin-derived molecules as CD4+ T cells, however the antigenic determents are presented on class I MHC molecules, which can be induced on a variety of CNS resident cells [146]. Lesions from the early-to-late stages of MS pathology show BBB breakdown and invading peripheral immune cells. Mostly macrophages are found abundantly in the lesions, followed by CD8+ T cells and CD4+ T cells, as well as B cells and differentiated antibody producing B cells called plasma cells which will be discussed next [135].

1.2.2.2 MS | B Cells

Typically, B cells reside in perivascular cuffs, but they can also distribute to the nearby parenchyma within MS lesion [147]. B cells become activated *via* interactions with an antigen that is recognized by an antigen-specific receptor presented on the surface of B cells, *via* the help of CD4+ T cells, these cells can then produce soluble antibodies against its receptor reactive antigen. Another hallmark of MS are so called oligoclonal band (OCB), which are antibodies or immunoglobulins isolated from CSF [148, 149]. *Via* antibodies different destructive pathways can be activated either through the antibodies or by antibody-complement to employ cellular cytotoxicity that contributes to the MS pathology [32, 150].

All cells discussed can be recruited to the inflammatory lesion *via* a selectin-dependent manner, which has been shown for B cells [151], CD8+ T cells [146, 152], and CD4+ T cells [67, 145] and other cells less typically found in MS lesions [153, 154]. Macrophages, discussed next, are also capable of entering the CNS *via* the selectins and other cell adhesion molecules [155-158].

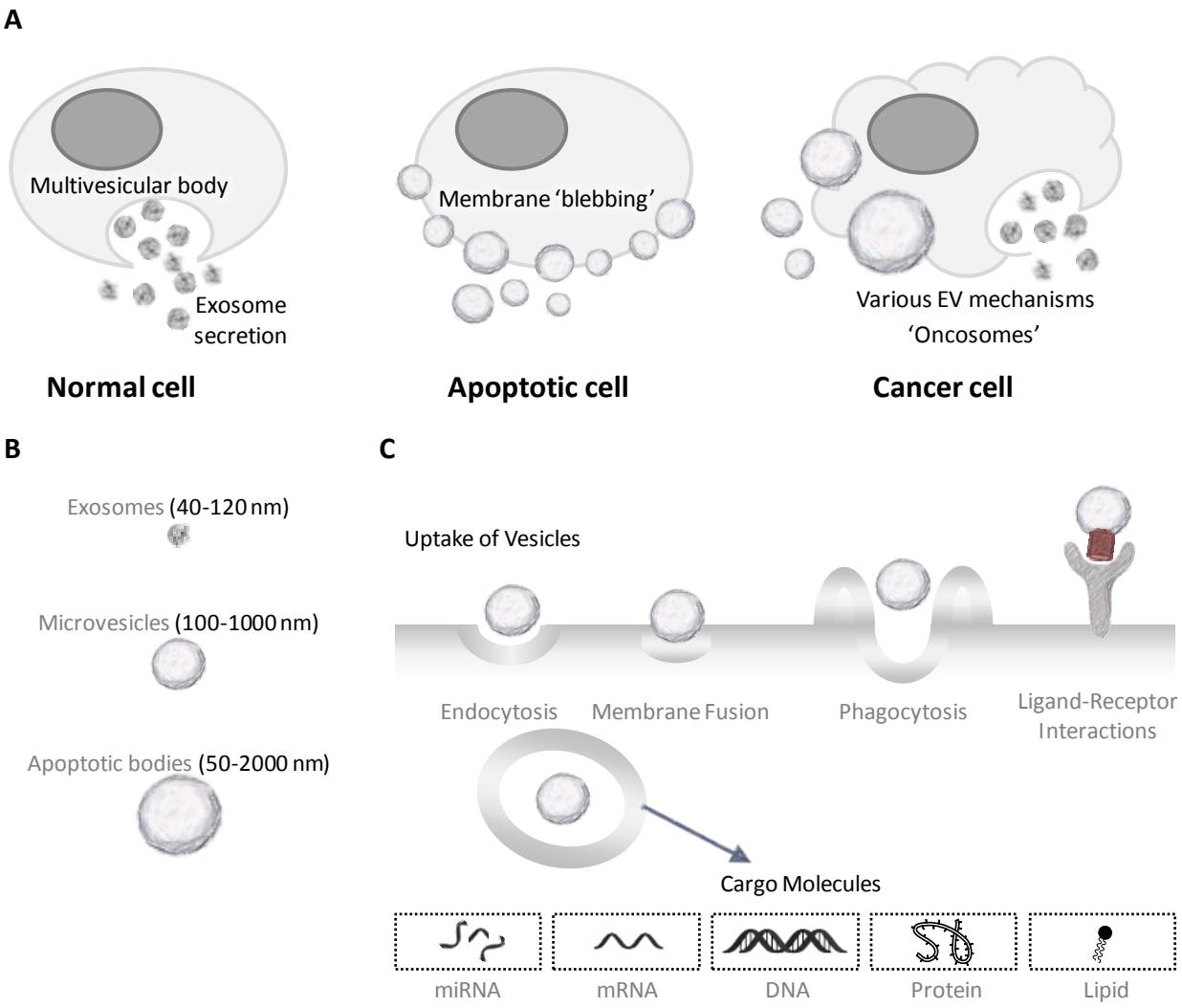
1.2.2.3 MS | Microglia and macrophages

As mentioned before, macrophages are found in lesions in the early stages of MS pathology [138]. Microglia are CNS-residing macrophages and are yolk sac derived from the early stages of embryonic development [133]. During a restricted embryonal period they populate the brain and then remain CNS resident throughout life. Microglia and other glial cells are the only CNS cells that continuously renew themselves, apart from O2A progenitor cells, without replacement from peripheral monocytes precursor cells and their reactivated state may reveal inflammation or injury [46]. However peripheral monocytes can adopt a microglia-like phenotype and replace damaged and dying microglia in the CNS during inflammation [159]. Microglial functions include scavenging of exogenous matter and cellular debris *via* phagocytosis, antigen presentation, homeostasis and synaptic pruning [160, 161]. Reactive microglia are capable of both repairing and damaging neurons and their activation status based on their expression levels for 'activation' can vary throughout disease progression [162, 163]. As microglia and macrophages can have both pro- and anti-inflammatory phenotypes, their roles during CNS diseases may vary and their secreted factors can have profound impact on the BBB [164, 165]. P2Y12, a protein found mostly on platelets, but also on microglia, can aid in chemotaxis and motility to injury-induced leaks in BBB and microglia recruited to the BBB rapidly repair the leaking BBB [164]. However, other factors secreted by reactive microglia, such as reactive oxygens species (ROS) and cytokines, may impair the BBB and destruct the myelin [13, 140, 165]. The CNS-resident microglia and the recruited immune cells can have a drastic impact on the integrity of the BBB and therefore the visualization of the early stages of brain inflammation during MS can be of great aid for disease management and treatment. As mentioned throughout this introduction, brain inflammatory lesions are often accompanied with disruption of the BBB. As these vascular cells are the entry point for immune cells from the periphery and the activation state of endothelial cells may signal downstream into the periphery *via* shedding of microvescilces from the endothelium, it is important to study the vascular and consequent peripheral aspects of these diseases, especially from an imaging point-of-view. This will be discussed in the next sections.

1.2.3 Other aspects of MS –vessels and vesicles

Early histological analysis of MS lesions showed that the vascular system of the CNS plays a pivotal role in the pathology [133]. As referred to before, active MS lesions show perivascular accumulation of immune cells, upregulation of adhesion molecules, leakage of serum proteins and deposition of complement on the luminal side of the endothelium. Interestingly, individuals who suffer from MS have an increased incidence of vascular disease [166, 167]. Some researchers

challenge the classical view of MS as an auto-immune disease and argue vascular abnormalities and dysfunction are part of the disease onset [167], while others argue that MS arises from dysfunction of the metabolism of lipids, with mechanisms similar - yet distinct - from atherosclerosis [168]. Part of the Acute Phase Response (APR) in response to infection and inflammation is the dramatic change in lipid metabolism and chemokine response by the liver [16, 168]. Elevated levels of APR proteins and lipid alterations are important regulators of brain inflammation and vascular pathology and dysregulation of the APR is associated with acute and chronic inflammatory diseases [169-172]. Until recently, it was unknown how the liver and the brain communicate during inflammation. Cytokines clearly play a role, but do not drive the inflammation in the brain, nor the atypical leukocyte recruitment per se [169]. However, increasing evidence suggests a role of vesicular components composed of proteins, nucleic acids and lipids derived from different cellular subsets to be (partially) responsible. **Figure 1.7** provides an overview of different extracellular vesicles (EV) - where they come from, their size and what cargo they carry - in a schematic manner. Historically, MS was the first disease where the presence of vesicular components, in this case exosomes, were detected and played a role in pathology. The exosomes of oligodendrocyte origin in the CSF of MS patients, were hypothesized to have a protective effect where recovery involved the release of complement vesicles from the surface of *via*ble cells [173]. Other cell types, including endothelial cells have altered secretion profiles of extracellular vesicles during MS. Endothelial micro particles (EMP) levels in serum derived from brain endothelial cells are raised in MS patients during the active phase of the disease when the BBB is open and lowered to baseline levels during remission [174]. The role of these microparticles and other extracellular vesicles remains elusive, however it has been shown that *in vitro* apoptotic bodies derived from apoptotic endothelial cells may signal to circulating stem cell progenitors to differentiate and facilitate the repair of injured endothelium [175]. Evidently, these extracellular particles play a role in MS and likely other brain inflammatory diseases. They may function as the mediator between the CNS and the peripheral immune system. Recently, EVs were shown to be involved in transferring sickness behaviour (stereotypical behaviour associated with disease, which reflects reprioritisation of behaviour rather than a functional loss) during brain inflammation. When naïve rats received EVs from rats that had a focal IL-1β inflammatory lesion in the brain, the naïve rats displayed sickness behaviour and the EVs were able to switch on the APR in these naïve animals [176]. These EVs were derived from activated endothelial cells and EVs derived from different cellular origins may have different outcomes on disease progression. In a different model of brain inflammation - traumatic brain injury (TBI) for instance - EVs derived from either plasma, endothelial cell cultures or macrophage cell cultures can alter the outcome of TBI and exacerbate CNS injury and the APR [177].



| Figure 1.7 | Extracellular vesicles: cellular origin, size range and uptake mechanism

|A| Extracellular vesicles can be synthesized and secreted *via* different mechanisms. Exosomes can be secreted by cells *via* multivesicular bodies, where vesicles are formed in lumen of multivesicular endosomes, and are secreted to the extracellular milieu. The contents of exosomes can vary but they typically contain markers shared with endosomes [178]. Microvesicles can 'bud' off the membrane of cells and typically contain cell surface plasma proteins and cytosolic components [179] . Apoptotic cells 'bleb' off a dying cell and can contain genomic DNA, organelles and phosphatidylserine. Besides signals, like phosphatidylserine for phagocytosis by macrophages, apoptotic bodies may signal in repair of the injured cell by replacement *via* stem cell progenitors [175]. Cancer cells can shed off a variety of extracellular vesicles, sometimes called oncosomes, that can aid in their invasiveness and can transform non-cancerous cells *via* horizontal transfer [180] **|B|** The overlapping sizes of the different classes of extracellular vesicles makes it difficult to distinguish their biogenesis. Exosomes are the smallest and can contain endosome-derived proteins. Microvesicles can vary in size and typically contain extracellular proteins on their surface. Apoptotic bodies are the largest and contain phosphatidylserine on their surface, which is normally facing the cytosol in *via*ble cells. **|C|** Recipient cells can take up extracellular vesicles and their cargo. Endocytosis, phagocytosis and receptor mediated uptake results in the endosomes containing the extracellular vesicles. Membrane fusion results in the direct delivery of the contents into the cytosol. Schematic adapted from the references supplied above.

Conceptually, it is interesting to study if EVs or exosomes can be manipulated in a manner so that we can understand their role in biology better and use them to modify or even treat diseases. Therefore, it is important identify specific exosomes markers that can aid with early diagnosis, disease stratification, and monitoring treatment response. Recent development of concentration-normalized electroanalytical assaying has overcome the limits of exosome concentration

necessary for conventional analysis and allows internal and external exosome marker discovery [181]. Recent reviews on extracellular vesicles and their cellular source, different pathways of biogenesis, targeting and role in health and CNS disease highlights their complexity and importance [182-184].

1.2.4 MS and MRI imaging of inflammation

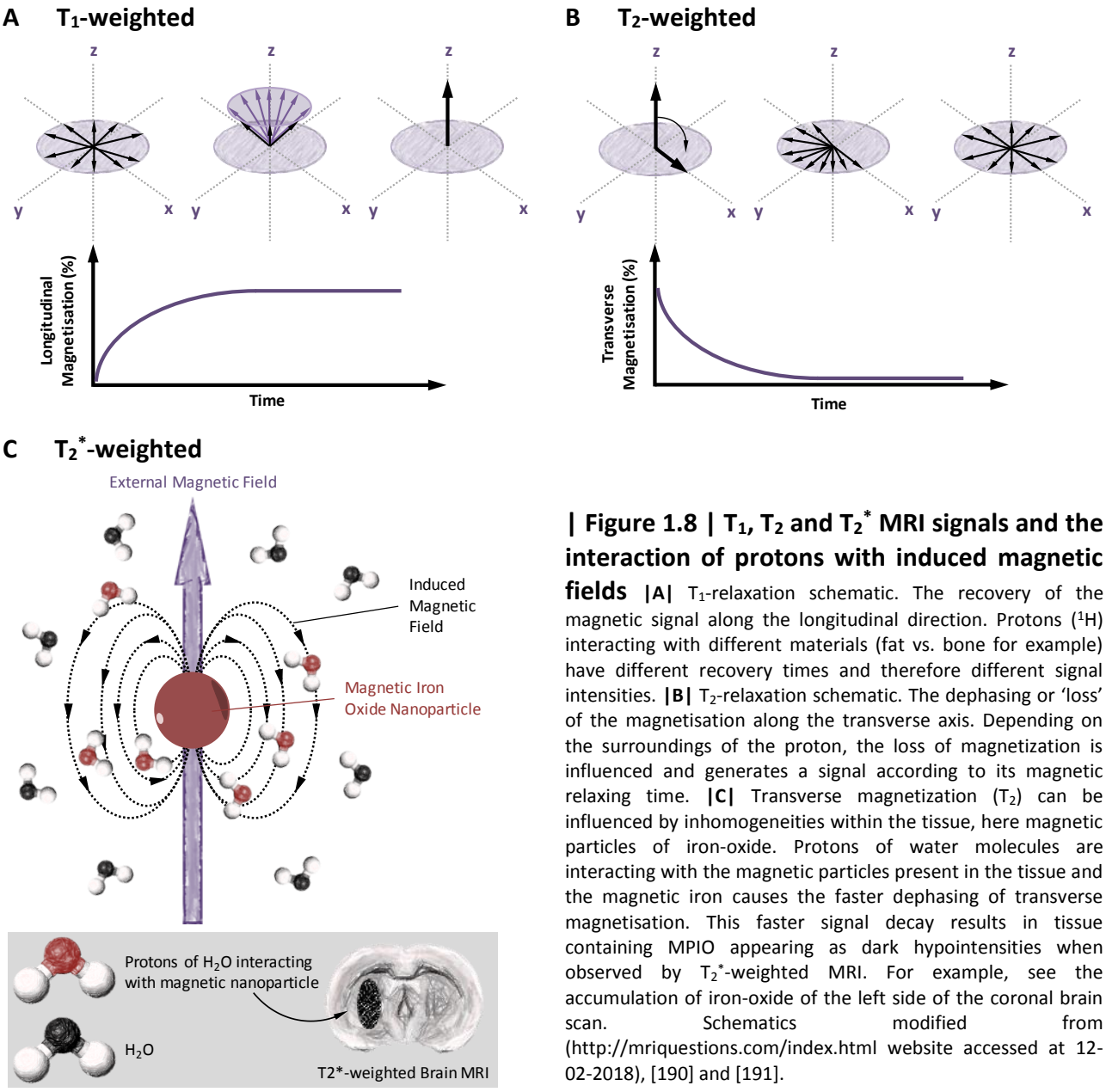
From an imaging point-of-view and for targeted drug delivery, studying the vascular changes of brain endothelial cells during inflammation can provide great insights in disease status and pre-clinical lesion formation, Magnetic Resonance Imaging (MRI) and Nuclear Magnetic Resonance (NMR) are based on the interaction of the magnetic moment of atomic nuclei with an externally applied magnetic field. ^{1}H-nuclei (or protons) are used for medical MRI as their molecular abundance within biological tissues is very high. Images acquired by MRI are obtained by the manipulation of the parameters in the imaging sequence, where in T_1 different tissues have different spin relaxing (the time at which excited protons return to equilibrium with the externally applied magnetic field) and T_2 spin coherence properties (the time at which excited protons reach equilibrium or go out of phase among the nuclei spinning perpendicular to the externally applied magnetic field). See **Figure 1.8 A** and **B**. The contrast can be enhanced by introducing paramagnetic material that can alter the signal intensity of the local ^{1}H-nuclei near the contrast material. This paramagnetic material (for this work, iron oxide particles) can cause inhomogeneities within the magnetic field when T_2 is measured and can cause a dark, hypointense signal as the paramagnetic material causes shorter T_2 relaxation times. This called T_2^*-weighted imaging. See **Figure 1.8 C**. Gadolinium (Gd), usually as Gd -DTPA (diethylenetriamine penta-acetic acid), is currently used to detect active brain inflammation lesions in MS. The Gd^{3+} is chelated in highly thermodynamically and kinetically stable complexes, as it is highly toxic on its own [185]. Gd provides T_1 contrast as Gd^{3+} has the highest possible number of unpaired electrons and slow electron spin relaxation. Accumulated Gd appears as hyper intense (white) signal on T_1 MRI as its unpaired electrons allow efficient relaxation of nearby protons [186]. These Gd-based contrast agents cannot cross the intact BBB. However, within active lesions BBB integrity fails and the Gd agent can enter the brain parenchyma and accumulate behind the BBB, which reveals these sites of active inflammation – known as a Gd-enhancing lesion. There are several safety issues concerning the repetitive use of Gd-based contrast agents including: nephrogenic systemic fibrosis, accumulation within the bone matrix and neural tissue deposition [185]. Beside these Gd-based agents, no other FDA-approved imaging techniques for MS are currently used. Although, several other imaging agents are available, technical difficulties and safety issues stop them from

being used in the clinic [3, 187]. There is an unmet need to reveal the early stages of brain inflammation as these early-inflammatory lesions are not accompanied by BBB breakdown or enhanced T_2-weighted signals. MRI is still the main method used to detect any abnormalities within the CNS as it is non-invasive and can provide information about the location of active lesions and their severity. In addition, their recurrence or onset can be monitored and can help clinicians to classify the type of MS present. Unfortunately, determining clinically definite MS is only 60% accurate at best according to the current McDonald criteria and relies heavily on active T_2-weighted lesions or abnormalities and T_1-weighted Gd-positive hyperintense MRI lesions [188, 189]. Thus the principal limitations of the use of MRI in the clinic is that the techniques used are largely sensitive to either late stage or gross neuropathology, at which point therapeutic intervention is of limited benefit. It is clear that the use of new molecular imaging agents is the way forward for MR-based technologies. The aim of molecular imaging is to visualise pathological processes at the cellular level, often long before disease symptoms become clinically apparent. This information will help clinicians to identify specific pathological processes, enabling the most appropriate therapeutic approach to be applied, and to monitor the outcome of therapy. It has been demonstrated that we can achieve *in vivo* detection of adhesion molecules for immune cells on blood vessels in the brain (e.g. VCAM-1, E/P-selectin) in a mouse model of acute inflammatory disease using magnetic resonance imaging, at a time when pathology is otherwise undetectable, but the contrast requires post imaging processing.

| Table 1.7 | MRI signals of CNS tissue using different magnetisation sequences

Signal	T_1-weighted	T_2-weighted	T_2^*-weighted
High	gadolinium, fat, subacute haemorrhage, protein rich fluid, slow flowing blood, lesions	high water content (oedema, tumour, infarct, inflammation, infection), subacute haemorrhage	
Medium	grey matter > white matter	white matter > grey matter	
Low	bone, CSF, air, high water content (oedema, tumour, infarct, inflammation, infection), haemorrhage, low proton density structures	bone, air, fat, low proton density structures (calcifications, blood cloth)	magnetic iron-oxide nanoparticles, haemorrhage, calcification, and iron deposition [190]

Typically T_1 and T_2-weighted images are made and the tissue differences between these types are shown in **Table 1.7**. When iron-oxide is placed in a magnetic field it develops a large magnetic moment which creates a local magnetic field gradient. This field shortens the time at which local excited ^{1}H-nuclei return to equilibrium with the externally applied magnetic field. T_2^*-weighted imaging of magnetic iron-oxide based contrast agents provides a hypo intense (black) signal on T_2 MRI and allows clear detection of these agents by the increased loss of transverse magnetization of interacting water molecules [190].



| Figure 1.8 | T_1, T_2 and T_2^* MRI signals and the interaction of protons with induced magnetic fields **|A|** T_1-relaxation schematic. The recovery of the magnetic signal along the longitudinal direction. Protons (^1H) interacting with different materials (fat vs. bone for example) have different recovery times and therefore different signal intensities. **|B|** T_2-relaxation schematic. The dephasing or 'loss' of the magnetisation along the transverse axis. Depending on the surroundings of the proton, the loss of magnetization is influenced and generates a signal according to its magnetic relaxing time. **|C|** Transverse magnetization (T_2) can be influenced by inhomogeneities within the tissue, here magnetic particles of iron-oxide. Protons of water molecules are interacting with the magnetic particles present in the tissue and the magnetic iron causes the faster dephasing of transverse magnetisation. This faster signal decay results in tissue containing MPIO appearing as dark hypointensities when observed by T_2^*-weighted MRI. For example, see the accumulation of iron-oxide of the left side of the coronal brain scan. Schematics modified from (http://mriquestions.com/index.html website accessed at 12-02-2018), [190] and [191].

As current criteria for identifying clinically definite MS still remain unimproved, having a targeted imaging T_2^*-based imaging agent that can visualise these early stages of brain inflammation before the destructive BBB breakdown occurs is highly desirable. Monitoring patients by a targeted MRI contrast agent in their pre-symptomatic stages of their disease may aid treatment design, follow-up frequency and give a more sensitive detection of novel therapies. Iron-oxide based nanoparticles have great potential to become part of CNS inflammation monitoring, however their size and clearance remain a translational issue for repetitive use [187, 192, 193]. For example the use of dextrans in the Ultra-Small Particles of Iron Oxide (USPIO) might lead to immunological responses. However, the use of USPIO, which are preferentially taken up by phagocytic macrophages, allows cellular imaging of *in vivo* macrophage activity [194]. However,

their dual role in MS pathology (neuroprotective and growth promoting or tissue damage by production of inflammatory mediators) may result in ambiguous MRI results when only USPIO are used because the presence of USPIO-filled macrophages may indicate the presence of a resolving lesion [162]. However, the combination of gadolinium and USPIO in MS patient may aid to identify additional active lesions compared to Gd only and allows contrast enhancement of more aggressive lesions otherwise not clearly visible with Gd only [195]. However, USPIO are not routinely used in the clinic. Recently, the limitation in their size, nonspecificity and biocompatibility has been overcome by bio-degradable multimeric magnetic particles of iron-oxide (mMPIO). These small dextran and iron-oxide based nanoparticles, approximately 60 nm in size, are linked together *via* peptidase cleavable peptide-linkers which increases there size up to 10-fold. This then allows a multivalent display of ligands for the detection of vascular makers on iron-oxide particles that can be broken down by the body [196]. As shown in **Figure 1.4**, Lewis^a-MPIO is a highly effective T_2^*-weighted MRI imaging agent to detect the early stages of brain inflammation, however the exact receptor or binding mechanism for Lewis^a remains unknown. Even though the disease mechanism of MS remains obscure, proteomics and genomics of inflammatory lesions in MS have provided scientists with great molecular insight into the pathology and these strategies have been employed in this thesis and will be discussed subsequently.

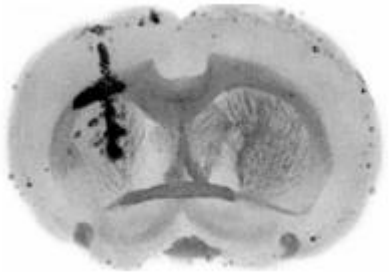
1.2.5 Proteomics and genomics of MS and animal models of MS

As highlighted in the previous sections, the heterogenic and complex nature of MS means its aetiology and exact pathogenesis remains unknown. CNS biopsies of patients for research are not readily available due to the invasive and dangerous nature of the procedure and post-mortem samples may not reflect the early stages of disease. Other bio-material, such as CSF and blood can be cumbersome to come by and need systematic handling procedures in order to compare patients, but can be very valuable for biomarker discovery [197]. Animal models of MS have provided researchers with disease models for discovering both the aetiology and treatment options for MS and other demyelinating diseases [142]. However, since the exact pathogenesis remains unknown these models are only approximations of the real disease. Nonetheless, they have been studied extensively and have led to some significant discoveries in treating MS [198]. Scientific advances in the field of proteomics and genomics have greatly aided in understanding MS on a molecular level and as part of this thesis makes use of these techniques; a concise overview on the proteomics and genomics of MS and the animal models of MS will be given here below.

1.2.5.1 MS | EAE and BCG animal models

Experimental Autoimmune (or Allergic) Encephalomyelitis (EAE) was first described in monkeys by injecting rabbit brain homogenate repeatedly in the periphery causing demyelination and meningitis [199]. Subsequent refinement of the model using adjuvants (Freund's adjuvants), resulted in a reproducible model of EAE in laboratory animals [200, 201]. As demyelination is the main feature of EAE that makes it a model for MS, many studies have tried to find how the immune system attacks the myelin sheets by genomics and proteomics and how to treat EAE with drugs. EAE can be induced peripherally, as mentioned, by CNS homogenates, purified myelin proteins and peptides against for example: MBP, PLP and MOG. Typical EAE disease follows an anticipated clinical course after a non-symptomatic period of 10–15 days followed by paralysis beginning in the tail and hind limbs and progressing to the fore-limbs. Different models may showcase different disease-forms of MS where now relapsing-remitting, progressive and chronic MS can been modelled by EAE [15]. Alternatively, a 'two-hit model' based on pre-sensitization rats with MOG followed by a stereotaxic injection of pro-inflammatory cytokines recapitulates MS-like lesion features including oedema, immune cell accumulation and demyelination that can be monitored by MRI [202]. The addition of adjuvants ensures the development of cell-mediated immune response, however, each model has its own characteristics that may cause a different onset time of EAE and different clinical signs. For example, immunisation with mannose-antigens elicits autoantibodies against these glycans but greatly reduces the severity of EAE when compared to without mannose [203]. Also, the difference between different models may affect the development of monoclonal antibody for clinical MS trials as some antibodies are effective in certain models of EAE and others not [204]. The role of E- and P-Selectin in the development of EAE and the recruitment of immune cells across the BBB remains unclear. Some studies have shown that E- and P-Selectin are not expressed during EAE [205] and that E- and P-Selectin knock out mice develop clinical EAE indistinguishable from wild-type mice [206]. These observations in EAE may not be reflective of MS as CNS, rather than peripheral cues, may cause Selectin expression. In addition, MS patients express E-Selectin in their vessels and Selectin ligands can be visualised using a different model of EAE and a delayed type hypersensitivity model [49, 137, 139] Therefore, EAE as a model for MS remains a topic of debate [14, 15]. Another, less frequently used model of MS is the Bacillus Calmette-Guérin (BCG)-model, in which a delayed-type hypersensitivity response is generated in the CNS by the intracranial injection of heat-killed BCG and a peripheral BCG immunization 2-6 week post intracranial injection [207]. The resulting lesion in the brain is accompanied by bystander demyelination and a myelomonocytic response. Bystander demyelination is the breakdown of myelin in the presence of immune cells, not necessarily directed against myelin. For example an immune response against Aquaporin4 in

neuromyelitis optica (NMO) can cause demyelination where the T cells and other immune cells that mount an immunological response against the astrocyte also damage myelin via the release of proteases[154]. The resulting demyelination is not direct demyelination, as it is caused by the myelin being in close proximity of the inflammatory event. When the peripheral immunisation is performed in complete Freund's adjuvant, the lesion is larger and more extensive and infiltrating cells are mostly mononuclear phagocytes and T cells. The adjuvant mediated peripheral challenge can still be detected in the CNS five months post immunisation, whilst the peripheral immunisation with only BCG lasts up to one month. Advantages of this model include the production of a demyelinating lesion at the site of the BCG injection so that the infiltrating immune cells can be studied in a quantitative and reproducible manner [137]. For this thesis the BCG model and the stereotactic injection of IL-1β in the brain are used as a model of acute inflammation and are explained in more detail in **Chapter 3**. Additionally, previous members from the laboratories of Daniel Anthony and Ben Davis also showed that Lewis^a-MPIO can acculumate in this BCG model and **Chapter 3** analyses the transcriptome of these lesions in order to find potential Lewis^a-MPIO interactors during this MS-model, see **Figure 1.9**.



| Figure 1.9 | Binding of Le^a-MPIO in a MS-neuroinflammatory lesion like model in the rat brain. Minimum intensity projection from an *ex vivo* high resolution T_2^*-weighted coronal MRI. Rats with a MS-lesion (intracerebral injection of BCG) in left hemisphere and intravenous injection of Le^a-MPIO (n=3). Dark left structure are accumulated Le^a-MPIO at the lesion location. ***Experiments performed by Daniel Anthony and Guillaume Bort.***

1.2.5.2 MS | Genomics and transcriptomics

Mendelian inheritance (the typical autosomal dominanat of resssive pattern of inheritance) does not apply to MS, although the incidence and prevalence is higher in family members of individuals who have MS, compared to the general population. However, not a single gene to date has been identified to cause MS. It appears that a combination of genes contributes to the susceptibility and that either a cumulative effect causes MS or external risk factors increase the likelihood [133, 208]. The major histocompatibility complex or human leukocyte antigen (MHC/HLA) genomic region has been identified as the largest contributor to the cumulative effects of this heterogenic disease [209]. There are more than 100 gene variants next to 103 variants in discrete loci outside

of the MHC identified for MS [210]. Analysis of the genes associated with MS can only account for 50% or the probability to develop the disease and the remaining risk is due to environmental risk factors [211]. As genetics alone cannot explain the disease, other dimensions of information are needed to understand MS. As mentioned before, MR imaging and animal models are very useful approaches to study the disease and metabolomics, proteomics, discussed next, and transcriptomics provide insight into the disease mechanism. Transcriptomics of chronic active lesions revealed, besides genes involved in immune function, altered gene transcription of lipid binding and uptake [212]. These alterations in lipids can also be monitored by metabolomics and can distinguish between MS and other similar demyelinating diseases of the CNS [213]. Cellular subsets can provide more detailed transcriptomes and reveal their specific roles in MS. Astrocyte transcriptomics revealed lipid-based alterations during EAE, specifically transcripts in cholesterol synthesis and immune regulation [214]. Microglia as mentioned before, can both have a protective and a destructive role in MS and their transcriptomes are different and can separate them from infiltrating macrophages [215]. These altered transcriptomes are not necessarily associated with genomic mutations and therefore provide more insight into the pathology, especially combined with proteomics. Transcriptomics and next generation sequencing has the power to detect alternative splicing and discovery of novel transcripts within MS and other diseases using a variety of techniques as reviewed in [216]. Transcriptomic mRNA and protein levels are generally considered to correlate, however, it has been shown that the cellular abundance of proteins is determined by the level of ribosomal translation, therefore the additional information on the protein level is required to firmly establish markers of the disease [217, 218].

1.2.5.3 MS | Proteomics

Over the years, several large-scale experiments have been performed to map the proteome of the brain in both health and disease. As the brain is the most complex organ in the human body, mapping the proteome by mass spectrometry (*MS**) seems a vast task and some great efforts have been made using mice as models [218, 219]. The proteome of MS lesions has been studied extensively as well. A summary of approximately 30 proteomics studies on EAE and MS analysing the brain, spinal cord, CSF and blood composition listed 200 proteins regularly found among them and whether they are up or down regulated among the many thousands of proteins present has been published [220]. An excellent example of studying the proteome and therapeutic development was the proteomic discovery of Protein C inhibitor and Tissue factor in MS lesions, both regulators of coagulation and inflammation. These proteins were found in post-mortem samples of acute plaques, chronic active plaques and chronic plaques of MS patients.

Pharmacological interference using either Hirudin (inhibitor of the procoagulant activity of thrombin) or mutant recombinant activated Protein C ameliorated the symptoms of mice with EAE [221]. Another study focussed on the *in silico* processing of post-mortem samples of acute plaques, chronic active plaques and chronic plaques of MS patients and used four different pathway analysis tools of bioinformatics which indicated that extracellular matrix components and integrin signalling proteins were key factors in the development of chronic lesions of MS [222]. Also EAE has been mapped for their altered protein expression in several studies and can provide more insight in the onset of EAE before the symptoms occur [223]. However, from a therapeutic or mechanistic point-of-view, analysis of cellular subsets or disease models of the brain can provide a more comprehensive and manageable set of data from which further experiments can be designed. The BBB has been a favourite for studies of both pharmacological and immune cell interactions; both rodent and human brain endothelial cells have mapped proteomes. Several techniques can be used to isolate brain microvascular endothelial cells including laser microdissection and also cellular compartmental isolations can aid in obtaining for example plasma membrane proteins of the BBB [219, 224, 225]. The lectins and cell adhesion molecules found on the cell surface of the BBB during inflammation are of particular interest for this work. Several potential lectins and adhesion molecules can be found in studies that interrogate the proteome of BBB cells. Mice cerebral artery proteome isolated from the circle of Willis contain the lectins Macrophage mannose receptor 1 and Galectin-1. Selectin ligands were identified as well, including PECAM1 and CD44 [226]. Brain microvascular endothelial cells have overlapping proteins with endothelial brain arterial cells and can also express cell adhesion molecules such as ICAM-1 and VCAM-1, but differ in their collagen composition [226, 227]. Species specific protein expression levels need to be taken into consideration as well, since rodents and human cells can have different levels of BBB specific proteins [228]. Marmosets have less than 2-fold expression differences between their BBB proteins and may be a better model for the human BBB than rodents [229]. As mentioned in section 1.1.3 Cell Adhesion Molecules, the selectins are not expressed in the brain vasculature and expression levels of E- and P-Selectin are undetectable in non-activated human brain micro vessels [66]. Therefore, comparative proteomics of ‘activated’ or ‘stimulated’ cells could provide more disease/inflammation relevant proteins and this is explored in Chapter 3. Using a non CNS-cell line, the proteome of IL-1β activated human umbilical vascular endothelial cells was studied before and E-Selectin, VCAM-1 and ICAM-1 expression was induced, where E-Selectin was undetectable in unstimulated cells [230].

1.2.5.4 Proteomic identification of targets using photo-crosslinkers

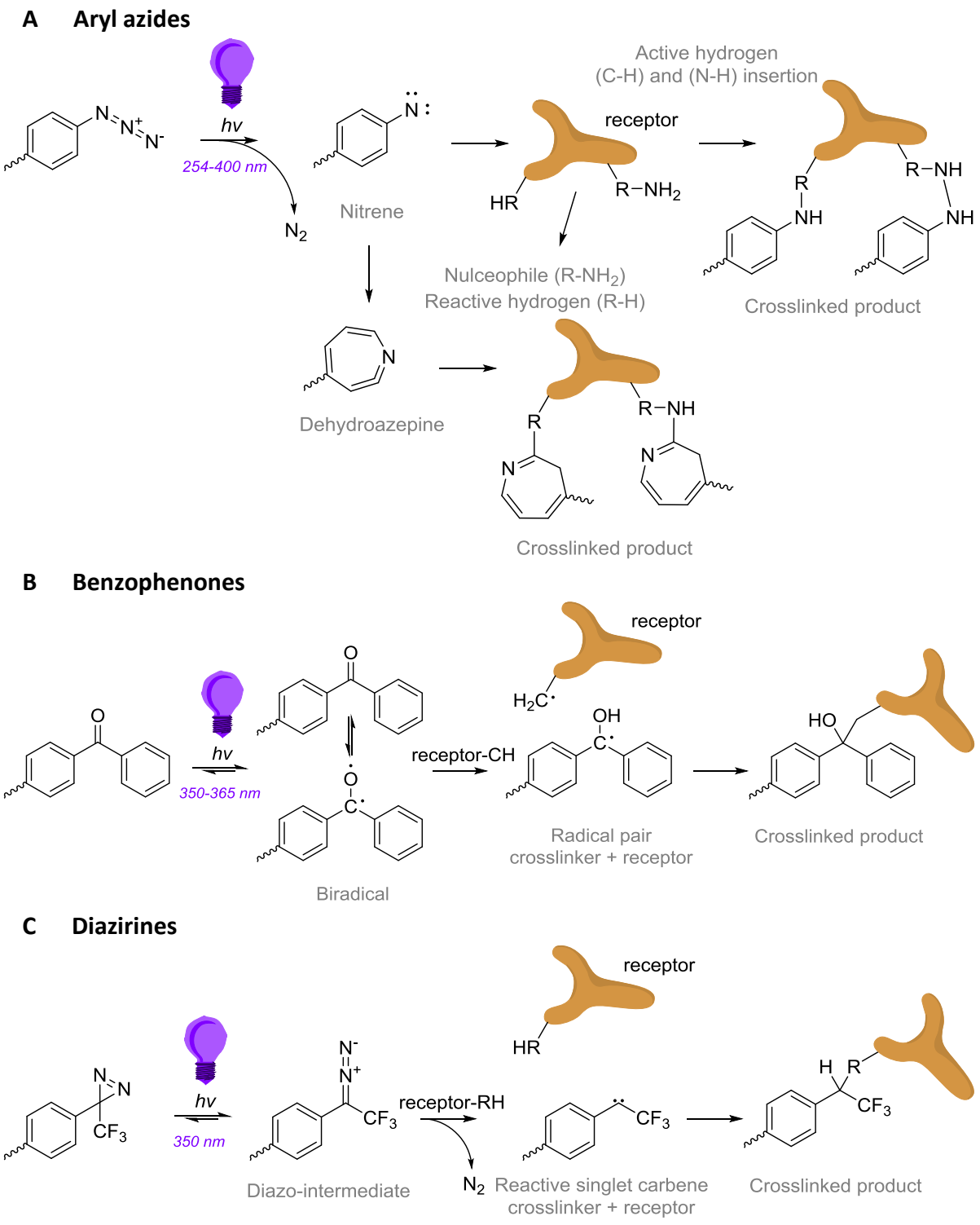
Lewis^a-MPIO, and, to a certain extent Lewis^b-MPIO, accumulate at the activated brain endothelium as shown in **Figure 1.4**. Although some lectins are known to interact with these carbohydrates, like E- and P-Selectin, MBL and DC-SIGN, their binding strength compared to sialyl Lewis^x could indicate that an alternative lectin is working in synergy with E-Selectin and is responsible for the observed accumulation of Le^a-MPIO on the activated endothelium. Therefore this thesis explores the possibility to selectively target Lewis carbohydrate-interacting proteins from brain endothelial cells by covalently trapping these interactions proteins onto the magnetic MPIOs with photo-crosslinkers. These covalently trapped Lewis carbohydrate-interacting proteins can then be identified by proteomics. The design of these particles will be discussed in the next chapter, Chapter 2, and the *in vitro* experiments in Chapter 3. The following section of this introduction will explain and discuss the use of crosslinkers and carbohydrates and how to identify their interacting lectins by proteomics.

In order to identify the lectin(s) involved using a crosslinker based proteomics tool, the tool must mimic the conditions during the brain inflammation MRI experiment as closely as possible. The proteomics tool should therefore have:

- A multivalent display of carbohydrates to enhance the binding [76],
- The easy retrieval of the scaffold used by magnetic isolation for instance to allow extensive washing and enrichment,
- And, an inducible cross linker to trap the transient interactions that occur between a single carbohydrate and its lectin to further aid in the enrichment and subsequent processing steps.

The Lewis^a-MPIOs fulfil to two of the three outlined criteria, and thus the introduction of an inducible cross linker onto the amine-particles might generate a highly effective proteomics tool.

Cross linking involves the introduction of irreversible covalent modifications at a reactive part of the cross linker and the side chains of a protein interacting in close proximity. Chemical cross linkers have been previously used successfully to identify proteins and protein complexes by proteomics, however for this system it was envisaged that the crosslinking-induced chemical changes could make proteomic identification by *MS**/*MS** cumbersome due to the introduction of modifications to the proteins [231, 232]. Although, methods have been developed with *MS**-



| Figure 1.10 | Photo-crosslinker structures and mechanisms of protein cross linking
|A| When irradiated, nitrogen is released and the aryl azide can either form an electrophilic nitrene that can insert into a carbon (R-H) to hydrogen covalent bond forming an amine or amide or a similar active hydrogen insertion can occur for amine-groups present in the protein (depicted in the scheme as the orange 'receptor' for illustrative purposes). Alternatively, an azepine from the nitrene can be formed that then *via* reactive hydrogen (R-H) or a nucleophilic ($R\text{-}NH_2$) reaction can form the cross-linked products with the protein receptor. **|B|** Benzophenones can, *via* a biradical mechanism, with the generated reactive triplet carbonyl activate inactive C–H bonds to cross link to proteins. **|C|** Diazirines, in this case 3-trifluoromethyl-3-phenyldiazirine, can upon irradiation *via* a diazo-intermediate release nitrogen to form the reactive carbene. This carbene can then subsequently form covalent bonds though addition reactions with protein side groups. [233], [234].

cleavable cross linkers that could overcome this problem, these type of linkers still require optimization for use in complex systems, such as cell lysates [235]. Therefore, photo-crosslinkers were explored for this work because of their advantages over chemical cross linkers. Firstly, photo-crosslinkers can be selectively installed onto the particles *via* the primary amines and activated by expose to UV light to initiate cross linking at will. Secondly, they are able to conjugate to common functional groups found in proteins. Lastly, photo-crosslinkers have the advantage of introducing a covalent modification at the site of interaction when exposed to the corresponding wavelength. This means that only the interacting domain close to the photo-crosslinker is modified, leaving the remainder of the protein intact for identification by *MS**/ *MS**. Several photo-crosslinker groups have been used in conjunction with biological systems and the most widely used groups are aryl azides, benzophenones and diazirines. See **Figure 1.10** for an overview of the most commonly used photo reactive groups for protein cross linking. Aryl azides are frequently used photo-crosslinkers, due to their straightforward synthesis, stability in the dark and high reactivity upon photo irradiation. The activation of an aryl azide generates a nitrene or a dehydroazepine that can react with protein side chains [236]. See **Figure 1.10 A**. These type of photo-crosslinkers have been previously used successfully in both affinity based profiling and metabolic incorporation and are reviewed elsewhere [233, 234, 237]. However their stability in ambient light is a drawback, but perfluoro- and other derivatives are even more stable [238]. Benzophenones are bulkier photo-crosslinkers that *via* a biradical mechanism can covalently trap proteins [239]. See **Figure 1.10 B**. Of all the commonly used photo-crosslinkers, benzophenones have the most off-target effects and require long irradiation times during which non-specific labelling can occur [233, 240]. Diazirines are relatively stable photo-crosslinkers that can be handled in ambient light and exposure to UV-light near 350 nm yields 35% of the diazoisomer and after release of nitrogen 65% of the corresponding carbene can then react with protein receptors [241]. See **Figure 1.10 C**. These yields are efficient for photo-crosslinking and reduce non-specific labelling, in addition the dark stability, rapid photolysis, and reactivity of the carbene made this molecule the choice for the work presented in this thesis [241]. A drawback is that the generated carbenes can easily be quenched by water affecting the labelling yields, however the diazirine photo-crosslinkers have been used successfully to identify proteins *via* affinity based profiling and compared to benzophenone has less off-target effects [240, 242-244]. Photo-crosslinkers and multivalent carbohydrate interactions have been studied before, however never as a one-system proteomics tool on magnetic nanoparticles. Most of these so called carbohydrate-based photoaffinity probes rely on a 3-way system where a carbohydrate (mono- or multivalent), a photo-crosslinker and a tag (usually biotin) for enrichment is used [245-247]. Also nanoparticles have been functionalized with carbohydrates and benzophenone or aryl azide photo-crosslinkers

[248]. However, no novel protein substrates were identified by *MS** and these systems were solely used to fish out spiked lectins from lystates. A 9-step synthesis was reported for a carboxylic acid trifluoromethyl phenyldiazirine which allowed through amide bond formation the functionalization of the primary amines present on the surface of the MPIOs used for Lewis^a [249]. More details regarding the use of photo-crosslinkers, lectins and carbohydrates will be given in **Chapter 2** that describes the synthesis and **Chapter 3** where the constructed bi-functional Lewis^a trifluoromethylphenyl diazirine magnetic pull-down particles are used in *in vitro* models of brain inflammation.

1.3 | NANOPARTICLES FOR ALTERNATIVE IMAGING MODALITIES

1.3.1 Introduction to nanoparticles as imaging modalities

Spherical inorganic nanoparticles (NP) provide a surface that can be modified with molecules of biological interest. Numerous targeting strategies have been employed and these emphasize the broad applicability of NP in biological systems [250-252]. The inherent surface properties of spherical particles allow for the display of multiple copies of the targeting molecule of interest and contribute to increased avidity and multivalent interactions [65, 251]. In addition, submicron size NP compared to smaller (<100 nm) particles are less susceptible to extravasation or nonspecific uptake by liver Kupffer cells and endothelial cells [64]. Imaging inorganic nanoparticles allows tracking the material, providing diagnostic information and potential toxicity issues where NP accumulate beyond their target. For iron-oxide based nanoparticles using MRI this has been done extensively [194, 253, 254]. Other imaging techniques used in the clinic, such as computed tomography (CT) and positron emission tomography (PET) have used other nanoparticles for imaging such as gold for CT and Fluorine^{18} labelled rare-earth nanoparticles and other radiolabelled nanoparticles for PET [255-257]. Imaging of several different inorganic nanoparticles, each targeted to a different marker, in biological materials is underexplored. As carbohydrates have high affinity for their receptors through a multivalent display, the study of lectins within biological materials requires nanoparticles for optimal binding [81]. In addition, inorganic nanoparticles provide a large dense object that can be identified within biological samples when resolution is on the submicron scale [250]. This thesis explores if the high binding strength of Lewis^a on iron-oxide nanoparticles can be translated to other inorganic nanoparticles using X-ray fluorescence imaging, which will be introduced next.

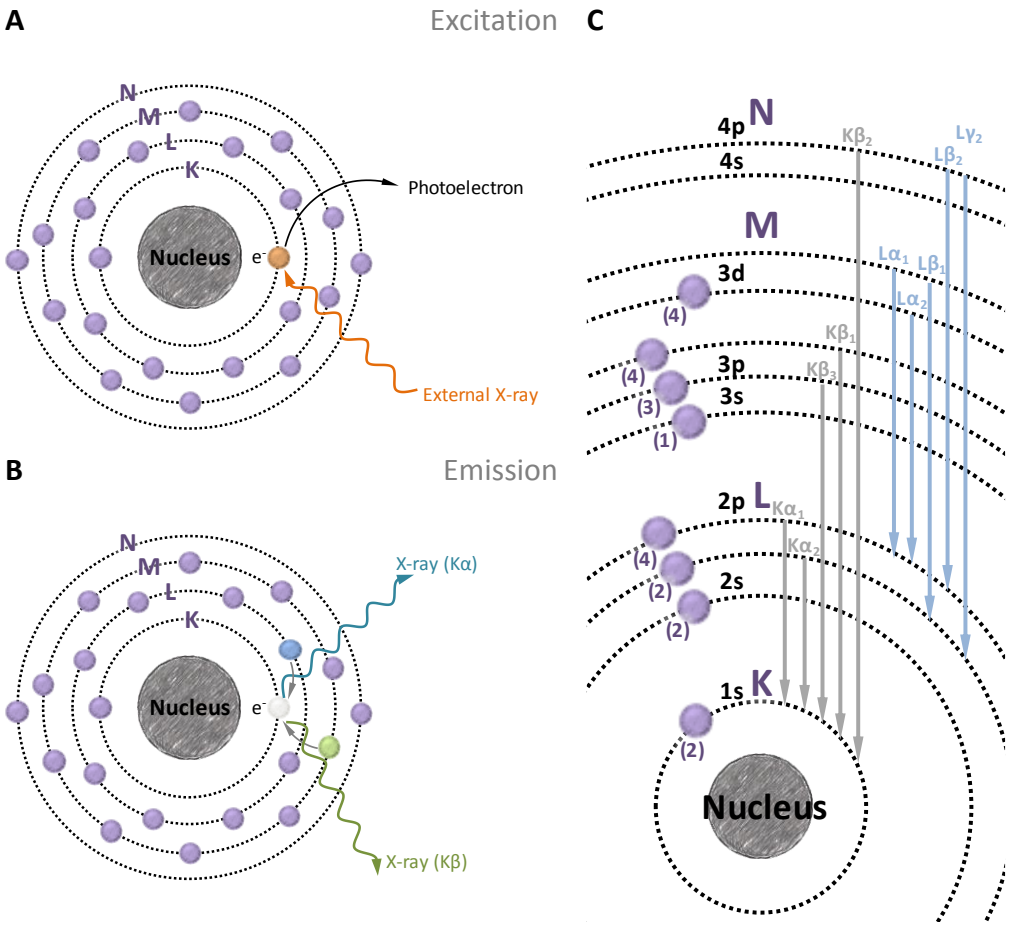
1.3.2 X-Ray fluorescence imaging

Synchrotron X-Ray Fluorescence (XRF) can image elements based on their X-ray emission spectrum after the element has been exited by high energy X-rays. An externally (for this thesis synchrotron generated) fired X-ray impinges on an atomic electron which is ejected from its orbital, as this is not energetically favourable, another higher orbital electron from the atom will occupy the empty space and by travelling down to the lower orbital it releases energy as an X-ray photon, see **Figure 1.11**. These X-rays photons or 'fluorescence' are unique for each element and

can therefore be used to map the elemental composition of materials and biological samples. Due to the destrictive nature of XRF, it can only be applied to post mortem specimens. When a highly focussed X-ray beam is used with a sensitive detector, nanoscale images of elemental maps of samples can be acquired [258, 259]. High-resolution imaging of naturally occurring elements of the cellular architecture has been successfully acquired using XRF and related principles [259-261]. Sub-cellular targets have been imaged with XRF as well with organelle-specific nanoparticles such as; targeted carbon nanotubes encapsulated with xenobiotic elements, quantum dots and gold-labelled antibodies [262-264]. *Ex vivo* brain samples have been of particular interest to image with XRF and will be discussed next.

1.3.2.1 XRF | Imaging of the brain

The resolution and the highly informative images that can be acquired with XRF allowed scientists to map elemental changes in the composition of trace metals in brain tissue and reveal metabolic and physiological alterations during disease progression [265-267]. Amyotrophic lateral sclerosis (ALS) is a CNS disease that causes the degeneration of the upper and lower motor neurons. The elemental composition of ALS differs from Parkinson's disease (PD), another motor neuron degenerative disorder, and differential metal accumulations have been implicated in the pathogenesis of these neurodegenerative diseases [268]. Early efforts used small post mortem brain slices (around 100 microns) of ALS and PD which were mapped by XRF failed to show any significant differences between the experimental groups, [269, 270]. However when larger areas (several centimetres) were mapped of the cerebellum, elemental iron, copper, and zinc were found to be differentially distributed within the white and grey matter of the healthy brain with sharp delineation [266]. This allowed observation of the elemental differences between PD and a healthy brain [271]. Subsequently, several neurological disorders and their mouse model equivalents have been mapped by XRF including; the afore mentioned PD [272], ALS [273], MS [274] and Alzheimer's disease (AD) [265, 275, 276] and show differential metal distributions in the brain as well on the micron-scale. Interestingly, CNS protein aggregation diseases, such as PD, AD and prion diseases 'chelate' metals such as copper in their protein plaques which often show highly regular structural fibrils or aggregates [268, 277]. The metal accumulation in these plaques, due to the chelation, may make these plaques more stable. Chelation treatment strategies can potentially aid in dissolving these plaques and XRF can assess the feasibility of these treatments [278]. Elements such as iron, copper, and zinc in CNS diseases are typically assessed by XRF as they are biologically relevant metals used for essential biological functions and their altered distribution may provide insights into pathology. However, XRF has been useful for studying



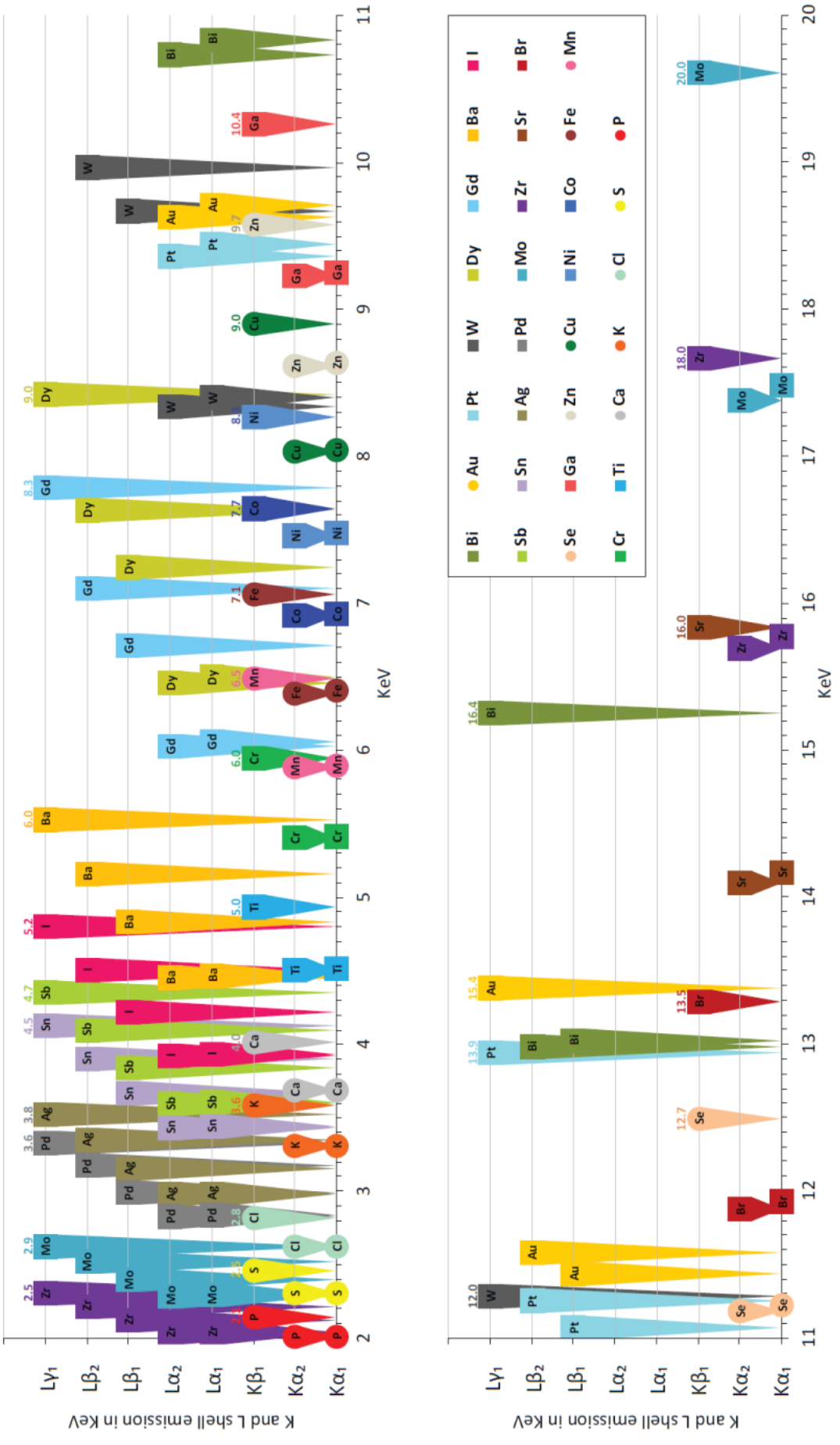
| Figure 1.11 | XRF principals **|A|** Externally applied X-rays can eject an electron (shown K shell here) from its orbital and a photoelectron is released. **|B|** The empty space where the electon was is replaced by an electron from another orbital and an X-ray photon is released by the electron travelling towards the lower orbital. **|C|** XRF emission lines for K- and L- shell emissions generates signals with distict KeV emissions that can be detected and allows elemental identification. Depending on the element, certain excitation energies are required to measure XRF. **Figure 1.12** shows the emission lines and excitation energies required to measure XRF of elements.

xenobiotic, toxic elemental deposits and their effects on the organismal level. Organomercury is highly toxic and can cause a range of pathological effects including CNS and peripheral neuropathy. Studying the uptake of several methyl and ethyl mercury derivatives in zebrafish, it was shown with XRF that mercury concentrated in the lens epithelium and to a certain extent in the brain, optic nerve and other organs [279]. Using XRF a new mechanism of mercury uptake was assessed [280]. As mentioned earlier, Gd-based MRI contrast agents can accumulate in the body when administered repetitively and have associated health implications. XRF of *ex vivo* tissue can be useful in preclinical pharmacological studies to assess the accumulation of Gd accumulation in tissue [281]. XRF has also been used to shown platinum accumulation in tumours of the anti-cancer drug cisplatin [282]. Nanoparticles have also been studied by XRF and will be discussed in the subsequent section.

1.3.2.2 XRF | Targeted imaging with nanoparticles

XRF analysis of the brain allows to multiplex the amount of markers that can be studied in disease models whilst simultaneously imaging biological elements that may be altered during disease state [267]. Targeting of the epidermal growth factor receptor (EGFR), a receptor that is often found to be upregulated in cancer, with EGFR-targeted Fe_3O_4@TiO_2 nanoparticles showed internalisation and nuclear translocation in cancer cells *via* XRF-imaging [283]. Another example of XRF-imaging of tumours was done by targeting the transferrin-receptor using gold nanoparticles [284]. XRF-imaging of nanoparticles on the the whole-organismal level has been done with cobalt nanoparticles in the nematode *Caenorhabditis elegans* and cadmium selenide quantum dots capped with zinc sulphide in fleas, though only bio-distribution was reported [285, 286]. The XRF imaging field lacks targeted imaging agents to study brain inflammation. As previously referred to, spherical nanoparticles provide a surface that can be modified with molecules of biological interest. Numerous targeting strategies have been employed and these emphasize the broad applicability of nanoparticles in biological systems [250-252]. Especially for carbohydrates and lectin targeting, the inherent surface properties of spherical particles allows for the display of multiple copies of the targeting molecule contributing to increased avidity [65, 251]. In addition, submicron size nanoparticles are less susceptible to extravasation or nonspecific uptake by endothelial cells than smaller (<100 nm) particles [64]. Nanoparticles used in biological systems are typically fabricated of iron-oxide (Fe_3O_4) [65], gold (Au) [264, 287] and silica (SiO_2) [288, 289] mostly due to their optical, imaging and magnetic properties and for the well-established knowledge of surface chemistries available [250, 251]. However for XRF imaging, the emission lines of these nanoparticles overlap with most common biological elements making them impractical to use in XRF targeted imaging, see **Figure 1.12**. Elements like Titanium (Ti) and Zirconium (Zr) have distinct XRF lines that would be most suitable for the design of targeted XRF imaging agents. Also, XRF requires *ex vivo* samples thus the brief exposure to toxic nanoparticles for targeted imaging poses no issues. Additionally, the size range of these particles (nano to micron sized) allows functionalisation of the surface with a higher density of molecules increasing the multivalent nanoparticle display. XRF imaging strategies is further explored in **Chapter 4**.

| Figure 1.12 | XRF emission lines compatible with the I18-Beamline at Diamond, Didcot UK – Figure on next page Listed here are the elements suitable for XRF-mapping using the I18-beamline from Diamond, Didcot UK. Square □ elements are xenobiotic and round ○ elements occur in biological specimens as indicated in the legend. The emission is shown on the lower axes in KeV and the lines on the left-side axis show the different K- and L- shell emissions in KeV. Indicated above the elements in the graph are the K- and L-edge excitation energies (shown in same colour as the element). The elements are chosen for their compatible K- and L-shell emission lines and can be made/purchased in nanoparticle form. It is taken into consideration that the I18 beamline becomes unstable above 15 KeV and that the K- and L-edges of certain elements have to fall within the range (mapping biological elements as well). Therefore the focus is on the elements with compatible excitations: Ba, Ti, Cr, Gd, Co, Dy, Ni, Ga, Pt, Au, W, Bi, Br, where the highest K-edge is Br (13.5 KeV) and the highest L-edge Au (15.4 KeV).


K and L shell emission in KeV
Kα1
Kα2
Kβ1
Lα1
Lα2
Lβ1
Lβ2
Lγ1
KeV
Bi
Au
Pt
W
Dy
Gd
Ba
I
Sb
Sn
Ag
Pd
Mo
Zr
Sr
Br
Se
Ga
Zn
Cu
Ni
Co
Fe
Mn
Cr
Ti
Ca
K
Cl
S
P

THESIS STRUCTURE

This thesis details the development and use of nanoparticles *in vitro* and *in vivo* to study the biological mechanism of carbohydrate Lewis^a binding during brain inflammation. Iron-oxide based nanoparticles were covalently functionalized with the carbohydrate Lewis^a and Lewis^b for *in vivo* MRI imaging of brain inflammation. In order to find the receptor and uncover the biological mechanism of binding during brain inflammation, several approaches were employed including transcriptomics of both acute IL-1β and chronic MS-like BCG brain inflammatory lesions in rats and proteomics of brain microvascular endothelial cells from mice. To reveal any unknown lectins that may contribute to the strong interaction of Lewis^a presented onto nanoparticles, a photo-crosslinker was introduced to generate bi-functional nanoparticles to covalently trap and analyse, *via* proteomics, the interacting Lewis^a molecules from cell membrane extracts of brain microvascular endothelial cells. The results from the *in vitro* transcriptomics and proteomics uncovered a role for neutrophils and the selectins in the binding of Lewis^a during brain inflammation, which was confirmed *in vivo* by MRI. Using the binding of Lewis^a to the inflamed vasculature, other experiment allowed perspectives for future work. Extracellular vesicles, were decorated with membrane-inserting Lewis^a-lipids to assess both the role of these lipids in inflammation and their use to re-target biological nanoparticles. Also initial efforts to develop a multiplexed imaging platform using synchrotron generated X-rays are presented, using xenobiotic nanoparticles to detect two different markers of brain inflammation, Lewis^a and VCAM-1, in *ex vivo* brain slices with XRF.

The strong *in vivo* binding of Lewis^a presented on iron-oxide nanoparticles investigated within this thesis shows promising evidence for using this carbohydrate as a targeted MRI imaging agent for the detection of the early stages of brain inflammation in diseases such as MS. Other nanoparticle platforms presented provide new imaging and delivery opportunities to detect and target brain inflammation and the strong binding of Lewis^a can aid in their development and validation.

Chapter 2 describes the synthesis of Lewis^a with an S-cyanomethyl (SCM) protecting group and a trifluoromethylphenyl diazirine photo-crosslinker with a carboxylic acid moiety. Both molecules bear groups reactive towards primary amines and the Lewis^a activation by the conversion to the reactive chemical group 2-imido-2-methoxy-ethyl (IME) group and peptide coupling of the photo-crosslinker allowed functionalization of nanoparticles with NH_2-groups. The chemical properties of the functionalized nanoparticles are described here as well.

Chapter 3 describes the *in vitro* and *in vivo* characterization of brain inflammation models using the synthesized nanoparticles described in chapter 2. Proteomics and transcriptomics of both *in vivo* and *in vitro* models of brain inflammation lead to a set of Selectin-blocking and neutrophil-depletion experiments which aided in the uncovering of the mechanism of Lewis^a binding *in vivo* using MRI.

Chapter 4 explores the use other nanoparticles in combination with Lewis^a, such as inorganic nanoparticles for XRF and lipid vescicles as a delivery vehicle. XRF experiments using nanoparticles and brain slides visualized elemental maps of early brain inflammation. Additionally, vesicles modified with Lewis^a-lipids allowed targeted delivery of liposomes to the inflamed brain *via* Lewis^a-lipids. These preliminary experiments hold promise for future work.

Chapter 5 summarises the work presented in this thesis and provides an outlook for future experiments.

2

|CHEMISTRY |

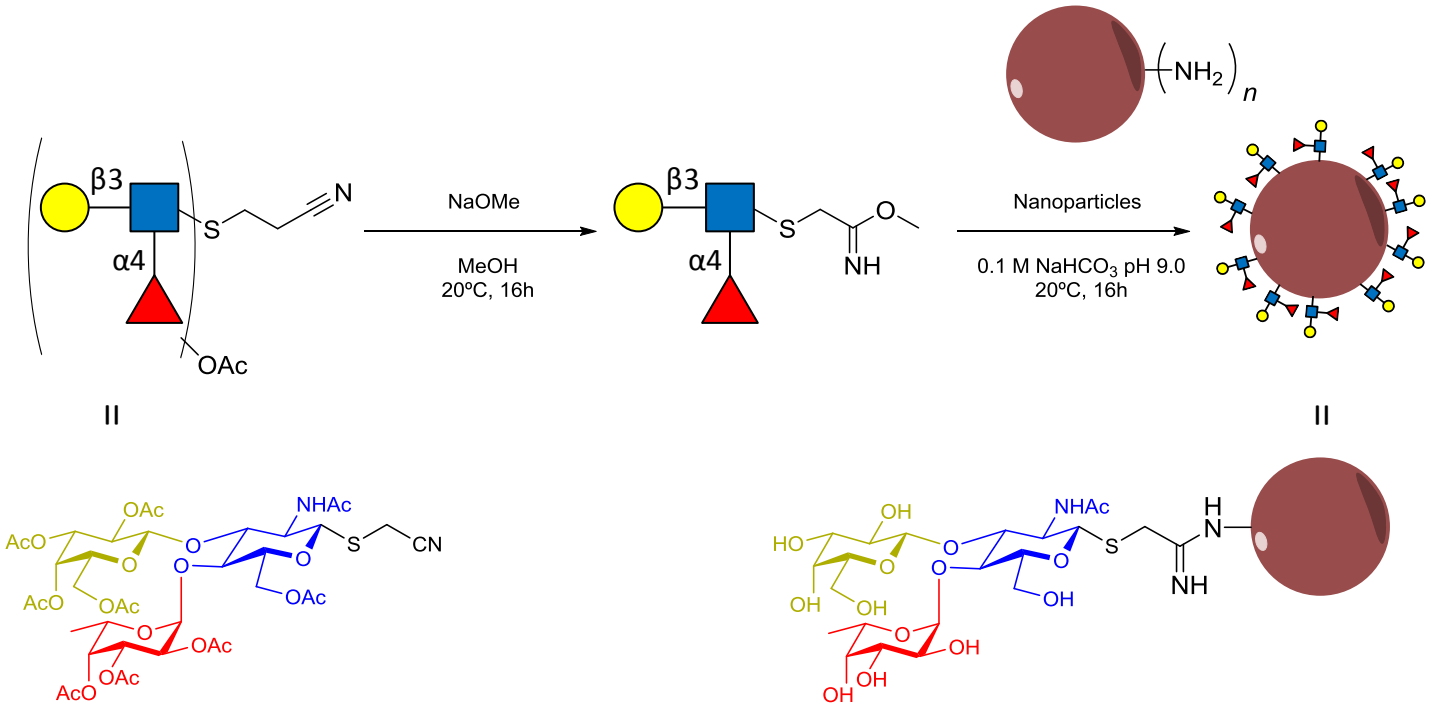
SYNTHESIS OF CARBOHYDRATE LEWIS[A],PHOTO-CROSSLINKER TRIFLUOROMETHYLPHENYLDIAZIRINE MOLECULES AND NANOPARTICLE FUNCTIONALISATION

The introduction of this thesis described that the strong binding observed for Lewis^a-MPIO is likely to be E- or P-Selectin, however other lectins or unknown proteins could be responsible for the binding. Therefore, a proteomics pull-down tool, based on these magnetic particles, was developed to study the early molecular changes at the plasma membrane surface of the activated brain endothelium and their interactions with Lewis^a. As most lectins are reliant on multivalent interactions that are transient, the design of the pull-down tool includes a photo-crosslinker which allows to covalently trap any interacting proteins onto the Lewis^a-MPIO to aid in proteomics sample processing and identification. This chapter describes the synthesis of Lewis^a with an S-cyanomethyl (SCM) functional group linker, which has been established within the Ben G. Davis group. The SCM linker activation reaction conditions generate the reactive chemical group 2-imido-2-methoxy-ethyl (IME) that can react with primary amines, as well as deprotects the acetyl groups of the acetylated carbohydrate to yield the linked desired carbohydrate onto the amine-terminated nanoparticles. For the proteomics pull-down tool, a trifluoromethylphenyldiazirine-based photo-crosslinker (PXL) was synthesized using a well-established literature procedure. The carboxylic acid of this photo-crosslinker allowed functionalisation of amine-terminated nanoparticles. Reactions to couple the photo-crosslinker onto the nanoparticles are described here in this chapter. Subsequently, proof-of-concept experiments were performed with the generated photo-crosslinker particles to determine their reactivity. In addition, the synthesis of Lewis^a-MPIO and Lewis^b-MPIO used for the *in vivo* experiments shown in **Chapter 3** are described. In summary, the synthesis of the precursor molecules to generate the bi-functional Lewis^a/Diazirine photo-crosslinker magnetic pull-down tool for proteomics and MRI particles used in **Chapter 3** are presented, including characterisations of the reactivity of the photo-crosslinker molecule on the nanoparticles.

2.1 | SYNTHESIS OF S-CYANOMETHYL-LEWIS[A]

2.1.1 Rationale for using IME-based chemistry to couple Lewis[a] onto amine nanoparticles

In order to covalently attach Lewis[a] molecules onto a primary amine-nanoparticle scaffold to display the carbohydrate in a multivalent manner, the Lewis[a] molecule requires a linker that can react with primary amines and remains stable during the synthesis conditions used to synthesize Lewis[a]. Amine linker chemistries have been widely used on lysine residues of proteins and a plethora of bio-orthogonal chemistries are available to modify primary amines [290], [291], [292]. However, this particular linker requires that the substrates and products are able to withstand the organic synthesis conditions required to make the tri-saccharide, to be water-soluble and to reacting rapidly and selectively with primary amines under mild conditions [65]. The linker used for Lewis[a] is 2-imido-2-methoxy-ethyl (IME) that is generated from the S-cyanomethyl (SCM) group using mild aqueous alkaline conditions, see **Figure 2.1**. Previously it has been shown that this IME-linker can functionalize the proteins α-amylase and lysozyme modified with IME-carbohydrates with retention of full enzymatic activity [293]. The generated imido ester that can then react with the primary amine to form the amidine linkage has the advantage of being small, hydrophilic, and positively charged at physiological pH, mimicking a lysine residue [294]. Because of the reasonable yields of this reactive linker (50-60%), and little or no change in pKa and mild aqueous conditions to generate it, it has been of particular use in modifying biologically-relevant molecules, such as viruses, proteins and primary amine-terminated magnetic iron-oxide nanoparticles (MPIO) [294], [295], [296], [65]. In addition, the acetate (Ac) protecting groups used during the synthesis of Lewis[a] are simultaneously deprotected with the sub-stoichiometric amounts of sodium methoxide in methanol used, yielding the IME-activated unprotected Lewis[a] for further functionalisation [293], [297]. Therefore for this work the SCM-Lewis[a] was synthesized in order to use it to functionalise MPIOs using an established method validated by previous members from the Ben G. Davis group (Régis C. Saliba and Sonia De Munari) [298], [299].

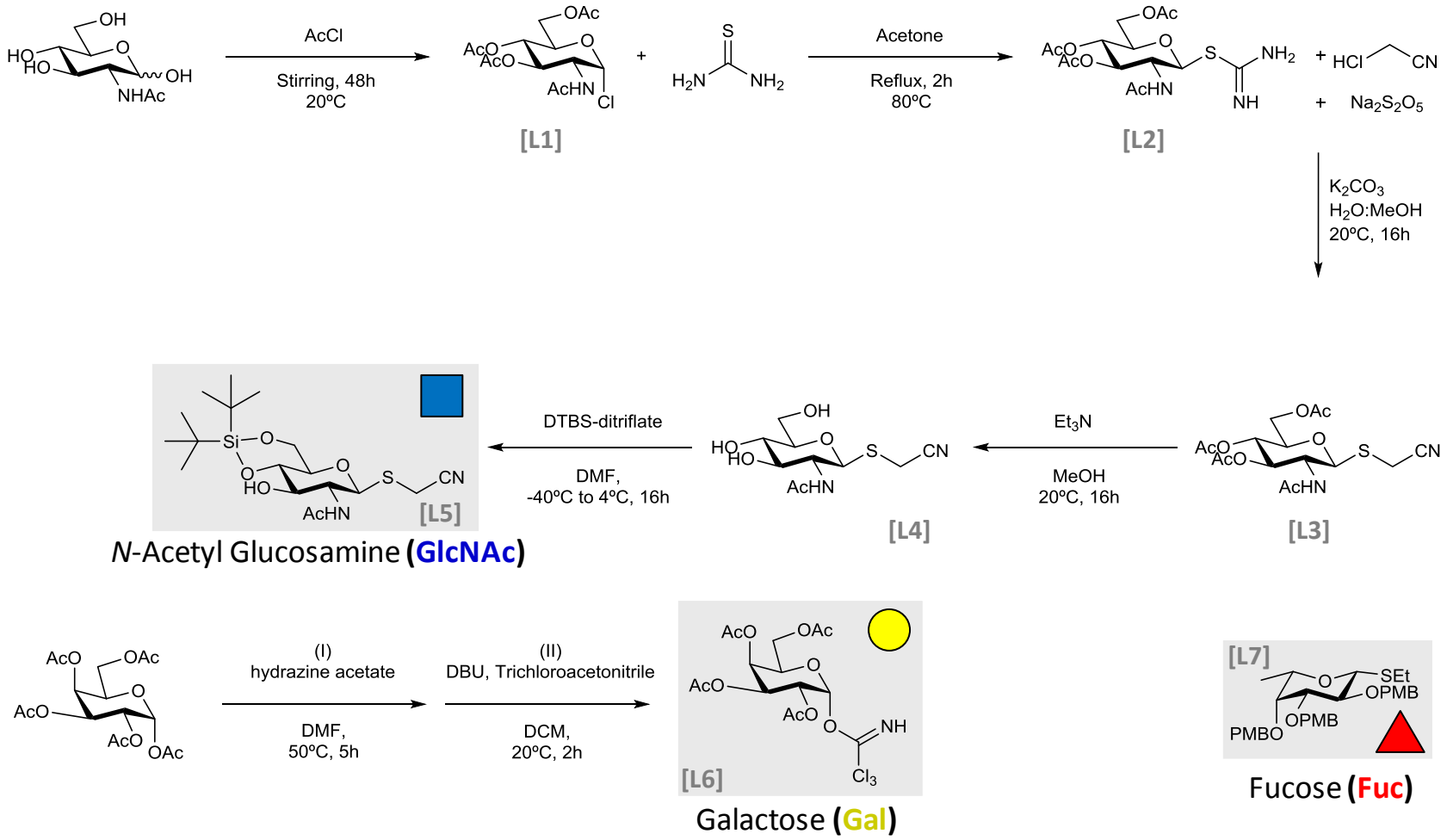


Galactose (Gal)
N-Acetyl Glucosamine (GlcNAc)
Fucose (Fuc)

| Figure 2.1 | IME-Lewis[a] enables amine-nanoparticle modification using mild aqueous conditions
Simultaneous activation of the SCM-group into IME and acetate (Ac) de-protecting of Lewis[a] using sub-stoichiometric amounts of sodium methoxide in methanol. The resulting deprotected IME-Lewis[a] can then be isolated and reacted onto amine-nanoparticles using an alkaline buffer. Cartoon representation of Lewis[a] is used though this thesis and the coloured structure shown here highlight the different mono-saccharide substructures that compose Lewis[a].

2.1.2 Synthesis of monosaccharides of Lewis[a]

Lewis[a] is composed of 3 different monosaccharide structures: a core *N*-acetyl glucosamine (GlcNAc) attached to a galactose (Gal) *via* β-1,3-linkage and to a fucose moiety *via* an α-1,4-linkage. A detailed synthesis route for the monosaccharides required to synthesize SCM-Lewis[a] was described by previous members of the group and the synthesis described here fully adhered to the reported procedures [298], [299]. See **Figure 2.2** for an overview. First GlcNAc was acetylated and chlorinated using acetyl chloride, resulting in the desired chlorinated α-anomer with 60% yield **[L1]**. This α-chloroglycoside was then reacted with thiourea by refluxing in acetone to obtain the stable thiouronium salt in 69% yield **[L2]**. The salt was converted to the S-cyanomethyl group with 59% yield **[L3]** by treatment with sodium metabisulfite and chloroacetonitrile. Deprotection of the acetate groups by triethylamine generated the.



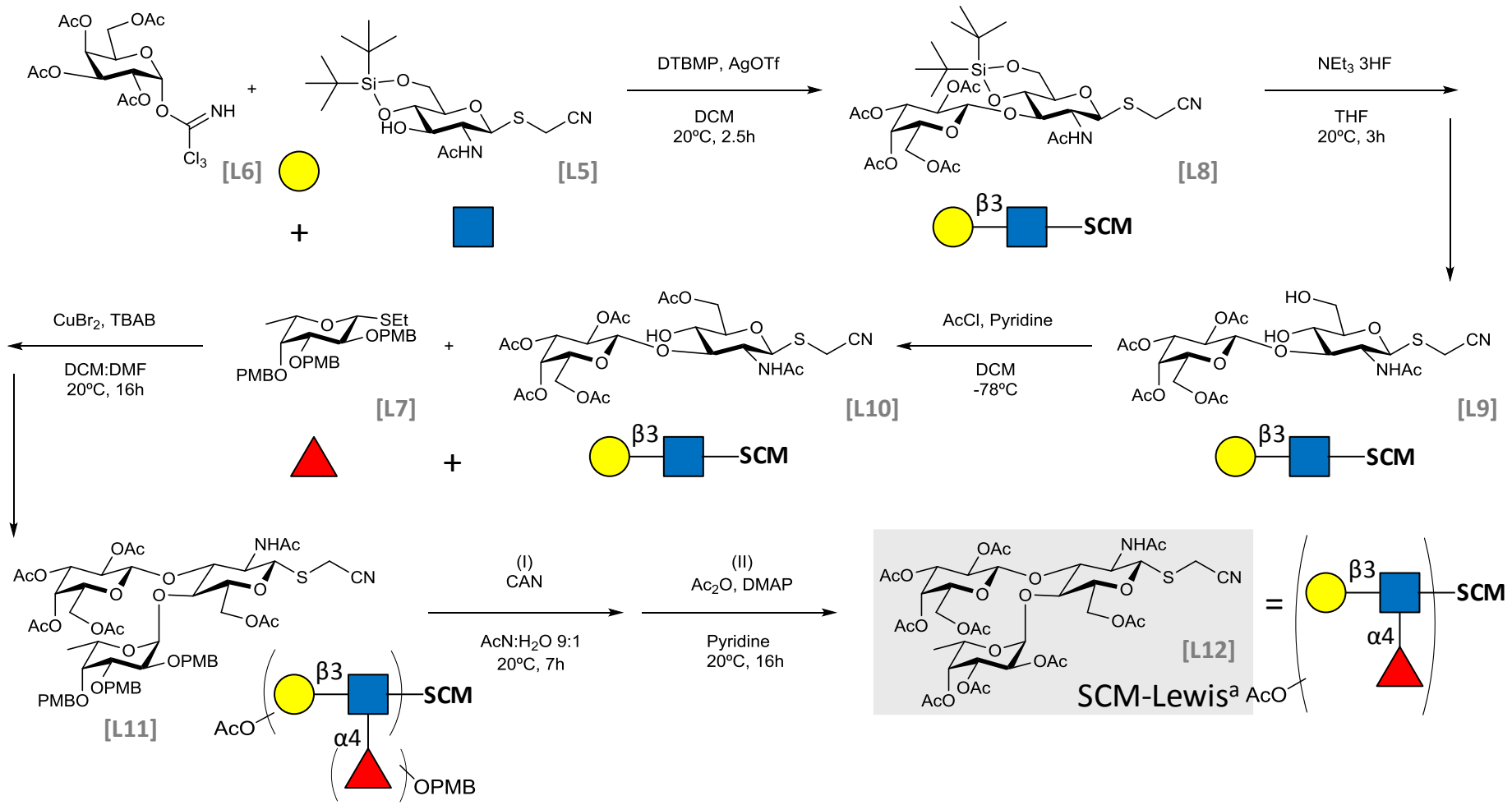
| Figure 2.2 | Synthesis of monosaccharides for SCM-Lewis[a]

As described in section 2.1.2 Synthesis of Monosaccharides of Lewis[a], introduction of the SCM-group to GlcNAc and selective protection of the 4- and 6-positions yielded the core GlcNAc. A two-step reaction using hydrazine acetate and DBU/trichloroacetonitrile yielded the Gal donor and Fuc was a kind gift from Sonia de Munari.

unprotected SCM-GlcNAc with 93% yield **[L4]**. For subsequent glycosylation reactions the β-1,3 linkage is required and the formation of a silylene ring linking the 4- and 6-positions together was achieved quantitatively using di-tertbutylsilylene (DTBS) **[L5]**. The resulting free hydroxyl group on the 3-position of the GlcNAc **[L5]** was then reacted with galactose (Gal), which will be described in the next **section 2.1.3** describing the glycosylation reactions to obtain Lewis[a]. For the next monosaccharide Gal, galactose pentaacetate was reacted with hydrazine acetate and the mid-work-up product was subjected to DBU and trichloroacetonitrile, resulting in the tetra-acetylated α-D-galactopyranoside trichloroacetimidate with an overall yield of 64% **[L6]**. The last monosaccharide Fucose (Fuc) **[L7]** was a kind gift from Sonia de Munari.

2.1.3 Glycosylation reactions to synthesise Lewis[a]

The three building blocks that compose Lewis[a] require glycosylation reactions to yield the linkages: GlcNAc attached to Gal *via* an β-1,3-linkage and GlcNAc to Fuc *via* an 1,4-α-linkage. As for the monosaccharides, a detailed synthesis route for the glycosylation reactions to obtain SCM-Lewis[a] was described by previous members of the group and the synthesis conditions for the glycosylation reactions described here fully adhered to the reported procedures [298], [299]. See **Figure 2.3** for an overview. Firstly, the Gal **[L6]** donor was reacted with the GlcNAc **[L5]** acceptor using the 2,6-di-tert-butyl-4-methylpyridine (DTBMP) reagent and silver triflate resulting in the desired 1,3-β-linked disaccharide in 68% yield **[L8]**. The deprotection of the DTBS with triethylamine trihydrofluoride was attained quantitatively yielding the disaccharide with the GlcNAc deprotected **[L9]**. These two reactions were performed early on in my DPhil and were executed together with an experienced chemist, Sonia de Munari, to ensure safe handling of the toxic and corrosive chemicals. The subsequent reaction conditions with pyridine and acetyl chloride yielded in 75% the selective acetylation of the 6-position of the GlcNAc, leaving the hydroxyl-group on the 4-position free for the next glycosylation reaction **[L10]**. Using the Fuc precursor **[L7]**, the PMB-protected tri-saccharide was obtained with the Fuc linked *via* an 1,4-α-linkage to the GlcNAc with 58% yield using copper bromide and tetrabutylammonium bromide (TBAB) **[L11]**. For the next reaction, yielding the Ac-protected SCM-Lewis[a] **[L12]** in 58% yield, **[L11]** was reacted under oxidising conditions with cerium ammonium nitrate (CAN) to deprotect the Fuc PMB protecting groups. Mid-work up, the subsequent deprotected Fuc was acetylated using acetic anhydride, pyridine and 4-dimethylaminopyridine (DMAP) and the final desired product was obtained after flash chromatography. Details regarding the synthesis can be found in the methods supplementary information section of this chapter.



| Figure 2.3 | Synthesis scheme of the glycosylation reactions for SCM-Lewis[a]: the precursor of IME-Lewis[a]

As described in **section SI.2.1 Glycosylation Reactions to Synthesise Lewis[a]**, the core SCM- GlcNAc was subjected to two regio-selective glycosylation reactions to obtain SCM-Lewis[a]. First donor Gal and acceptor GlcNAc were reacted to selectively form the desired 1,3-β-linked disaccharide. Selective protection of the 6-position of the GlcNAc and reaction with Fuc yielded the 1,4-α-linkage between Fuc and GlcNAc. Subsequent deprotection and acetylation yielded the SCM-Lewis[a] product that was used to functionalize nanoparticles using IME chemistry.

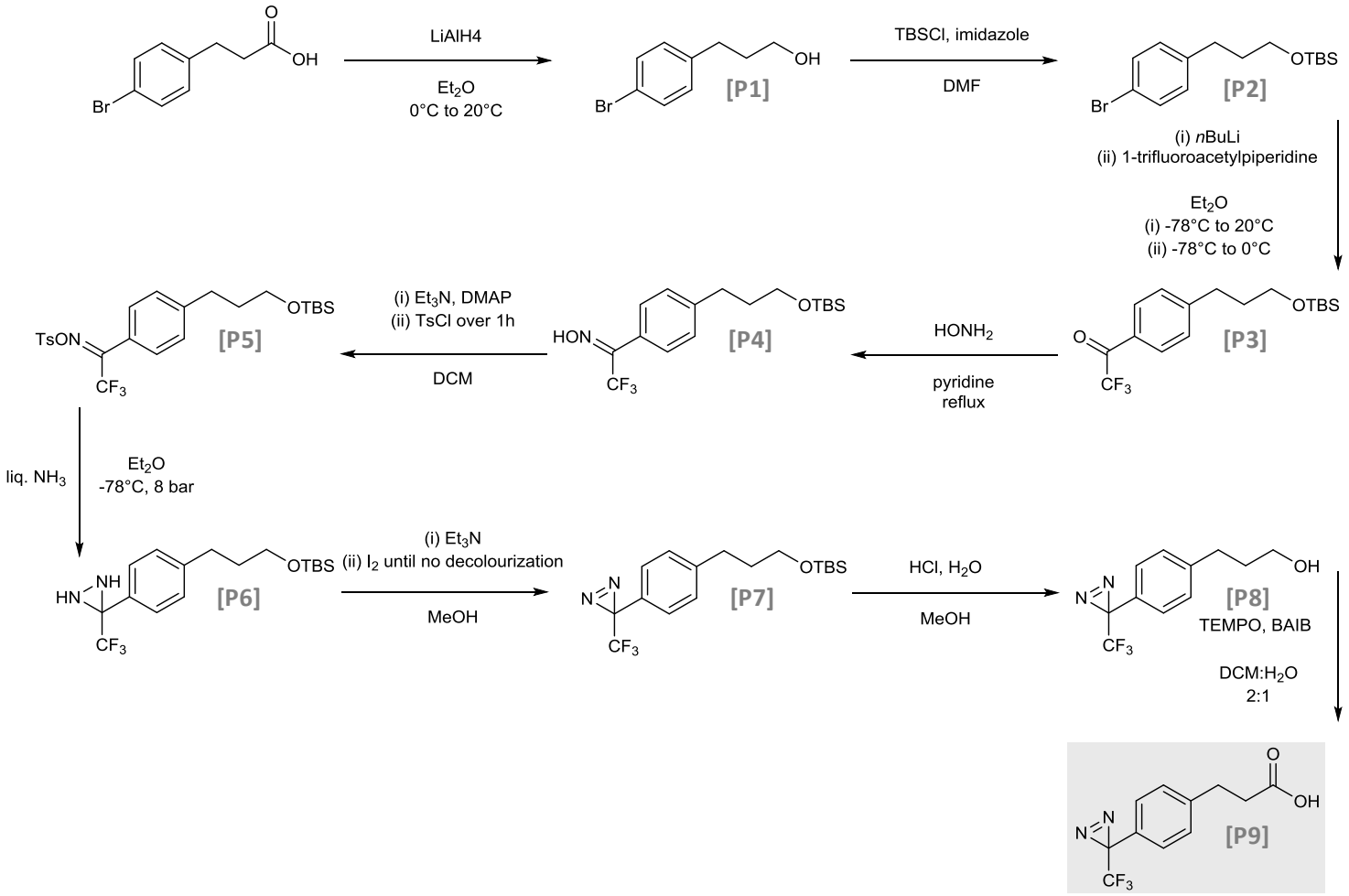
2.2 | SYNTHESIS OF TRIFLUOROMETHYL-DIAZIRIN-PHENYL-PROPANOIC ACID

2.2.1 Rationale for using trifluoromethyl-diazirin-phenyl-propanoic acid to couple onto amine-nanoparticles bearing Lewis^a

It was envisaged that the addition of a photo-crosslinker molecule onto the Lewis^a-MPIO could aid with the pull down of the interaction receptor(s) by covalently trapping these Lewis^a interacting receptors onto the magnetic particles. The covalently trapped proteins onto the MPIO would be able to withstand extensive washing of non-specific interacting proteins, allowing unbiased proteomic identification of the crosslinked Lewis^a interacting receptors. Because photo-crosslinkers, upon light activation with the correct wavelength, can react with nearby groups, it could allow covalent trapping of interacting proteins [241], [244], [242], [300]. However, the light reactivity also makes handling these compounds cumbersome and requires, for some photo-crosslinking moieties, protection from ambient light. Here, as the functionalisation of nanoparticles was required and subsequent further decoration with Lewis^a, a relatively stable photo-crosslinker was needed. As amine-terminated nanoparticles were required for Lewis^a functionalisation, the photo-crosslinker had to be stable enough to be used in proteomics trapping experiments, allow functionalisation with primary amine groups and not require completely dark synthesis conditions for practical reasons. A straight-forward and high-yielding synthesis was reported for trifluoromethyl-diazirin-phenyl-propanoic acid. See **Figure 2.4** for the reported reaction scheme yielding into **[P9]** [249]. Subsequent incorporation of the reported photo-crosslinker into peptides also ensured that the molecule remains stable during peptide coupling conditions. Peptide coupling reactions were also required in this thesis to couple the photo-crosslinker to the amine magnetic particles.

2.2.2 Synthesis of the photo-crosslinker

3-(4-Bromophenyl) propanoic acid was reduced to the alcohol **[P1]** using lithium aluminium hydride and the alcohol was then protected with tertbutylchlorodimethylsilane (TBSCl). This allowed further functionalisation of the Br-group to generate the trifluoro diazirine. The TBS-group remained stable during the synthesis conditions. The TBS ether **[P2]** was subjected to a halogen-lithium exchange using *n*-BuLi and reaction with 1-trifluoroacetyl piperidine yielded the trifluoroethanone **[P3]**. Ketone condensation using hydroxylamine hydrochloride resulted in the oxime **[P4]**. The oxime was then tosylated using tosyl chloride to generate the *O*-tosyl oxime **[P5]**. *O*-tosyl oxime diaziridine **[P6]** formation was achieved by a nucleophilic reaction with liquid ammonia. Subsequent diaziridine oxidation to the diazirine **[P7]** was accomplished by reacting the diaziridine with I_2. Deprotection to the alcohol **[P8]** was attained by acidolysis of the TBS ether. The desired carboxylic acid was completed by a TEMPO/BAIB ((2,2,6,6-Tetramethylpiperidin-1-yl)oxyl/bis(acetoxy)iodobenzene) oxidation of the alcohol to the carboxylic acid **[P9]**. Details regarding the synthesis can be found in the methods supplementary information section of this chapter.

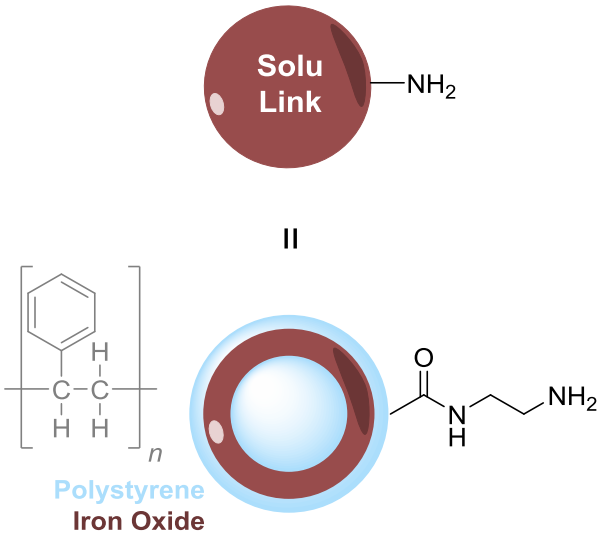


| Figure 2.4 | Synthesis scheme for the synthesis of trifluoromethyl-diazirin-phenyl-propanoic acid used to generate the bi-functional pull down particles Synthesis conditions as described in **section SI.2.2** and [249]. The acid was first transformed into the alcohol and subsequent TBS-ether. This TBS-ether remained stable during the synthesis conditions outlined. Dehalogenation and introduction of trifluoroethanone allowed the introduction of the diaziridine over 4 steps. Subsequent re-introduction of the carboxylic acid yielded the desired photo-crosslinker.

2.3 | AMINE-NANOPARTICLE FUNCTIONALISATION

2.3.1 Determining the free amine content of commercial nanoparticles (MPIOs) and coupling conditions for photo-crosslinker

Towards the development of a proteomics tool for identifying the ligand of Lewis[a], a diazirine photo-crosslinker and IME-Lewis[a] were synthesized (see **sections 2.1 and 2.2**). Commercial (SoluLink) 0.8 µm sized particles with an iron-oxide core (magnetic) and an amine coating were used as a scaffold for this pull-down tool. Other commercial particles were tested as well. However the Dynal (hydrophilic Dynabeads®, 2.8 µm with amine groups) that were used in earlier studies from my laboratories, anti-VCAM-1 antibody attached using the tosyl-activated version of these type of particles did not perform as well for the conditions described here in this section and the methods section of this chapter [64]. Different amine coupling approaches were employed and ultimately a HATU/DIPEA with the photo-crosslinking precursor 3-(4-bromophenyl) propanoic acid proved to be a reproducible model strategy to control the loading of the particles. Detection of the remainding of free amines was achieved by Fmoc-numbering using an >15K molar excess of Fmoc-Gly-OH and HATU/DIPEA as a coupling agent. A general method to assess amine loading and functionalisation levels are presented as well, including an ELISA-based approach to quickly screen particle batches reacted with Lewis[a].

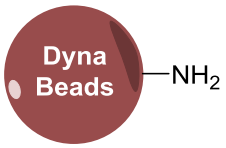
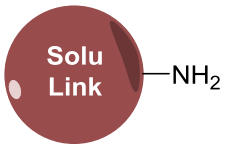


| Figure 2.5 | Chemistry of the commercial MPIO used
Commercial SoluLink amine-terminated nanoparticles. Top representation of the nanoparticles used throughout the thesis. Bottom representation of the particle depicts the linker and the polystyrene (PS) content.
Information retrieved from http://www.solulink.com/ at 13-03-2018.

2.3.2 Fmoc-numbering yields a quantitiative method to determinine amine-content on MPIOs and modification levels

Several methods are available to determine the amine content of species containing primary amines, in this case MPIOs. Most methods were developed to determine the amine content of proteins and the protein-based methods translated to MPIOs are listed in **Table 2.1** and described in the methods **section 2.7.2** at the end of this chapter.

| Table 2.1 | Amine-reactive detection methods explored in this thesis.

Particle	 DynaBeads	 SoluLink	References
Size	2.7 µm	0.8 µm	
NH_2 loading*	150 µmol/mg	41.2 nmol/mg	
Fluorescamine	X	Yes	[301], [299], [298], [302]
Phthaldialdehyde	X	X	[303]
Picrylsulfonic Acid	X	X	[304]
Fmoc-Numbering	X	Yes	[302]

Using Fmoc-numbering, only the SoluLink particles were able to give a read-out of the amine content present on the particles. Subsequently different coupling methods were used to couple Fmoc-Gly-OH and Fmoc-Cl onto the nanoparticles with the aim to react every amine and obtain minimal precipitation that may interfere with the nanoparticles. The precipitates are urea byproducts that occur during the Fmoc-numbering reactions using carbodiimides. The results are presented in **Table 2.2**.

| Table 2.2 | Different coupling conditions for Fmoc-numbering

Samples	Absorbance at 300 nm	Calculated Loading (nmol/mg)
20% Piperdine in DMF	-0.0002	0
SoluLink/Fmoc-Gly-OH/EDC/NHS	0.0762	175
SoluLink/Fmoc-Gly-OH/DCC/NHS	0.0998	228
SoluLink/Fmoc-Gly-OH/DIC/HOBT	0.2460	562
SoluLink/Fmoc-Gly-OH/HATU/DIPEA	***0.1825***	***417***
SoluLink/Fmoc-Cl/Et_3N	0.1667	381
SoluLink only	0.0001	0.0

Loading (mmol/mg) = (Abs_{sample})/ (mg of sample x 1.75*) * Based on ε = 5253 M^{-1} cm^{-1}
Formula from Reference: *W. C. Chan, P. D. White, Fmoc Solid Phase Peptide Synthesis, Oxford University Press, Oxford, 2000*

Both Fmoc-Gly-OH/DCC/NHS and Fmoc-Cl/Et_3N showed precipitation after the O/N reaction and particle pellets were significantly larger and more difficult to handle. Also Fmoc-Cl has the potential to react with hydroxyl groups, which could lead to false results if a Fmoc-Cl based method would be used to determine the loading of Lewis^a functionalised particles [305]. Although DIC/HOBT yielded the highest coupling yields, some discoloration was observed in the supernatant that could be responsible for the higher absorbance value. The particles treated with HATU/DIPEA appeared to withstand the reaction conditions well and the particles pelleted nicely against the magnet without any signs of aggregation or precipitates from the reaction conditions. The release of the dibenzofulvene from the Fmoc-species was initially tested with 20% piperidine in DMF (v/v). Although results with HATU/DIPEA were satisfactory with the 20% piperidine cleavage mix (see **Table 2.2**), a more stable spectroscopic readout can be achieved with a cleavage mixture containing the base DBU, as this base is unable to further react with the liberated dibenzofulvene [306]. Also the amount of amines determined did not correspond to the amount stated by the supplier and may be due to different detection methods used. The following procedure **(2.7.4)** was used throughout this work to determine the amine content of MPIOs. As these conditions were suitable to couple the Fmoc-protected amino acid glycine onto the nanoparticles, HATU/DIPEA was used to couple the photo-crosslinker onto the nanoparticles.

2.3.3 Dual functionalisation of nanoparticles with photo-crosslinker and Lewis^a

For the pull-down and MRI experiments described in **Chapter 3** both bi-functional Lewis^a/diazirine photo-crosslinker MPIOs were used and Lewis^a and Lewis^b functionalised MPIOs. This part of **Chapter 2** describes the functionalisation of these particles and measuring the amine content to determine the level of functionalisation of these two molecules. Including observations made about the amine numbers, size and charge of particles treated with different aprotic solvent. Using the same coupling methods established in **section 2.7.3**, a photo-crosslinker mimic was used to obtain a photo-crosslinker amine-loading of around 20%. This semi-arbitrary loading was chosen so that 80% of the remaining amines could react with IME-Lewis^a. By employing a 4-fold excess of Lewis^a over the photo-crosslinker on the MPIO, specific binding to Lewis^a is favoured with minimal a-specific binding to the photo-crosslinker during the pull-down experiments. A degree of coverage control was obtained and subsequently this strategy was employed to the photo-crosslinker **[P9]** to functionalise the MPIOs. Subsequently, Lewis^a was coupled to generate the bi-functional pull-down particles, including the determination of loading, particle charge and size. This will be presented next.

| Table 2.3 | Overview of the batches reported in thesis and experiments conducted

Carboxylic Acid	Amount (nmol)	Amine MPIO (nmol)	Functionalisation (%)	Figure	Table	Experiment
3-(4-bromophenyl) propanoic acid propanoic acid	See table	831 (batch I)	See table	2.6	2.4	Loading
Trifluoromethyl-diazirin-phenyl-propanoic acid	0	1040 (batch II)	0			
	61.8		unsuccessful			
	892.7		unsuccessful			
	92.7		unsuccessful			
	123.6		26 %			+ Lewis[a] Chapter 3 (3.1.4.2)
Trifluoromethyl-diazirin-phenyl-propanoic acid	0	711 (batch III)	See table	2.7	2.5	
	123.6		18 %	and		+ Lewis[a] Brain Recovery
	123.6		10 %	2.8		+ Lewis[a] Brain Recovery
	123.6		13 %			+ Lewis[a] Brain Recovery
	123.6		41%			Brain Recovery + BSA Cross Link
	123.6		12 %			Brain Recovery + BSA Cross Link
	123.6		26 %			Brain Recovery + BSA Cross Link

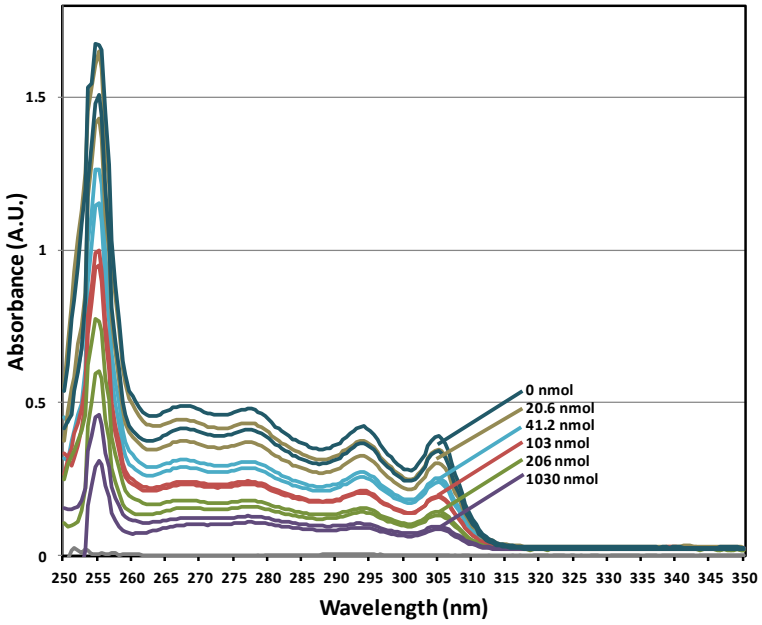
2.3.4 Functionalisation of nanoparticles with the photo-crosslinker, Lewis[a] and particle characteristics of treated particles

For the pull-down and MRI experiments described in **Chapter 3** both bi-functional Lewis[a]/diazirine photo-crosslinker MPIOs were used and Lewis[a] and Lewis[b] MPIOs. This part of **Chapter 2** describes the functionalisation of the MPIOs with the photo-crosslinker.

| Table 2.4 | Coverage calculations (305 nm) of MPIO-NH_2 using different equivalants of a photo-crosslinker mimic

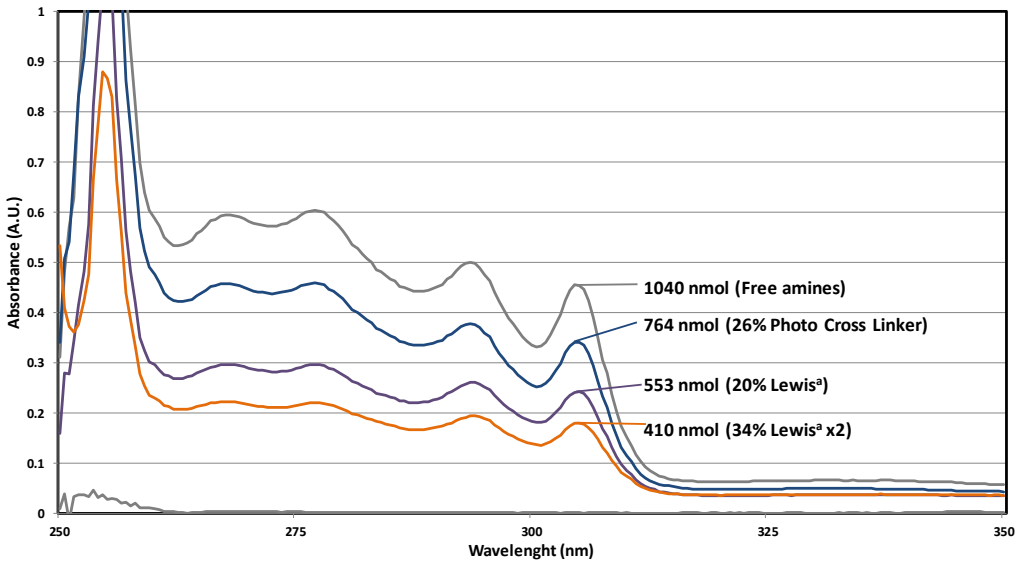
Equivalents used based on suppliers amine content	0	0	1	2	5	10	50
Amount used in nmol	Blank	0	20.6	41.2	103	206	1030
Fmoc numbering of free amines (nmol/mg)	0	831	739	560	438	313	207
% Coverage based on 0 nmol of Acid	0	0	11	33	47	62	75
Theoretical Load (nmol) based on 0 nmol Acid		831	810	790	728	625	-199

Solulink: 41,2 nmol/mg from supplier, using 0,5 mg/reaction. Averaged values (n=2). Loading (mmol/mg) = (Abs_{sample})/ (mg of sample x 1.75*) * Based on ε = 5253 M^{-1} cm^{-1} Formula from Reference: *W. C. Chan, P. D. White, Fmoc Solid Phase Peptide Synthesis, Oxford University Press, Oxford, 2000*



| Figure 2.6 | Coverage control of the amount of functionlised amines on amine-nanoparticles (MPIO) using 3-(4-bromophenyl) propanoic acid Solulink amine coated particles (MPIO) were first reacted with the indicated amounts of 3-(4-bromophenyl) propanoic acid using 0.98 equiv. HATU and 2 equiv. DIPEA. See **section 2.7.3** for the method used. The remaining free amines were reacted with Fmoc-Gly-OH to determine the load of 3-(4-bromophenyl) propanoic acid using a photo spectrometric readout at 305 nm which is indicative of amine-functionlisation (n=2).

These results indicate that either the amount of amines calculated is incorrect - most likely an overestimate - or not every photo-crosslinker molecule is coupled. All the batches of SoluLink particles used in this thesis were determined by the supplier to have 41.2 nmol/mg. Fmoc numbering yielded different loadings for each batch and other amine methods were unsuccessful to determine the amine amount of these particles. Therefore, for each batch the amine content was determined using Fmoc-numbering prior to functionalisation. When particles were treated with ≥15K molar excess of Fmoc-Gly-OH without any coupling agent, no absorbance at 305 was observed indicating that absorbance from the reactions with coupling agent were covalent and that the washing steps were sufficient to remove the excess of reagents used. From these results it appeared that a degree of control over the coverage that can be obtained and an estimate based on the spectroscopic read-outs can be indicative of functionalisation. To generate the desired bi-functional Le[a]-PXL MPIOs, the procedures described in **methods section 2.7.5** and **2.7.6** were used and the results are presented below.



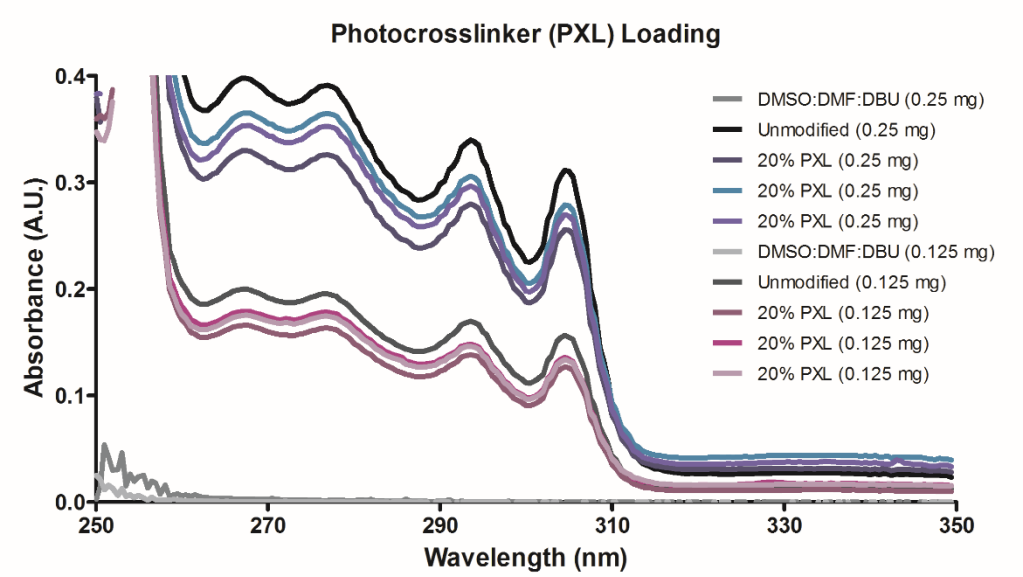
| Figure 2.7 | Amine functionalisation coverage of pulldown particles (MPIO) using the photo-crosslinker and Lewis[a] Solulink amine coated particles (0.25 mg measured as shown) were first reacted with the photo-crosslinker as described in **2.7.3**. Then the remaining free amines were reacted with IME-activated Lewis[a] **2.7.6.** An initial coupling of Lewis[a] yielded in a 20 % load onto the photo-crosslinker containing particles. Another IME-activated Lewis[a] batch was added and resulted in a total Lewis[a] loading of 34%. Fmoc- numbering was performed as described in **2.7.4.** to determine the load using a photo spectrometric read-out at 305 nm which is indicative of amine-functionlisation (n=1). Particles were used for **Chapter 3** pull-down experiments.

The pull-down particles used in **Chapter 3** were made successfully after a two-batch Lewis[a] functionalisation yielding in a 26% loading of the photo-crosslinker and a 34% loading of Lewis[a]. As these reaction conditions were effective in obtaining the desired loading levels, subsequent batches were made and are presented next.

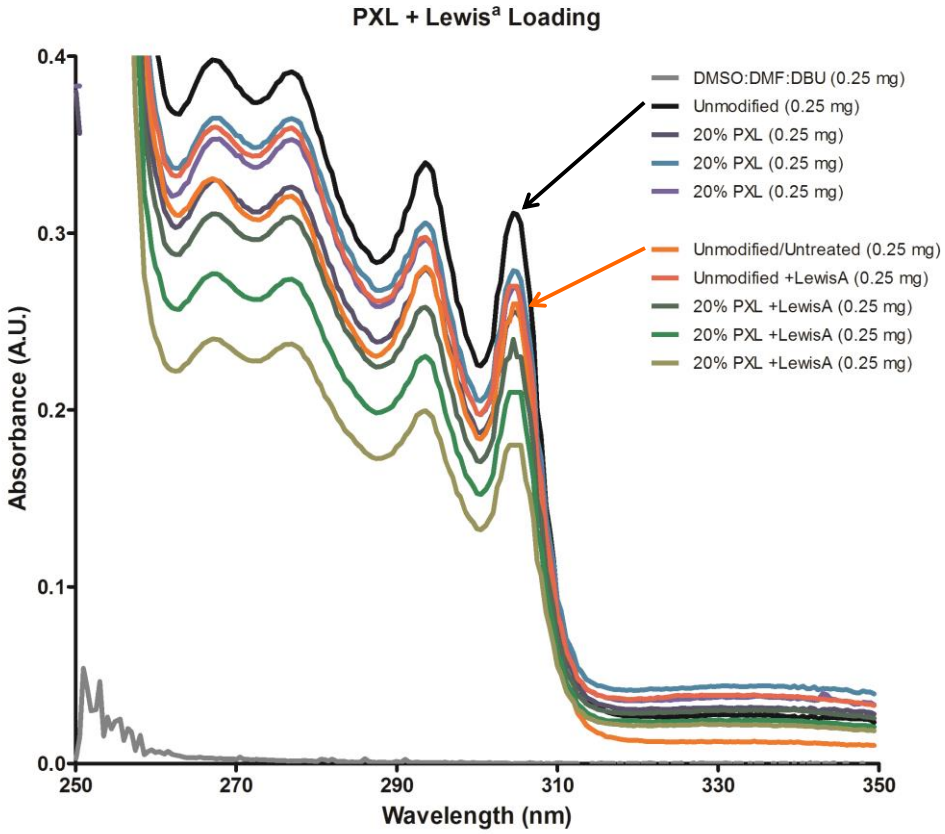
| Table 2.5 | Coverage control of MPIO-NH_2 using substoichiometric amounts of coupling agent and the diazirine photo-crosslinker

Sample Name	Wavelength (305 nm)	nmol/mg	PXL Loading (%)
DMSO:DMF:DBU (0.25 mg) ...	0.000	0	n/a
Unmodified (0.25 mg) ...	0.311	711	0 %
I 20% PXL (0.25 mg) ...	0.256	584	18 %
II. 20% PXL (0.25 mg) ...	0.279	637	10 %
III. 20% PXL (0.25 mg) ...	0.270	617	13 %
DMSO:DMF:DBU (0.125 mg) ...	0.000	0	n/a
Unmodified (0.125 mg) ...	0.157	716	0 %
I. 20% PXL (0.125 mg) ...	0.127	581	19 %
II. 20% PXL (0.125 mg) ...	0.136	621	13 %
III. 20% PXL (0.125 mg) ...	0.134	611	15 %

Numerical values of Fmoc- numbering from graph below. (*n=2*, using 0.5 mg and 0.125 mg of particles).



| Figure 2.8 | Coverage determination of MPIO-NH_2 functionalised with the photo-crosslinker as measured by Fmoc-numbering Solulink amine coated particles (MPIO, 1.5 mg) were first reacted with the photo-crosslinker as described in **2.7.3**. Fmoc- numbering was performed as described in **2.7.4.** to determine the loading using a photo spectrometric read-out at 305 nm which is indicative of amine-functionlisation (n=2, using 0.25 mg and 0.125 mg of particles). See Table above for loading results.



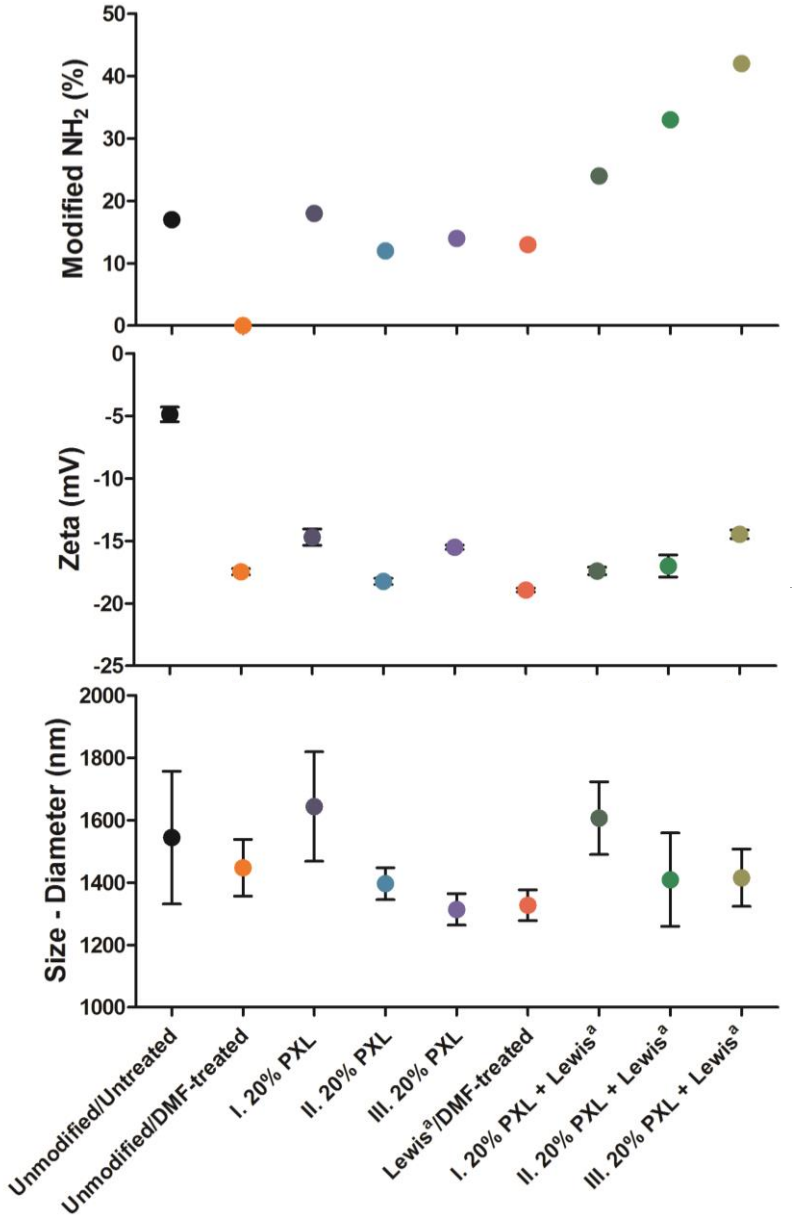
| Figure 2.9 | Coverage determination of MPIO-NH_2 functionalised with the photo-crosslinker and Lewis[a] as measured by Fmoc-numbering Solulink amine coated particles (MPIO, 0.95 mg) were first reacted with the photo-crosslinker as described in **2.7.3** and subsequently functionalised with IME-Lewis[a] as described in **2.7.6**. Fmoc- numbering was performed as described in **2.7.4** to determine the loading using a photo spectrometric read-out at 305 nm which is indicative of amine-functionlisation (*n=1*, using 025 mg of particles). Particles were used for brain pull-down experiments described **2.7.16**. See **Table 2.6** for loading results.

|Table 2.6 | Size (nm), charge (ζ) and coverage (Fmoc) of MPIO-NH_2 covered with a photo-crosslinker and Lewis[a]

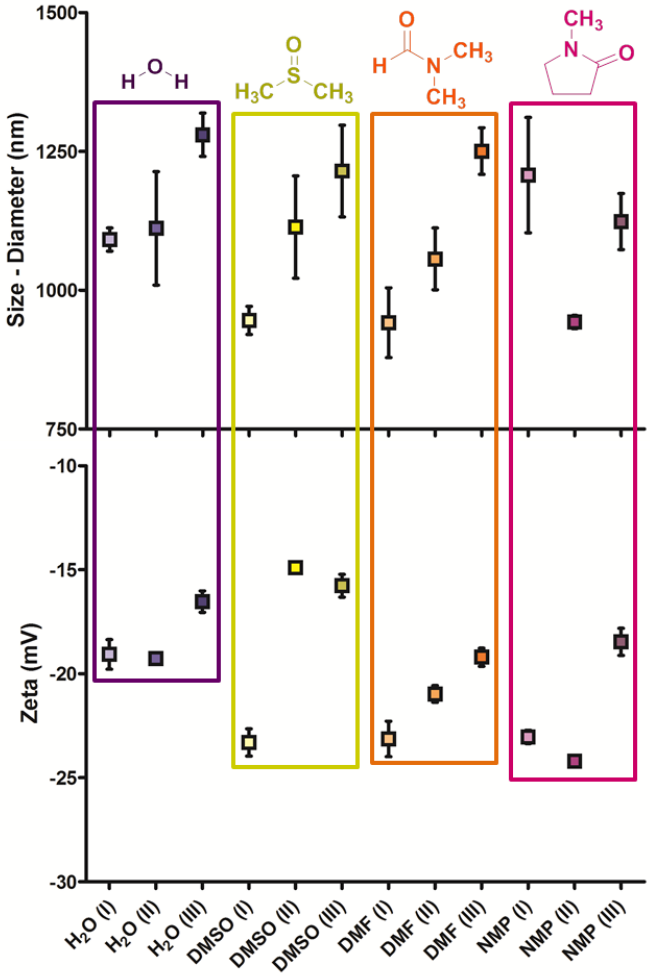
Sample Name …	Diameter (nm)	STDEV ± (nm)	ζ (mV)	STDEV ± (mV)	Fmoc Loading (%) PXL	Fmoc Loading (%) Lewis[a]	Fmoc Loading (%) Total
Unmodified/Untreated …	1544	213	-4.9	0.58	17(!)	---	17(!)
Unmodified/DMF-treated …	1448	91	-17.5	0.25	0	---	0
I. 20% PXL …	1644	176	-14.7	0.66	18	---	18
II. 20% PXL …	1397	51	-18.2	0.25	12	---	12
III. 20% PXL …	1314	50	-15.5	0.17	14	---	14
Lewis[a]/DMF-treated …	1328	49	-18.9	0.15	---	13	13
I. 20% PXL + Lewis[a] …	1607	116	-17.4	0.30	---	6	24
II. 20% PXL + Lewis[a] …	1409	150	-17.0	0.89	---	21	33
III. 20% PXL + Lewis[a] …	1415	92	-14.5	0.35	---	28	42

Size was measured 3 times, using 3 reads/measurement. Zeta (ζ) potential measured in mV (n=3, 10 measurements/run). Numerical values of the graphs above. Size was measured using the Malvern ZetaSizer (Light Scattering plus Zeta Potential Measurement).

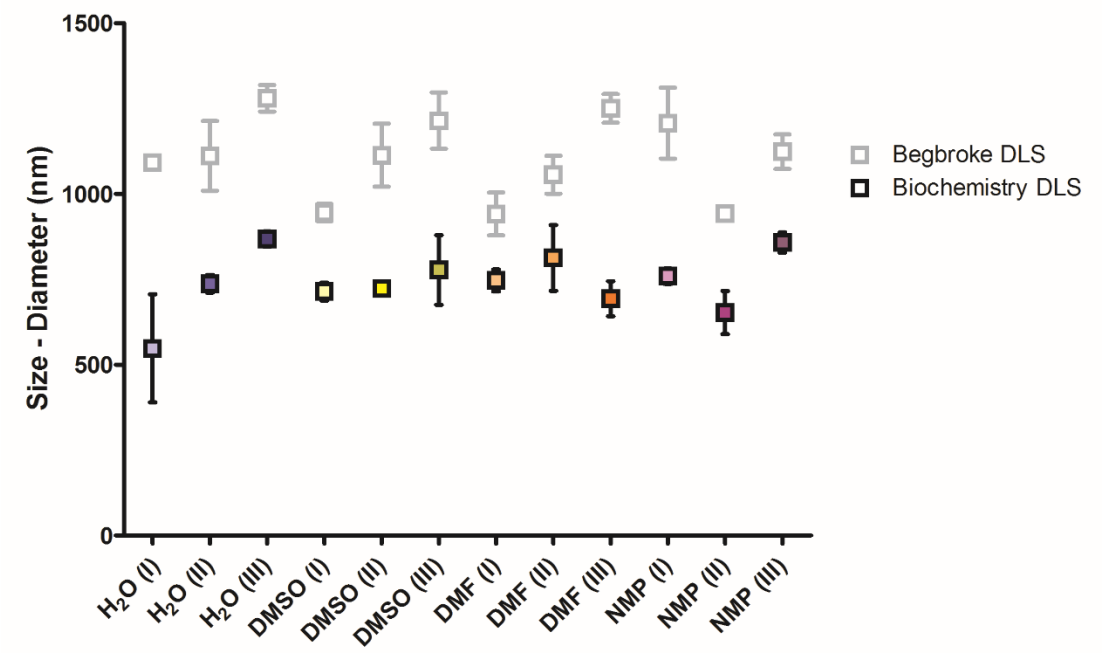
Previously it was suggested that the amount of amines calculated could de*via*te and be not highly accurate. The charge of the particles was anticipated to change upon functionalisation of the positively charges amines with neutral molecules. To determine if other particle characteristics could be indicative of functionalisation, the Zeta (charge) and size (nm) was measured as well. However the results presented in **Figure 2.8, 2.9** and **Table 2.6** revealed that the unmodified, but DMF treated (black line) particles without any coupling agents have more amines than untreated particles. This observation indicates that the particles may 'swell' upon DMF exposure. Although typically DMF and polystyrene are not compatible, the amine functionalised polystyrene iron-oxide nanoparticles were stated by the suppliers to be stable when exposed to DMF and other solvents** (see link in reference list). In order to test this, the particles were exposed to the manual steps (see **Figure 2.27** in the **methods section**) of the protocol (without any PXL, coupling agents or IME-Lewis[a]) whilst exposed to different aprotic solvents, such as NMP, DMSO and DMF and the alkaline buffer used for the IME-coupling. As a control, water was used to assess if the handling may change the surface chemistry of these particles. In addition, the size of the particles deviate significantly from the manufacturers reported size of ~800 nm. The Zeta measurements met the quality parameters from the machine used (concentration of particles etc.). However, when the same machine, after resuspending and flicking the folded capillary cells used for measuring, was used to measure the size of the particles the quality report stated sedimentation and inaccurate measurement. Another size determining machine was assessed as well to measure the size of these particles and if swelling occurs (size increase). This will be presented next in the **Figures 2.10**, **2.11** and **2.12**.



| Figure 2.10 | Overview of amine-coverage (Fmoc), charge (ζ) and size (nm) of MPIO-NH^2 particle characteristics presented in Table 2.6 Particle characterization of 3 batches (labelled I, II, III) modified with the photo-crosslinker (PXL) and subsequently Lewis[a], including an unmodified/untreated control which was only exposed to the Fmoc-numbering procedure and an unmodified/DMF-treated control which was exposed to the same coupling procedures for the photo-crosslinker without the coupling agents and photo-crosslinker. Top to bottom: **Top.** Percentage of amines covered based on Fmoc-numbering. Note: Unmodified/Untreated (not pre-treated with DMF) particles appear to have a 'loading' when compared to Unmodified/DMF treated. Calculated amount of amines for unmodified/untreated is 590 nmol/mg and for Unmodified/DMF treated is 711 nmol/mg (0.25 mg based, *n=1*). **Middle.** Zeta (ζ) potential measured in mV (*n=3, 10 measurements/run)*. Note: Unmodified/Untreated (i.e. not pre-treated with DMF) particles appear to have a higher ζ-potential when compared to Unmodified/DMF treated. **Bottom.** Size distribution of the particles appeared to larger than the 800 nm stated by the supplier (*n=3, 3 measurements/run)*. Error bars are represented as standard error.



| Figure 2.11 | Overview of size (nm) and charge (ζ, mV) of the different solvent-treated MPIO particles using a Malvern Zetasizer Nano ZS To determine the effects of different solvent treatments on the particle properties, the particles underwent the steps of the modification protocols without the coupling agents or functional groups. See **section 2.7.7** for the methods used. Batches were treated with the indicated solvents. Different treatments for the particles (I), (II) and (III) were measured in triplicate (n=3). **Top.** Size distribution of the particles (*n=3, 3 measurements/run)*. Note the size de*via*tion from the 800 nm stated by the supplier. **Bottom.** Zeta (ζ) potential measured in mV (*n=3, 10 measurements/run)*. Error bars are represented as standard error.



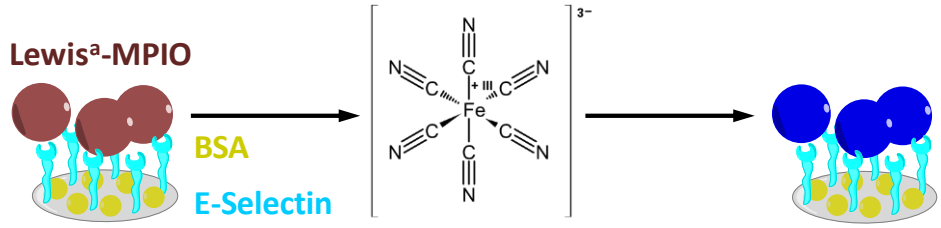
| Figure 2.12 | Size measurement comparison of the two different DLS machines Size data from **Figure 2.13** (Biochemistry DLS) and **Figure 2.12** (Begbroke DLS) summarized. There is a large measurement difference between the two machines. Solulink states their particles are 0.8 µm and when using the Biochemistry DLS machine, the stated size corresponds approximately (Size range 741 nm ± 88 nm). But when using the Begbroke machine, the particles are almost twice the size. For future size measurements use the Biochemistry DLS machine.

Previously, different particle sizes and charges were observed when the photo-crosslinker molecules and Lewis[a] molecules were introduced onto the particles. Indicating that treatment and both functionalization could have an effect on the physical properties of these particles. The particles were treated with different aprotic solvents (DMF –the solvent used for PXL couplings and Fmoc-numbering, DMSO, NMP) and water to assess the effects on the physical properties of these particles. **Figure 2.11** and **2.12** shows that both size and zeta (mV) change upon different treatment procedures used for introducing PXL and Lewis[a], but these differences could be within the scatter/error of measurement. In addition, two DLS machines were compared and the DLS machine at Biochemistry is more accurate than the DLS at Begbroke and this machine will be used for future measurements. The results are not conclusive, but there seems to be a trend that when the particles are stored in their respective solvents prior to the measurement (treatment (**III**)) and only are solvent exchanged to water (the solvent used for measuring charge and size) without vigorous, shaking their size and charge are more affected. The charge is decreased and this treatment (**III**) seems to increase the size of the particles too. It is likely that the vigorous shaking prior to measurements used in treatment (**I)** and (**II**) prevents the particles from swelling and that the surface chemistry might be effected too (see **Figures 2.9** and **2.11**). For future reference, for each step performed an 'unmodified' batch should be included for every modification and measurement. Moreover, other methods should be sought to better characterisze these

nanoparticles during the reaction conditions used. In addition, the exposure of aprotic solvents makes surface functionalisation difficult and other methods to assess the reactivity of both the photo-crosslinker and Lewis[a] on the MPIOs are presented in **section 2.3.5**.

2.3.5 Determining Lewis[a] functionalisation levels of MPIO with an ELISA-based method

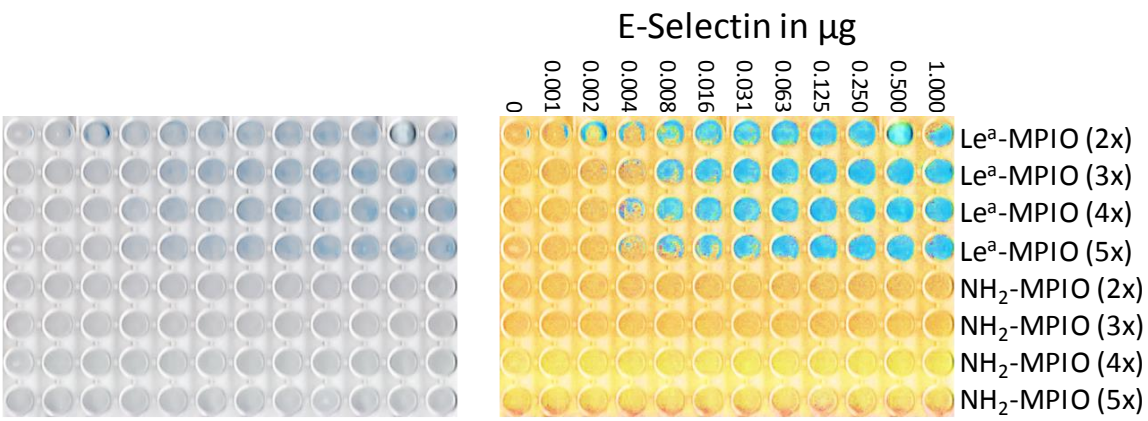
As shown in **Figure 2.8**, the Fmoc-numbering can be perfomed with a minimal of 0.125 mg of particles. For the Lewis[a] and Lewis[b]-MPIOs a more efficient loading determination method was sought. Using the principles of the Perls' Prussian Blue stain, an ELISA based method, using E-Selectin coated wells was developed. This allowed batches to be rapidly screened for similar loading levels. Particles with similar levels were pooled and collectively determined for their loading levels using the established Fmoc-numbering method and were used in the MRI experiments described in **Chapter 3**.



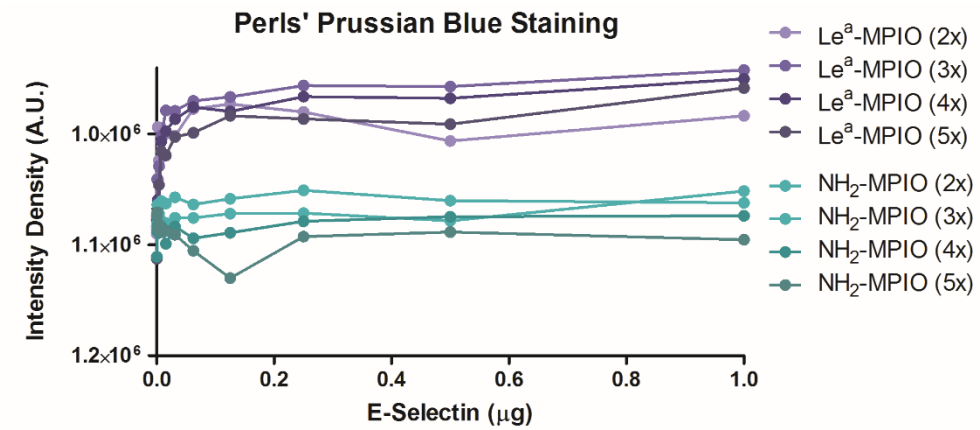
| Figure 2.13 | Schematic of the assay principle using the Perls' Prussian Blue stain
Lewis[a]-MPIOs are bound to E-Selectin coated wells and are invisble to the naked eye. To visualise the iron present in the MPIOs potassium ferrocyanide and acid are used to form a blue complex of hydrated ferric ferrocyanide deposits *in situ* that can be seen by the naked eye and is semi-quantifiable when used with a reference.

To establish if the screening method was sensitive towards detergent and if the binding could be disrupted by vigorous washing steps, the wells of the E-Selectin coated ELISA plate were incubated with Lewis[a]-MPIO and treated differently as shown in **Figure 2.14.** Wells were washed vigorously at the indicated times (…x) and showed that the washing has a non-significant effect on the binding. As E-Selectin is a C-type lectin which requires Ca^{2+} in order to bind Lewis carbohydrates, the influence of calcium-dependence of MPIO-Lewis[a] binding was assessed by using the chelator EDTA to disrupt this binding. This is shown in **Figure 2.15**. Wells were washed and incubated with PBS+EDTA or PBS+Tween and washed 3x with the indicated diluent and showed that the binding of Le[a]-MPIO to E-Selectin is Ca^{2+}-dependent.

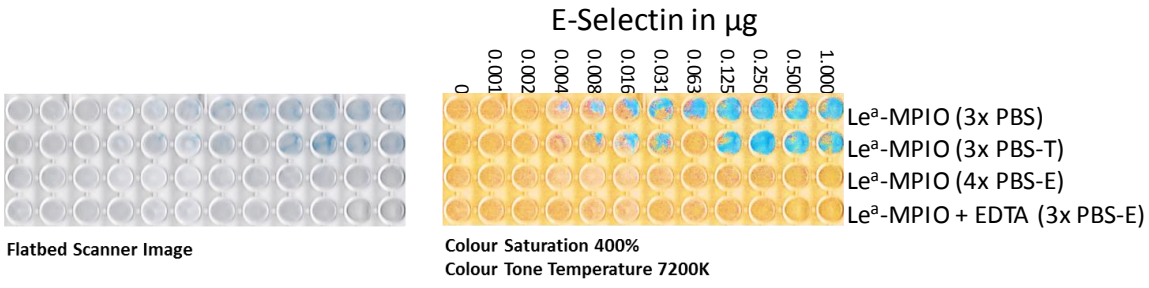
A



B

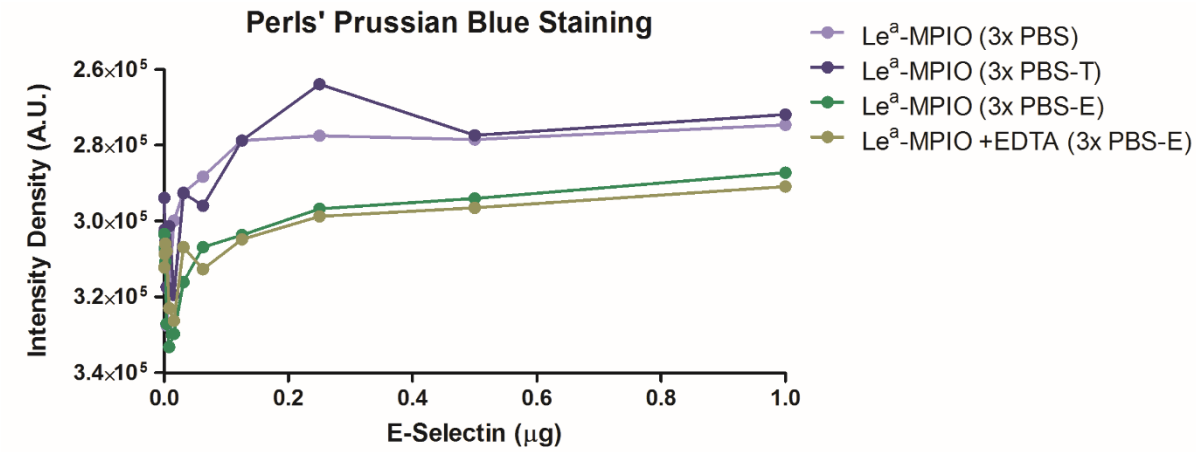


| Figure 2.14 | The influence of washing on the E-Selectin : Lewis^a-MPIO interaction and binding measured by the Perls' Prussian Blue ELISA method **|A|** Binding of Lewis^a-MPIO to rat recombinant E-Selectin FC-chimera proteins bound to a high binding ELISA plate can be observed by the naked eye. Scanned images of the plate analysed and colour enhancement for display purposes shows the binding in the top 4 rows with the highest concentration of E-Selectin on the right and the different treatements as specified in **section 2.7.8**. **|B|** The plotted values are from the scanned images where the pixel intensity density was calculated per well using ImageJ. The (..x) indicated the amount of washes used as specified in **section 2.7.8**.



A

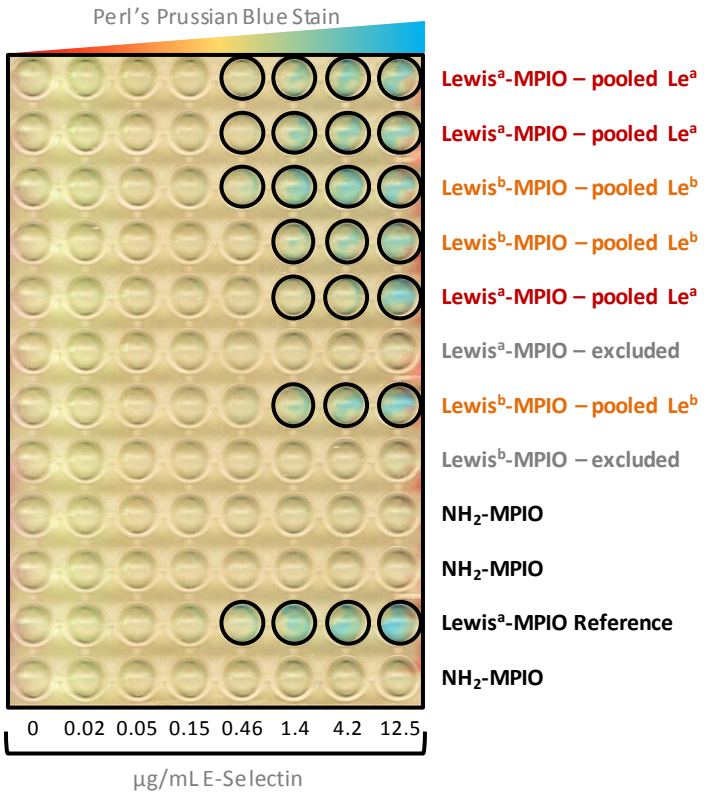
B



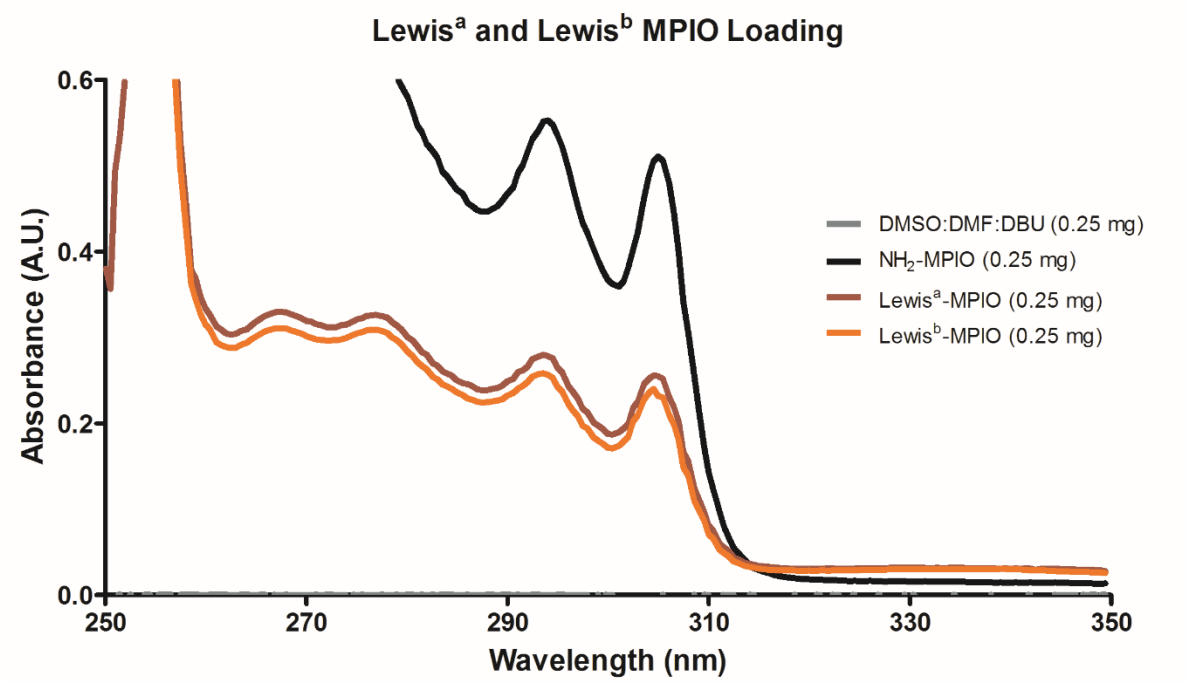
| Figure 2.15 | The influence of Calcium-chelation on the E-Selectin : Lewis^a-MPIO interaction and binding measured by the Perls' Prussian Blue ELISA method

|A| Binding of Lewis^a-MPIO to rat recombinant E-Selectin FC-chimera proteins bound to a high binding ELISA plate treated with detergent and a chelator can be observed by the naked eye. Scanned images of the plate analysed and colour enhancement for display purposes shows the binding in the 4 rows shown with the highest concentration of E-Selectin on the right and the different treatements as specified in **section 2.7.8**. EDTA (PBS-E) disrupts the binding between E-Selectin and the Lewis^a-MPIO as seen by the lack of blue precipitate. **|B|** The plotted values are from the scanned images where the pixel intensity density was calculated per well using ImageJ. The (..x) indicates the buffers with either a detergent (T, for Tween) or a chelator (E, for EDTA) and the amount of washes used as specified in **section 2.7.8**.

Using this method, semi-quantitatively Lewis[a]-MPIO binding can be assessed. The binding of the particles to E-selectin is specific, as shown by the removal of calcium from E-Selectin and the absence of Lewis[a]-MPIO binding in the BSA-only treated wells. This method was subsequently used to screen several Lewis[a] and Lewis[b]-MPIO batches for their binding strength, comparing them with particles with a known (Fmoc-numbering determined) Lewis-reference. This allowed screening of batches with minimal material (≥ 10x less material required than Fmoc-numbering, 0.01 mg vs 0.125 mg minimal for Fmoc-numbering). Subsequently multiple small aliquots (ranging from 1-1.5 mg of MPIO/batch) from a single MPIO batch were activated with IME-Lewis[a] and IME-Lewis[b]. Batches with similar binding strength as the reference batches were pooled and then collectively determined for their functionalisation levels using Fmoc-numbering. These particles were used for the MRI experiments presented in **Chapter 3**.



| Figure 2.16 | Rapid screening method for Lewis[a] and Lewis[b] functionalised MPIO batches using the Perls' Prussian Blue ELISA method Scanned image of a plate to test the binding of Lewis carbohydrate MPIO to rat recombinant E-Selectin bound to a high binding ELISA plate. Screen was used to rapidly determine batches with similar loading levels (Lewis[a]-MPIO reference 40%). Batches were pooled and the collective loading level was determined with Fmoc-numbering, see **Figure 2.17**



| Figure 2.17 | Graph of the measured coverage of MPIO-NH_2 and Lewis[a] and Lewis[b] functionalised MPIO using Fmoc-numbering Solulink amine coated particles (MPIO) were reacted with IME-Lewis[a] and IME-Lewis[b] as described in **2.7.10**. Fmoc- numbering was performed as described in **2.7.4** to determine the loading using a photo spectrometric read-out at 305 nm which is indicative of amine-functionlisation (n=1, using 0.25 mg of particles). See **Table 2.7** below for numerical loading results.

|Table 2.7 | Coverage of MPIO-NH2 and Lewis[a] and Lewis[b] functionalised MPIO measured by Fmoc-numbering

Sample Name	Wavelength (305 nm)	nmol/mg	Lewis Loading (%)
DMSO:DMF:DBU (0.25 mg) ...	0.000	0	n/a
NH_2-MPIO (0.25 mg) ...	0.505	1155	0 %
Lewis[a]-MPIO (0.25 mg) ...	0.251	575	49 %
Lewis[b]-MPIO (0.25 mg) ...	0.230	525	54 %

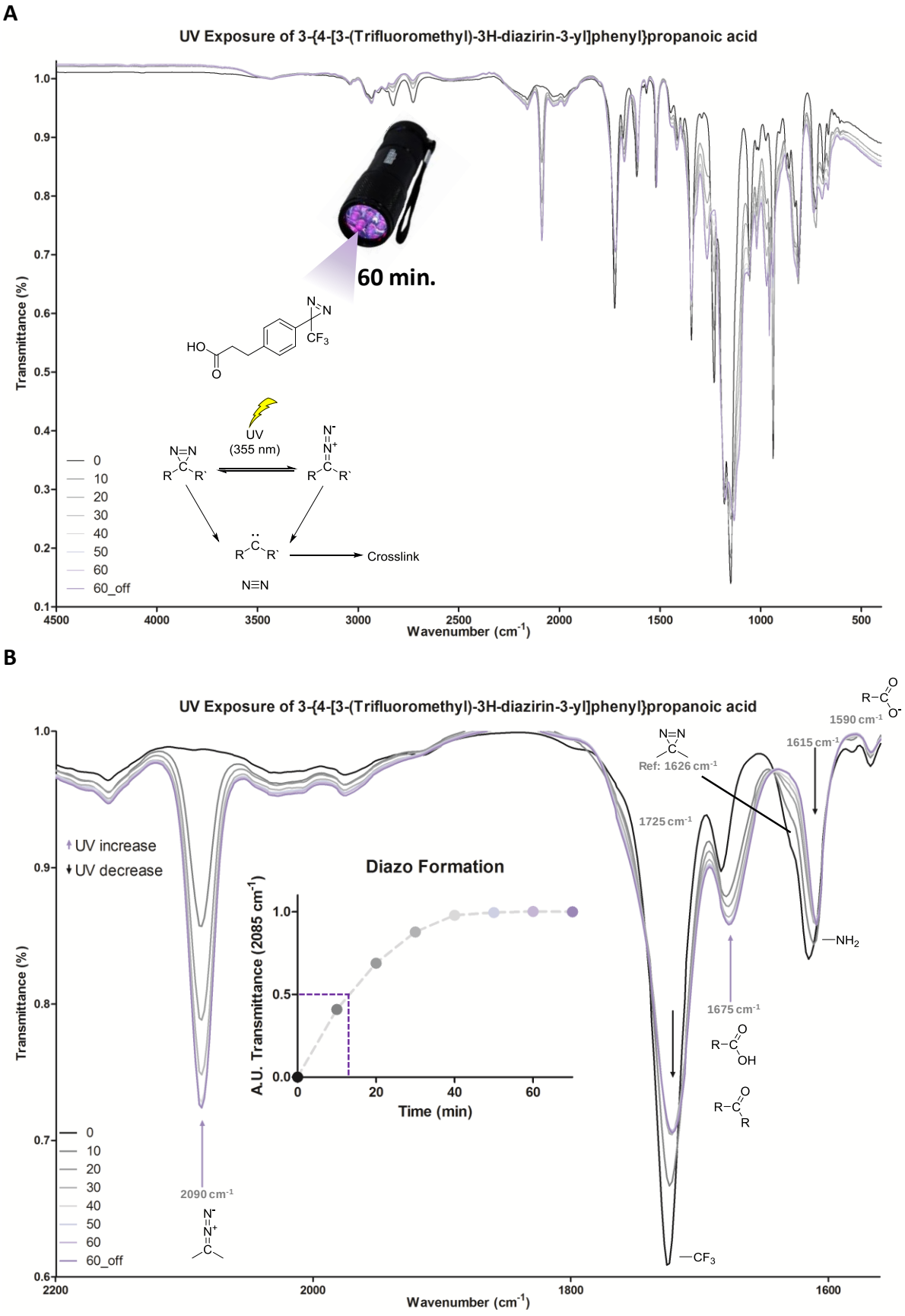
2.4 | DETERMINING THE PHOTO-CROSSLINKER REACTIVITY AND EFFECTIVENESS ON NANOPARTICLES

2.4.1 UV activation of trifluoromethyl-diazirin-phenyl-propanoic acid and the photo-crosslinker on MPIOs

The amine functionalisation of the photo-crosslinker onto the MPIOs did not determine if the diazirine could be UV-activated onto the nanoparticles in order to covalently trap proteins interacting with Lewis[a] when both are present on the MPIO. If the Lewis[a] interacting proteins could be covalently trapped with the photo-crosslinker it would allow to aid in proteomics sample processing and identification. The photo-crosslinker molecule synthesized was exposed to UV light and monitored by FT-IR to determine its reactivity. This allowed observing a reported IR-frequency that could be used to monitor the activity of the photo-crosslinker on nanoparticles [307]. In addition, proof-of-principle cross linking experiments, using BSA, were executed to determine the crosslinking efficiency of the photo-crosslinker towards a general protein at high concentrations. To conclude, an *in vivo* injection of bi-functionalised particles and PXL-functionalised and an *ex vivo* isolation method were trialled and optimised for future experiments.

2.4.2 UV activation of trifluoromethyl-diazirin-phenyl-propanoic acid measured by FT-IR

As shown in **Figure 2.19**, IR is an informative technique to observe the formation of a diazo-intermediate using the synthesized trifluoromethyl-diazirin-phenyl-propanoic acid **[P9]**. Several IR-active peaks are observed upon UV irridation, including the reported IR-frequency at 1625 cm^{-1} [307]. Structures indicated in **Figure 2.18 B** are IR-active groups. Although a change in the reported diazirine group can be observed, the formation of the diazo-species at 2090 cm^{-1} has a more distinct IR-peak than the diazirine. Monitoring the IR spectrum, whilst irradiating with a 3W UV-lamp, a 50% conversion rate was observed around 13 minutes and the recorded spectral changes could be used to monitor photo-crosslinking efficiencies onto nanoparticles which will be presented next.



| Figure 2.18 | The formation of a diazo intermediate upon UV exposure of the photo-crosslinker

|A| Full FT-IR spectrum of the trifluoromethyl-diazirin-phenyl-propanoic acid exposed to UV-light as in **section 2.7.11**.
|B| The formation of a diazo-intermediate (2090 cm^{-1}) was observed. 50% of the intermediate is formed in 13 minutes.

2.4.3 UV activation of photo-crosslinker modified MPIOs measured by FT-IR

Previously the the trifluoromethyl-diazirin-phenyl-propanoic acid **[P9]** showed several IR-active peaks indicative of UV-activation, see **Figure 2.18**. To assess if the photo-crosslinker on MPIOs can be activated in a similar manner, the PXL-MPIOs were exposed to UV irradiation and measured by IR afterwards see **section 2.7.12** for more details. Acetic acid was added for some reactions in order to observe an additional acetate peak that could indicate crosslinking. The formation of a diazo-intermediate was observed previously with the PXL **[P9]** around 2090 cm^{-1}. PXL modified particles treated with UV light and acetic acid display a broad stretch around the same region with multiple peaks. However, these results are likely to be subject to measuring artefacts. For example, when modified nanoparticles were used, some IR-frequencies such as the stretch at 1605 cm-1 could indicate the diazirine is present and the 1495 cm-1 stretch for the amide-bond formation between the photo-crosslinker and the amines of the MPIO. However, treating the PXL-MPIO with acetic acid did not result in a clear IR spectrum with an acetate peak nor the disappearance of the 1605 cm^{-1}diazirine peak. As the nanoparticles are very dark brown and contain iron-oxide, the transmittance is not as good as for the PXL only, making recording IR spectra of these particles less informative. In addition, the PXL-MPIO (UV-AA) samples could have D_2O contamination, masking or obscuring the diazo-peak region [308]. Therefore a functional read-out was sought to determine the reactivity of the diazirine on the MPIO, where the model protein BSA was covalently trapped onto the modified nanoparticles and quantitatively measured by trypsin peptide cleavage. These experiments will be discussed next.

2.4.4 Photo-crosslinking of BSA to particles to determine crosslinking efficiency

To determine if the photo-crosslinker covalently attached to the magnetic nanoparticles can trap proteins, the particles were incubated with the globular protein BSA at a high concentration whilst being exposed to UV-light. Determining if the photo-crosslinker can trap the protein onto the nanoparticles, enzymatic cleavage of particle-bound BSA was determined spectroscopically. The results of these experiments are presented below and the methods used are described in **2.7.14** in the **methods section** of this chapter.

| Table 2.8 |Photo-crosslinked BSA peptides can be cleaved from PXL-MPIO with trypsin

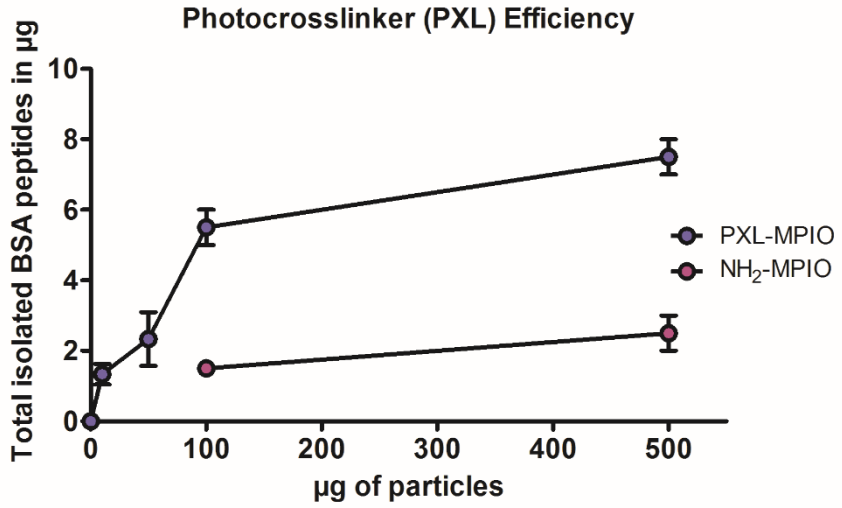
	Measured mg/mL			Measured - Trypsin µg/mL		
Number of measurements	**1**	**2**	**3**	**1**	**2**	**3**
0. Trypsin	0.04	0.05	0.06	-	-	-
1. 50 µL 500 µg of particles (368 nmol PXL)	0.20	0.19	0.18	200	190	180
2. 10 µL 100 µg of particles (73.6 nmol PXL)	0.16	0.14	0.15	160	140	150
3. 5 µL 50 µg of particles (36.8 nmol PXL)	0.10	0.09	0.07	100	90	70
4. 1 µL 10 µg of particles (7.4 nmol PXL)	0.07	0.07	0.06	70	70	60
5. 50 µL 500 µg of particles (NH_2)	0.09	0.10	0.08	90	100	80
6. 10 µL 100 µg of particles (NH_2)	0.07	0.07	0.07	70	70	70

Absorbance at 280 nm was used to perform calculations. Samples were blanked against ABC buffer used for trypsin cleavage ad for yields the absorbance of trypsin was subtracted from the signal measured in the samples (1 to 6).

| Table 2.9 |Efficiency of photo-crosslinking and the amount of PXL molecules present per BSA molecule

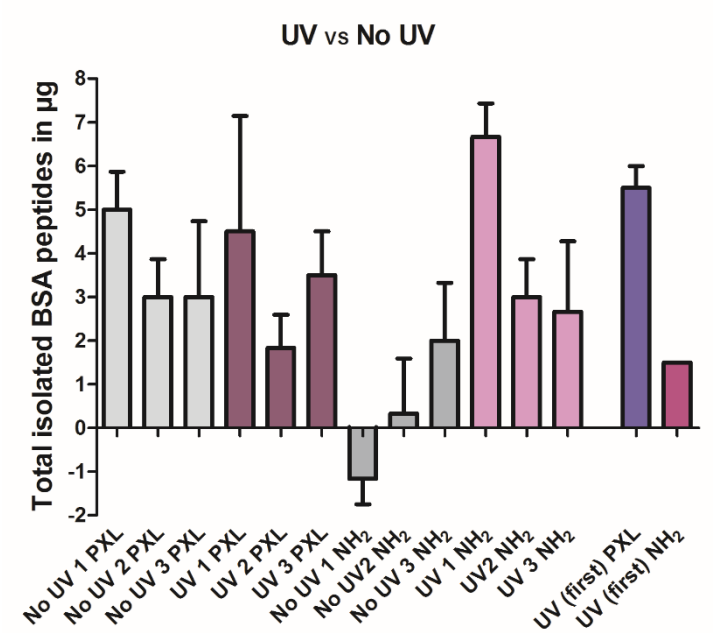
	pmol BSA digested	BSA molecules present	nmol PXL used	PXL molecules present	PXL molecules per BSA molecule
1. 50 µL 500 µg of particles (368 nmol PXL)	113	6.81×10^{13}	368	2.22×10^{14}	3.26
2. 10 µL 100 µg of particles (73.6 nmol PXL)	83	5.00×10^{13}	73.6	4.43×10^{13}	0.89
3. 5 µL 50 µg of particles (36.8 nmol PXL)	35	2.11×10^{13}	36.8	2.22×10^{13}	1.05
4. 1 µL 10 µg of particles (7.4 nmol PXL)	20	1.20×10^{13}	7.4	4.46×10^{12}	0.37
5. 50 µL 500 µg of particles (NH_2)	38	2.29×10^{13}	0	0.00	0.00
6. 10 µL 100 µg of particles (NH_2)	23	1.39×10^{13}	0	0.00	0.00

Amount of PXL molecules bound to BSA was calculated using 6.0221415×10^{23} for Avogadro's number.



| Figure 2.19 | Comparison of trypsin cleaved, isolated BSA peptides from PXL- and NH_2-MPIO incubated with BSA and UV light Non-specific BSA binding is observed for NH_2-MPIO, however a 2.9 and 3.6 times increase is observed for the isolation of BSA peptides when using 500µg and 100 µg of amine particles containing 43% PXL are used. Error bars represent standard de*via*tion.

In order to examine if the particles are capable of crosslinking, BSA was crosslinked to the particles and cleaved off using trypsin. A high concentration of BSA (145.69 mg/mL) was used and different concentrations of particles with (43% loading) and without photo-crosslinker molecule were incubated with the BSA under UV-irradiation. The trypsin cleaved peptides that came off the PXL particles after several washing steps (**Table 2.12** and **Figure 2.27**, see **methods**) was 3 times higher than the plain amine particles, see and **Table 2.9 and 2.19**. To assess the specificity of this reaction, the experiment was repeated without UV light and the results are presented next.



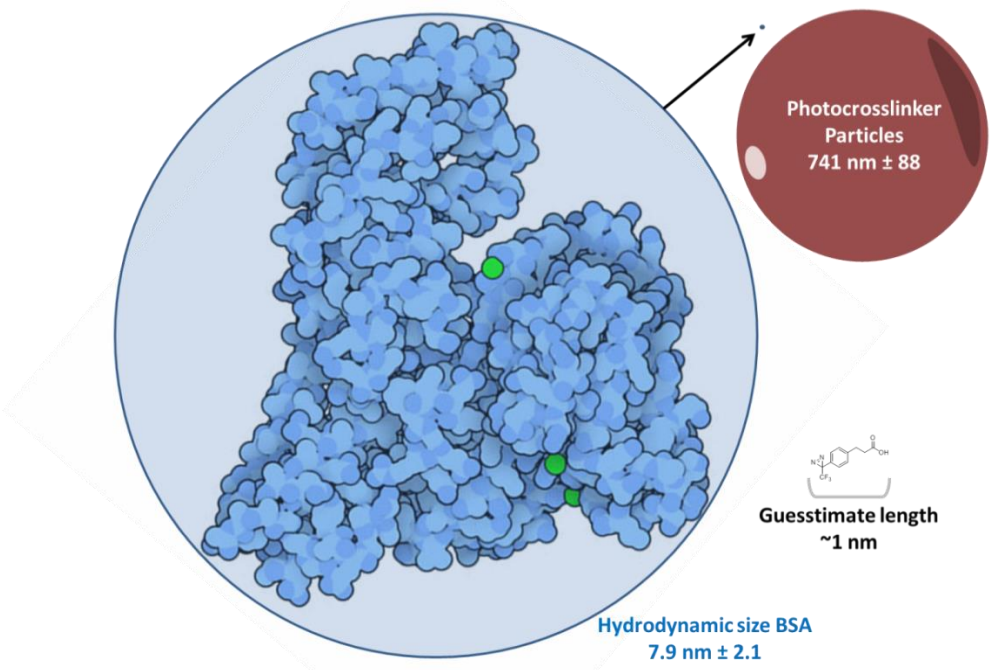
| Figure 2.20 | Comparison of isolated BSA peptides from UV-treated and non UV-treated PXL- and NH_2-particles incubated with BSA 4 particle groups performed in triplicate (and measured in triplicate) were measured for the ability to crosslink BSA. First no UV PXL (1 to 3, see **table 2.10** for PXL loading levels) was tested if the particles modified with the photo-crosslinker can bind BSA in the absence of UV light. Second the UV PXL (1-3) particles were incubated with BSA in the precence of UV light to test if UV light increases the amount of BSA on the particles. Third and last, the no UV and UV treatment was applied to the unmodified amine-MPIO (NH_2) as well in the presence of BSA. Non-specific BSA binding is observed for NH_2-MPIO when UV-treated. Non-UV treated PXL-MPIO also non-specifically bound more BSA than Non-UV treated NH_2-MPIO. A comparison is made by using the data from the previous experiment (100 µg of particles). Error bars represent standard de*via*tion.

| Table 2.10 | Trypsin-cleaved BSA peptides from PXL-MPIO and NH_2-MPIO treated with UV light and a non UV-treated control

Sample	PXL Loading	Average peptide yield UV	Average peptide yield No UV
1 PXL	41%	4.5	5.0
2 PXL	12 %	1.8	3.0
3 PXL	26 %	3.5	3.0
1 NH_2	0%	6.7	-1.2
2 NH_2	0%	3.0	0.3
3 NH_2	0%	2.7	2.0
PXL	43%	5.5	*n.d.*
NH2	0	1.5	*n.d.*

Total peptide yield of 100 µg of particles. Absorbance at 280 nm was used to perform calculations. Samples were blanked against ABC buffer used for trypsin cleavage and for yields the absorbance of trypsin was subtracted from the signal measured in the samples.

When the experiment was repeated with an added control of *no UV* treatment it was established that the presence of UV on unmodified NH_2-MPIO can cause non-specific BSA retention on the particles (see **Figure 2.20** and **Table 2.10**). Additionally, *no UV* treatment also causes BSA to interact with the MPIO (both amine and PXL modified). Therefore it is not clear if the photo-crosslinking has worked, using this type of analysis and experimental set-up. The dark coloured iron-oxide particles might quench the UV-irradiation necessary for the diaziridine to crosslink to interacting proteins. Or the photo-crosslinker is quenched by the surrounding buffer/water layer around the particles, preferring to hydrolyse instead of protein crosslinking. Additionally, the MPIO (both amine and PXL modified) bind BSA non-specifically, which makes this method unlikely to succeed. Potentially, the Lewis[a]-moiety may be required to direct the Lewis[a]-binding protein in close proximity to the photo-crosslinker to gain more specificity onto the nanoparticles to cross link, **Chapter 3** explores the proteome of IL-1β activated brain microvascular endothelial cells incubated with the bi-functional pull-down particles.



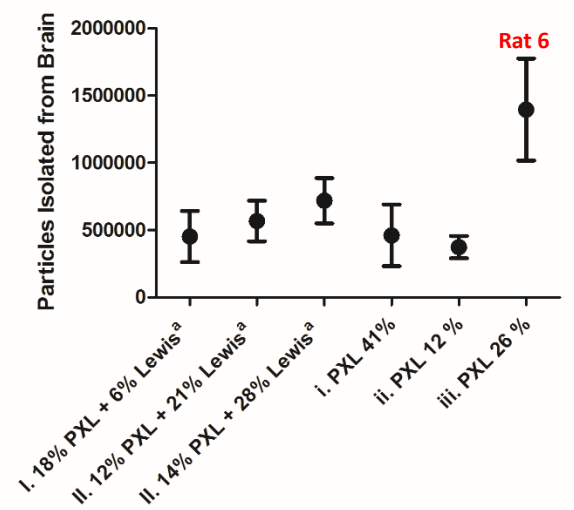
| Figure 2.21 |Size considerations of the nanoparticles, BSA and the photo-crosslinker
Model to show the sizes of the components used in the photo-crosslinking of BSA to particles to determine cross linking efficiency. BSA is 8 times bigger than the PXL molecule and BSA is a 100 times smaller than the particles.

2.4.5 Optimising MPIO recovery from brain tissue

Bi-functional MPIOs with both Lewis[a] and the photo-crosslinker have the potential to identify novel Lewis[a] interacting proteins *in vivo*. When injected into animals with IL-1β induced brain inflammation, the Lewis[a] targets the particles towards the site of inflammation as shown in **Figure 1.4** in **Chapter 1**. The addition of a photo-crosslinker could trap these interactions and allow proteomic identification of the proteins involved in the binding. This section described the experiments performed to optimize the recovery yield of these MPIOs from brains of animals injected with the synthesized bi-functional MPIOs, brain homogenate and testing different magnetic isolation methods in order to obtain sufficient material for proteomic identification.

2.4.6 Optimising MPIO recovery from brain tissue using bi-functional nanoparticles and photo-crosslinker nanoparticles

As described in the **methods section 2.7.16**, the left, IL-1β activated, striatum was obtained using the dissection guide presented in **Figure 2.28**, see **methods**. The isolated brain section was then homogenised to isolate the magnetic nanoparticles. 5 of the 6 animals were treated by cannulating a saline solution containing (Lewis[a]+PXL or PXL) MPIOs (0.5 mg total in sterile saline) into the carotid artery. Rat 6, highlighted in red, was first saline flushed *via* the intracarotid injection before the MPIO injection, thus having no blood present at the time of MPIO injection. Brain homogenate from the isolated brains was incubated with a magnet (Dynal, Fisher Scientific) to pellet the particles present in the brain. Subsequently the particles were counted and the yields were calculated and shown below. To increase the recovery yield, different isolation methods and dilutions of the brain homogenate resulted in an optimised method.



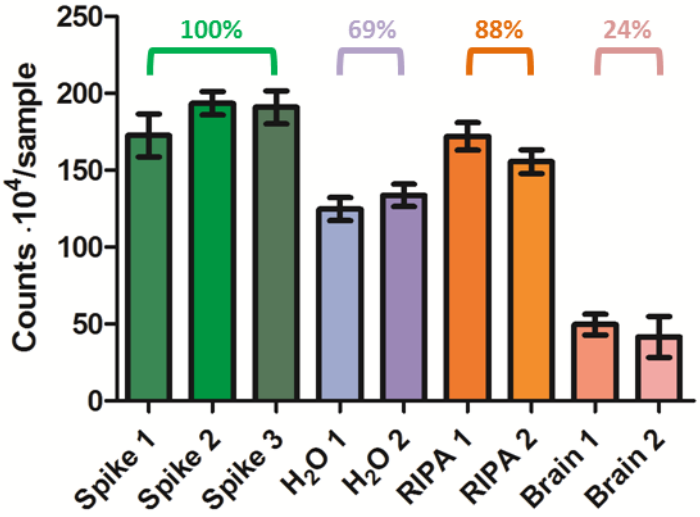
| Figure 2.22 | Recovery of particles from the left IL-1β inflamed striatum from animals injected with bi-functional MPIOs and photo-crosslinked modified MPIOs Recovery numbers of particles isolated from brain (left striatum as shown/described above). I-III are animals treated with bi-functional particles (Lewisa/photo-crosslinker-MPIO) and should have an increase in numbers due to Lewis[a] targeting. i-iii are animals treated with the photo-crosslinker MPIOs. Note: The increased numbers of isolated particles from **rat 6** that was treated differently by pre-clearing the brain from blood before MPIO injection. See methods **section 2.7.16** for more details.

| Table 2.11 | Recovery of the particles from the left IL-1β inflamed striatum from animals injected with bi-functional MPIOs and photo-crosslinked modified MPIOs

Rat	Recovered mass (µg)	STDEV ± (µg)	Recovery (%)	Particles
1	0.20	0.08	0.04 %	I. 18% PXL + 6% Lewis[a]
2	0.25	0.07	0.05 %	II. 12% PXL + 21% Lewis[a]
3	0.32	0.07	0.06 %	II. 14% PXL + 28% Lewis[a]
4	0.20	0.10	0.04 %	i. PXL 41%
5	0.16	0.04	0.03 %	ii. PXL 12 %
6(*)	**0.61**	**0.17**	**0.12 %**	**iii. PXL 26 %**

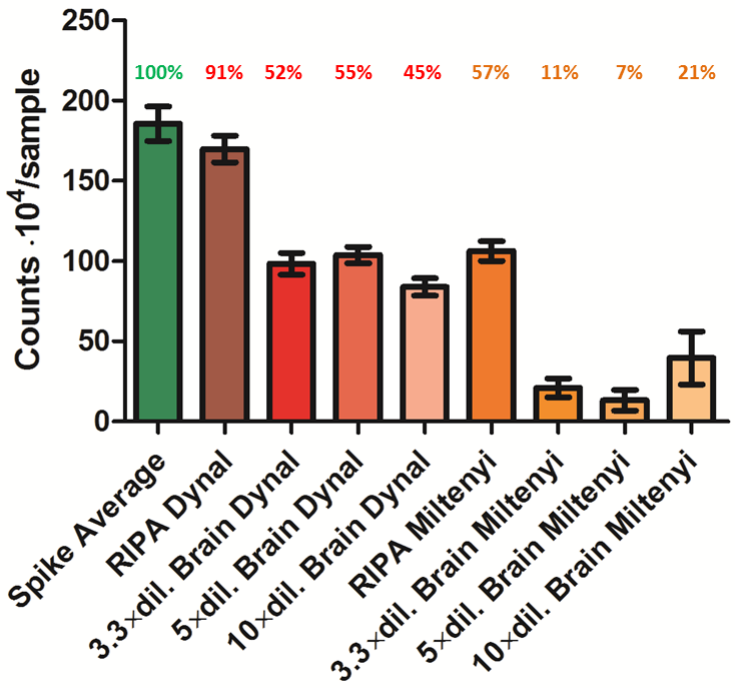
Recovered mass was calculated by dividing the particle numbers isolated by the number of particles/µg (2.3×10^6). Recovery (%) was calculated by dividing the recovered mass by the mass of particles injected (0.5 mg = 500 µg) multiplying the number by a 100%. Note: **Rat 6** was treated differently as mentioned in the methods. Particles used were as before.

Low recovery yield was obtained from the left striatum that was activated with IL-1β. Also no difference between the PXL-MPIO and PXL-Lewis[a]-MPIO was observed; indicating no increased targeting with Lewis[a] towards the inflamed endothelium. Rat 6 was treated differently as described in the methods section. This method increased the yield approximately two-fold. Nonetheless, these numbers were very low and not enough for proteomic identification. Therefore the isolation method was optimised by spiking NH_2-MPIO into different buffers and brain homogenate to assess the recovery yield and improve the isolation method. This is shown in **Figure 2.23** and **Figure 2.24**.



| Figure 2.23 | Spike recovery of particles from H_2O, RIPA buffer and brain homogenate to assess isolation yield A known amount of particles was spiked into H_2O, RIPA buffer and brain homogenate and then isolated using a magnet, see **section 2.7.17.** Counted (left axis) spike samples were set to 100% (green). Each sample was performed in duplicate (except the spike only, not using any isolation medium) and counted twice and for each count the 4 corner squares were used for counting (*n=8*), see methods for particle counting protocol. Error bars represent standard de*via*tion.

Using H_2O as an isolation medium, the recovery was 69% (lilac), indicating that RIPA buffer (orange) yield 88%, decreases the surface tension, maintaining particles better in suspension for increased isolation. When using brain homogenate in RIPA buffer, the isolation yield was 24%. To improve the isolation yield of the particles from brain homogenate, different dilutions of brain homogenate in RIPA buffer were trialled and different magnetic isolation methods and are presented next.



| Figure 2.24 | Spike recovery of particles comparing different magnets and brain homogenate dilutions Counted Spike samples were set to 100% from **Figure 2.26**. Each sample was spiked with a known amount of particles and from the different brain homognetae dilutions (3.3xdil, 5xdil, and 10xdil) particles were iolated using either a Dynal magnet of a Miltenyi magnet, see **section 2.7.18**. Each experiment was counted twice and for each count the 4 corner squares were used for counting (*n=8*). Error bars represent standard de*via*tion.

Using RIPA as an isolation medium, the recovery was 91% for the Dynal magnet and 57% for the Miltneyi magnet indicating that the Miltenyi magnetic columns retain more particles in the magnetic column than the Dynal magnet. Increased recovery is obtained when the particles are kept in the tube during the wash steps using the Dynal magnet. For the Dynal magnet, any dilution had an increase on the isolated yield, going from 24% (see **Figure 2.23** –no dilution) to ~50% (**Figure 2.24**).

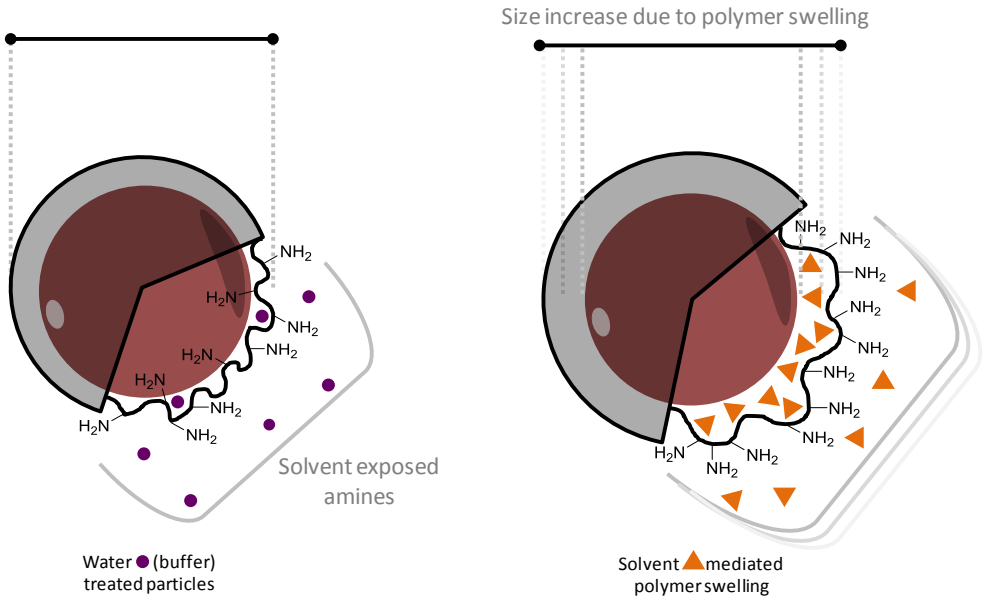
2.5 | DISCUSSION

This chapter described the synthesis of the molecules, Lewis[a] and the trifluoromethylphenyl diazirine photo-crosslinker, both bearing amine reactive groups for the functionalisation of amine-MPIO. The amine-functionalisation levels on the MPIO of both molecules were established by using a spectroscopic read-out with Fmoc-numbering. For the Lewis, only modified MPIOs an ELISA based method allowed screening of successful reactions using 10 times less material than the Fmoc-based method. Additionally, it was discovered that the functionalisation methods and solvent exposure influences the amine-levels on the MPIO. Also, functional assays were performed to establish if the photo-crosslinker on MPIO was effective in crosslinking when exposed to UV light.

2.5.1 Amine loading determination and the influence of solvent exposure on nanoparticle characteristics

Assessing the functionalisation of amine-MPIOs with the synthesized trifluoromethyl-diazirin-phenyl-propanoic acid and IME-Lewis[a], generated from SCM-Lewis[a], has proven to be challenging. The main challenge was to determine a reliable measure of amine functionalisation that was independent of the nanoparticles, that is, the read-out is a 'cleaved-off' product that can be determined spectroscopically without the nanoparticles obscuring the read-out. Some methods, such as the fluorescamine method, rely on a fluorescent product generated onto the nanoparticles. However, despite successful use by others, this method was unsuitable for the particles presented in this chapter [301], [302], [299], [298]. Even when experienced scientists attempted to measure the loading of the MPIOs (Solulink), they were unsuccessful (data not shown). As alluded to in **section 2.3.2.** Fmoc-Cl has the potential to react with hydroxyl groups, though it has the advantage of a spectroscopic readout of the released dibenzofulvene after cleaving the Fmoc with a base [305]. Therefore a peptide coupling with Fmoc-Gly-OH using a large excess of the Fmoc-species was used to determine the amine loading. Assessing different coupling agents; HATU/DIPEA IN DMF was determined to be the most compatible with the particles used [309]. See **Table 2.2**. In addition, another challenge was overcome by which low levels of particles, only 0.125 mg of nanoparticles, was sufficient for measuring within the range and allowed fewer particles to be used for loading determination. Subsequent functionalisation of the photo-crosslinker, using the same HATU/DIPEA IN DMF method as for the Fmoc-numbering, the desired ±20% loading was achieved, although the stated amount of amines (in nmol/mg) on the particles

did not correspond with the supplier's number. Using Fmoc-numbering and amounts based on previous reactions on the same batch of particles, desired functionalisation levels were attained, see **Figure 2.8**. Subsequently these particles were covered with IME-Le[a] and used for experiments presented in the next chapter. For other batches, the Le[a] coverage of the particles ranged from 6-28% using 20 equiv. of IME- Le[a]. Surprisingly, when the Le[a] + PXL particles were tested for their coverage using Fmoc-numbering, an observation was made between the unmodified/DMF-treated and unmodified/untreated particles as shown in **Figure 2.10**. In order to couple the PXL to the particles, DMF was used as a solvent and the particles were exposed to the solvent at least twice for more than 12h whilst vigorously shaking. As a control, particles without coupling agents were exposed to the same DMF treatment as the PXL reactions. When particles were merely washed (3 times) in DMF and then exposed to the Fmoc-numbering method a lower Fmoc-loading was observed (17% less amines) than the control particles exposed to DMF without coupling agents and then tested for their amine content. Potentially, the DMF swells the polymer coating of the iron-oxide particles exposing more amines when the particles were in contact with the DMF for longer [310], [311]. These observations indicate that the polymer (polystyrene-based) used for the amines may swell upon contact with DMF for prolonged periods. However, particles show no obvious size increase/decrease trend when treated differently as described and measured by DLS, measured on two different dynamic size scattering (DLS) machines. However, storing them solvent (including water) adds a modest size increase to the particles and may allow amines to become more exposed, which is in line with this theory. Also, the treatment (I), as described in **section 2.7.7**, which mimics the functionalisation of both photo-crosslinker coupling and Lewis[a] functionalisation, where the particles are exposed multiple times to shaking in the solvent, has the most effect on the charge indicating again that more amines are exposed. **Figure 2.27** explains this theory. Accounting for the amount of swelling the particles may display when exposed to DMF and the treatment used to functionalise (or other aprotic solvents, including water), makes the measuring of amine-functionalisation cumbersome and variable. Other amine detection methods proved not possible with these particular particles and perhaps an alternative photo-crosslinker soluble in water and aqueous amine coupling reactions could overcome this. However these were not explored in this work. For the Lewis[a]-ony decorated particles used for the MRI experiments described in the next chapter, two methods of loading were used. First, an ELISA-based method using E-Selectin allowed rapid screening and selecting of Lewis[a]-functionalised nanoparticles of similar loading using minimal material and then pooling them into a large batch. Second, subsequent Fmoc-numbering was performed as before, but these particles are only exposed to DMF for the analysis of the Fmoc-numbering as the IME-reaction is aqueous. Using this method, Lewis[a]- and Lewis[b]-functionalised MPIOs were made with similar loading levels.



| Figure 2.26 | Model for the increased numbers of amines after solvent exposure Upon solvent treatment, the polymer swells and more amines are 'pushed' to the surface resulting in an increased exposure of amines affecting loading and charge.

2.5.2 UV activation of the photo-crosslinker on MPIO *in vitro* is challenging

Assessing functionality and translatability of these particles to be used *in vitro* and *in vivo*, the last part of this chapter explores the reactivity of the photo-crosslinker when on particles and how to retrieve these particles from brains. First the photo-crosslinker molecule and attached to the MPIOs was exposed to UV light whilst recording an IR-spectrum in order to elucidate if the trifluoromethyl-diazirin-phenyl-propanoic acid can be UV-activated. The 'free' molecule was exposed to UV-light and revealed the formation of the diazo-intermediate (50% formed in 13 minutes, hand-held UV-lamp, 3 W). See **Figure 2.19.** When MPIO were compared with and without PXL modification, the results were inconclusive and IR is not able to quantitatively record the functionalisation of a small molecule coupled onto a large nanoparticle of iron-oxide coated with polystyrene and amines. However, though some IR-stretches could be indicative of the diazirine and amide-bond between the PXL and the particles, no evidence was found that the photo-crosslinker could be activated on the nanoparticles. As these particles were intended to trap proteins and pull them out of a mixture, a simplified pull-down using BSA and the photo-crosslinked MPIOs was performed. Subsequent cleavage of the trapped BSA with trypsin from the MPIOs functionalised with photo-crosslinker was performed. Although initially the BSA seemed to crosslink onto UV exposed PXL-MPIOs preferentially, it was subsequently revealed that merely UV exposure of MPIOs (with and without PXL) in the presence of BSA was causative of the increased

amount of isolated BSA peptides. This may be due to the UV-induced unfolding of the protein, exposing hydrophobic patches that could preferentially bind to the photo-crosslinker and the polystyrene coating [312], [313]. Unsure if these artefacts were due to an incompatible model system, another *in vivo* model system was explored where the targeting of Lewis[a] was used in a brain inflammation model. As the MRI experiment in Chapter 1 showed accumulation of Lewis[a]-MPIO in the left (IL-1β activated) hemisphere, it was expected that the particles with Lewis[a] and PXL would also preferentially accumulate into the left (IL-1β activated) hemisphere. To rule out any a-specific binding of the PXL, the Lewis[a] and PXL particles were compared with PXL only particles. However, very low particle yield were obtained altogether, with no significant difference between the photo-crosslinker modified control particles and the bi-functional particles. Isolation of these particles from the brain was difficult and translating *in vitro* to *in vivo* binding of Lewis[a] has proven to be challenging, mostly because the *in vivo* recovery of the particles is very low (0.06%, or 0.88 µg of 0.5 mg particles injected). Rat 6 was treated differently from the rest of the group, as described in **section 2.7.16.** Under anaesthesia an intracarotid injection was secured into the carotid artery. Then rat 6 was deeply anaesthetised with sodium pentobarbitone, after the heart stopped pumping, the rat was pre-flushed with saline and then with the particles, followed by another saline flush. This method increases the particle recovery rate (**Figure 2.23**) and can be used future follow-up experiments. Even though the recovery rate and difference was neither promising nor significant, increasing the isolation method may aid in determining if these particles are suitable for *de novo* protein identification of Lewis[a] binders using the photo-crosslinker to covalently trap the interacting proteins. However, initial results were not promising and no preferentially accumulated Lewis[a] and PXL particles were isolated from left (IL-1β activated) hemisphere and may indicate that the PXL could influence the binding.

The proteomics facility (Biochemistry, University of Oxford, UK) has as a *MS*/MS** run minimum 1 µg of recombinant protein. In order to identify a mixture of proteins the following basic calculations were made: 20% PXL loading = 142.6 nmol/mg of particles = 0.1426 nmol/µg of particles. Assuming 100% PXL efficiency and assuming 'average' molecular weight (MW) of a protein is 41250 Da*. 0.1426 nmol of 'average' protein is 5.9 µg. In order to get a 'confident' at least 10 µg of particles are required for confident *MS*/MS** protein identification. Therefore spike-recovery experiments were performed on brain homogenate to optimize the isolation yield of the particles. For the spike-recovery, trialling two different isolation methods and several dilutions of the brain homogenate, a two-fold increase in particle isolation from brain was achieved using an improved isolation method, as shown in **Figure 2.25**. Although the method used to inject the particles, *via* the carotid artery, was not trialled before. To ensure optimal particle

binding in the brain, an experimental set-up testing different injection sites and using MRI to determine the MPIO binding in the brain could improve future experiments.

2.6 | CONCLUSION

The previously well-established synthesis routes to SCM-Lewis[a] and trifluoromethyl-diazirin-phenyl-propanoic acid were reproduced and allowed functionalisation of amine-terminated MPIOs. Using Fmoc-numbering the amount of functionalised amines was determined, however it was also shown that the solvent used to couple the photo-crosslinker onto the nanoparticles alters the amounts of amines exposed on the surface of the nanoparticles making the exact functionalisation levels difficult to determine and unreliable. Whilst the exact levels of photo-crosslinker functionalisation were estimated and were indicative of photo-crosslinker being covalently coupled onto the MPIOs, the reactivity of the diazirine on the nanoparticles has not been established. Although the trifluoromethyl-diazirin-phenyl-propanoic acid itself can be UV-activated forming the reactive diazo-intermediate, it is unclear whether this happens on when the molecule is coupled onto the MPIOs and if the diazirine is capable of cross linking proteins onto the nanoparticles. BSA was not a good model protein to determine if the photo-crosslinker could covalently trap BSA onto the particles and it appeared that UV irradiation could trap BSA onto the particles independently of the photo-crosslinker. It was then established that the additional 'targeting' of Lewis[a] on the bi-functional pull-down particles did not increase the yield when used in a brain inflammation model to target these particles to the inflamed brain *via* Lewis[a]. However, an improved isolation method to isolate the particles from brain homogenate doubled the yield and could be a useful method for nanoparticle isolations in to the future.

2.7 | METHODS

2.7.1 Reagents and buffers used

Reagents were from Sigma unless specified otherwise. Tubes used were exclusively Protein LoBind microcentrifuge tubes (0.5, 1.5 and 2 mL) from Eppendorf. Dry solvents were from Acros Organics with molecular sieve and AcroSeal. Argon was used when solvent was removed from the bottle. DMSO was from Fisher BioReagents. Sodium methoxide was bought from Sigma as a 25% wt. solution in methanol, or made fresh the night before the experiment with cut Na in mineral oil, rinsed with hexane, weighed and placed a flask with dry methanol (1 % wt.) topped with a drying tube containing calcium chloride. Magnet for 1.5 mL tubes was from Dynal, Invitrogen. Buffers prepared were 0.22 µ-filtered and stored up to 6 months. Dulbecco's Phosphate Buffered Saline (DPBS) with calcium and magnesium was from Sigma (Cat # D1283).

2.7.2 Determination of (free) amine content on nanoparticles

For brevity a general procedure is written down here for the determination of the amount of free amines on DynalBeads (DB) and SoluLink (SL) using two Fmoc-species. Methods explored are summarized in **Table 2.1**. Experiments marked with **X** are not covered in this thesis due to their lack of success. The following references for the methods were used, originally designed to detect free (primary) amines in proteins, did not work for both the nanoparticle systems. [304],[303], [301], [302], [299], [298]. For the Fmoc-numbering: Take out 0.5 mg (50 µL SL, 16.7 µL DB) of particles and wash the particles with 1 mL DMF-dry 3 times by vortexing and using a magnet to remove the excess wash solution. Note: The particles do not readily dissolve in DMF-dry, after vortexing, spin (1 minute, 2000 xg) and sonicate before removing excess DMF. Repeat 3 times. Resuspend the beads in 50µL DMF-dry. Fmoc-Gly-OH was dissolved in DMF-dry (50µL) and the indicated (see below) coupling reagents were dissolved in 50µL each and mixed. The mix was added to the Fmoc-species, briefly mixed on the vortex and added to the 50µL of suspended particles to obtain a 200µL final reaction volume. Seal the tubes with film and vigorously shake (1000 rpm) the reactions overnight at room temperature. Briefly spin and place the tubes on a magnet and remove the reaction mixtures. Wash the particles with DMF 3 times as described above and resuspend the particles in 100 µL of cleavage mix 20% piperidine in DMF (v/v) and vigorously shake (1000 rpm) the reaction for 1.5h. Take out 50 µL and dilute in 950 µL MeOH.

Measure an absorbance spectrum between 250 and 350 nm using a quartz cuvette and a photo spectrometer.

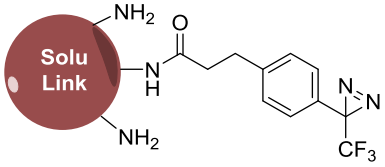
Summary of conditions used and tested (**Table 2.2** for results):

- Large excess (≥15K equiv.) of either Fmoc-Gly-OH of Fmoc-Cl was dissolved in DMF.
- Coupling agents were dissolved in DMF and added according to methods described in W. C. Chan, P. D. White, Fmoc Solid Phase Peptide Synthesis, Oxford University Press, Oxford, 2000
- Equivalents relative to the Fmoc-species.

Fmoc-Gly-OH (1 equiv.)	EDC (5 equiv.)	NHS (5 equiv.)
Fmoc-Gly-OH (1 equiv.)**	DCC (5 equiv.)	NHS (5 equiv.)
Fmoc-Gly-OH (1 equiv.)	DIC (1 equiv.)	HOBT (1 equiv.)
Fmoc-Gly-OH (1 equiv.)	HATU (0.98 equiv.)	DIPEA (2 equiv.)
Fmoc-Cl (1 equiv.)**	Et_3N (2 equiv.)	

- Final Reaction volume 200 µL and the reaction was vigorously shaken (1000 rpm) overnight (16h).
- **Fmoc-Gly-OH/DCC/NHS and Fmoc-Cl/NEt_3 showed precipitation after the O/N reaction and particle pellets were significantly larger and challenging to handle.

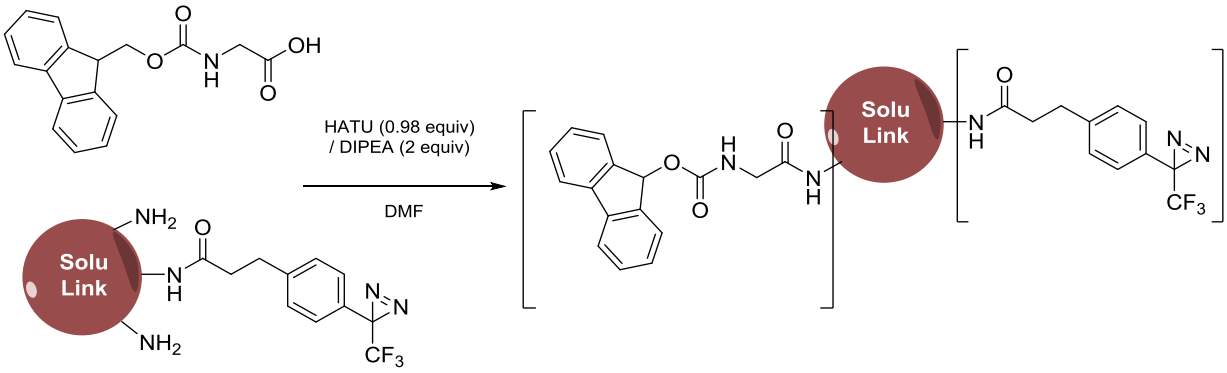
2.7.3 Coupling of photo-crosslinker onto SoluLink amine MPIO



Note: All of these steps were performed with minimal light and incubations were kept under aluminum foil. Take out 1.5 mg of particles (150 µL Solulink, 10 mg/mL) and wash the particles with 1 mL DMF-dry 3 times by vortexing and using a magnet (1 min) to remove the excess wash solution. Note: The particles do not readily dissolve in DMF-dry, after vortexing, spin (1 minute, 2000 xg) and sonicate before removing excess DMF. Repeat 3 times. Resuspend the beads in 150 µL DMF-dry. The diazririne photo-crosslinker molecule was dissolved in DMF and 0.98 equiv. of HATU was added and 2 equiv. of DIPEA with respect to the PXL. This mixture was premixed on a shaker (1500 rpm, RT) for 10 minutes (observe yellow/orange colour change) before adding the different equivalents (61.8, 92.7 and 123.6 nmol) of the acid to the amount of free amine on the particles (41.2 nmol/mg, 61.8 for 1.5 mg). The amount of acid was dissolved in a volume of 100 µL, adding to the particles this yielded in a final volume of 150 µL. Incubate the reactions at room temperature for overnight under vigorous shaking (1500 rpm). After 16h the reactions were

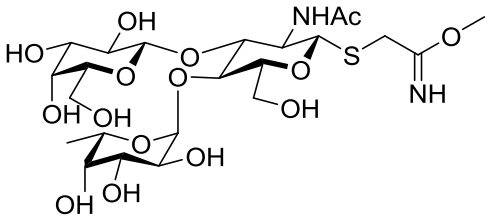
vortexed for 30 sec and spun down. The tubes were placed on the tube on the magnet for 1 min and the supernatant was discarded. As described above, wash the particles with 1 mL DMF wash three times. Take out 0.05 mg for particle characterization.

2.7.4 Free amine determination using Fmoc-numbering



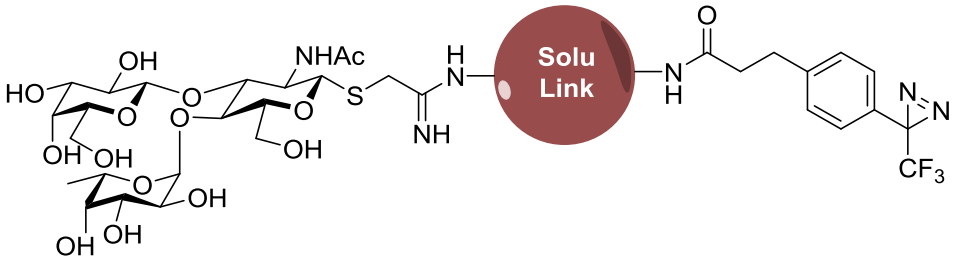
Note: All of these steps were performed with minimal light and incubations were kept under aluminum foil. Determine the loading with Fmoc-numbering using a 15K molar excess of Fmoc-species. Take out 0.5 mg of particles and suspend in 50µL DMF-dry. Fmoc-Gly-OH (10 mg) was dissolved in DMF-dry (50µL) and HATU (13.3 mg) was dissolved in 50 µL (DMF) and mixed with Fmoc-Gly-OH. DIPEA (12,5 µL) was added to the Fmoc-Gly-OH/HATU mix. The mix was incubated for 10 minutes (observe yellow colour change). The Fmoc-Gly-OH/HATU/DIPEA mix was vortexed and added to the 50µL of suspended particles to obtain a 150µL final reaction volume. Vigorously shake (1500 rpm) the reaction for overnight. Briefly spin and place the tubes on a magnet and remove the supernatant. Wash the particles with DMF 3 times and resuspend the particles in 100 µL of cleavage mix (1:24:25 DBU:DMSO:DMF). Vigorously shake (1500 rpm) the reaction for 2.5h. Take out 50 µL (equivalent to 0.25 mg of particles), dissolve in 950 µL of MeOH and measure the Absorbance at 305 nm in a quartz cuvette. When fewer particles were used (0.25 mg or 0.125 mg) the same amount of reagents were used (lowering the particle concentration in solution), but cleavage was performed with 50 or 25 µL respectively.

2.7.5 SCM-Le[a] deprotection and IME-activation



Fully protected IME-Lewis[a] 10 mg, 10.9 µmol, 1 equiv. was dissolved in 500 µL dry MeOH. A 25% solution of sodium methoxide in methanol (4.4 µL, 4.4 µmol, 0.4 equiv.) was added and the reaction was left to stir overnight under nitrogen. TLC (8:2 Acetone:H_2O) revealed complete consumption of starting material. The reaction was evaporated under reduced pressure without heating and left under high vacuum for 30 minutes. Lewis[a] was dissolved in 200 µL 0.6 M TAPS buffer pH 7.0 and the pH was measured of the solution using pH paper and appeared between pH 8 and 9. This method was used for the particles used for the pull-down experiments described in **Chapter 3**. For the MRI particles and the particles used for the isolation experiment described later in this chapter the following procedure was used. Fully protected SCM-Lewis[a] (1 equiv.) was dissolved in 300 µL dry MeOH. A 1% solution of sodium methoxide in methanol was freshly prepared the day before (0.4 equiv.) was added and the reaction was left to stir overnight under nitrogen. TLC (8:2 Acetone:H_2O) revealed consumption of starting material. The reaction was evaporated under reduced pressure without heating and left under high vacuum for 30 minutes. Lewis[a] was dissolved in 200 µL 0.1 M $NaHCO_3$ buffer pH 9.0 and the pH was measured of the solution using pH paper and appeared between pH 8 and 9.

2.7.6 Bi-functional Lewis[a]/diazirine photo-crosslinker MPIO

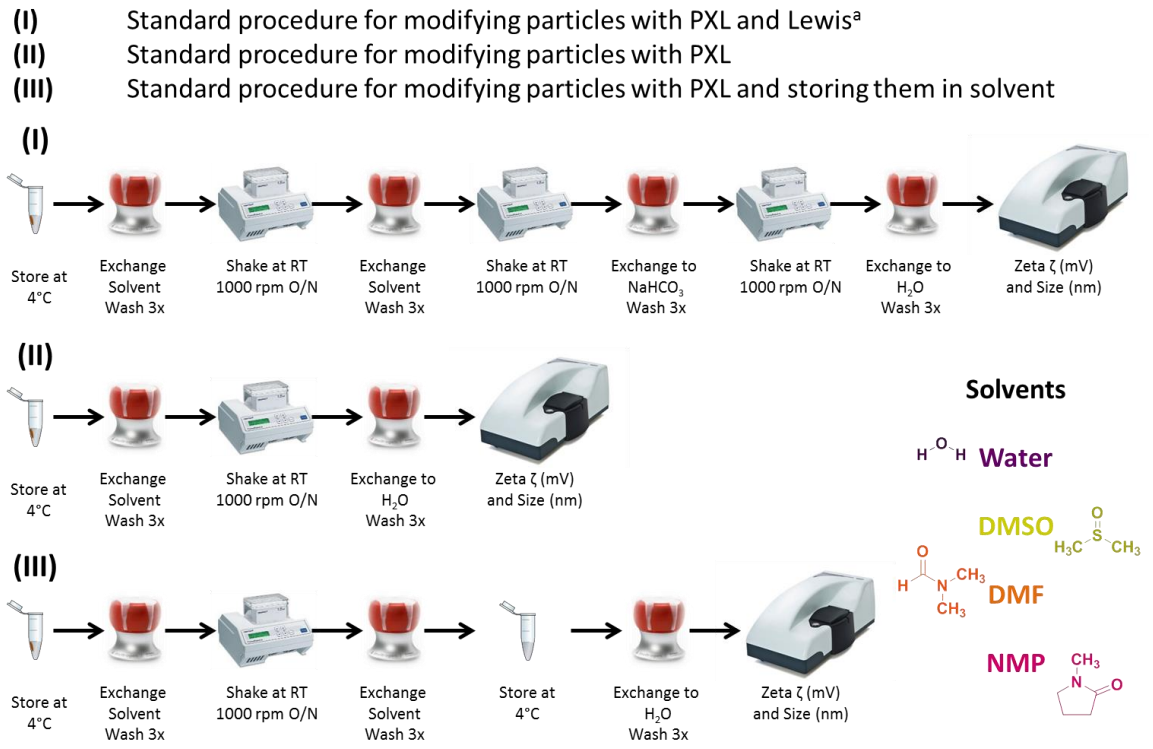


Note 1: All of these steps were performed with minimal light and incubations were kept under aluminum foil. 2 mg of diazirine-loaded SoluLink particles were washed 3 times (using a magnet) with 1 mL of 0.6 M TAPS buffer pH 7.0. The particles (2 mg, 1.58 µmol amines, 126.3 nmol photo-crosslinker, 26%) were resuspended with Lewis[a] (6.8 equiv.) in TAPS buffer at pH 8-9 to give a final volume of in 200 µL. The reaction was left overnight in a bench-top shaker (1500 rpm, room temperature). The particles were washed 3 times with 0.6 M TAPS buffer pH 7.0. 0.25 mg was taken out and the loading was determined using Fmoc-numbering. Take out 0.05 mg for particle

characterization. *Note 2*: To increase the amounts of Le[a] on the particles, this protocol was repeated on particles already containing (20%) Le[a] and diaziridine (see figure below). Particles were used for the pull-down experiments described in **Chapter 3**.

2.7.7. The effects of different aprotic solvents on the amine particles characteristics

Figure 2.28 presents an overview of the steps performed to determine the effects of different aprotic solvents on the amine particles characteristics. Start for **(I)**, **(II)** and **(III)**; take out 0.5 mg of particles (50 µL Solulink, 10 mg/mL) and wash the particles 'Exchange Solvent Wash' with 1 mL (H_2O, DMF-dry, DMSO or NMP) 3 times by vortexing, placing the tubes in a minufuge table top spinner (5 sec, 2000xg approximately) and using a magnet (1 min) to remove the excess wash solution. Note: The particles do not readily dissolve in DMF-dry (larger clumps that need extra vortexing to dissolve), DMSO (more particles in supernatant) and NMP (larger clumps that need extra vortexing to dissolve). Resuspend the beads in 150 µL of the appropriate solvent. Incubate the particles at room temperature for overnight under vigorous shaking (1000 rpm). After 16h the reactions were vortexed for and spun down using a minifuge for a few seconds.



| Figure 2.26 | Overview of particle treatment to test the effects of aprotic solvent exposure

For **(I)**, the tubes were placed on the tube on the magnet for 1 min and the supernatant was discarded. Wash the particles 'Exchange Solvent Wash 3x' with 1 mL (H_2O, DMF-dry, DMSO or NMP) 3 times by vortexing, placing the tubes in a minufuge table top spinner (5 sec, 2000xg approximately) and using a magnet (1 min) to remove the excess wash solution. Resuspend the beads in 150 µL of the appropriate solvent used. Incubate the particles at room temperature for overnight under vigorous shaking (1000 rpm). After 16h the reactions were vortexed for 30 sec and spun down. The tubes were placed on the tube on the magnet for 1 min and the supernatant was discarded. wash the particles 'Exchange Solvent Wash 3x' with 1 mL 0.1 M $NaHCO_3$ buffer pH 9.0 3 times by vortexing, placing the tubes in a minufuge table top spinner (5 sec, 2000xg approximately) and using a magnet (1 min) to remove the excess wash solution. Resuspend the beads in 150 µL 0.1 M $NaHCO_3$ buffer pH 9.0.. Incubate the particles at room temperature for overnight under vigorous shaking (1000 rpm). The tubes were spun down for a few seconds in the minifuge and the tubes were placed on the tube on the magnet for 1 min and the supernatant was discarded. The particles were washed with H_2O three times. Take out 0.05 mg in 750 µL H_2O for Zeta and size determination.

For **(II)**, the tubes were placed on the tube on the magnet for 1 min and the supernatant was discarded. Wash the particles with H_2O three times. Take out 0.05 mg in 750 µL H_2O for Zeta and size determination.

For **(III)**, after the 16h the reactions were vortexed for 30 sec and spun down using the minufuge. The tubes were placed on the tube on the magnet for 1 min and the supernatant was discarded. Wash the particles 'Exchange Solvent Wash 3x' with 1 mL (H_2O, DMF-dry, DMSO or NMP) 3 times by vortexing, placing the tubes in a minufuge table top spinner (5 sec, 2000xg approximately) and using a magnet (1 min) to remove the excess wash solution. The tubes were stored at 4°C for 2 days. The tubes were spun down for a few seconds in the minifuge and the tubes were placed on the tube on the magnet for 1 min and the supernatant was discarded. The particles were washed with H_2O three times. Take out 0.05 mg in 750 µL H2O for Zeta and size determination. Zeta (mV) determination and DLS size (nm) was performed using a Malvern Zetasizer Nano ZS at Begbroke Science Park (Oxford). See **Figure 2.12**. DLS Size (nm) was also determined using the new DLS machine (Wyatt DynaPro Plate Reader II) at Biochemistry (Oxford). See **Figure 2.13**.

2.7.8 Rat E-Selectin *in vitro* screening experiment

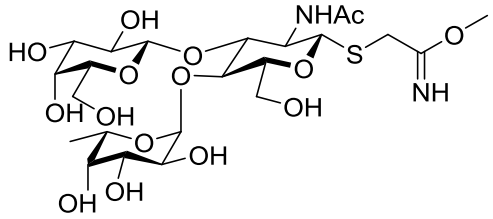
ELISA 96 well plates from Greiner Bio-One (Polystyrene, flat bottom, MICROLON® 600, high binding, clear Cat # 655 061) were coated with 50 µL/well. E-Selectin was from Stratech, Sino Biological Inc. Rat E-Selectin/CD62E/SELE (FC Tag) (Cat # 80033-R02H-SIB-100ug). Serial dilutions were made using PBS (as specified concentrations in the graphs presented) a 100 µL final volume in each well. Control wells were PBS only. The plate was covered and incubated overnight at 4°C. The content of the plate was tipped out and patted dry on paper towels. Wells were washed with 150 µl of PBS twice before incubating with 150 µl 3% BSA in PBS for 2h at RT. Wells were washed with 150 µl of PBS twice before incubating with particles. The wells were filled with 40 µL of PBS and a MPIO-$Le^{a/b}$ (or MPIO-NH_2 for control) solution was prepared by diluting the particles a 100 times and using 10 µL (1 µg/well) and placing this solution into 40 µL of PBS in well plate to a final volume of 50 µL. The plate was incubated for 2h on a plate rocker (Biometra®, WT, speed setting 4). The bound MPIO-$Le^{a/b}$ particles were washed with 150 µl PBS 3 times and after the last wash the wells were pipetted empty. The Perls Prussian Blue stain for iron was performed (50 µL/well) by freshly mixing 20% HCl (~6.5M) with 10% (w/w) $K_4Fe(CN)_6$ $3{\cdot}H_2O$ (Cat # 094403, FluoroChem) 1 to 1, which results in a ~3.2M HCl solution and left to stain for 20 min at room temperature. A blue precipitate was observed where MPIO-$Le^{a/b}$ were present. Notes for optimal results: pipetting from disposable white polystyrene reagent reservoirs or mixing in a polystyrene bijou tube (7mL) will result in an opaque blue stain, which is still quantifiable. Pipetting from a glass reservoir and mixing in a polypropylene tube will result in a clear well view with blue precipitate. Optimized staining is achieved using TipOne® 200 µL graduated filter tips (sterile) (StarLab, #S1120-8810), which appear to be more acid resistant than other tips tested, that can cause white precipitates in the wells after ≥ 10 minutes of incubation with the Perl stain. Only after an extended period of time (≥24h) the plate turns opaque and the negative control wells will turn (lighter) blue as well. Optimal measuring 'scanning' time is between 10 and 60 minutes. In addition, a plate rocker improves the stain, but has to be a side-to-side rocker like the Biometra® (WT, speed setting 4), an orbital rocker will produce an obscured result that leads to particle and precipitate accumulation in the middle of the well. Plates can either be scanned by a flatbed scanner or by measuring the plate in a photo spectrometer BMG SPECTROstar Omega platereader (BMG Labtech) at various wavelengths.

Several parameters of this assay were assessed and are presented below. For **Figure 2.15** the effects of washing were assessed after the addition of the MPIO-$Le^{a/b}$ or MPIO-NH_2. 2 µL of E-Selectin in 198 µL PBS times 4 = 800 µL (for row A to H), add 100 µL to each well and perform a

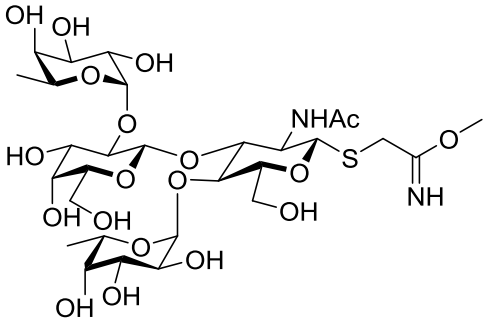
1:1 serial dilution of the solution made in PBS. Column 12 is PBS only. Rows A to D were filled with MPIO-Le[a] and rows E to H with MPIO-NH_2 for control. To assess the binding strength of the particles and the influence of the washing steps row A and E were washed two times by pipetting out the liquid and pipetting 100 µL into the well and resuspending the volume 3 times. Take out the wash solution. And repeat once more and take out the last wash solution. Row B and F were washed as rows A and E, but 3 times. Row C and F were washed 4 times and rows D and H were washed 5 times.

For **Figure 2.16** the influence of calcium-dependent of MPIO-Lewis[a] binding was assessed by using the chelator EDTA. The same procedure described in **2.7.8** was executed with the following alterations: Row A (top) particles were incubated in PBS and washed with PBS 3 times after particle incubation. Row B particles were incubated in PBS and washed with PBS-T (PBS, with 0.05% Tween-20) 3 times after particle incubation. Row C particles were incubated in PBS and washed with PBS-E 3 times after particle incubation. (PBS-E was prepared by adding 350 mg EDTA into 48 mL of Calcium and Magnesium-free PBS, pH adjusted to pH 7.4 with NaOH. 25 mM EDTA. Noticed small precipitate on the bottom after pipetting it into the wells, only used top 'clear' solution). Add to Row D 40 µL of the PBS-E solution and 10 µL of particles and incubate as the others. Wash with PBS-E 3 times after particle incubation.

2.7.9 . Le[a] deprotection and IME-activation

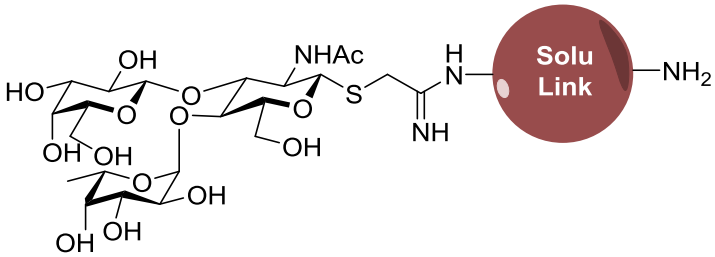


Fully protected SCM-Lewis[a] (1 equiv.) (range of 10-15 µmol) was dissolved in 300 µL dry MeOH. A 1% solution of sodium methoxide in methanol was freshly prepared the day before (0.4 equiv.) was added and the reaction was left to stir overnight under nitrogen. TLC (8:2 Acetone:H_2O) revealed consumption of starting material. The reaction was evaporated under reduced pressure without heating and left under high vacuum for 30 minutes. Lewis[a] was dissolved in 200-500 µL 0.1 M $NaHCO_3$ buffer pH 9.0 and the pH was measured of the solution using pH paper and appeared between pH 8 and 9.



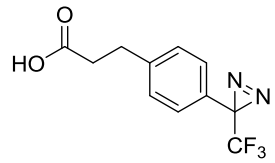
Fully protected SCM-Lewis[b] was from Régis C. Saliba as reported and activated as stated above for Lewis[a] [299].

2.7.10 Coupling of IME-Le[a] or Le[b] onto amine MPIO



1 mg (or 1.5 mg when more IME-Lewis was weighted out, ~10 equiv. of carbohydrate) of SoluLink particles were washed 3 times (using a magnet and centrifuge) with 1 mL of 0.1 M $NaHCO_3$ buffer pH 9.0. The particles were resuspended with Lewis carbohydrate in buffer at pH 8-9 to give a final volume of in between 200-500 µL, depending on the solubility of the carbohydrate. The reaction was left overnight in a bench-top shaker (1000 rpm, room temperature). The particles were washed 3 times with 0.1 M $NaHCO_3$ buffer pH 9.0. Particles were washed 3 times with PBS containing 0.05% sodium azide and stored at 4 °C at a concentration of 10 mg/mL. 1 µL was used to screen the binding strength of as described in **2.7.8** and shown in **Figure 2.18**. Batches with similar binding patterns were pooled and 0.25 mg was taken out and the loading was determined using Fmoc-numbering as described in **2.7.4.** and shown in **Figure 2.19**.

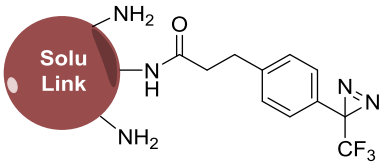
2.7.11. FT-IR monitoring of a diazo intermediate



Note: All of these steps were performed with minimal light and experiments were kept under aluminium foil. The trifluoromethyl-diazirin-phenyl-propanoic acid **[P9]** was put onto the FT-IR (Surface Analysis Facility, Department of Chemistry, Oxford) detector, enough to cover the probe. A hand-held UV-lamp (365 nm LED, 3 W) was placed as close as possible to the sample without

touching the spectrometer and an IR spectrum was recorded (aluminium foil covered to block ambient light) and labelled '0'. Subsequently the UV lamp was switched on and a spectrum was recorder every 10 minutes for 1 hour. After 1 hour the lamp was switched off and a final spectrum was obtained labelled '60_off'. The spectra are shown in **Figure 2.10** and additional spectra can be found in the supplementary information of this chapter.

2.7.12. FT-IR monitoring of a diazo intermediate on MPIO



Note: All of these steps were performed with minimal light and experiments were kept under aluminium foil. The trifluoromethyl-diazirin-phenyl-propanoic acid **[P9]** was coupled using 100 equiv. onto 3 mg of amine-MPIO using the method reported in **2.3.3.2.** In addition a NH_2-MPIO batch treated with DMF (without coupling agents and photo-crosslinker) was included. After the reaction (no Fmoc-numbering performed), the particles were washed 3 times (using a magnet and centrifuge) with 1 mL of dry-DMF. Subsequently the batch suspended in 1 mL H_2O was divided in 3 (333 µL, 1 mg each) and placed in separate tubes. Of two PXL-modified batches, the liquid was removed by magnet pelleting and replaced by acetic acid (AA) and the particles were washed 3 times (using a magnet and centrifuge) with 1 mL of acetic acid. The particles in 1 mL acetic acid each were placed in a 6 well plate and 3 wells were covered with aluminium foil (1 for the PXL-MPIO in acetic acid, 1 for the PXL-MPIO in H_2O and 1 for control NH_2-MPIO in H_2O) for, leaving 1 exposed with the PXL-MPIO and acetic acid. The plate was UV-treated on ice with an UVP Chromato-Vue Transilluminator, model TM-20 (220/240 V, 50 Hz, 1.5 Amp). A total of 20 minutes of irradiation using midrange UV (8W) 302nm and longwave (8W) 365nm for 20 minutes was performed at a depth of 20 mm on the samples whilst maintaining agitation (60 rpm) on ice. The particles were recovered from the plate and the wells were washed with H_2O a couple of times and pelleted onto the magnet. The particles were exchanged into D_2O by washing 3 times (using a magnet and centrifuge). The D_2O was removed as much as possible, whilst still being able to pipette the concentrated particle solution. The particle paste was pipetted onto the FT-IR (Surface Analysis Facility, Department of Chemistry, Oxford) detector) and allowed to dry before an IR spectrum was recorded (aluminium foil covered to block ambient light). The spectra are shown in **Figure 2.11** using the detailed schematic for the MPIOs as shown in **Figure 2.6** and additional spectra can be found in the supplementary information of this chapter.

2.7.13 Buffers and reagents used for crosslinking experiments

Reagents were from Sigma unless specified otherwise. Modified RIPA buffer: Tris Buffer pH 7.5: 25 mM Tris·HCl, 150 mM NaCl, 0.25% sodium deoxycholate, 1% Triton. BSA was from Sigma (Cat # A7906) and Trypsin was from Thermo Fisher and prepared by Jitka Dadova (Pierce™ Trypsin Protease, MS Grade, Cat # 90057). ABC buffer, ammonium bicarbonate solution: 50 mM in H_2O. Plastic ware for tissue culture was from Corning exclusively and Protein LoBind microcentrifuge tubes (0.5, 1.5 and 2 mL) were from Eppendorf, other tubes (15 and 50 mL) were from Falcon, all sterile before use. Fresh buffers were prepared for each experiment and 0.22 µ-filtered before use.

2.7.14 BSA crosslinking onto photo-crosslinker modified MPIO

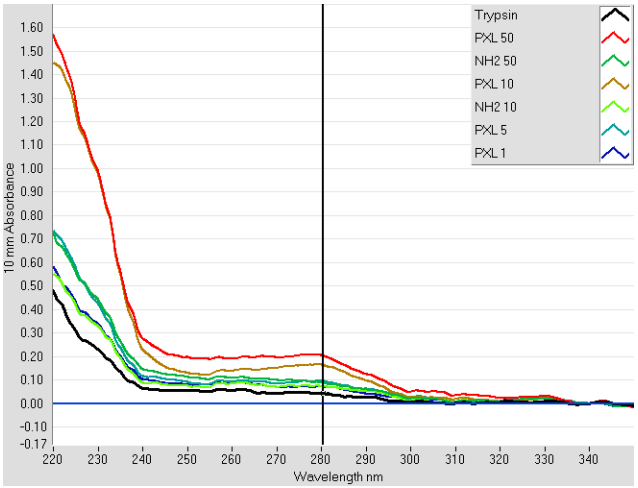
A solution of 0.2 mg/mL of BSA was prepared in RIPA buffer. A 6 well plate was coated with 2mL of 0.1 mg/mL BSA for 1h at RT whilst shaking (200 rpm) on an orbital plate rocker. The wells were washed with 2 mL RIPA buffer each for 3 times. The plate was incubated with 2 mL of RIPA buffer for 1h at RT under gentle shaking (200 rpm) conditions on an orbital plate rocker. A dilution in RIPA buffer of photo-crosslinker (PXL 43% loading) particles was made, distributing over the wells 0.5 mg, 0.1 mg, 0.05 mg, 0.01mg of particles in 1 mL of 0.15 mg/mL BSA in RIPA buffer. *(For the repeat experiment 0.1 mg of the specified particles, see **Table 2.11**, were used.)* The plate was placed on ice and UV-irradiated with a UVP Chromato-Vue Transilluminator, model TM-20 (220/240 V, 50 Hz, 1.5 Amp). A total of 20 minutes of irradiation using midrange UV (8W) 302nm for 30 minutes and longwave (8W) 365nm for 20 minutes was performed at a depth of 20 mm on the samples whilst maintaining agitation on an orbital plate rocker (200 rpm) on ice. *(For the repeat experiment the samples that were not UV-treated were covered with aluminium foil.)* The samples were collected in 1.5 mL Eppendorf Protein LoBind tubes and placed on a magnet for 2 minutes. The supernatant was discarded and the wells of the plate used were rinsed with 1 mL RIPA buffer and added to the tubes on the magnet. The wash supernatant was removed after 2 minutes and this step was repeated once more. The samples were spun at 10.000xg for 5 minutes at 4°C and the particles were washed with RIPA buffer 3 times. See measured wash protein residue measurements below (see **Table 2.12**). The particles were washed with 1mL ABC buffer and then the ABC was removed and the particles were resuspended in 47 µL ABC. 3 µL (2 µg/µL) of Trypsin Stock was added and the tubed were incubated for 16h at 37°C, 1000 rpm. After the incubation the tubes were spun down for 5 minutes at 10.000xg and placed on the magnet for 2 minutes. The resulting supernatant was measured by Nanodrop 3 times (see **Figure 2.21**) and

spotted on TLC plates using 10 µL of sample (Running solvents: 1:1 Acetonitrile:Water, developed with Nynhydrin and Sulphuric Acid). Unfortunately the stains were very faint and not informative (not shown).

| Table 2.12 |Protein concentration of the wash supernatant

BSA solution for Crosslinking 145.69 mg/mL	BSA mg/mL Wash 1	Wash 2	Wash 3
1. 50 µL 500 µg of particles (368 nmol PXL)	1.87	-0.03	-0.13
2. 10 µL 100 µg of particles (73.6 nmol PXL)	0.98	0.01	-0.06
3. 5 µL 50 µg of particles (36.8 nmol PXL)	2.2	0.05	-0.01
4. 1 µL 10 µg of particles (7.4 nmol PXL)	1.68	-0.06	-0.09
5. 50 µL 500 µg of particles (NH_2)	2.26	-0.07	-0.04
6. 10 µL 100 µg of particles (NH_2)	1.29	-0.01	-0.54

Absorbance at 280 nm was used to check if protein was present in the washes.



| Figure 2.27 | NanoDrop trace of photo-crosslinked BSA peptides cleaved off PXL-MPIO particles with trypsin
Absorbance at 280 nm was used to perform calculations. Samples were blanked against ABC buffer used for trypsin cleavage.

2.7.15 Buffers and reagents used for the recovery of MPIOs from the brain

Modified RIPA buffer: Tris Buffer pH 7.5: 25 mM Tris·HCl, 150 mM NaCl, 0.25% sodium deoxycholate, 1% Triton. 1% Triton X-100 Surfact-Amps X-100 proteomics-grade (10% solution) was from Life Technologies (Cat # 28314, Lot# QD215923), cOmplete™ EDTA-free Protease Inhibitor Cocktail 3 tablets/50 mL from Roche, Recombinant Rat IL-1 beta/IL-1F2 Protein, CF was from R&D Systems (Cat # 501-RL-050/CF). All other reagents were from Sigma, BioUltra-grade or higher. Plastic ware for tissue culture was from Corning exclusively and Protein LoBind microcentrifuge tubes (0.5, 1.5 and 2 mL) were from Eppendorf, other tubes (15 and 50 mL) were

from Falcon, all sterile before use. Fresh buffers were prepared for each experiment and 0.22 µ-filtered before use.

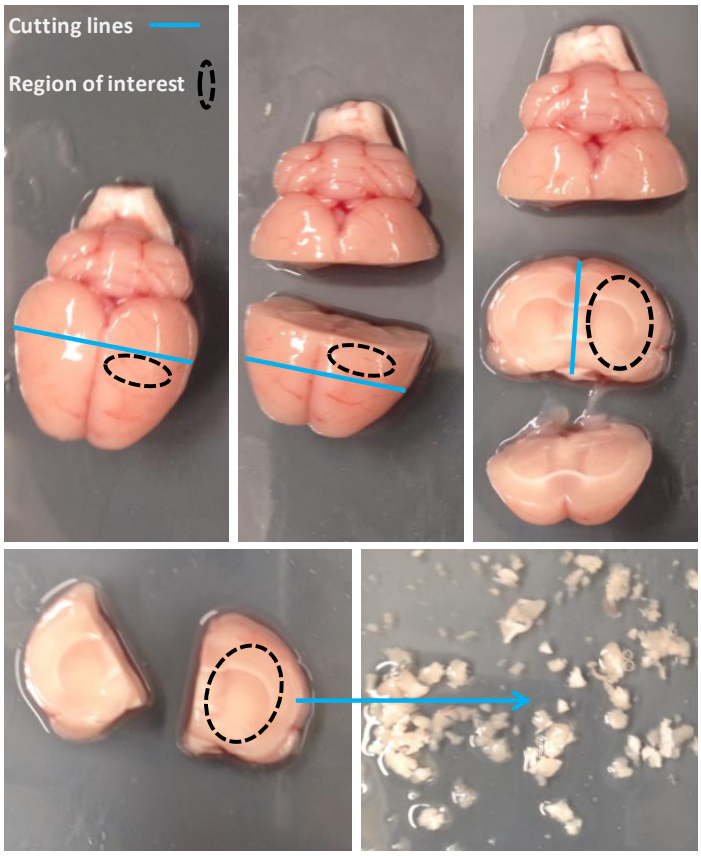
2.7.16 Recovery of MPIOs from an acute IL-1β brain inflammation model in rats

Rats (Wistar, male, *(n=6)* weighing approximately 120 g, Charles River UK) were anesthetized with 2–3% isoflurane in oxygen in an anaesthetic chamber. Upon induction of the anaesthesia, the absence of reflexes was confirmed and the animal was placed in a stereotaxic frame on a surgical heating pad whilst maintaining the anaesthesia *via* a nose cone. A midline incision was made in the scalp and the skull was exposed. A small hole was drilled in the skull and a stereotactic injection of IL-1β (1 µL, 10 ng in sterile saline) using a <50 µm tipped sterile glass capillary was made in the left brain hemisphere at 1 mm anterior, 3 mm lateral from Bregma and at a 4 mm depth into the left striatum. The solution was injected slowly and the capillary was left for 1 minute after the injection before removing it from the injection site. The skin was sutured and the animals were left to recover. Animals were anaesthetized as described above after 4 h of IL-1β activation. An intracarotid injection of a 500 µL of a saline solution containing (Lewis[a]+PXL or PXL) MPIOs (0.5 mg total in sterile saline) was cannulated into the carotid. *Via* the intracarotid injection, animals were flushed with approximately 200 µL of saline and were decapitated immediately after flushing. **(*) Rat 6** was deeply anaesthetised with sodium pentobarbitone and perfused with saline *via* the carotid. A solution containing PXL MPIOs (4 mg/kg, 0.5 mg total in sterile saline) was cannulated into the carotid. *Via* the intracarotid injection rat 6 was flushed with approximately 400 µL of saline and was decapitated immediately after flushing. After dissection, the brains were transferred into ice cold sterile saline. Brain sections were made as shown in **Figure 2.29** onto disposable petri dishes on ice. Chopped sections were submerged in 10 mL of ice-cold RIPA buffer (see recipe above) and UV-treated on ice with an UVP Chromato-Vue Transilluminator, model TM-20 (220/240 V, 50 Hz, 1.5 Amp). A total of 20 minutes of irradiation using midrange UV (8W) 302nm for 30 minutes and longwave (8W) 365nm for 20 minutes was performed at a depth of 20 mm on the samples whilst maintaining agitation (60 rpm) on ice. Treated samples were collected into protein LoBind (Eppendorf) tubes on ice using a 1 mL pipette with the tip cut off and modified ice-cold RIPA lysis buffer with protease inhibitors (3 tablets/50 mL) was added to dishes and the tubes to collect all reaming tissue fragments. Samples were spun down at 10000 xg for 5 minutes (at 4°C). Supernatant was discarded and the tissue fragments were pooled into 1 tube/sample and resuspended again in RIPA buffer. Samples were spun down at 10000 xg for 5 minutes (at 4°C) and the supernatant was discarded. The tissue-pellet was treated with a homogenizer for 15 seconds and the pestle was washed with ice-cold RIPA buffer

and collected in the same tube on ice. The homogenate was vortexed for 15 seconds and spun briefly (< 2 sec) at 2000 xg before placing it onto a ice-cold magnet for 20 minutes, the homogenate was transferred into a fresh tube onto another magnet and was left to incubate on ice again for 20 minutes. The pooled magnetic fractions (on the side of the tube whilst on the magnet –not visible by eye) were collected into 1 tube/sample and washed 3 times (2-minute magnet incubations) with ice-cold RIPA buffer. After the last wash, 20 µL of ice-cold RIPA buffer was added, vortexed and spun down spun for a brief moment (< 2 sec) at 2000 xg before storing the samples at 4 °C. The next day the particles were counted by vortexing the samples for 5 seconds and pipetting out a small volume. The sample was diluted with Milli-Q H_2O and counted with a haemocytometer (Improved Neubauer), using the formula below.

$$\frac{\left((\text{counted particles} * \text{dilution factor}) * 10^4\right) = \text{particles/mL}}{1000 * 20\mu\text{L} = \text{total particles isolated}}$$

Particle numbers were calculated as followed from the supplier's stock concentration (10 mg/ml). Dilute 1 µL (of 10 mg/mL particles) into 999 µL Milli-Q H2O = 1000-fold dilution = 10 µg/mL. Count 10 µL = 2.3×10^7 particles/mL = 2.3×10^6 particles/µg. (Average count of dilution 2276 particles/counting chamber, STDEV ± 1302 particles, n=6).



| Figure 2.28 | Dissection guide to obtain left striatum

Brains were dissected as shown and chopped up as finely as possible to allow maximum UV penetration.

| Table 2.13 | Overview of experiment

Rat	Injection time	Particles	Decapitation
1	10:55	I. 18% PXL + 6% Lewis^a	16:05
2	11:05	II. 12% PXL + 21% Lewis^a	16:25
3	11:25	II. 14% PXL + 28% Lewis^a	16:55
4	11:45	i. PXL 41%	17:15
5	12:00	ii. PXL 12 %	17:35
6(*)	**12:30**	**iii. PXL 26 %**	**17:55**

Note: Rat 6 was treated differently as mentioned in the experimental.

2.7.17 Spike recovery of particles from brain tissue

An adult rat 'control' saline injected brain was used for this experiment. The fresh-frozen, non-fixed brain embedded in OCT was left on ice for 15 minutes. The OCT was removed with blunt forceps and remaining residues were gently rinsed away under the tap with cold water. The midsection (as described before) of the brain was isolated, discarding the cerebellum and front section, keeping the striatum. The striatum was cut in half and each half was placed into a Petri dish on ice. Using a razorblade, the brain sections were chopped-up as finely as possible. 3 mL of ice cold RIPA buffer was added and the Petri dishes whilst being on ice were placed on a shaker (60 rpm) for 40 minutes. The homogenates were collected into two 1,5 mL Eppendorf (Protein LoBind) tubes and spun for 5 minutes at 5000xg (4°C). The supernatant was discarded and the remainder of the brain pieces was added on top of the pellet, resulting in 1 half of a brain section per tube (~0.5 g). The Petri dishes were rinsed out once with 1 mL RIPA and added to the pellet of brain pieces and the spin step was repeated. The supernatant was removed and 200 µL of ice cold RIPA buffer was added to the brain pieces. To spike the sample with a known amount of particles and to calculate the recovery rate 10 µL of spike particles (1 ug/mL in RIPA buffer) was added to the brain pieces, to a separate tube with Milli-Q H_2O (490 µL) and a tube with RIPA (490 µL). Each tube went through a pestle homogenising step, using a clean pestle for each tube, where the pestle was carefully moved up and down for 20 seconds. After the homogenization step the pestle was rinsed with 1 mL of ice cold RIPA buffer. The tubes were spun down for 5 minutes at 5000xg (4°C), placed on a magnet for 10 minutes and the supernatant was removed. Fresh ice cold RIPA buffer (1,5 mL/tube) was added and the washing steps was repeated 3 times. At the last magnet isolation step all the liquid was carefully removed and the particles were resuspended in 10 µL of RIPA buffer and stored at 4°C until counting. Counting of the particles was performed using a Neubauer improved counter. The particles were diluted with 990 µL RIPA and 10 µL of particles were counted per counting chamber. 4 counting chambers for each sample were

counted and the count for each sample was repeated. Average counts per area (4x4 corner squares) were multiplied by 10^4 = particles per mL.

2.7.18 Magnet and dilution trial of spike recovery of particles from brain tissue

An adult rat 'control' saline injected brain was used for this experiment. The fresh, non-fixed frozen brain embedded in OCT was left on ice for 15 minutes. The OCT was removed with blunt forceps and remaining residues were gently rinsed away under the tap with cold water. The midsection (**Figure 2.29**) of the brain was isolated, discarding the cerebellum and front section, keeping the striatum. The striatum was cut in half and each half was placed into a Petri dish on ice. Using a razorblade, the brain sections were chopped-up as finely as possible. 3 mL of ice cold RIPA buffer was added and the Petri dishes whilst being on ice were placed on a shaker (300 rpm) for 30 minutes. The homogenates were collected into two 1,5 mL Eppendorf (Protein LoBind) tubes and spun for 5 minutes at 5000xg (4°C). The supernatant was discarded and the remainder of the brain pieces was added on top of the pellet, resulting in 1 half of a brain section per tube (~0.250 mg tissue/tube). The supernatant was removed and 500 µL/tube of ice cold RIPA buffer was added to the brain pieces. The brain was homogenised by carefully moving the pestle up and down for about 20 seconds. After the homogenization step the following dilutions were made in duplicate.

Brain Homogenate
300 + 700 µL RIPA = 3.3x diluted
200 + 800 µL RIPA = 5x diluted
100 + 900 µL RIPA = 10x diluted
0 + 1000 µL RIPA = no dilution

To these dilutions, a known amount of particles was added to calculate the recovery rate; 10 µL of spike particles (1 ug/mL in RIPA buffer) was added to the brain homogenate dilutions and buffer only. Two separate isolation methods of the particles were tested and described below.

2.7.18.1 Dynal magnet method

DynalMag Magnet



The tubes were spun down for 5 minutes at 5000xg (4°C), placed on a magnet for 10 minutes and the supernatant was removed. Fresh ice cold RIPA buffer (1,5 mL/tube) was added and the washing steps was repeated 3 times. At the last magnet isolation step all the liquid was carefully removed and the particles were resuspended in 10 µL of RIPA buffer and stored at 4°C until counting.

2.7.18.2 Miltenyi magnet method

Miltenyi Magnet

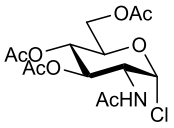


4 magnetic columns were prewashed with 5 mL of ice cold RIPA buffer. Once the meniscus reached the top of the magnetic column the samples were added to the columns. Once the samples ran though, the columns were washed 3 times with a reservoir-volume of ice cold RIPA buffer. After the washes the tubes were removed from the magnetic holder and placed onto a 15 mL tube. The reservoir was filled with ice cold RIPA buffer and the supplied plunger was used to push through the samples. This was repeated twice yielding a 15 mL of flow through/tube and the samples were spun down 3000xg (4°C) for 20 minutes. The supernatant was carefully removed and approximately 1 mL was left, samples were resuspended and transferred to a 1,5 mL Eppendordf (Protein LoBind) tube. 0.5 mL RIPA was used to rinse out the tube and was added to the 1,5 mL tube. The tubes were spun down for 5 minutes at 5000xg (4°C). Then placed on the Dynal magnet for 10 minutes and all the liquid was carefully removed. The particles were resuspended in 10 µL of RIPA buffer and stored at 4°C until counting. Counting of the particles was performed using a Neubauer improved counter and was done as described before.

|SUPPLEMENTARY INFORMATION CHAPTER 2|

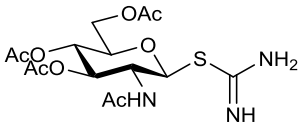
SI.2.1 Synthesis of SCM-Lewis[a]

2-*N*-Acetamido-3,4,6-tri-*O*-acetyl-1-chloro-2-deoxy-*α*-D-glucopyranoside [L1]



Commercially available *N*-Acetyl glucosamine (2.0 g, 9.04 mmol, 1.0 equiv.) was slowly added to a 25 mL round-bottom flask containing acetyl chloride (5.8 mL, 81.37 mmol, 9 equiv.) under strong stirring and Ar-atmosphere. The suspension was stirred for 48h at room temperature. DCM (20 mL) was added to the slightly discoloured solution. The mixture was poured into ice water (50 mL). Phases were separated and the organic layer transferred without delay into a beaker with a sat. $NaHCO_3$-solution (100 mL). The mixture was stirred until the gas-production was finished and transferred to a separatory funnel and the layers were separated. The organic layer was extracted with saturated aq. $NaHCO_3$ and brine (100 mL, each), dried with $MgSO_4$ and concentrated under reduced pressure. The product was precipitated with 20 mL of cold Et_2O and heated until clear. The product was left to crystallize at room temperature and the procedure was repeated. The product **[L1]** was obtained as colourless crystals after high vacuum (1.98 g, 5.42 mmol, 60%). **^{1}H NMR** (400 MHz, $CDCl_3$) δ = 1.95, 2.01, 2.05 (d, *J*=6.9, 5H, d *J*=0.9, 8H, 4xAc + extra H), 4.05 – 4.13 (m, 1H, H-6_b), 4.19 – 4.28 (m, 2H, , H-5, H-6_a), 4.50 (ddd, *J*=10.7, 8.7, 3.7, 1H, , H-2), 5.13 – 5.22 (m, 1H, H-4), 5.29 (dd, *J*=10.8, 9.4, 1H, H-3), 6.07 (d, *J*=8.7, 1H, NH), 6.15 (d, *J*=3.7, 1H, H-1). The spectroscopic data correspond with those reported in the thesis procedures [298], [299].

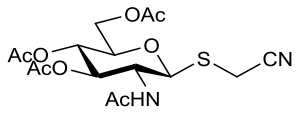
(2-*N*-acetamido-3,4,6-tri-*O*-acetyl-1-chloro-2-deoxy-*α*-D-glucopyranosyl-1-thiouronium) chloride [L2]



Crude chloride **[L1]** (1.98 g, 5.42 mmol, 1.0 equiv.) was dissolved in dry acetone (100mL). To this solution thiourea (0.82 g, 10.83 mmol, 2 equiv.) was added and the mixture was heated to reflux

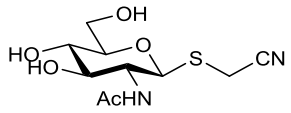
(80 °C). After 2 h the solution was cooled to room temperature and a white solid appeared. The solid was filtrated and washed with ice-cold dry Et_2O (30 ml). The filtrate was concentrated under reduced pressure. The wash of the first filtration was filtrated again. The filtrate was concentrated under reduced pressure and the combined solid fractions gave **[L2]** as white powder (1.64 g, 3.72 mmol, 69%). **^{1}H NMR** (400 MHz, DMSO-d_6) δ = 1.76 – 2.06 (m, 12H, 4 x Ac), 3.38 (s, 22H, H_2O, DMSO), 3.95 – 4.10 (m, 2H, H-2, H-6_b), 4.10 – 4.29 (m, 2H, , H-5, H-6_a), 5.02 (d, *J*=, 9.7, 1H, H-3, H-4), 5.65 (d, *J*=10.5, 1H, H-1), 8.41 (d, *J*=9.2, 1H, (Ac)NH), 9.17 (s, 2H, (S)NH_2), 9.37 (s, 2H, (S)NH_2). The spectroscopic data correspond with those reported in thesis procedures [298], [299].

2-*N*-acetamido-3,4,6-tri-*O*-acetyl-2-deoxy-1-thio-(*S*-cyanomethyl)-*β*-D-glucopyranoside [L3]



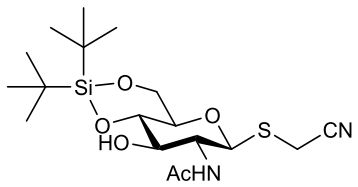
The thiouronium chloride **[L2]** (1.64 g, 3.72 mmol, 1.0 equiv.) was dissolved in a H_2O:acetone mixture (1:1, 40 mL) and sodium metabisulphite (1.56 g, 8.19 mmol, 2.2 equiv.), potassium carbonate (0.67 g, 4.84 mmol, 1.3 equiv.) and chloroacetonitrile (4.48 mL, 70.73 mmol, 19 equiv.) were added. After 16h at room temperature the darkened solution was poured into ice-water (40 mL) and stirred for 2h. The mixture was transferred to a separatory funnel and the organic layers was extracted with CH_2Cl_2 (3 × 100 mL). The combined organic layers were washed with Brine (2 × 150 mL) and dried with $MgSO_4$ and concentrated under reduced pressure. The product **[L3]** was obtained as a white solid after high vacuum. (yield: 0.97 g, 2.40 mmol, 65%). **^{1}H NMR** (400 MHz, $CDCl_3$) δ = 1.98 (s, 3H, 1 x Ac), 2.05 (d, *J*=2.0, 6H, 2 x Ac), 2.10 (s, 3H, 1 x Ac), 3.32 (d, *J*=17.0, 1H, SCH_2CN), 3.67 (d, *J*=17.0, 1H, SCH_2CN), 3.75 (ddt, *J*=7.2, 4.8, 2.4, 1H, H-5), 4.13 – 4.20 (m, 1H, H-6_b), 4.20 – 4.22 (m, 1H, H-6_a), 4.23 – 4.29 (m, 1H, H-2), 4.76 (d, *J*=10.3, 1H, H-1), 5.07 – 5.27 (m, 2H, H-4, H-3), 5.76 (d, *J*=9.2, 1H, NH). The spectroscopic data correspond with those reported in thesis procedures [298], [299].

2-*N*-acetamido-2-deoxy-1-thio-(S-cyanomethyl)-*β*-D-glucopyranoside [L4]



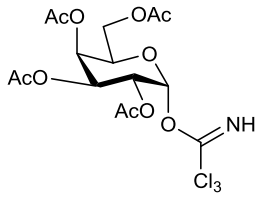
To a suspension of **[L3]** (0.97 g, 2.40 mmol, 1.0 equiv.) in MeOH (30 mL), Et_3N (1.88 mL, 13.64 mmol, 5.6 equiv.) was added and stirred at room temperature for 24h. Solvents were removed under high vacuum and the mixture was co-evaporated with toluene (3 x 30 mL). The product **[L4]** was obtained as a white solid after high vacuum (yield: 0.62 g, 2.24 mmol, 93%). **^{1}H NMR** (400 MHz, DMSO-d_6) **^{13}C NMR** (400 MHz, DMSO-d_6)δ = 1.81 (s, 3H, Ac), 3.09 (ddd, *J*=9.7, 8.2, 5.4, 1H, H-5), 3.12 – 3.17 (m, 1H, H-4), 3.30 (ddd, *J*=9.9, 8.2, 5.6, 1H, H3), 3.45 (dt, *J*=11.7, 5.7, 1H, H-6_b), 3.55 (q, *J*=9.8, 1H, H-2), 3.65 – 3.72 (m, 1H, H-6_a), 3.75 (s, 1H, SCH_2CN), 3.81 (s, 1H, SCH_2CN), 4.46 – 4.54 (m, 2H, H-1, OH-6), 5.11 (dd, *J*=8.7, 5.4, 2H, OH-3, OH-4), 7.89 (d, *J*=9.2, 1H, NH). The spectroscopic data correspond with those reported in thesis procedures [298], [299].

2-*N*-acetamido-2-deoxy-4,6-di-tert-butyldimethylsilylidene-1-thio-(S-cyanomethyl)-*β*-D-glucopyranoside [L5]



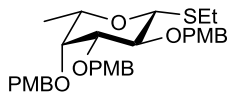
Compound **[L4]** (0.62 g, 2.24 mmol, 1 equiv.) was dissolved in dry DMF (18 mL) and cooled to -40°C (dry ice/AcN). DTBS-ditriflate (11.7 mL, 35.8 mmol, 1.05 equiv.) was slowly added and the mixture was stirred overnight from -40°C to 4°C under argon atmosphere. Pyridine (0.5 mL) was added to quench the reaction and was stirred for 15 min at 4°C. The crude was diluted in EtOAc and washed with water (3 x 100 mL) and Brine (100 mL) and dried with $MgSO_4$ and concentrated under reduced pressure. The product **[L5]** was obtained as a white solid after high vacuum. (yield: 0.99 g, 2.39 mmol, quantitative). **^{1}H NMR** (400 MHz, MeOD) δ = 0.95 – 1.13 (m, 18H, $SiC(CH_3)_6$), 1.98 (s, 3H, Ac), 3.48 – 3.54 (m, 1H, H-3), 3.55 – 3.62 (m, 2H, H-5, H-6_a), 3.67 – 3.78 (m, 2H, H-1, H-6_b), 3.86 (dt, *J*=16.5, 10.1, 2H, H-4, H-2), 4.20 (dd, *J*=10.1, 5.0, 1H, OH-3), 4.72 (d, *J*=10.5, 1H, NH). The spectroscopic data correspond with those reported in thesis procedures [298], [299].

2,3,4,6-tetra-*O*-acetyl-*α*-D-galactopyranoside trichloroacetimidate [L6]



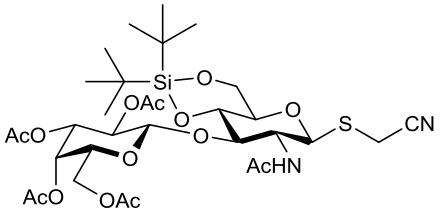
Commercially available β-D-galactose pentaacetate (200 mg, 0.512 mmol, 1 equiv.) was dissolved in dry DMF (2.5 mL) and hydrazine acetate (51.9 mg, 0.564 mmol, 1.1 equiv.) was added to the solution. The solution was heated to 50 °C and stirred for 4.5h. After TLC analysis revealed a completed reaction, twice the volume of EtOAc was added. The organic layer was extracted 3 x with saturated aq. $NaHCO_3$ and Brine (30 mL, each), dried with $MgSO_4$ and concentrated under reduced pressure. The mid-work-up product was dissolved in dry DCM (2.5 mL) under argon atmosphere. DBU and trichloroacetonitrile were added. After 1,5h the reaction was concentrated under reduced pressure and purified by flash chromatography (1:9 to 1:1 in EtOAc in PE). The pure fractions were pooled and concentrated under reduced pressure. The product **[L6]** was obtained as a white solid after high vacuum. (yield: 157 mg, 0.33 mmol, 64%). **^{1}H NMR** (400 MHz, $CDCl_3$) δ = 1.98 – 2.05 (m, 12H, 4 x Ac), 4.04 – 4.17 (m, 3H, H,5 H-6_a), 4.20 (ddd, *J*=10.3, 4.1, 2.1, 1H), 4.27 (dd, *J*=12.3, 4.1, 1H, H-6_b), 5.09 – 5.15 (m, 1H, H-2), 5.18 (d, *J*=10.0, 1H, H-4), 5.55 (t, *J*=9.9, 1H, H-3), 6.54 (d, *J*=3.7, 1H, H-1), 8.71 (s, 1H, NH). The spectroscopic data correspond with those reported in thesis procedures [298], [299].

1-ethylthio-2,3,4-tri-*O*-paramethoxybenzyl-6-deoxy-*β*-L-galactopyranose [L7]



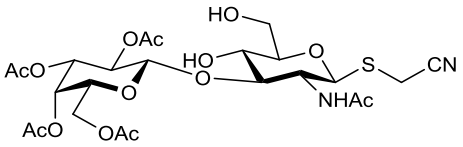
A kind gift from Sonia De Munari. The spectroscopic data correspond with those reported in thesis procedures [298], [299].

4,6-*O*-di-tert-butyldimethylsilylidene-3-*O*-[2,*3*,4,6-tetra-*O*-acetyl-*β*-D-galactopyranose]-1-thio-*S*-cyanomethyl-2-*N*-acetimido-2-deoxy-*β*-D-glucopyranoside [L8]



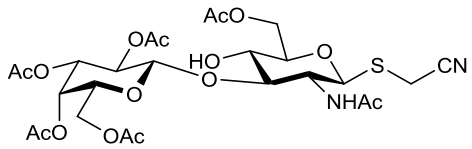
Acceptor **[L6]** (1.0 g, 2.4 mmol, 1 equiv.) and donor **[L5]** (1.48 g, 3.6 mmol, 1.5 equiv.) were dried under high vacuum for 1h in a flame dried flask containing MS4Å and stir bar. Dry DCM was added and the solution was stirred at room temperature for 1h before addition of DTBMP (493 mg, 2.4 mmol, 1 equiv.) and AgOTf (1.4 g, 5.5 mmol, 2.3 equiv.). The mixture was covered by aluminium foil and stirred at room temperature. After 16h the reaction mixture was filtered over Celite and rinsed with DCM. The filtered reaction was concentrated under reduced pressure and purified by flash chromatography (1:2 to 1:0 in EtOAc in PE). The pure fractions were pooled and concentrated under reduced pressure. The product **[L8]** was obtained as a white solid after high vacuum. (yield: 1.22 g, 1.5 mmol, 68%). **^{1}H NMR** (400 MHz, $CDCl_3$) **^{13}C NMR** (400 MHz, $CDCl_3$). *Reaction performed together with Sonia De Munari.* The spectroscopic data correspond with those reported in thesis procedures [298], [299].

3-*O*-[2,*3*,4,6-tetra-*O*-acetyl-*β*-D-galactopyranose]-1-thio-*S*-cyanomethyl-2-*N*-acetimido-2-deoxy-*β*-D-glucopyranoside [L9]



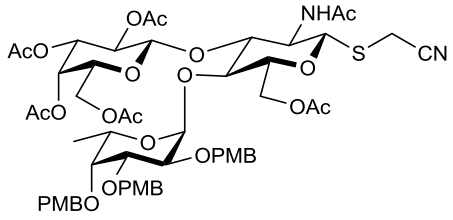
Product **[10]** (1.2 g, 1.63 mmol, 1 equiv.) was dissolved in dry THF (15 mL) and $NEt_3.3HF$ (560 µL, 3.34 mmol, 2.1 eq) was added. After 5h the reaction was concentrated under reduced pressure and co-evaporated with MeOH (1x 50 mL) and toluene (3 x 50 mL). The product **[L9]** was obtained as a white solid after high vacuum. (yield: 1.20 g, 1.6 mmol, quantitative). *Reaction performed together with Sonia De Munari.* The spectroscopic data correspond with those reported in thesis procedures [298], [299].

6-*O*-Acetyl-3-*O*-[2,*3*,4,6-tetra-*O*-acetyl-*β*-D-galactopyranose]-1-thio-*S*-cyanomethyl-2-*N*-acetimido-2-deoxy-*β*-D-glucopyranoside [L10]



Unprotected disaccharide **[L9]** (200 mg, 0.33 mmol, 1 equiv) was dissolved in dry DCM (3.5 mL) and dry pyridine (107 µL, 1.32 mmol, 4 equiv.) under argon atmosphere at -78°C. To the cooled mixture AcCl (59 µL, 0.82 mmol, 2.5 eq) was added. After 1h MeOH was carefully added in portions to quench the reaction. The mixture was stirred until the gas-production was finished. The reaction was warmed to room temperature and MeOH was carefully added. The absence of gas-production was used as an indicator for a quenched reaction. The reaction was concentrated under reduced pressure and dissolved in DCM. The organic layer was transferred to a separatory funnel and the layers were separated. The organic layer was extracted with aq. 1 M HCl, saturated aq. $NaHCO_3$ and Brine (50 mL, each), dried with $MgSO_4$ and concentrated under reduced pressure. The product **[L10]** was obtained as colourless powder after high vacuum (161 mg, 0.25 mmol, 75%). **^{1}H NMR** (400 MHz, $CDCl_3$) δ = 1.97 (s, 3H, Ac), 2.02 (s, 3H, Ac), 2.04 – 2.12 (m, 6H, Ac), 2.15 (s, 6H, Ac), 2.92 (d, *J*=34.4, 1H, SCHCN), 3.35 (d, *J*=17.1, 1H, SCHCN), 3.56 (q, *J*=2.9, 2.5, 2H, H-4, H-5), 3.70 – 3.80 (m, 1H, H-2), 3.96 (dd, *J*=9.7, 7.3, 1H, H-3), 4.01 – 4.19 (m, 3H, H'-5, H'-6b, H'-6a), 4.24 (dd, *J*=12.0, 4.9, 1H, H'-6b), 4.45 (dd, *J*=12.2, 1.5, 1H, H-6a), 4.61 (d, *J*=8.0, 1H, H'-1), 4.89 (d, *J*=10.3, 1H, H-1), 5.02 (dd, *J*=10.5, 3.4, 1H, H'-3), 5.20 (dd, *J*=10.5, 7.9, 1H, H'-2), 5.37 (dd, *J*=3.4, 1.1, 1H, H'-4), 6.36 (d, *J*=8.7, 1H, NH). The spectroscopic data correspond with those reported in thesis procedures [298], [299].

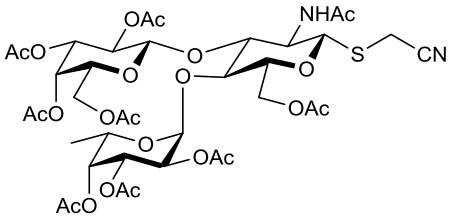
6-*O*-acetyl-4-*O*-[2,3,4-tri-*O*-paramethoxybenzyl-6-deoxy-*α*-L-galactopyranose]-3-*O*-[2,3,4,6-tetra-*O*-acetyl-*β*-D-galactopyranosyl]-2-deoxy-1-thio-*S*-cyanomethyl-2-acetamido-2-deoxy-*β*-D-glucopyranoside [L11]



[L10] (161 mg, 0.25 mol, 1.0 equiv.) and **[L7]** (280 mg, 0.50 mmol, 2.0 equiv.) were dried under high vacuum for 1h in a flame dried flask containing MS4Å and stir bar. The mixture was dissolved

in dry DCM:DMF 1:1 mixture (1.5 mL) and stirred for 1h at room temperature before copper(II) bromide (111 mg, 0.50 mmol, 2.0 equiv) and tetra-butylammonium bromide (168 mg, 0.52 mmol, 2.1 eq) were added. The mixture was covered by aluminium foil and stirred at room temperature. After 16h the reaction mixture was filtered over Celite and rinsed with EtOAc (100 mL). The organic layer was washed twice with aq. NH_4Cl, pH9 (100 mL each) and Brine (100 mL), dried with $MgSO_4$ and concentrated under reduced pressure. The concentrated crude was purified by flash chromatography (1:2 to 1:0 in EtOAc in PE). The pure fractions were pooled and concentrated under reduced pressure. The product **[L11]** was obtained as a white powder after high vacuum. (yield: 167 mg, 0.14 mmol, 58%). **^{1}H NMR** (400 MHz, $CDCl_3$) δ = 1.84 (s, 3H, Ac), 1.92 (s, 3H, NHAc), 1.95 (s, 3H, Ac), 2.01 (s, 3H, Ac), 2.04 (s, 3H, Ac), 2.07 (s, 3H, Ac), 3.56 (d, *J*=17.2, 1H, CHCN), 3.67 – 3.74 (m, 2H, SCHCN, H''-4), 3.76 – 3.85 (m, 11H, H-5, 3 x OMe), 3.89 (t, *J*=7.3, 2H, H-4, H'-5), 3.94 (s, 1H, H-3), 4.04 (d, *J*=7.1, 2H, H-2, H'-6), 4.09 (s, 1H, , H'-6b), 4.35 (dd, *J*=12.2, 3.9, 1H. H-6b), 4.40 – 4.50 (m, 2H, H''-5, H-6a), 4.61 – 4.69 (m, 2H, 2 x , CH_2PMB), 4.69 – 4.83 (m, 6H, 3 x CH_2PMB, H''-1), 4.85 (d, *J*=3.9, 1H, CH_2PMB), 4.89 – 4.97 (m, 2H, H'-3), 5.12 (dd, *J*=10.4, 8.1, 1H, H'-2), 5.35 (d, *J*=3.4, 1H, H'-4), 6.26 (d, *J*=9.2, 1H, NH), 6.80 – 6.88 (m, 4H, CH_{Ar}), 6.91 (d, *J*=8.3, 2H, CH_{Ar}), 7.23 – 7.33 (m, 4H, CH_{Ar}), 7.36 (d, *J*=8.3, 2H, CH_{Ar}). The spectroscopic data correspond with those reported in thesis procedures [298], [299].

6-*O*-acetyl-4-*O*-[2,3,4-tri-*O*-acetyl-6-deoxy-*α*-L-galactopyranose]-3-*O*-[2,3,4,6-tetra-*O*-acetyl-*β*-D-galactopyranosyl]-2-deoxy-1-thio-*S*-cyanomethyl-2-acetamido-2-deoxy-*β*-D-glucopyranoside [L12]



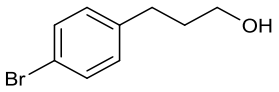
Molecular Weight: 920.89

Compound **[L11]** (197mg, 0.14 mmol, 1.0 equiv.) was dissolved in a mixture of AcN:H_2O (9:1, 3 mL). CAN (2.2 g, 4.1 mmol, 6.05 eq) was added to the mixture and the solution was stirred at room temperature for 7h. 10 mL of H_2O was added to the reaction mixture and the aqueous layer was extracted with 3 x EtOAc and 2 x $CHCl_3$:isopropanol (3:1) (50 mL each). The organic layers were combined, dried with $MgSO_4$ and concentrated under reduced pressure. The oil was dissolved in Ac_2O (10 mL) and pyridine (15 mL) and DMAP was added (1.8 mg, 0.01 mmol, 0.1 equiv.). The mixture was stirred at room temperature. After 16h the reaction was cooled to 0°C

and MeOH was added to quench the reaction. The mixture was stirred until the gas-production was finished. The reaction was warmed to room temperature and MeOH was carefully added. The absence of gas-production was used as an indicator for a quenched reaction. Solvents were removed under high vacuum and the mixture was co-evaporated with toluene (3 x 30 mL). The concentrated crude was purified by flash chromatography (1:1 to 1:0 in EtOAc in PE). The pure fractions were pooled and concentrated under reduced pressure. The protected Lewis[a] **[L12]** was obtained as a white powder after high vacuum. (yield: 83.3 mg, 0.09 mmol, 63%). **^{1}H NMR** (400 MHz, $CDCl_3$) δ = 1.24 (s, 3H, H''-6,) , 2.01 – 2.11 (m, 30H, 9 x Ac + NHAc, + additional Ac), 3.37 (dd, *J*=27.2, 17.2, 2H, SCHCN, H-5), 3.56 (d, *J*=3.8, 1H, SCHCN), 3.86 – 3.91 (m, 1H, H-6b), 3.96 (d, *J*=8.8, 1H, H'-5), 4.06 (d, *J*=9.8, 1H, H-3), 4.10 (d, *J*=7.2, 1H, H-4), 4.12 – 4.16 (m, 1H, H-2), 4.50 (dd, *J*=11.4, 5.7, 1H, H'-6b), 4.59 (qd, *J*=8.9, 7.5, 4.3, 3H, H-1, H-6a, H'-6a), 4.78 – 4.83 (m, 1H, H'-1), 4.96 (d, *J*=3.4, 1H, H'-3), 5.01 (s, 1H, H''-5), 5.04 (d, *J*=2.7, 1H, H''-1), 5.08 – 5.13 (m, 1H, H'-2), 5.18 (dd, *J*=11.0, 3.0, 1H, H''-3), 5.23 (dd, *J*=11.1, 3.4, 1H, H''-2), 5.34 (dt, *J*=5.0, 2.6, 1H, H''-4), 5.37 – 5.41 (m, 1H, H'-4), 6.59 (s, 1H, NH). The spectroscopic data correspond with those reported in thesis procedures [298], [299].

SI.2.2 Synthesis of Trifluoromethylphenyldiazirine

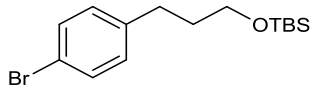
3-(4-Bromophenyl)propanol [P1]



Commercially available 3-(4-bromophenyl) propanoic acid **[0]** (2g, 8.73 mmol, 1 equiv.) was dissolved in dry Et_2O (50 mL) in a flame dried flask under argon atmosphere and cooled to 0 °C. To this solution was carefully added $LiAlH_4$ (1.3 equiv., 11.7 mmol, 11.7 mL of 1 M solution). The reaction was slowly warmed to room temperature in 1 h. TLC analysis was performed in PE:EtOAc (2:1 + drop of acetic acid) and showed a complete conversion after 2h. The reaction was cooled again to 0 °C and 430 µL H_2O was slowly added (Fieser&Fieser work-up, X mg of $LiAlH_4$ = X µL of H_2O). 430 µL of 25% NaOH in H_2O was added and subsequently 3x430=1290 µL H_2O was added. The solution was left to stir for 5 minutes and a white precipitate was formed. The solution was filtered over celite and the remaining solid in the flask was washed and sonicated with Et_2O (20 mL), this was repeated three times. The filtrate was dried with $MgSO_4$ and concentrated under reduced pressure. The product **[P1]** was obtained as a colourless oil after high vacuum. (yield: 1.6934 g, 7.87 mmol, 90%) **^{1}H NMR** (400 MHz, $CDCl_3$) δ = 1.66 – 1.83 (m, 2H, CH_2), 1.87 – 2.05 (m,

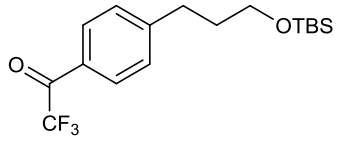
1H, OH), 2.46 – 2.62 (m, 2H, $PhCH_2$), 3.53 (dt, *J*=9.2, 6.4, 2H, OCH_2), 6.88 – 7.13 (m, 2H, Ph), 7.13 – 7.33 (m, 2H, Ph). The spectroscopic data correspond with those reported in literature [249].

[3-(4-Bromophenyl)propoxy](tert-butyl)dimethylsilane [P2]



3-(4-bromophenyl)propanol **[P1]** (1.6934g, 7.87 mmol, 1 equiv.) was dried under high vacuum in a flame dried flask. Dry DMF (20 mL) under argon atmosphere was used to dissolve **[P1]** and imidazole (1.5 equiv., 11.81 mmol, 804 mg) and TBSCl (1.1 equiv., 8.66 mmol, 1.31 g) were added. The reaction was left to stir for 2 h at room temperature. TLC analysis was performed in PE:EtOAc (2:1) and showed a complete conversion after 2h. While stirring, 100 mL of H_2O was added to the reaction. The mixture was transferred to a separating funnel and the water mixture was extracted with PE (50 ml) 3 times. The organic layers were combined and were extracted with H_2O (50 mL) 4 times and Brine (50 mL), dried with $MgSO_4$ and concentrated under reduced pressure. The TBS-protected product **[P2]** was obtained as a colourless oil after high vacuum. (yield: 2.5933 g, 7.8 mmol, quantitative). **^{1}H NMR** (400 MHz, $CDCl_3$) δ = 0.05 (s, 6H, 2·$SiCH_3$), 0.91 (s, 9H 3·CH_3), 1.85 (ddd, *J*=12.3, 6.8, 4.1, 2H, CH_2), 2.79 (dd, *J*=8.7, 6.8, 2H, $PhCH_2$), 3.64 (t, *J*=6.1, 2H, OCH_2), 7.36 (d, *J*=8.2, 2H, Ph), 7.99 (d, *J*=8.0, 2H, Ph). The spectroscopic data correspond with those reported in literature [249].

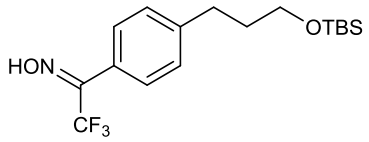
1-{4-[3-(tert-butyldimethylsilyloxy)propyl]phenyl}-2,2,2-trifluoroethanone [P3]



The TBS-protected bromide **[P2]** was (2.59g, 7.8 mmol, 1 equiv.) was dried under high vacuum in a flame dried flask. Dry Et_2O (30 mL) under argon atmosphere was used to dissolve **[P2]** and the reaction was cooled to -78°C in an acetone/dry-ice bath. Carefully n-BuLi was added dropwise (1.25 equiv., 9.8 mmol, 0.63 g, 4.1 mL of a 2.5 M solution in hexanes). The reaction was allowed to warm up to room temperature over the course of 3 h (previously KW29 was not checked, used literature ref 1h). The reaction was cooled again to -78°C in an acetone/dry-ice bath and a solution of 1-trifluoroacetylpiperidine (1.1 equiv., 8.65 mmol, 1.57 g, 1.8 mL) was slowly added to

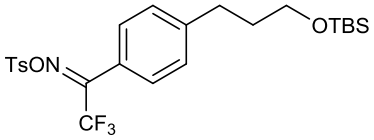
the reaction. The reaction was allowed to warm up to 0°C over the course of 2 hours (literature ref: completion). The reaction turned into a yellowish solution. TLC (1:9 EtOAC:PE) indicated incomplete conversion and another 0.2 equiv. of the 1-trifluoroacetylpiperidine was added and left to stir at 0°C. After 2h another 0.2 equiv. was added and the reaction was left to stir for another 2h. TLC revealed ≥ 80% conversion. Whilst on ice and stirring, (50 mL) of sat. aq. NH_4Cl was added. The mixture was transferred to a separating funnel and the organic layer was separated. The Et_2O layer was extracted with sat. aq. NH_4Cl, H_2O and Brine (50 mL each), dried with $MgSO_4$ and concentrated under reduced pressure whilst heating at 77 °C to get rid of the 1-trifluoroacetyl piperidine. The crude ketone **[P3]** was obtained as a yellowish/colourless oil after high vacuum and was purified by column chromatography (10-30% Toluene gradient in PE). Yield: 52% (1.4207 g). **^{1}H NMR** (400 MHz, $CDCl_3$) δ = 0.05 (s, 6H, 2x $SiCH_3$), 0.91 (s, 9H, 3x CH_3), 1.85 (ddd, *J*=12.3, 6.8, 4.1, 2H, 2x CH_2), 2.79 (dd, *J*=8.7, 6.8, 2H, $PhCH_2$), 3.64 (t, *J*=6.1, 2H, OCH_2), 7.36 (d, *J*=8.2, 2H, Ph), 7.99 (d, *J*=8.0, 2H, Ph). The spectroscopic data correspond with those reported in literature [249].

1-{4-[3-(tert-butyldimethylsilyloxy)propyl]phenyl}-2,2,2-trifluoroethanone Oxime [P4]



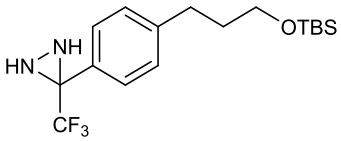
The ketone **[P3]** (1.42 g, 4.10 mmol, 1 equiv.) was dissolved in pyridine (5 mL). To this solution hydroxylamine $HONH_2$(0.855 g, 12.3 mmol, 3 equiv.) was added and the mixture was stirred and heated to reflux (115°C). After 2 h TLC revealed a complete conversion (9:1 in PE:EtOAc) and the reaction was cooled to room temperature. Solvents were removed under high vacuum. The concentrated crude was dissolved in EtOAc and aq. 0.2 M citric acid was added (30 mL each) and the mixture was transferred to a separating funnel and the organic layer was separated. The organic layer was extracted twice with aq. 0.2 M citric acid, H_2O and Brine (30 mL each), dried with $MgSO_4$ and concentrated under reduced pressure. The oxime **[P4]** was obtained as a colourless oil after high vacuum (yield: 1.2919 g, 3.57 mmol, 87%).**^{1}H NMR** (400 MHz, $CDCl_3$) δ = 0.06 (d, J=2.7, 6H, 2·$SiCH_3$), 0.91 (s, 9H, 3·CH_3), 1.81 – 1.94 (m, 2H, CH_2), 2.68 – 2.77 (m, 2H, $PhCH_2$), 3.66 (t, J=6.3, 2H, OCH_2), 7.28 – 7.38 (m, 2H, Ph), 7.45 (d, J=8.0, 2H, Ph), 8.80 (s, 1H, NOH). The spectroscopic data correspond with those reported in literature [249].

1-{4-[3-(tert-butyldimethylsilyloxy)propyl]phenyl}-2,2,2-trifluoroethanone O-Tosyl Oxime [P5]



The oxime **[P4]** (1.292 g, 3.57 mmol, 1 equiv.) was dissolved in DCM (10 mL). To this solution NEt_3 (780 µL, 5.59 mmol, 1.5 equiv.) and DMAP (9 mg, 0.07 mmol, 0.02 equiv.) was added and the mixture was stirred for a couple of minutes. TsCl (711 mg, 3.57 mmol, 1 equiv. in 10 mL DCM) was added to the reaction with a syringe pump on the slowest setting. The reaction was left to stir for 16h. After TLC (1:1 Toluene:PE) revealed complete conversion 50 mL of aq. 0.2 M citric acid was added and the mixture was transferred to a separating funnel and the organic layer was separated. The organic layer was extracted with aq. 0.2 M citric acid and Brine (50 mL each). TLC analysis revealed product in the Brine layer and was re-extracted with 20 mL of DCM. The combined organic layers were dried with MgSO4 and concentrated under reduced pressure. The tosylate **[P5]** was obtained as a faint yellow oil after high vacuum (yield: 1.5764 g, 3.06 mmol, 57%). **^{1}H NMR** (400 MHz, $CDCl_3$) δ = 0.02 (s, 6H, 2·$SiCH_3$), 0.87 (s, 9H, 3·CH_3), 1.76 – 1.85 (m, 2H, CH_3), 2.42 (d, *J*=8.2, 3H $PhCH_3$), 2.63 – 2.71 (m, 2H, $PhCH_2$), 3.57 – 3.62 (m, 2H, OCH_2), 7.23 – 7.28 (m, 2H, Ph), 7.30 (d, *J*=8.2, 2H, Ph), 7.32 – 7.37 (m, 2H, Ph), 7.85 (d, *J*=8.4, 1H, Ph). The spectroscopic data correspond with those reported in literature [249].

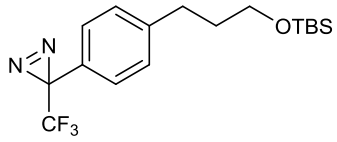
3-{4-[3-(tert-butyldimethylsilyloxy)propyl]phenyl}-3-(trifluoromethyl)diaziridine [P6]



The tosyl-activated oxime **[P5]** (1.5767 g, 3.06 mmol, 1 equiv.) was dissolved in DCM (5 mL) and cooled to -40°C. Gaseous ammonia (NH_3) was condensed by the means of a cold finger into liquid ammonia. About 15 mL of liquid ammonia was added to the cooled reaction and the reaction was left to stir for about 2h at -40°C after TLC (1:1 Toluene:PE and 1:4 EtOAc:PE). The reaction was taken out of the cooling bath (dry ice+acetone) and left to warm up over the course of 16h. During this period the ammonia was left to evaporate. The remaining slurry (ammonium tosylate) was redissolved in DMC (10 mL) and filtered over celite. The filtrate was washed with 2 x 10 mL. The organic layer was extracted three times with H_2O and Brine once (50 mL each), dried with

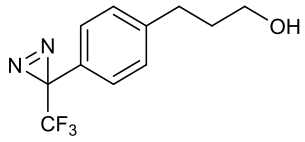
$MgSO_4$ and concentrated under reduced pressure. (yield: 1.1091 g, 3.08 mmol, quantitative). **^{1}H NMR** (400 MHz, $CDCl_3$) δ = 0.06 (s, 6H, 2x $SiCH_3$), 0.92 (s, 9H, 3x CH_3), 1.79 – 1.88 (m, 2H, CH_2), 2.21 (d, *J*=8.7, 1H, NH), 2.63 – 2.73 (m, 2H, $PhCH_2$), 2.77 (d, *J*=8.8, 1H, NH), 3.64 (t, *J*=6.2, 2H, OCH_2), 7.25 (d, *J*=8.1, 2H, Ph), 7.50 (dd, *J*=13.4, 7.9, 2H, Ph). The spectroscopic data correspond with those reported in literature [249].

3-{4-[3-(tert-butyldimethylsilyloxy)propyl]phenyl}-3-(trifluoromethyl)-3H-diazirine [P7]



The diaziridine **[P6]** (1.1091 g, 3.08 mmol, 1 equiv.) was dissolved in MeOH (5 mL). To this solution NEt_3 (857 µL, 6.15 mmol, 2 equiv.) was added and the mixture was stirred for a couple of minutes. I_2 was added in portions (796 mg, 3.08 mmol, 1 equiv). After each portion the reaction was left to decolourize until eventually the reactions doesn't decolourize anymore (dark-brown/orange). After 30 minutes TLC revealed a complete conversion (1:9) EtOAc:PE. 30 mL of aq. 10% (w/w) citric acid was added and the mixture was transferred to a separating funnel. The mixture was extracted twice with Et_2O (30 mL each) and the layers were separated and combined. The organic layer was extracted with aq. 10% (w/w) citric acid, sat. aq. $NaHSO_4$ and Brine (80 mL each), dried with $MgSO_4$ and concentrated under reduced pressure. The diazirine **[P7]** was obtained as a white/colourless slurry/oil after high vacuum (yield: 0.8997 g, 2.51 mmol, 82%). **^{1}H NMR** (400 MHz, $CDCl_3$) δ = 0.11 (d, *J*=3.5, 6H, 2x $SiCH_3$), 0.96 (d, *J*=3.4, 9H, 3x CH_3), 1.81 – 1.92 (m, 2H, CH_2), 2.61 – 2.84 (m, 2H, $PhCH_2$), 3.67 (t, *J*=6.1, 2H, OCH_2), 7.14 (dd, *J*=11.5, 8.4, 2H, Ph), 7.21 – 7.33 (m, 2H, Ph). The spectroscopic data correspond with those reported in literature [249].

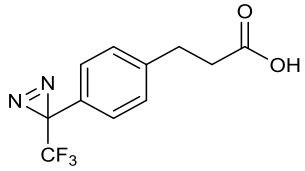
3-{4-[3-(Trifluoromethyl)-3*H*-diazirin-3-yl]phenyl}propan-1-ol [P8]



The diazirine **[P7]** (0.8997 g, 2.51 mmol, 1 equiv.) was dissolved in MeOH (5 mL). To this solution concentracted HCl (37% w/v, 12M) (351 µL, 3.78 mmol, 1.5 equiv.) was added. After 2h complete consumption of the starting material was observed including 2 other spots (3:2) EtOAc:PE (TBS

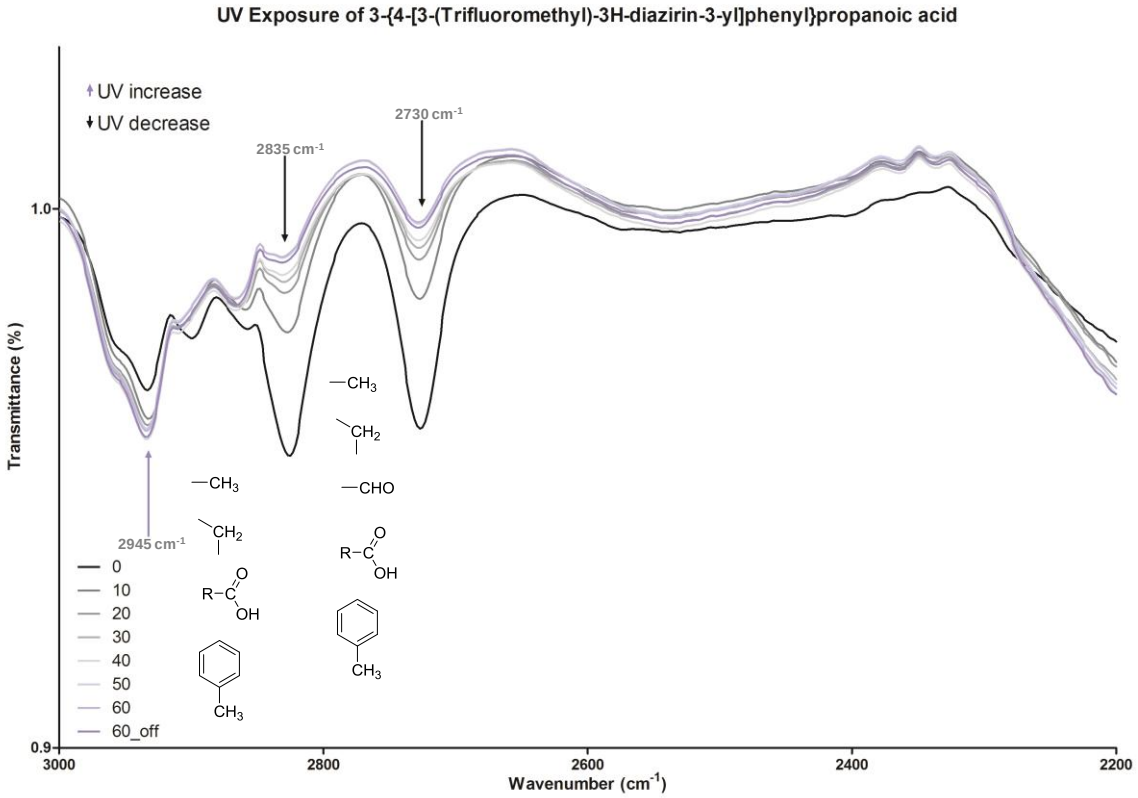
and unknown). The MeOH was removed by evaporation and the concentrated crude was dissolved in Et_2O. The organic layer was extracted twice with sat. aq. $NaHCO_3$ and twice with Brine (30 mL each), dried with $MgSO_4$ and concentrated under reduced pressure. The crude was purified by column chromatography (10-60% EtOAc in PE). The deprotected diazirine **[P8]** was obtained as a colourless oil after high vacuum (yield: 0.3964 g, 1.62 mmol, 65%). **^{1}H NMR** (400 MHz, $CDCl_3$ δ = 1.56 (s, 1H, OH), 1.82 – 1.94 (m, 2H, CH2), 2.72 (dd, *J*=8.7, 6.8, 2H, $PHCH_2$), 3.66 (t, *J*=6.4, 2H, OCH_2), 7.12 (d, *J*=8.1, 2H, Ph), 7.17 – 7.34 (d, *J*=8.1, 2H, Ph). The spectroscopic data correspond with those reported in literature [249].

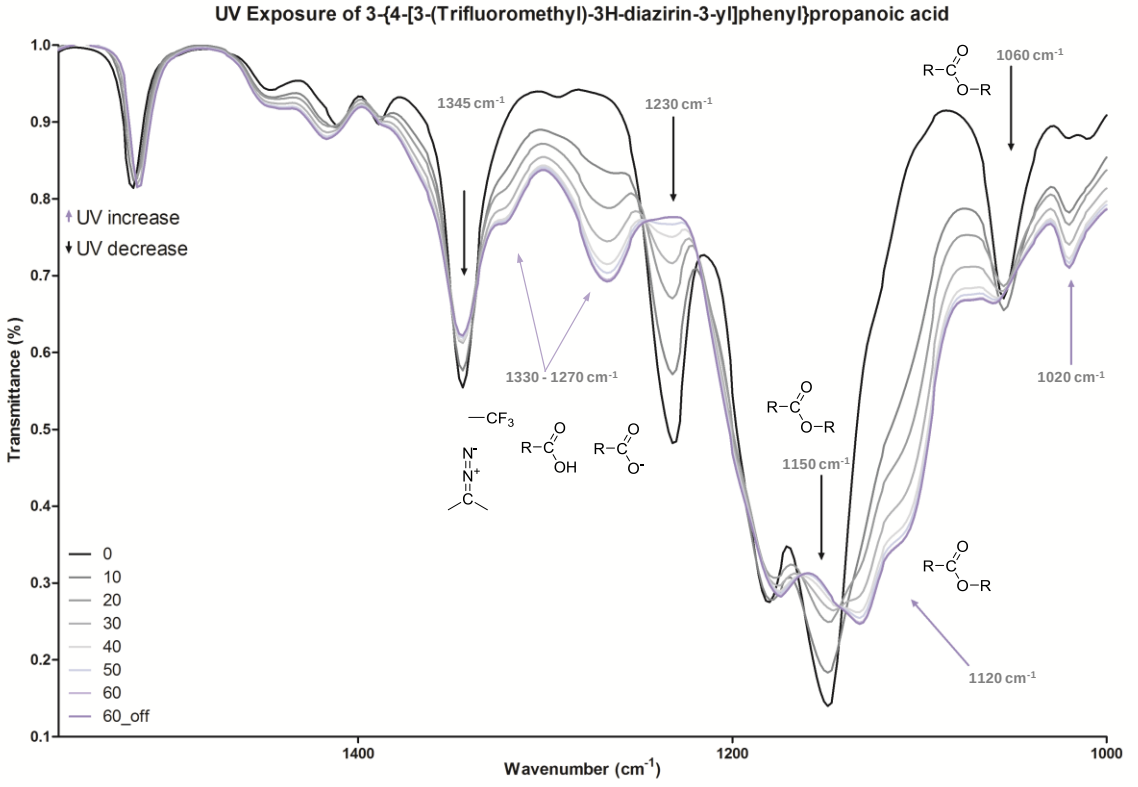
3-{4-[3-(Trifluoromethyl)-3*H*-diazirin-3-yl]phenyl}propanoic acid [P9]

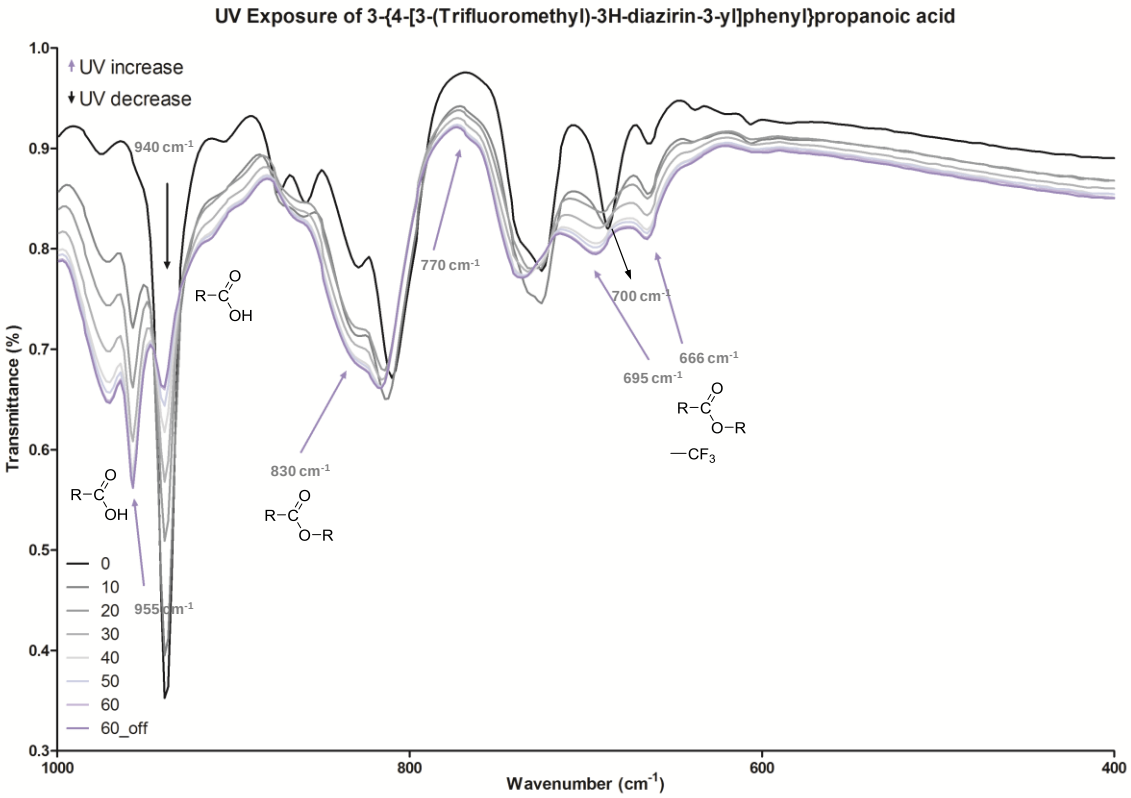


The alcohol **[P8]** (0.3964 g, 1.62 mmol, 1 equiv.) was dissolved in a H_2O:DCM (1:2) mixture. TEMPO (25.4 mg, 0.16 mmol, 0.1 equiv.) and BAIB (1.307 g, 4.06 mmol, 2.5 equiv.) were added and the reaction was left to stir vigorously overnight (16h). TLC revealed an incomplete reaction and the reaction was left to stir for another 8h (3:7) EtOAc:PE + 0.1 mL of NEt3 per 10 mL of running solvent. Sat. aq. $Na_2S_2O_3$ was added after 24h and stirred vigorously for 5 min. EtOAc was added and the mixture was transferred to a separating funnel and the organic layer was separated. The organic layer was extracted with 1M aq. HCl and Brine (20 mL, each), dried with $MgSO_4$ and concentrated under reduced pressure. The crude was purified by flash chromatography (10-30% EtOAc in PE). The acid **[P9]** was obtained as a colourless oil (should be white solid) after high vacuum (yield: 143.3 mg, 34%). **^{1}H NMR** (400 MHz, $CDCl_3$) δ = 2.73 – 2.82 (m, 1H, CH_2), 2.83 (d, *J*=7.0, 1H, CH_2), 2.99 (d, *J*=7.4, CH_2), 3.02 (s, 1H, CH_2), 7.15 (s, 1H, Ph), 7.17 (s, 1H, Ph), 7.25 (d, *J*=15.8, 1H, Ph), 7.28 (s, 1H, Ph), 9.84 (q, *J*=1.2, 1H, COOH). The spectroscopic data correspond with those reported in literature [249].

SI.3.3 Additional IR spectra of UV-irradiated trifluoromethylphenyldiazirine






UV Exposure of 3-{4-[3-(Trifluoromethyl)-3H-diazirin-3-yl]phenyl}propanoic acid
UV increase
UV decrease
940 cm-1
770 cm-1
700 cm-1
695 cm-1
666 cm-1
830 cm-1
955 cm-1
0
10
20
30
40
50
60
60_off
Transmittance (%)
Wavenumber (cm-1)
1.0
0.9
0.8
0.7
0.6
0.5
0.4
0.3
1000
800
600
400

3

|BIOLOGY |

IN VITRO AND *IN VIVO* CHARACTERISATION OF BRAIN INFLAMMATION MODELS USING LEWIS^{A}-NANOPARTICLES

Thus far, the synthesis, construction, and characterization of nanoparticles bearing Lewis[a] and a diazirine-based photo-crosslinker have been described in Chapter 2 and their application for proteomic identification *in vitro* and binding studies *in vivo* will be presented here. This chapter describes the validation and testing of different *in vitro* and *in vivo* models of brain inflammation with the aim of identifying a carbohydrate binding receptor for Lewis[a]. As alluded to in the introduction, there are multiple lectins in the human body that can bind Lewis[a] and studying the immune response in the brain following an inflammatory stimulus by IL-1β was considered to be a manner in which they might be identified. An *in vitro* approach, using brain microvascular endothelial cell cultures, was used to study the interactions of Lewis[a] and the vasculature. By incubating IL-1β-stimulated cells with the bi-functional nanoparticles, a covalent trap of the Lewis[a]-interacting endothelial lectins E-Selectin and/or P-Selectin was expected. However, proteomic identification of the pulled down interacting proteins did not include any (known) lectins. Subsequently, the experiment was repeated without crosslinking, using only Lewis[a]-functionalised nanoparticles. Again, this approach did not trap any lectins. When the whole cell proteome was studied, the second most upregulated protein by IL-1β was identified as E-Selectin, which served to highlight this ligand as a potential target for the Lewis[a] and Lewis[b] carbohydrates. As the *in vitro* experiments mimic the blood vessel luminal surface that would be exposed to an intravascular agent, other blood-borne proteins and immune cells that may contribute to the Lewis[a] binding *in vivo*, may be absent in these *in vitro* experiments. Therefore, the transcriptome of IL-1β rat brain lesions was studied to find the up-regulated mRNA transcripts of this acute brain inflammation model. In this case, E-selectin was the third most upregulated transcript upon IL-1β stimulation. Taken together, these two experiments confirmed E-Selectin as an IL-1β-upregulated protein in the models used and led to a set of *in vivo* blocking experiments using antibodies against E- and P-Selectin. As E-selectin ligands are expressed by neutrophils, such as PSGL-1, which are recruited to the early-inflamed site via chemotaxis, neutrophils were depleted in rats and the binding of Lewis[a] was assessed in the absence of these immune cells. These experiments revealed that the binding of Lewis[a] is E-Selectin dependent with only a minor role of P-Selectin. Additionally, the absence of neutrophils allowed more Lewis[a]-MPIO to bind to the IL-1β inflamed endothelium. Using the MRI results and immunohistochemistry a model for *in vivo* binding of Lewis[a] during acute IL-1β is presented.

3.1 | PROTEOME ANALYSIS OF LEWIS^A INTERACTING MOLECULES USING BI-FUNCTIONAL NANOPARTICLES *IN VITRO*

3.1.1 Trapping multivalent carbohydrate interactions with nanoparticles using a photo-crosslinker and proteomics

Proteomics has the power to provide an unbiased screening method and comprehensive overview of proteins involved in disease processes and provides insight into understanding essential biologicals mechanisms upon various stimuli. By comparing the proteome of healthy cells or tissue versus diseased cells or tissue, proteins that either are up or down regulated in the disease state may reveal protein targets crucial in the disease development and provide targets for drug intervention. The cell membrane or plasma membrane and its associated glycocalyx are involved in cell adhesion, cell signalling and cell homeostasis; it is the main cellular component that is connected with its surrounding environment and can interact with other cells. Upon a stimulus or cell contact, signalling *via* cell surface receptors can transmit environmental changes into the cell body and nucleus, where proteomic changes can occur *via* transcription initiation.

Brain microvascular endothelial cells form the Blood-Brain-Barrier (BBB) and any molecular changes at the cell membrane of these cells may be indicative of ongoing pathology behind a closed BBB. Leukocyte recruitment of brain inflammatory diseases (e.g. multiple sclerosis (MS)) can take place across intact, but activated brain endothelium [314], [315], [316]. Current Gadolinium-based contrast agents rely on late stage BBB permeability despite the fact that, for many inflammatory brain diseases, BBB breakdown is already accompanied by severe symptoms [3]. The molecular changes of the early-activated cerebral endothelium before BBB breakdown have been successfully visualized before and rely on cell adhesion markers [65], [64]. Iron-oxide nanoparticles functionalized with an anti-endothelial Vascular Cell Adhesion Molecule (VCAM-1) antibody enabled *in vivo* MRI detection of early inflammatory lesions, hallmarked by immune cell recruitment, but no BBB breakdown or gadolinium accumulation [64, 141]. Using the Lewis sugar sialyl Lewis^x (sLe^x) conjugated to iron-oxide nanoparticles the early-activated cerebral endothelium was visualized *via* MRI by targeting E- and P-Selectin [65]. The use of iron-oxide nanoparticles in these studies greatly enhances the MRI contrast observed at the early activated endothelium and provides a multivalent display of ligand to the receptor, increasing the binding avidity [317]. In the case of sLe^x, this is highlighted by the only modest increase of ~3% contrast enhancement of a singular sLe^x-mimetic conjugated to a Gadolinium-based contrast agent used for BBB breakdown detection [318]. Multivalent display of E-Selectin ligands can greatly enhance

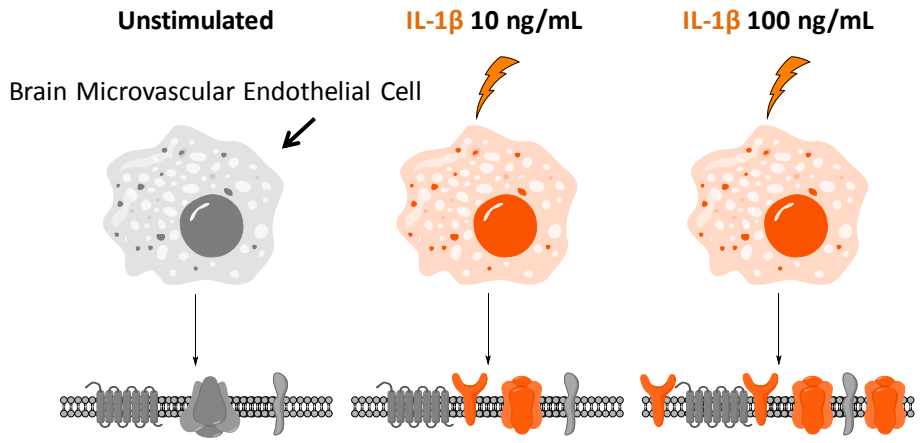
the potency of inhibitors by up to 700-fold [76] and linker and immobilization chemistries can have a profound effect on the binding of sLe^x and sulphated analogues to the E-, P- and L-Selectin [77]. Another example of multivalent targeting of a lectin made use of gold nanoparticles functionalized with α-fucosylamine which allowed effective targeting of the cell surface lectin DC-SIGN, a dendritic cell specific lectin [319]. Nanoparticle scaffolds have been used extensively to study the interactions between lectins and their carbohydrate ligands and a variety of scaffolds and display-types can overcome the low affinity of a single carbohydrate binding to lectins expressed on cells. Multivalent glyconanoparticles, glycofullerenes, glycodendrimers, and glycolipids incorporated into liposomes all have been used successfully to target lectins, as reviewed in [81]. The use of photo-crosslinkers and multivalent carbohydrate interactions have been studied before and proven to be a useful tool in studying carbohydrate interactions [245]. Using a tri-valant galactose probe with a tri-fluoro diazirine and a biotin, the spiked lectin RCA120 (*Ricinus communis* Agglutinin I) was pulled out of an E. coli lysate and an asialoglycoprotein receptor on intact mammalian cells was identified by Western Blot [246]. However, no novel protein substrates were identified. Another example compared two different photo-crosslinkers, alkyl diazirine and a trifluoromethylphenyl diazirine, for their ability to crosslink the carbohydrate protein PNA (lactose-binding lectin, peanut agglutinin) to its ligand D-lactose. By using post-photo-crosslinking fluorescence detection *via* a copper-catalysed azide-alkyne cycloaddition, the researchers were able to tag the lectin and do comparative analysis between the yield of crosslinking between the two photo-crosslinkers used [247]. Subsequently, the same researchers utilized gold nanoparticles, decorated them with D-lactose and with either a benzophenone or an aryl azide photo-crosslinker and showed that they could trap spiked peanut agglutinin (PNA) from mammalian cell lysate proteins at a ratio of 1:100 (w/w) [248]. These examples highlight the feasibility of this strategy and the rationale for the bi-functional Lewis[a] trifluoromethylphenyl diazirine

3.1.2 Design of the *in vitro* pull-down experiments using the bi-functional nanoparticles

In order to study the interactions of multivalent Lewis[a] presented on a nanoparticle scaffold (Solulink, NanoLink™ Amino Magnetic Beads, 741 nm ± 88nm diameter (current supplier TriLink Bioctehchnologies)) and its interacting (lectin) receptors using a proteomic approach a bi-functional nanoparticle was developed. SoluLink particles were used because they are homogenously suspended in aqueous solutions and their size is compatible for *in vivo* (as mentioned in the introduction –**Chapter 1**) studies. The SoluLink particles show moderate stability in polar aprotic solvents (presented earlier in **Chapter 2**). These properties, including their

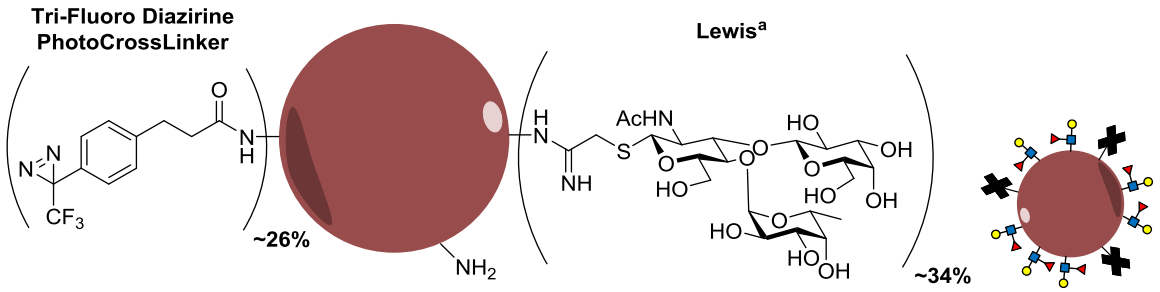
magnetic properties, make them ideal for using them as the bi-functional nanoparticles for proteome discovery of the interacting receptors. A photo-crosslinker was introduced onto these particles to trap the Lewis[a]-interacting receptors on the particles to allow the multivalent display binding needed for Lewis[a] binding. As alluded to in the previous chapter, the diazirine photo-crosslinker molecule[249] is introduced onto the nanoparticle to covalently trap more transient interactions and to aid in the pull down and subsequent sample processing steps [244, 320]. It was envisaged that a 20% functionalisation of the photo-crosslinker and the remaining 80% of amines on the MPIOs for Lewis[a] would allow enough engagement with the receptor via the Lewis[a] moiety. The 20% photo-crosslinker coverage on the MPIO would be able to crosslink the Lewis[a] interacting receptors onto the nanoparticles and subsequently then allow proteomic identification of proteins covalently trapped onto the MPIOs. Rodent brain microvascular cells were used for the experiments presented in this thesis, as the initial *in vivo* results are indicative of vascular binding. GP8.3 Rat brain microvascular endothelial cells (Daniel C. Anthony in-lab culture derived from [321]) and bEnd.3 mouse brain microvascular endothelial cells (bEnd.3, ATCC CRL-2299) were used interchangeably as both species are capable of binding Lewis[a] during IL-1β brain inflammation, as presented in the introduction. A simplified schematic overview of the experimental design is presented in **Figure 3.1**.

A

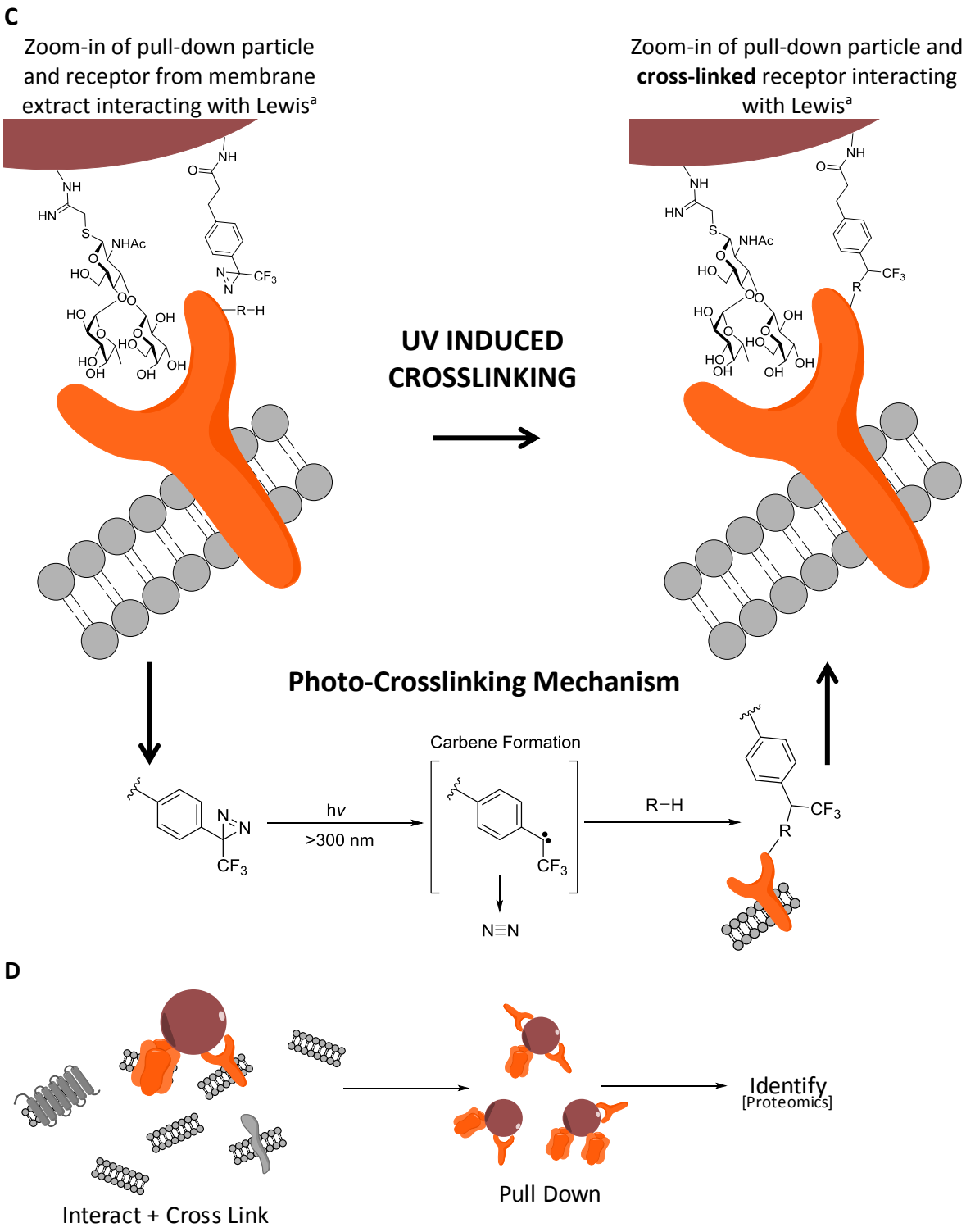


Altered plasma membrane proteome (orange) upon IL-1β stimulation
that could be potential Lewis[a]-MPIO binders

B



The bi-functional nanoparticles



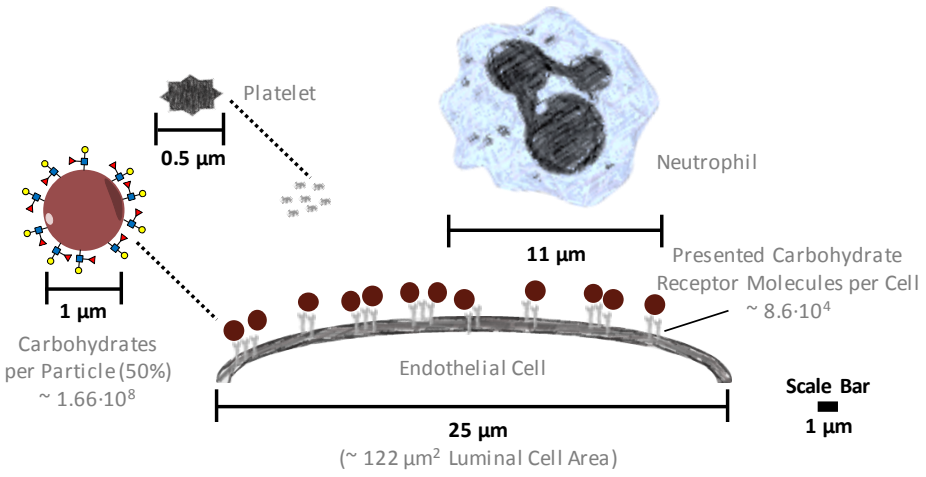
| Figure 3.1 | Experimental overview and design of a bi-functional Lewis[a]/Diazirine photo-crosslinker magnetic pull-down tool for proteomics *in vitro* **|A|** Rodent brain microvascular endothelial cells stimulated with IL-1β changes the cell surface expression of proteins (orange) that interact with Lewis[a] nanoparticles. **|B|** The designed magnetic particles of iron-oxide created with both Lewis[a], for receptor interactions, and a diazirine photo-crosslinker, to trap the transient multivalent interactions. Note the particle on the right is a cartoon representation. **|C|** The interacting (orange) cell surface molecules from a membrane extract interacting with Lewis[a] presented on the nanoparticles. Subsequent UV-induced crosslinking could trap the interacting receptor onto the pull-down particles. **|D|** The interacting membrane proteins with Lewis[a] are crosslinked onto the particles (orange receptors) and a magnetic pull down enriches the interacting proteins and extensive washing ensures only proteins with highly specific binding remain. Identification of the proteins was performed using a proteomics approach.

3.1.3 Calculations and anticipated results

Using an *in vitro* approach with brain microvascular endothelial cells, enabled a reductionist approach of identifying interacting proteins with Lewis^a upon IL-1β stimulation. The designed bi-functional nanoparticles allowed a potential method to trap the Lewis^a interactors. As presented in the introduction, there are a number of known cell surface lectins which can bind Lewis^a, endothelial cells can present E- and P-Selectin [322], [65] and the mannose receptor CD206 on macrophages and immature dendritic cells [323]. In addition, DC-SIGN or CD209 on the cell surface of macrophages and dendritic cells can bind Lewis^a also [324], [325]. This reductionist approach will not account for soluble, blood-derived lectins that can bind Lewis^a, like the mannan-binding lectin MBL, which is expressed in the liver during the acute phase response [113] or any immune cell derived ones. As evidenced by previous work, endothelial cells were the anticipated cells responsible for the observed Lewis^a binding *in vivo*. Previously, using sLe^x magnetic particles of iron-oxide, the inflamed endothelial cells were imaged by targeting E- and P-Selectin expression [65]. Therefore, rodent brain microvascular cells were used and calculations below rationalize the numbers of cells, particles and photo-crosslinker molecules used in the experiments that will be described in the next section.

1.7×10^5 E-Selectin molecules can be presented by a singular endothelial cell [326]. Assuming only the luminal side (or the 'up' facing side *in vitro*) is responsible for the E-Selectin binding, this value is halved, therefore, it is reasonable to assume that approximately 8.6×10^4 E-Selectin molecules are presented by an activated endothelial cell in a vessel. These numbers are derived from a reference where E-Selectin expression was induced at the cell surface of lung microvascular endothelial cells using IL-1α. The maximum number of molecules was reached after 3.5h and remained stable 5h post stimulation and resulted in 702 ± 18 molecules of E-Selectin per μm^2 of cell surface area [326]. These calculations are highly speculative and will only provide a rough estimate to justify the numbers used. Alternatively, a confluent 75 cm^2 tissue culture flask of rat GP8.3 cells yields ~8×10^6 cells and provides large surface that can be activated. The area of a typical endothelial cell (common human iliac artery endothelial cell) lining the blood vessels is 245.0 ± 115.1 μm^2 [24]. Of a typical cell, about 50% of its mass of the plasma membrane is protein, with the remainder lipids [327]. Taken into account that rodent cells are typically 10-20% smaller than human cells [328], on which some of the calculations are based, a flask of the rodent cells grown to confluency will provide nearly 75 cm^2 of surface for the particles to interact with. Keeping E-Selectin as a model, Rat E-Selectin is 60,080 Da. Using the earlier mentioned value of 8.6×10^4 E-Selectin molecules being presented by an activated endothelial cell, up to 210 ng or

2.06×10^{12} molecules of E-Selectin could be isolated per experiment using three 75 cm^2 flasks. The concentration of SoluLink nanoparticles = 2.3×10^{6} particles/µg ± 1.3×10^{6} STDEV (*n* = 6, counts are of individually prepared dilutions) and free primary amine loadings range from 831-1710 nmol/mg (experimentally determined and used throughout this thesis). Assuming an average loading of 1.27 nmol/ µg, each particle has an amine content of µg 0.55 fmol/particle which corresponds to 3.31×10^{8} primary amine molecules per particle (using 6.0221415×10^{23} for Avogadro's number for number of molecules per mole). As designed, approximately 20% of amines were functionalized with the diazirine, resulting in 6.62×10^{7} molecules per particle. Efficiency of the crosslinking and trapping 'yield' is dependent or numerous variables and can range from anywhere between 5% up to 70% in solvent lacking electron-rich groups or bonds [238], but typical yields are reported to range between 10% and 20% because the carbine is quickly quenched by water molecules in aqueous buffers [329], [243], [247]. A conservative yield of 10% will result in 6.62×10^{6} photo-crosslinker molecules that could potentially trap the Lewis[a] receptor(s). 300 µg of the particles has the potential of trapping 4.57×10^{15} molecules, which is a ~2000 excess of the E-Selectin molecules that can be presented on a cell. This excess is to account for other receptors, non-specific binding, intra-particle crosslinking, multiple crosslinking sites per receptor and other small molecules that could hinder the reactive carbine generated by the photo-catalysed reaction. As for the targeting moiety Lewis[a], an 'ideal' Lewis[a] load of 50% (or higher) will then present 1.66×10^{8} sugars per particle. As shown in **Figure 3.2** which is drawn to scale, numerous particles can bind a single endothelial cell and for the experiments conducted up to 30 particles per cell were used.



| Figure 3.2 | Cell size considerations of a model of an endothelial cell binding Lewis[a] MPIO A hypothetical model of the numbers of carbohydrate receptor molecules presented on the surface of an endothelial cell. Sizes of the brown dots representing the carbohydrate particles give an indication of the amount of particles that can cover an average endothelial cell (2D-projection). The size of murine platelets and neutrophils (human platelets are 1-2 µm and human neutrophils range from 12-15 µm) are depicted to scale. Dotted lines represent a zoom in of the cartoons and the scale bar is 1 micron. For illustrative purposes, the schematics used throughout this thesis will not use the images to scale.

3.1.4 Pulldown experiments using the synthesised MPIOs

Using the generated Lewis^a-functionalised MPIOs and the bi-functional Lewis^a/Diazirine photo-crosslinker magnetic pull down tool from **Chapter 2**, two proteomics experiments were performed. First, a Lewis^a photo-crosslinker pulldown was performed on GP8.3 rat brain microvascular endothelial cells. These cells were stimulated for 4 hrs with two concentrations of IL-1β (10 and 100 ng/mL of media) and an unstimulated control. A cell-membrane extract was generated from the differentially treated cells and incubated with the pull down particles whilst being UV-exposed (see **methods section 3.6.2**) . Second, a similar experiment was performed as for the Lewis^a photo-crosslinker pulldown, but only using the Lewis^a-functionalised MPIOs (see **methods section 3.6.3**). Lastly, a whole cell proteome was generated from immortalized bEnd.3 mouse brain microvascular endothelial cells stimulated with IL-1β and compared to an unstimulated control to assess general protein up- and down-regulation (see methods **section 3.6.4**). See **Table 3.1** for the experiments performed with the synthesised particles.

| Table 3.1 | Data nomenclature and experimental overview for proteomics files using pulldown particles

Sample Names used in Data Analysis	**Unstimulated Control**	**IL-1β treated with 10 ng/mL**	**IL-1β treated with 100 ng/mL**
Photo-crosslinked samples using bi-functional Lewis^a/Diazirine	Ctrl	10ng	100ng
MS*/MS* peptide count ion series (technical quality)	✔	✔	✔
Pulldown samples using Lewis^a MPIO	0ng	10ng	100ng
MS*/MS* peptide count ion series (technical quality)	✔	✔	✔ low ion count
Pulldown samples using unmodified NH_2- MPIO	0ng_ctrl	10ng_ctrl	100ng_ctrl
MS*/MS* peptide count ion series (technical quality)	✔	✔	✔

Overview of pulldown experiments performed using GP8.3 rat brain microvascular endothelial cells and the pull down particles used The ion series (technical quality) of the runs is indicated with coloured a tick (green = good, red = low ion count). Experiments listed were run once.

3.1.5 Proteomic results using the bi-functional Lewis^a/photo-crosslinker pulldown particles yielded no lectins

1452 proteins were identified in the 3 runs (Control '*Ctrl*', '*10ng*' and '*100ng*' IL-1β treated). Pulldown results are shown in **Table 3.2**. Values were sorted on Significance B and on the absence (value of -6) or low abundance of peptides in the 'Ctrl'. Proteins identified were selected on their gene ontology (GO) (http://geneontology.org/) using the following recognised identifiers: membrane, plasma membrane, extracellular, extracellular matrix and secreted. These proteins are highlighted in BLUE for the pull down experiments. Further data processing was done using Excel. High values are colored in red and low values colored in blue. Protein information was retrieved from uniprot.org and thebiogrid.org. Typically human protein functions were assigned to identified rat genes assuming similar functions. See **method 3.6.5** for proteomic data analysis details.

3.1.6 Proteomic results using the Lewis^a only pulldown particles also yields no lectins

522 proteins were identified in the 6 runs (Le^a-particles Control '*0ng*', '*10ng*' and '*100ng*' IL-1β treated and NH_2-particles Control '*0ng_Ctrl*', '*10ng_Ctrl*' and '*100ng_Ctrl*' IL-1β treated). Pulldown results are shown in **Table 3.3** below. Values were sorted on the absence of peptides in the NH_2-particles control samples '*0ng_Ctrl*', '*10ng_Ctrl*' and '*100ng_Ctrl*'. The identified proteins identified in the NH_2-particles control samples are regarded as non-specific. The samples were then sorted on IL-1β treated and on the absence/low abundance of peptides in Le^a-particles Control '*0ng*'. *Note:* Le^a-particles '*100ng*' run yielded very low peptide counts for unknown reasons. Therefore, the data is presented for the proteins identified in the 10ng run, but the 100 ng Le^a-pulldown results are not included in **Table 3.3**. Similar colour coding and criteria as before were used highlighting these proteins in BLUE. High values are colored in red and low values colored in blue. See **method 3.6.5** for proteomic data analysis details.

| Table 3.2 | Data summary of bi-functional Lewis[a]/Diazirine photo-crosslinker magnetic particle pulldown on GP8.3 rat brain microvascular endothelial cells

10ng / Ctrl B significant	100ng / Ctrl B significant	Peptides Identified	Unique peptides	Sequence coverage [%]	10ng_x-y_Ctrl Significance B	100ng_x-y_Ctrl Significance B	10ng / Ctrl	100ng / Ctrl	Ctrl	Gene Symbol	Protein Names
+	+	2	2	26.9	11.5	16.7	5	6	-6	**Fkbp1a**	Peptidyl-prolyl cis-trans isomerase FKBP1A
+	+	2	2	1.7	4.6	17.1	3	6	-6	**Atp13a1**	ATPase type 13A1
+	+	1	1	11.2	13.2	18.1	6	6	-6	**Nme1;Nme2**	Nucleoside diphosphate kinase A;B
+	+	2	2	5.7	3.8	8.2	3	4	-6	**Idh3a**	Isocitrate dehydrogenase [NAD] subunit alpha
+	+	1	1	14.1	2.9	3.7	2	3	-6	**Mrpl20**	Mitochondrial Ribosomal Protein L20
	+	1	1	6.6	1.7	4.6	2	3	-6	**Nsdhl**	Sterol-4-alpha-carboxylate 3-dehydrogenase
+	+	1	1	5.3	9.1	3.8	5	3	-6	**Cers2**	Ceramide synthase 2
+	+	1	1	5.1	5.8	7.6	4	4	-6	**Galk2**	N-acetylgalactosamine kinase
+	+	1	1	3.4	6.9	8.6	4	4	-6	**Sec13**	Protein SEC13 homolog
+	+	1	1	3.2	5.3	6.4	3	3	-6	**RGD1565002**	Protein similar to Dehydrogenase/reductase SDR family member 7 precursor
+	+	1	1	3.1	5.2	6.5	3	4	-6	**Tufm**	Elongation factor Tu, mitochondrial
	+	1	1	2.9	0.9	4.4	1	3	-6	**Csde1**	Cold shock domain-containing protein E1
+	+	1	1	2.6	8.9	6.3	5	3	-6	**Creb1;Crem;Atf1**	Cyclic AMP-responsive element-binding protein 1
	+	1	1	2.1	2.1	4.3	2	3	-6	**Gpd2**	Glycerol-3-phosphate dehydrogenase, mitochondrial
+	+	1	1	2	6.5	6.9	4	4	-6	**Slc2a1**	GLUT1, Solute carrier family 2, facilitated glucose transporter member 1
+	+	1	1	1.8	8.8	11.7	5	5	-6	**Palld***	Palladin
+	+	1	1	1.6	5.6	4.5	4	3	-6	**Col5a1**	Collagen alpha-1(V) chain
+	+	1	1	1.4	8.0	6.7	4	4	-6	**Atp6v0a1**	V-type proton ATPase 116 kDa subunit a isoform 1
+	+	1	1	1.3	5.8	5.0	4	3	-6	**Vps11**	Vacuolar protein sorting 11 homolog (S. cerevisiae)
+	+	1	1	1.1	5.4	4.2	3	3	-6	**Zeb2**	Zinc finger E-box binding homeobox 2
+	+	1	1	0.8	5.6	7.0	4	4	-6	**Msh6**	DNA mismatch repair protein Msh6
	+	1	1	0.5	0.2	4.3	0	3	-6	**Dsp**	Desmoplakin
+	+	252	218	76.4	8.9	2.9	3	2	11	**Myh9****	Myosin-9
+	+	14	13	85.4	8.8	3.8	3	2	6	**Myl6**	Myosin light polypeptide 6
+	+	13	13	41.6	10.6	2.8	4	2	0	**Actr3**	Actin-related protein 3
	+	13	13	23.2	0.5	2.7	-1	-2	4	**Sdad1**	Protein SDA1 homolog
	+	10	10	33.1	1.8	3.0	1	2	3	**Rpl7**	60S ribosomal protein L7
+	+	10	10	12.8	4.8	3.7	3	2	0	**Rai14**	Ankycorbin
	+	9	9	32.9	0.5	8.1	0	3	3	**Rps6**	40S ribosomal protein S6
+	+	7	7	27.8	4.1	3.3	-2	-2	3	**Bcap31**	B-cell receptor-associated protein 31
+	+	7	7	24.7	8.3	2.5	3	2	0	**Arpc2**	Actin-related protein 2/3 complex subunit 2
+	+	7	7	15.6	5.9	2.6	3	2	-1	**Xrcc6**	X-ray repair cross-complementing protein 6
	+	7	7	3.3	0.5	2.9	-1	-2	0	**Atm**	Ataxia telangiectasia mutated
+	+	6	6	27.5	2.7	2.8	2	2	2	**Rpl15**	60S ribosomal protein L15
+	+	6	6	14.4	13.1	4.0	5	3	-3	**Lrrfip2**	Leucine-rich repeat flightless-interacting protein 2
	+	6	6	6.8	2.1	4.1	2	2	-1	**Flii**	Flightless I homolog protein
+	+	5	5	19.3	8.5	2.6	4	2	-3	**Tmod3**	Tropomodulin 3
+	+	5	5	10.8	16.5	10.0	-5	-4	3	**Mars**	Methionyl-TRNA Synthetase
	+	4	4	14.1	0.0	3.3	0	-2	0	**Noc4l**	Nucleolar complex protein 4 homolog
	+	4	4	11.3	1.1	2.5	-1	-2	0	**Aifm2**	Apoptosis-Inducing Factor, Mitochondrion-Associated, 2
	+	4	4	5.7	0.6	2.5	1	2	-2	**Cwc22*****	CWC22 Spliceosome-Associated Protein
+	+	4	4	1.8	5.2	2.6	3	2	-3	**Pcm1**	Pericentriolar material 1
+	+	13	3	66.3	9.1	3.3	3	2	4	**Rlc-a**	Myosin regulatory light chain RLC-A
+	+	18	3	50.4	8.2	3.9	3	2	2	**Tpm1**	Tropomyosin alpha-1 chain
+	+	3	3	15.8	3.1	4.2	2	2	-1	**Bri3bp**	Bri3 binding protein
	+	3	3	13.7	0.6	5.2	1	2	-1	**Stom**	Stomatin, human erythrocyte integral membrane protein band 7
	+	3	3	10.4	1.4	3.1	2	2	-3	**Pgam5**	Serine/threonine-protein phosphatase PGAM5
+	+	3	3	7.5	8.1	8.6	3	3	-3	**Zbtb20**	Zinc finger and BTB domain-containing protein 20
+	+	14	3	5.9	8.3	3.5	3	2	2	**Myh14**	Myosin, Heavy Chain 14, Non-Muscle
	+	3	3	2.2	0.3	3.0	0	2	-3	**Thoc2**	THO Complex 1
+	+	13	2	27.7	3.3	3.0	-2	-2	1	**Exoc1**	Exocyst complex component 1
	+	2	2	8	0.2	3.9	0	-3	0	**Ppap2b**	Lipid phosphate phosphohydrolase 3
	+	2	2	5.7	0.3	2.8	0	2	-1	**Psmc3**	26S protease regulatory subunit 6A
	+	2	2	5.4	0.4	3.1	0	-2	-1	**Fip1l1**	Pre-mRNA 3-end-processing factor FIP1
+	+	2	2	5	4.3	4.9	3	3	-4	**Stt3a**	Serine/threonine-protein kinase Chk1
	+	2	2	4.9	0.0	3.7	0	-2	0	**Ptdss1**	Phosphatidylserine synthase 1
	+	2	2	4.8	0.2	3.3	0	2	-4	**Ncoa5**	Nuclear receptor coactivator 5
	+	2	2	4.6	2.3	2.6	2	2	-3	**Stau1**	Staufen Double-Stranded RNA Binding Protein 1
	+	2	2	3.7	1.2	4.3	1	2	-2	**Lepre1**	Prolyl 3-hydroxylase 1
+	+	2	2	3.4	9.6	7.8	-5	-4	0	**Rasa2**	Ras GTPase-activating protein 2
	+	1	1	18.8	0.2	6.1	0	-3	1	**Rpl38******	60S ribosomal protein L38
+	+	2	1	12	8.1	2.8	3	2	2	**Myl3;Myl1**	Myosin light chain 3;1
	+	1	1	5.2	0.2	6.4	0	-3	0	**Kdelr2;Kdelr1**	ER lumen protein retaining receptor 2;1
	+	2	1	3.7	0.0	14.4	0	4	-4	**Fmr1**	Fragile X mental retardation protein 1 homolog
+	+	1	1	2.3	3.3	4.5	3	3	-5	**Lap3**	Cytosol aminopeptidase
+	+	1	1	2.3	3.6	3.3	-2	-2	0	**Impdh2**	Inosine-5-monophosphate dehydrogenase 2
+	+	12	0	54.7	21.4	13.6	5	4	-2	**Myl12b**	Myosin regulatory light chain 12B

Additional gene information *LOC100360205;Mypn, ** LOC100911597, ***LOC680519, **** LOC686066; RGD1561636

| Table 3.3 | Data summary of Lewis[a] magnetic particle pulldown on GP8.3 rat brain microvascular endothelial cells

Peptides Identified 10ng	Sequence coverage 10ng [%]	Intensity 10ng_x-y_Intensity 0ng Significance B	Gene Symbol	Protein Names
2	23.4	0.2	**Hmga1;RGD1564836**	High mobility group protein HMG-I/HMG-Y
2	22.2	0.9	**LOC687711**	Protein Snrpd3
4	12.5	0.5	**U2af2**	Splicing factor U2AF 65 kDa subunit
1	11.8	0.3	**Cxcl12**	CXCL12
1	11.6	0.2	**Atp6v0c**	V-type proton ATPase 16 kDa proteolipid subunit
1	11.5	0.1	**Rps24;LOC100363469**	40S ribosomal protein S24
5	10.5	0.5	**Immt**	Mitochondrial inner membrane protein
2	10.1	0.4	**Lrrc59**	Leucine-rich repeat-containing protein 59
	9.9	0.8	**Vdac1**	Voltage-dependent anion-selective channel protein 1
1	9.8	1.0	**LOC288913**	Leydig cell tumor 10 kDa protein
1	9.8	0.7	**Tceb1**	Transcription elongation factor B polypeptide 1
1	9.4	0.6	**Glipr2**	Golgi-associated plant pathogenesis-related protein 1
1	8	0.1	**Prdx5**	Peroxiredoxin-5, mitochondrial
1	7.8	0.1	**Rras2;Rras**	Ras-related protein R-Ras
5	7.6	0.8	**Supt16h**	FACT complex subunit SPT16
1	7.5	0.4	**Nudt21**	Cleavage and polyadenylation specificity factor subunit 5
2	7.4	0.6	**Aldoa;Aldoart2**	Fructose-bisphosphate aldolase A;Fructose-bisphosphate aldolase
1	7.2	0.2	**Srsf2**	Serine/arginine-rich splicing factor 2
2	6.9	0.9	**Cdc37**	Hsp90 co-chaperone Cdc37;Hsp90 co-chaperone Cdc37, N-terminally processed
2	6.6	0.9	**Cyr61**	Protein CYR61
1	6.5	0.6	**Eif4e**	Eukaryotic translation initiation factor 4E
2	6.4	0.6	**Tufm**	Elongation factor Tu, mitochondrial
1	6.3	0.2	**Sdcbp**	Syntenin-1
1	5.8	0.6	**Cdc42**	Cell division control protein 42 homolog
1	5.7	0.4	**Chchd3**	MICOS complex subunit
1	5.6	0.1	**Stom**	Stomatin, human erythrocyte integral membrane protein band 7
1	5.5	1.0	**Skp1**	S-phase kinase-associated protein 1
1	5.2	0.3	**Srsf5**	Serine/arginine-rich splicing factor 5
1	5.2	0.2	**Capza2**	F-actin-capping protein subunit alpha-2
1	5.1	1.0	**Ppib**	Peptidyl-prolyl cis-trans isomerase B
1	4.6	1.0	**Chchd6**	Coiled-coil-helix-coiled-coil-helix domain-containing protein 6, mitochondrial
1	4.5	1.0	**Gipc1**	PDZ domain-containing protein GIPC1
2	4.5	1.0	**Atp6v1a**	V-type proton ATPase catalytic subunit A
2	4.5	0.1	**Ipo9**	Importin-9
1	4.4	0.1	**Nap1l1**	Nucleosome assembly protein 1-like 1
2	4.3	0.7	**Atp5a1**	ATP synthase subunit alpha, mitochondrial;ATP synthase subunit alpha
1	4.2	0.5	**Dimt1**	rRNA adenine N(6)-methyltransferase
1	4.2	0.5	**Rasl2-9;RGD1306195;Ran**	GTP-binding nuclear protein Ran, testis-specific isoform;GTP-binding nuclear protein Ran
1	4.2	0.1	**Eif3s6ip**	Eukaryotic translation initiation factor 3 subunit L
1	4	0.5	**Srsf1**	Serine/arginine-rich splicing factor 1
1	4	0.4	**Snrnp40**	U5 small nuclear ribonucleoprotein 40 kDa protein
1	3.9	0.4	**Mfap1a**	Protein Mfap1a
1	3.8	0.9	**Ctsb**	Cathepsin B;Cathepsin B light chain;Cathepsin B heavy chain
1	3.7	0.8	**Zc2hc1a**	Family with sequence similarity 164, member A
1	3.5	0.2	**Fkbp8**	Peptidyl-prolyl cis-trans isomerase FKBP8
1	3.4	0.3	**Prss23**	Serine protease 23
1	3.4	0.3	**Csnk1a1**	Casein kinase I isoform alpha
1	3.3	0.7	**Htra1**	Serine protease HTRA1
1	3.3	0.4	**Dock7**	Dedicator of cytokinesis protein 7
1	3.2	0.1	**Anxa11**	Annexin A11
1	3.1	0.5	**Tsg101**	Tumor susceptibility gene 101 protein
1	3.1	0.5	**Stoml2**	Stomatin-like protein 2, mitochondrial
1	2.9	0.5	**Psmc4**	26S protease regulatory subunit 6B
1	2.8	0.7	**Ctnnb1**	Catenin beta-1
2	2.8	0.6	**Rtn4**	Reticulon-4
2	2.8	0.6	**Ddx39a**	ATP-dependent RNA helicase DDX39A
1	2.8	0.4	**Slc25a3**	Phosphate carrier protein, mitochondrial
1	2.8	0.3	**Crmp1;Dpysl2;Dpysl3**	Dihydropyrimidinase-related protein 1;Dihydropyrimidinase-related protein 2;Dihydropyrimidinase-related protein 3
1	2.6	1.0	**Sdpr**	Serum deprivation-response protein
1	2.6	0.3	**Zfp207**	Protein Zfp207
1	2.6	0.3	**Paics**	Multifunctional protein ADE2;Phosphoribosylaminoimidazole-succinocarboxamide synthase
1	2.6	0.3	**Hspa4**	Heat shock 70 kDa protein 4
1	2.5	0.9	**Nono**	Non-POU domain-containing octamer-binding protein
1	2.3	0.4	**Arcn1**	Coatomer subunit delta
1	2.1	0.4	**Maged1**	Melanoma-associated antigen D1
1	1.8	0.1	**Elp3**	Elongator complex protein 3
1	1.7	0.4	**Specc1l**	Cytospin-A

1	1.6	1.0	**Cdc5l**	Cell division cycle 5-like protein
1	1.6	0.2	**Plod1**	Procollagen-lysine,2-oxoglutarate 5-dioxygenase 1
1	1.5	0.7	**Vps35**	Vacuolar protein sorting-associated protein 35
2	1.4	0.4	**Snrnp200**	U5 small nuclear ribonucleoprotein 200 kDa helicase
1	1.2	1.0	**Prpf40a**	Pre-mRNA processing factor 40 homolog A
1	1.2	0.7	**Hsph1**	Heat shock protein 105 kDa
1	1.1	0.6	**Eprs**	Protein Eprs
1	0.9	0.8	**Phldb2**	Pleckstrin homology-like domain family B member 2
1	0.9	0.2	**Col4a2**	Collagen alpha-2(IV) chain
1	0.9	0.0	**Usp48**	Ubiquitin carboxyl-terminal hydrolase 48
1	0.4	0.6	**Prpf8**	Pre-mRNA processing factor 8, isoform CRA_a
1	0.4	0.2	**Trio**	Protein Trio
1	0.3	0.7	**Aspm**	Abnormal spindle-like microcephaly-associated protein

3.1.7 Proteome of bEnd.3 mouse brain microvascular endothelial cells stimulated with IL-1β reveals E-Selectin as the second highest upregulated protein

3594 proteins were identified in the 6 runs (Control '*Unstimulated_1_2_3*' and '*100ng*' IL-1β Stimulated_1_2_3). Results of the top 20 upregulated and bottom 20 downregulated proteins are shown in **Table 3.4**. Values were sorted on the highest difference between unstimulated and IL-1β stimulated samples. The low abundant or absent peptides in the control samples were compared against the presence of highly abundant (i.e. upregulated) peptides that appear in the IL-1β stimulated samples. Values were then sorted on the p-value, which provides a confidence level for the results. Values were generated using Perseus 1.5.4.1 software. Highlighted in **blue** are immune-related upregulated proteins. See **method 3.6.5** for proteomic data analysis details.

| Table 3.4 | Data summary of whole cell proteome of bEnd.3 mouse brain microvascular endothelial cells stimulated with IL-1β reveals E-Selectin as the second highest and VCAM-1 as the highest upregulated proteins

	Intensity						Sequence coverage [%]									
# Proteins	Unstimulated 1	Unstimulated 2	Unstimulated 3	IL-1β Stimulated 1	IL-1β Stimulated 2	IL-1β Stimulated 3	Unstimulated 1	Unstimulated 2	Unstimulated 3	IL-1β Stimulated 1	IL-1β Stimulated 2	IL-1β Stimulated 3	-Log Student's T-test p-value Sample_Control	Student's T-test Difference Sample_Control	Gene names	Protein names
1	-6.0	-6.0	-6.0	2.5	3.3	3.1	0	0	0	20.8	32.1	29.8	5.59	8.98	Vcam1	Vascular cell adhesion protein 1
2	-6.0	-2.3	-6.0	3.1	2.9	3.4	0	2.6	0	29.1	28.6	35.8	2.51	7.91	Sele	E-selectin
3	-6.0	-6.0	-6.0	-1.9	0.8	-0.1	16.7	26.2	26.2	28.6	39.3	39.3	2.66	5.61	Rps27	40S ribosomal protein S27
4	-6.0	-6.0	1.6	0.7	0.8	0.5	0	0	0.3	0.6	0.3	0.3	0.74	4.11	Kiaa1109	Uncharacterized protein KIAA1109
5	-6.0	-6.0	-6.0	-2.4	-2.6	-0.8	0	0	0	3.1	5.4	4.7	2.67	4.02	Sema4c	Semaphorin-4C
6	-6.0	-6.0	-6.0	-0.7	-6.0	0.0	0	0	0	27.1	0	32.3	0.93	3.74	Cxcl1	Growth-regulated alpha protein;KC(5-72)
7	-6.0	-6.0	-1.3	-0.6	-0.8	-0.7	0	0	4.9	4.9	4.9	4.9	1.12	3.74	Unchar.Pr.	Uncharacterized protein 2210010C04Rik
8	-3.8	-6.0	-6.0	-1.7	-0.2	-2.7	3.9	0	0	6	13.3	13	1.62	3.70	Vps37b	Vacuolar protein sorting-associated protein 37B
9	-6.0	-6.0	-6.0	-1.6	-2.6	-2.8	0	0	0	3.2	3.4	2	3.20	3.68	Slfn5	Schlafen family member 5
10	-6.0	-6.0	-6.0	-0.8	-6.0	-0.2	0	0	0	8.1	2.8	8.1	0.93	3.67	Cx3cl1	Fractalkine;Processed fractalkine
11	-6.0	-6.0	-6.0	-6.0	-0.9	-0.1	0	0	0	0	1.1	1.1	0.93	3.67	Grid2	Glutamate receptor ionotropic, delta-2
12	-6.0	-6.0	-1.5	-1.6	-1.1	-0.1	0	0	4.1	4.1	4.7	6.7	1.08	3.57	B3galtl	β-1,3-glucosyltransferase
13	-1.2	-6.0	-1.0	0.3	1.7	0.4	8.5	0	8.5	8.5	8.5	8.5	0.98	3.54	Myl1;Myl3	Myosin light chain 1/3, skeletal muscle isoform
14	-6.0	4.8	-6.0	4.9	-6.0	4.5	0	1.2	0	1.2	0	1.2	0.28	3.54	Mis18bp1	Mis18-binding protein 1
15	-6.0	-6.0	-6.0	-6.0	-1.5	-0.1	0	0	0	0	7.6	7.6	0.91	3.49	Gpkow	G patch domain and KOW motifs-containing protein
16	-2.0	-1.9	-6.0	0.5	-0.2	-0.1	3.6	6.6	0	15.5	11.6	10.8	1.18	3.42	Nploc4	Nuclear protein localization protein 4 homolog
17	-2.4	-2.7	-6.0	-1.6	3.3	-2.9	6.8	4.2	0	11	15.6	6.8	0.68	3.33	Bpnt1	3(2),5-bisphosphate nucleotidase 1
18	-6.0	-6.0	-6.0	-1.3	-6.0	-0.7	0	0	0	5.4	0	10.8	0.93	3.32	Ccl2	C-C motif chemokine 2
19	-6.0	-6.0	-3.0	-0.8	-2.4	-2.0	0	0	4.8	16.1	4.8	11.2	1.40	3.28	Pdlim4	PDZ and LIM domain protein 4
20	-2.2	-2.6	-6.0	0.0	0.1	-1.0	10	10	3.5	21.7	13	10.3	1.22	3.27	H2-K1;H2-D1	H-2 class I histocompatibility antigen, K-B; D-K α chain
3578	-2.8	-1.9	0.2	-3.8	-6.0	-6.0	5.5	4.2	10.9	2.3	4.2	0	1.50	-3.78	Ppox	Protoporphyrinogen oxidase
3579	-1.1	-2.1	-3.0	-6.0	-6.0	-6.0	9.7	6.9	2.2	0	0	0	2.68	-3.95	Xpnpep3	Probable Xaa-Pro aminopeptidase 3
3580	-0.3	0.2	-6.0	-6.0	-6.0	-6.0	42.9	47.4	28.9	27.5	35.9	27.2	0.93	-3.96	Pgam5	Serine/threonine-protein phosphatase, mitochondrial
3581	-2.0	-2.0	-2.0	-6.0	-6.0	-6.0	5.9	8.4	5.3	0	0	5.3	13.92	-3.97	Coq6	Ubiquinone biosynthesis monooxygenase COQ6
3582	-0.7	-0.1	0.1	-0.6	-6.0	-6.0	2.7	2.7	4.2	2.7	0	0	1.03	-3.97	Slc6a6	Sodium- and chloride-dependent taurine transporter
3583	-2.8	-1.5	-1.6	-6.0	-6.0	-6.0	0.9	1.7	1.7	0	0	0	3.13	-4.02	Cad	Carbamoyl-phosphate synthetase 2
3584	0.6	0.2	0.3	-3.8	-1.2	-6.0	15.4	14.9	14.9	6.1	9.9	0	1.35	-4.03	Slc25a24	Calcium-binding mitochondrial carrier protein
3585	0.0	0.3	-0.1	-6.0	-6.0	-0.4	15.8	15.8	15.8	0	0	15.8	1.06	-4.18	Cox6c	Cytochrome c oxidase subunit 6C
3586	-0.6	-0.5	-4.1	-6.0	-6.0	-6.0	11.7	18.2	6.6	0	0	0	1.65	-4.26	Ndufb7	NADH dehydrogenase [ubiquinone] 1 β subunit 7
3587	1.3	-0.3	-1.2	-1.3	-6.0	-6.0	32.3	10.8	15	17	0	0	1.20	-4.38	Brix1	Ribosome biogenesis protein BRX1 homolog
3588	-1.2	-1.5	-2.1	-6.0	-6.0	-6.0	11.4	5.5	5.5	0	0	0	4.12	-4.43	Mvb12a	Multivesicular body subunit 12A
3589	-3.0	-0.9	-0.6	-6.0	-6.0	-6.0	4.2	6.2	6.4	1.7	1.7	1.7	2.39	-4.50	Ubqln4	Ubiquilin-4
3590	-1.3	-1.6	-1.7	-6.0	-6.0	-6.0	6.3	6.3	7.4	3.7	0	0	5.55	-4.50	Rfc2	Replication factor C subunit 2
3591	-0.2	-1.3	-0.5	-3.5	-6.0	-6.0	25.2	21.4	13	8.4	0	0	2.12	-4.51	Ndufa6	NADH dehydrogenase [ubiquinone] 1 α subunit 6
3592	-1.2	-1.6	-1.6	-6.0	-6.0	-6.0	12.8	6.1	6.1	0	0	0	5.38	-4.54	Nif3l1	NIF3-like protein 1
3593	-1.3	-0.4	-2.0	-6.0	-6.0	-6.0	4.9	8.9	4.9	0	0	0	3.29	-4.76	Cyc1	Cytochrome c1, heme protein, mitochondrial
3594	0.5	-1.6	-1.4	-6.0	-6.0	-6.0	13.5	3.1	3.1	0	0	0	2.80	-5.19	Map2k1	Mitogen-activated protein kinase kinase 1
3595	-0.7	-0.5	-1.1	-6.0	-6.0	-6.0	20	12.1	21.4	0	0	0	4.90	-5.22	Cst3	Cystatin-C
3596	2.4	1.2	2.4	2.0	-6.0	-6.0	7.6	7.6	7.6	7.6	0	0	0.92	-5.31	Bloc1s5	Biogenesis of lysosome-related organelles
3597	-2.8	-2.0	6.8	-6.0	-6.0	-6.0	2.4	5	3.9	0	0	0	1.01	-6.67	Scin	Adseverin

Top 20 highest upregulated and downregulated proteins from the whole-cell proteome. The two cell adhesion molecules VCAM-1 and E-Selectin are the two highest upregulated proteins upon IL-1β stimulation.

The proteomic identification of Lewis^a-interacting proteins was not achieved successfully with the designed bi-functional proteomics pull down tool, nor particles functionalised with Lewis^a only. No proteins were identified with lectin domains or any prior literature regarding the binding of any Lewis-antigens. The limitations of the photo-crosslinker modified particles described in **Chapter 2** could be responsible for this and the pull down conditions used may not be optimal for pulling out the binders of Lewis^a. The whole cell proteome of stimulated brain endothelial cells identified the Lewis^a-binding lectin E-Selectin as the second highest upregulated protein and could very likely be the candidate for Lewis^a. So the unsuccessful activation of the photo-crosslinker as described in **Chapter 2** and the conditions used for the pulldown presented here in this chapter could be limitations for the proteomic identification of Lewis^a-interacting proteins, therefore a genomics approach was used to find potential novel lectins for Lewis^a. The transcriptomic analysis of brain lesions will be discussed next.

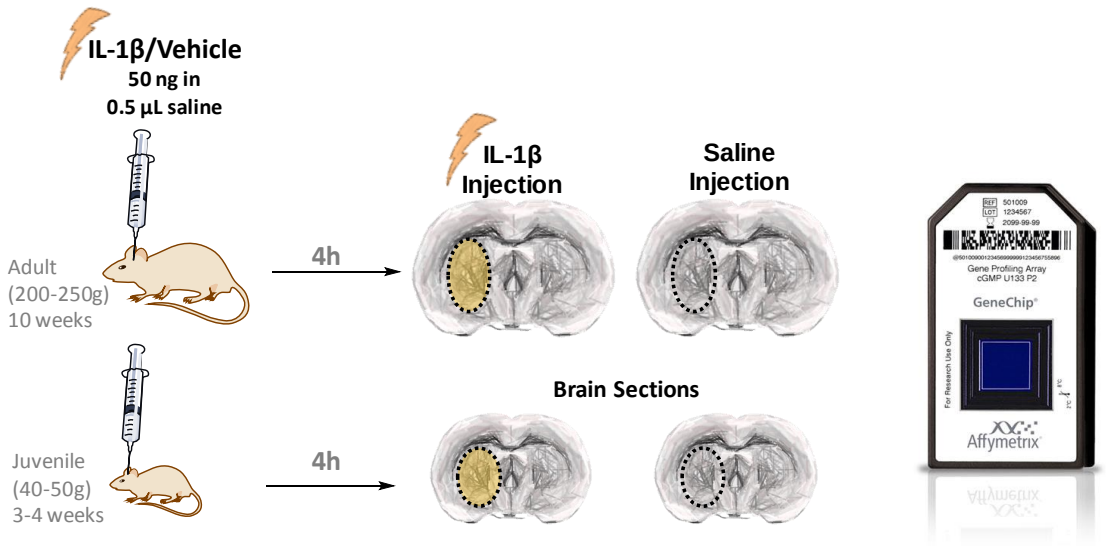
3.2 | TRANSCRIPTOMIC ANALYSIS OF ACUTE IL-1β BRAIN INFLAMMATION AND BCG MS-LIKE LESION MODEL

Transcriptomics allows studying the molecular changes at a transcript level upon stimuli that initiate gene transcription of the genes and ultimately the proteins involved. Messenger RNA (mRNA) is the information carrier in the central dogma of molecular biology for the translation of proteins from active gene transcription [330]. mRNA and protein levels are generally considered to correlate however, it has been shown that the cellular abundance of proteins is determined by the level of ribosomal translation [217]. As proteins are the functional components of cells, their complexity and and their relative abundance can go undetected in the proteomic identification of proteins due to technical limitations. Hence, combining both proteomics and transcriptomics, will provide a truer and unbiased insight into studying the molecular changes during brain inflammation, than either of the techniques used alone. By studying the changes of transcriptomics, a correlation can be made of proteomic results obtained and will allow an unbiased and more informed decision of the potential hits [331]. An elegant study where the proteome and the transcriptome was compared from the mouse brain and its major brain regions and cell types that occur in the brain, showed an remarkable overlap of the expressed genes (mRNA transcripts) and the identified proteins [218].

There are different techniques to study the transcriptomic changes. Presented in this thesis is the use of U34 rat genome GeneChip® arrays from the company Affymetrix (currently part of Thermo Fisher). In brief, total RNA of the brains is isolated and *via* reverse transcription turned into (copy) cDNA. Subsequently from this cDNA using 3' *in vitro* translation biotin-uracil is incorporated into the cRNA. By random fragmentation the biotin-labelled cRNA is hybridized onto the GeneChip® expression array. Unbound cRNA fragments are washed off and the bound biotin-labelled cRNA is hydridized to the chip (source: https://www.affymetrix.com/). Binding, and hence abundance, is visualized with a fluorophore-conjugated Steptravidin and the fluorescence intensity is scanned and quantified. In order to study the transcriptome of two similar, but distinct models of brain inflammation, two experiments were conducted (by Daniel Anthony) and shown in the **Figures 3.3** and **3.4** of these experimental forms of brain inflammation are able to bind Lewis[a] magnetic nanoparticles *in vivo*, therefore they were both analysed for their transcriptome and compared to the proteomics experiments discussed previously. All the information from the GeneChips®, their

specifications and the databases used were found on https://www.affymetrix.com/ and details regarding to the analysis are summarized below in the and in **methods 3.6.8** and **3.6.9.**

First, gene expression arrays of the IL-1β model of acute brain inflammation were 3' IVT Expression Profiled using a GeneChip® Rat Genome 230 2.0 Array, see **Figure 3.3** and **method section 3.6.6**. The array used is comprised of more than 31,000 probe sets and can analyse over 30,000 transcripts and variants from over 28,000 rat genes. Second and last, a BCG (Bacillus Calmette-Guérin) model of MS-like brain inflammation [207],[332] were 3' IVT Expression Profiled using a GeneChip® Rat Genome Genome U34A Set, consisting of three GeneChip® arrays. The experimental design and samples taken are shown in **Figure 3.4**, **Table 3.5** and **methods section 3.6.7**. This array can examine more than 24,000 mRNA transcripts and Expressed Sequence Tags (EST) clusters from the UniGene database (Build 34). Array A of the set approximately analyses 7,000 full-length sequences 1,000 EST clusters. Arrays B and C each analyse approximately 8,000 EST clusters. We can use the data from the proteomics and from the GeneChip® arrays to narrow down a list of probable cell-surface/extracellular proteins with lectin domains that could be responsible for the binding observed in the MRI images presented in the introduction of this thesis. In addition, other transcripts and proteins identified can gain insights into the molecular changes that occur during the different brain inflammation models used.

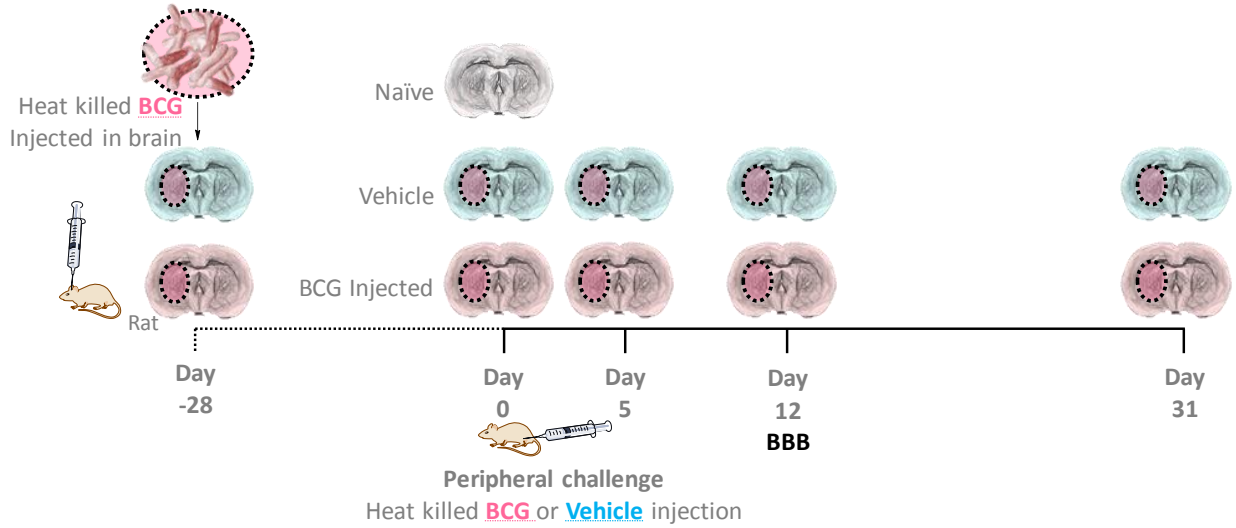


| Figure 3.3 | Experimental overview of GeneChip® experiment using IL-1β as a model of brain inflammation Schematic overview of the GeneChip experiment performed. Adult rats and p21 juvenile rats (*n=3* for each group) received an intracerebral injection of IL-1β in the left brain hemisphere 4h later brain sections indicated by the dashed lines were taken for GeneChip® analysis using the GeneChip® Rat Genome 230 2.0 Array. See **methods section 3.6.6**.

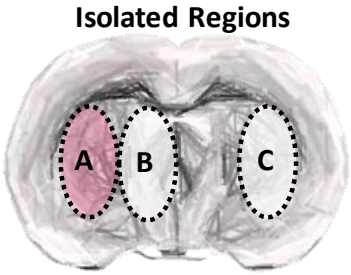
| Table 3.5 | *N*-numbers of experiments and GeneChip-runs

N-numbers Experiments		Sections Isolated (based on Figure 3.5) A	B	C
MS-Like Lesion Model using BCG				
Naïve	**Day 0**	3	2	3
BCG	**Day 0**	3	4	4
	Day 5	3	3	3
	Day 12	3	3	3
	Day 31	3	3	3
Vehicle	**Day 0**	5	4	5
	Day 12	3	3	3
IL-1β Acute Brain Inflammation Model				
Adult	**IL-1β**	3		
	Vehicle	3		
Juvenile	**IL-1β**	3		
	Vehicle	3		

A



B

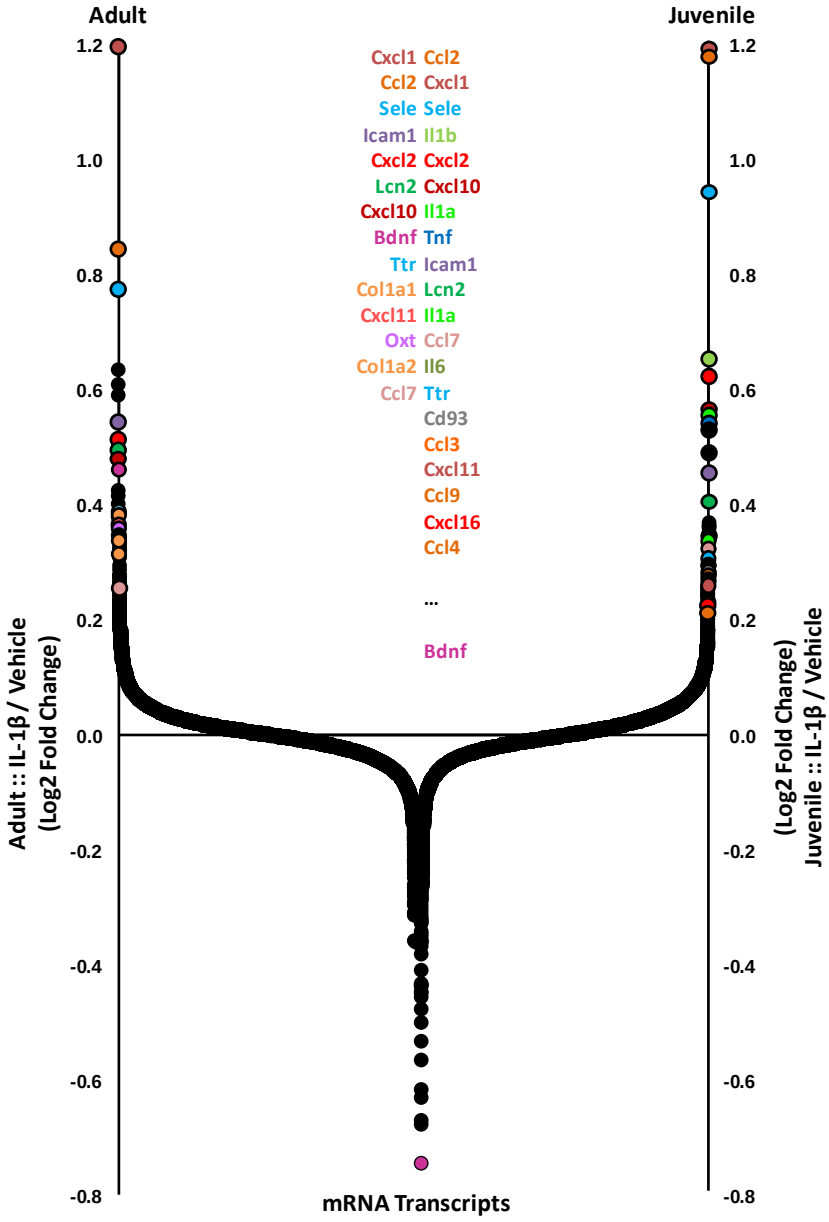


A | Lesion (heat killed BCG injection)

B | Non-lesioned area –same side as lesion

C | Contralateral control

| Figure 3.4 | Experimental overview of GeneChip® experiment using BCG as a model of MS-like brain inflammation **|A|** Schematic overview of the experiment performed. Rats received an intracerebral injection of heat-killed BCG in the left brain hemisphere. 28 days post BCG brain injection; animals were peripherally challenged with either BCG in Freund's Complete Adjuvant (CFA) or CFA 'Vehicle' on day 0. On day 12 for BCG challenged animals BBB breakdown occurs: source Daniel Anthony. **|B|** Indicates the selection sites for the samples collected in panel **A** and **Table 3.5** which were taken on days 0, 5, 12 and 31. The brain regions were isolated (A, B, and C) and taken for GeneChip® analysis using the GeneChip® Rat Genome Genome U34A Set. See **methods section 3.6.7**.



| Figure 3.5 | Results of mRNA transcripts upregulated by IL-1β during brain inflammation in the adult and juvenile rat Double scatterplot of mRNA transcripts sorted on Log2 fold change (IL-1β/Vehicle). Top dots are the highest upregulated transcripts upon IL-1β stimulation (left adult, right juvenile). Coloured dots represent the similarly coloured transcripts highlighted in the middle of the graph and are selected on their immune-related functions.

3.2.1 Transcriptome of IL-1β acute brain inflammation in adult and juvenile rats

Analysing the transcriptome of both adult and juvenile models of IL-1β induced acute brain inflammation, a striking cluster of immune-related and cell adhesion molecules was found to be upregulated. In the adult and juvenile brain the 3 highest upregulated genes are *Cxcl1*, *Ccl2* and *Sele*; the anticipated Lewis[a] binder E-Selectin. **Figure 3.5** and **Table 3.8** highlight the immune-relevant transcripts between the two groups. Noticeable is that the juvenile rats produce more CXCL- and CCL-chemokines and other immune related transcripts. As the major neutrophil chemoattractant CXCL1 (also known as Cytokine-Induced Neutrophil Chemoattractant 1 (CINC-1)) is shared between both adult and juvenile rats as a top 3 upregulated gene, it implies a differential mechanism of brain inflammation between the two age groups. It has been shown, using the same model of acute IL-1β-mediated brain inflammation, that juvenile rats produce a more extreme neutrophil-mediated CNS immune response mediated by CXCL-1 than adult rats. Furthermore, neutrophil-mediated blood–brain barrier damage *via* CXCL-1 in juvenile rats was attenuated by an anti-neutrophil serum and an anti CXCL-1 antibody [333]. This difference in CNS immune response between juvenile and adult brain inflammation may be indicative of alternative, protective mechanisms in adults and suggest that CXCL-1 may act as a catalyst in juvenile rat brains to produce more chemokines, as presented here, which drive the more prolific immune response. In addition, as shown in **Figure 3.5** and **Tables 3.6** and **3.7**, juvenile rats produce both pyrogenic interleukins IL-1α and IL-1β, CCL3, CCL4 and tumour necrosis factor, whilst in the adult rat brains these pyrogens are downregulated upon IL-1β stimulation (*data not shown*). Taken together, this indicates adult rats are less susceptible to proinflammatory challenges than juvenile rats and that the febrile and immune response and the recruitment of immune cells is greater in juvenile rats. As it is known that the susceptibility to inflammatory stimuli like IL-1β differs between age groups [334], the data presented here in this thesis allows a more mechanistic insight in the transcriptomic differences between adult and juvenile CNS inflammation. As mentioned before, juvenile rats express the pyrogenic molecules IL-1α and β, CCL3, CCL4 and TNF, whilst adults do not. However, they also express IL-6; a CNS cytokine that can have both inflammatory effects like B-cell differentiation and maturation to antibody-producing plasma cells and physiological effects like neurogenesis [335]. IL-6 acts on the liver hepatocytes to induce the synthesis of acute phase proteins [32]. It is implied to play a role in diseases like MS, as IL-6 knock-out mice cannot develop EAE induced by myelin oligodendrocyte glycoprotein (MOG) [336] by differentially activating autoreactive T cells [337]. As shown here, and by others [338], in response to IL-6, BDNF levels are lowered as highlighted in **Figure 3.5**, where BDNF is the most

downregulated transcript in the juvenile brain. On the contrary, adult rat brains produce BDNF in response to IL-1β where it may have a neuroprotective role [339], [340] and may attenuate ICAM-1 expression on endothelial cells during IL-1β activation [341]. Similarly, another way adult brains may attenuate the effects of a full-blown immune response including BBB, is by preventing CCL2 to 'open' the BBB and by reducing leukocyte recruitment, especially neutrophils. As CCL2 is implied in monocyte and neutrophil recruitment and BBB breakdown [342], [343], metalloproteinase-dependent BBB breakdown can occur in inflammatory lesions in the brain, but is dependent of the type of lesion [344],[345]. However, BBB breakdown is not seen in adult rat brains during this acute model of brain inflammation, highlighting again that the juvenile brain is less capable of supressing CNS inflammation but the BBB breakdown seems not to be mediated by the expression of metalloproteinases, as these are no upregulated transcripts in both adult and juvenile brains. Most likely the increased immune cell infiltration and BBB breakdown in the juvenile brain is the result of a greater and different chemokines-panel. In particular, the chemokines and pyrogens CCL3 and CCL4 are not upregulated in the adult brain. These chemokines, together with CCL2, are capable of all the steps required for neutrophil-mediated disruption of the perivenular basement membrane resulting in microvascular leakage, including recruitment, *de novo* protein synthesis, adherence, activation and generation of proinflammatory mediators, like platelet activation factor [346], [347], [348],[343]. The lack of CCL3 and CCL4 and less neutrophil-recruitment at this stage of acute brain inflammation in adults may be the mechanism of action and explain the differences between adult and juvenile responses to IL-1β in the brain. As it is evident that neutrophils play a pivotal role in the early stages of brain inflammation [19],[333],[349] and in more chronic diseases like MS [154], in the next **subchapter** (**3.3**) the role of neutrophils and Lewis^a-binding will be assessed, in addition to the function of E- and P-Selectin during IL-1β acute brain inflammation models [104].

| Table 3.6 | Overview of selected immune-related transcripts and their functions

Protein	Alias	Gene	Upregulated in	Recruits	Function
			CCL-Chemokines		
CCL2	Monocyte Chemoattractant Protein 1 (MCP1)	*Ccl2*	Both	Neutrophils, Monocytes, Basophils, Memory T cells, Dendritic cells	Expressed by microglial cells in the brain during inflammation
CCL3	Macrophage Inflammatory Protein 1-α (MIP-1-α)	*Ccl3*	Juvenile	Neutrophils, Macrophages, Monocytes	Pyrogen, recruitment and activation of polymorphonuclear leukocytes
CCL4	Macrophage Inflammatory Protein 1-β (MIP-1-β)	*Ccl4*	Juvenile	Macrophages, Natural Killer cells, Monocytes	Chemoattractant
CCL7	Monocyte-Chemotactic Protein 3 (MCP3)	*Ccl7*	Both	Monocytes	Macrophage regulator
CCL9	Macrophage Inflammatory Protein 1-γ (MIP-1-γ)	*Ccl9*	Juvenile	CD11b+, CCr1+ Dendritic cells	Expressed constitutively by macrophages and myeloid cells
			CXCL-Chemokines		
CXCL1	Cytokine-Induced Neutrophil Chemoattractant 1 (CINC-1)	*Cxcl1*	Both	Neutrophils	CXCL1 is expressed by macrophages, neutrophils and epithelial cells
CXCL2	Macrophage Inflammatory Protein 2-α (MIP-2-α)	*Cxcl2*	Both	Polymorphonuclear cells	Secreted by monocytes and macrophages
CXCL10	Interferon gamma-induced protein 10 (IP-10)	*Cxcl10*	Both	Macrophages, Monocytes, T cells, Natural Killer cells, Dendritic cells	Secreted by monocytes, endothelial cells and fibroblasts
CXCL11	Interferon-inducible T-cell alpha chemoattractant (I-TAC)	*Cxcl11*	Both	T cells	Highly expressed in peripheral blood leukocytes, pancreas and liver
CXCL16		*Cxcl16*	Juvenile	T cells, Natural Killer cells	
			Cell Adhesion		
E-Selectin	CD62E (Cluster of Differentiation 62 Endothelial)	*Sele*	Both	Neutrophils *via* ESL-1 and PSGL-1 and Eosinophils, Monocytes, T cells, Natural Killer cells	Initial rolling for immune cell recruitment *via* endothelial expression
ICAM-1	CD54 (Cluster of Differentiation 54)	*Icam1*	Both	Leukocyte recruitment	
			Interleukins		
Interleukin-1 α	IL-1α, Hematopoietin 1	*Il1a*	Juvenile	Leukocytes *via* induced chemokine expression	Pyrogen, Produced by activated macrophages, neutrophils, epithelial cells, endothelial cells
Interleukin-1 β	IL-1β, Leukocytic pyrogen	*Il1b*	Juvenile	Leukocytes *via* induced chemokine expression	Pyrogen, Produced by activated macrophages
Interleukin-2 Receptor subunit γ	CD132 (Cluster of Differentiation 132) Common γ Chain (γc)	*Il2rg*	Both		Expressed on most lymphocytes
Interleukin-6		*Il6*	Juvenile		Procuded by vascular cells, T cells and macrophages. Repression of *Bdnf* expression in the brain. Acute phase protein synthesis, neutrophil production, growth of B cells
			Tumor necrosis factor		
TNF	Tumour necrosis factor	*Tnf*	Juvenile		Pyrogen, Produced by activated macrophages, neutrophils, natural killer cells, mast cells, eosinophils and neurons
			Clusters of Differentiation		
CD14		*Cd14*	Juvenile		Innate immune function, co-receptor for TLR4 for LPS
CD93		*Cd93*	Juvenile	Apoptotic cells	C-type lectin transmembrane receptor for cell adhesion expressed by platelets, monocytes, microglia, neutrophils, macrophages, B cells, endothelial cells.
			Other Secreted		
Transthyretin	Prealbumin	*Ttr*	Both (BCG-model)		Transports T_4 and retinol (Vit. A) *via* binding with retinol-binding protein RBP
BDNF	Brain-Derived Neurotrophic Factor	*Bdnf*	Adult (BCG-model)		Growth factor for the maintenance of neurons
Oxytocin		*Oxt*	Adult (BCG-model)		Hormone and neuropeptide
Lipocalin-2	Neutrophil Gelatinase-Associated Lipocalin (NGAL)	*Lcn2*	Both (BCG-model)		Expressed by neutrophils to sequester iron (innate immunity)
Galanin		*Gal*	Adult		Neuropeptide, various functions
Factor V	Factor 5	*F5*	Adult		Binding to activated platelets

Table information derived from Gene ontology information and Uniprot and NCBI information and the following references [350], [42], [351],[59]

| Table 3.7 | Data summary of IL-1β upregulated mRNA transcripts in adult rat brains reveals E-selectin as the third highest upregulated gene

IL-1β Lesion Compared to Vehicle Injected Site					
Fold Change	tTest	Log2 Fold Change	-Log10 tTest	Gene Symbol	Gene Title
2.3	0.5	1.2	0.3	**Cxcl1**	chemokine (C-X-C motif) ligand 1
1.8	0.4	0.8	0.4	**Ccl2**	chemokine (C-C motif) ligand 2
1.7	0.0	0.8	1.3	**Sele**	**selectin E**
1.5	0.8	0.5	0.1	**Icam1**	intercellular adhesion molecule 1
1.4	0.7	0.5	0.1	**Cxcl2**	chemokine (C-X-C motif) ligand 2
1.4	0.1	0.5	0.9	**Lcn2**	lipocalin 2
1.4	0.6	0.5	0.2	**Cxcl10**	chemokine (C-X-C motif) ligand 10
1.4	0.2	0.5	0.6	**Bdnf**	brain-derived neurotrophic factor
1.3	0.3	0.4	0.5	**F5**	coagulation factor V (proaccelerin, labile factor)
1.3	0.2	0.4	0.7	**Ttr**	transthyretin
1.3	0.0	0.4	1.5	**Col1a1**	collagen, type I, alpha 1
1.3	0.7	0.4	0.2	**Gal**	galanin/GMAP prepropeptide
1.3	0.3	0.4	0.5	**Stra6**	stimulated by retinoic acid 6
1.3	0.2	0.4	0.7	**Cxcl11**	chemokine (C-X-C motif) ligand 11
1.3	0.1	0.4	1.1	**Oxt**	oxytocin/neurophysin 1 prepropeptide
1.3	0.0	0.3	2.1	**Col1a2**	collagen, type I, alpha 2
1.2	0.5	0.3	0.3	**Sostdc1**	sclerostin domain containing 1
1.2	0.0	0.3	1.6	**Col1a2**	collagen, type I, alpha 2
1.2	0.6	0.3	0.2	**Trhr**	thyrotropin releasing hormone receptor
1.2	0.5	0.3	0.3	**Stra6**	stimulated by retinoic acid 6
1.2	1.0	0.3	0.0	**Cldn2**	claudin 2
1.2	0.3	0.3	0.5	**Hcrtr2**	hypocretin (orexin) receptor 2
1.2	0.1	0.3	1.1	**Crh**	corticotropin releasing hormone
1.2	0.1	0.3	0.9	**Ibsp**	integrin-binding sialoprotein
1.2	0.1	0.3	0.8	**Slc7a3**	solute carrier family 7 (cationic amino acid transporter, y+ system), member 3
1.2	0.1	0.3	0.9	**Adcyap1**	adenylate cyclase activating polypeptide 1
1.2	0.6	0.2	0.2	**Ccl7**	chemokine (C-C motif) ligand 7
1.2	0.2	0.2	0.7	**Galr2 /// LOC100910349**	galanin receptor 2 /// galanin receptor type 2-like
1.2	0.1	0.2	1.0	**RT1-CE10 /// RT1-EC2**	RT1 class I, locus CE10 /// RT1 class Ib, locus EC2
1.2	0.9	0.2	0.1	**Trhr**	thyrotropin releasing hormone receptor
1.2	0.5	0.2	0.3	**Scgb1c1**	secretoglobin, family 1C, member 1
1.1	0.0	0.2	1.5	**Asic2**	acid-sensing (proton-gated) ion channel 2
1.1	0.1	0.2	1.1	**Gast**	gastrin
1.1	0.1	0.2	1.3	**Igfbp2**	insulin-like growth factor binding protein 2
1.1	0.0	0.2	2.7	**Il2rg**	interleukin 2 receptor, gamma

Top 150 upregulated transcripts, filtered on: membrane, plasma membrane, extracellular, extracellular matrix and secreted.

| Table 3.8 | Data summary of IL-1β upregulated mRNA transcripts in juvenile rat brains reveals E-selectin as the third highest upregulated gene

IL-1β Lesion Compared to Vehicle Injected Site					
Fold Change	tTest	Log2 Fold Change	-Log10 tTest	Gene Symbol	Gene Title
2.3	0.0	1.2	4.3	**Ccl2**	chemokine (C-C motif) ligand 2
2.3	0.0	1.2	3.4	**Cxcl1**	chemokine (C-X-C motif) ligand 1
1.9	0.0	1.0	1.5	**Sele**	**selectin E**
1.6	0.1	0.7	1.0	**Il1b**	interleukin 1 beta
1.5	0.1	0.6	1.0	**Cxcl2**	chemokine (C-X-C motif) ligand 2
1.5	0.0	0.6	2.6	**Cxcl10**	chemokine (C-X-C motif) ligand 10
1.5	0.3	0.6	0.6	**Il1a**	interleukin 1 alpha
1.5	0.0	0.5	1.4	**Tnf**	tumor necrosis factor
1.4	0.0	0.5	2.5	**Icam1**	intercellular adhesion molecule 1
1.3	0.0	0.4	1.3	**Lcn2**	lipocalin 2
1.3	0.3	0.3	0.6	**Il1a**	interleukin 1 alpha
1.3	0.1	0.3	1.1	**Ccl7**	chemokine (C-C motif) ligand 7
1.3	0.2	0.3	0.7	**Il6**	interleukin 6
1.2	0.4	0.3	0.4	**Ttr**	transthyretin
1.2	0.4	0.3	0.5	**Cd93**	CD93 molecule
1.2	0.1	0.3	0.9	**Ccl3**	chemokine (C-C motif) ligand 3
1.2	0.0	0.3	1.8	**Tas2r107**	taste receptor, type 2, member 107
1.2	0.0	0.3	2.0	**Cxcl11**	chemokine (C-X-C motif) ligand 11
1.2	0.1	0.2	0.9	**Clcf1**	cardiotrophin-like cytokine factor 1
1.2	0.1	0.2	0.9	**Angpt2**	angiopoietin 2
1.2	0.4	0.2	0.4	**Ccl9**	chemokine (C-C motif) ligand 9
1.2	0.1	0.2	1.3	**Cxcl16**	chemokine (C-X-C motif) ligand 16
1.2	0.2	0.2	0.8	**Slc14a1**	solute carrier family 14 (urea transporter), member 1
1.2	0.2	0.2	0.7	**Ccl4**	chemokine (C-C motif) ligand 4
1.2	0.3	0.2	0.5	**Adamts1**	ADAM metallopeptidase with thrombospondin type 1 motif, 1
1.2	0.0	0.2	2.5	**Il2rg**	interleukin 2 receptor, gamma
1.2	0.1	0.2	1.2	**Anxa1**	annexin A1
1.2	0.1	0.2	1.0	**Adamts19**	ADAM metallopeptidase with thrombospondin type 1 motif, 19
1.1	0.4	0.2	0.4	**Stra6**	stimulated by retinoic acid 6
1.1	0.1	0.2	1.2	**Cd14**	CD14 molecule
1.1	0.3	0.2	0.5	**Slc4a1**	solute carrier family 4 (anion exchanger), member 1
1.1	0.0	0.2	1.4	**Tmem252**	transmembrane protein 252
1.1	0.3	0.2	0.6	**Slc44a4**	solute carrier family 44, member 4
1.1	0.1	0.2	0.9	**Tfpi2**	tissue factor pathway inhibitor 2
1.1	0.2	0.2	0.7	**Slco4a1**	solute carrier organic anion transporter family, member 4a1

Top 150 upregulated transcripts, filtered on: membrane, plasma membrane, extracellular, extracellular matrix and secreted.

| Table 3.9 | Data summary of BCG lesion specific upregulated mRNA transcripts compared to vehicle treated and naïve brains

Day 31 BCG Lesion [A] Compared to Day 0 Vehicle [A]				Day 31 BCG Lesion [A] Compared to Day 0 Naïve [A]					
Fold Change	tTest	Log2 Fold Change	-Log10 tTest	Fold Change	tTest	Log2 Fold Change	-Log10 tTest	Gene Symbol	Gene Title
1.4	0.2	0.4	0.7	1.7	0.1	0.8	1.1	**B2m***	beta-2 microglobulin
1.3	0.3	0.3	0.6	1.5	0.1	0.6	0.8	**Igkv28****	similar to NGF-binding Ig light chain
1.3	0.3	0.3	0.5	1.5	0.2	0.6	0.8	**Igkv28****	similar to NGF-binding Ig light chain
1.3	0.0	0.3	1.5	1.4	0.0	0.5	1.8	**Aif1**	allograft inflammatory factor 1 *(IBA1)*
1.1	0.4	0.2	0.4	1.4	0.1	0.4	1.1	**Cxcl13**	chemokine (C-X-C motif) ligand 13
1.1	0.0	0.1	2.4	1.3	0.3	0.4	0.6	**Olfm1**	olfactomedin 1
1.3	0.1	0.4	1.1	1.3	0.1	0.4	1.0	**Col1a1**	collagen, type I, alpha 1
1.2	0.1	0.3	1.2	1.3	0.0	0.4	2.5	**Aif1**	allograft inflammatory factor 1 *(IBA1)*
1.3	0.0	0.3	1.7	1.3	0.0	0.4	2.5	**Cd48**	Cd48 molecule
1.0	0.0	0.1	2.1	1.3	0.3	0.4	0.5	**Scg3**	secretogranin III
1.1	0.3	0.2	0.5	1.3	0.1	0.4	1.0	**Lcn2**	lipocalin 2
1.1	0.6	0.1	0.3	1.3	0.1	0.4	1.2	**Spp1**	secreted phosphoprotein 1
1.2	0.3	0.2	0.5	1.3	0.2	0.3	0.7	**Igkv28****	similar to NGF-binding Ig light chain
1.2	0.3	0.2	0.5	1.2	0.2	0.3	0.7	**Igkv28****	similar to NGF-binding Ig light chain
1.1	0.4	0.2	0.4	1.2	0.2	0.3	0.6	**Cd74**	Cd74 molecule, major histocompatibility complex, class II invariant chain
1.1	0.4	0.2	0.4	1.2	0.2	0.3	0.7	**Igkv28****	similar to NGF-binding Ig light chain
1.2	0.1	0.2	1.0	1.2	0.1	0.3	1.1	**Pafah1b1**	platelet-activating factor acetylhydrolase 1b, regulatory subunit 1
1.1	0.3	0.2	0.5	1.2	0.2	0.3	0.8	**Cd74**	Cd74 molecule, major histocompatibility complex, class II invariant chain
1.1	0.2	0.2	0.7	1.2	0.1	0.3	1.0	**Igkv28****	similar to NGF-binding Ig light chain
1.1	0.1	0.2	0.9	1.2	0.0	0.3	1.7	**Dbi**	diazepam binding inhibitor acyl-CoA binding protein)
1.3	0.0	0.4	1.7	1.2	0.0	0.3	1.8	**Rapgef4**	Rap guanine nucleotide exchange factor (GEF) 4
1.1	0.3	0.1	0.5	1.2	0.0	0.3	1.6	**C3**	complement component 3
1.0	0.5	0.0	0.3	1.2	0.3	0.3	0.5	**Ctsh**	cathepsin H
1.2	0.0	0.2	3.3	1.2	0.0	0.3	1.7	**Rasa1**	RAS p21 protein activator (GTPase activating protein) 1
1.2	0.5	0.2	0.3	1.2	0.4	0.2	0.4	**Oxt**	oxytocin/neurophysin 1 prepropeptide
1.2	0.0	0.2	2.4	1.2	0.0	0.2	1.7	**Cadps2**	Ca++-dependent secretion activator 2
1.3	0.0	0.3	2.1	1.2	0.0	0.2	2.1	**Ptprz1**	protein tyrosine phosphatase, receptor-type, Z polypeptide 1
1.2	0.2	0.2	0.8	1.2	0.1	0.2	0.9	**Crp*****	C-reactive protein, pentraxin-related
1.2	0.0	0.3	2.5	1.2	0.0	0.2	1.4	**Gclm**	glutamate cysteine ligase, modifier subunit
1.2	0.0	0.3	2.2	1.2	0.0	0.2	1.8	**Scn1a**	sodium channel, voltage-gated, type I, alpha subunit
1.1	0.1	0.1	1.2	1.2	0.0	0.2	2.3	**Il18**	interleukin 18
1.2	0.0	0.2	2.5	1.2	0.0	0.2	3.6	**Ptprz1**	protein tyrosine phosphatase, receptor-type, Z polypeptide 1
1.1	0.1	0.2	0.9	1.2	0.1	0.2	1.1	**Crp**	C-reactive protein, pentraxin-related
1.0	0.7	0.1	0.2	1.2	0.1	0.2	1.2	**Ttr**	Transthyretin
1.2	0.1	0.2	0.9	1.2	0.1	0.2	1.2	**Kcnc2**	potassium voltage gated channel, Shaw-related subfamily, member 2
1.2	0.0	0.3	1.8	1.2	0.0	0.2	1.8	**Ptn**	Pleiotrophin
1.1	0.0	0.2	1.4	1.2	0.0	0.2	1.8	**Sepp1**	selenoprotein P, plasma, 1
1.1	0.0	0.2	1.4	1.2	0.0	0.2	4.1	**B2m**	beta-2 microglobulin
1.2	0.2	0.2	0.7	1.2	0.2	0.2	0.7	**Bdnf**	brain-derived neurotrophic factor
1.3	0.1	0.3	1.0	1.2	0.2	0.2	0.7	**Col1a1**	collagen, type I, alpha 1
1.1	0.0	0.1	1.7	1.2	0.0	0.2	1.5	**Atp2b1**	ATPase, Ca++ transporting, plasma membrane 1
1.1	0.3	0.1	0.5	1.2	0.2	0.2	0.7	**Cd74**	Cd74 molecule, major histocompatibility complex, class II invariant chain
1.1	0.1	0.2	0.9	1.1	0.1	0.2	1.2	**Igkv28**	immunoglobulin kappa chain variable 28 (V28)
1.1	0.2	0.2	0.7	1.1	0.2	0.2	0.7	**Ednrb**	endothelin receptor type B
1.1	0.1	0.1	1.0	1.1	0.1	0.2	1.0	**Igkv28**	immunoglobulin kappa chain variable 28 (V28)

*/// LOC689064 /// Pfdn1 /// Rn18s /// Rn45s /// Rpl4 [/// beta-globin /// prefoldin subunit 1 /// 18S ribosomal RNA /// 45S pre-ribosomal RNA /// ribosomal protein L4]
**/// LOC500180 /// LOC500183 [/// similar to IG KAPPA CHAIN V-V REGION K2 PRECURSOR /// similar to NGF-binding Ig light chain]
***/// LOC100233206 /// LOC100362110 /// LOC317588 /// LOC361942 /// LOC501503 /// Serinc1 [/// uncharacterized LOC100233206 /// LRRGT00155-like /// hypothetical protein LOC317588 /// similar to ORF4 /// nucleic acid binding protein 5 /// serine incorporator 1] Top 150 upregulated transcripts, filtered on: membrane, plasma membrane, extracellular, extracellular matrix and secreted. First two columns show BCG lesions from day 31 (section [A], see **Figure 3.6**) are compared to day 0 vehicle (which have a BGC lesion), second two columns show BCG lesions from day 31 compared to naïve animals without any BGC lesions. Data is sorted on day 31 BCG lesion [A] compared to day 0 Naïve [A].

3.2.2 Transcriptome of MS-like lesions using a BCG inflammation model of chronic brain inflammation

Analysing the transcriptome of the BCG time course, a more innate and adaptive cluster of immune-related molecules was found. See **Table 3.9** and the supplementary section of this chapter for addition time course graphs. The anticipated Lewis[a] binders E-Selectin nor P-Selectin were not found to be upregulated (*data now shown*) in this model. Although, this model may resemble a more MS-like phenotype, no other cell adhesion molecules, such as VCAM-1 and ICAM-1 (*data now shown*), associated with the activated endothelium in MS were found to be highly upregulated [49]. However, it is known that E-Selectin and mutations of it are strongly associated with MS-pathology in humans [49],[352],[353] and that this rodent model is capable of binding Lewis[a] (this thesis, see introduction). In comparison, in the IL-1β model of brain inflammation no VCAM-1 transcripts were found to be highly upregulated, however this model has been used successfully to develop an iron-oxide based imaging agent of inflammation by using VCAM-1 antibodies conjugated to the nanoparticle [64]. Also, VCAM-1 was the highest IL-1β upregulated protein in the whole cell proteome experiment using brain microvascular endothelial cells (**Chapter 3.1**). This indicates again that a dual approach, using both proteomics and transcriptomics, can effectively, but not exclusively, identify and confirm chief players in disease models. Furthermore, different models of brain inflammation, both acute and chronic, may reveal common genes and proteins among them, but may also downplay potential markers that are not found to be upregulated. Though the BCG-model used does not allude to any lectins capable of binding Lewis[a], this does not imply they are not there –they are merely not upregulated at the transcript level or the different GeneChip® (E-Selectin transcript L25527_at for IL-1β model and 1388018_at for BCG model from GeneChip® Rat Genome 230 2.0 Array and GeneChip® Rat Genome Genome U34A Set respectively) used may have different binding or splicing efficiencies resulting in no upregulation of E-Selectin in the BCG model (*not further investigated*). Therefore this particular model (including that the model is more technically challenging and time consuming) was not further investigated with regard to Lewis[a]-binding, but some interesting insights and transcripts overlapping between the two transcriptomics experiments performed will be presented next.

Studying the time course of transcripts during this model, a set of genes were selected based on their upregulated transcripts during the course. The transcripts listed below (or certain subsets of transcripts, as 1 gene may have multiple transcripts within the chip) are upregulated when the day 31 BCG lesions [A] are compared to naïve [A], but not to vehicle [A] (indicated in **Table 3.9** in black numbers). Transcripts may be more specifically upregulated in the BCG peripherally challenged BCG

animals than in the BCG lesions challenged with CFA only, implying that the transcripts below are part of 'active lesions'.

Cxcl13	chemokine (C-X-C motif) ligand 13
Olfm1	olfactomedin 1
Scg3	secretogranin III
Spp1	Osteopontin, secreted phosphoprotein 1
C3	complement component 3
Igkv28	immunoglobulin kappa chain variable 28 (V28)
Il18	interleukin 18
Crp	C-reactive protein, pentraxin-related
Ttr	transthyretin
B2m	beta-2 microglobulin
Atp2b1	ATPase, Ca++ transporting, plasma membrane 1
Cd74	Cd74 molecule, major histocompatibility complex, class II invariant chain
Igkv28	immunoglobulin kappa chain variable 28 (V28)
Ctsh	cathepsin H

In the supplementary part of this chapter, expression profiles over time are shown of the identified genes (both BCG lesions compared to naïve and vehicle). Gene ontology (GO) function and interactions were selected from the open-access protein and gene databases https://thebiogrid.org and http://www.uniprot.org/. Briefly, these transcripts of 'active' lesions (or lesions challenged by BCG in Freund's Complete Adjuvant) listed above fit well with a pattern I MS-lesion (complement independent) which are hallmarked by complement and antibody depositions [354],[355]. There are a number of *Igkv28 (*immunoglobulin kappa chain variable 28) transcripts upregulated, CXCL13 a B-cell activation cytokine [356], osteopontin (*Spp1*) a secreted protein which enhances B cell antibody production [357] and IL-18, which can induce B-cells to produce self-reactive IgM and IgG antibody responses [358]. The transcripts of β_2m (beta-2 microglobulin) and MHC-II invariant chain (CD74) also indicate antigen presentation and involvement of MHC-II which is an established marker for MS [49],[149],[359]. In addition to the antibody-production and B-cell involved transcripts, the complement components C3 and CRP were found to be upregulated. E-Selectin is not upregulated in this model, an alternative mechanism of Lewis[a] binding *via* other lectins may be possible *via* complement component C3, and this will be briefly discussed now. C3 is a component of the complement system and is produced in the liver as an acute phase protein [172]. It plays a central

role in the complement system as it is the central protein that is enzymatically cleaved by C3 convertase and can then go onto different pathways; the classical pathway that involves antigen:antibody complexes, the alternative pathway that forms the membrane attack complex for the lysis of pathogens and the mannan-binding lectin (MBL) pathway that requires the binding of MBL to carbohydrate structures and then binding of convertase cleaved C3, C3b that aids in the phagocytosis of the carbohydrate bearing structures [32]. MBL is also an acute phase protein and can cause damage to the vasculature when it is activated by the complement system [122], [360]. It is capable of binding Lewis[a/b] structures [113], and therefore it may be responsible for the binding to the inflamed endothelium *via* vascular deposits of C3 and C4 *(not in top up regulated transcripts)* on the vascular wall [119]. Depending on the carbohydrate structures presented, MBL may exert different activities that are C3-independent [113]. In addition, C3 can bind to collagen (which will be discussed later) directly and C3 can bind to platelets, platelet-derived microvescicles and polymorphonuclear (PMN) cells initiating platelet-PMN complexes *via* a C3 contact-activated manner [361].

3.2.3 Comparing the transcriptome of chronic vs. acute brain inflammation

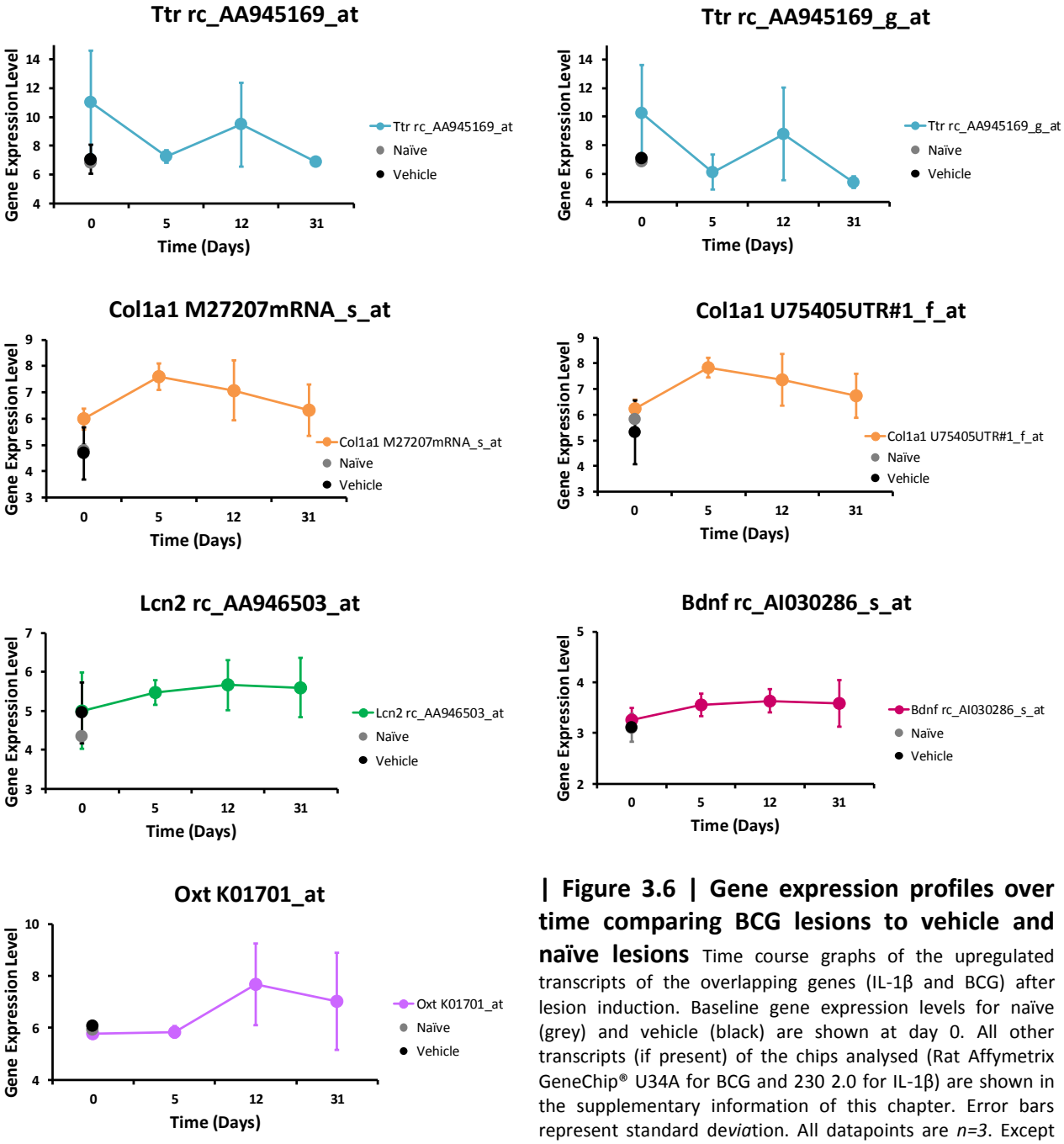
The IL1-β and BCG gene expression profiles were generated from different arrays; however there is an overlap of a select set of genes between the two different experiments, which are listed below.

Bdnf	brain-derived neurotrophic factor*
Ttr	transthyretin*
Oxt	oxytocin/neurophysin 1 prepropeptide*
Lcn2	lipocalin 2*
Col1a1	collagen, type I, alpha 1*

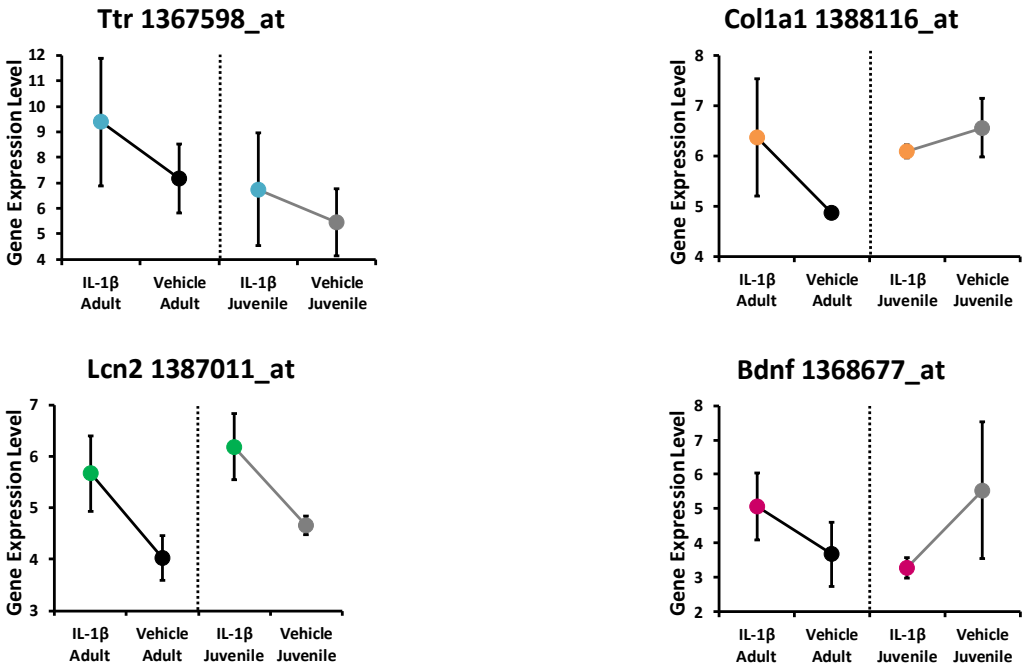
* No lectin/carbohydrate, GAG or other potential obvious Lewis[a] binding domains have been found using NCBI Search for Conserved Domains within a protein or coding nucleotide sequence (http://www.ncbi.nlm.nih.gov/Structure/cdd/wrpsb.cgi).

Figure 3.6 shows the time profiles of these genes comparing the transcripts from the BCG lesions to vehicle and naïve lesions. Transthyretin shows an initial high gene expression level at day 0, which is 28 days post BCG injection. The expression levels return to baseline at day 5 and increase again at day 12 when there is BBB breakdown before returning again to baseline levels at day 31. Collagen 1 α1 shows higher initial gene expression levels, peaking at day 5 and lowering slightly over the measured 26 days. BDNF and lipocalin 2 steadily increase their expression levels over the time course, remaining stabile at day 12 and 31. Oxytocin transcripts only appear higher at day 12 and 31. **Figure 3.7** compares the gene expression profiles of the overlapping genes between adult and

juvenile IL-1β activated brains. Transthyretin shows a similar profile, albeit lower in the juvenile experimental group. Collagen 1 α1 shows an opposite trend in the juvenile brains, where the transcripts are lower in the IL-1β treated juvenile brains. The same opposite trend is shown for BDNF, however BDNF is one of the highest downregulated genes in the juvenile IL-1β treated brains. Lipocalin 2 transcript levels reveal an almost identical profile between adults and juveniles and oxytocin transcripts are only higher in the adult brains. Additional gene information can be found in the discussion section of this chapter.



| Figure 3.6 | Gene expression profiles over time comparing BCG lesions to vehicle and naïve lesions Time course graphs of the upregulated transcripts of the overlapping genes (IL-1β and BCG) after lesion induction. Baseline gene expression levels for naïve (grey) and vehicle (black) are shown at day 0. All other transcripts (if present) of the chips analysed (Rat Affymetrix GeneChip® U34A for BCG and 230 2.0 for IL-1β) are shown in the supplementary information of this chapter. Error bars represent standard de*via*tion. All datapoints are *n=3*. Except BCG time course vehicle, where *n=5*.



| Figure 3.7 | Gene expression profiles comparing adult and juvenile IL-1β lesions to vehicle Graphs with the upregulated transcripts of the overlapping genes (IL-1β and BCG). Dotted line separates Adult (left) from Juvenile (right). Vehicle gene expression levels are shown in bloack for both adult and juvenile. All other transcripts (if present) of the chips analysed (Rat Affymetrix GeneChip® U34A for BCG and 230 2.0 for IL-1β) are shown in the supplementary information of this chapter. Error bars represent standard de*via*tion. All datapoints are *n=3*.

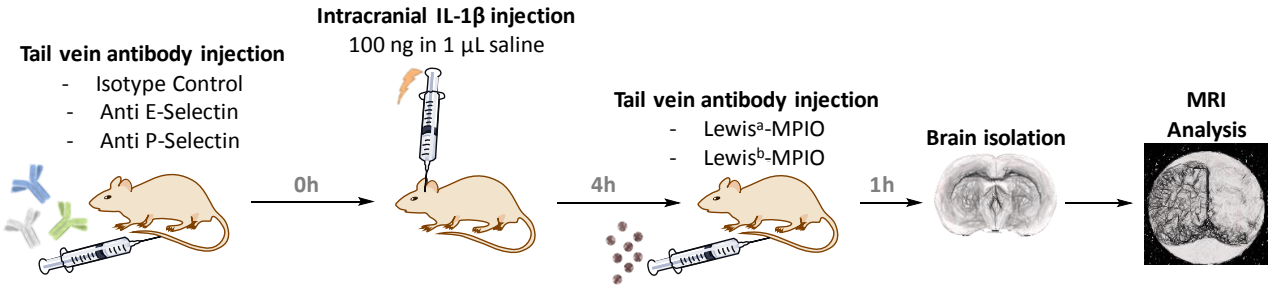
3.3 | *IN VIVO* LEWIS[A] BLOCKING EXPERIMENTS OF ACUTE IL-1β BRAIN INFLAMMATION

The *in vitro* experiments using cell lines illustrate the challenge of mimicking the complex environment, which may be responsible for Lewis[a] binding, which occurs *in vivo*. In particular, the immune system orchestrates an intricate interplay of immune cells, immune components (including proteins, peptides and small molecules), and whole organ 'activation', such as the acute phase response [170]. Mimicking these cascades of reactions, protein mediators, and recruitment of immune cells is nearly impossible in an *in vitro* setting. While the *in vitro* experiments indicate that lectin E-Selectin was the evident hit, the intricate mechanism of Lewis[a] binding *in vivo* under flow conditions could not be derived from these experiments. The limitation of the brain microvascular endothelial cell proteomics experiments is that there is only 1 cell type present; even though these are highly likely the cells responsible for the binding, no flow, immune cells, or blood components that could alter the Lewis[a] binding to these cells were present. The *in vivo* transcriptomics could overcome this in part as it sampled the inflammatory IL-1β lesion from the rat brain containing all the cells necessary for the binding of Lewis[a]. However, the source of the upregulated transcripts cannot be traced back to a particular cell type and will only provide a mechanism at the transcript level. While these experiments described in the previous subchapters have their limitations, they were instrumental in designing the two *in vivo* experiments presented herein.

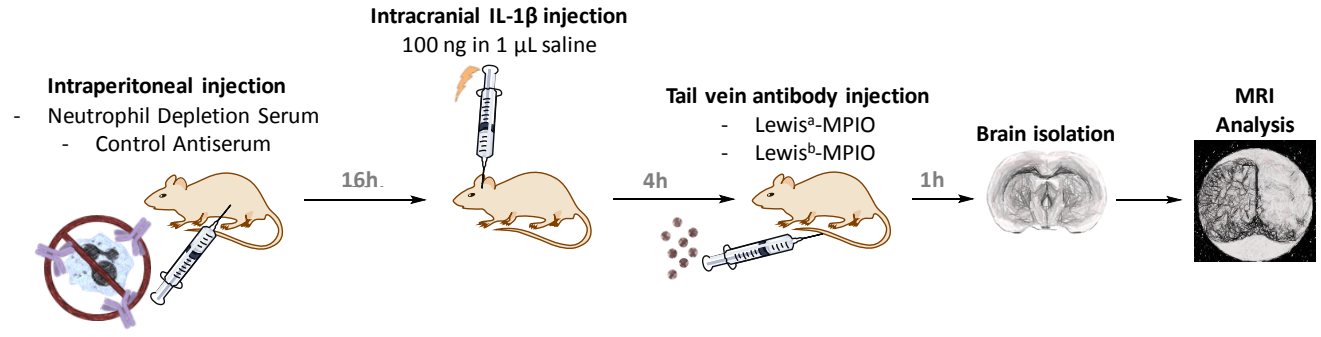
In order to elucidate how Lewis[a]-MPIO accumulate at the IL-1β inflamed endothelium in the brain *in vivo,* the speculated components identified to facilitate binding *in vitro* were systematically removed/blocked from the system. The two types of experiments used are shown in **Figure 3.8**.
First, the blockade of either E- or P- selectins was employed. E-selectin was considered the most likely lectin involved from the experiments described in the proteomics and genomics sections before. Like E-selectin, P-selectin is expressed by endothelial cells, plays a role in neutrophil recruitment to the brain [104], and is known to bind to Lewis[a]. A role for P-selectin, or perhaps a synergistic role of both selectins, could not be ruled out by the *in vitro* data, and thus P-selectin's role in Lewis[a] binding was also studied [53]. P-Selectin was detected, but not upregulated (*data not shown*) in the proteome of brain microvascular endothelial cells. However, the transportation of P-selectin to the cell surface, from α-granules, if present, and Weibel-Palade bodies [362], could not be detected with his method.

In addition, the transcriptome cannot be used for pre-stored proteins, which translocate to the cells surface upon activation. However, an indirect role of platelets was implied by the *bdnf* transcripts detected, described in subchapter 3.2, as platelets can be a source of *bdnf* mRNA [363], [364], [365]. Second, because both E- and P-Selectin mediate neutrophil recruitment, the effect of neutrophil depletion was investigated. Neutrophils play a role in acute brain inflammation, as they are the primary cells to arrive at the early inflamed endothelium [4]. Neutrophils bind E- and P-Selectin and thus may interact with Lewis[a] as well, [55]. Human neutrophils can display Lewis[a] structures [98] and by studying the role of neutrophils in rodents (that have a Lewis[a]-*null* background due to their lack of the Lewis-gene) Lewis[a] binding independently from Lewis[a] presented on neutrophils can be assessed. The role of neutrophils and the Lewis[a] binding *in vivo* will be presented after the blocking experiments in this part of the thesis.

A



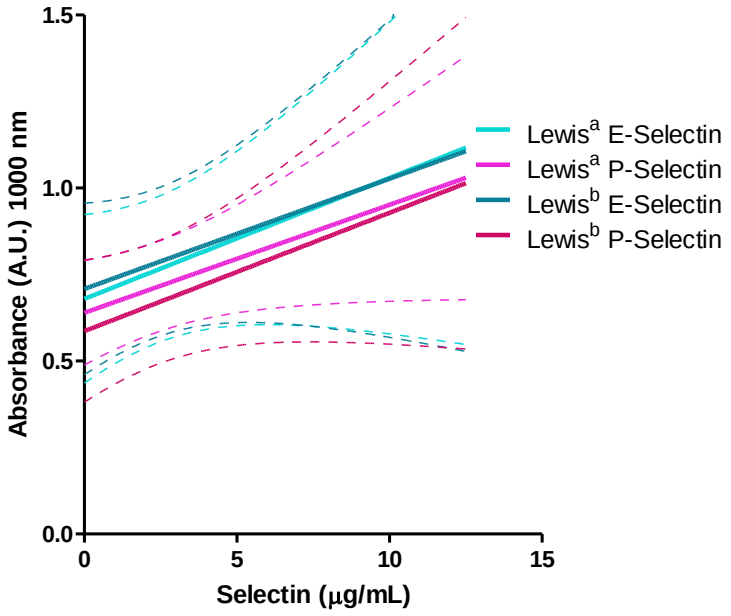
B



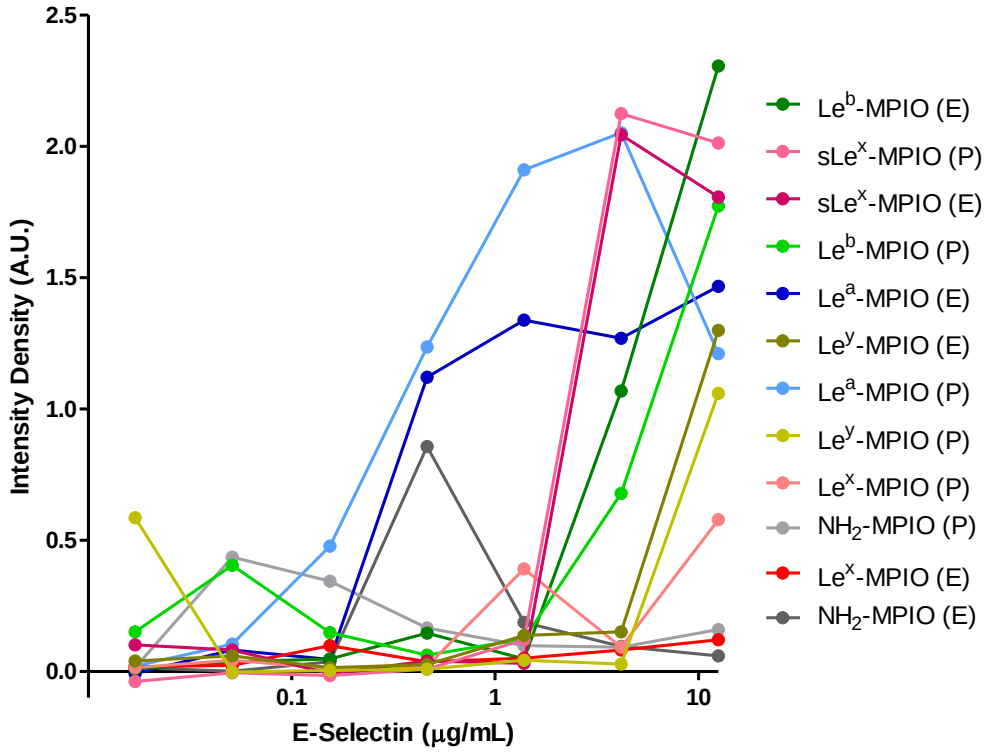
| Figure 3.8 | Experimental overview *in vivo* Lewis[a] and Lewis[b] blocking experiments of acute IL-1β brain inflammation **|A|** E- and P-Selectin were blocked with antibodies prior to inducing IL-1β mediated acute brain inflammation. Lewis[a/b]-MPIO binding was quantified using MRI to assess the role of the selectins *in vivo* for Lewis[a/b]-MPIO binding. **|B|** Neutrophils were depleted with an anti-neutrophil serum prior to inducing IL-1β mediated acute brain inflammation. Lewis[a/b]-MPIO binding in the presence an absence of neutrophils was quantified using MRI.

3.3.1 *In vitro* binding of Lewis[a], Lewis[b] and other Lewis antigens to E-Selectin and P-Selectin

Using the ELISA-based method described in **Chapter 2**, the binding of Lewis[a] and Lewis[b] present on MPIO was compared against E- or P-selectin. See the method details in **section 3.6.12.** There was no significant difference between the binding of Lewis[a] and Lewis[b] to either E-selectin or P-Selectin. But in general both Lewis[a] and Lewis[b] bind slightly stronger to E-Selectin than P-Selectin and Lewis[a] binds slightly stronger than Lewis[b], as shown in **Figure 3.9**. The binding was also assessed using the other Lewis antigens, see **Figure 3.10**. However the experiment was only perfomed once and the data presented is not clear. Some observations were made nonetheless and decribed here: Both sLe[x] and Le[b] bind the strongest to both E- and P-Selectin at high concentrations of Selectins, Le[x] only shows binding to P-Selectin and Le[y] has moderate binding to both selectins, but only at high concentrations. (*) Le[a] has the strongest binding at the lower concentrations of both Selectins. *N=1* for all data points shown. **Table 3.10** shows the binding order of the Lewis antigens tested, note (*) that Lewis[a] binds the strongest at lower concentrations of the selectins, but is ranked second best binder.



| Figure 3.9 | Binding of Lewis[a/b]-MPIO to rat recombinant E- and P-Selectin reveals no significant difference in binding between the Lewis antigens and the Selectins E- and P-Selectin binding of Lewis[a] and Lewis[b] MPIO using the Perls' Prussian Blue stain for iron particle detection (see section **2.7.8**). Slopes of the lines are not significantly different. Both Lewis[a] and Lewis[b] can bind to both lectins in a dose-dependent manner. Lewis[a] and Lewis[b] bind more strongly to E-Selectin. Plotted lines are average values of 6 independent assays, normalized and the standard deviation is plotted as dashed lines.



| Figure 3.10 | Binding of Lewis antigens on MPIO to rat recombinant E- and P-Selectin shows that Lewis[a] binds E-Selectin at lower concentrations E- and P-Selectin binding of Lewis MPIO using the Perl's Prussian Blue stain for iron particle detection (see **section 2.7.8**). Lewis-MPIO are indicated and (E) denotes E-Selectin and (P) denotes P-Selectin. Experiment was performed once, *n*=1. Table 3.10 summarises the binding order.

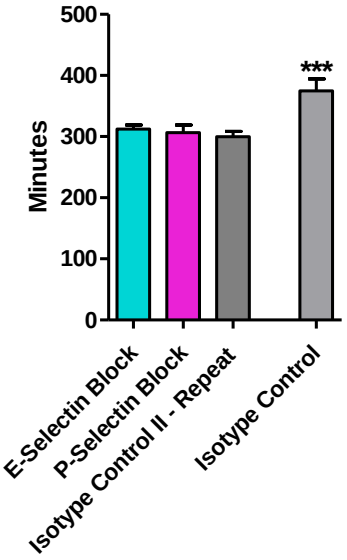
| Table 3.10 | Lewis-antigens used for the E- and P-Selectin ELISA

MPIO	Loading (%) Fmoc	Synthesized by	E-Selectin Binding Order	P-Selectin Binding Order
Le^a	49	KW	++ (*)	+ (*)
Le^b	54	KW	+++	+++
Le^x	67	SDM [298]	-	±
sLe^x	72	SDM [298]	+++	+++
Le^y	62	SDM [298]	+	+
NH_2	0	n/a	-	-

(-) none (±) trace (+) weak (++) moderate (+++) strong (nd) not determined.

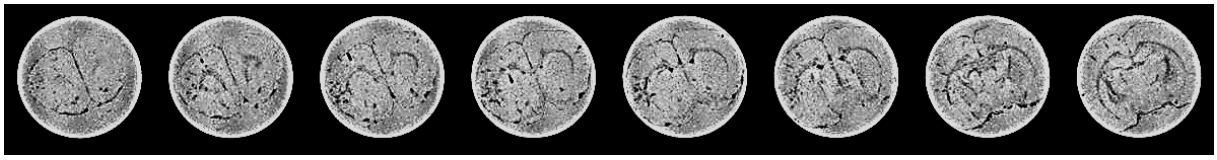
3.3.2 Considerations and overview of experimental details of the *ex vivo* MRI data presented

The IL1-β brain inflammation model used to assess the biding of Lewis[a] and Lewis[b] *in vivo* is described in the methods section. Four animals were used for each experimental group. For the Selectin blockade experiment (**3.6.13**), The significantly (****P ≤ 0.001*) longer experimental timings of the Isotype control subset resulted in a large variation of the control Le[a]-MPIO and Le[b]-MPIO binding analysed by MRI for the Selectin blockade group (see results and data analysis further on). Both the IL-1β incubation time (~5h instead of 4h) and the MPIO incubation time (~1.5h instead of 1h) were longer. Therefore a repeat experiment was performed labelled 'Isotype Control II- Repeat'. To assess the level of neutrophil depletion in the circulation as described in **3.6.14**, blood samples were taken as descried in **3.6.15**. **Figure 3.12** and **Figure 3.13** show the data analysis parameters used in **3.6.18**. These parameters shown allowed uniform data analysis of the samples. **Figure 3.12** shows the region of interest based on the stereotactic injections performed. **Figure 3.13** shows representative image analysis and applied exclusions, so each sample was measured in a constant manner.



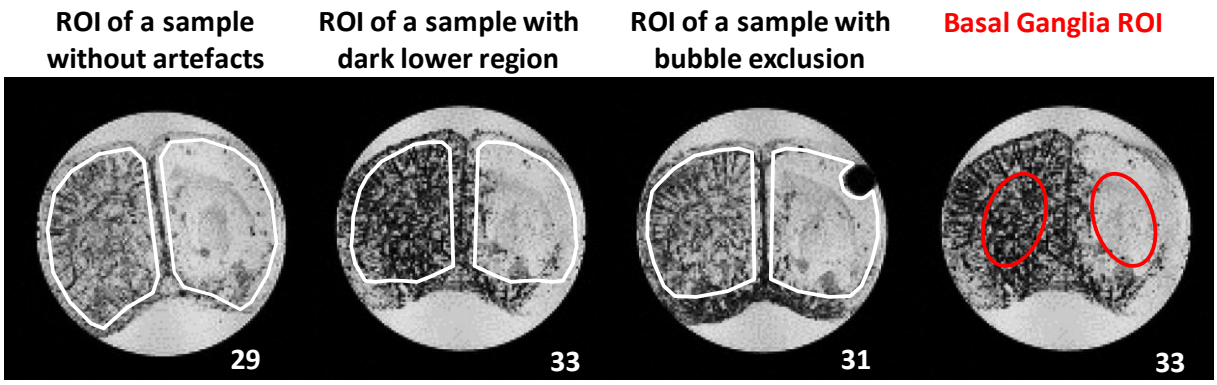
| Figure 3.11 | Variable experimental timings resulted in altered Lewis[a/b]-MPIO binding

Overview of experimental timings showing the total time of each animal averaged per indicated group. 1 way ANOVA using a Bonferroni's Multiple Comparison Test (**P* ≤ 0.05, ***P* ≤ 0.01,****P* ≤ 0.001, NS not significant).



| Figure 3.12 | Overview of coronal MRI sections of a rat brain used to generate Z-stacks

Z-stacks were generated from the MRI images using the stereotactic coordinates for the injection and the rat brain atlas. Each generated Z-stack file contains 35 sections and encompasses the regions of interest of the brain shown above.



| Figure 3.13 | Representative ROIs for image analysis Two methods were used to analyse the Lewis[a] and Lewis[b] MPIO binding in the generated Z-stacks. First method (white) includes most of the hemisphere and artefacts are excluded. The second method (red) uses fixed-size eclipse shaped ROIs covering only the basal ganglia (BG). Data comparisons will be presented further using BG when only the basal ganglia are analysed.

3.3.3 Blood analysis of the experimental groups reveals an altered blood profile for IL-1β treated animals and shows effective neutrophil depletion for animals treated with an antiserum

To assess the changes of the immune cell populations of the treated animal groups (Selectin-blockade and neutrophil depletion), blood samples were taken and analysed with a haemocytometer (see method **3.6.15**). **Table 3.11** and **Figure 3.14** show an overview of the blood parameters of the experimental groups. **Figure 3.15** shows that the red blood cell count remains stable between all groups analysed. Tail vein samples from naïve animal groups resulted in some haemolysis but did not affect white blood cell counts. Total white blood cell count is significantly lower in the neutrophil depleted animals when compared with the control (both naïve and IL-1β) and the IL-1β treated neutrophil depleted animals have significantly lower WBC when compared to the E- and P-Selectin treated groups, $**P \leq 0.01$ and $*P \leq 0.05$ respectively. Platelet numbers are significantly lower in the neutrophil depleted animals when compared to its control group and to the E- and P-Selectin treated groups. Lymphocyte numbers remain stable between the IL-1β treated groups and lower upon IL-1β treatment in both control serum and anti-neutrophil serum treated animals. This is also shown in **Figure 3.14**. For a breakdown of the immune cell subsets, see **Figure 3.16**. Neutrophils are depleted from the circulation in the neutrophil anti-serum treated animals. Numbers of neutrophils lower upon IL-1β treatment, but not significantly. In addition, neutrophil numbers differ significantly between the two isotype control groups, where the light grey group had significantly longer experimental timings (see **Figure 3.11**). The neutrophil numbers are significantly lower the neutrophil depleted animals when compared to all groups. Monocyte count is significantly lower in the neutrophil depleted animals when compared with the control (both naïve and IL-1β) and the IL-1β treated neutrophil depleted animals have significantly lower monocytes when

compared to the E- and P-Selectin treated groups, **P ≤ 0.01 and *P ≤ 0.05 respectively. Eosinophil numbers lower upon IL-1β treatment and only neutrophil depleted animals have lower eosinophil numbers compared to the other IL-1 β treated groups. Basophil numbers remain stable between all groups and treatments.

| Table 3.11 | Tabular overview of full blood counts of the experiments used for statistical analysis

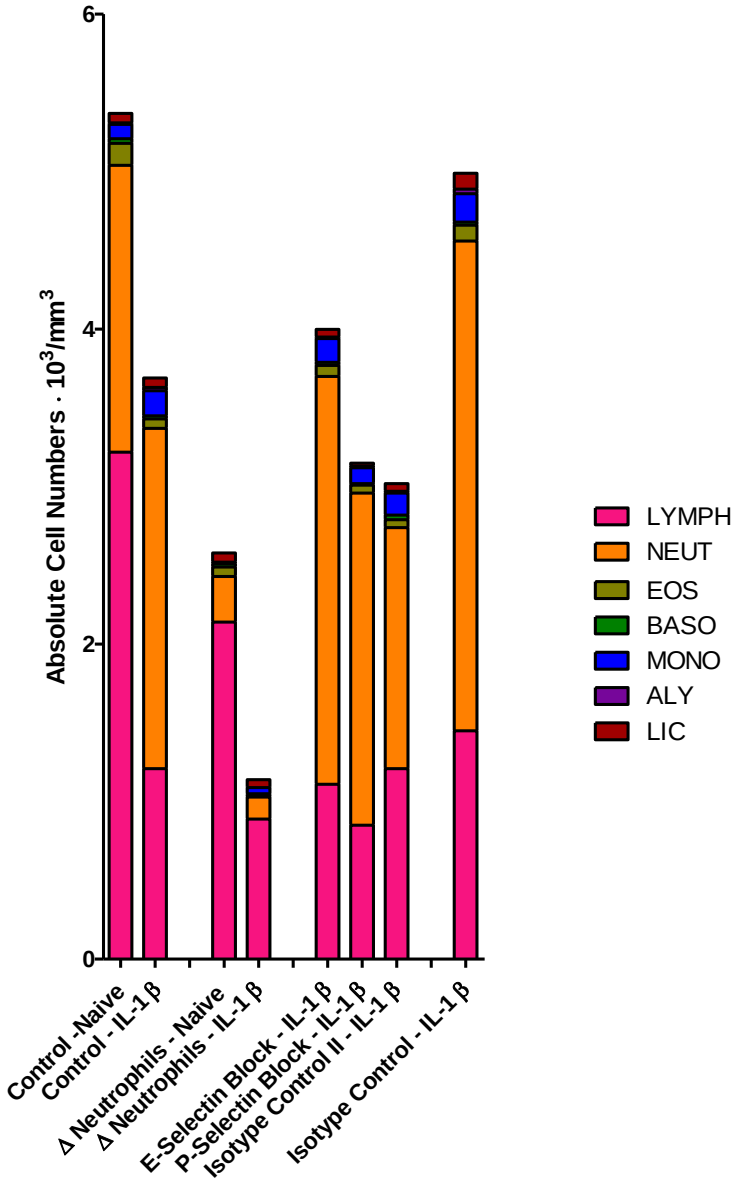
		Serum Control Naïve Avg	Serum Control IL-1β Avg	Δ Neutrophil Naive Avg	Δ Neutrophil IL-1β Avg	Isotype Control IL-1β Avg	Isotype Control II* IL-1β Avg	E-Selectin Block IL-1β Avg	P-Selectin Block IL-1β Avg
WBC	**(10^3/mm^3)**	4.6	3.8	2.5	1.1	4.6	3.0	3.9	3.1
	Stdev	± 2.2	± 1.0	± 1.1	± 0.3	± 1.8	± 0.9	± 1.5	± 0.9
RBC	**(10^6/mm^3)**	3.0	5.5	3.5	5.2	4.8	5.5	5.0	5.2
	Stdev	± 1.2	± 0.3	± 1.5	± 0.3	± 0.4	± 0.3	± 0.5	± 0.3
HGB	**(g/dL)**	16.0	28.6	19.1	28.3	26.2	12.1	26.5	27.2
	Stdev	± 6.3	± 1.3	± 7.9	± 1.3	± 1.4	± 0.5	± 2.5	± 1.3
HCT	**(%)**	18.4	28.4	21.5	27.9	28.2	35.7	28.6	30.3
	Stdev	± 7.2	± 1.7	± 8.9	± 1.5	± 3.0	± 1.4	± 2.8	± 1.6
MCV	**(fL)**	62.3	51.9	62.0	54.0	58.1	64.8	57.3	58.9
	Stdev	± 3.3	± 3.3	± 2.7	± 2.1	± 2.1	± 1.4	± 2.1	± 1.4
MCH	**(pg)**	54.2	52.4	55.6	54.9	53.0	22.0	53.1	52.9
	Stdev	± 2.3	± 1.1	± 2.7	± 2.3	± 1.0	± 0.5	± 1.4	± 1.3
MCHC	**(g/dL)**	87.4	101.2	89.6	101.7	91.3	34.0	92.8	89.8
	Stdev	± 6.0	± 6.1	± 4.2	± 5.3	± 1.9	± 0.3	± 1.5	± 1.0
RDW	**(%)**	19.5	15.0	17.2	14.9	16.6	14.5	19.4	18.3
	Stdev	± 3.1	± 1.9	± 1.6	± 1.3	± 2.0	± 0.6	± 3.8	± 4.7
PLT	**(10^6/mm^3)**	452.5	637.9	315.7	422.0	552.4	580.5	508.0	577.1
	Stdev	± 252.9	± 60.7	± 128.3	± 52.9	± 142.2	± 57.0	± 84.3	± 48.0
MPV	**(fL)**	6.7	5.7	6.3	5.9	6.0	5.8	5.5	5.5
	Stdev	± 1.0	± 0.2	± 0.4	± 0.3	± 0.6	± 0.5	± 0.2	± 0.3
PCT	**(%)**	0.3	0.4	0.2	0.2	0.3	0.3	0.3	0.3
	Stdev	± 0.1	± 0.0	± 0.1	± 0.0	± 0.1	± 0.0	± 0.0	± 0.0
LYMPH	**(%)**	58.0	32.8	80.3	82.9	31.7	40.6	29.2	26.9
	Stdev	± 8.0	± 4.4	± 7.9	± 5.2	± 10.9	± 4.0	± 5.3	± 2.8
MONO	**(%)**	1.5	4.2	0.5	3.0	4.0	4.4	4.0	3.1
	Stdev	± 1.3	± 1.1	± 0.2	± 3.1	± 1.3	± 1.1	± 1.5	± 0.7
NEUT	**(%)**	36.5	60.9	14.5	12.2	61.7	51.9	65.0	67.9
	Stdev	± 7.6	± 5.2	± 5.7	± 2.9	± 11.5	± 4.2	± 5.1	± 3.2
EOS	**(%)**	3.0	1.7	3.6	1.0	2.2	1.9	1.8	1.7
	Stdev	± 1.1	± 0.3	± 2.0	± 0.9	± 1.3	± 0.5	± 0.6	± 0.4
BASO	**(%)**	1.0	0.4	1.1	0.8	0.5	1.1	0.5	0.4
	Stdev	± 0.9	± 0.2	± 0.7	± 0.7	± 0.4	± 0.5	± 0.3	± 0.2
ALY	**(%)**	0.2	0.4	0.1	0.3	0.6	0.4	0.4	0.2
	Stdev	± 0.2	± 0.2	± 0.1	± 0.1	± 0.4	± 0.1	± 0.3	± 0.1
LIC	**(%)**	1.4	1.9	2.4	5.4	2.1	1.3	1.5	0.6
	Stdev	± 0.8	± 1.6	± 1.1	± 6.0	± 2.0	± 1.5	± 1.5	± 0.7
	Rats	*n=4***	*n=8*	*n=6***	*n=8*	*n=8*	*n=8*	*n=7*	*n=8*
	# of measurements	1	3	1	3	3	3	3	3

* Isotype control experiment II was a repeat experiment as experimental timings were significantly different from the other experiments (see **Figure 3.11**). ** Numbers of tail vein samples of naïve (before IL-1β injection) were not always sufficient for a full blood count (≥70 µL), repeat tail veins were not attempted.

| Table 3.12 | Overview of data comparison groups for statistics

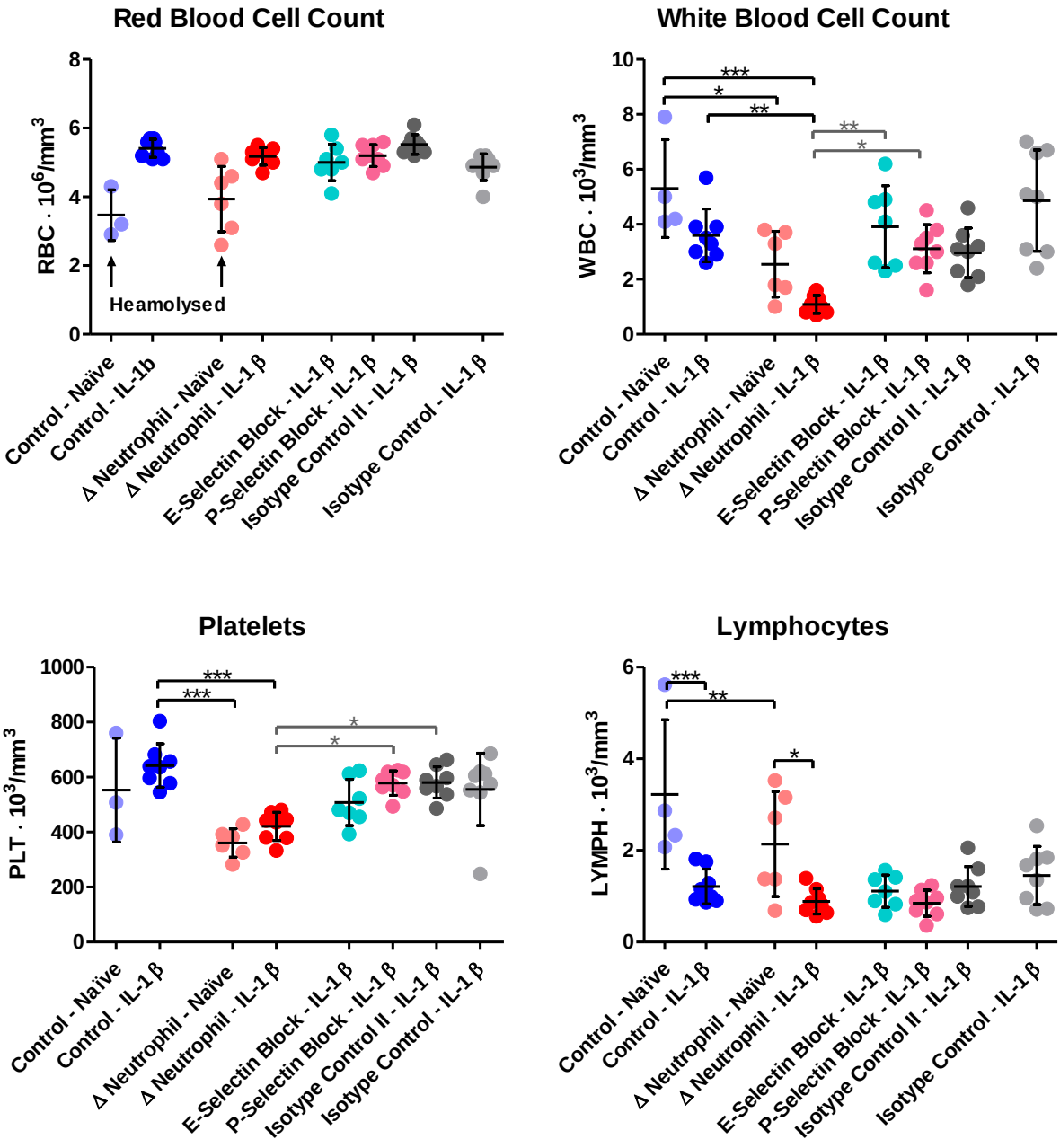
Groups	Details	Error bar colour
Control Serum and Neutrophil Depletion Serum	Compare Naïve vs IL-1β	**Black**
All IL-1β groups	Exclude first Isotype Control - IL-1β	**Dark Grey**
Isotype Control group	Compare Isotype Control vs the repeat experiment Isotype Control II	**Light Grey**

Isotype control experiment II was a repeat experiment as experimental timings were significantly different from the other experiments, therefore Isotype Control will not be included in the analysis. As only for the neutrophil depletion experiment naïve (no IL-1β brain inflammation) blood was taken, these will not be compared with the IL-1β treated animals from the Selectin blockade experiment.

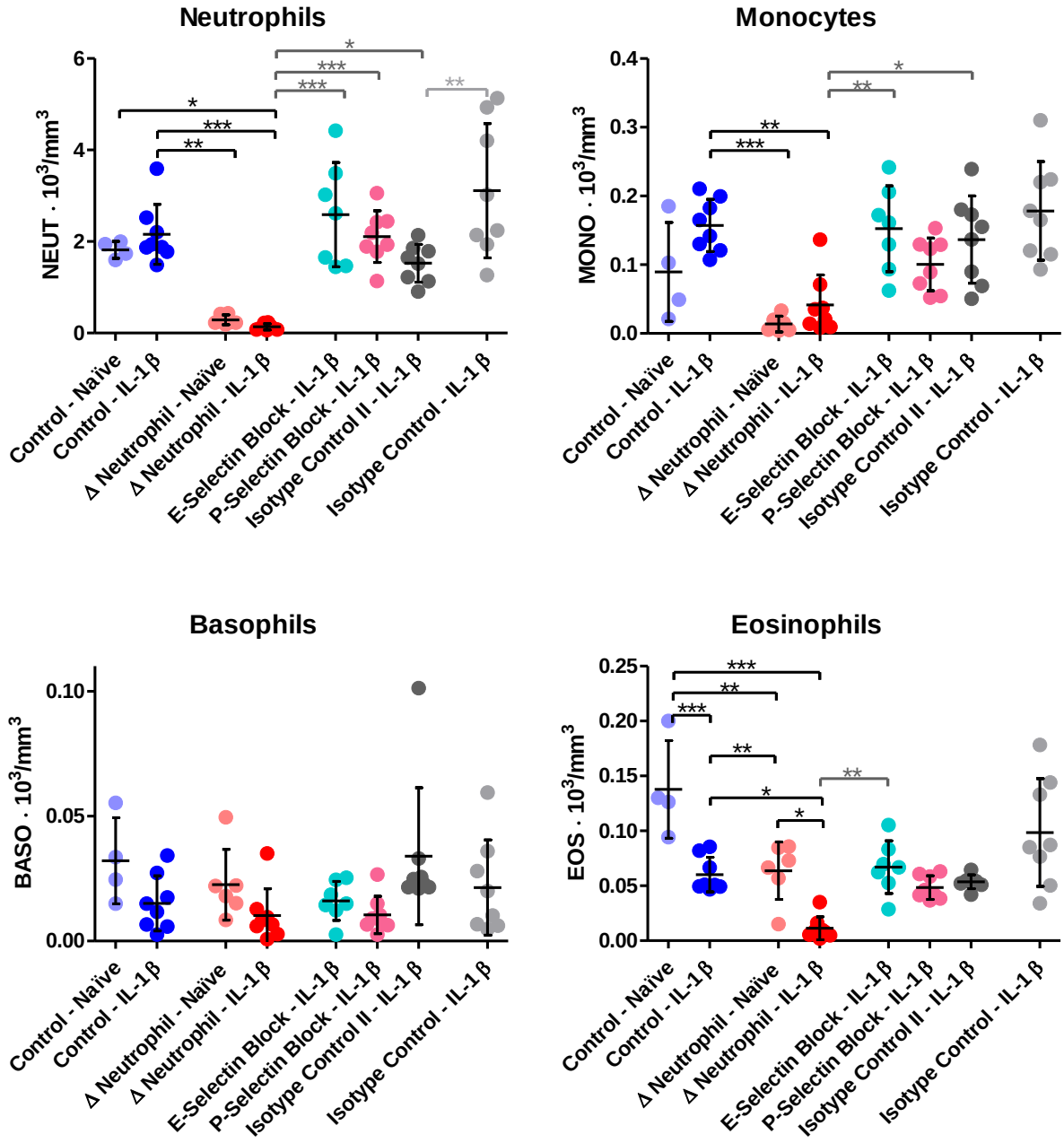


| Figure 3.14 | Absolute Cell numbers of the experimental groups shows an altered white blood cell composition and effective neutrophil depletion in the antiserum treated animals

Colour coded overview of absolute white blood cell counts calculated from **Table 3.11**. Breakdown and statistical analysis of the individual cell types can be found in **Figure 3.15** and **3.16**. Note: IL-1β treatment decreases WBC numbers. Orange shows the neutrophil populations in the experimental groups and reveals that the antiserum treated animals have lower neutrophil numbers.



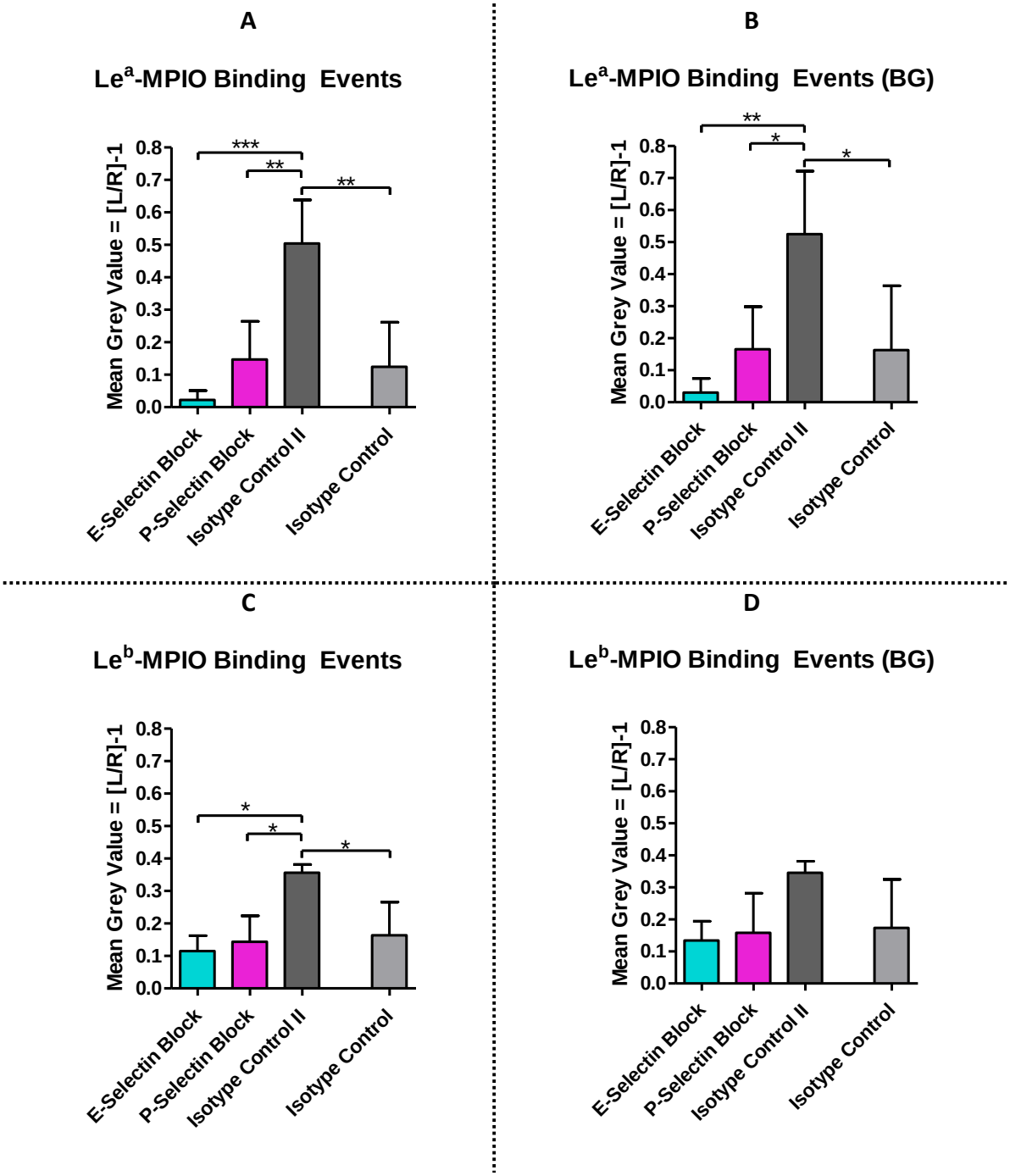
| Figure 3.15 | Blood parameters of the experimental groups studied for Lewis[a/b]-MPIO binding – Graphs 1 Absolute numbers for blood counts. Please refer to **Table 3.12** for error bar legend. 1 way ANOVA using a Bonferroni's Multiple Comparison Test (*P ≤ 0.05, **P ≤ 0.01,***P ≤ 0.001).



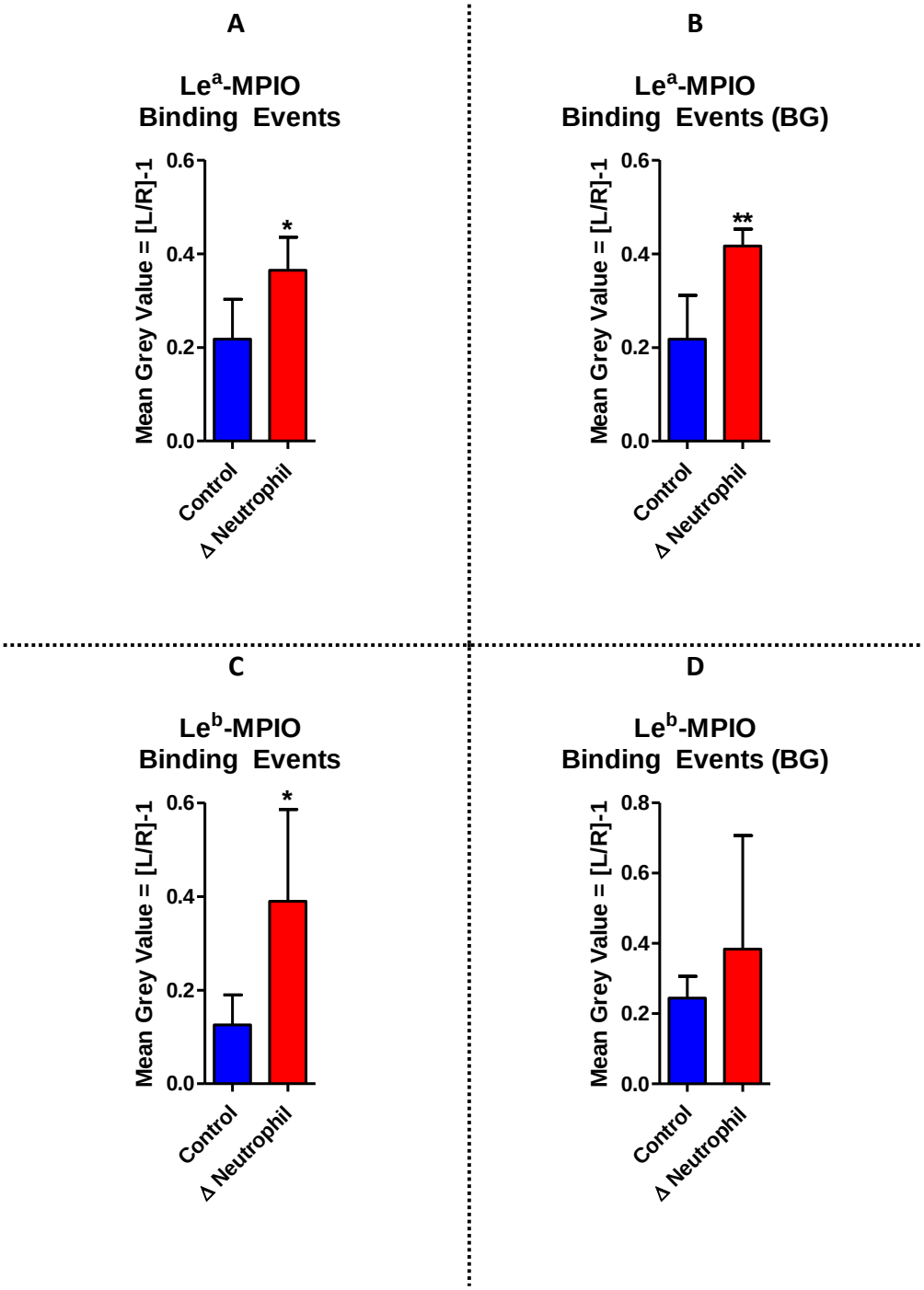
| Figure 3.16 | Blood parameters of the experimental groups studied for Lewis[a/b]-MPIO binding – Graphs 2 Absolute numbers for blood counts. Please refer to **Table 3.12** for error bar legend. 1 way ANOVA using a Bonferroni's Multiple Comparison Test (*P ≤ 0.05, **P ≤ 0.01,***P ≤ 0.001).

3.3.4 Lewis-MPIO quantification of the IL-1β inflamed brain using MRI

Figure 3.19 shows representative MRI Z-stacks as described in **3.6.18** and the experimental details for each animal. Grouped analysis and quantification of the Lewis-MPIO binding events in the brains is shown in **Figure 3.17** and **3.18**. Two ROIs, as shown in **Figure 3.12**, were used to analyse the Lewis-MPIOs in the brain MRI- Z-stacks. The (BG)-indicated graphs show the result from the basal ganglia, whilst the other graphs include the entire hemisphere with the earlier specified exclusion criteria. For the Selectin-blockade results, see **Figure 3.17**. Lewis[a]-MPIO binding is significantly (*$***P \leq 0.001$*) reduced when E-Selectin is blocked with an anti-E-Selectin antibody. P-Selectin blockade results in a less significant (*$**P \leq 0.01$*) reduction of Lewis[a]-MPIO binding. Comparing the isotype controls shows that longer experimental timings (**Figure 3.11**) results in significantly (*$**P \leq 0.01$*) less Lewis[a]-MPIO binding events. Analysis of only the basal ganglia (BG) ROI as shown in **Figure 3.13**, results in less significant values of Lewis[a]-MPIO binding. Quantified binding events show significantly fewer (*$*P \leq 0.05$*) Lewis[b]-MPIO binding events when the Selectins are blocked. Also Lewis[b]-MPIO binding is significantly (*$*P \leq 0.05$*) affected by longer experimental timings and significant binding events are abolished when only basal ganglia (BG) are measured. When Neutrophils are depleted (see **Figure 3.18**), there is significantly (*$*P \leq 0.05$*) more Lewis[a]-MPIO present in the neutrophil depleted animals and when the basal ganglia is quantified it results in a more significant value (*$**P \leq 0.01$*). As for Lewis[b]-MPIO, there is significantly (*$*P \leq 0.05$*) more Lewis[b]-MPIO present in the neutrophil depleted animals and the significant binding events are abolished when only basal ganglia (BG) are compared for Lewis[b]-MPIO binding.

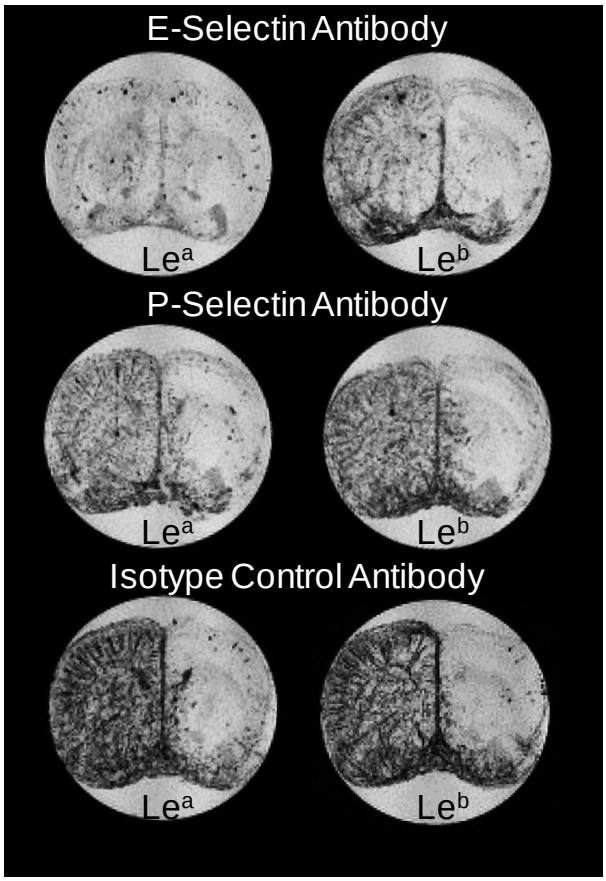


| Figure 3.17 | Quantified MRI analysis of the hemisphere and basal ganglia (BG) reveals E-Selectin mediated Lewis[a]-MPIO binding and E- and P-Selectin medated binding for Lewis[a]-MPIO during the Selectin Blockade experiments **|A|** Quantified binding events of Selectin-blocked and isotype controls animals comparing the left and right hemisphere with the formula as described in **section 3.6.18**. **|B|** Analysis of only the basal ganglia (BG) ROI as shown in **Figure 3.13**, for Lewis[a]-MPIO binding. **|C|** Quantified binding events of Lewis[b]-MPIO binding of the hemispheres. **|D|** Analysis of only the basal ganglia (BG) ROI as shown in **Figure 3.13**, for Lewis[b]-MPIO binding. 1 way ANOVA using a Bonferroni's Multiple Comparison Test (*P ≤ 0.05, **P ≤ 0.01,***P ≤ 0.001, Numbers: *n=4* for all, except E-Selectin Block Lewis[b] and Isotype Control II Lewis[b] which are *n=3*.

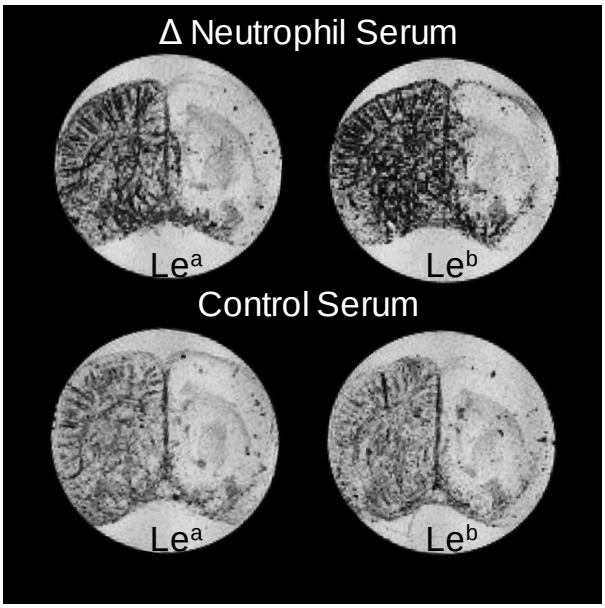


| Figure 3.18 | Quantified MRI analysis of hemisphere and basal ganglia shows a role for neutrophils in the binding of Lewis[a/b]-MPIO during the neutrophil depletion experiments **|A|** Quantified binding events of control and neutrophil depleted animals comparing the left and right hemisphere with the formula as described in **section 3.6.18**. **|B|** Analysis of only the basal ganglia (BG) as shown in **Figure 3.13**. **|C|** Quantified binding events of control and neutrophil depleted animals for Lewis[b]-MPIO binding. **|D|** Analysis of only the basal ganglia (BG) for Lewis[b]-MPIO binding. Two-tailed unpaired t test. (*P ≤ 0.05, **P ≤ 0.01,***P ≤ 0.001). Numbers: *n=4* for all.

A



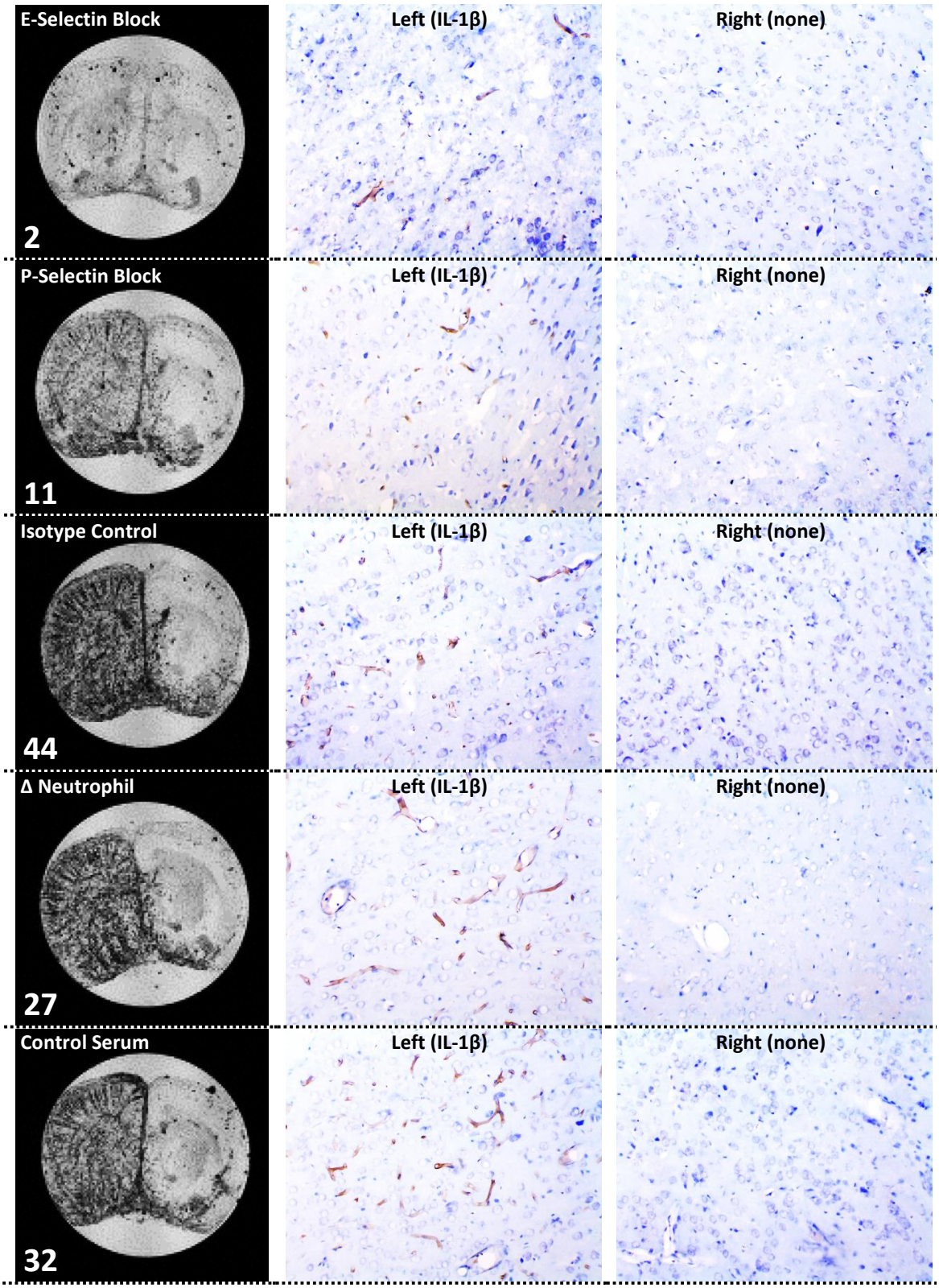
B



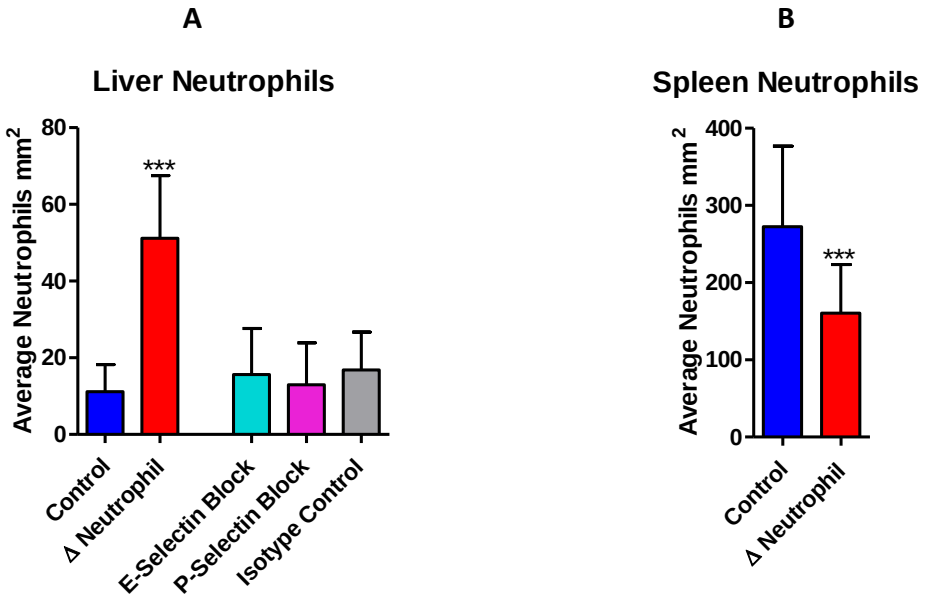
| Figure 3.19 | Representative Z-stacks of MRI images of the Selectin Blockade and Neutrophil Depletion experiments performed **|A|** Representative coronal Z-stacks of MRI images acquired during the Selectin Blockade experiments, see Methods for all the acquired Z-stacks and other experimental parameters. Representative of data presented in **Figure 3.17**. **|B|** Representative coronal Z-stacks of MRI images acquired during the Neutrophil Depletion experiments, see Methods for all the acquired Z-stacks and other experimental parameters. Representative of data presented in **Figure 3.18**.

3.3.4 Immunohistochemical analysis of E-Selectin and neutrophils in the experimental groups

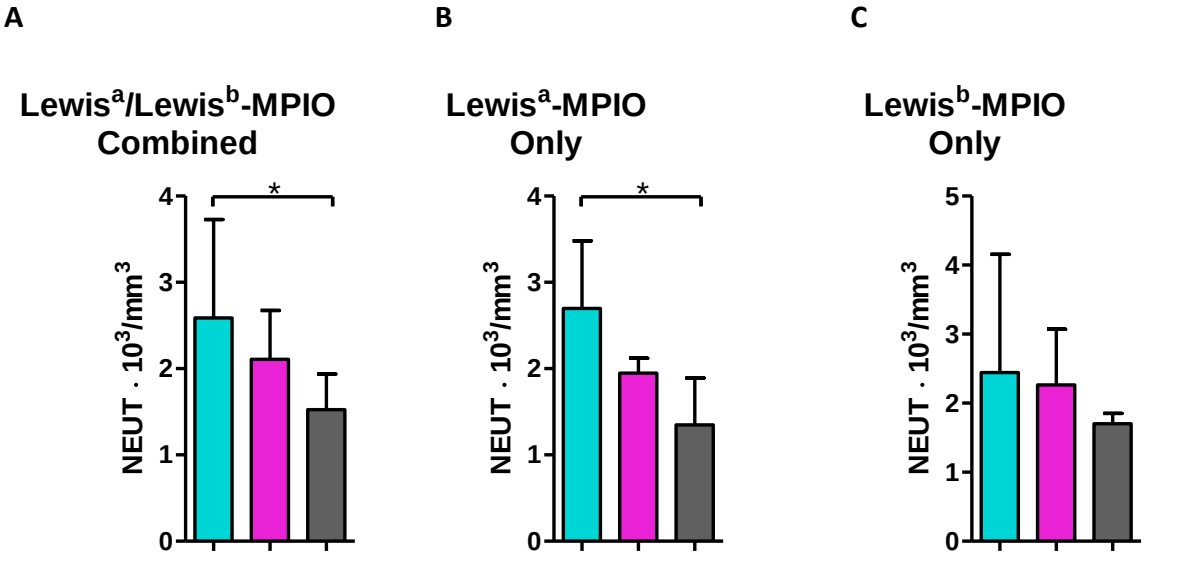
To assess if E-Selectin blockade resulted in less E-Selectin expression in the brain, the indicated brains in **Figure 3.20** were analysed for their E-Selectin expression levels with immunohistochemistry. As shown for E-Selectin blocked animal number two, E-Selectin is still present in the vessels when analysed with immunohistochemistry. Blood analysis revealed previously that neutrophils were significantly depleted from the animals treated with the anti-neutrophil serum. Peripheral tissue (liver and spleen, see **Figure 3.21**) were stained for the presence of neutrophils and quantified by counting three tissue sections and three regions per section for only the Lewis[a]-MPIO treated animals. Anti-Neutrophil serum immunoreactivity in the liver was significantly (***P ≤ 0.001) elevated in neutrophil depleted animals (as part of the clearance mechanism), but analysis of the spleen data revealed a significant reduction of neutrophils in the neutrophil depleted animals. Further analysis of the role of neutrophils in the experimental groups is shown in **Figure 3.22**. Shown here is the difference of absolute neutrophil numbers from the blood compared between Lewis[a]-MPIO and Lewis[b]-MPIO in the Selectin-blocked animals. Absolute neutrophil number is significantly (*P ≤ 0.05) increased in E-Selectin blocked animals and neutrophil numbers remain significantly higher (*P ≤ 0.05) in the E-Selectin blocked animals injected with Lewis[a]-MPIO. Neutrophil numbers are not significantly different from animals injected with Lewis[b]-MPIO.



| Figure 3.20 | Immunohistochemical analysis of E-Selectin Expression in brains of Lewis[a]-MPIO animals reveals E-Selectin expression in all treatment groups
Immunohistochemistry of 10 µm coronal brain slides of the IL-1β lesion reveals the presence of E-Selectin using an E-Selectin antibody. Left basal ganglia (IL-1β) compared to untreated right basal ganglia regions shows that all groups have E-Selectin expression on the left IL-1β treated side of the brain. Brown DAB staining of vessels reveals E-Selectin and sections are counterstained with cresyl violet. Representative sections of the indicated (numbered) brains are shown.



| Figure 3.21 | Immunohistochemical quantification of neutrophils in peripheral tissue of Lewis[a]-MPIO animals **|A|** Neutrophil accumulation in the liver of the Lewis[a]-MPIO treated animals using a 1 way ANOVA using a Bonferroni's Multiple Comparison Test (*P ≤ 0.05, **P ≤ 0.01,***P ≤ 0.001). **|B|** Analysis of the spleen neutrophils in the neutrophil depleted animals. Two-tailed unpaired t test. (*P ≤ 0.05, **P ≤ 0.01,***P ≤ 0.001). Numbers: n=4 for all, only Lewis[a]-MPIO tissue was analysed. Average of 9 counts. 3 tissue sections, 3 regions per section.



| Figure 3.22 | Neutrophil blood numbers for the Selectin Blockade Experiment shows a difference between Lewis[a] and Lewis[b] **|A|** Absolute neutrophil numbers from whole blood for the-Selectin-blockade treatment groups . *N=7* for E-Selectin, and *n=8* for P-Selectin and Isotype control. **|B|** Neutrophil numbers of the animals injected with Lewis[a]-MPIO. *N=4* for E-Selectin, P-Selectin and Isotype control. **|C|** Neutrophil numbers from animals injected with Lewis[b]-MPIO. *N=3* for E-Selectin, and *n=4* for P-Selectin and Isotype control. 1 way ANOVA using a Bonferroni's Multiple Comparison Test (*P ≤ 0.05, **P ≤ 0.01,***P ≤ 0.001, NS not significant).

3.4 | DISCUSSION

This chapter describes the *in vitro* and *in vivo* experiments performed to discover whether E-Selectin is a significant contributor to the binding of Lewis[a]-MPIO. The proteomics experiments performed with both the bi-functional Lewis[a]/photo-crosslinker MPIO and the Lewis[a]-MPIO revealed that this system was unable to selectively 'fish-out' any lectins from a membrane extract generated from *in vitro* IL-1β stimulated brain microvacular endothelial cell lines. However, when the whole cell proteome was analysed of *in vitro* IL-1β stimulated brain microvacular endothelial cells, E-selectin was among the highest upregulated proteins. Additionally, transcriptomics of adult and juvenile brain IL-1β lesions also confirmed E-Selectin upregulation *in vivo*. The transcriptome of the acute IL-1β model and a chronic MS-like lesion model were compared and showed overlapping genes that could imply a role for platelets and neutrophils. Subsequently a set of E- and P-Selectin antibody blocking and neutrophil depletion experiments confirmed E-Selectin as the binder of Lewis[a] *in vivo*. Also, neutrophils influence the binding between E-Selectin and Lewis[a] *in vivo* as reveleaed by the depletion experiments.

3.4.1 Proteomic pull-down experiments and whole cell proteome

3.4.1.1 Proteomics data comparison of pull-down results yields no obvious lectins

When the two pull down experiments, using first the bi-functional Lewis[a]/photo-crosslinker MPIOs and second the Lewis[a]-MPIO only, are compared there is very little overlap between the results. As eluded to in Chapter 2, it is unclear if the photo-crosslinker molecule coupled onto nanoparticles is capable of forming the reactive carbine to trap covalent interactions. While E- and P-Selectin were suspected to be the lectins present on activated endothelial cells that were interacting with Lewis[a], they were not identified in the pull-down experiments. Even though these molecules are present, their affinity may have been too low during *in vitro* conditions [321] or the membrane extract may have resulted in the loss of the multivalent display needed to trap the transient interactions [317]. Bovine serum does not contain any competing Lewis[a]-structures and therefore does not interfere with the binding [366]. Nonetheless, the lectin E-Selectin was the second highest upregulated protein upon IL-1β stimulation in the whole cell proteome *in vitro* experiment. The only overlapping 'hit' between the two pull down proteomic experiments was *Stom* Stomatin (human erythrocyte integral membrane protein band 7) which is one of the two major cell surface proteins on erythrocytes/red blood cells (RBC) along with SLC2A1 (Band 4.5 protein) GLUT1 (glucose transporter), – which was identified in the photo-crosslinked experiment [367]. Lewis[a] (and [b]) are

sugar antigens present on the cell surface of RBC and, as described in the introduction, these structures can be adsorbed from plasma [86], [87], [367]. However, their absorption mechanism is unknown. *Stom* Stomatin and SLC2A1, identified in the pull-down experiments, do not contain any lectin domains; however they may have recognition domains for Le[a] which have not yet been described or identified. Other proteins which interact with Stomatin are: SLC4A1 (Band 3 protein) AE1,a calcium and bicarbonate antiporter; Palladin, which associates with GLUT 1[368] (significant in photo-crosslinker experiment); Calnexin (identified in both photo-crosslinker and Le[a] only pull down experiments); and Calreticulin (identified in both photo-crosslinker and Le[a] binding only). This suggests that these particles (both with and without photo-crosslinker) are capable of pulling out protein complexes and that the photo-crosslinker might aid in trapping more transient interactions as well (due to GLUT1 being only present in the photo-crosslinked samples). No elevated levels of transcripts were found for any of these proteins in the gene chip experiments and no analysis was performed to see if any crosslinked species were found in the *MS*/MS** runs.

3.4.1.1 Selected other hits from Lewis[a] only pull down

As the photo-crosslinker strategy for the pull down is not proven to work yet as shown in **Chapter 2** extensively, the more classical pull down with just Lewis[a] only presented on the magnetic nanoparticles was anticipated to pull out some relevant molecules with possible lectin domains. However, as mentioned before this was not the case. The following section will briefly describe some pulled out proteins that were only identified in the IL-1β stimulated samples with Lewis[a] pull down particles. *Col4a2* encodes the alpha-2 chain of type IV collagen. Type IV collagen is associated with laminin, entactin, and heparan sulphate proteoglycans to form the sheetlike basement membranes that separate epithelium from connective tissue. Col4a1 and Col4a2 are the most abundant type IV collagens, are ubiquitously expressed in basement membranes, and play a role in the susceptibility for intracerebral haemorrhage[369]. Other collagen molecules have been implicated in brain physiology, MS, and other CNS diseases [370], [371],[222], [372]. CXCL12 is a chemoattractant that can act on T-lymphocytes and monocytes, but not neutrophils. It activates the C-X-C chemokine receptor CXCR4 to induce a rapid and transient rise in the level of intracellular calcium ions and chemotaxis. It also stimulates migration of monocytes and T-lymphocytes through its receptors, CXCR4 and ACKR3, and decreases monocyte adherence to surfaces coated with ICAM-1, a ligand for beta-2 integrins (uniprot). Besides binding to its receptors, it also binds to cell surface proteoglycans heparan and heparin [373],[374] and has different glycosaminoglycan GAG-domains, no further experiments were performed to assess the role of CXCL12 in brain inflammation. Neither

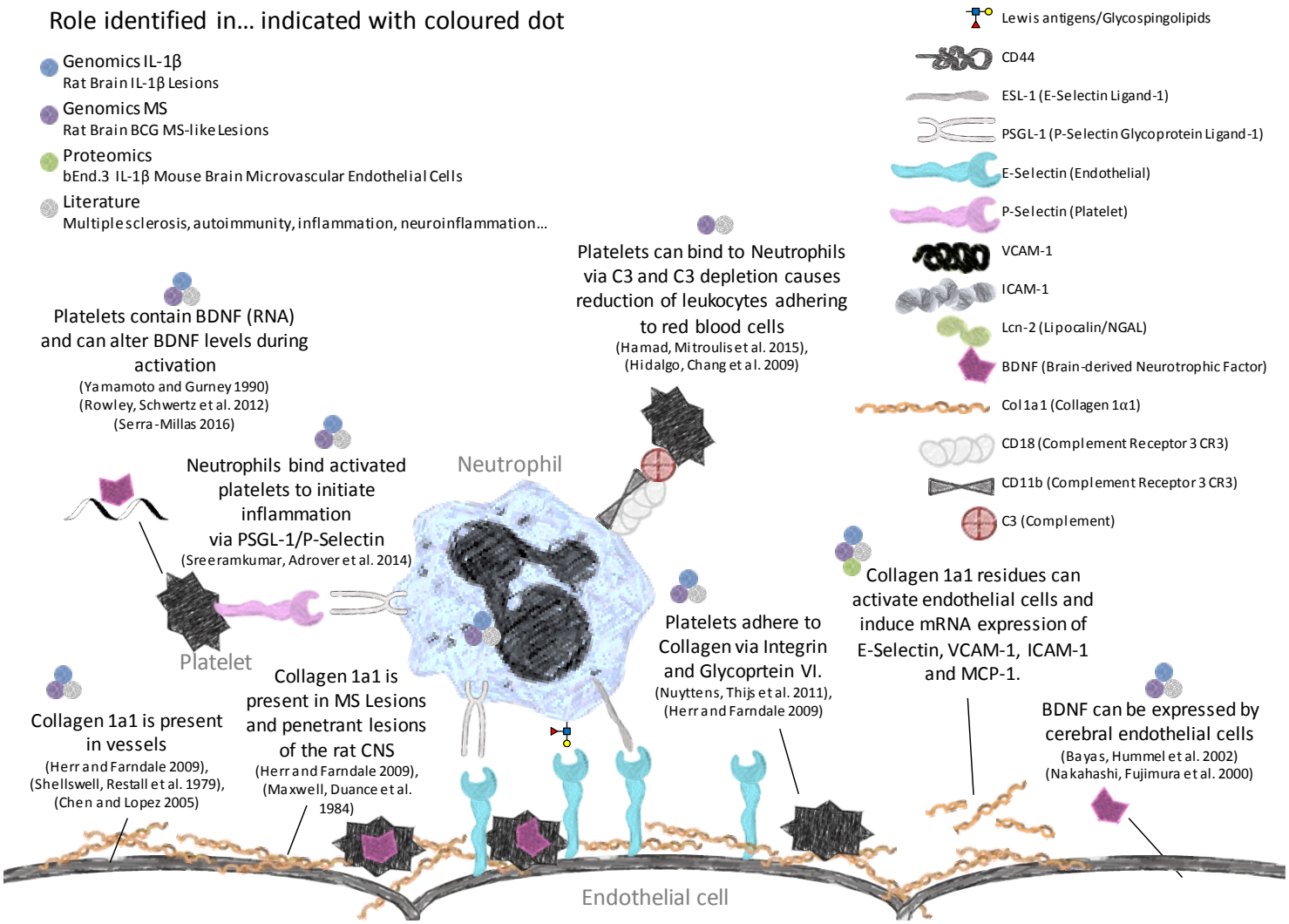
Col4a2 nor CXCL12 were identified in the transcriptomic experiment, nor were they upregulated in the whole cell proteome experiment. To conclude, the whole cell proteome was the main proteomics experiment used to further design the *in vivo* blocking experiments, as E-Selectin is a known Lewis[a] binder and together with CXCL1 and CCL2 were highly upregulated and overlapping with the transcriptomics results of IL-1β stimulated brain lesions, which will be discussed next.

3.4.2 Transcriptomic Experiments

3.4.2.1 Overlapping transcriptomic results can be explained by neutrophils and platelets

E-Selectin is the third highest upregulated transcript in the *in vivo* IL-1β transcriptomic experiments and it also being the second highest upregulated protein in the whole cell proteome experiment it provided enough evidence to pursue the Selectin-lectin family as a potential binder of Lewis[a] discussed in **3.4.3**. The following part of the discussion discusses the other observations made from the GeneChip® experiments performed. Shared gene analysis between lesions of IL-1β acute brain inflammation and BCG MS-lesion model rat brains uncovered a set of 5 genes. Although these genes are shared between experiments and are significantly upregulated. Their validity needs to be proved by additional assays such as qPCR or Western Blot for example. Nonetheless, this data was crucial to design the in vivo experiments. Until now, it was challenging to correlate to Lewis[a/b] binding events observed in both brain lesions. Adding platelets and neutrophils to the system may explain these results and sparked interest in testing how these immune components may influence the binding of Le[a/b]-MPIO *in vivo*, possibly *via* E- and/or P-Selectin. The shared genes are Brain-derived Neurotrophic Factor (*Bdnf*), Collagen 1α1 (*Col1a1*), Transthyretin (*Ttr*), Lipocalin (*Lcn-2* or NGAL), and Oxytocin (*Oxt*). Below, each gene and protein function will be discussed and figures will schematically illustrate how these proteins may interact with the activated endothelium, platelets, and neutrophils in the context of brain inflammation. Each figure comes with a legend using cartoon representations used throughout this thesis and experimental and literature evidence is indicated for each component presented in the figures. Literature evidence is shown by a grey dot, proteomics evidence by a green dot and the genomic evidence from the IL-1β model and the BCG model are indicated by blue and purple dots respectively.

| Figure 3.23 | The role of Collagen and BDNF in brain inflammation



Literature references used for the images are linked to the following numbers in an alphabetical manner. More information can be found in the text describing Col1a1 and BDNF.

Baronas-Lowell Lauer-Fields et al. 2004 [375]
Bayas, Hummel et al. 2002 [376]
Chen and Lopez 2005[377]
Hamad, Mitroulis et al. 2015[361]
Herr and Farndale 2009 [378]
Hidalgo, Chang et al. 2009 [379]
Maxwell, Duance et al. 1984 [371]
Nakahashi, Fujimura et al. 2000 [364]
Nuyttens, Thijs et al. 2011 [380]
Rowley, Schwertz et al. 2012 [381]
Serra-Millas 2016 [365]
Shellswell, Restall et al. 1979 [370]
Sreeramkumar, Adrover et al. 2014 [382]
Yamamoto and Gurney 1990 [363]

3.4.2.2 Brain derived neurotrophic factor (*Bdnf*)

BDNF is a neurotrophic factor that promotes neuronal survival and supports nerve growth and differentiation of new neurons and synapses. BDNF is considered to be neuroprotective and BDNF can be found in MS lesions, CFS and in serum. However, the role of BDNF as a biomarker for inflammatory brain diseases is not yet fully understood [383]. *In vitro*, BDNF can inhibit intercellular adhesion molecule 1 (ICAM-1) expression and when IL-1β treated endothelial cells are incubated with BDNF the adherence of neutrophils to the endothelium is decreased [341]. Other immune cells, like autoreactive T cells, mononuclear cells and macrophages have been shown to immunolocalize with BDNF, however these cells do not appear at IL-1β induced lesions on a short timeframe (4h) [384]. Another study has shown that BDNF is primarily present in immune cells (T cells, macrophages/microglia) and reactive astrocytes found at the lesion. The BDNF receptor gp145trkB is found in neurones in the immediate vicinity of the multiple sclerosis plaques as well as in reactive astrocytes within the lesion, but not in immune cells [339]. Conversely, platelets are a source of BDNF and BDNF mRNA and can alter the levels of BDNF during platelet activation [363], [381], [365]. This marked increase in BDNF that we observed may come from platelets recruited to the lesions, but other report have shown that BDNF can be expressed by cerebral endothelial cells, but no increased levels in the proteomic experiments was observed [364], [376].

3.4.2.3 Collagen 1 alpha 1 (*Col1a1*)

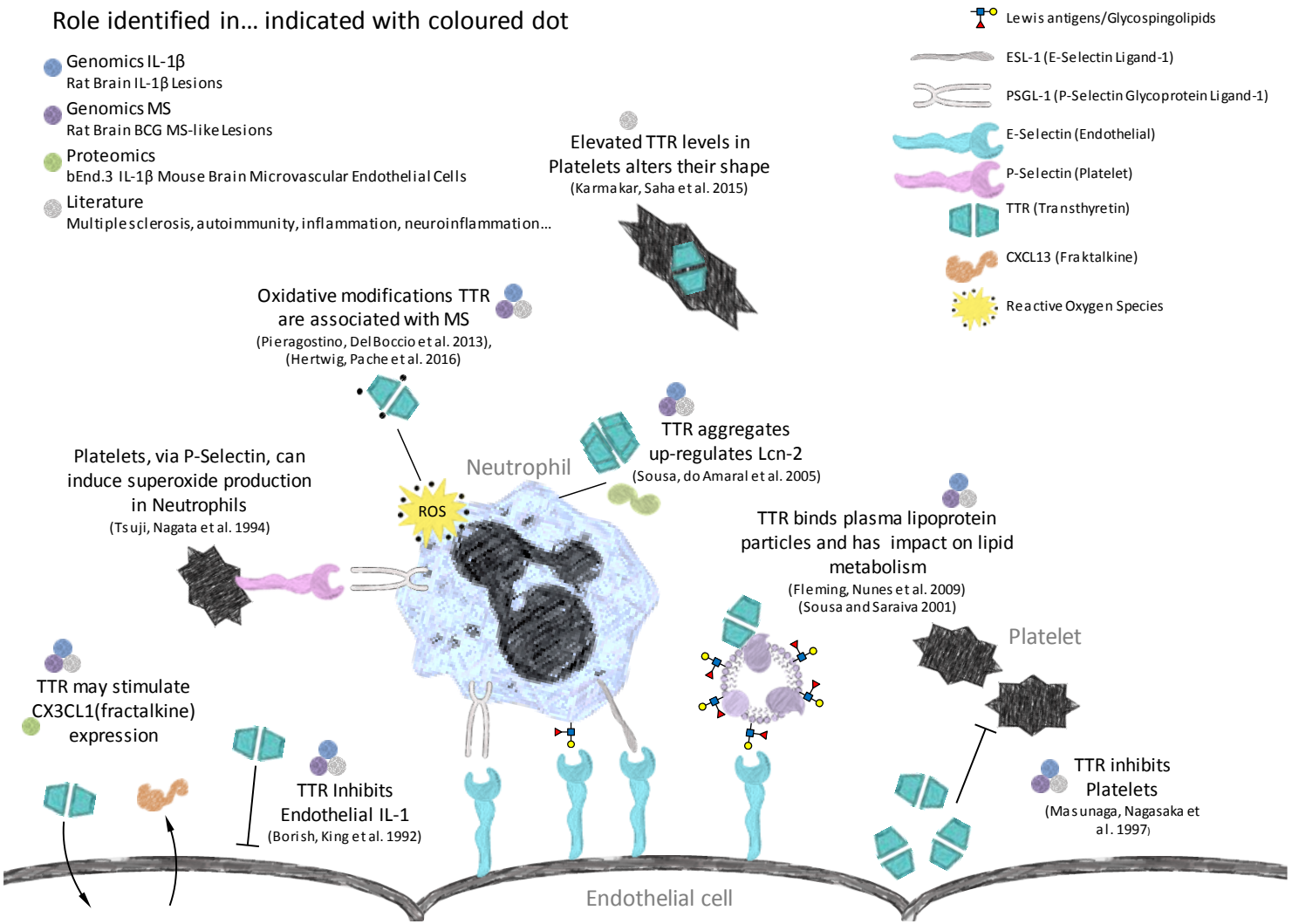
Collagen 1α1 is typically not expressed by brain microvascular cells. However, Col1a1 is present in the abluminal parenchymal tissue but not the blood vessels [370]. Collagen is a potent platelet activator and adhesion molecule [378], [377], [380]. However, the location of Col1a1 within the IL-1β lesions is unknown and it is uncertain if platelets and neutrophils can reach and adhere to these collagenous fibres. In human MS lesions, Col1a1 expression (together with Col3a1, Col5a1 and Col5a2) is induced strongly in active lesions and even more in inactive lesions. These structures are largely found between the endothelium and astrocytic glia limitans in the perivascular space packed with infiltrating immune cells, but these are post BBB breakdown events [372]. COL1A1 has been shown to interact with (matrix metalloprotease-2) MMP-2 and binding to COL1A1 stabilizes *in vitro* MMP-2 activity by reducing the rate of autolytic inactivation[385]. MMPs have a broad spectrum of functions and their role at the BBB in neuroinflammation and neuro degenerative diseases has been established [386]. MMPs are also differentially expressed in cases of multiple sclerosis and stroke [344] and MMP inhibitors can reduce the excitotoxicity and leukocyte recruitment in the brain [345]. Interestingly, the expression levels of MMPs in the IL-1β and BCG MS-like lesions are unchanged, implying a differential role for COL1A1. *In vitro* astrocytes are capable of expressing fibrillary

collagen structures and may play a role in lesion formation and regeneration [81]. Interestingly, Collagen 1a1 residues (peptide 496-507) can activate endothelial cells and induce mRNA expression and protein synthesis of E-Selectin, VCAM-1, ICAM-1 and MCP-1 [375]. It may be possible that the collagen produced in the lesions by cells like astrocytes can have downstream effects on endothelial activation. Nonetheless, the Col1a1 results remains elusive and it is unknown if neutrophils and platelets could directly interact with Col1a1 in our IL-1β-model, but collagen 1a1 residues (peptide 496-507) indeed could indirectly *via* E-Selectin.

3.4.2.4 Transthyretin (*Ttr*)

TTR is a transporter protein in serum and cerebrospinal fluid (CSF) that binds the thyroid hormone thyroxine (T_4) and retinol-binding protein RBP bound to retinol. Serum TTR is mainly produced by the liver and the choroid plexus secretes TTR into the CSF. Besides functioning as a transporter, TTR is a protease, cleaving natural substrates in the nervous system, including apoA-I (apolipoprotein A-I) and amidated NPY (neuropeptide Y) [387]. Spinal cord tissue transcriptional changes of a chronic relapsing and secondary progressive EAE (pEAE) Biozzi ABH mouse model of MS showed that TTR is the most significantly downregulated gene [388], whilst the results presented in this thesis show a marked increase in gene upregulated expression in CNS lesions. TTR has been associated with MS and other CNS diseases, including, familial amyloidotic polyneuropathy (FAP), where TTR (most commonly implicated protein), apolipoprotein A1, and gelsolin form protein aggregates and/or amyloid fibril formations in the CNS [389]. CSF and serum levels of TTR in MS patients (or Alzheimer's [390]) have not been found to be altered, however it has not been established as a reliable marker for disease progression and/or detection and its role in disease progression unknown [391],[197]. TTR has also been found to be post-translationally modified (PTM) by oxidative modifications and cerebral oxidised TTR can change its folding and function and its PTMs could be associated with multiple sclerosis [392]. Since neutrophils can produce reactive oxygen species, they may be the modifiers of TTR in MS. *In vitro* TTR was found to inhibit LPS-stimulated IL-1 production in monocytes and endothelial cells [393]. Blocking Il-1β signalling with the selective (IL1) receptor antagonist Anakinra (brand name Kineret) provides a disease modifying benefits for mice suffering from TTR amyloid forming plaques, implying that interfering with the interleukin-1 signalling pathway could be a therapeutic target in TTR amyloidosis [394]. TTR aggregates have also an effect on neutrophils and Lcn-2 (next to be described) is upregulated by TTR. In addition, TTR may have immune-modifying effects *via* platelets, since TTR can inhibit platelet aggregation [395] and elevated TTR levels can alter the shape of platelets [396]. Furthermore, Lcn-2 is upregulated in a NF-κB depend manner by TTR in amyloid poly neuropathy of TTR plaques [397].

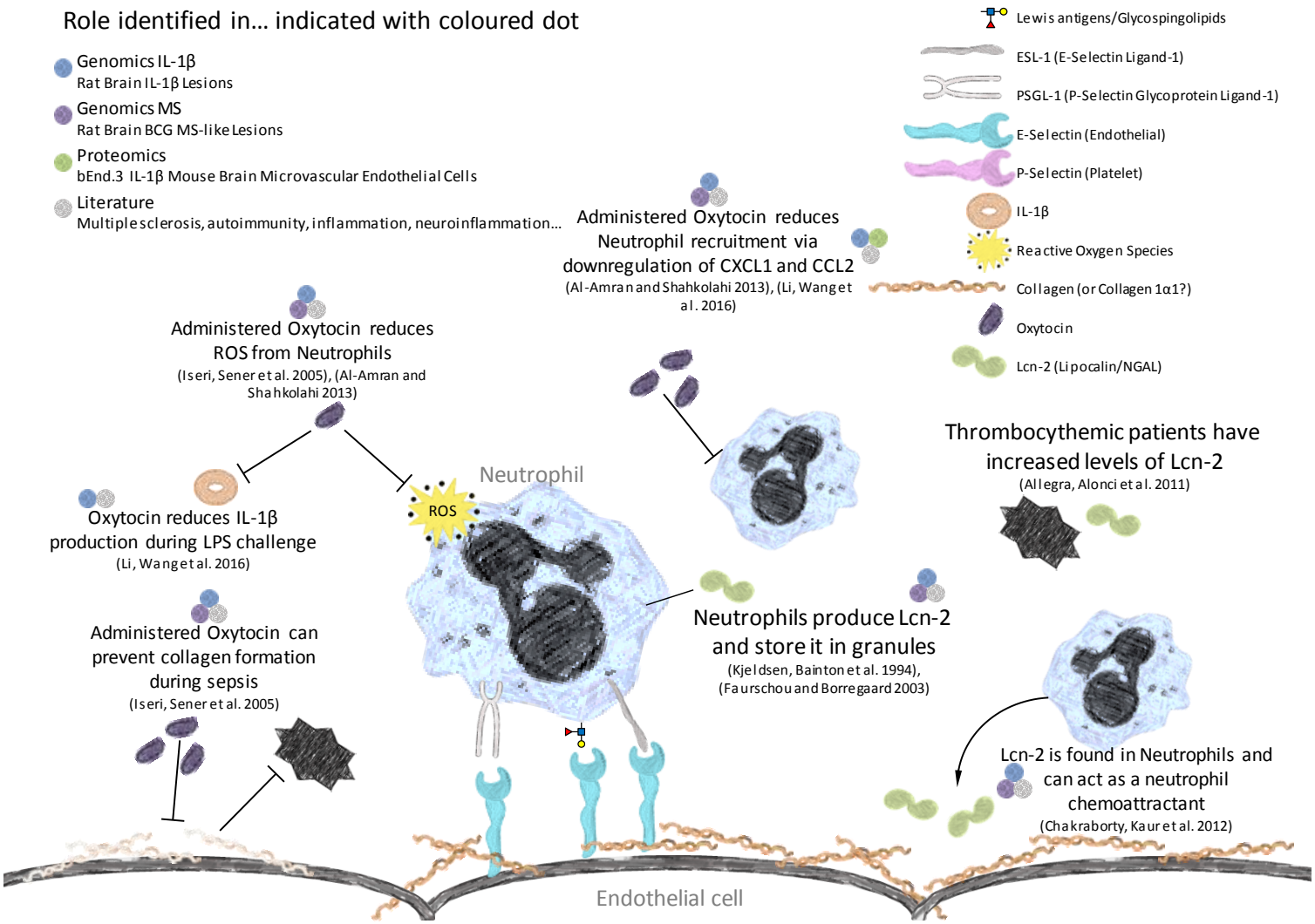
| Figure 3.24 | The role Transthyretin in brain inflammation



Literature references used for the images are linked to the following numbers in an alphabetical manner. More information can be found in the text describing Ttr.

Borish, King et al. 1992 [393]
Davis, Glinsky et al. 2016 [398]
Fleming, Nunes et al. 2009 [399]
Hertwig, Pache et al. 2016 [154]
Karmakar, Saha et al. 2015 [396]
Masunaga, Nagasaka et al. 1997 [395]
Pieragostino, Del Boccio et al. 2013 [395]
Sousa and Saraiva 2001 [400]
Sousa, do Amaral et al. 2005 [397]
Tsuji, Nagata et al. 1994 [401]

| Figure 3.25 | The role of Oxytocin and Lcn-2 in brain inflammation



Literature references used for the images are linked to the following numbers in an alphabetical manner. More information can be found in the text describing Oxt and Lcn-2.

Al-Amran and Shahkolahi 2013 [402]
Allegra, Alonci et al. 2011 [403]
Chakraborty, Kaur et al. 2012 [404]
Faurschou and Borregaard 2003 [405]
Iseri, Sener et al. 2005 [406],[407]
Kjeldsen, Bainton et al. 1994 [408]
Li, Wang et al. 2016 [409]

Interestingly, TTR has also been shown as a new putative transcytosis transporter for nanomedicines across the BBB. 1 µm quantum-dots (QDs) conjugated to TTR were able to cross the BBB *in vivo* in rats and in *in vitro* in trans well assays, where unconjugated QDs were unable to do so [410].

3.4.2.5 Lipocalin-2 (*Lcn2*), neutrophil gelatinase-associated lipocalin (NGAL)

Lcn-2 or Neutrophil Gelatinase-Associated Lipocalin (NGAL) is expressed in neutrophils *via* IL1R signalling in a NF-κB depent manner [408], [405]. It acts as an iron-binding and trafficking protein involved in apoptosis, innate immunity and renal development. It can also be upregulated *via* a Toll-like receptor mediated manner and it acts in innate immunity by sequestering iron from bacterial sidopores reducing their growth [411]. It is mainly expressed by neutrophils [404].Besides neutrophils producing Lnc-2 they can also be recruited to tissues that express Lcn-2 so it is considered a chemoattractant for neutrophils too [408]. An excess of platelets induces increased levels of Lcn-2, indicating that both platelets and neutrophils could contribute to these elevated levels [403]. In ischemic stroke Lcn2/NGAL expression is induced and contributes to neuronal cell death, neurotoxic glial activation, neuroinflammation, and BBB disruption[412]. When astrocytes are incubated *in vitro* with Lcn2/NGAL, they upregulate the chemokines: CCL20, CCl4, CXCL1, CXCL1, CCL3, CCL5, CXCL7, CXCL10 and CXCL9 [413]. Increased levels of Lcn2/NGAL are found in progressive MS patients (in both plasma and CFS) and treatment with the anti-cell adhesion molecule α4-integrin Natalizumab lowers CSF Lcn2/NGAL levels. Moreover, an *in vitro* model suggests that Lcn2/NGAL has an inhibitory effect on remyelination [414]. Lcn2/NGAL has been identified as an upregulated gene in two other studies using gene expression profiling of experimental autoimmune encephalomyelitis (EAE). The first study characterized the transcriptome of the choroid plexus (CP) of a mouse EAE model and analysed CSF of MS and the optic neuritis (ON) patients. Among Lcn2/NGAL, adhesion molecules, chemokines and cytokines were upregulated. In addition, immunostaining revealed that infiltrating neutrophils were responsible for increased Lcn2/NGAL and within the brain Lcn2/NGAL was also detected in astrocytes [415]. The second study characterized the transcriptome of EAE spinal cords of mice and identified Lcn2/NGAL as being significantly upregulated at the onset of EAE using an Affymetrix gene array screen. Human Lcn2/NGAL expression in MS was studied as well and it was shown that Lcn2 expression is increased in the serum and CSF of MS patients and it can be detected in MS lesions in the brain [416].Additional information can be found in the comprehensive review by Chakraborty *et al.* [405].

3.4.2.6 Oxytocin (*Oxt*)

Oxytocin is a small peptide hormone and IL-1β can have a profound effect on hypothalamo-pituitary hormones in the brain. It has been described that IL-1β reactive neurons in the hypothalamus can co-localize with Oxt. IL-1β produced by activated glial cells in the hypothalamus of MS patients may contribute to the activation of the hypothalamic neurons, but the activation of other cell types within the brain has not been studied [417]. Oxt in the Il-1β model may have an anti-inflammatory effect to the IL-1β challenge. Administered Oxt can reduce neutrophil recruitment to the inflamed site by down regulation of the cytokines CXCL1 and CCL2 [402],[409]. In addition, administered Oxt can also prevent collagen formation during sepsis, which is another upregulated gene from our experiment [406]. As highlighted before, LPS is a potent pro-inflammatory stimulus and induces IL-1β formation, however Oxt reduces the amount of IL-1β produced during an LPS challenge [409]. Neutrophil recruitment is accompanied by oxidative damage caused by the neutrophils producing reactive oxygen species and Oxt can reduce the levels of proceed ROS from neutrophils [407], [402]. All these examples highlight that Oxt can have a immunomodularly effect on IL-1β induced inflammation and has a likely anti-inflammatory effect upon this potent stimulus, especially on neutrophils.

3.4.2.7 Other observations relating *Stra6* and *Col1a2*

TTR is closely associated to Vitamin A as it binds to RBP that in turn binds retinol, the receptor for RBP. Stimulated by Retinoic Acid 6 STRA6 acts as a membrane transporter and a cell surface receptor[418] (gene upregulated in IL-1β, two transcripts, gene not present in U34A GeneChip). Upon binding of RBP and transport of retinol, STRA6 can activate the JAK/STAT pathway *via* a cytosolic retinol binding protein [419]. Retinol and the metabolite of retinol; retinoic acid may have implications in MS and it's known to be responsible for a multitude of neuroimmunological functions. A comprehensive review of retinol, retinoic acid, MS and EAE highlights its importance and protective effects where retinoic acid can inhibit an inflammatory response in EAE[420]. In more detail, activated astrocytes in MS lesions can produce retinoic acid. This in turn can induce endothelial immune quiescence and decrease monocyte adhesion. The role of retinoic acid on the BBB might protect it from immune cell infiltration [421],[422]. COL1A1, a group I collagen, is composed of two collagen 1 pro-α1 chains and one pro-α2 chain. The latter is produced from the Col1a2 gene, also highly upregulated (two transcripts) in only the IL-1β GeneChip® Array.

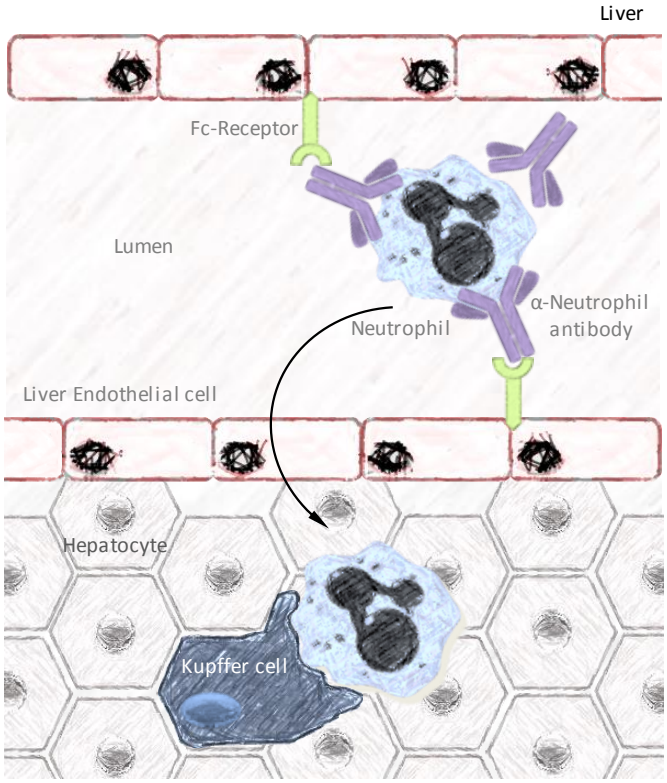
3.4.3 *In vivo* blocking experiments

3.4.3.1 Proteomics, transcriptomics lead to Selectin-blockade and neutrophil depletion experiments

As mentioned above, the lectin E-Selectin was the sole known Lewis[a] binder identified in the whole cell proteome and the transcriptome of both adult and juvenile IL-1β lesions. This taken together with the prominent role of neutrophils at the early stages of acute brain inflammation, a set of blocking and depletion experiments was successfully performed and a model was generated to explain the unusually strong binding of Lewis[a] particles observed, which will be discussed next.

3.4.3.2 Blood analysis and peripheral immunohistochemistry shows neutrophils are depleted *via* a liver-mediated mechanism.

Blood analysis of the experimental groups summarized in **Table 3.11** and shown in **Figure 3.14**, **3.17** and **Figure 3.16** shows that neutrophils can effectively be depleted from rats using an antiserum against polymorphonuclear (PMN) cells. Red blood cell (RBC) analysis shown in **Figure 3.15** shows that RBCs are not affected in the different treatment groups and that samples taken from tail veins instead of cardiac punctures results in haemolysis. Upon IL-1β treatment, total white blood cell (WBC) counts are lowered, but not significantly. The neutrophil depleted animals have lower overall numbers for WBC than the other experimental groups and that is accounted for by the significant reduction of neutrophils from these experimental groups. Also platelets are lower in the neutrophil depleted animals, but this might be due to the platelets interacting with the neutrophils [423]. Lymphocytes also significantly lower upon IL-1β treatment as do eosinophils as shown in **Figure 3.16**. There are no significant differences between the basophil numbers in all the groups analysed and monocytes are lower in the neutrophil deleted animals. Neutrophils are successfully depleted form the antiserum treated animals and compared to any of the other groups have almost no neutrophils left in the circulation. The experimental group with the significantly longer experimental timings (Isotype control – IL-1β) has significantly more neutrophils than its matched group (Isotype control II –IL-1β) that was timed in accordance with all the other experimental groups. To take into consideration, depending on the sampling site (tail vein vs cardiac puncture) WBC may be significantly different and WBC counts appear to be higher from tail veins than from cardiac puncture in mice [424]. Also, the haemocytometer used was fully calibrated using the recommended calibration solutions provided by the supplier, but is designed for human cells. Rat and human cells differ in size and granularity and the WBC composition differs [328], the data presented is solely used for a differential between experimental groups.



| Figure 3.26 | Liver-mediated neutrophil clearance
Model for the clearance of neutrophils coated by antiserum antibodies *via* the liver's residing macrophages; Kupffer cells.

In order to assess how the neutrophils were depleted from the animals, the spleen and the liver were analysed with immunohistochemistry for the presence of neutrophils. As anticipated, there was a significant decrease of neutrophils in the spleen (**Figure 3.21 B**), as an overall lower neutrophil tissue pattern was expected. Unexpectedly, neutrophils appear to accumulate in the liver (**Figure 3.21 A**). When antibodies are tracked in mice, they appear to be preferentially cleared by the liver *via* liver FC-receptors (41%) and only a fraction (1.8%) is taken up by the spleen [425]. Additionally, adhesion molecules bound to neutrophils may promote Kupffer-neutrophil interactions [426]. CXC chemokine activated neutrophils may be sequestered in the liver [427], and multiple CXC chemokines are produced in the IL-1β brain inflammation model and were discussed previously in the introduction and shown in the transcriptomics section of this chapter. Therefore the model shown in in **Figure 3.26** may explain the increase of neutrophils seen in the livers of the neutrophil depleted animals. The Fc-receptors on liver endothelial cells capture the antibody covered neutrophils and Kupffer-cells (liver macrophages) can phagocytose the antibody coated neutrophils in the liver. It is possible that at a later time point (liver and spleen collected 24h after the intraperitoneal injection of the anti-PMN-serum) the liver may have effectively cleared the neutrophils and counts could be lower then. A time course of the depletion experiment may confirm

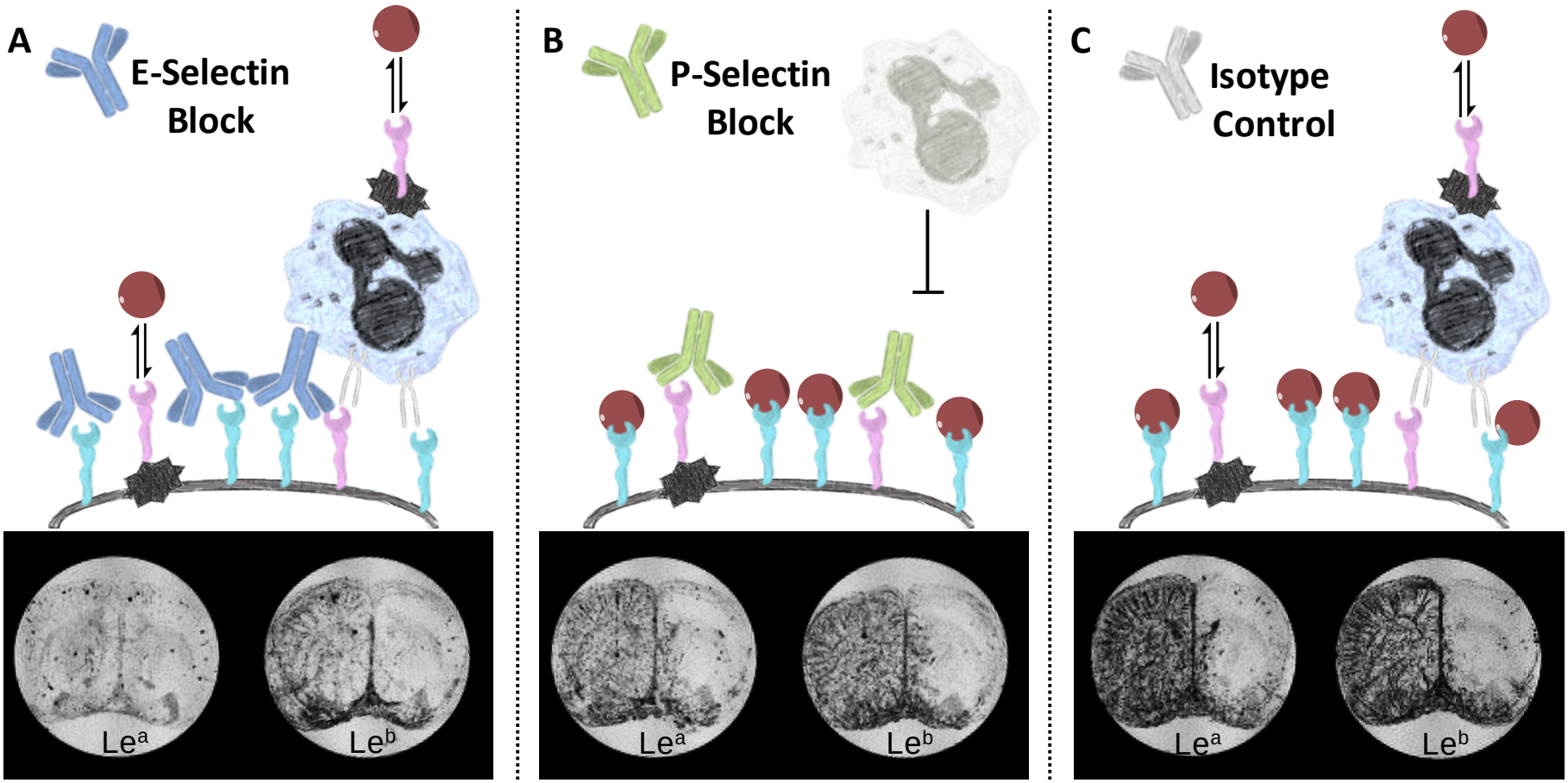
if the mechanism proposed is valid and additional immunohistochemistry may reveal co-localization of Kupffer-cells and neutrophils.

3.4.3.3 Lewis[a] binds strongly to E-Selectin *in vivo* and the interaction is blocked with monoclonal antibodies

In vitro E-Selectin and P-Selectin can bind both Lewis[a] and Lewis[b], as in accordance with the literature [53], [54], [51], [111] and **Figure 3.9.** P-Selectin can only bind Lewis[a] when presented at high densities [428] and can also bind Lewis[b], as shown in **Figure 3.9.** There is no significant difference between the binding (or the slopes of the lines) of both Lewis[a] compared to Lewis[b] and E-Selectin binding compared to P-Selectin binding. **Figure 3.20** reveals that E-Selectin micro vessel staining is only present in the left (IL-1β) hemisphere (basal ganglia) and that all experimental groups appear to have E-Selectin present in their vessels and can be seen as tubular and circular structures. E-Selectin staining (polyclonal rabbit IgG for IHC) may appear less prominent in the E-selectin blocked animals and is perhaps due to epitopes being blocked by the E-selectin antibody (clone RME-1, mouse monoclonal IgG1, κ) used *in vivo*. Nonetheless, vessels in the E-Selectin blocked animals do have E-Selectin, but no Lewis[a]-MPIO binding, as shown in **Figure 3.17**, indicating that the antibody is an effective blocker for Lewis[a]-MPIO E-Selectin binding. The absence of Lewis[a]-MPIO in the E-selectin blocked animals indicates that Lewis[a] in the preferred binder for E-Selectin *in vivo* and that binding to P-Selectin is weak *in vivo*. P-Selectin blockade still has Lewis[a]-MPIO-binding to remaining E-Selectin. As P-Selectin blockade results in the reduction of neutrophils to the inflamed endothelium, more E-Selectin in available in the P-Selectin blocked animals than in the isotype controls and the E-Selectin blocked animals [104]. As Neutrophils are significantly higher in E-Selectin blocked animals (see **Figure 3.22**) they can compete for E- and P-Selectin, reducing the available sites for the MPIO to bind to.

For Lewis[b]-MPIO, shown in **Figure 3.17**, an overall less binding is observed in the isotype control when compared with Lewis[a], however the binding in the E-Selectin blocked animals is higher than in Lewis[a]-MPIO animals. This might be due to Lewis[b]-MPIO binding stronger to P-Selectin *in vivo* than Lewis[a]-MPIO. It appears the binding of Lewis[b]-MPIO to E-Selectin is similarly moderate as for P-Selectin. Therefore an additive Lewis[b]-MPIO binding is observed in the isotope control. Also, binding of Lewis[b] may be sequestered by neutrophils in a Selectin-independent manner, as there are fewer neutrophils in the E-Selectin blocked animals than for the Lewis[a]-MPIO group (see **Figure 3.22**) which may explain the residual Lewis[b]-MPIO binding in the E-Selectin blocked animals.

The comparison of **Figure 3.17** for the regions analysed shows that the variation of binding in the full left and right hemisphere (as explained in **Figure 3.13**) (**Figure 3.17 A** & **C**) or only the basal ganglia (**Figure 3.18 B** & **D**) is similar but more accurate measurements with less standard de*via*tions can be



| Figure 3.27 | Lewis$^{a/b}$-MPIO binding is dependent on the availably of E-selectin **|A|** Lewis^{a}-MPIO is a strong *in vivo* E-Selectin binder and blocking E-Selectin does not significantly reduce the numbers of neutrophil-recruitment, as shown before [104]. Therefore only the moderate binding of Lewis^{a} to P-Selectin is still remaining, but some P-Selectin sites are taken by neutrophil ligands. In addition, any unblocked E-Selectin can be occupied by increased neutrophil numbers (as shown in **Figure 3.16**) or may be impaired by neutrophil-mediated cell surface remodelling (not shown in cartoon) by activated proteases generated from the recruited neutrophils [429]. **|B|** Lewis^{a}-MPIO is a moderate *in vivo* P-Selectin binder and blocking P-Selectin does not only reduce the available P-Selectin sites but also reduces neutrophil recruitment by 85% and the associated platelets *(numbers not significantly different –data not shown)* [104]. As there are fewer neutrophils available to block E-selectin and P-Selectin, some of the binding of Lewis^{a}-MPIO to the remaining E-selectin is retained. **|C|** When no Selectins are blocked, Lewis^{a}-MPIO possibly can outcompete the natural ligands from the neutrophils. In addition lower neutrophil numbers are present in the circulation in these animals (as shown in **Figure 3.16**) making more E-Selectin available. When both E- and P-Selectin are available, Lewis^{a}-MPIO can adhere (P-Selectin) and roll (E-Selectin) onto the activated endothelium, and the moderate P-Selectin interactions can be captured by E-Selectin in a dynamic manner. Brown spheres represent MPIO with Lewis-antigens. Dark hypointensities from MRI images correlate with the amount of MPIO's depicted in the schemes.

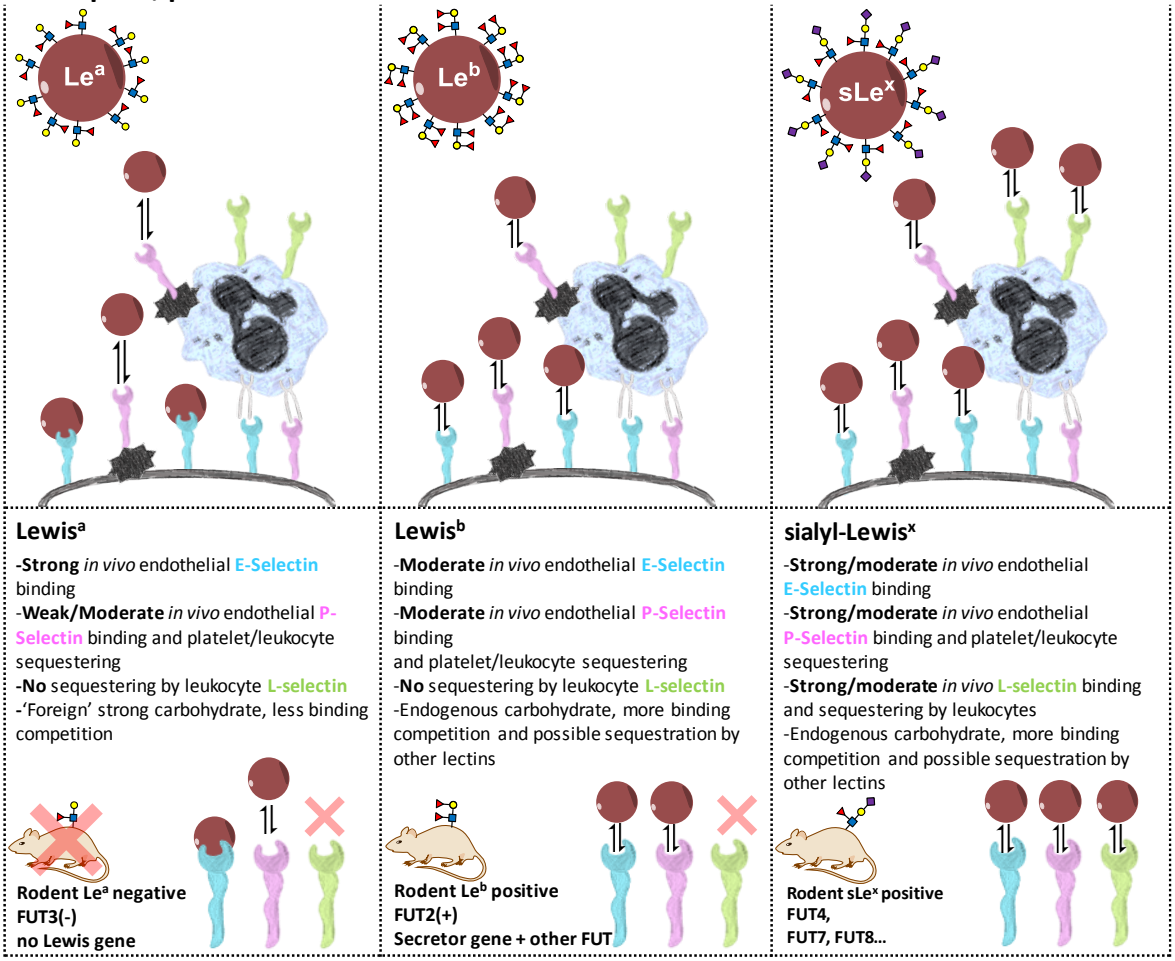
made by analysing the full hemisphere for both Lewis^a and Lewis^b-MPIO. This is also true for the neutrophil depletion experiments as shown in **Figure 3.18**, which will be discussed later.

To summarize, **Figure 3.27** explains that Lewis^a-MPIO binding is dependent on the availably of E-selectin and the figure legend will explain the different experimental groups and how binding is affected in the 3 different conditions. The binding of Lewis^b may operate in a similar fashion, but the different binding strengths to the selectins may alter this model slightly. Further on in this section a comparison between Lewis^a, Lewis^b and sialyl-Lewis^x is made that will refine the model.

3.4.3.4 *In vitro* results can be misrepresentative and *in vivo* experiments confirms Lewis^a as the superior E-Selectin binder over sialyl-Lewis^x

Sialyl-Lewis^x is the common binder for all 3 selectins [52]. Its strong *in vitro* binding and it being generally accepted as the dominant E- and P-Selectin binder lead to the development of using it as an imaging tool to visualize inflammation of the brain, however, as an imaging agent presented onto magnetic iron-oxide particles it is less superior than Lewis^a [65]. *In vitro* binding experiments can be misleading and do not necessarily translate into *in vivo* binding as blood flow and other carbohydrates/glycosylated proteins may interfere with binding [54]. **Figure 3.12** shows that sialyl-Lewis^x and Lewis^b have high binding to E- and P-Selectin and that Lewis^a has the strongest binding at lower E- and P-Selectin concentrations. This highlights the difference observed between *in vitro* and *in vivo* experiments, as the binding of these antigens is markedly different *in vivo*. A comparative study of Lewis^x and Lewis^a and their sialylated counterparts, showed Lewis^a is preferred over sialyl-Lewis^x. Even though human cells were used and the binding was assessed in the absence of flow, Lewis^a was the preferred binder to E- and P-selectin positive human colon cell lines over the other 3 tested carbohydrates sialyl-Lewis^a, Lewis^x, sialyl-Lewis^x [101]. The results presented here indicate that strong *in vitro* binding, as for sialyl-Lewis^x, does not automatically translate in strong *in vivo* binding, as Lewis^a and Lewis^b bind equally well *in vitro* but have distinct E-Selectin binding profiles *in vivo* as shown in **Figure 3.17**. In addition, as mentioned in the introduction, using fully glycosylated E- and P-Selectin, as expressed by the rat endothelial cells, in the *in vivo* binding assays may result in better Lewis^a binding as the recombinant differentially glycosylated used *in vitro* could have an altered binding for the Lewis antigens [51], [53], [111], [101]. A model was generated based on the *in vivo* binding data to explain the binding patterns observed and is shown in **Figure 3.28.**

| Figure 3.28 | Proposed *in vivo* model to explain the observed strong Lewis[a] binding compared to its β3-linkage isoform Lewis[b] and sialyl-Lewis[x] and the interaction with neutrophils, platelets and the inflamed endothelium *via* the Selectins



3.4.3.5 Lewis[a] binds strongly to E-Selectin *in vivo* and the E-Selectin availability is dependent on the presence of neutrophils

As seen in **Figure 3.18** there is significantly more binding of both Lewis[a] and Lewis[b] magnetic particles at the inflamed hemisphere in the absence of neutrophils. Neutrophils can clearly interfere with the binding as the first isotype control experiment not only had longer experimental timings, but also more neutrophils. Although not significant, when the neutrophil numbers of serum control animals and the isotype control II repeat are compared to the first isotype control experiment, there are about 1.5 times more neutrophils present in the first isotype control experiment when compared with the repeat experiment and 2.2 times more for the serum control. This may explain the reduced binding events of both Lewis[a] and Lewis[b]-MPIO in these animals. As the brains from the first isotype control experiments were 1.5h longer than the other experiments (6.5h instead of 5h total time, see **Figure 3.11**), the binding of particles was reduced. It has been shown that the shedding of E-Selectin can occur 6-12 hours after activation of human umbilical vein endothelial cells [430]. Over this longer period the shedding of E-Selectin

from the endothelial cells by proteases may occur *in vivo via* a P-selectin glycoprotein ligand (PSGL-1) dependent manner and could explain the reduced binding of particles to E-Selectin in this experimental group [431]. Neutrophils and platelets express both PSGL-1 on their cell surface and store multiple proteases that can be released upon activation by binding to selectins and can be responsible for the proteolytic cleavage of the membrane-bound adhesion molecules [432].

So the increase in neutrophils can also cause the decrease of cell surface E-Selectin by shedding and therefore fewer binding sites are available or the particles may be sequestered by the soluble E-Selectin. In addition, there is a weak correlation between neutrophil numbers and mean grey values of the basal ganglia (r^2=0.32) in total when comparing all samples to each other and a moderate correlation (r^2=0.42) for Le^b binding in the basal ganglia and neutrophils numbers. A strong relationship (r^2=0.69) was found for Le^a binding in the basal ganglia and neutrophils numbers. (*Calculations not shown in figures, using Pearson's correlation coefficient*).

Another observation made was that possibly the rabbit serum used in these experiments may have a minor inhibitory effect in the rats for Lewis^a and Lewis^b-MPIO binding, as the overall binding events are lower in the serum control group when compared with isotype control (II). Exogenously administered serum, especially IgG, from another organism may have an overall immune modifying effect that has not been described fully in rodents, but is evident in humans when using human donor IgG [433]. Differences of Lewis$^{a/b}$-MPIO binding between the serum control (intraperitoneal rabbit serum with a mixture of serum components and immunoglobulins) and the isotype control (intravenous purified mouse IgG of a single clone) may be the accidental neutralization of some inflammatory molecules present in the rabbit serum by the immunoglobulins, whilst the isotype control antibodies were selected for their negative binding to mouse, rat and human tissues. As shown for human neutrophils, IgG molecules from pooled donors may block IL-1α and therefore reduce neutrophil transmigration by reducing endothelial activation, it may be possible a similar phenomenon is occurring in the serum treated animals regulating the binding of the Lewis$^{a/b}$-MPIO [434]. Similarly, rabbits, like mice and rats, do not have FUT3 (*Lewis gene*) but do have putative FUT2 (*Secretor gene*) and may produce Lewis^b-products which can be absorbed into the circulation from the peritoneum and partially block binding [435]. When stimulated with IL-1β, human cells upregulate multiple fucosyltransferases, although studies in humans may not correlate to expression activities in rodents.[436]. In contrary, human cells downregulate FUT3 (not in rodents) the Lewis^a gene in response to cytokines Il-1β and IL-6 [437] . To place this into the human context and the role of Le^a-glycolipids, it is likely that E-Selectin can bind Lewis^a-structures presented as glycolipids on immune cells, including platelets, and that is what these particles are essentially mimicking. Mouse neutrophils treated with a protease are incapable of rolling onto presented E-selectin, however human

neutrophils are still capable of rolling and adhering to E-Selectin when protease-treated, implying a role for glycosphingolipids like sLe^x and Le^a as these are protease resistant [438], [439]. This indicates that E-Selectin binding in rodents is dependent on carbohydrates presented on proteins as rodents are not capable of synthesizing Le^a glycospingolipids nor glycolated proteins bearing this structure [93], [94], [440]. In addition, human neutrophils have Lewis^a structures and can adsorb the glycosphingolipids from plasma [98], [441]. Therefore the binding of Lewis^a presented on MPIO may be greater in rodents than in humans, as there is less competition from endogenous (lower affinity) antigens.

3.5 | CONCLUSION

This chapter has shown that E-Selectin in the major binder of Lewis[a]-MPIO *in vivo*. E-Selectin is known to bind Lewis[a] *in vitro*, but its sialyated counter-part sLe[a] and isoform sLe[x] have been reported to bind with higher affinity to E-Selectin. *In vitro* experiments on brain microvascular endothelial cells revealed that upon IL-1β stimulation E-Selectin is among the highest upregulated proteins. This result was confirmed *in vivo* by measuring the transcriptomic changes in the brain upon IL-1β stimulation, as E-Selectin was again among the highest upregulated transcripts. Both the proteome and transcriptome had no other upregulated (known) lectins. The E-Selectin from the transcriptomic experiments is derived from the brain microvascular endothelial cells and could be the responsible Lewis[a] binder *in vivo*. However, *in vivo* other lectins are present in the circulation and on other cell types that could influence the binding observed previously and could not have been detected with either the proteomics or the transcriptomics experiments performed. From literature and the transcriptomics results from this thesis, a prominent role of neutrophils and possibly platelets in the early stages of IL-1β induced brain inflammation and BCG MS-like lesions was hypothesized. Neutrophils and platelets, *via* their glycosylated receptors, can bind E-Selectin and were therefore experimentally depleted from rats to determine their role in the binding *in vivo*. Also, the endothelial lectins E- and P-Selectin were blocked to assess which lectin is responsible for the binding. The *in vivo* MRI binding results of Lewis[a] and Lewis[b]-MPIO and the haematological analysis shows that Lewis[a]-MPIO binding is dependent on the availability of E-Selectin. When E-Selectin is blocked, no binding is observed of Lewis[a]-MPIO and when higher numbers of neutrophils are present in the animals; the available E-Selectin is partially blocked by neutrophils and results in fewer MRI binding signals of Lewis[a]-MPIO in the brain. Lewis[b]-MPIO shows a similar binding pattern as for Lewis[a]-MPIO, however its binding to E-Selectin is as strong as it is for P-Selectin, whereas Lewis[a]-MPIO shows only very weak binding to P-Selectin *in vivo*. Lewis[b]-MPIO binds P-Selectin equally well as E-Selectin, but the overall binding strength when compared to Lewis[a] is less.

To conclude, the results presented here in this thesis show that *in vivo* experiments, where all the necessary conditions are met including blood flow and immune cell populations, is ideal to study endothelial cell surface lectin interactions. A model that explains the observed strong binding for Lewis[a]-MPIO *in vivo* is presented and highlights the necessity of studying carbohydrate-lectin interactions *in vivo* to obtain a true binding profile as the *in vitro* experiments may not reveal the strongest *in vivo* Selectin binders. Also, these *in vivo* results formed the basis for a set of proof-of-principle studies using Lewis[a] for retargeting of biological nanoparticles and other particle formats which will be presented in the translational chapter of this thesis.

3.6 | METHODS

3.6.1 Reagents and buffers used for the proteomics experiments

Tris Buffer pH 8: 25 mM Tris·HCl, 150 mM NaCl, 5 mM $CaCl_2$,1 mM $MgCl_2$. Non denaturing lysis buffer pH 8: 25 mM Tris·HCl, 150 mM NaCl, 5 mM $CaCl_2$,1 mM $MgCl_2$. 1% Triton X-100 Surfact-Amps X-100 proteomics-grade (10% solution) was from Life Technologies (Cat # 28314, Lot# QD215923), 1 cOmplete™ EDTA-free Protease Inhibitor Cocktail Tablet/50 mL from Roche, 5mM iodoacetamide, 0.1mg/mL PMSF. Tris stock buffer for making dilutions, pH 7.8: 100 mM Trizma Base. Urea buffer: 6 M Urea, 25 mM Tris (from stock). Iodoacetamide buffer: 200 mM iodoacetamide, 25 mM Tris (from stock). Dithiothreitol (DTT) buffer: 200 mM Dithiothreitol, 25 mM Tris (from stock). Ammonium bicarbonate (ABC) solution: 50 mM in H_2O. Dulbecco's Phosphate Buffered Saline (DPBS) with calcium and magnesium was from Sigma (Cat # D1283). Dulbecco's Modified Eagle's Medium (DMEM) was from Sigma (Cat # D6046), Fetal Calf Serum (FCS) was from the Daniel Anthony lab stock and was heat inactivated for 30 minutes at 56°C, Penicillin-Streptomycin (P/S) was from Sigma (Cat # P4333), Recombinant Rat IL-1 beta/IL-1F2 Protein, CF was from R&D Systems (Cat # 501-RL-050/CF). NuPAGE LDS (lithium dodecyl sulfate) Sample Buffer (4X) was from Thermo Fisher (Cat # NP0007) with added NuPAGE Sample Reducing Agent (10X) from Thermo Fisher (Cat # NP0009). All other reagents were from Sigma, BioUltra-grade or higher. Plastic ware for tissue culture was from Corning exclusively and Protein LoBind microcentrifuge tubes (0.5, 1.5 and 2 mL) were from Eppendorf, other tubes (15 and 50 mL) were from Falcon, all sterile before use. Fresh buffers were prepared for each experiment and 0.22 µ-filtered before use. All experimental samples that were submitted for proteomic analysis were kept clean as much as possible to avoid any contamination.

3.6.2 Pulldown using bi-functional Lewis[a]/Diazirine photo-crosslinker magnetic particles

GP8.3 rat brain microvascular endothelial cells (passage number 7) were grown to confluency (≥ 90%) in DMEM supplemented with 10% FCS and P/S in a T75 (15 mL media/flask for maintaining the culture). For the experiment 3 control T75 flasks (10 mL media = 30 mL), 3 T75 flasks IL-1β stimulated using 10 ng/mL (10 mL media = 30 mL, 300 ng of IL-1β from an 1 µg/µL stock = 0.3µL) and 3 T75 flasks IL-1β stimulated using 100 ng/mL (10 mL media = 30 mL, 3000 ng of IL-1β from an 1 µg/µL stock = 3µL) of cells were used. The cells were incubated with the IL-1β or control for 4h

at 37°C, 5% CO_2.The flasks were placed on ice and the media was removed and discarded. The cells were washed with Tris-buffer (see above for recipes -with Calcium and Magnesium). The buffer was removed, then ice-cold lysis buffer (2 mL / flask + 3 mL to rinse the flask and scraper = 5 mL in total/flask) was added to the flask and the cells were scraped off the dish using a pre-cooled plastic cell scraper. The cell suspension was gently placed into a pre-cooled 15 mL Falcon tube. To disrupt the cell surface membrane, 1% Triton X-100 was used, at this concentration the nuclear membrane and organelle-membranes remain intact. Constant agitation was maintained for 30 minutes at 4°C to disrupt the cell surface membranes. Place the 15 mL/tube of each experiment into separate 2 mL pre-cooled Lo-Bind tubes and centrifuge at 4°C, 12,000xg for 10 minutes to pellet nuclei and large organelles. Carefully remove tubes from centrifuge and place on ice, aspirate the supernatant and place in a fresh Lo-Bind tube kept on ice. Take 100 µL and freeze to determine the protein concentration using a BCA assay. Results BCA: Control 0 ng/mL IL-1β 0.26 mg/mL, 10 ng/mL IL-1β 0.29 mg/mL and 100 ng/mL IL-1β 0.30 mg/mL. Use the remainder for the pull-down. Pool the tubes for each experiment into a 15 mL Falcon tube per experiment and add 0.3 mg = 30 µL of the bi-functional pull-down particles to each tube (see previous chaper, 26% diazirine photo-crosslinker, 34% Lewis[a] or the free amines). Maintain constant agitation for 60 minutes at 4°C. Transfer the solution to a 100 mm (55 cm^2) dish without the lid and place the samples under a hand-held UV-lamp (365 nm LED, 3 W) and irradiate for 20 minutes under gentle agitation (50 rpm) on ice at a depth of 20 mm. Upon performing this step, it was discovered that the light source is very weak and an alternative UV-source was used for the remainder of the experiment. A UVP Chromato-Vue Transilluminator, model TM-20 (220/240 V, 50 Hz, 1.5 Amp) was used. A total of 40 minutes of irradiation using midrange UV (8W) 302nm for 30 minutes and longwave (8W) 365nm for 10 minutes was performed at a depth of 20 mm on the samples whilst maintaining agitation (50 rpm) on ice. After irradiation, the samples were placed in a Lo-Bind 1.5 mL tube and spun down at 4°C, 12,000xg for 3 minutes and placed on an Invitrogen DYNAL DynaMag magnet for 2 minutes (cold room) and the supernatant was removed. Resuspend the particles of every tube with ice cold lysis buffer and repeat until all particles are in 1 tube per experiment. The supernatant was kept separate and frozen. The particles were washed with ice-cold lysis buffer w/o triton-X100, 2 times (1 mL per experiment/tube and kept for 2 minutes on magnet in the cold room. 100 µL of 6 M Urea was added to the particles and the particles were resuspend. Upon contact with the urea the particles aggregated and pelleting by magnetization was greatly reduced. The particles stick to the pipette tips and some sample loss occurred. To the urea treated particles, 5 µL DTT was added and the particles were incubated at room temperature in the tubes for 20 minutes under gentle agitation (200 rpm). 20 µL of iodoacetamide was added and the particles were incubated at room temperature in the tubes for 20 minutes under gentle

agitation (200 rpm). Add 20 µL of DTT and incubate the particles at room temperature in the tubes for 20 minutes under gentle agitation (200 rpm). Spin down the tubes at 2000xg, for 5 minutes and place for 2 minutes on the magnet. Keep the supernatant and freeze it. Finally, wash the particles with 100 µL ammonium bicarbonate buffer (ABC) twice by spinning down the tubes at 2000xg, for 5 minutes and by placing them on the magnet for 2 minutes and removing the supernatant. Resuspend the particles in 50 µL ABC and add 3 µL (2 µg/µL) of Ritu's Proteomics-Grade Trypsin Stock and incubate for 16h at 37°C, 1000 rpm. After the incubation, spin down the tubes at 2000xg, for 5 minutes and place them on the magnet for 2 minutes. Keep the supernatant do not discard, these contain the peptides. Wash the particles with 50 µL ABC and spin down the tubes at 2000xg, for 5 minutes and place them on the magnet for 2 minutes. Pool the supernatant containing the peptides and freeze down.

3.6.3 Pulldown using Lewis[a] and amine magnetic particles

GP8.3 rat brain microvascular endothelial cells (passage number 11) were grown to confluency (≥ 80%) in DMEM supplemented with 10% FCS and P/S in a T75 (15 mL media/flask for maintaining the culture). For the experiment 5 control T75 flasks (10 mL media = 50 mL), 5 T75 flasks IL-1β stimulated using 10 ng/mL (10 mL media = 50 mL, 500 ng of IL-1β from an 1 µg/µL stock = 0.5µL) and 5 T75 flasks IL-1β stimulated using 100 ng/mL (10 mL media = 50 mL, 5000 ng of IL-1β from an 1 µg/µL stock = 5µL) of cells were used. The cells were incubated with the IL-1β or control for 4h at 37°C, 5% CO_2.The flasks were placed on ice and the media was removed and discarded. The cells were washed with ice-cold Tris-buffer (see above for recipes -with Calcium and Magnesium). The buffer was removed, then ice-cold Tris-buffer (2 mL / flask + 3 mL to rinse the flask and scraper = 5 mL in total/flask) was added to the flask and the cells were scraped off the dish using a pre-cooled plastic cell scraper. The 25 mL cell suspension was gently placed into a pre-cooled 50 mL Falcon tube and the scraped cells were pelleted for 5 minutes at 4°C, 600xg. The supernatant was removed and the cell pellet was resuspended in ice-cold lysis buffer, transferred to a 2 mL Lo-Bind tube and briefly (5 seconds) vortexed. The individual tubes were wrapped with a sealing film and placed in 50 mL tubes filled with ice. These 50 mL tubes were then placed onto a tube roller in the cold room at 4°C for 30 minutes. The tubed were centrifuged at 4°C, 12,000xg for 10 minutes to pellet nuclei and large organelles. The tubes were removed from the centrifuge and placed on ice, the supernatant was aspirated and place into a fresh Lo-Bind tube kept on ice. Take 20 µL and freeze to determine the protein concentration using a BCA assay. Results BCA: Control 0 ng/mL IL-

1β 0.46 mg/mL, 10 ng/mL IL-1β 0.38 mg/mL and 100 ng/mL IL-1β 0.56 mg/mL. The remainder was used for the pull-down and divided over the following 6 tubes and add the pulldown particles.

1	0 ng/mL IL-1β + Lewis^a-MPIO (0.45 mg) + 1800 µL sample	**4**	NH_2-MPIO only (0.1 mg) + 200 µL sample
2	10 ng/mL IL-1β+ Lewis^a-MPIO (0.5 mg) + 1800 µL sample	**5**	NH_2-MPIO only (0.1 mg) + 200 µL sample
3	100 ng/mL IL-1β+ Lewis^a-MPIO (0.5 mg) + 1800 µL sample	**6**	NH_2-MPIO only (0.1 mg) + 200 µL sample

Using Lewis^a-MPIO particles with a loading of ~40% and amine-MPIO only particles (10 mg/mL stocks). Leave the particles to incubate and maintain constant agitation for 24h. Spin down the tubes at 5000xg, for 5 minutes and place for 2 minutes on the magnet. Remove the supernatant and freeze. Wash the particles with 200 µL ice-cold lysis buffer, place on the magnet, remove the supernatant and freeze. Add to the beads the volume initially used (10 mg/mL particle stock, 50µL for 0.5 mg and 10µL for 0.1 mg) and add 4x SDS loading buffer with reducing agents and heat for 5 minutes at 95°C with regular vortexing every minute. Spin down the particles for 5 minutes at 5000xg (4°C) and take the supernatant. Freeze down.

3.6.4 Whole cell proteome of IL-1β treated mouse brain microvascular endothelial cells

Mouse brain microvascular endothelial cells bEnd.3 (passage number 16) were grown to confluency (≥ 90%) in DMEM supplemented with 10% FCS and P/S in a T75 (15 mL media/flask for maintaining the culture). Three control T75 flasks (10 mL media = 30 mL) and 3 T75 flasks IL-1β stimulated using 100 ng/mL (10 mL media = 30 mL, 3000 ng of IL-1β from an 1 µg/µL stock = 3µL) of cells were used. The cells were incubated with the IL-1β or control for 4h at 37°C, 5% CO_2. The flasks were placed on ice and the media was removed and discarded. The cells were washed twice with 10 mL ice-cold sterile DPBS containing calcium and magnesium. To each flask, 2,5 mL of ice-cold DPBS was added and the adherent cells were scraped off the dish using a cold plastic cell scraper and then the cell suspension was gently transferred into a pre-cooled 15 mL Falcon tube. 2.5 mL of ice-cold PBS was used to rinse out the flask and scraper and was added this to the tube. The control cells were pooled in 1 Falcon tube and the IL-1β cells in a separate tube, the cells were spun down for 10 minutes at 500xg at 4°C. The supernatant was discarded and the pellet was resuspended in 3 mL of ice-cold PBS and distributed for each experimental procedure over 3 tubes. Cells were spun for 10 minutes at 500xg at 4°C, PBS was removed and the cells were frozen -20°C. Samples were run by Dr. Brian Lyons (Benjamin G. Davis Laboratory, Chemical Biology Group, Department of Chemistry, University of Oxford) who used these samples as part of his

induction to proteomics under the proteomics facility director Professor Shabaz Mohammed. He was aided by Dr. Monika Stegmann for the sample processing.

3.6.5 Proteomics data analysis details

Samples were submitted to, and run by Dr. Monika Stegmann from the Advanced Proteomics Facility (Department of Biochemistry, University of Oxford) under the facility director Professor Shabaz Mohammed. Samples from the 3.1.4.2 pulldown using bi-functional Lewis[a]/Diazirine photo-crosslinker magnetic particles were run as prepared. Samples from the 3.1.4.3 pulldown using Lewis[a] and amine magnetic particles were submitted to filter aided sample preparation (FASP), performed by Dr. Monika Stegmann, prior to liquid chromatography. Samples from the 3.1.4.4 whole cell proteome were processed by Dr. Brian Lyons and Dr. Monika Stegman, using their in-house protocols for whole cell sample processing. All samples were run on a Q Exactive™ Hybrid Quadrupole-Orbitrap™ Mass Spectrometer using a 1 hour gradient and BSA washes in-between runs to prevent contamination from previous runs. Peptides were identified using the Mascot Server from the University of Oxford. Data was further analysed using Perseus 1.5.4.1 software and for the 3.1.4.2 experiment significance B was used (selected expression/numerical columns containing the intensities for the "Significance B" (Maxquant - Perseus 1.5.4.1 software), were calculated using the ratios of Control '*Ctrl*' over '*10ng*' or '*100ng*' IL-1β treated). To highlight the differences in proteins identified between the control and IL-1β treated samples, Significance B for peptide intensity was used, a P value depending on protein intensity and protein ratio between the experiments. Please note that any real 'significance' calculated for the hits needs to be verified by repeat experiments. This value was merely used to more confidently select any potential hits to compare to other data sets. Both data sets (pulldown with photo-crosslinker and without) were analysed for low or absent peptides in the control sample. As the whole cell proteome from 3.1.4.4 was run as a technical triplicate, statistical p-values were assigned to the identified proteins and log transformed with the Perseus software and the means of the triplicates were compared in a t-test. The values were then plotted against each other to generate a scatter plot. Proteins identified were selected on their gene ontology (GO) (http://geneontology.org/) for membrane, plasma membrane, extracellular, extracellular matrix and secreted. These proteins are highlighted in BLUE for the pull-down experiments. Further data processing was done using Excel. Protein information was retrieved from uniprot.org and thebiogrid.org. Typically, human protein functions were assigned to identified rat genes assuming similar functions.

3.6.6 Acute IL-1β brain inflammation model in rats for transcriptomics

Rats (Wistar, male, juvenile *(n=3)*: 3-4 weeks old, range 40-50 g, adult *(n=3)*: 10 weeks old, range 200-250 g, Charles River UK) were anesthetized with 2–3% isoflurane in oxygen in an anaesthetic chamber. Upon induction of the anaesthesia, the absence of reflexes was confirmed and the animal was placed in a stereotaxic frame on a surgical heating pad whilst maintaining the anaesthesia *via* a nose cone. A midline incision was made in the scalp and the skull was exposed. A small hole was drilled in the skull and a stereotactic injection of IL-1β (0.5 µL, 50 ng in sterile saline) using a <50 µm tipped sterile glass capillary was made in the left brain hemisphere at 1 mm anterior, 3 mm lateral from Bregma and at a 4 mm depth into the left striatum. The solution was injected slowly and the capillary was left for 1 minute after the injection before removing it from the injection site. The skin was sutured and the animals were left to recover. Animals were anaesthetized as described above after 4 h of IL-1β activation. Animals were terminally anesthetised and perfused *via* the left ventricle with heparinized saline (5000 U/L, 0.9% NaCL) until tissue was clear from blood. The brain was removed from the skull using rongeurs and fresh frozen immediately to preserve mRNA. GeneChip® sample preparation was prepared as described by the manufacturer. Experiments performed by Daniel Anthony.

(See http://www.affymetrix.com/support/technical/byproduct.affx?product=rat230-20 for protocols.)

3.6.7 Chronic BCG MS-Like brain inflammation model in rats for transcriptomics

Rats (Wistar, *n*= specified in table 3.5, male, 50-100g, Charles River UK) were allowed to acclimatize for 1 week before the start of the experiment. Animals were anesthetized with 2–3% isoflurane in oxygen in an anaesthetic chamber. Upon induction of the anaesthesia, the absence of reflexes was confirmed and the animal was placed in a stereotaxic frame on a surgical heating pad whilst maintaining the anaesthesia *via* a nose cone. A midline incision was made in the scalp and the skull was exposed. A small hole was drilled in the skull and a stereotactic injection of heat-killed BCG (1×10^5 cells in 2 µL phosphate-buffered saline) using a 10 µL Hamilton syringe (Sigma Aldrich) was made in the left brain hemisphere at 1 mm anterior, 3 mm lateral from Bregma and at a 4 mm depth into the left striatum. The solution was injected slowly and removed from the injection site. The skin was sutured and the animals were left to recover. 28 days after the intracranial injections, the brain lesions were activated by a peripheral challenge using either an intradermal injection of BCG (1.5 mg) in 100 µL emulsion of CFA (complete Freund adjuvant, Sigma Aldrich) or 'vehicle' 100 µL emulsion of CFA mixed with 100 µL of phosphate-buffered

saline. Brains were collected at days 0 (day -28 after the initial intracranial injection) 5, 12 and day 31. This was done by terminally anesthetising the animals and perfusion *via* the left ventricle with heparinized saline (5000 U/L, 0.9% NaCL) until tissue was clear from blood. The brain was removed from the skull using rongeurs and fresh frozen immediately to preserve mRNA. Sections were made from the lesion (A), from the side next to the lesion (B) and from the contralateral side (C). **Table 3.5** shows the n-numbers and the sections taken from the GeneChip® experiments. GeneChip® sample preparation was prepared as described by the manufacturer. Experiments performed by Daniel Anthony.

(See http://www.affymetrix.com/support/technical/byproduct.affx?product=rat230-20 for protocols.)

3.6.8 Data analysis of IL-1β brain inflammation model using R Script

The following script was developed with Dr. Fay Probert from the Experimental Neuropathology Laboratory (Daniel C. Anthony Group, Department of Pharmacology, University of Oxford). The script can be copied and modified in 'R' and #'s will guide users through the script. In the next section Affymetrix Expression Console was used to analyse the BCG MS-like brain inflammation transcripts. Both methods yield the same output file and no difference in results was found (data not shown). Values (normalized intensity values) were further processed and analysed in Excel. The R-script can be found in the supplementary section of this chapter.

3.6.9 Data analysis of brain inflammation models using Affymetrix Expression Console (2014)

This section will provide a quick method to extract the e data the data from the .CEL files for analysis. Load the .CEL files, Click Analysis > 3' Expression Arrays > RMA. To .rma.chp transform the .CEL file and to scale the data to a log2 scale. Comprehensive data analysis reports will follow. Data presented here used the manual and the recommended settings for 3' Expression Arrays loading the correct library files and merge paths (GeneChip® Rat Genome 230 2.0 Array for IL-1β and GeneChip® Rat Genome Genome U34A Set for the BCG samples). Excel spreadsheet were generated with the log2 values. Statistical significance was calculated using a t-Test (all samples were from triplicate animals (or more –if available)). The t-Test was calculated using T.TEST(array1,array2,tails,type). If tails = 2, T.TEST uses the two-tailed distribution. If type = 3 T.TEST uses Two-sample unequal variance (heteroscedastic). Genes upregulated were sorted on Log2 fold change and plotted for scatterplots (**Figure 3.5**) against the –log10 for the t-Test. The top 150 for both data sets had a fold change cut-off of around 1.15 and the top 150 genes

upregulated were selected on their gene ontology (GO) (http://geneontology.org/) for membrane, plasma membrane, extracellular, extracellular matrix and secreted. These proteins are listed in the tables provided. Protein information was retrieved from uniprot.org and thebiogrid.org. Typically human protein functions were assigned to identified rat genes assuming similar functions.

3.6.10 Buffers and reagents used for the *ex vivo* MRI experiments

Dulbecco's Phosphate Buffered Saline (DPBS) with calcium and magnesium was from Sigma (Cat # D1283). Recombinant Rat IL-1 beta/IL-1F2 Protein, CF was from R&D Systems (Cat # 501-RL-050/CF). E-Selectin antibody RME-1 (mouse monoclonal IgG1, κ) and P-Selectin antibody RMP-1 (mouse monoclonal IgG2a, κ) were a generous gift from Professor Andrew C. Issekutz (Department of Pediatrics, Dalhousie University, Izaak Walton Killam Health Centre, Halifax, Nova Scotia, Canada). Isotype control antibodies (mouse monoclonal IgG1/IgG2a, κ) were from Biolegend, Clone MG1-45 is mouse IgG1 (Cat # 401408 Ultra-LEAF™) and clone MOPC-173 is mouse IgG2a (Cat # 400264 Ultra-LEAF™). Rabbit anti rat polymorphonuclear (PMN) serum is from Accurate Chemicals (Cat # AIA51140) and control Rabbit Serum (normal) is from Sigma-Aldrich (Cat # R4505-20ML). Antibodies were certified endotoxin and azide free and suitable for *in vivo* experiments. EDTA (0.5 M, pH 8.0). Heparinized saline (5000 U/L, 0.9% NaCL) was from Sigma-Aldrich (Cat # H3149). 0.1 M phosphate buffer (Acid $H_2NaO_4P{\cdot}H_2O$ 2.63 g/L Base HNa_2O_2P 11.47 g/L, pH 7.4), 4% paraformaldehyde (pH 7.4, in 0.1 M phosphate buffer). Sucrose 30% (pH 7.4, in 0.1 M phosphate buffer). Non-sterile PBS was from Thermo-Fisher (Cat# BR0014G). Crysyl Violet stain; cresyl violet acetate was from Sigma-Aldrich (Cat # C5042), 5 g was dissolved in 1 L of water whilst heating it to 60°C, once dissolved it was left to stir overnight, filtered, and acetic acid was added until pH 3.0. Unless specified, all other reagents were from Sigma, BioUltra-grade or higher. For antibody mixing and nanoparticle dilutions Protein LoBind microcentrifuge tubes (0.5, 1.5 and 2 mL) were used from Eppendorf, other tubes (15 and 50 mL) were from Falcon, all sterile before use. For injecting substances into the animals, Terumo 1ml Insulin Syringe & Needles were used (Cat# BS-01H2516). MRI tubes were from Sarstedt (Cat # 62.558.201) Fresh buffers were prepared for each experiment and filtered using general purpose laboratory filters before use. Other reagents and wares not mentioned here will be specified within the methods.

3.6.11 Animals

Rats were obtained from Charles River UK. Male Wistar rats (4-5 weeks old, average weight: 60 g) were housed under standard conditions with *ad libitum* standard chow and water on Level 2 in the BMS (University of Oxford). Upon arrival animals acclimatized for 3 days prior to experiments. Home office approval was obtained for all of the animal experiments described in this thesis.

3.6.12 Rat E- and P-Selectin *in vitro* binding experiment

ELISA 96 well plates from Greiner Bio-One (Polystyrene, flat bottom, MICROLON® 600, high binding, clear Cat # 655 061) were coated with 50 µL/well. E-Selectin or P-Selectin were from Stratech, Sino Biological Inc. Rat E-Selectin/CD62E/SELE (FC Tag) (Cat # 80033-R02H-SIB-100ug), Rat P-Selectin/CD62P/SELP (FC Tag) (Cat # 80451-R02H-SIB-50ug). 1:3 Serial dilution was made using PBS, pipetting a 150 µL (12,5 µg/mL E- or P-Selectin 9 µl in 1800 µL PBS in first well ROW A) into the first column of the 96 well plate, transferring 50 µL into the next well filled with 100 µL PBS and so on, leaving a 100 µL final volume in each well. Last well H PBS only. The plate was covered and incubated overnight at 4°C. The content of the plate was tipped out and patted dry on paper towels. Wells were washed with 150 µl of PBS twice before incubating with 150 µl 3% BSA in PBS for 2h at RT. Wells were washed with 150 µl of PBS twice before incubating with particles. The wells were filled with 40 µL of PBS and 10 µL of a 100 times dilution of MPIO-Le$^{a/b}$ (or MPIO-NH_2 for control). The plate was incubated for 2h on a plate rocker (Biometra®, WT, speed setting 4). The bound MPIO-Le$^{a/b}$ particles were washed with 150 µL PBS 3 times and after the last wash the wells were pipetted empty. The Perls Prussian Blue stain for iron was performed (50 µL/well) by freshly mixing 20% HCl (~6.5M) with 10% (w/w) $K_4Fe(CN)_6$ $3{\cdot}H_2O$ 1 to 1, which results in a ~3.2M HCl solution and left to stain for 20 min at room temperature. A blue precipitate was observed where MPIO-Le$^{a/b}$ were present. Notes for optimal results: pipetting from disposable white polystyrene reagent reservoirs or mixing in a polystyrene bijou tube (7mL) will result in an opaque blue stain, which is still quantifiable. Pipetting from a glass reservoir and mixing in a polypropylene tube will result in a clear well view with blue precipitate. Optimized staining is achieved using TipOne® 200 µL graduated filter tips (sterile) (StarLab, #S1120-8810), which appear to be more acid resistant than other tips tested, that can cause white precipitates in the wells after ≥ 10 minutes of incubation with the Perl stain. Only after an extended period of time (≥24h) the plate turns opaque and the negative control wells will turn (lighter) blue as well. Optimal measuring 'scanning' time is between 10 and 60 minutes. In addition, a plate rocker improves the stain, but has to be a side-to-side rocker like the Biometra® (WT, speed setting 4), an

orbital rocker will produce an obscured result that leads to particle and precipitate accumulation in the middle of the well. Plates can either be scanned by a flatbed scanner or by measuring the plate in a photo spectrometer BMG SPECTROstar Omega platereader (BMG Labtech) at various wavelengths.

3.6.13 Selectin blockade experiment

Rats (Wistar, male, 4-5 weeks old, average weight: 66 g, range 50-90 g) were anesthetized with 2–3% isoflurane in oxygen in an anaesthetic chamber. Upon induction of the anaesthesia, the absence of reflexes was confirmed and the animal was placed in a stereotaxic frame on a surgical heating pad whilst maintaining the anaesthesia *via* a nose cone. For the selective blockade of E- and P-Selectin, a tail vein injection with a 25 gauge insulin syringe was performed using either the E-Selectin antibody RME-1 (mouse monoclonal IgG1, κ, 3.3 mg/kg), P-Selectin antibody RMP-1 (mouse monoclonal IgG2a, κ, 3.3 mg/kg) or a mixture of the isotype control antibodies (mouse monoclonal IgG1/IgG2a, κ, 3.3 mg/kg of each, 6.6 mg in total) in a total volume of 100 µl in sterile phosphate buffered saline, pH 7.4. Immediately after the tail vein injection, a midline incision was made in the scalp and the skull was exposed. A small hole was drilled in the skull and a stereotactic injection of IL-1β (1 µL, 100 ng in sterile saline) using a <50 µm tipped sterile glass capillary was made in the left brain hemisphere at 1 mm anterior, 3 mm lateral from Bregma and at a 4 mm depth into the left striatum. The solution was injected slowly and the capillary was left for 1 minute after the injection before removing it from the injection site. The skin was sutured and the animals were left to recover. Animals were anaesthetized as described above after 4 h of IL-1β activation and either Lewis[a] or Lewis[b] MPIO (4 mg/kg in sterile saline in a total volume of 100 µl) was injected intravenously in the tail vein. Animals were left to recover and after 1h the animals were terminally anesthetised and >1 mL of blood was taken *via* a cardiac puncture using an EDTA (0.5 M, pH 8.0) treated syringe with a 23G needle. Animals were perfused *via* the left ventricle with heparinized saline (5000 U/L, 0.9% NaCL) until tissue was clear from blood and followed by 4% paraformaldehyde (pH 7.4, in 0.1 M phosphate buffer) fixation until rigid. Liver, spleen, kidney and lungs were extracted for further histochemistry studies and the brain was removed from the skull using rongeurs. Collected tissue was stored at 4 °C in 4% paraformaldehyde (PFA), pH 7.4 (phosphate buffer 100 mm, pH 7.4). During storage and imaging the PFA was exchanged for freshly prepared PFA every 14 days. Brain samples were placed at the 1 mL marking from the conical base and imaged in Sarstedt 5 ml tubes (56.61 x 15.30 mm, cap width: 17.83 mm, length with cap: 60.58 mm flat/conical base, PP, # 62.558.201) filled with

freshly prepared PFA, which was sonicated and flushed with N_2 gas for 20 minutes before sample preparations in the tubes. Great care was taken to avoid air bubbles. Brains were left to equilibrate to room temperature 2 hours prior to imaging on a 9.4T MRI in collaboration with Dr. Sean Smart at the Imaging core (Department of Oncology, University of Oxford).

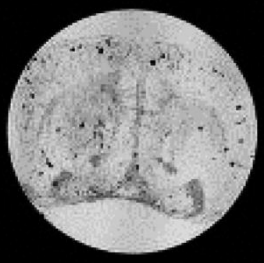
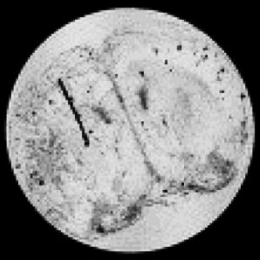
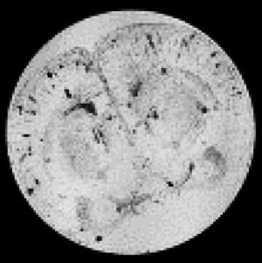
3.6.14 Neutrophil depletion experiment

Rats (Wistar, male, 4-5 weeks old, average weight: 76 g, range 55-90 g) were given an intraperitoneal injection of either a rabbit anti rat polymorphonuclear serum (dose: 3.3 µL/g, Accurate Chemicals) or control serum at the same dose using a 25 gauge insulin syringe 16h before surgery. Animals were anesthetized with 2–3% isoflurane in oxygen in an anaesthetic chamber. Upon induction of the anaesthesia, the absence of reflexes was confirmed and the animal was placed in a stereotaxic frame on a surgical heating pad whilst maintaining the anaesthesia *via* a nose cone. Blood ≤100 µL was taken from the tail vein using a EDTA (0.5 M, pH 8.0) treated syringe with a 23G needle. A midline incision was made in the scalp and the skull was exposed. A small hole was drilled in the skull and a stereotactic injection of IL-1β (1 µL, 100 ng in sterile saline) using a <50 µm tipped sterile glass capillary was made in the left brain hemisphere at 1 mm anterior, 3 mm lateral from Bregma and at a 4 mm depth into the left striatum. The solution was injected slowly and the capillary was left for 1 minute after the injection before removing it from the injection site. The skin was sutured and the animals were left to recover. Animals were anaesthetized as described above after 4 h of IL-1β activation and either Lewis[a] or Lewis[b] MPIO (4 mg/kg in sterile saline in a total volume of 100 µl) was injected intravenously in the tail vein. Animals were left to recover and after 1h the animals were terminally anesthetised and ≥1 mL of blood was taken *via* a cardiac puncture using a EDTA (0.5 M, pH 8.0) treated syringe with a 23G needle. Animals were perfused *via* the left ventricle with heparinized saline (5000 U/L, 0.9% NaCL) until tissue was clear from blood and followed by 4% paraformaldehyde (pH 7.4, in 0.1 M phosphate buffer) fixation until rigid. Liver, spleen, kidney and lungs were extracted for further histochemistry studies and the brain was removed from the skull using rongeurs. Collected tissue was stored at 4 °C in 4% paraformaldehyde (PFA), pH 7.4 (phosphate buffer 100 mm, pH 7.4). During storage and imaging the PFA was exchanged for freshly prepared PFA every 14 days. Brain samples were placed at the 1 mL marking from the conical base and imaged in Sarstedt 5 ml tubes (56.61 x 15.30 mm, cap width: 17.83 mm, length with cap: 60.58 mm flat/conical base, PP, # 62.558.201) filled with freshly prepared PFA, which was sonicated and flushed with N_2 gas for 20 minutes before sample preparations in the tubes. Great care was taken to avoid air bubbles.

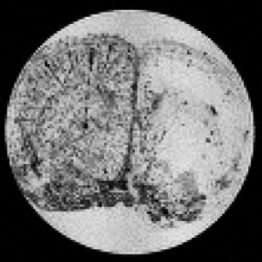
Brains were left to equilibrate to room temperature 2 hours prior to imaging on a 9.4T MRI in collaboration with Dr. Sean Smart at the Imaging core (Department of Oncology, University of Oxford).

| Figure 3.29 | MRI Z-Stacks for Lewis[a]-MPIO binding – Overview 1 E- and P-Selectin Block

Lewis[a] Experiment	Antibody Clone	Species	Dose
E-Selectin Block	RME-1	Mouse monoclonal IgG1, κ	3.3 mg/kg

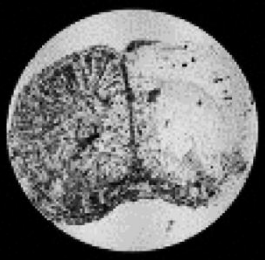
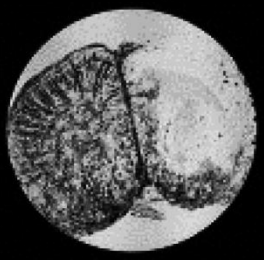
1	2	3	4
			
IL-1β incubation time: 4:19 **Le[a]-MPIO incubation time:** 1:05 **Weight rat:** 55 gram **Neutrophil count:** 63.9% ± 1.4 **Z-Stacks:** 200-235 **Experimental Notes:**	**IL-1β incubation time:** 4:22 **Le[a]-MPIO incubation time:** 0:55 **Weight rat:** 55 gram **Neutrophil count:** 63.5% ± 5.2 **Z-Stacks:** 211-246 **Experimental Notes:**	**IL-1β incubation time:** 4:19 **Le[a]-MPIO incubation time**: 0:53 **Weight rat:** 57 gram **Neutrophil count:** 72.8% ± 1.2 **Z-Stacks:** 193-228 **Experimental Notes:**	**IL-1β incubation time:** 4:10 **Le[a]-MPIO incubation time:** 0:59 **Weight rat:** 55 gram **Neutrophil count:** 61.7% ± 4.8 **Z-Stacks:** 200-235 **Experimental Notes:** Bad perfusion

P-Selectin Block	RMP-1	Mouse monoclonal IgG2a, κ	3.3 mg/kg

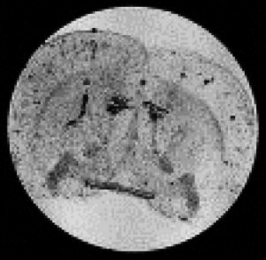
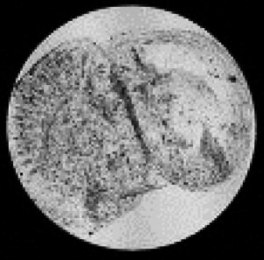
9	10	11	12
			
IL-1β incubation time: 4:15 **Le[a]-MPIO incubation time:** 1:14 **Weight rat:** 50 gram **Neutrophil count:** 68.4% ± 1.7 **Z-Stacks:** 208-243 **Experimental Notes:**	**IL-1β incubation time:** 4:06 **Le[a]-MPIO incubation time:** 1:14 **Weight rat:** 70 gram **Neutrophil count:** 66.4% ± 3.2 **Z-Stacks:** 223-258 **Experimental Notes:**	**IL-1β incubation time:** 3:53 **Le[a]-MPIO incubation time:** 1:13 **Weight rat:** 51 gram **Neutrophil count:** 72.7% ± 1.5 **Z-Stacks:** 223-258 **Experimental Notes:** Bad tail vein injection of Le[a]-MPIO	**IL-1β incubation time:** 3:50 **Le[a]-MPIO incubation time:** 1:16 **Weight rat:** 54 gram **Neutrophil count:** 64.5% ± 1.2 **Z-Stacks:** 236-271 **Experimental Notes:**

| Figure 3.30 | MRI Z-Stacks for Lewis[a]-MPIO binding – Overview 2 Isotype Controls

Lewis[a] Experiment	Antibody Clone	Species	Dose
Isotype Control	MG1-45 (IgG1) + MOPC-173 (IgG2a)	Mouse monoclonal IgG1 + IgG2a, κ	3.3 mg/kg + 3.3 mg/kg

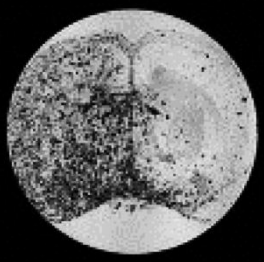
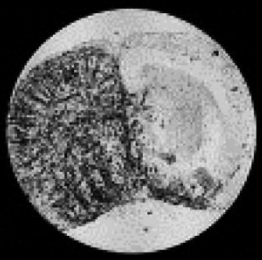
41	42	43	44
			
IL-1β incubation time: 4:13 **Le[a]-MPIO incubation time:** 1:01 **Weight rat:** 64 gram **Neutrophil count:** 49.2% ± 1.4 **Z-Stacks:** 209-244 **Experimental Notes:** Heparinized Blood sample measured 2h post mortem	**IL-1β incubation time:** 4:04 **Le[a]-MPIO incubation time:** 1:04 **Weight rat:** 61 gram **Neutrophil count:** 50.3% ± 1.3 **Z-Stacks:** 197-232 **Experimental Notes:** Heparinized Blood sample measured 2h post mortem	**IL-1β incubation time:** 4:02 **Le[a]-MPIO incubation time:** 1:00 **Weight rat:** 66 gram **Neutrophil count:** 58.1% ± 2.0 **Z-Stacks:** 201-236 **Experimental Notes:** Heparinized Blood sample measured 2h post mortem	**IL-1β incubation time:** 4:00 **Le[a]-MPIO incubation time:** 1:01 **Weight rat:** 70 gram **Neutrophil count:** 46.5% ± 1.9 **Z-Stacks:** 217-252 **Experimental Notes:** Heparinized Blood sample measured 2h post mortem

Isotype Control	MG1-45 (IgG1) + MOPC-173 (IgG2a)	Mouse monoclonal IgG1 + IgG2a, κ	3.3 mg/kg + 3.3 mg/kg

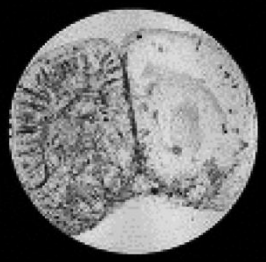
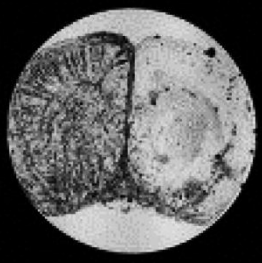
17	18	19	20
			
IL-1β incubation time: 5:27 **Le[a]-MPIO incubation time:** 1:18 **Weight rat:** 67 gram **Neutrophil count:** 42.8% ± 1.4 **Z-Stacks:** 210-245 **Experimental Notes:** No saline perfusion, only PFA perfusion / Le[a]-MPIO incubation time too long	**IL-1β incubation time:** 5:07 **Le[a]-MPIO incubation time:** 1:21 **Weight rat:** 60 gram **Neutrophil count:** 76.6% ± 1.1 **Z-Stacks:** 228-263 **Experimental Notes:** Le[a]-MPIO incubation time too long	**IL-1β incubation time:** 4:53 **Le[a]-MPIO incubation time:** 1:31 **Weight rat:** 64 gram **Neutrophil count:** 59.3% ± 1.2 **Z-Stacks:** 203-238 **Experimental Notes:** Le[a]-MPIO incubation time too long	**IL-1β incubation time:** 4:45 **Le[a]-MPIO incubation time:** 1:35 **Weight rat:** 64 gram **Neutrophil count:** 64.6% ± 2.7 **Z-Stacks:** 218-253 **Experimental Notes:** Unsucsessfull tail vein injection of Le[a]-MPIO / Le[a]-MPIO incubation time too long

| Figure 3.31 | MRI Z-Stacks for Lewis[a]-MPIO binding – Neutrophil Depletion

Lewis[a] Experiment	Serum	Species	Dose
Neutrophil Depletion	Anti Rat Polymorphonuclear Serum	Rabbit polyclonal	3.3 µL/g

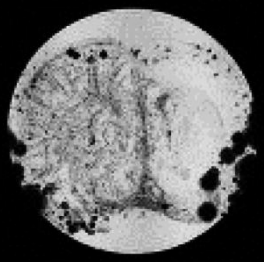
25	26	27	28
			
IL-1β incubation time: 4:23 **Le[a]-MPIO incubation time:** 1:22 **Weight rat:** 78 gram **Neutrophil count:** 17.2% **Z-Stacks:** 230-265 **Experimental Notes:** Blood measured once	**IL-1β incubation time:** 4:18 **Le[a]-MPIO incubation time:** 1:29 **Weight rat:** 85 gram **Neutrophil count:** 7.7% **Z-Stacks:** 228-263 **Experimental Notes:** Blood measured once	**IL-1β incubation time:** 4:08 **Le[a]-MPIO incubation time**: 1:32 **Weight rat:** 68 gram **Neutrophil count:** 9.6% **Z-Stacks:** 222-257 **Experimental Notes:** Blood measured once	**IL-1β incubation time:** 4:03 **Le[a]-MPIO incubation time:** 0:52 **Weight rat:** 84 gram **Neutrophil count:** 12.7% **Z-Stacks:** 222-257 **Experimental Notes:** Blood measured once

Serum Control	Control Serum	Rabbit polyclonal	3.3 µL/g

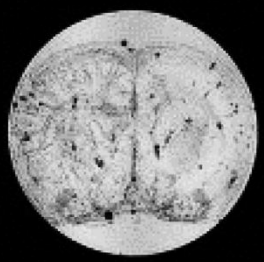
29	30	31	32
			
IL-1β incubation time: 4:14 **Le[a]-MPIO incubation time:** 1:00 **Weight rat:** 71 gram **Neutrophil count:** 59.2% **Z-Stacks:** 216-251 **Experimental Notes:** Blood measured once	**IL-1β incubation time:** 4:01 **Le[a]-MPIO incubation time:** 1:09 **Weight rat:** 64 gram **Neutrophil count:** 66.7% **Z-Stacks:** 213-257 **Experimental Notes:** Blood measured once	**IL-1β incubation time:** 4:02 **Le[a]-MPIO incubation time:** 1:06 **Weight rat:** 90 gram **Neutrophil count:** 48.0% **Z-Stacks:** 219-254 **Experimental Notes:** Blood measured once	**IL-1β incubation time:** 4:09 **Le[a]-MPIO incubation time:** 1:00 **Weight rat:** 55 gram **Neutrophil count:** 57.3% **Z-Stacks:** 223-258 **Experimental Notes:** Blood measured once

| Figure 3.32 | MRI Z-Stacks for Lewis[b]-MPIO binding – Overview 1 E- and P-Selectin Block

Lewis[b] Experiment	Antibody Clone	Species	Dose
E-Selectin Block	RME-1	Mouse monoclonal IgG1, κ	3.3 mg/kg

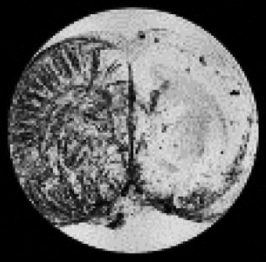
5	6	7	8
			†
IL-1β incubation time: 4:08 **Le[b]-MPIO incubation time:** 1:04 **Weight rat:** 60 gram **Neutrophil count:** 71.3% ± 1.1 **Z-Stacks:** 210-245 **Experimental Notes:**	**IL-1β incubation time:** 3:59 **Le[b]-MPIO incubation time:** 1:07 **Weight rat:** 55 gram **Neutrophil count:** 58.7% ± 1.2 **Z-Stacks:** 237-202 **Experimental Notes:**	**IL-1β incubation time:** 3:53 **Le[b]-MPIO incubation time**: 1:12 **Weight rat:** 56 gram **Neutrophil count:** 63.0% ± 1.4 **Z-Stacks:** 215-251 **Experimental Notes:**	**IL-1β incubation time:** … **Le[b]-MPIO incubation time:** … **Weight rat:** 58 gram **Neutrophil count:** … **Z-Stacks:** … **Experimental Notes:** Did not recover

P-Selectin Block	RMP-1	Mouse monoclonal IgG2a, κ	3.3 mg/kg

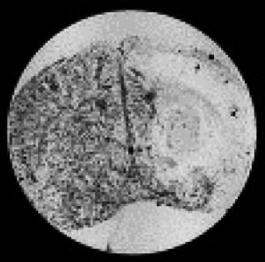
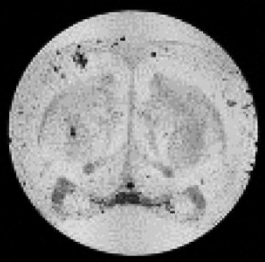
13	14	15	16
			
IL-1β incubation time: 4:04 **Le[b]-MPIO incubation time:** 1:00 **Weight rat:** 54 gram **Neutrophil count:** 68.0% ± 1.9 **Z-Stacks:** 189-224 **Experimental Notes:**	**IL-1β incubation time:** 3:52 **Le[b]-MPIO incubation time:** 1:02 **Weight rat:** 59 gram **Neutrophil count:** 71.1% ± 0.7 **Z-Stacks:** 211-246 **Experimental Notes:**	**IL-1β incubation time:** 3:51 **Le[b]-MPIO incubation time:** 1:04 **Weight rat:** 56 gram **Neutrophil count:** 64.3% ± 0.6 **Z-Stacks:** 224-259 **Experimental Notes:** Bad tail vein injection of Le[a]-MPIO	**IL-1β incubation time:** 3:45 **Le[b]-MPIO incubation time:** 1:12 **Weight rat:** 70 gram **Neutrophil count:** 69.2% ± 1.3 **Z-Stacks:** 218-253 **Experimental Notes:**

| Figure 3.33 | MRI Z-Stacks for Lewis[b]-MPIO binding – Overview 2 Isotype Controls

Lewis[b] Experiment	Antibody Clone	Species	Dose
Isotype Control	MG1-45 (IgG1) + MOPC-173 (IgG2a)	Mouse monoclonal IgG1 + IgG2a, κ	3.3 mg/kg + 3.3 mg/kg

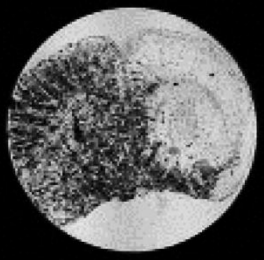
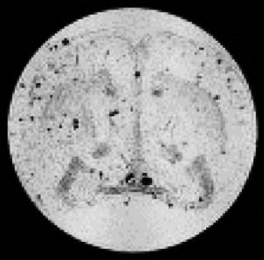
45	46	47	48
			
IL-1β incubation time: 4:00 **Le[b]-MPIO incubation time:** 0:58 **Weight rat:** 69 gram **Neutrophil count:** 49.6% ± 0.8 **Z-Stacks:** 201-236 **Experimental Notes:** Heparinized Blood sample measured 2h post mortem / Unsucsessfull tail vein injection of Le[b]-MPIO	**IL-1β incubation time:** 3:52 **Le[b]-MPIO incubation time:** 1:00 **Weight rat: 70** gram **Neutrophil count:** 50.6% ± 2.1 **Z-Stacks:** 209-244 **Experimental Notes:** Heparinized Blood sample measured 2h post mortem	**IL-1β incubation time:** 3:49 **Le[b]-MPIO incubation time:** 1:02 **Weight rat:** 70 gram **Neutrophil count:** 58.0% ± 0.6 **Z-Stacks:** 217-252 **Experimental Notes:** Heparinized Blood sample measured 2h post mortem	**IL-1β incubation time:** 3:56 **Le[b]-MPIO incubation time:** 0:56 **Weight rat:** 64 gram **Neutrophil count:** 53.1% ± 0.7 **Z-Stacks:** 207-242 **Experimental Notes:** Heparinized Blood sample measured 2h post mortem

Isotype Control	MG1-45 (IgG1) + MOPC-173 (IgG2a)	Mouse monoclonal IgG1 + IgG2a, κ	3.3 mg/kg + 3.3 mg/kg

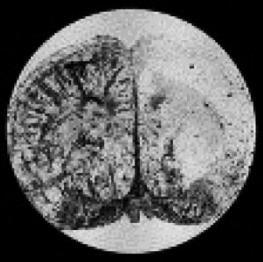
21	22	23	24
			
IL-1β incubation time: 5:05 **Le[b]-MPIO incubation time:** 1:13 **Weight rat:** 60 gram **Neutrophil count:** 52.9% ± 1.6 **Z-Stacks:** 210-245 **Experimental Notes:** Le[b]-MPIO incubation time too long	**IL-1β incubation time:** 4:57 **Le[b]-MPIO incubation time:** 1:07 **Weight rat:** 56 gram **Neutrophil count:** 72.3% ± 0.8 **Z-Stacks:** 214-249 **Experimental Notes:** Le[b]-MPIO incubation time too long	**IL-1β incubation time:** 4:57 **Le[b]-MPIO incubation time:** 1:00 **Weight rat:** 63 gram **Neutrophil count:** 63.7% ± 1.7 **Z-Stacks:** 215-250 **Experimental Notes:** Le[b]-MPIO incubation time too long	**IL-1β incubation time:** 4:40 **Le[b]-MPIO incubation time:** 1:02 **Weight rat:** 73 gram **Neutrophil count:** 70.5% ± 0.8 **Z-Stacks:** 220-255 **Experimental Notes:** Le[b]-MPIO incubation time too long

| Figure 3.34 | MRI Z-Stacks for Lewis[b]-MPIO binding – Neutrophil Depletion

Lewis[b] Experiment	Serum	Species	Dose
Neutrophil Depletion	Anti Rat Polymorphonuclear Serum	Rabbit polyclonal	3.3 µL/g

33	34	35	36
			
IL-1β incubation time: 5:10 **Le[b]-MPIO incubation time:** 1:15 **Weight rat:** 89 gram **Neutrophil count:** 16.5% ± 0.2 **Z-Stacks:** 230-265 **Experimental Notes:** Blood measured once	**IL-1β incubation time:** 5:04 **Le[b]-MPIO incubation time:** 1:04 **Weight rat:** 78 gram **Neutrophil count:** 11.0% ± 0.6 **Z-Stacks:** 228-263 **Experimental Notes:** Blood measured once	**IL-1β incubation time:** 4:50 **Le[b]-MPIO incubation time**: 1:04 **Weight rat:** 71 gram **Neutrophil count:** 10.8% ± 1.1 **Z-Stacks:** 222-257 **Experimental Notes:** Blood measured once	**IL-1β incubation time:** 4:54 **Le[b]-MPIO incubation time:** 1:02 **Weight rat:** 84 gram **Neutrophil count:** 11.0% ± 0.6 **Z-Stacks:** 222-257 **Experimental Notes:** Blood measured once

Serum Control	Control Serum	Rabbit polyclonal	3.3 µL/g

37	38	39	40
			
IL-1β incubation time: 4:49 **Le[b]-MPIO incubation time:** 1:05 **Weight rat:** 70 gram **Neutrophil count:** 64.7% ± 0.3 **Z-Stacks:** 207-242 **Experimental Notes:** Blood measured once	**IL-1β incubation time:** 4:47 **Le[b]-MPIO incubation time:** 1:03 **Weight rat:** 75 gram **Neutrophil count:** 64.7% ± 0.8 **Z-Stacks:** 215-250 **Experimental Notes:** Blood measured once	**IL-1β incubation time:** 4:44 **Le[b]-MPIO incubation time:** 1:04 **Weight rat:** 71 gram **Neutrophil count:** 63.0% ± 0.3 **Z-Stacks:** 230-265 **Experimental Notes:** Blood measured once	**IL-1β incubation time:** 4:40 **Le[b]-MPIO incubation time:** 1:03 **Weight rat:** 84 gram **Neutrophil count:** 55.4% ± 1.9 **Z-Stacks:** 228-263 **Experimental Notes:** Blood measured once

3.6.15 Full blood count

A calibrated haemocytometer with the recommended fluidics (Horiba UK) for human blood analysis was used for generating the differentials (ABX Pentra 60, Horiba UK). Samples (≤ 100 µL) from tail veins were taken with EDTA (0.5 M, pH 8.0) treated 1 mL syringes with 23G needles. Syringes were filled with 1 mL of EDTA and just before sampling, the EDTA was ejected and the syringe was used. Blood was collected in 1.5 mL micro centrifuge tubes, pre-filled with EDTA, which was discarded before the blood was placed into the tube. Blood (≥1 mL) derived from a cardiac puncture was collected using a EDTA treated 1 mL syringe with a 23G needle, as before but leaving 25 µL residual EDTA in the syringe. Blood was collected in 1.5 mL micro centrifuge tubes, pre-filled with EDTA, which was discarded before the blood was placed into the tube. All blood samples were gently swirled or inverted to prevent clotting and were measured immediately after sampling. All samples derived from cardiac punctures were measured 3 times and data is represented as the average of 3. All samples from tail vein collections were measured 1 time. Samples were measured by Pascal Kilian.

3.6.16 Immunohistochemistry for peripheral tissue

Tissue was collected at the perfusion stage and was stored at 4 °C in 4% paraformaldehyde (PFA), pH 7.4 (phosphate buffer 100 mm, pH 7.4). Tissue was left in PFA for 14 days. PFA was replaced by 30% sucrose and was stored at 4 °C (30 g sucrose + 70 mL phosphate buffer 100 mm, pH 7.4. Once dissolved, fill up to 100 mL) and exchanged the next day, after 3 days the tissues were gently dabbed dry on tissue paper and coated with a layer of OCT. Organs (liver, spleen, lung, kidney) were placed into a premoulded aluminium foil cup with a layer of OCT, taking care to avoid air bubbles and arranging them for a Smörgåsbord-type arrangement, and then completely covered with OCT. The cups were placed in a pre-cooled tub with a layer of isopentane cooled by dry-ice for quick freezing. Once frozen, the organs in OCT were stored in -20°C until sectioning. Tissue was sectioned at 10 µm using a cryostat and collected onto gelatinized slides with phosphate buffer and dried overnight at room temperature. Slides were stored at -20°C until staining. Slides were dried at 37°C for 15 minutes and then briefly washed in PBS. Endogenous peroxidase activity was quenched by incubating the slides in methanol with 1% H_2O_2 for 10 minutes. The slides were washed in PBS and placed into sequenza (Shandon Scientific) clips whilst being submerged in PBS. Once placed into the holder, the slides were washed with PBS (5 min) twice. Endogenous biotin was blocked with avidin in PBS (120 µL/ sequenza clip) for 15 minutes at room temperature. The

slides were washed with PBS (5 min) twice before blocking the remaining avidin sites with free biotin in PBS (120 µL/ sequenza clip) for 15 minutes at room temperature (Avidin/Biotin Blocking Kit Vector Laboratories). The slides were washed with PBS (5 min) twice and incubated with 10% serum (of the animal in which the secondary antibody was raised) in PBS for 1 hour at room temperature (120 µL/ sequenza clip). The primary antibody was then added in 1% serum in PBS (120 µL/ sequenza clip) and incubated overnight at 4 °C, see table below for concentrations used. The next day, the slides were washed with PBS (5 min) three times and then incubated with the secondary antibody with 1% serum in PBS for 2 hours at room temperature (120 µL/ sequenza clip). The slides were washed with PBS (5 min) three times before incubation with the ABC mix which was prepared 30 minutes prior to incubation and kept at room temperature (VECTASTAIN® ABC-HRP Kit Vector Laboratories), the slides were incubated with ABC for 1 hour at room temperature (120 µL/ sequenza clip). The slides were washed with PBS and then placed into a metal rack whilst being submerged in 0.1 M phosphate buffer, pH 7.4 (Acid $H_2NaO_4P{\cdot}H_2O$ 2.63 g/L Base HNa_2O_2P 11.47 g/L). Once racked, the slides were incubated with DAB (frozen aliquot of 5 mL at a concentration of 50 mg/mL in 0.1 M phosphate buffer, pH 7.4, thawed and dissolved in 280 mL 0.1 M phosphate buffer, pH 7.4) and 0.05% H_2O_2. Once the desired level of staining was obtained by inspecting slides carefully under the microscope, the slides were washed in phosphate buffer and counterstained with Harris-haematoxylin for 5 minutes. The excess stain was washed off by running the slides under tap water, the slides were differentiated in acidified alcohol (1% (v/v) concentrated HCL (37%) to 99% (v/v) 70% EtOH). The slides were gradually dehydrated by increasing alcohol concentrations (80%, 95%, EtOH absolute, EtOH absolute). Subsequently slides were further dehydrated in xylene twice for 5 minutes and mounted with DPX mounting medium from Fisher Scientific (Cat # D/5319/05) and coverslips. The slides were left to dry and harden for 24h.

3.6.17 Immunohistochemistry for brain tissue

Brains were collected at the perfusion stage and were stored at 4 °C in 4% paraformaldehyde (PFA), pH 7.4 (phosphate buffer 100 mm, pH 7.4). During storage the PFA was exchanged for freshly prepared PFA every 14 days. Prior to imaging brain samples were placed in freshly prepared PFA, which was sonicated and flushed with N2 gas for 20 minutes before sample preparations in the tubes. After MRI imaging, the samples were stored at 4°C and PFA was replaced by 30% sucrose and was stored at 4 °C (30 g sucrose + 70 mL phosphate buffer 100 mm, pH 7.4. Once dissolved, fill up to 100 mL) and exchanged the next day, after 3 days the brains

were gently dabbed dry on tissue paper and coated with a layer of OCT. Brains were placed into a premoulded aluminium foil cup with a layer of OCT, taking care to avoid air bubbles and arranging them for coronal sectioning. The cups were placed in a pre-cooled tub with a layer of isopentane cooled by dry-ice for quick freezing. Once frozen, the brains in OCT were stored in -20°C until sectioning. Brains were sectioned at 10 µm using a cryostat and collected onto gelatinized slides with phosphate buffer and dried overnight at room temperature. Slides were stored at -20°C until staining. Slides were dried at 37°C for 15 minutes and then briefly washed in PBS. Endogenous peroxidase activity was quenched by incubating the slides in methanol with 1% H_2O_2 for 10 minutes. The slides were washed in PBS and placed into sequenza (Shandon Scientific) clips whilst being submerged in PBS. Once placed into the holder, the slides were washed with PBS (5 min) twice and incubated with 10% serum (of the animal in which the secondary antibody was raised) in PBS for 1 hour at room temperature (120 µL/ sequenza clip). The primary antibody was then added in 1% serum in PBS (120 µL/ sequenza clip) and incubated overnight at at 4 °C, see table below for concentrations used. The next day, the slides were washed with PBS (5 min) three times and then incubated with the secondary antibody with 1% serum in PBS for 2 hours at room temperature (120 µL/ sequenza clip). The slides were washed with PBS (5 min) three times before incubation with the ABC mix which was prepared 30 minutes prior to incubation and kept at room temperature (VECTASTAIN® ABC-HRP Kit Vector Laboratories), the slides were incubated with ABC for 1 hour at room temperature (120 µL/ sequenza clip). The slides were washed with PBS and then placed into a metal rack whilst being submerged in 0.1 M phosphate buffer, pH 7.4 (Acid $H_2NaO_4P{\cdot}H_2O$ 2.63 g/L Base HNa_2O_2P 11.47 g/L). Once racked, the slides were incubated with DAB (frozen aliquot or 5 mL at a concentration of 50 mg/mL in 0.1 M phosphate buffer, pH 7.4, thawed and dissolved in 280 mL 0.1 M phosphate buffer, pH 7.4) and 0.05% H_2O_2.. Once the desired level of staining was obtained by inspecting slides carefully under the microscope, they were washed with phosphate buffer and transferred to acidified water () for 5 minutes. Then slides were transferred to Cresyl Violet for 5 minutes and rinsed in distilled water. The slides were gradually dehydrated by increasing alcohol concentrations (80%, 95%, EtOH absolute, EtOH absolute) leaving the slides in 95% EtOH untill the desired crysyl violet intensity was obtained. Subsequently slides were further dehydrated in xylene twice for 5 minutes and mounted with DPX mounting medium from Fisher Scientific (Cat # D/5319/05) and coverslips. The slides were left to dry and harden for 24h.

| Table 3.13 | Antibodies used for immunohistochemistry

Primary Antibody Details	Primary antibody concentration	Secondary antibody*	Dilution
In-house anti neutrophil antibody (Daniel Anthony Lab stock)	1:10.000	Goat-anti-Rabbit (BA-1000)	1:200
Polyclonal Rabbit IgG against Rat P-Selectin (CD62P Ala58-Cys158 Accession # P98106) From Cloud-Clone Corp. Cat # PAA569Ra01	10 µg/mL	Goat-anti-Rabbit (BA-1000)	1:100
Polyclonal Goat IgG against Rat E-Selectin (CD62E Trp22-Pro494 Accession # P98105) From R&D Systems, Cat # AF977	10 µg/mL	Horse-anti-Goat (BA-8000)	1:100

* Biotinylated antibodies from Vector Laboratories Ltd (Cambridgeshire, UK)

3.6.18 MRI imaging parameters for MPIO quantification

All files were processed the same and were blinded. Open .nii MRI file in ImageJ 1.48v. The two bars below the image are centred. Use Echo 4 (out of 8). The top bar (Z) is placed to 64 (128/2=64) and the Echo (▶) to 4 (8/2=4). Image > Adjust > Brightness and Contrast (B&C) > Auto. A sagittal image of a rat brain appears. Select the opened file and Image > Stacks > Reslice [/] > Untick flip vertically and tick (✔) Rotate 90 degrees (✔) Avoid interpolation. A Reslice file is generated and repeat Image > Stacks > Reslice [/] > Tick flip vertically (✔) and untick Rotate 90 degrees, keep (✔) Avoid interpolation. The now coronal should be flipped horizontally so the left side is the IL-1β injected side. Orientation can be changed using Image > Transform > … . Save the file as a .Tiff. Using the rat brain atlas, identify the slides 6 *4.83 (+4.20)* – 7 *5.11 (+3.60)* till 24 *9.31 (-1.33)* – 25 *9.47 (-1.53).* This should cover on average the sections between 4.95 and 9.39 = 4.42 mm of the coronal sections. When these sections are identified in the image they should span 4.375 mm (35 slides, ~125 µm/pixel) (slide ~17 = bregma). See exemplary **Figure 3.12** for an overview of the coronal sections used for analysis. Use these 35 slides to generate a Z stack by Image > Stacks > Z Project. Insert the identified start and end section (35 slides) and select Min Intensity and untick All time frames. Save the file as a .Tiff and a .Jpeg. .Tiff images are used to calculate the mean grey values in ImageJ by drawing an ROI as shown in **Figure 3.13** and measuring: Area ROI, Mean Grey Value (Min and Max), Intensity Density and the raw intensity density 'RawIntDen'.

$$\text{Formula}=\left(\frac{\text{Mean Grey Value Right Hemisphere}}{\text{Mean Grey Value Left Hemisphere}}\right)\text{-}1$$

Typical image analysis (black font, white ROI) excludes the outer regions of the brain (meningeal bubbles, as seen most prominently in sample 33) and if present, dark lower regions. Large bubbles as in sample 31 were excluded and no ROI area compensation was performed as the mean grey value was used. ROI image analysis of the basal ganglia region simplifies the ROI (all areas of the

eclipse were equal and set to an area of 10) and excludes any outer regions artefacts. For illustrative purposes open the .Jpeg file in paint.exe and resize to 500%. Copy the image and paste in PowerPoint, adjust the image setting with Picture Tools > Format > Corrections > Brightness -20% / Contrast +40%.

|SUPPLEMENTARY INFORMATION CHAPTER 3|

SI.3.1 R Script

```
#set source location for libraries
#if you cannot download the library you may have incorrect source google on biocunductor webiste will
find this
source("https://bioconductor.org/biocLite.R")

#install required libraries
biocLite("affy")
biocLite("oligo")
biocLite("limma")

#load affy library
library(affy)

#set path location to your folder containing CEL files

setwd("C:/Users/Fay/Documents/Work/Kim/")

#ReadAffy will automatically read all CEL files in this folder

data <- ReadAffy()

#to check that it has been read correctly look at the data object

data

# AffyBatch object
# size of arrays=834x834 features (21 kb)
# cdf=Rat230_2 (31099 affyids)
# number of samples=12
# number of genes=31099
# annotation=rat2302
# notes=

#annotation tells you the chip that was used
#download the .db file for this chip

biocLite("rat2302.db")

#load the the library for the .db file

library(rat2302.db)

#to see what information it is possible to extract from the db file type

rat2302()

#information in the package will be named in the form rat2302ACCNUM, rat2302GENENAME etc.

#before extracting the data in to a table various normalisation and quality control steps need to be
completed
#this is not an extensive list

#normalisation using rma algorithm
data.rma <- rma(data)

#or normalisation using gcrma algorithm

data.gcrma <- gcrma(data)

#write
write.exprs(data.gcrma,file="gcrmaNormalisedData.txt")

# load colour libraries
library(RColorBrewer)
 # set colour palette
 cols <- brewer.pal(8, "Set1")
 # plot a boxplot of unnormalised intensity values
 boxplot(data, col=cols)
 # plot a boxplot of normalised intensity values, affyPLM is required to interrogate celfiles.gcrma
 library(affyPLM)
 boxplot(data.gcrma, col=cols)
 # the boxplots are somewhat skewed by the normalisation algorithm
 # and it is often more informative to look at density plots
 # Plot a density vs log intensity histogram for the unnormalised data
 hist(data, col=cols)
 # Plot a density vs log intensity histogram for the normalised data
 hist(data.gcrma, col=cols)
```

```
# Perform probe-level metric calculations on the CEL files:
 data.qc <- fitPLM(data)
 # Create an image of the first file:
 image(data.qc, which=1, add.legend=TRUE)
 # to make a heat map of the other files change the number after which=
 image(data.qc, which=4, add.legend=TRUE)
 # affyPLM provides more informative boxplots
 # RLE (Relative Log Expression) plots should have values close to 0 so check for outliers

 RLE(data.qc, main="RLE")

 # We can also use NUSE (Normalised Unscaled Standard Errors).
 # The median standard error should be 1 for most genes - check for outliers

 NUSE(celfiles.qc, main="NUSE")

#you can also do some cluster analysis

eset <- exprs(data.gcrma)
 distance <- dist(t(eset),method="maximum")
 clusters <- hclust(distance)
plot(clusters)


#extract the annotated chip info that you want from the .db file

Annot <- data.frame(ACCNUM=sapply(contents(rat2302ACCNUM), paste, collapse=", "),
SYMBOL=sapply(contents(rat2302SYMBOL), paste, collapse=", "), DESC=sapply(contents(rat2302GENENAME),
paste, collapse=", "), UNIPROT=sapply(contents(rat2302UNIPROT), paste, collapse=",
"),REFSEQ=sapply(contents(rat2302REFSEQ), paste, collapse=", "))

#make a data frame with the expression data from your normalised .cel file data

my_frame <- data.frame(exprs(data.gcrma))

#now combine the two

all <- merge(Annot, my_frame, by.x=0, by.y=0, all=T)

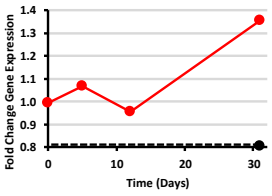
#and write to a tab-delimited text file, this can be opened in excel (select tab-delimited)

write.table(all,file="Annoted_Normalised_Data.txt",sep="\t")
```

SI.3.2 Additional time course graphs from the BCG MS-like lesion model in rats

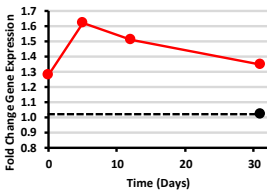
| Supplemental Table 3.1| Data summary of gene expression transcripts over time comparing BCG lesions to vehicle lesions

B2m



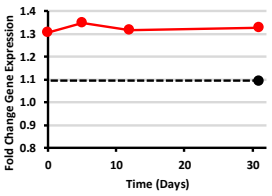
Beta-2-microglobulin
antigen processing and presentation of peptide antigen *via* MHC class I
cytokine-mediated signaling pathway
innate immune response
interferon-gamma-mediated signaling pathway
regulation of defense response to virus by virus
regulation of immune response
viral process

Col1a1



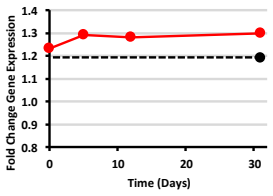
Collagen type I, alpha 1
blood coagulation
blood vessel development
collagen biosynthetic process
extracellular matrix organization
leukocyte migration
platelet activation
positive regulation of epithelial to mesenchymal transition

Rapgef4



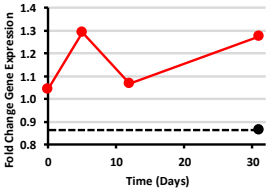
Rap guanine nucleotide exchange factor 4
G-protein coupled receptor signaling pathway
blood coagulation
energy reserve metabolic process
platelet activation
positive regulation of GTPase activity
positive regulation of Ras GTPase activity
regulation of insulin secretion
small molecule metabolic process

Slc1a3



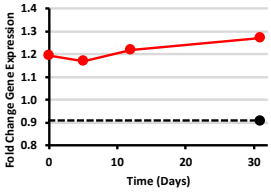
solute carrier family 1 (glial high affinity glutamate transporter), member 3
D-aspartate import
L-glutamate import
L-glutamate transmembrane transport
ion transport
neurotransmitter uptake
synaptic transmission
transmembrane transport [TAS]

Igkv28 /// LOC500183



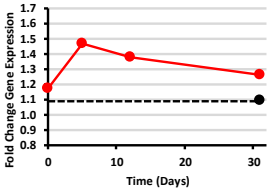
Igkc immunoglobulin kappa constant
Fc-epsilon receptor signalling pathway
Fc-gamma receptor signalling pathway involved in phagocytosis
complement activation
complement activation, classical pathway
immune response
innate immune response
regulation of immune response

Aif1 /// IBA1



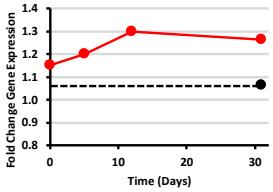
Allograft inflammatory factor 1, ionized calcium-binding adapter molecule 1 (IBA1)
DNA catabolic process
activation of cysteine-type endopeptidase activity involved in apoptotic process
apoptotic DNA fragmentation
apoptotic process
chromosome condensation
intrinsic apoptotic signaling pathway in response to endoplasmic reticulum stress
mitochondrial respiratory chain complex I assembly
neuron differentiation
positive regulation of apoptotic process

Col1a1



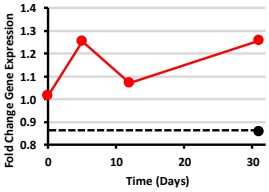
Collagen type I, alpha 1
blood coagulation
blood vessel development
collagen biosynthetic process
extracellular matrix organization
leukocyte migration
platelet activation
positive regulation of epithelial to mesenchymal transition

Ptprz1



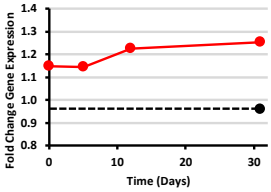
protein tyrosine phosphatase, receptor-type, Z polypeptide 1
central nervous system development
learning or memory
oligodendrocyte differentiation
peptidyl-tyrosine dephosphorylation
protein dephosphorylation
regulation of oligodendrocyte progenitor proliferation

Igkv28 /// LOC500183



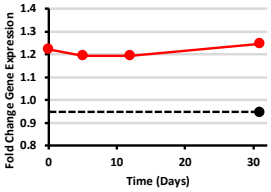
Igkc immunoglobulin kappa constant
Fc-epsilon receptor signalling pathway
Fc-gamma receptor signalling pathway involved in phagocytosis
complement activation
complement activation, classical pathway
immune response
innate immune response
regulation of immune response

Cd48



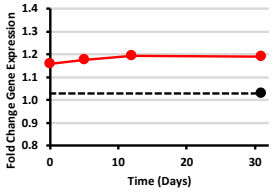
CD48 antigen
blood coagulation
defense response
leukocyte migration

Aif1 /// IBA1



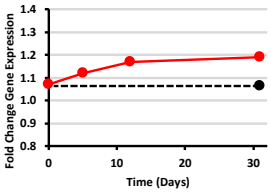
Allograft inflammatory factor 1, ionized calcium-binding adapter molecule 1 (IBA1)
DNA catabolic process
activation of cysteine-type endopeptidase activity involved in apoptotic process
apoptotic DNA fragmentation
apoptotic process
chromosome condensation
intrinsic apoptotic signaling pathway in response to endoplasmic reticulum stress
mitochondrial respiratory chain complex I assembly
neuron differentiation
positive regulation of apoptotic process

Ptn



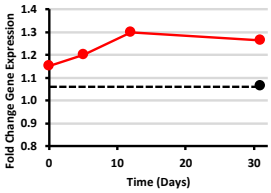
Pleiotrophin, heparin-binding brain mitogen (HBBM), heparin-binding growth factor 8 (HBGF-8), neurite growth-promoting factor 1 (NEGF1)
heparin binding
proteoglycan binding
vascular endothelial growth factor binding
brain development
cellular response to hypoxia
cellular response to platelet-derived growth factor stimulus
endothelial cell differentiation
liver development
negative regulation of cell migration
negative regulation of epithelial cell proliferation
positive regulation of cell-substrate adhesion
positive regulation of hepatocyte proliferation

Gria3



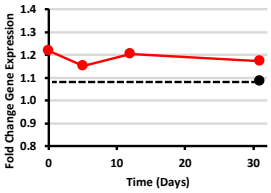
Glutamate receptor 3
glutamate receptor signaling pathway
ion transmembrane transport
ionotropic glutamate receptor signaling pathway
synaptic transmission
synaptic transmission, glutamatergic transport

Ptprz1



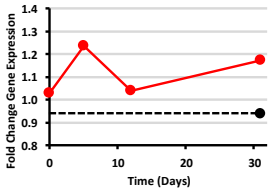
protein tyrosine phosphatase, receptor-type, Z polypeptide 1
central nervous system development
learning or memory
oligodendrocyte differentiation
peptidyl-tyrosine dephosphorylation
protein dephosphorylation
regulation of oligodendrocyte progenitor proliferation

Nktr



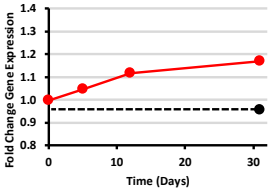
NK-tumor recognition protein
cyclosporin A binding
peptidyl-prolyl cis-trans isomerase activity
protein folding

Igkv28 /// LOC500183



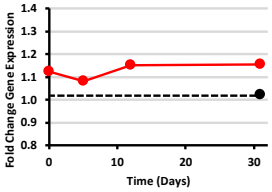
Igkc immunoglobulin kappa constant
Fc-epsilon receptor signalling pathway
Fc-gamma receptor signalling pathway involved in phagocytosis
complement activation
complement activation, classical pathway
immune response
innate immune response
regulation of immune response

Pafah1b1



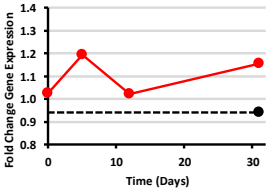
Platelet-activating factor acetylhydrolase IB subunit alpha
dynactin binding
dynein binding
heparin binding
microtubule binding
phospholipase binding
phosphoprotein binding
actin cytoskeleton organization
brain morphogenesis

Il33



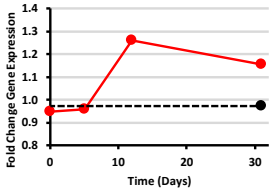
Interleukin-33
positive regulation of chemokine secretion
positive regulation of inflammatory response
positive regulation of macrophage activation
positive regulation of transcription from RNA polymerase II promoter
type 2 immune response

Igkv28 /// LOC500183



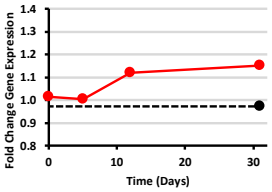
Igkc immunoglobulin kappa constant
Fc-epsilon receptor signalling pathway
Fc-gamma receptor signalling pathway
involved in phagocytosis
complement activation
complement activation, classical pathway
immune response
innate immune response
regulation of immune response

Oxt



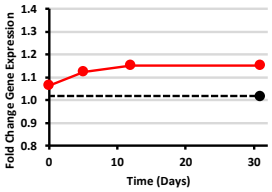
Oxytocin, neurophysin I prepropeptide
neuropeptide hormone activity
oxytocin receptor binding
memory
positive regulation of blood pressure
response to glucocorticoid
response to mechanical stimulus
response to retinoic acid
response to steroid hormone
various

Crp



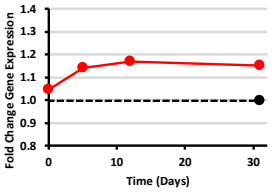
C-reactive protein
acute-phase response
defense response to Gram-positive bacterium
inflammatory response
negative regulation of lipid storage
negative regulation of macrophage derived foam cell differentiation
negative regulation of vasodilation
opsonization
positive regulation of gene expression
positive regulation of superoxide anion generation
regulation of interleukin-8 secretion

Slc6a1



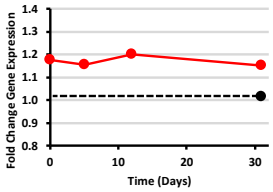
Sodium- and chloride-dependent GABA transporter 1
gamma-aminobutyric acid import
gamma-aminobutyric acid transport
negative regulation of synaptic transmission, GABAergic
neurotransmitter transport
positive regulation of gamma-aminobutyric acid secretion
protein homooligomerizatio

Bdnf



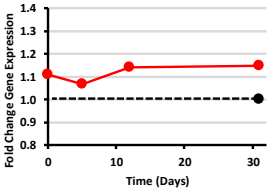
Brain-derived neurotrophic factor
negative regulation of neuron apoptotic process
nervous system development
neuron projection morphogenesis
regulation of synapse assembly
regulation of neuron differentiation
transmembrane receptor protein tyrosine kinase signaling pathway

Gabra4



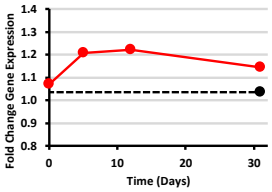
Gamma-aminobutyric acid receptor subunit alpha-4
benzodiazepine receptor activity
chloride channel activity
extracellular ligand-gated ion channel activity
GABA-A receptor activity
central nervous system development
chemical synaptic transmission, postsynaptic

Endrb



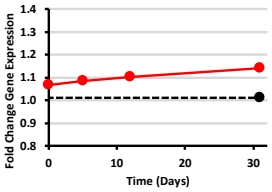
Endothelin receptor type B
endothelin receptor signaling pathway
enteric nervous system development
enteric smooth muscle cell differentiation
macrophage chemotaxis
negative regulation of cellular protein metabolic process
nervous system development
vasoconstriction
vein smooth muscle contraction

Acta2



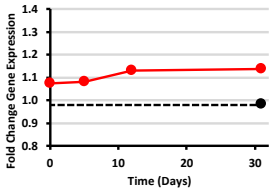
Actin, aortic smooth muscle
glomerular mesangial cell development
muscle contraction
response to virus

Alcam



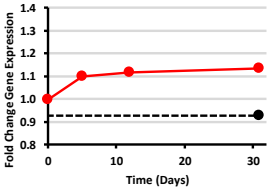
CD166 antigen, Activated leukocyte cell adhesion molecule
adaptive immune response
axon extension involved in axon guidance
cell adhesion
heterophilic cell-cell adhesion *via* plasma membrane cell adhesion molecules
motor neuron axon guidance
neuron projection extension
retinal ganglion cell axon guidance

Sepp1



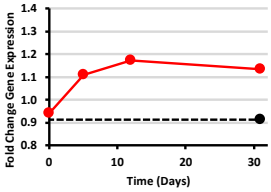
Selenoprotein P
brain development
growth
locomotory behavior
platelet degranulation
post-embryonic development
response to oxidative stress
selenium compound metabolic process

CD74



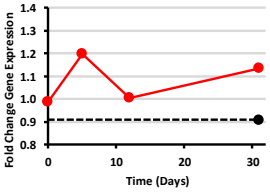
CD74 antigen, H-2 class II histocompatibility antigen gamma chain
T cell selection
antigen processing and presentation of exo- and endogenous peptide antigen *via* MHC class II
cell proliferation
immunoglobulin mediated immune response
positive regulation of B cell proliferation
positive regulation of chemokine (C-X-C motif) ligand 2 production
positive regulation of cytokine-mediated signaling pathway
positive regulation of macrophage cytokine production
positive regulation of neutrophil chemotaxis

CD74



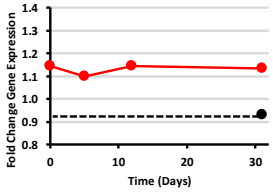
CD74 antigen, H-2 class II histocompatibility antigen gamma chain
T cell selection
antigen processing and presentation of exo- and endogenous peptide antigen *via* MHC class II
cell proliferation
immunoglobulin mediated immune response
positive regulation of B cell proliferation
positive regulation of chemokine (C-X-C motif) ligand 2 production
positive regulation of cytokine-mediated signaling pathway
positive regulation of macrophage cytokine production
positive regulation of neutrophil chemotaxis

Igkv28 /// LOC500183



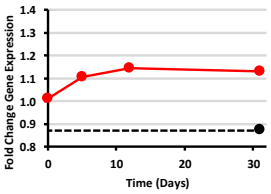
Igkc immunoglobulin kappa constant
Fc-epsilon receptor signalling pathway
Fc-gamma receptor signalling pathway involved in phagocytosis
complement activation
complement activation, classical pathway
immune response
innate immune response
regulation of immune response

Dbi



Diazepam binding inhibitor (GABA receptor modulator, acyl-CoA binding protein)
benzodiazepine receptor binding
lipid binding
phosphatidylcholine acyl-chain remodelling
transport

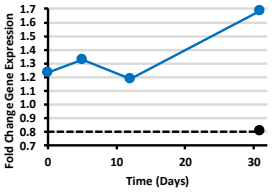
Lcn2



Lipocalin-2, Neutrophil gelatinase-associated lipocalin (NGAL)
cellular response to interleukin-1
cellular response to lipopolysaccharide
cellular response to nutrient levels
cellular response to tumor necrosis factor
innate immune response
ion transport and homeostasis
positive regulation of cell projection organization
response to bacterium
response to oxidative stress
response to virus
siderophore transport

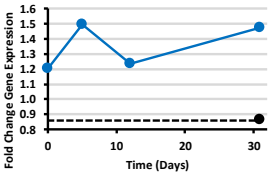
| Supplemental Table 3.2| Data summary of gene expression transcripts over time comparing BCG lesions to naïve brain lesion-sites

B2m



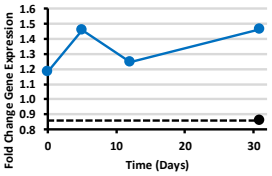
Beta-2-microglobulin
antigen processing and presentation of peptide antigen *via* MHC class I
cytokine-mediated signaling pathway
innate immune response
interferon-gamma-mediated signaling pathway
regulation of defense response to virus by virus
regulation of immune response
viral process

Igkv28 /// LOC500183



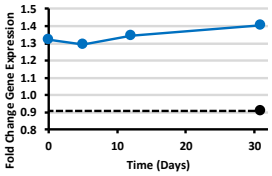
Igkc immunoglobulin kappa constant
Fc-epsilon receptor signalling pathway
Fc-gamma receptor signalling pathway involved in phagocytosis
complement activation
complement activation, classical pathway
immune response
innate immune response
regulation of immune response

Igkv28 /// LOC500183



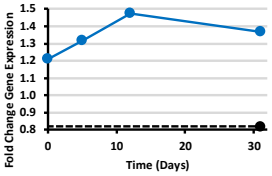
Igkc immunoglobulin kappa constant
Fc-epsilon receptor signalling pathway
Fc-gamma receptor signalling pathway involved in phagocytosis
complement activation
complement activation, classical pathway
immune response
innate immune response
regulation of immune response

Aif /// IBA1



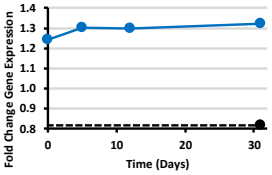
Allograft inflammatory factor 1, ionized calcium-binding adapter molecule 1 (IBA1)
DNA catabolic process
activation of cysteine-type endopeptidase activity involved in apoptotic process
apoptotic DNA fragmentation
apoptotic process
chromosome condensation
intrinsic apoptotic signaling pathway in response to endoplasmic reticulum stress
mitochondrial respiratory chain complex I assembly
neuron differentiation
positive regulation of apoptotic process

Cxcl13



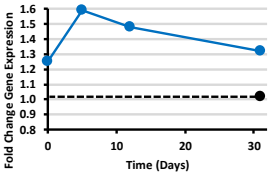
Chemokine (C-X-C motif) ligand 13, B lymphocyte chemoattractant (BLC)
B cell chemotaxis
activation of Rap GTPase activity
cell surface receptor signaling pathway
cell-cell signaling
chemokine-mediated signaling pathway
chronic inflammatory response
defense response to bacterium
endothelial cell chemotaxis to fibroblast growth factor
germinal center formation
lymphocyte chemotaxis across high endothelial venule
positive regulation of cell-cell adhesion mediated by integrin
positive regulation of integrin activation
response to lipopolysaccharide

Olfm1



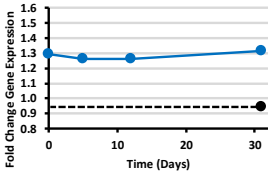
Olfactomedin 1, noelin 1
atrioventricular valve formation
cardiac epithelial to mesenchymal transition
negative regulation of gene expression
neuronal signal transduction
positive regulation of epithelial to mesenchymal transition
positive regulation of gene expression
regulation of axon extension

Col1a1



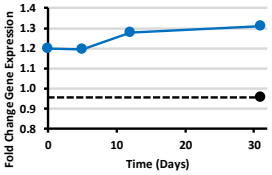
Collagen type I, alpha 1
blood coagulation
blood vessel development
collagen biosynthetic process
extracellular matrix organization
leukocyte migration
platelet activation
positive regulation of epithelial to mesenchymal transition

Aif1 /// IBA1



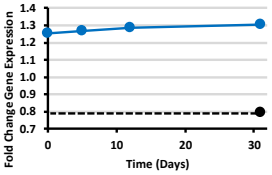
Allograft inflammatory factor 1, ionized calcium-binding adapter molecule 1 (IBA1)
DNA catabolic process
activation of cysteine-type endopeptidase activity involved in apoptotic process
apoptotic DNA fragmentation
apoptotic process
chromosome condensation
intrinsic apoptotic signaling pathway in response to endoplasmic reticulum stress
mitochondrial respiratory chain complex I assembly
neuron differentiation
positive regulation of apoptotic process

CD48



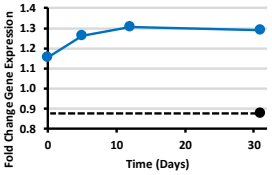
CD48 antigen
blood coagulation
defense response
leukocyte migration

Scg3



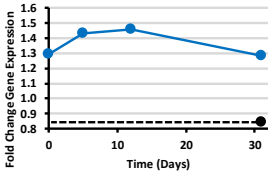
Secretogranin III
blood coagulation
platelet activation
platelet degranulation

Lcn2

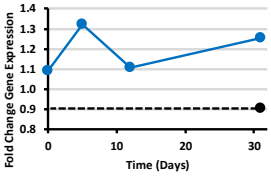


Lipocalin-2, Neutrophil gelatinase-associated lipocalin (NGAL)
cellular response to interleukin-1
cellular response to lipopolysaccharide
cellular response to nutrient levels
cellular response to tumor necrosis factor
innate immune response
ion transport and homeostasis
positive regulation of cell projection organization
response to bacterium
response to oxidative stress
response to virus
siderophore transport

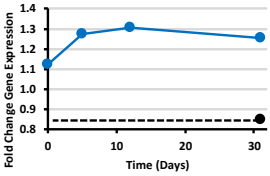
Spp1



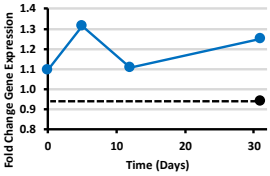
secreted phosphoprotein 1, Osteopontin, bone sialoprotein I (BSP-1), early T-lymphocyte activation (ETA-1)
biomineral tissue development
cell adhesion
decidualization
embryo implantation
extracellular matrix organization
inflammatory response
negative regulation of collateral sprouting of intact axon in response to injury
osteoblast differentiation
response to steroid hormone
response to vitamin D



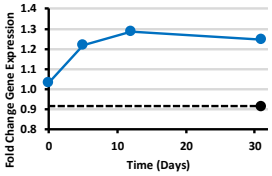
Igkc immunoglobulin kappa constant
Fc-epsilon receptor signalling pathway
Fc-gamma receptor signalling pathway
involved in phagocytosis
complement activation
complement activation, classical pathway
immune response
innate immune response
regulation of immune response



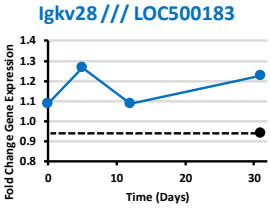
Neuronatin
brain development
neuron differentiation
positive regulation of insulin secretion
protein lipoylation



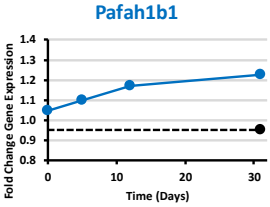
Igkc immunoglobulin kappa constant
Fc-epsilon receptor signalling pathway
Fc-gamma receptor signalling pathway
involved in phagocytosis
complement activation
complement activation, classical pathway
immune response
innate immune response
regulation of immune response



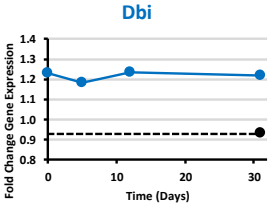
CD74 antigen, H-2 class II histocompatibility antigen gamma chain
T cell selection
antigen processing and presentation of exo- and endogenous peptide antigen *via* MHC class II
cell proliferation
immunoglobulin mediated immune response
positive regulation of B cell proliferation
positive regulation of chemokine (C-X-C motif) ligand 2 production
positive regulation of cytokine-mediated signaling pathway
positive regulation of macrophage cytokine production
positive regulation of neutrophil chemotaxis



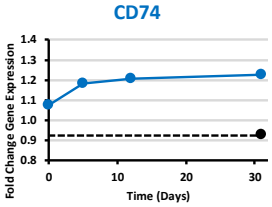
Igkc immunoglobulin kappa constant
Fc-epsilon receptor signalling pathway
Fc-gamma receptor signalling pathway
involved in phagocytosis
complement activation
complement activation, classical pathway
immune response
innate immune response
regulation of immune response



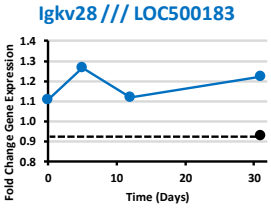
Platelet-activating factor acetylhydrolase IB subunit alpha
dynactin binding
dynein binding
heparin binding
microtubule binding
phospholipase binding
phosphoprotein binding
actin cytoskeleton organization
brain morphogenesis



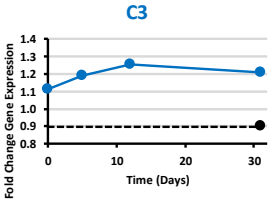
Diazepam binding inhibitor (GABA receptor modulator, acyl-CoA binding protein)
benzodiazepine receptor binding
lipid binding
phosphatidylcholine acyl-chain remodelling
transport



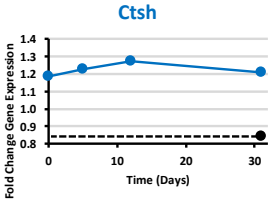
CD74 antigen, H-2 class II histocompatibility antigen gamma chain
T cell selection
antigen processing and presentation of exo- and endogenous peptide antigen *via* MHC class II
cell proliferation
immunoglobulin mediated immune response
positive regulation of B cell proliferation
positive regulation of chemokine (C-X-C motif) ligand 2 production
positive regulation of cytokine-mediated signaling pathway
positive regulation of macrophage cytokine production
positive regulation of neutrophil chemotaxis



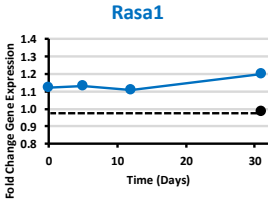
Igkc immunoglobulin kappa constant
Fc-epsilon receptor signalling pathway
Fc-gamma receptor signalling pathway
involved in phagocytosis
complement activation
complement activation, classical pathway
immune response
innate immune response
regulation of immune response



Complement component 3
blood coagulation
complement activation
complement activation, alternative pathway
complement activation, classical pathway
immune response
positive regulation of activation of membrane attack complex
positive regulation of angiogenesis positive regulation of apoptotic cell clearance
positive regulation of vascular endothelial growth factor production

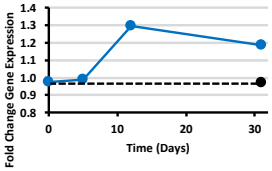


Cathepsin H
T cell mediated cytotoxicity
activation of cysteine-type endopeptidase activity involved in apoptotic process
adaptive immune response
antigen processing and presentation
cellular response to thyroid hormone stimulus
membrane protein proteolysis
positive regulation of cell migration
positive regulation of cell proliferation
positive regulation of epithelial cell migration
proteolysis



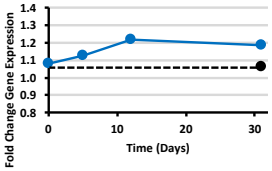
Ras GTPase-activating protein 1
glycoprotein binding
blood vessel morphogenesis
intracellular signal transduction
negative regulation of cell adhesion
negative regulation of cell-matrix adhesion
regulation of actin filament polymerization
vasculogenesis

Oxt



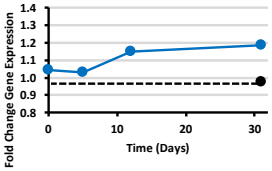
Oxytocin, neurophysin I prepropeptide
neuropeptide hormone activity
oxytocin receptor binding
memory
positive regulation of blood pressure
response to glucocorticoid
response to mechanical stimulus
response to retinoic acid
response to steroid hormone
various

Ptprz1



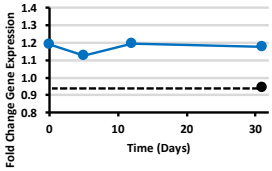
protein tyrosine phosphatase, receptor-type, Z polypeptide 1
central nervous system development
learning or memory
oligodendrocyte differentiation
peptidyl-tyrosine dephosphorylation
protein dephosphorylation
regulation of oligodendrocyte progenitor proliferation

Crp



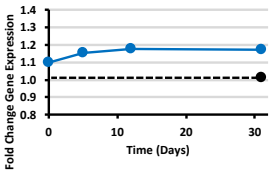
C-reactive protein
acute-phase response
defense response to Gram-positive bacterium
inflammatory response
negative regulation of lipid storage
negative regulation of macrophage derived foam cell differentiation
negative regulation of vasodilation
opsonization
positive regulation of gene expression
positive regulation of superoxide anion generation
regulation of interleukin-8 secretion

Il18



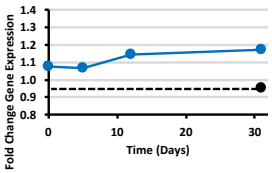
Interleukin-18
T-helper 1 type immune response
angiogenesis
cell-cell signaling
chemokine biosynthetic process
immune response
positive regulation of NK T cell proliferation
positive regulation of activated T cell proliferation
positive regulation of granulocyte macrophage colony-stimulating factor production
positive regulation of tissue remodelling
regulation of cell adhesion
sleep
type 2 immune response

Ptprz1



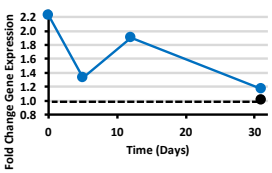
protein tyrosine phosphatase, receptor-type, Z polypeptide 1
central nervous system development
learning or memory
oligodendrocyte differentiation
peptidyl-tyrosine dephosphorylation
protein dephosphorylation
regulation of oligodendrocyte progenitor proliferation

Crp



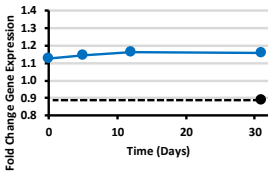
C-reactive protein
acute-phase response
defense response to Gram-positive bacterium
inflammatory response
negative regulation of lipid storage
negative regulation of macrophage derived foam cell differentiation
negative regulation of vasodilation
opsonization
positive regulation of gene expression
positive regulation of superoxide anion generation
regulation of interleukin-8 secretion

Ttr



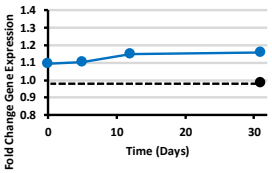
Transthyretin
thyroxine (T_4) and retinol-binding
extracellular matrix
phototransduction, visible light
retinoid metabolic process [TAS]

Ptn



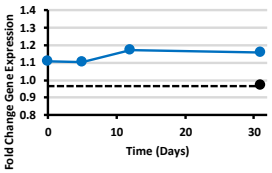
Pleiotrophin, heparin-binding brain mitogen (HBBM), heparin-binding growth factor 8 (HBGF-8), neurite growth-promoting factor 1 (NEGF1)
heparin binding
proteoglycan binding
vascular endothelial growth factor binding
brain development
cellular response to hypoxia
cellular response to platelet-derived growth factor stimulus
endothelial cell differentiation
liver development
negative regulation of cell migration
negative regulation of epithelial cell proliferation
positive regulation of cell-substrate adhesion
positive regulation of hepatocyte proliferation

Sepp1



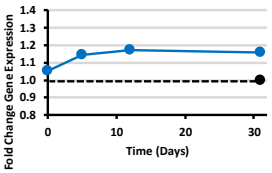
Selenoprotein P
brain development
growth
locomotory behavior
platelet degranulation
post-embryonic development
response to oxidative stress
selenium compound metabolic process

B2m



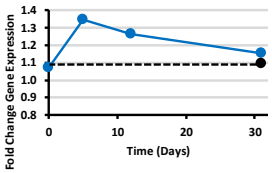
Beta-2-microglobulin
antigen processing and presentation of peptide antigen *via* MHC class I
cytokine-mediated signaling pathway
innate immune response
interferon-gamma-mediated signaling pathway
regulation of defense response to virus by virus
regulation of immune response
viral process

Bdnf



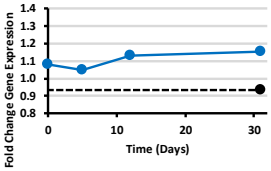
Brain-derived neurotrophic factor
negative regulation of neuron apoptotic process
nervous system development
neuron projection morphogenesis
regulation of synapse assembly
regulation of neuron differentiation
transmembrane receptor protein tyrosine kinase signaling pathway

Col1a1



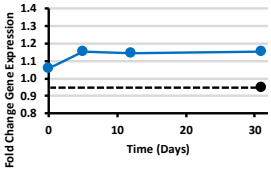
Collagen type I, alpha 1
blood coagulation
blood vessel development
collagen biosynthetic process
extracellular matrix organization
leukocyte migration
platelet activation
positive regulation of epithelial to mesenchymal transition

Atp2b1



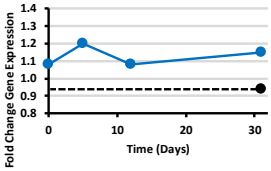
ATPase, Ca^{++} transporting, plasma membrane 1
blood coagulation
ion transmembrane transport
transmembrane transport
brain development

CD74



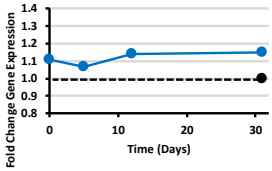
CD74 antigen, H-2 class II histocompatibility antigen gamma chain
T cell selection
antigen processing and presentation of exo- and endogenous peptide antigen *via* MHC class II
cell proliferation
immunoglobulin mediated immune response
positive regulation of B cell proliferation
positive regulation of chemokine (C-X-C motif) ligand 2 production
positive regulation of cytokine-mediated signalling pathway
positive regulation of macrophage cytokine production
positive regulation of neutrophil chemotaxis

Igkv28 /// LOC500183



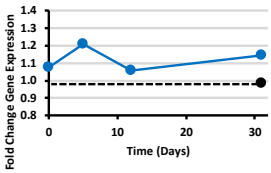
Igkc immunoglobulin kappa constant
Fc-epsilon receptor signalling pathway
Fc-gamma receptor signalling pathway involved in phagocytosis
complement activation
complement activation, classical pathway
immune response
innate immune response
regulation of immune response

Ednrb



Endothelin receptor type B
endothelin receptor signaling pathway
enteric nervous system development
enteric smooth muscle cell differentiation
macrophage chemotaxis
negative regulation of cellular protein metabolic process
nervous system development
vasoconstriction
vein smooth muscle contraction

Igkv28 /// LOC500183



Igkc immunoglobulin kappa constant
Fc-epsilon receptor signalling pathway
Fc-gamma receptor signalling pathway involved in phagocytosis
complement activation
complement activation, classical pathway
immune response
innate immune response
regulation of immune response

4

| FUTURE APPLICATIONS |

ELEMENTAL MAPPING OF BRAIN INFLAMMATION AND LEWIS^A-LABELLING OF EXTRACELLULAR VESICLES

The unprecedented binding of Lewis[a]-MPIO to E-Selectin during the acute *in vivo* model of brain inflammation has great potential to develop new contrast agents and targeted delivery systems. This chapter summarises performed pilot-experiments that could potentially be future applications of Lewis[a]-based tools. As mentioned in the introduction, XRF can simultaneously map the naturally occurring elements in biological tissue and xenobiotic elements that are administered. The power of XRF analysis of the brain allows visualisation of the amount of markers at a time using xenobiotic elements as 'contrast agents' whilst simultaneously imaging biological elements. The changes in naturally occurring elements during a disease model such as acute brain inflammation and the xenobiotic contrast agent could potentially reveal interesting elemental changes. The brain endovascular inflammation markers E-Selectin:Lewis[a] and previously established VCAM-1 have never been assessed together before and XRF could allow imaging of these markers in one specimen by using two distinct xenobiotic nanoparticles. The use of nanoparticles of different non-biological elements is in this case is of key importance because Lewis[a] can only effectively function as an imaging tool when conjugated to nanoparticles. This chapter describes the initial proof-of-concept experiments for XRF-based imaging of brain inflammation. The last part includes the modification of extracellular vesicles (EV) and liposomes with Lewis[a]-lipids for retargeting purposes. The tracking of these EVs is challenging as their elemental composition is similar to the tissue analysed. Using an established fluorescent-labelling protocol to label the vesicles for fluorescence microscopy, aggregation issues and high background fluorescence required a different strategy to label and detect these EVs in tissue. Using a non-mammalian miRNA to transfect the EVs proved to work, however no retargeting was observed using Lewis[a]-lipid labelled EVs transfected with the miRNA in the IL-1β brain inflammation model. A reductionist model using liposomes labelled with Lewis[a]-lipids in the IL-1β brain inflammation model worked in a single proof-of-concept experiment and could provide basis for further experiments.

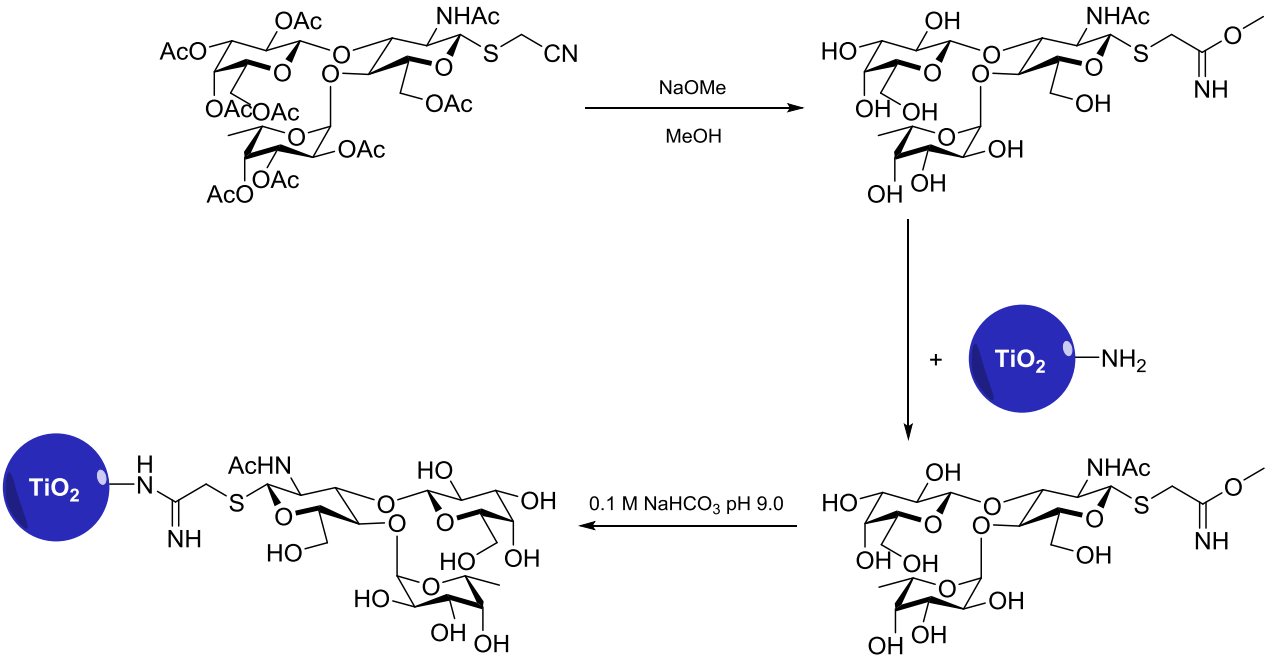
4.1 | XRF IMAGING OF BRAIN INFLAMMATION USING XENOBIOTIC TARGETED NANOPARTICLES

4.1.1 Strategy for the generation of targeted XRF imaging agents using the I18 beamline at Diamond

XRF imaging is typically not combined with a 'contrast agent' and no brain specimens to date have been generated where an agent is specifically targeted to a site within the brain. Due to the resolving power of XRF and the detailed information about the elemental composition of the specimen, XRF brain imaging with nanoparticles of xenobiotic elements could prove to be a useful technique to study brain inflammation. Additionally, Lewis[a] MPIO nanoparticles accumulate at the inflamed site and could provide a useful 'tool' to explore the use of other nanoparticles for XRF imaging. Nanoparticles typically used for imaging have XRF emission lines that overlap with most common biological elements and therefore are not suitable to use in XRF targeted imaging. See **Chapter 1**, **Figure 1.12** for an overview of compatible elements for XRF imaging. In addition, The XRF imaging field lacks targeted imaging agents to study brain inflammation, whilst simultaneously mapping the biological elements at a high resolution. Elements like Titanium (Ti) and Zirconium (Zr) with distinct XRF lines (falling within the Diamond I18 Beam-Line range) are most suitable for the design of targeted XRF probes. Additionally, the size range of these particles (nano-to micron sized) allows us to functionalize the surface with a higher density of molecules increasing the multivalent nanoparticle display. Due to the brief exposure (1h) of these nanoparticles in the experimental animals, no adverse side effects are expected of the associated toxicity of these nanoparticles [442], [443], [444]. Titanium, combined with iron, has been successfully used before to XRF image nuclear translocation in cancer cells [290]. However, Zr-based nanoparticles have not yet been used in XRF imaging. Although zirconium nanoparticles were tested without biological tissue (*data not shown)* and provided a clear signal, Zr requires a higher excitation energy (11.000 KeV). Due to this higher excitation energy, any samples of biological tissue with Zr nanoparticles would require two excitation rounds to visualise both the biologically occurring elements and Zr. Therefore Ti was trialled first, as with the same excitation energy (9.000 KeV) both exogenously administered Ti and the biologically occurring elements can be visualised in one round.

4.1.2 Functionalisation of titanium oxide nanoparticle XRF probes with Lewis[a]

Using the same Lewis[a]-functionalisation strategies as described in **Chapter 2**, Lewis[a]-Ti NP were generated from commercially available amine terminated titanium nanoparticles, see **Figure 4.1** below for the reaction scheme. Fluorescamine loading revealed a 46% coverage (*n*=1) using the protocol described elsewhere [298], [299].



| Figure 4.1 | Ti-nanoparticle functionalisation with IME-Lewis[a] The SCM-Lewis[a] product as described in **Chapter 2** and in **section 4.7.2** and **4.7.3** was used to functionalize the commercial Ti-nanoparticles using IME chemistry. The generated amine-reactive IME-Lewis[a] is coupled onto TiO_2 nanoparticles using mild aqueous conditions.

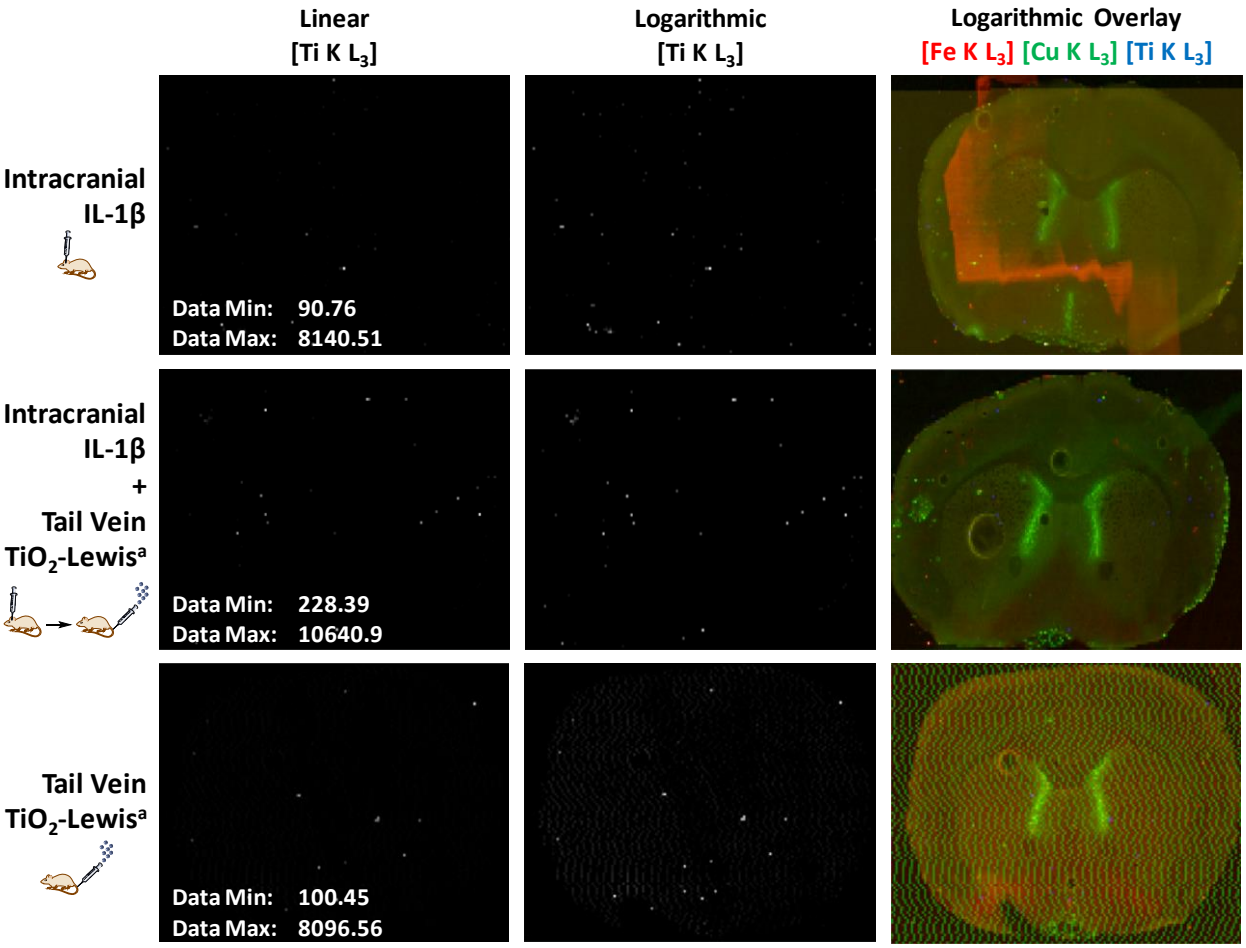
4.1.3 XRF Imaging of the generated XRF-Probes in brain sections at Diamond reveals Titanium contamination

An initial beam-time session at the Diamond Synchrotron I18 beam line (Didcot, UK) allowed only to generate three images (out of 10 samples) of 50 micron thick mouse brain sections with targeted Ti-nanoparticles using 9.000 KeV excitation energy. See section **4.5.4**.

Brain **#2**: an intracranial IL-1β injection in the left hemisphere to assess if there are any elemental changes in the left, inflamed hemisphere upon a 4h IL-1β stimulus.

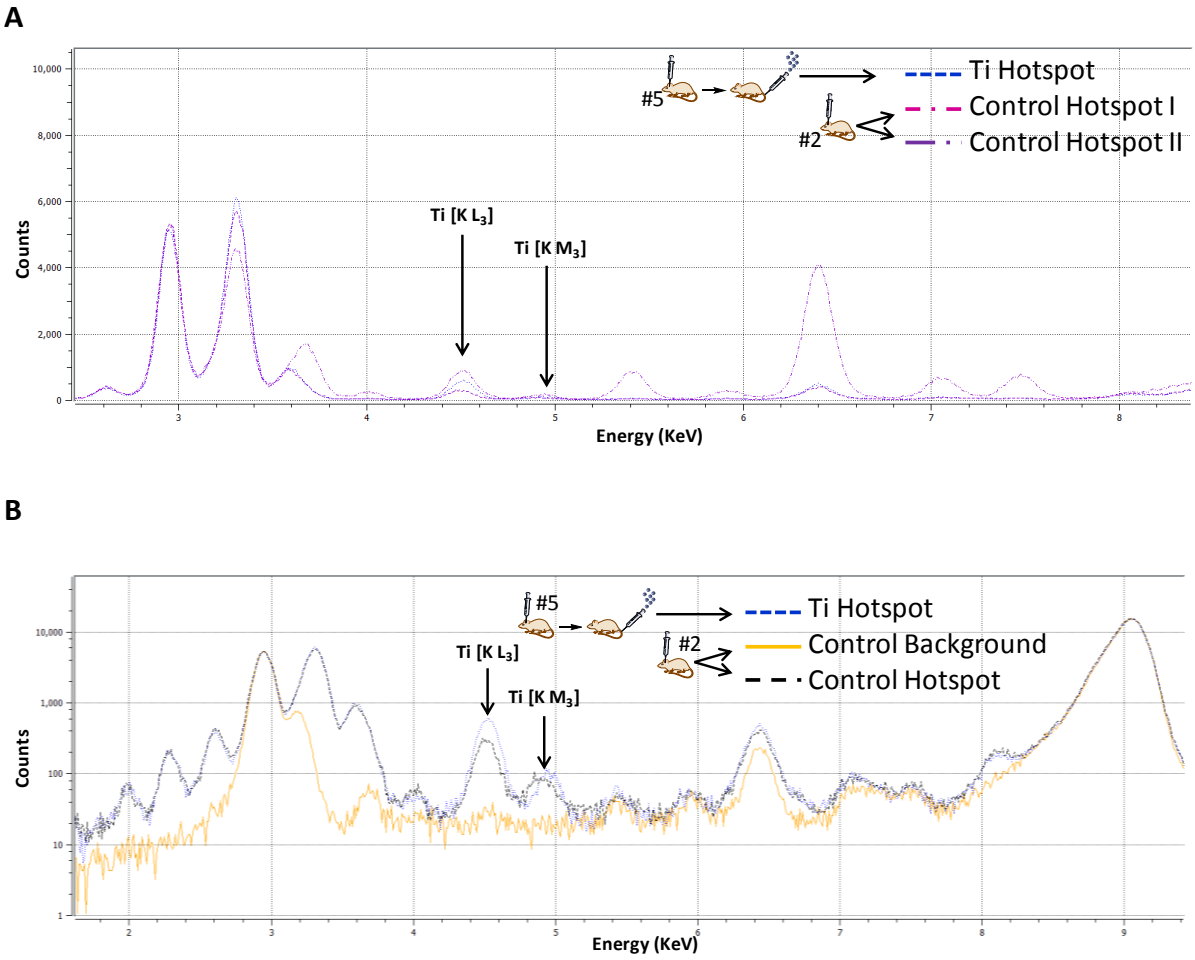
Brain **#5**: an intracranial IL-1β injection in the left hemisphere and a tail vein injection of titanium nanoparticles functionalised with Lewis^a (TiO_2-Lewis^a) after the 4h IL-1β stimulation to assess if the TiO_2-Lewis^a could be similarly accumulated to the inflamed left hemisphere as the MPIO-Lewis^a.

Brain **#6**: was untreated and a tail vein injection of TiO_2-Lewis^a was performed as a negative control and to assess the background levels of titanium when these particles are injected.

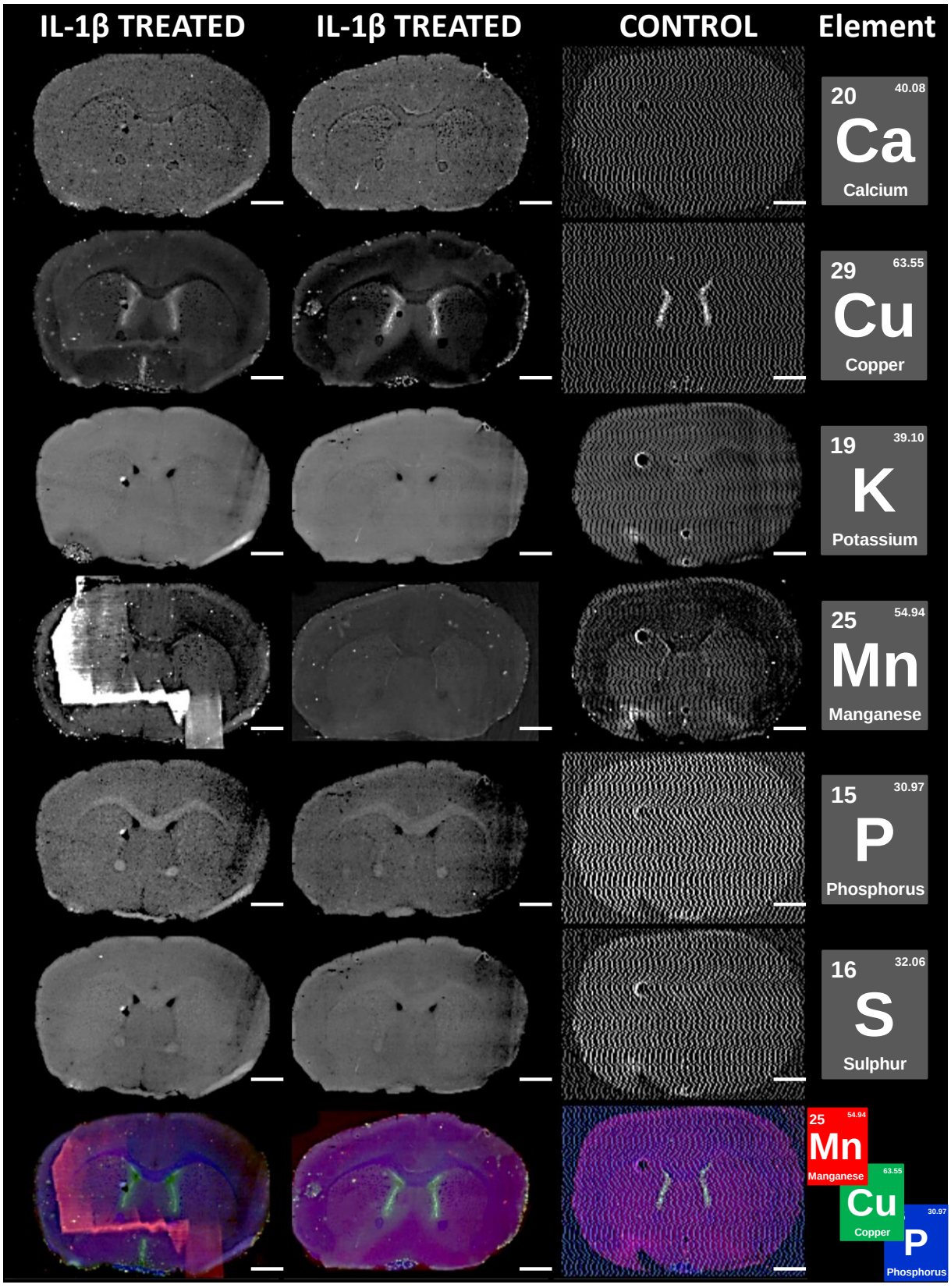


| Figure 4.2 | XRF elemental map of brain inflammation using the NP TiO_2-Lewis^a XRF probe reveals a Ti-contamination in the untreated brain Top to bottom are the samples measured: **#2** Intracranial IL-1β (115x170 data points), **#5**: IntracranialIL-1β + Tail Vein TiO_2-Lewis^a (105x163 data points), **#6** Tail Vein TiO_2-Lewis^a (113x161 data points). Left to right are different imaging modes for Titanium. Data Min and Data Max denote signal of the Ti K L_3 emission line measured (both linear and logarithmic). First panel (Linear Ti K L_3) shows the data points plotted in a linear mode, with a white signal being the highest intensity and back being the lowest. Second panel (Logarithmic Ti K L_3) plots the data points in a similar way using a logarithmic function. The last panel is a RGB overlay of the logarithmic signals from the (red) Fe K L_3, (green) Cu K L_3 and Ti K L_3(blue) emission lines to generate an image where anatomical features of the mouse brain can be seen.

The data analysis plotting for the most abundant Ti signal (K L_3) revealed a titanium contamination in all samples, whilst only brain **#5** (intracranial IL-1β + tail vein TiO_2-Lewis^a) was envisaged to reveal a titanium signal at the left inflamed hemisphere. As shown in **Figure 4.2**, Titanium is present in all samples and no significant NP TiO_2-Lewis^a accumulation is observed in the left hemisphere (IL-1β inflamed). Sample **#2** 'intracranial IL-1β only' should not contain any titanium, however hotspot analysis in **Figure 4.3** reveals the presence of Titanium. Conversely, when titanium is injected in the sample **#5** (intracranial IL-1β + tail vein TiO_2-Lewis^a) titanium is present at similar levels to the sample that does not contain any titanium. Due to a Ti-contamination, the visualization of Ti was unreliable and also no increased accumulation at the left inflamed site was seen using the NP TiO_2-Lewis^a.

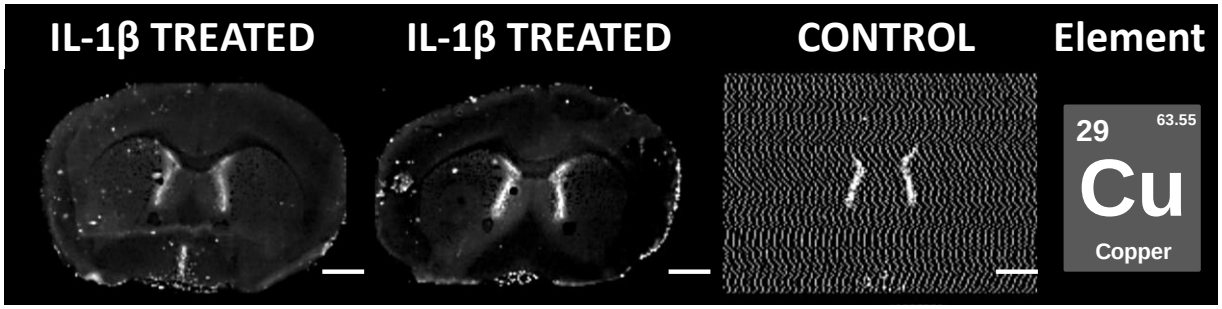


| Figure 4.3 | XRF Ti-hotspot analysis reveals the Ti-contamination **|A|** Hotspot analysis shows the XRF emission lines in KeV for a pixel/region from the acquired images. Ti hotspots (see image for line specifications) are present in all images acquired. **|B|** When the background (black pixels from **Figure 4.17**) is included in the hotspot analysis there is an absence of Ti signal, indicating hotspots do contain a measurable level of titanium.



| Figure 4. 4 | An XRF elemental map of endogenous elements in the inflamed brain An acute brain inflammation mouse model was used by injecting interleukin type 1 β (IL-1β) in the left hemisphere of the brain. 1h post XRF-probe injection 50 µm cryofixed brain sections were prepared. XRF maps of the endogenous elements were plotted and reveal district structural features. Scale bar 1 mm.

Although no NP TiO_2-Lewis[a] could be observed, the biological elements were mapped of the measured specimens to assess if there were any changes in biological elements that could be indicative of inflammation (left IL-1β hemisphere vs right control hemisphere), see **Figure 4.4** below. A manganese artefact can be observed and is probably iron-based (see **Figure 1.12**, for the close emission lines between Fe and Mn) and likely due to microtome cutting or uncareful handling. A zoom-in of Copper is shown in **Figure 4.5** and reveals accumulation of hotspots on the left-inflamed site. The resolution of these images is superior to other imaging techniques like Positron emission tomography (PET) and Magnetic resonance imaging (MRI), where only the distribution of one marker and/or ligand can be observed in the brain. However, no targeted imaging was observed for the Titanium nanoparticles functionalised with Lewis[a] as shown in **Figure 4.2**, however, Cu-accumulation can be seen in the left IL-1β inflamed hemisphere and will be discussed in **section 4.3**.



| Figure 4.5 | An XRF elemental map of Cu (copper) in the inflamed brain shows Cu-hotspots on the left IL-1β inflamed side XRF maps of the endogenous element Cu (Copper) in an acute brain inflammation mouse using interleukin type 1 β (IL-1β) injections in the left hemisphere of the brain to induce a local inflammatory response. The left hemisphere of the IL-1β treated brains shown Cu-hotspots (white specks). Scale bar 1 mm.

4.2 | RETARGETING OF BIOLOGICAL NANOPARTICLES TO SITES OF BRAIN INFLAMMATION WITH LEWIS[A]

4.2.1 Biological Functions of Lewis Antigens in Inflammation

There are 35 blood group systems and since humans can have an enormous variety of blood types (including ABH) and Lewis combinations, an evolutionary role of protecting the body against infections by having a variety of blood group antigens has been debated since blood group frequencies were shown to be different between individuals [445], [94]. Although extensive research has established that Lewis antigens and secretor status can play a role in bacterial, viral, parasitic and fungal adhesion, by either acting as an carbohydrate receptor or as a decoy for pathogens, their role in auto-immune diseases remains elusive [96]. Lewis[a/b] and/or secretor status is associated with multiple immune diseases which will be listed next. For Crohn's disease it has been shown that FUT2 polymorphisms can alter the gut microbiome and increase the risk for Crohn's disease [446], [447]. In obesity where especially Lewis[a/b] negative individuals have a marked increase in body weight and a higher risk of ischaemic heart disease [448]. Individuals with ischemic heart disease, without obesity, is more prevalent in Lewis[a/b] negative patients [449], [450]. And also, an altered gut microbiome can be influenced by the Lewis antigens presented at the exocrine epithelial cells of the intestinal mucosal epithelium and may have an influence on autoimmunity [451], [452], [453], [454], [455]. Blood type differences in neurological auto-immune diseases, like multiple sclerosis (MS), remains a topic of debate [133]. Whilst some reports [456], [457] have found no differences between blood group frequencies or secretor status in MS populations, others have shown differences, albeit unconvincingly, in Rhesus, ABO(H) and Lewis antigens associated with MS [458].

As shown in **Chapter 3**, the binding of Lewis[a]-MPIO in brain inflammation *via* an E-Selectin-mediated mechanism provokes what the role of Lewis[a] on biological nanoparticles may entail. As mentioned in **Chapter 1**, Lewis[a] and Lewis[b] glycolipids are synthesized by exocrine epithelial cells and secreted into the blood stream and passively absorbed by the cells present in the blood from blood lipoprotein particles [84]. Although the specific role of extracellular vesicles (EVs) in health and disease are still largely unknown, their role in disease and their increased or decreased levels can be indicative of ongoing inflammation and refer to **section 1.2.3** for more information regarding this. Interestingly, most isolated and purified circulating extracellular vesicles from blood used to study the roles of these vesicles have lipoprotein and chylomicron vesicles as a

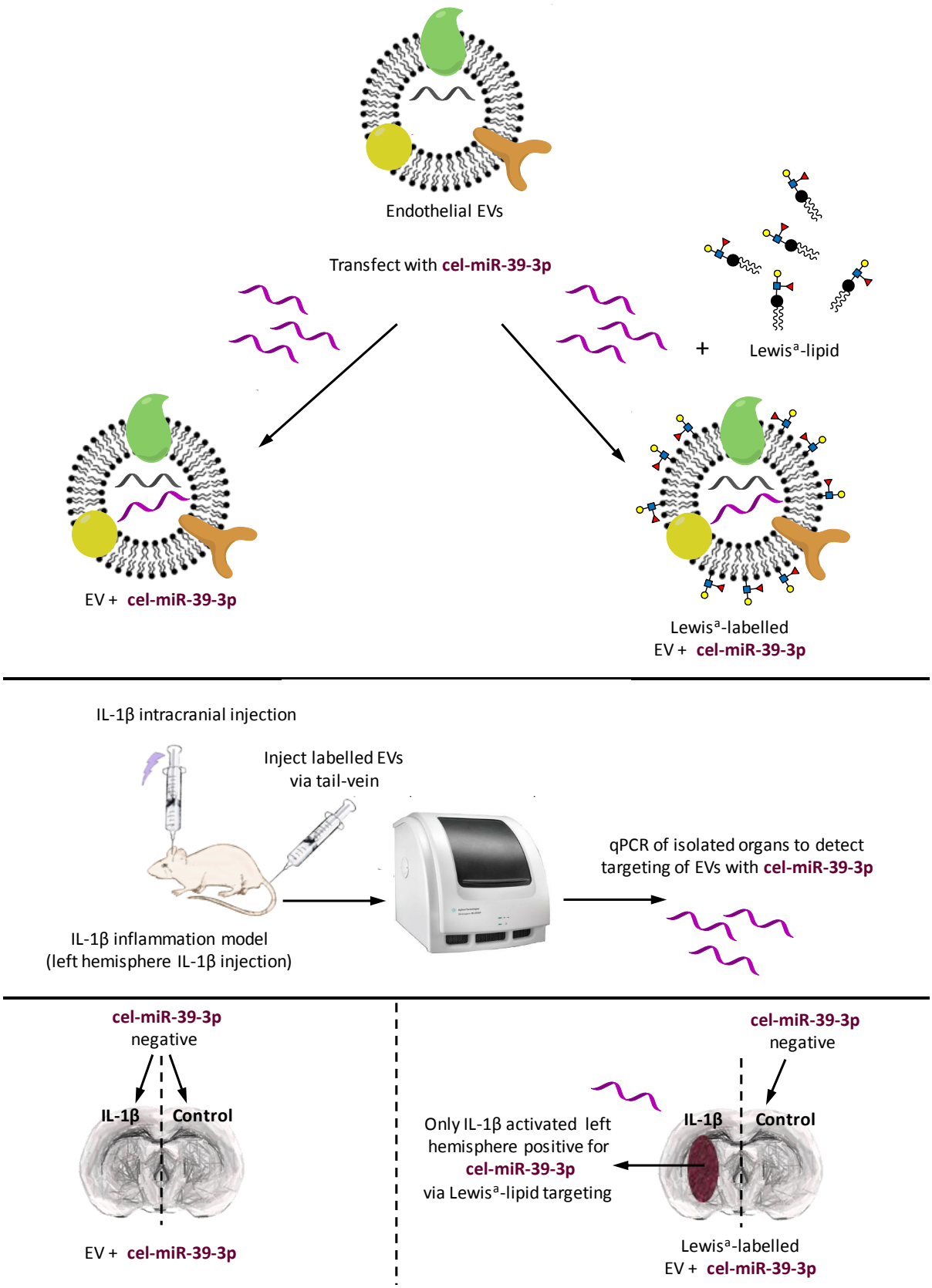
contaminant [459]. These 'contaminants' can mimic the characteristics of extracellular vesicles but are also the blood-derived source of Lewis[a] and Lewis[b] glycolipids. From these lipoprotein particles and chylomicrons blood cells (erythrocytes, leukocytes and platelets) can passively absorb the Lewis lipids onto their membranes [86], [87].

4.2.2 Labelling of extracellular vesicles for *in vivo* tracking

In order to establish if Lewis[a] glycolipids may play a role in inflammation or could be used as a re-targeting tool, this part of the thesis explores the Lewis[a] glycolipid manipulation of cell-culture derived extracellular vesicles from endothelial cells to make them Lewis[a] positive. By using rodent cells and EVs derived from culture instead of blood, the EVs are Lewis[a]-negative and have no lipoprotein and chylomicron vesicles. Because mice do not have FUT3 to synthesize Lewis[a] and the serum used for growing these cells was depleted from EVs, lipoprotein and chylomicron vesicles by ultra-centrifugation of the growth-media prior to culturing conditions (bovine serum also does not contain any Lewis[a] structures).

To examine the fate of exogenously administered EVs, typically EVs are tagged with membrane reactive fluorophores, such as Di-8-ANEPPS. However when using a literature procedure, large dye aggregates and high background fluorescence made the Di-8-ANEPPS labelling of EVs for tracking purposes unsuitable [460], [461], [462] (*data not shown*). Another labelling strategy was explored and made use of non-mammalian miRNAs. Exogenous miRNA transfected into EVs can be quantified selectively by using quantitative PCR and allows tracking of these labelled EVs *in vivo*. Previously, this strategy has worked successfully by tracking the non-mammalian miRNA labelled EVs in a myocardial infarction model where endothelium-derived EVs promoted splenic monocyte mobilization [463]. Together with Naveed Akbar (Cardiovascular Medicine, University of Oxford), this labelling strategy was used in conjunction with Lewis[a]-lipid labelling of extracellular vesicles [464]. The resulted non-mammalian miRNA Lewis[a]-lipid labelled EVs were tested for their targeting capacities using the IL-1β acute brain inflammation model and the methods used are described in **section 4.5.13**. See **Figure 4.6** for an experimental overview of the miRNA labelling experiment.

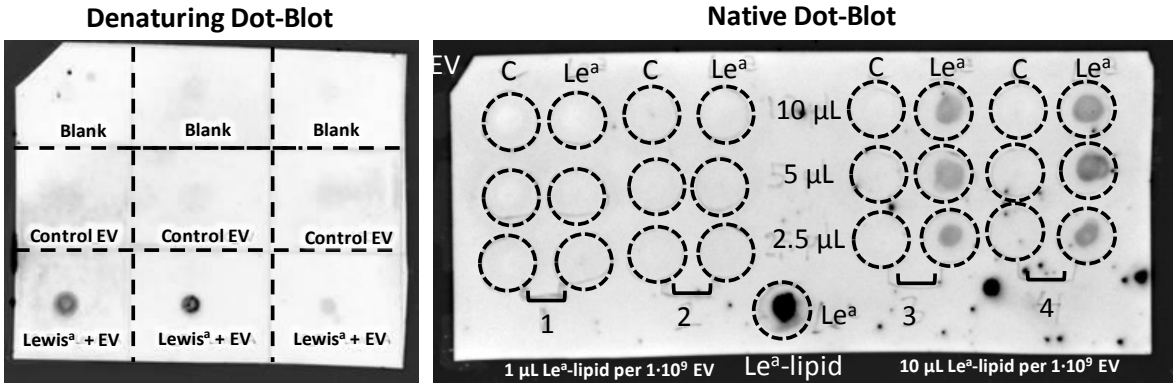
It was envisaged that only the Lewis[a]-lipid labelled EVs + the cel-miR-39-3p miRNA would reveal a positive qPCR signal for the non-mamallian miRNA at the left inflamed hemisphere. See **Figure 4.6.**



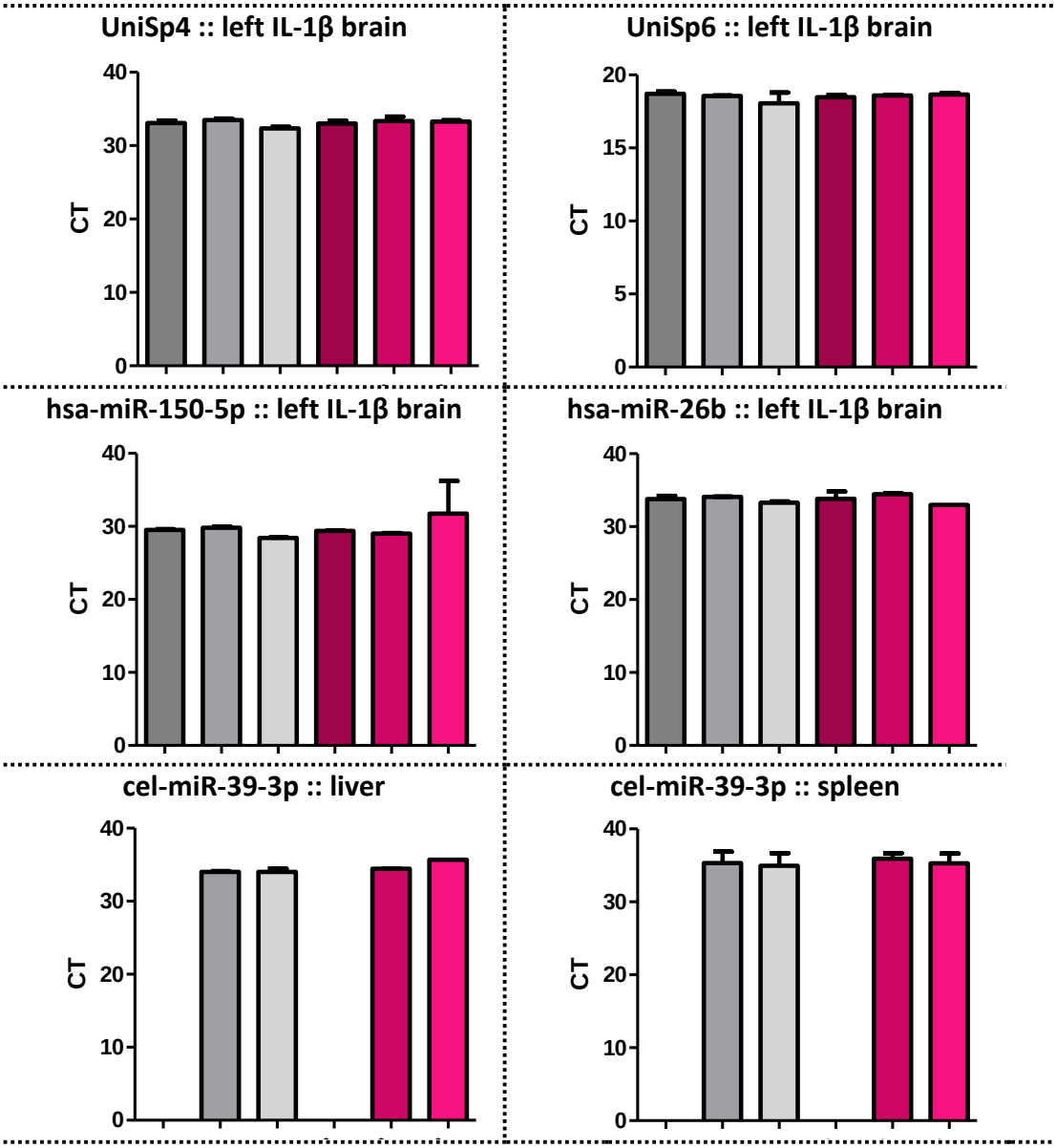
| Figure 4.6 | Experimental overview of targeting labelled EVs with a Lewis^a-lipid and a non-mammalian miRNA using the IL-1β brain inflammation model Left (IL-1β activated) and right striatum brain sections are isolated of mice injected with EVs labelled with a non-mammalian miRNA and Lewis^a-lipids. Lewis^a targeted delivery of EVs to the IL-1β activated site allows cel-miR-39-3p PCR amplification from isolated sections.

4.2.3 miRNA and Lewis^a-lipid labelling of extracellular vesicles for *in vivo* brain inflammation targeting was unsuccessful

Using a commercially available Lewis^a-lipid that inserts into biological membranes, EVs were labelled with Lewis^a and the labelling was detected by using an antibody against Lewis^a (7LE). See **section 4.5.14**. As shown in **Figure 4.7**. The Lewis^a-lipid labelling, transfection of EVs with the *C. elegans* miRNA cel-miR-39-3p and subsequent injection into the IL-1β brain inflammation model mice was performed as described **section 4.5.13**. All mice received an IL-1β injection into the left striatum and 4h post activation 3 mice received control EVS with cel-miR-39-3p (1.5 x 10^{10} EVs/animal) and 3 mice received the Lewis^a-lipid labelled EVS with cel-miR-39-3p (1.5 x 10^{10} EVs/animal). 30 minutes after the EV injections, relevant organs were taken. From the harvested tissues (liver, spleen and the left and right striatum of the brain) miRNAs were isolated and several spike-ins were used prior to isolation to quantify the efficiency of isolation. Also spike-ins were used to assess the cDNA PCR efficiency. The qPCT CT values are shown in **Figure 4.8** qPCR of the isolated UniSp4 and UniSp6 miRNA revealed that the RNA isolation efficiency across the 6 samples of the left isolated striatum was consistent. hsa-miR-150-5p and hsa-miR-26b miRNAs showed that the spiked miRNA for the cDNA PCR efficiency was also consistent across the 6 samples of the left isolated striatum. The cel-miR-39-3p used to label the EVs can be detected in the spleen and liver in two of the control EV-treated animals and two of the Lewis^a-lipid labelled EV treated animals. However no cel-miR-39-3p was detected in the brain (*data not shown*). Therefore a more reductionist model for biological vesicles was explored using fluorescently labelled liposomes labelled with the Lewis^a lipid to assess if they can be redirected to the IL-1β inflamed brain *via* E-Selectin.



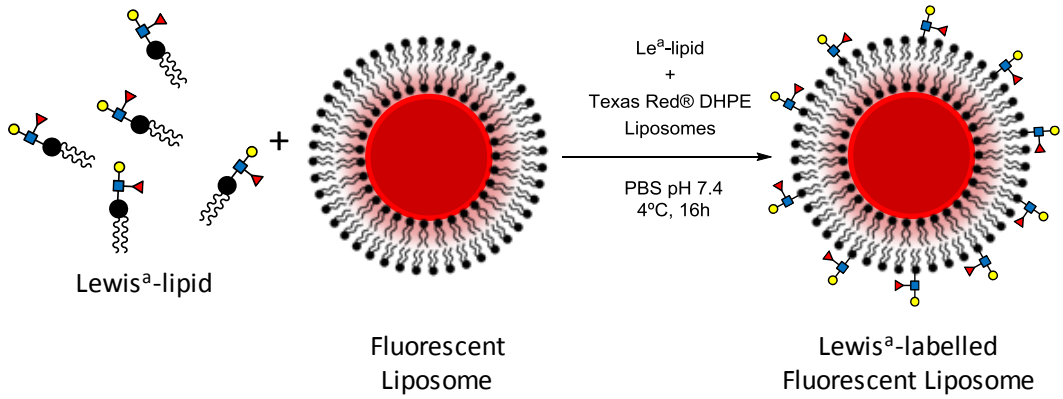
| Figure 4.7| Lewis^a-lipid labelling of endothelial cell derived EVs and detection of labelling using denaturing and native dot-blots Denaturing dot-blot shows Lewis^a-positive dots for the Lewis^a-lipid labelled EVs. Using 10 µL of Lewis^a-lipid per labelling reaction as described in **section 4.7.25**, the labelled EVs show positive dots. The Control (C.) EVs mock labelled are all negative. Blank is the PBS buffer used. *Note: specks outside the dotted lines are contaminants.*



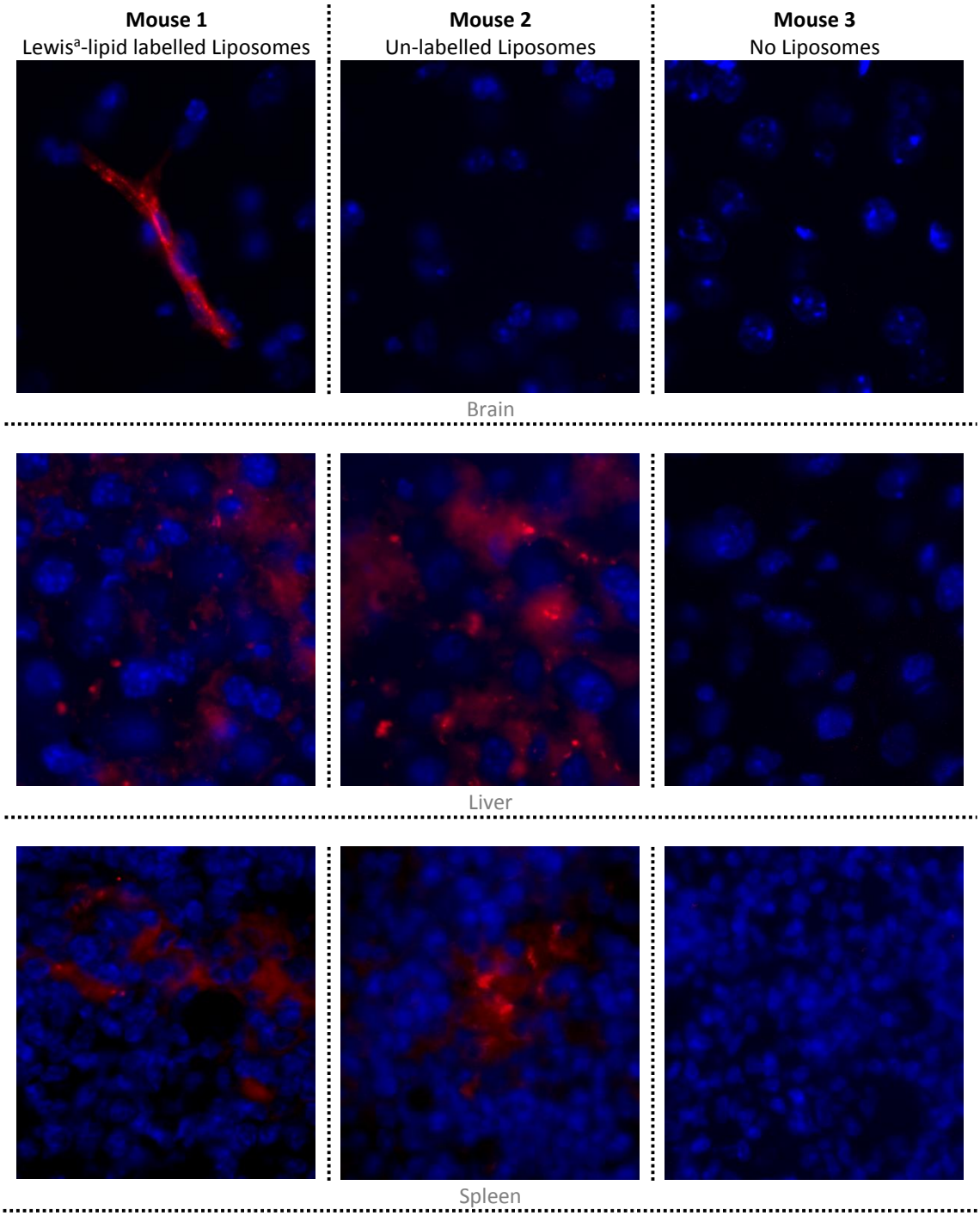
| Figure 4.8 |qPCR cycle threshold (CT) values of the spike-ins and the cel-mIR-39-3p in selected tissues Selection of miRNA quantified by qPCR. UniSp4 and UniSp6 spike-ins allowed quantification of the RNA isolation efficiency of the left isolated striatum. hsa-miR-150-5p and hsa-miR-26b spike-ins allowed quantification of the cDNA PCR efficiency of the left isolated striatum. No cel-miR-39-3p was found in the left isolated striatum (*data not shown*). cel-miR-39-3p was found in the liver and spleen in 4 of the 6 animals.

4.2.4 Lewis[a]-lipid labelling of fluorescent liposomes reveals *in vivo* brain inflammation targeting

Extracellular vesicles labelled with Lewis[a]-lipid were unable to be redirected to the IL-1β inflamed brain. To assess if this was due to complex nature of the EVs, as they have membrane proteins, a reductionist approach was trialled using commercial fluorescent liposomes (300 nm). These liposomes were labelled with the same Lewis[a]-lipid and tracked *in vivo* using fluorescence microscopy. Refer to methods **section 4.5.15** for the labelling conditions and the experimental details. Using the Lewis[a]-lipid labelled liposomes with the following composition: 1,2-dioleoyl-*sn*-glycero-3-phosphocholine (DOPC) / cholesterol (CHOL) / Texas Red™ 1,2-dihexadecanoyl-*sn*-glycero-3-phosphoethanolamine (TR-DHPE) / Lewis[a]-lipid (48:40:1:11 mol/mol), targeted brain delivery was achieved to the IL-1β inflamed side, as shown in **Figure 4.10**. Vesicle staining in red (for the liposomes) is only observed in the Lewis[a]-lipid labelled liposomes and at the left IL-1β inflamed side of the brain. Both the labelled and unlabelled liposomes are taken up by the spleen and liver. Background fluorescence staining was not present, as an untreated animal showed no fluorescent signal in the red channel. For each experimental condition only 1 animal was used, but the initial results indicate that Lewis[a]-lipids can redirect liposomes to E-Selectin expressing sites of inflammation.



| Figure 4.9 | Lewis[a]-lipid labelling of fluorescent liposomes Overview of the labelling reaction performed in **section 4.5.15**.



| Figure 4.10 | Fluorescence microscopy images of organ sections taken from mice injected with fluorescent liposomes labelled with Lewis[a]-lipid to target the IL-1β inflamed brain Representative fluorescent images from the brain (left IL-1β activated basal ganglia), liver and spleen of mice injected with Lewis[a]-lipid labelled liposomes (panel 1), un-labelled liposomes (panel 2) and untreated (panel 3). Red = liposomes with Texas Red® DHPE, Blue = DAPI nuclear stain. Top left image shows brain microvessel staining with the Lewis[a]-lipid labelled liposomes indicative of targeted localisation. Images shown are at 40x magnification.

4.3 |DISCUSSION

4.3.1 Lewis^a-mediated targeting of xenobiotic nanoparticles to brain inflammation sites was not observed by XRF imaging

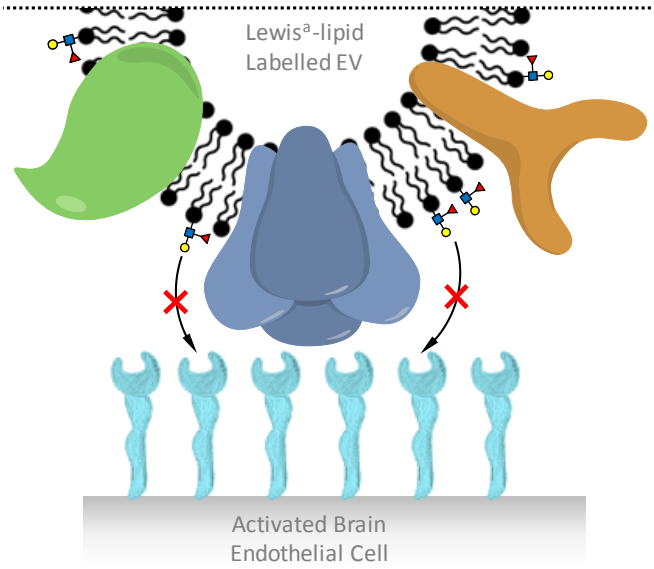
The commercially available amine-titanium nanoparticles were used for the modification with Lewis^a and the method to detect the modification levels was fluorescamine-based. As shown in Chapter 2, the fluorescamine method was not suitable the MPIO used, however did work for the titanium nanoparticles presented in this chapter. For future modification reactions it would be good to use the developed Fmoc-based method as well and to compare the loading levels between the different amine functionalisation methods. In addition, rigorous analysis of the generated precursor particles was not performed and is required for future experiments to assess the yields of modification. The initial experiments performed with these particles were proof-of-concept and no further investigations were undertaken as no additional XRF beam time was granted for this project to investigate the nanoparticle targeting of xenobiotic elements in the brain. Three brain sections were imaged at 9.000 KeV which allowed the visualisation of the biological elements and the xenobiotic element Ti. Despite acquiring good resolution for the two IL-1 β-activated brains that were treated with the Lewis^a-Ti nanoparticles, a significant amount of titanium was present in all samples analysed (see **Figure 4.2**). This contamination is likely from 'dust' or dead skin that has been treated with cosmetics or sun cream [465]. The OCT embedding matrix (KMA-0100-00A, CellPath Ltd) used to prepare the fresh cryopreserved brain sections contains the following trace impurities per 100g of product: Cl ≤5 µg, sulphate (SO_4^{2-}): ≤5 µg, Ca: ≤5 µg, Cd: ≤5 µg, Co: ≤5 µg, Cu: ≤5 µg, Fe: ≤5 µg, K: ≤5 µg, Ni: ≤5 µg, Pb: ≤5 µg, Zn: ≤5 µg. Interestingly, elemental analysis of sample **#2** Intracranial IL-1β, showed an unusual structure in the left bottom side of the brain. Further analysis revealed that the trace metals present in the OCT embedding matrix could be found back in this structure (*data not shown*). It is plausible that this structure is a contamination from the embedding matrix. Titanium signals of both K K M_3 and K K L_3 emission lines show no overlap with this structure. This could imply that the titanium contamination is not from the embedding matrix as mentioned before. This means that for future experiments great care need to be taken to avoid any exogenous materials that could cause contaminations that might interfere with elemental analysis of the XRF probes and biological tissue.

4.3.2 XRF analysis of acute IL-1β brain inflammation may reveal enzymatic activity

Despite the lack of success in targeting xenobiotic elements to brain inflammatory sites, an elemental map of the early stages of IL-1β induced brain inflammation was obtained as shown in **Figure 4.4**. The XRF elemental map of endogenous elements in the inflamed brain reveals several interesting anatomical structures that will be discussed next. Ca and K provide a general anatomic overview of the brain section with little distinction between grey matter and white matter in the brain. P and S to a certain extent visualize the white matter of the brain. Especially phosphorus clearly shows anatomical features which are rich in phospholipids, phosphoric acid and ATP and may be useful for visualising demyelination [3]. Due to the abundance of phosphorus it provided a structure to superimpose manganese and copper. Both Mn and Cu are elements associated with an oxidative environment that is created by immune cell recruitment because of the Cu and Mn binding enzymes involved in oxidative stress. Both Mn and Cu is used in the active site of the enzyme superoxide dismutase (SOD) [401]. Also 6-phosphogluconate dehydrogenase has Mn as a cofactor and is the main generator of NADPH, which is involved in protecting against the toxicity of reactive oxygen species (ROS) caused by neutrophil accumulation [268], [278]. The activation state of neutrophils may differ between different neuroinflammatory diseases and the measurement of ROS *via* elemental analysis may aid in structural analysis of the oxidative environment during inflammation [154]. Manganese in the brain described in this thesis not informative due to an unknown measuring artefact. Copper on the other hand showed clear XRF images and was able to visualize Cu-transporters, like Copper Transport Protein (Ctr1) and other Cu trafficking proteins are located at the choroid plexus [466], [467]. In addition, due to better Cu-signal some accumulation of Cu was seen at the left, IL-1β inflamed, side of the brain as shown in **Figure 4.5** and may be indicative of inflammation [468]. As mentioned before, Cu is used in the active site of the enzyme SOD and altered Cu homeostasis has been associated in diseases like Parkinson's Disease, Alzheimer's disease and Amyotrophic lateral sclerosis [469], [470], [275], [276], [273]. Although there may be an increase of Cu on the left side, the source remains unidentified and may be due to trace metals present in the OCT embedding matrix used or a measuring artefact as the right side of both the IL-1β treated brains (also clearly shown by P and S in **Figure 4.4**) appears to have less signal. Future imaging of the acute brain inflammation model using XRF and proteomic / genomic / immunohistochemical analysis of Cu-containing enzymes is required to confirm the presence of Cu [466], [471].

4.3.3 Labelling of biological nanoparticles with a non-mammalian miRNA and a Lewis[a]-lipid

The membrane reactive Di-8-ANEPPS allows selective labelling of membranes [462], however, labelling of EVs was not successful (*data not shown*). Using a different approach to label the EVs, endothelium derived EVs were labelled with a Lewis[a]-lipid and a non-mammalian miRNA derived from *C. elegans* (cel-miR-39-3p). This miRNA allowed quantitative measurements of EV tracking *in vivo* using qPCR [463]. However when used with the Lewis[a]-labelled EVs, no specific targeting to the inflamed brain was detected. The spike-ins used determined that the different stages of the RNA isolation and amplification of cDNA were efficient and are shown in **Figure 4.8**. This indicated that the technical aspects of the experiment worked, but the labelling or the targeting may not have worked. Using the labelling strategy employed, for every two lipid molecules in the EV one is a Lewis[a]-lipid. This was estimated using the following assumptions that a 100 nm liposome, which is comparable with EV size, contains 8×10^5 lipid molecules per liposome***. 10 µL of a 1 mg/mL Lewis[a]-lipid per 1×10^9 EVs was used which equals to 4.1×10^5 Lewis[a]-lipids per EV assuming 100% insertion. To compare this to the membrane of a red blood cells, these typically carry 12×10^6 glycolipid molecules of which 10^6 are polyglycosylated glycolipids [89]. Only a qualitative measurement of the Lewis[a]-lipid labelling of EVs was performed using the dot-blot (**Figure 4.7**) and for future experiments quantitative detection methods need to be sought. The size of the Lewis[a]-lipid may also be a confounder for two reasons: One, the there are fewer molecules presented on a surface that can interact with E-Selectin on activated brain endothelial cells [81]. Two, as the surface of the EVs are coated with large glycoproteins; the small Lewis[a]-lipid may not be reached by E-Selectin as it is hindered by the EV proteins on the surface [183], see **Figure 4.11**.



| Figure 4.11 |Steric hindrance model of Lewis[a] presented on extracellular vesicles

"It is like looking for a bungalow in New York City…"

Daniel Anthony.

Therefore this could imply that possibly only Lewis^a-structures presented as part of glycans on proteins may have a biological function in humans [88], [98]. In order to test the hypothesis of the steric hindrance model of Lewis^a presented on extracellular vesicles, fluorescent liposomes with an estimated 10% Lewis^a-lipid content were used for brain inflammation targeting *via* E-Selectin. As shown in **Figure 4.10**, these liposomes show targeting to the inflamed microvessels and hold great promise for targeted drug delivery *via* liposomes [472],[473],[107]. Of note, these experiments were performed once with low *n*-numbers and need to be further validated. Alternatively, for the retargeting of EVs with Lewis-glycolipids, these could be protease-treated [474] or enzymatically deglycosylated to make the membrane presented Lewis^a more accessible.

4.4 |CONCLUSION

This chapter has explored the possibilities of translating the strong Lewis[a] : E-Selectin binding onto other targeting modalities. Starting, the imaging power of X-Ray Fluorescence (XRF) imaging was explored to visualise the elemental composition of the IL-1β inflamed brain with xenobiotic Lewis[a]-nanoparticles. An initial trial to make Ti-nanoparticles with Lewis[a] was attempted, however no targeting was observed and detailed particle characterisation is needed. Nonetheless, an elemental map of brain inflammation was made using biological elements and a potential role of copper was showed. Due to the limited sample numbers, no further investigations were performed. However, the resolution of these samples is superior to other imaging techniques on the whole organ scale and richly informative about the elemental composition. XRF imaging, albeit without targeted imaging agents, promises a great potential to study metal-containing enzymes in brain inflammatory diseases.

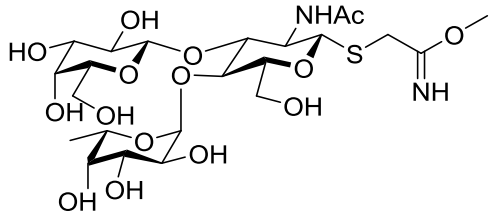
To conclude, the last part of this chapter explored the targeting capacities of Lewis[a] on biological nanoparticles: extracellular vesicles (EVs) and liposomes. As EVs in biology serve as vehicles for transfer and communication between cells, they do so by sharing membranes, lipids, cytosolic and membrane proteins and genomic material which are usually RNA-species. As naturally occurring Lewis[a] in humans can occur on both glycolipids and glycoproteins, the EV Lewis[a]-lipid model used could have unveiled an interesting role for Lewis[a] lipids in inflammation and biology. To study the role and fate of exogenously administered endothelial derived EVs in an IL-1β brain inflammation model, these EVs, were labelled with a Lewis[a]-lipid that inserts itself into membranes and a non-mammalian miRNA from *C. elegans.* It was envisaged that these EVs could be re-directed to the site of brain inflammation *via* an E-selectin mediated mechanism. However these Lewis[a]-lipid labelled EVs transfected with the non-mammalian miRNA were unable to do so as quantified by qPCR. A speculative mechanism was presented on why EVs are potentially an unsuitable carrier for Lewis[a]-lipid mediated retargeting, due to their large membrane protein components blocking the interacting between Lewis[a] and E-Selectin on these biological nanoparticles. A reductionist approach of this model, using liposomes, showed that Lewis[a]-labelled liposomes can be redirected to the inflamed brain and holds great promise for targeted drug and therapy delivery.

4.5 | METHODS

4.5.1 Buffers and reagents used

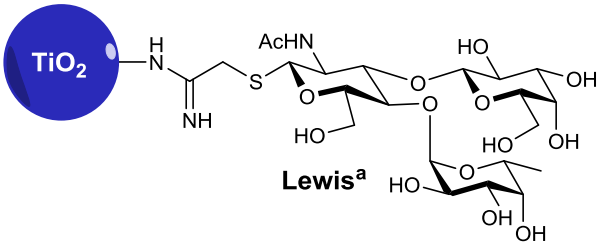
Reagents were from Sigma unless specified otherwise. Tubes used were exclusively Protein LoBind microcentrifuge tubes (0.5, 1.5 and 2 mL) from Eppendorf. Dry solvents were from Acros Organics with molecular sieve and AcroSeal. Argon was used when solvent was removed from the bottle. DMSO was from Fisher BioReagents. Magnet for 1.5 mL tubes was from Dynal, Invitrogen. Buffers prepared were 0.22 µ-filtered and stored up to 6 months. Roswell Park Memorial Institute (RPMI)-1640 Medium was from Sigma (Cat # R8758), Fetal Calf Serum (FCS) was from the Daniel Anthony lab stock and was heat inactivated for 30 minutes at 56°C, Penicillin-Streptomycin (P/S) was from Sigma (Cat # P4333). Dulbecco's Phosphate Buffered Saline (DPBS) with calcium and magnesium was from Sigma (Cat # D1283). Recombinant Rat IL-1 beta/IL-1F2 Protein, CF was from R&D Systems (Cat # 501-RL-050/CF). For injecting substances into the animals, Terumo 1ml Insulin Syringe & Needles were used (Cat# BS-01H2516). FSL-LEa(tri) referred to in the thesis as Lewis[a]-lipid was from Sigma (Cat# F9682). Handling tools (forceps etc.) for preparing the XRF samples were carbon-based to prevent metal contaminations.

4.5.2 Le[a] deprotection and IME-activation



Fully protected Lewis[a] (10 mg, 10.9 µmol, 1 equiv.) was dissolved in 500 µL dry MeOH. A 25% solution of sodium methoxide in methanol (4.4 µ:L, 4.4 µmol, 0.4 equiv.) was added and the reaction was left to stir overnight under nitrogen. TLC (8:2 Acetone:H_2O) revealed incomplete consumption of starting material. The reaction was quenched with Dowex H^+ till neutral (pH paper: pH ~6-7) and was filtered over cotton wool. The reaction was evaporated under reduced pressure without heating and left under high vacuum for 30 minutes.

4.5.3 NP TiO_2-Le[a]



2.5 mg of commercial TiO_2-NH_2 (C-TiO-0.95NH2, 10 mL of 25 mg/mL, Corpuscular Inc. #220392-10) particles were washed 3 times (fixed angle, 17K x g, 5 minutes) with 1 mL of 0.1 M $NaHCO_3$ pH 9.0. The particles were resuspended in 200 µL of the sodium bicarbonate buffer. Dry deprotected and activated Lewis[a] was dissolved in 200 µL of sodium bicarbonate buffer and added to the particles to give a final volume of in 400 µL. The reaction was left overnight under gentle rotation. The particles were washed twice with sterile saline (0.9% NaCl). Fluorescamine loading revealed a 46% coverage using the protocol described elsewhere [298], [299].

4.5.4 *In vivo* models of brain inflammation and XRF-probe administration

Adult C57BL/6 "black 6" mice weighing approximately 30 g were anesthetized with isoflurane. Il-1 β (50 ng in 0.5 µL saline) or particles (see **Table 4.2**) were injected intracerebrally using a 50-µm-tipped glass pipette. Animals were allowed to recover from anaesthesia for about 3.5 h, at which point they were reanesthetized as before and 150 µL of a solution containing either TiO_2-Lewis[a] (two different doses) or TiO_2-VCAM-1 (*data not shown for synthesis of these particles*) were injected *via* a tail vein (see table above). Animals were allowed to recover from anaesthesia. After the recovery period the animals were deeply anaesthetised with sodium pentobarbitone and and transcardially perfused with saline. After dissection, the brains were frozen in OCT embedding matrix with isopentane on dry ice. Frozen, 50-µm thick sections of the injection site were mounted onto sapphire disks. Sections were left to dry, frozen at -20°C overnight and were used as such the next day for XRF elemental mapping (I18 beam line, Diamond, Didcot, UK). XRF samples were measured at 9.000 KeV and average acquisition time including handling was approximately 4,5h per sample. Imaging dwell time was 0.5 seconds and pixel resolution was 2µm. Datapoints (pixels) per sample: **#2** Intracranial IL-1β (115x170), **#5**: IntracranialIL-1β+Tail Vein TiO2-Lewis[a] (105x163), **#6** Tail Vein TiO2-Lewis[a] (113x161). Limited beam time was available and the rest of the samples were not acquired.

| Table 4.2 |Experimental overview

#	Sample	Inflammation?	Time IL-1β injections	Type of particle injection	Time particle injections
1	No Particles	Control	N/A	None	N/A
2	No particles	IL-1β (50 ng in 0,5 µL saline)	14:30 (27-05-2015)	None	
3	TiO_2-NP α-VCAM-1 Single Dose	IL-1β (50 ng in 0,5 µL saline)	14:45 (27-05-2015)	Tail vein (132 µg in 150 µL saline (4.5 mg/kg [~30 g mice])	18:25 (27-05-2015)
4	TiO_2-NP Lewis-A Single Dose	IL-1β (50 ng in 0,5 µL saline)	14:50 (27-05-2015)	Tail vein (132 µg in 150 µL saline (4.5 mg/kg [~30 g mice])	18:28 (27-05-2015)
5	TiO_2-NP Lewis-A Triple Dose	IL-1β (50 ng in 0,5 µL saline)	14:55 (27-05-2015)	Tail vein (394 µg in 150 µL saline (13.5 mg/kg [~30 g mice])	18:30 (27-05-2015)
6	TiO_2-NP Lewis-A Triple Dose	Control		Tail vein (394 µg in 150 µL saline (13.5 mg/kg [~30 g mice])	18:20 (27-05-2015)
7	TiO_2-NP Lewis-A	Control		Intracranial (1 µg, 2 µg/µL)	16:00 (27-05-2015)

4.5.5 Data analysis using the XRF-fitting software PyMca

XRF imaging was performed at the I18 beamline at Diamond Synchrotron (Didcot, UK) and assistance was provided by Kalotina (Tina) Geraki. Samples were mounted onto supplied sapphire disks from Diamond. Brains were excited by XRF at selected energies after optimised visualisation of the selected xenobiotic elements. XRF samples were measured at 9.000 KeV and average acquisition time including handling was approximately 4,5h per sample. Imaging dwell time was 0.5 seconds and pixel resolution was 2µm. Datapoints (pixels) per sample: #2 Intracranial IL-1β (115x170), #5: IntracranialIL-1β+Tail Vein TiO2-Lewis[a] (105x163), #6 Tail Vein TiO2-Lewis[a] (113x161). Limited beam time was available and the rest of the samples were not acquired. After data collection the images were generated by fitting and deconvolution of the data with the following configuration file setting as presented in **Figure 4.12** below. All the parameters changes from the standard settings are described here. Intensity of the maps (pixels) corresponds to the net XRF peak areas for all elements of interest at each map pixel.



Highlighted in yellow are the elements included in the fit. Same fit was used for all the data in this report.

FIT

Fit function:	Mca Hypermet
Continuum type:	NO continuum
Polynomial order:	1
Non-analytical (or estimation) background algorithm:	SNIP
Strip background width:	1
Strip background iterations:	20000
Strip background smoothing with (Savitsky-Golay):	1
Statistical weighting of data:	Poisson (1/Y)
Number of iterations:	10
Minimum chi^2 difference (%):	0.001
Include:	Stripping and Escape peaks

DETERCTOR

Detector composition:	Si
Maximum number of escape energies:	4
Spectrometer zero (KeV): -	0.00521932138567 δ +/- 0.1
Spectrometer gain (KeV/ch):	0.0100089176637 δ +/- 0.001
Detector noise (KeV):	0.1 δ +/- 0.05
Fano factor (Si~ 0.012, Ge ~0.1):	0.114 δ +/- 0.114
Pile-up factor:	1e-08 δ +/- 1e-08

BEAM

Excitation Energy (KeV): 9.000 *(For Zr, 11.000)*

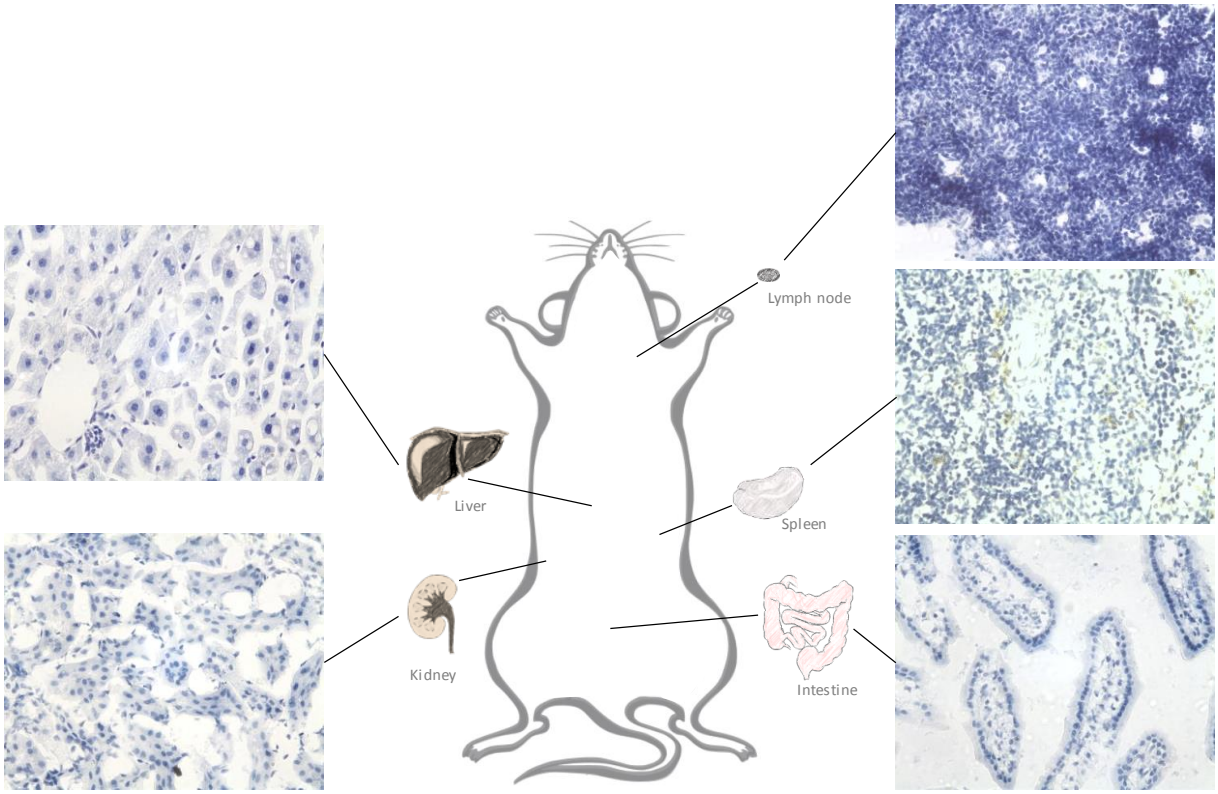
PEAKS

PEAKSHAPE, ATTENUATORS, MATRIX, CONCENTRATIONS and **XRFMC** were all on default settings.

| Figure 4.12| XRF fitting parameters using PyMca software (version 4.7.4)

4.5.6 Immunohistochemical analysis of Lewis[a] in mouse tissue

Standard immunohistochemical for Peripheral Tissue described in section 3.6.16 was performed on 4% PFA fixed tissue generated by Jay Roodselaar from CD20 control mice. The following reagents were used: Mouse monoclonal [7LE] for Lewis[a] (Insight Biotech, EXB-11-385-C100) was used 1:100 in PBS Goat Serum (1%). Goat Serum was used for blocking (10% in PBS). Goat anti Mouse secondary antibody (Vector Labs, BA-9200) was used in 1:200 in PBS Goat Serum (1%).



| Figure 4.13 | Immunohistochemical analysis of Lewis[a] structures in mice 40x magnification images of indicated organs of CD20 control mouse (n=1) stained for Lewis[a]. Tissue is expected to be negative and no staining (dark brown) is observed for the tissues analysed. An non-specific stain was observed in the spleen that showed a very similar pattern when other sections of the spleen were stained with the same secondary antibody used (*data not shown*).

4.5.7 Lewis[a]-labelling and miRNA-transfection of EVs for acute brain inflammation targeting using qPCR

Using a modified protocol from a previously reported method the following procedures were followed to obtain cel-miR-39-3p transfected EVs labelled with Lewis[a]-lipid. EVs were provided by Naveed Akbar (Cardiovascular Medicine, University of Oxford) and were isolated from unstimulated murine endothelioma s.END1 cells as described in [463]. 10 µL Lewis[a]-lipid at a concentration of 1 mg/mL per 1×10^9 EVs in 100 µL PBS were used for labelling reactions and were incubated in sealed Eppendorf tubes at 37°C for 1h under gentle rotation. Mock-labelled EVs underwent the same reaction conditions and were supplemented with the Lewis[a]-lipid vehicle

(PBS, pH 7.4). EVs were labelled using an exosomal transfection kit (Exo-Fect, System Bioscience) with a non-mammalian miRNA derived from *C. elegans* (cel-miR-39-3p transcript (Exiqon)) according to the manufacturer's instructions with the following modification: $1x10^8$ EVs were used per labelling reaction instead of the recommended $1x10^7$ EVs. EVs were then washed by ultra-centrifuging at 120,000 xg for 120 minutes in 13 ml PBS as described in [463]. Isolated EV reactions were pooled (keeping Lewis^a-lipid and control separate) and resuspended in 200 µL steile PBS pH 7.4. NTA measurements yielded a total of $4×10^{10}$ in 200 µL for 'control' EVs and $5×10^{10}$ in 200 µL for 'Lewis^a-lipid' EVs. The EVs were stored at 4°C and used the next day for injections. Labelled EVs were injected into mice using the following procedure. Mice (C57BL/6 "black 6", male, 11 weeks old (n=6): were anesthetized with 2–3% isoflurane in oxygen in an anaesthetic chamber. Upon induction of the anaesthesia, the absence of reflexes was confirmed and the animal was placed in a stereotaxic frame on a surgical heating pad whilst maintaining the anaesthesia *via* a nose cone. A midline incision was made in the scalp and the skull was exposed. A small hole was drilled in the skull and a stereotactic injection of IL-1β (1 µL, 100 ng in sterile saline) using a <50 µm tipped sterile glass capillary was made in the left brain hemisphere at 0.8 mm anterior, 2 mm lateral from Bregma and at a 2.3 mm depth into the left striatum. The solution was injected slowly and the capillary was left for 1 minute after the injection before removing it from the injection site. The skin was sutured and the animals were left to recover. Animals were anaesthetized as described above after 4 h of IL-1β activation and the indicated EV solutions in sterile PBS were injected *via* a tail vein using an insulin syrine. Lewis^a-lipid-labelled cel-miR-39-3p transfected EVs were injected at 1.5 x 10^{10} EVs/animal (n=3) and cel-miR-39-3p transfected control EVs were also injected at 1.5 x 10^{10} EVs/animal (n=3). The animals were left to recover and after 30 minutes of EV circulation time the animals were deeply anaesthetised with isoflurane and transcardially perfused with heparinized saline (5000 U/L, 0.9% NaCL) until tissue was clear from blood at which point sections from the liver, and spleen were taken and the left and right striatum were isolated. Isolated organs were immediately snap frozen in pre-cooled tubes on dry-ice and stored at -80°C. Isolated tissue was homogenised using a Tissuelyser LT (Qiagen) small bead mill with 7 mm sterile stainless steel beads at 50 Hz oscillation for 2 minutes. The tubes were spun down for 8000 xg for 5 min at 4°C and the supernatant was collected. Total RNA was isolated from cells using the miRCURY™ RNA Isolation Kit and the following synthetic RNA spike-ins were added as a control for isolation and cDNA synthesis/PCR efficiencies: UniSp2, UniSp4, UniSp5 (Exiqon) were added to the lysis buffer used at the recommended concentrations. These spike-ins allowed quantification of the RNA isolation efficiency. hsa-miR-129-3p, hsa-miR-150-5p, hsa-miR-266-5p (Exiqon) were added to reverse transcriptase mix used at the recommended concentrations. These spike-ins allowed quantification of the cDNA PCR efficiency.

miRNAs were prepared using miRCURY Cells and Tissue RNA, Biofluids and Cell and Plant isolation kits, and Universal cDNA was synthesis kits II (Exiqon), and transcript levels were quantified using miRCURY LNA microRNA PCR, ExiLENT SYBR master mix with ready-to-use PCR, human panel I and II or cel-miR-39-3p, LNA control primer set kits (Exiqon) according to the manufacture's protocol.

4.5.8 Lewis[a] detection in labelled extracellular vesicles for using a dot-blot

EVs were provided by Naveed Akbar (Cardiovascular Medicine, University of Oxford) and were isolated from unstimulated murine endothelioma s.END1 cells as described in [463]. 1 or 10 µg/mL final Lewis[a]-lipid concentration (1 mg/mL stock) reactions were made using 1×10^9 EVs in 1000 µL PBS. The labelling reactions were incubated in sealed Eppendorf tubes at 37°C for 1h under gentle rotation. Mock-labelled EVs underwent the same reaction conditions and were supplemented with the Lewis[a]-lipid vehicle (PBS, pH 7.4). EVs were then washed by ultra-centrifuging at 120,000 xg for 120 minutes in 13 ml PBS as described in [1]. For the denaturing blot EV pellets were resusupended in 100 µL RIPA buffer and were performed by Naveed Akbar. For the Native Dotblot EV pellets were resusupended in 100 µL PBS. Nitrocellulose membrane was spotted with the indicated amounts and dried for 1h. Blocking was performed by using 3% BSA in PBS for 1h. Washing was performed with PBS, exchanging the solution 3 times every 5 minutes. Mouse monoclonal [7LE] for Lewis[a] (Insight Biotech, EXB-11-385-C100) was used 1:100 in PBS BSA (1%) overnight at 4°C under gentle rocking conditions. Washing was performed with PBS, exchanging the solution 3 times every 5 minutes. An anti-mouse secondary HRP-conjugated antibody (Cardiovascular Medicine, Naveed Akbar) was used in 1:10000 in PBS BSA (1%). Washing was performed with PBS, exchanging the solution 3 times every 5 minutes. The blot was gently dried by dabbing the sides onto paper tower and by incubating the blot in an ECL chemiluminescent substrate (Cardiovascular Medicine, Naveed Akbar). Chemiluminesence was visualised using a BioRad ChemiDoc™ Imaging System.

4.5.9 Fluorescent tracking of Lewis[a]-lipid labelled fluorescent liposomes *in vivo*

Note: protect the fluorescent liposomes from light and perform all incubations under aluminium foil. Experiment performed together with Megan Sealy. Dilute the 300nm DOPC/CHOL liposomes labeled with Texas-Red™ DHPE (Cat# F60103F3-R, 30 mg/mL FormuMax Scientific, Inc.) to 2.5 mg/mL in 500 µL sterile PBS (1.25 mg total, 541.6 µL). For the Lewis[a]-lipid labelled liposomes, dissolve the liposomes in 500 µL of the Lewis[a]-lipid solution (1 mg/mL, sterile PBS pH 7.4) (Cat#

F9682, Sigma-Aldrich). Briefly vortex to mix and seal the tubes with parafilm and cover with foil. Place the tubes in a 50 mL falcon tube. The labelling and control reactions were incubated on a tube roller for 18 hours at 4°C in the dark. Spin the reactions at 1500xg (4°C) using filter-aided centrifation (3 MWCO, PES Membrane, VivaSpin, Sartorius) untill concentrated to appromimately 200 µL. 2 Mice (C57BL/6 "black 6", female, ex-breeders): were anesthetized with 2–3% isoflurane in oxygen in an anaesthetic chamber. Upon induction of the anaesthesia, the absence of reflexes was confirmed and the animal was placed in a stereotaxic frame on a surgical heating pad whilst maintaining the anaesthesia *via* a nose cone. A midline incision was made in the scalp and the skull was exposed. A small hole was drilled in the skull and a stereotactic injection of IL-1β (1 µL, 100 ng in sterile saline) using a <50 µm tipped sterile glass capillary was made in the left brain hemisphere at 0.8 mm anterior, 2 mm lateral from Bregma and at a 2.3 mm depth into the left striatum. The solution was injected slowly and the capillary was left for 1 minute after the injection before removing it from the injection site. The skin was sutured and the animals were left to recover.4h post-injection the animals were placed under anaesthesia, the absence of reflexes was confirmed and liposomes (control and Lewis[a]-labelled) were injected *via* a tail vein using an insulin syringe. Animals were allowed to recover from anaesthesia and 30 minutes after the injection the animals were deeply anaesthetised with isoflurane and transcardially perfused with heparinized saline (5000 U/L, 0.9% NaCL) until tissue was clear from blood at which point sections from the liver, spleen, kidney and lungs were taken and followed by the brain. Collected tissues were immediately frozen in OCT on dry-ice with pentane and kept frozen at -80°C. Tissue was sectioned at 10 µm using a cryostat and collected onto gelatinized slides and post- fixed in 4% PFA (in 0.1 M Phosphate buffer, pH 7.4). for 5 minutes before mouting the slides with VECTASHIELD Antifade Mounting Medium with DAPI (Cat# H-1200, VectorLabs).Tissue was analysed at 40x magnification using a fluorescence microscope. Acquired images were analysed by Megan Sealy.

Lewis[a]-lipid labelled liposomes

Animal received a bolus of:

1.40 µmoles of DOPC:
1.17 µmoles of CHOL: cholesterol
20 nmoles of Texas Red® DHPE
342 nmoles of Lewis[a]-lipid

Unlabelled Liposomes

Animal received a bolus of:

1.40 µmoles of DOPC:
1.17 µmoles of CHOL: cholesterol
20 nmoles of Texas Red® DHPE
0 nmoles of Lewis[a]-lipid

(1,2-dioleoyl-*sn*-glycero-3-phosphocholine (DOPC)
cholesterol (CHOL)
Texas Red™ 1,2-dihexadecanoyl-*sn*-glycero-3-phosphoethanolamine (TR-DHPE)

5

| SUMMARY AND FUTURE OUTLOOK |

5.1 | SUMMARY

5.1.1 Principal findings of this thesis

This thesis has been subdivided in three thematic chapters and the principal findings of each experimental chapter are summarized below. The main aim and title of this thesis is the '*Development and use of Nanoparticles to Study the Biological Mechanism of Carbohydrate Lewis^a Binding during Brain Inflammation*' and each chapter aided in uncovering the biological mechanism, using different nanoparticle scaffolds, described in this thesis.

Chapter 2 describes the development and characterisation of commercial MPIOs that were functionalised with chemically synthesized IME-Lewis^a and a trifluoromethylphenyl diazirine photo-crosslinker. Amine functionalisation levels of both Lewis^a and the photo-crosslinker molecules covalently conjugated to the MPIOs was made possible by using an Fmoc-based detection method. It was also possible to rapidly screen batches of Lewis^a and Lewis^b functionalised MPIOs using an ELISA-based method that required less material to measure particle-batches with similar loading levels. Proof-of-principle reactions using FT-IR and BSA protein to study the UV-induced crosslinking capacities of the photo-crosslinker on MPIOs demonstrated to be challenging.

Chapter 3 was subdivided into three biological subchapters to determine whether E-selectin might bind Lewis^a during CNS inflammation using the generated functionalised MPIOs with Lewis^a and the photo-crosslinker from **Chapter 2**

The first proteomics subchapter used the bi-functional Lewis^a/diazirine photo-crosslinker on MPIOs in conjunction with IL-1β activated brain microvascular endothelial cells (GP8 rat). These pulldown experiments yielded however no lectin-domain bearing proteins. Subsequent pulldown experiments with Lewis^a functionalised MPIOs without the photo-crosslinker also yielded no lectins. When the whole cell proteome of IL-1β activated brain microvascular endothelial cells was studied (bEnd.3 mouse), it revealed the known Lewis^a-binding lectin E-Selectin as the second highest upregulated protein and VCAM-1 as the highest upregulated protein.

The second transcriptomic subchapter used two models of brain inflammation, an acute IL-1β induced model in adult and juvenile rats and a BCG MS-like lesion model. The acute brain inflammation model showed in both the adult and juvenile rats E-Selectin as one of the most upregulated transcripts following IL-1β-induced acute brain inflammation, which suggested that

E-Selectin was a good candidate for Lewis^a-binding during brain inflammation. The other BCG MS-like lesion model uncovered a transcriptome fitting with a pattern I type MS-lesion. E-Selectin was however not found to be upregulated at the transcript level in this model and alternative mechanisms were proposed. The overlapping upregulated transcripts between the two models compared showed a potential role for neutrophils and platelets as well.

The last *in vivo* subchapter used E- and P-Selectin blocking antibodies and a neutrophil depletion model in rats to assess the binding of Lewis^a-MPIO and Lewis^b-MPIO using MRI during IL-1β induced acute brain inflammation. The binding of Lewis^a-MPIO was abolished by blocking E-Selectin, which indicated that E-Selectin is the principal binder of Lewis^a in vivo. P-Selectin neutralisation only partially blocked Lewis^a-MPIO binding and an additional role for neutrophils was postulated to account for this observation. For Lewis^b-MPIO, a similar, yet distinct, binding pattern was observed. Lewis^b binds less strongly to the inflamed endothelium when compared to Lewis^a. However, a moderately stronger binding to P-Selectin was observed when Lewis^b was compared to E-Selectin to Lewis^b in this model. Neutrophil depletion was achieved with the antiserum and confirmed by blood analysis and loss of neutrophils in the liver. The difference between Lewis^a and Lewis^b MPIO binding in this model is small and a similar binding pattern was shown in the absence of neutrophils. The lack of neutrophils implied that when neutrophil numbers are low, more E-Selectin is available and more binding is observed for the Lewis-MPIO as both compete for E-Selectin on the activated endothelium.

Chapter 4 explored the use of other nanoparticles for future applications. The XRF imaging experiments performed on brain sections of IL-1β induced acute brain inflammation using Titanium Lewis^a-functionalised nanoparticle revealed Titanium contaminants. However, an 'elemental map' of acute brain inflammation was generated and showed a potential role for copper. Although XRF is a highly informative technique, the work presented in this thesis needs optimisation and better particle characterisation in order to understand the biology of brain inflammation. Biological nanoparticles also were functionalised with a Lewis^a-lipid and transfected with a non-mammalian siRNA with the aim to redirect endothelial cell derived extracellular vesicles (EV) to E-Selectin in the acute IL-1β induced brain inflammation model and detect the redirected EVs with quantitative PCR. Redirected targeting with the Lewis^a-lipid was not observed by qPCR for the non-mammalian siRNA and a reductionist liposome model revealed that either steric hindrance of the Lewis^a-lipid by EV proteins or the size of the EVs is limiting. The Lewis^a-lipid mediated brain delivery of fluorescent liposomes hold great promise for targeted drug delivery

5.1.2 General Discussion

This thesis has established a role for E-selectin in the binding of Lewis^a-MPIO to the activated brain endothelium and reveals how this contrast agent might be used to detect the inflammation in the brain in the absence of blood-brain barrier breakdown. Several findings regarding Lewis^a are notable and will be discussed next.

5.1.2.1 The unknown role of Lewis^a in human during health and disease

For such an old and well-established blood group, there is surprisingly little known of the roles of Type 1 Lewis antigens (both Lewis^a and Lewis^b) in humans during normal physiology and disease. Establishing the role of the Lewis-antigens may have been hampered by the fact that most the most well-studied mammalian model organisms for inflammation, rat and mice do not have FUT3, the enzyme to synthesize Lewis^a [93], [475]. *C. Elegans* is a classical model organism (nematode) and has several FUT3 genes; however, the carbohydrates produced by these FUTs appear to be Lewis^x and not Lewis^a [476]. Similarly, bovine FUT3 produces Type 2 epitopes and Lewis^a was not detected in any bovine tissue. [366]. Our closest ancestors from the homininae subfamily appear to have FUT3 genes, but these functions are not supported by literature and are solely inferred from alignments, biological aspect of ancestor and electronic annotations (see Uniprot). In humans, it is not clear what the functions are for Lewis^a (Lewis^b) as a glycolipid and part of a glycoprotein and it is unclear if these antigens bind E- and P-Selectin during normal physiology or during inflammation. It is known that Lewis^a (and Lewis^b) glycolipids are likely synthesised in the digestive tract by exocrine epithelial cells and in the liver and that the circulating Lewis-glycolipids can be absorbed by membranes of blood-cells *via* lipoprotein particles [441],[87]. Type 1 structures can also be found as part of glycoproteins and human neutrophils carry Lewis^a structures [88]. No clear functionality has yet been assigned to Lewis^a glycoproteins or lipids, but immune cells bearing Lewis^a can be recruited to the inflamed intestinal mucosa and blocking of Lewis^a enhances their transmigration, implying a role in gut immune regulation *via* an unknown mechanism [98]. Conversely, the role of sialylated Lewis^a and its overexpression in cancer (mostly in colon cancer) is very much established and the metastasis is mediated by E-Selectin [101], [436] [477], [478].

5.1.2.2 Lewis antigens and the vasculature

This thesis work focussed primarily on the vasculature in the brain and therefore the importance of Lewis antigens, as a blood group, was expected to conceivably show a difference is vascular

diseases. Indeed, Lewis$^{a/b}$ negative individuals have a marked increase in body weight and a higher risk of ischaemic heart disease [448]. Also ischemic heart disease, without obesity, is more prevalent in Lewis$^{a/b}$ negative patients [449], [450]. Though these studies only reveal an association and do not provide mechanistic insight. E- and P-selectin are overexpressed during atherosclerosis and immune cell adhesion to the atherosclerotic plaque plays a significant role in the disease aetiology [479],[480]. Potentially the presence of Lewis$^{a/b}$ glycolipids present on the lipoprotein particles and blood cells in the blood may act as a decoy for immune cells reacting to the excess of cholesterol and lipids in the walls of blood vessels or may modulate their activity; however this role has not been addressed yet. In addition, diabetes may also be more prevalent in Lewis$^{a/b}$ negative individuals [481]. However, this may be due to the Lewis-binding lectin MBL which can contribute to the pathogenesis of vascular complications in type 1 diabetes [360].

5.1.2.3 Other Selectin imaging agents and the possible antigenicity of Lewis antigens

Although the initial finding of the strong Lewis^{a} binding observed during the pilot experiment shown in **Figure 1.4** was somewhat serendipitous, it meant that a relatively easy carbohydrate moiety could be used to effectively target inflammation. Sialyl Lewis^{x} was explored before as an E- and P-Selectin targeting moiety, but the synthesis is cumbersome in comparison to Lewis^{a} [65]. In addition, Lewis^{a} showed a better MRI contrast image than the previously reported sialyl Lewis^{x}. Therefore, Lewis^{a} holds great promise as an early-stage brain inflammation contrast agent. As mentioned in the introduction, the recently developed biodegradable iron-oxide based imaging tool (mMPIO) could combined with Lewis^{a} be a highly informative and safe technique to monitor disease progression in MS [196]. Although, the use of nanoparticles in humans needs to be further studied in order to deem it safe. The studies presented here have been performed in rats and E-Selectin protein homology between rats and humans is 70% identical with 84% identical carbohydrate domains (using NCBI blast, with P16581 (LYAM2_HUMAN) and P98105 (LYAM2_RAT)). How these differences may affect the translatability from rodent to human is unknown, however human E-Selectin is fully capable of binding Lewis^{a} and similar results from the rats are expected in humans [51], [53], [111], [101]. As E-Selectin is upregulated in MS [49], other scientists have tried to visualize E-Selectin as a marker of inflammation using anti E-Selectin antibodies. However, none show the superior contrast as described in this thesis. Anti-human E-selectin conjugated to iron oxide is capable of binding live IL-1β stimulated human endothelial umbilical vein (HUVEC) cells and shows promising binding by MRI, however the binding *in vivo* was not trialled [482]. Another group tested the anti-human E-selectin conjugated to iron oxide *in*

vivo in an ear inflammation model and showed accumulation of the agent at the inflamed ear. The rationale for the strong Lewis^a binding in comparison to antibodies is most like due to the multivalent effect, which typically not occurs for IgG-based antibodies [317]. The use of antibodies (even fully human monoclonal antibodies) and therapeutic proteins also has the risk of immunogenicity, hypersensitivity and neutralisation which can result in morbidity and mortality [483]. The immunogenicity of the Lewis-antigens on the MPIO contrast agent are considered to be negligible as Lewis-antigens are typically not screened for in blood transfusions [84]. Cold agglutination may occur, as anti-Lewis antibodies can agglutinate at lower temperatures, but should not pose a problem if the agent is warmed up to room temperature prior to injection [484], [90]. In addition, 90% of the population is Lewis-positive, so the contrast agent would only be not available to a small proportion of the population who may have reactive Lewis-antibodies, if agglutination poses any issues [90], [84].

5.1.2.4 Facile preparation of targeted liposomal delivery using Lewis antigens

Finally, the 300nm Lewis^a-lipid-mediated liposome binding may allow for targeted drug delivery. Using a different system, based on the cell adhesion molecule VCAM-1, liposomal delivery of encapsulated neuroprotective citicoline using anti VCAM-1 antibodies as the targeting agent has been successfully shown before. This method, which uses a similar strategy as the E-Selectin mediated-delivery described here, allowed liposome delivery to areas of ischemia with BBB breakdown in a model of ischemic stroke [485]. Although, the targeting worked in this case, the preparation of the liposomes and the coupling of the VCAM-1 antibody is laborious. Also, the use of antibodies has the risk of immunogenicity and lack the multivalent effect as mentioned before [483], [317]. Although, it is believed that the strong Lewis^a : E-Selectin binding observed here in this thesis is due to the multivalent effect, there are examples where one-on-one molecule interaction are able to retain liposomes. This has been shown for a single Annexin 5 molecule anchored to a liposome which was able to bind to a phosphatidylserine-containing membrane support, however it is unknown if this interaction can withhold under flow conditions *in vivo* [486]. It is envisaged that the Lewis^a-lipid : E-Selectin model could achieve effective targeting without the risk of immunogenicity and with easier preparation as the Lewis^a-lipid inserts spontaneously into membranes and remains stable over prolonged periods [464]. Other targeted delivery systems can be explored as well, including siRNA, immunomodulatory drugs and other types of contrast agents encapsulated in liposomes [487], [488], [489], [490].

5.2 | FUTURE OUTLOOK

Lewis^a on biodegradable mMPIO for clinical translation. Combining the targeting power of Lewis^a and the safe, biodegradable multimeric MPIOs, a new contrast agent to monitor disease progression in brain inflammatory diseases, such as MS, would be possible. Although, as discussed before, the potential antigenicity of Lewis^a would probably not pose any issues, the assessment of Lewis^a antigenicity presented on nanoparticles needs to be performed before clinical translation.

Assessment of the differences between the transcriptome of adult and juvenile rat brains in response to IL-1β. Differences in mRNA transcripts upregulated by IL-1β during brain inflammation in the adult and juvenile rat could allow more tailored treatment strategies to be developed. Further studies regarding the differences could establish the molecular changes between the adult and juvenile brain when undergoing inflammation.

EV modification using Lewis^a to re-direct vesicles to sites of inflammation. Two different strategies could allow EV modifications with Lewis^a re-directing of EVs to sites of inflammation. First, a cargo-delivery method independent from the proteins exposed on EVs should include protease treatment of EVs to expose Lewis^a-lipids to E-Selectin. This would allow the internal cargo of EVs to be delivered. Second, if such a protease treatment would impair the integrity of the EV, a milder modification strategy could be employed where the existing glycan structures on the EV proteins could be extended with Lewis^a structures.

Targeted drug delivery to the inflamed brain using Lewis^a-lipid modified liposomes. Shown in this thesis is the successful targeting of fluorescent liposomes modified with Lewis^a-lipids to sites of IL-1β induced inflammation in the brain. The next stages to explore regarding the Lewis^a-mediated delivery is the capability of these liposomes to pass the intact BBB and assess if drug-cargo can be delivered behind the BBB. Potential cargo could include; siRNA against cell adhesion molecules which could be assessed by qPCR and immunohistochemistry and immunomodulatory drugs which could be assessed by evaluating microglial and astrocytic activation.

REFERENCES

1. Banks, W.A. and M.A. Erickson, *The blood-brain barrier and immune function and dysfunction.* Neurobiol Dis, 2010. **37**(1): p. 26-32.
2. Zlokovic, B.V., *The blood-brain barrier in health and chronic neurodegenerative disorders.* Neuron, 2008. **57**(2): p. 178-201.
3. Ciccarelli, O., et al., *Pathogenesis of multiple sclerosis: insights from molecular and metabolic imaging.* Lancet Neurol, 2014. **13**(8): p. 807-22.
4. Campbell, S.J., et al., *Central nervous system injury triggers hepatic CC and CXC chemokine expression that is associated with leukocyte mobilization and recruitment to both the central nervous system and the liver.* Am J Pathol, 2005. **166**(5): p. 1487-97.
5. Minagar, A. and J.S. Alexander, *Blood-brain barrier disruption in multiple sclerosis.* Mult Scler, 2003. **9**(6): p. 540-9.
6. Cartier, L., et al., *Chemokine receptors in the central nervous system: role in brain inflammation and neurodegenerative diseases.* Brain Res Brain Res Rev, 2005. **48**(1): p. 16-42.
7. Frijns, C.J. and L.J. Kappelle, *Inflammatory cell adhesion molecules in ischemic cerebrovascular disease.* Stroke, 2002. **33**(8): p. 2115-22.
8. Yilmaz, G. and D.N. Granger, *Cell adhesion molecules and ischemic stroke.* Neurol Res, 2008. **30**(8): p. 783-93.
9. Ransohoff, R.M., P. Kivisakk, and G. Kidd, *Three or more routes for leukocyte migration into the central nervous system.* Nat Rev Immunol, 2003. **3**(7): p. 569-81.
10. Schwartz, M., et al., *How do immune cells support and shape the brain in health, disease, and aging?* J Neurosci, 2013. **33**(45): p. 17587-96.
11. Galea, I., I. Bechmann, and V.H. Perry, *What is immune privilege (not)?* Trends Immunol, 2007. **28**(1): p. 12-8.
12. Bechmann, I., I. Galea, and V.H. Perry, *What is the blood-brain barrier (not)?* Trends Immunol, 2007. **28**(1): p. 5-11.
13. Larochelle, C., J.I. Alvarez, and A. Prat, *How do immune cells overcome the blood-brain barrier in multiple sclerosis?* FEBS Lett, 2011. **585**(23): p. 3770-80.
14. Sriram, S. and I. Steiner, *Experimental allergic encephalomyelitis: a misleading model of multiple sclerosis.* Ann Neurol, 2005. **58**(6): p. 939-45.
15. McCarthy, D.P., M.H. Richards, and S.D. Miller, *Mouse models of multiple sclerosis: experimental autoimmune encephalomyelitis and Theiler's virus-induced demyelinating disease.* Methods Mol Biol, 2012. **900**: p. 381-401.
16. Mardiguian, S., et al., *The contribution of the acute phase response to the pathogenesis of relapse in chronic-relapsing experimental autoimmune encephalitis models of multiple sclerosis.* J Neuroinflammation, 2017. **14**(1): p. 196.
17. Galea, I., et al., *An antigen-specific pathway for CD8 T cells across the blood-brain barrier.* J Exp Med, 2007. **204**(9): p. 2023-30.
18. Bolton, S.J. and V.H. Perry, *Differential blood-brain barrier breakdown and leucocyte recruitment following excitotoxic lesions in juvenile and adult rats.* Exp Neurol, 1998. **154**(1): p. 231-40.
19. Anthony, D.C., et al., *Age-related effects of interleukin-1 beta on polymorphonuclear neutrophil-dependent increases in blood-brain barrier permeability in rats.* Brain, 1997. **120 (Pt 3)**: p. 435-44.
20. Campbell, S.J., et al., *Altered chemokine expression in the spinal cord and brain contributes to differential interleukin-1beta-induced neutrophil recruitment.* J Neurochem, 2002. **83**(2): p. 432-41.
21. Ukkonen, M., et al., *Cell surface adhesion molecules and cytokine profiles in primary progressive multiple sclerosis.* Mult Scler, 2007. **13**(6): p. 701-7.

22. Kutzelnigg, A., et al., *Cortical demyelination and diffuse white matter injury in multiple sclerosis.* Brain, 2005. **128**(Pt 11): p. 2705-12.
23. van Horssen, J., et al., *The blood-brain barrier in cortical multiple sclerosis lesions.* J Neuropathol Exp Neurol, 2007. **66**(4): p. 321-8.
24. van der Valk, P. and S. Amor, *Preactive lesions in multiple sclerosis.* Curr Opin Neurol, 2009. **22**(3): p. 207-13.
25. Allan, S.M., P.J. Tyrrell, and N.J. Rothwell, *Interleukin-1 and neuronal injury.* Nat Rev Immunol, 2005. **5**(8): p. 629-40.
26. Watkins, L.R., et al., *Dynamic regulation of the proinflammatory cytokine, interleukin-1beta: molecular biology for non-molecular biologists.* Life Sci, 1999. **65**(5): p. 449-81.
27. Goshen, I. and R. Yirmiya, *Interleukin-1 (IL-1): a central regulator of stress responses.* Front Neuroendocrinol, 2009. **30**(1): p. 30-45.
28. Dujmovic, I., et al., *The analysis of IL-1 beta and its naturally occurring inhibitors in multiple sclerosis: The elevation of IL-1 receptor antagonist and IL-1 receptor type II after steroid therapy.* J Neuroimmunol, 2009. **207**(1-2): p. 101-6.
29. Murray, K.N., A.R. Parry-Jones, and S.M. Allan, *Interleukin-1 and acute brain injury.* Front Cell Neurosci, 2015. **9**: p. 18.
30. Galea, J. and D. Brough, *The role of inflammation and interleukin-1 in acute cerebrovascular disease.* J Inflamm Res, 2013. **6**: p. 121-8.
31. Perkins, N.D., *Integrating cell-signalling pathways with NF-kappaB and IKK function.* Nat Rev Mol Cell Biol, 2007. **8**(1): p. 49-62.
32. Murphy, K., et al., *Janeway's immunobiology*. 8th ed. 2012, New York: Garland Science. xix, 868 p.
33. Kern, J.A., L.J. Warnock, and J.D. McCafferty, *The 3' untranslated region of IL-1beta regulates protein production.* J Immunol, 1997. **158**(3): p. 1187-93.
34. Asson-Batres, M.A., et al., *Evolutionary conservation of the AU-rich 3' untranslated region of messenger RNA.* Proc Natl Acad Sci U S A, 1994. **91**(4): p. 1318-22.
35. Eder, C., *Mechanisms of interleukin-1beta release.* Immunobiology, 2009. **214**(7): p. 543-53.
36. Lopez-Castejon, G. and D. Brough, *Understanding the mechanism of IL-1beta secretion.* Cytokine Growth Factor Rev, 2011. **22**(4): p. 189-95.
37. Hara, H., et al., *Inhibition of interleukin 1beta converting enzyme family proteases reduces ischemic and excitotoxic neuronal damage.* Proc Natl Acad Sci U S A, 1997. **94**(5): p. 2007-12.
38. Spulber, S., T. Bartfai, and M. Schultzberg, *IL-1/IL-1ra balance in the brain revisited - evidence from transgenic mouse models.* Brain Behav Immun, 2009. **23**(5): p. 573-9.
39. Gutierrez, E.G., W.A. Banks, and A.J. Kastin, *Blood-borne interleukin-1 receptor antagonist crosses the blood-brain barrier.* J Neuroimmunol, 1994. **55**(2): p. 153-60.
40. Arend, W.P., *The balance between IL-1 and IL-1Ra in disease.* Cytokine Growth Factor Rev, 2002. **13**(4-5): p. 323-40.
41. Arend, W.P., et al., *Interleukin-1 receptor antagonist: role in biology.* Annu Rev Immunol, 1998. **16**: p. 27-55.
42. Felix, J. and S.N. Savvides, *Mechanisms of immunomodulation by mammalian and viral decoy receptors: insights from structures.* Nat Rev Immunol, 2017. **17**(2): p. 112-129.
43. Wang, D., et al., *Structural insights into the assembly and activation of IL-1beta with its receptors.* Nat Immunol, 2010. **11**(10): p. 905-11.
44. Butcher, E.C., *Leukocyte-endothelial cell recognition: three (or more) steps to specificity and diversity.* Cell, 1991. **67**(6): p. 1033-6.
45. Springer, T.A., *Traffic signals for lymphocyte recirculation and leukocyte emigration: the multistep paradigm.* Cell, 1994. **76**(2): p. 301-14.
46. Anthony, D.C. and F.J. Pitossi, *Special issue commentary: the changing face of inflammation in the brain.* Mol Cell Neurosci, 2013. **53**: p. 1-5.

47. Cayrol, R., et al., *Activated leukocyte cell adhesion molecule promotes leukocyte trafficking into the central nervous system.* Nat Immunol, 2008. **9**(2): p. 137-45.
48. Elices, M.J., et al., *VCAM-1 on activated endothelium interacts with the leukocyte integrin VLA-4 at a site distinct from the VLA-4/fibronectin binding site.* Cell, 1990. **60**(4): p. 577-84.
49. Washington, R., et al., *Expression of immunologically relevant endothelial cell activation antigens on isolated central nervous system microvessels from patients with multiple sclerosis.* Ann Neurol, 1994. **35**(1): p. 89-97.
50. Phillips, M.L., et al., *ELAM-1 mediates cell adhesion by recognition of a carbohydrate ligand, sialyl-Lex.* Science, 1990. **250**(4984): p. 1130-2.
51. Larkin, M., et al., *Spectrum of sialylated and nonsialylated fuco-oligosaccharides bound by the endothelial-leukocyte adhesion molecule E-selectin. Dependence of the carbohydrate binding activity on E-selectin density.* J Biol Chem, 1992. **267**(19): p. 13661-8.
52. Foxall, C., et al., *The three members of the selectin receptor family recognize a common carbohydrate epitope, the sialyl Lewis(x) oligosaccharide.* J Cell Biol, 1992. **117**(4): p. 895-902.
53. Nelson, R.M., et al., *Higher-affinity oligosaccharide ligands for E-selectin.* J Clin Invest, 1993. **91**(3): p. 1157-66.
54. Varki, A., *Selectin ligands.* Proc Natl Acad Sci U S A, 1994. **91**(16): p. 7390-7.
55. Hidalgo, A., et al., *Complete identification of E-selectin ligands on neutrophils reveals distinct functions of PSGL-1, ESL-1, and CD44.* Immunity, 2007. **26**(4): p. 477-89.
56. Cerutti, C. and A.J. Ridley, *Endothelial cell-cell adhesion and signaling.* Exp Cell Res, 2017.
57. Palabrica, T., et al., *Leukocyte accumulation promoting fibrin deposition is mediated in vivo by P-selectin on adherent platelets.* Nature, 1992. **359**(6398): p. 848-51.
58. Somers, W.S., et al., *Insights into the molecular basis of leukocyte tethering and rolling revealed by structures of P- and E-selectin bound to SLe(X) and PSGL-1.* Cell, 2000. **103**(3): p. 467-79.
59. Carlos, T.M. and J.M. Harlan, *Leukocyte-endothelial adhesion molecules.* Blood, 1994. **84**(7): p. 2068-101.
60. Wagner, D.D. and P.S. Frenette, *The vessel wall and its interactions.* Blood, 2008. **111**(11): p. 5271-81.
61. Marki, A., et al., *Role of the endothelial surface layer in neutrophil recruitment.* J Leukoc Biol, 2015. **98**(4): p. 503-15.
62. Hess, D.C., et al., *E-selectin expression on human brain microvascular endothelial cells.* Neurosci Lett, 1996. **213**(1): p. 37-40.
63. Minagar, A., et al., *Multiple sclerosis as a vascular disease.* Neurol Res, 2006. **28**(3): p. 230-5.
64. McAteer, M.A., et al., *In vivo magnetic resonance imaging of acute brain inflammation using microparticles of iron oxide.* Nat Med, 2007. **13**(10): p. 1253-8.
65. van Kasteren, S.I., et al., *Glyconanoparticles allow pre-symptomatic in vivo imaging of brain disease.* Proc Natl Acad Sci U S A, 2009. **106**(1): p. 18-23.
66. Carvalho-Tavares, J., et al., *A role for platelets and endothelial selectins in tumor necrosis factor-alpha-induced leukocyte recruitment in the brain microvasculature.* Circ Res, 2000. **87**(12): p. 1141-8.
67. Kivisakk, P., et al., *Human cerebrospinal fluid central memory CD4+ T cells: evidence for trafficking through choroid plexus and meninges via P-selectin.* Proc Natl Acad Sci U S A, 2003. **100**(14): p. 8389-94.
68. Dorovini-Zis, K. and H.K. Huynh, *Ultrastructural localization of factor VIII-related antigen in cultured human brain microvessel endothelial cells.* J Histochem Cytochem, 1992. **40**(5): p. 689-96.
69. Rudd, P.M., et al., *Glycosylation and the immune system.* Science, 2001. **291**(5512): p. 2370-6.

70. Haslam, S.M., et al., *Characterizing the glycome of the mammalian immune system.* Immunol Cell Biol, 2008. **86**(7): p. 564-73.
71. Varki, A., *Nothing in glycobiology makes sense, except in the light of evolution.* Cell, 2006. **126**(5): p. 841-5.
72. Rudd, P.M. and R.A. Dwek, *Glycosylation: heterogeneity and the 3D structure of proteins.* Crit Rev Biochem Mol Biol, 1997. **32**(1): p. 1-100.
73. Allen, H.J. and E.C. Kisailus, *Glycoconjugates : composition, structure, and function*. 1992, New York: Dekker. viii, 685 p.
74. Sharon, N., *Lectins: carbohydrate-specific reagents and biological recognition molecules.* J Biol Chem, 2007. **282**(5): p. 2753-64.
75. DeFrees, S.A., et al., *Sialyl Lewis x liposomes as a multivalent ligand and inhibitor of E-selectin mediated cellular adhesion.* Journal of the American Chemical Society, 1996. **118**(26): p. 6101-6104.
76. Thoma, G., et al., *Nanomolar E-selectin inhibitors: 700-fold potentiation of affinity by multivalent ligand presentation.* J Am Chem Soc, 2001. **123**(41): p. 10113-4.
77. Pavlovic, D., et al., *Chemically synthesized solid phase oligosaccharide probes for carbohydrate-binding receptors - Interactions of the E-, L- and P-selectins with sialyl-Le(X) and O-sulphated forms linked to biotin or to polyacrylamide.* Journal of Immunological Methods, 2002. **264**(1-2): p. 53-58.
78. Dernedde, J., et al., *Dendritic polyglycerol sulfates as multivalent inhibitors of inflammation.* Proc Natl Acad Sci U S A, 2010. **107**(46): p. 19679-84.
79. Garcia-Vallejo, J.J., et al., *Glycodendrimers prevent HIV transmission via DC-SIGN on dendritic cells.* Int Immunol, 2013. **25**(4): p. 221-33.
80. Kennedy, D.C., et al., *Glycosylated nanoscale surfaces: preparation and applications in medicine and molecular biology.* Chemistry, 2013. **19**(12): p. 3794-800.
81. Lepenies, B., J. Lee, and S. Sonkaria, *Targeting C-type lectin receptors with multivalent carbohydrate ligands.* Adv Drug Deliv Rev, 2013. **65**(9): p. 1271-81.
82. Cecioni, S., A. Imberty, and S. Vidal, *Glycomimetics versus multivalent glycoconjugates for the design of high affinity lectin ligands.* Chem Rev, 2015. **115**(1): p. 525-61.
83. Parsons, T.B., et al., *Optimal Synthetic Glycosylation of a Therapeutic Antibody.* Angew Chem Int Ed Engl, 2016. **55**(7): p. 2361-7.
84. Daniels, G., *Human blood groups*. 2nd ed. 2002, Malden, MA: Blackwell Science. x, 560 p.
85. Mourant, A.E., *A new human blood group antigen of frequent occurrence.* Nature, 1946. **158**: p. 237.
86. Sneath, J.S. and P.H. Sneath, *Transformation of the Lewis groups of human red cells.* Nature, 1955. **176**(4473): p. 172.
87. Marcus, D.M. and L.E. Cass, *Glycosphingolipids with Lewis blood group activity: uptake by human erythrocytes.* Science, 1969. **164**(3879): p. 553-5.
88. Babu, P., et al., *Structural characterisation of neutrophil glycans by ultra sensitive mass spectrometric glycomics methodology.* Glycoconj J, 2009. **26**(8): p. 975-86.
89. Viitala, J. and J. Jarnefelt, *The Red-Cell Surface Revisited.* Trends in Biochemical Sciences, 1985. **10**(10): p. 392-395.
90. Henry, S., R. Oriol, and B. Samuelsson, *Lewis histo-blood group system and associated secretory phenotypes.* Vox Sang, 1995. **69**(3): p. 166-82.
91. Ramsey, G., et al., *The Lewis blood group system in liver transplantation.* Transplant Proc, 1987. **19**(6): p. 4591-4.
92. Henry, S.M., B.E. Samuelsson, and R. Oriol, *Immunochemical and immunohistological expression of Lewis histo-blood group antigens in small intestine including individuals of the Le(a+b+) and Le(a-b-) nonsecretor phenotypes.* Glycoconj J, 1994. **11**(6): p. 600-7.
93. Costache, M., et al., *Evolution of fucosyltransferase genes in vertebrates.* J Biol Chem, 1997. **272**(47): p. 29721-8.

94. Garratty, G., *Blood groups and disease: a historical perspective.* Transfus Med Rev, 2000. **14**(4): p. 291-301.
95. Magalhaes, A., et al., *Fut2-null mice display an altered glycosylation profile and impaired BabA-mediated Helicobacter pylori adhesion to gastric mucosa.* Glycobiology, 2009. **19**(12): p. 1525-36.
96. Marionneau, S., et al., *ABH and Lewis histo-blood group antigens, a model for the meaning of oligosaccharide diversity in the face of a changing world.* Biochimie, 2001. **83**(7): p. 565-73.
97. Mondal, N., A. Buffone, Jr., and S. Neelamegham, *Distinct glycosyltransferases synthesize E-selectin ligands in human vs. mouse leukocytes.* Cell Adh Migr, 2013. **7**(3): p. 288-92.
98. Brazil, J.C., et al., *Expression of Lewis-a glycans on polymorphonuclear leukocytes augments function by increasing transmigration.* J Leukoc Biol, 2017.
99. Brazil, J.C., et al., *Targeting of Neutrophil Lewis X Blocks Transepithelial Migration and Increases Phagocytosis and Degranulation.* Am J Pathol, 2016. **186**(2): p. 297-311.
100. Feizi, T., *Blood Group-Related Oligosaccharides Are Ligands in Cell-Adhesion Events.* Biochemical Society Transactions, 1992. **20**(2): p. 274-278.
101. Hittelet, A., et al., *Binding sites for Lewis antigens are expressed by human colon cancer cells and negatively affect their migration.* Lab Invest, 2003. **83**(6): p. 777-87.
102. Kim, Y.J. and A. Varki, *Perspectives on the significance of altered glycosylation of glycoproteins in cancer.* Glycoconj J, 1997. **14**(5): p. 569-76.
103. Coisne, C., et al., *Differential expression of selectins by mouse brain capillary endothelial cells in vitro in response to distinct inflammatory stimuli.* Neurosci Lett, 2006. **392**(3): p. 216-20.
104. Bernardes-Silva, M., et al., *Recruitment of neutrophils across the blood-brain barrier: the role of E- and P-selectins.* J Cereb Blood Flow Metab, 2001. **21**(9): p. 1115-24.
105. Morel, A., et al., *Flow cytometric analysis reveals the high levels of platelet activation parameters in circulation of multiple sclerosis patients.* Mol Cell Biochem, 2017.
106. Zamora, C., et al., *Binding of Platelets to Lymphocytes: A Potential Anti-Inflammatory Therapy in Rheumatoid Arthritis.* J Immunol, 2017.
107. Jubeli, E., et al., *E-selectin as a target for drug delivery and molecular imaging.* J Control Release, 2012. **158**(2): p. 194-206.
108. Jubeli, E., et al., *Preparation of E-selectin-targeting nanoparticles and preliminary in vitro evaluation.* Int J Pharm, 2012. **426**(1-2): p. 291-301.
109. Green, P.J., et al., *High affinity binding of the leucocyte adhesion molecule L-selectin to 3'-sulphated-Le(a) and -Le(x) oligosaccharides and the predominance of sulphate in this interaction demonstrated by binding studies with a series of lipid-linked oligosaccharides.* Biochem Biophys Res Commun, 1992. **188**(1): p. 244-51.
110. Kogelberg, H. and T.J. Rutherford, *Studies on the three-dimensional behaviour of the selectin ligands Lewis(a) and sulphated Lewis(a) using NMR spectroscopy and molecular dynamics simulations.* Glycobiology, 1994. **4**(1): p. 49-57.
111. Martin, M.J., et al., *An investigation of the interactions of E-selectin with fuco-oligosaccharides of the blood group family.* Glycobiology, 2002. **12**(12): p. 829-35.
112. Anthony, D.C. and Y. Couch, *The systemic response to CNS injury.* Exp Neurol, 2014. **258**: p. 105-11.
113. Muto, S., T. Takada, and K. Matsumoto, *Biological activities of human mannose-binding lectin bound to two different ligand sugar structures, Lewis A and Lewis B antigens and high-mannose type oligosaccharides.* Biochim Biophys Acta, 2001. **1527**(1-2): p. 39-46.
114. Loveless, R.W., et al., *Bovine serum conglutinin is a lectin which binds non-reducing terminal N-acetylglucosamine, mannose and fucose residues.* Biochem J, 1989. **258**(1): p. 109-13.
115. Feizi, T., *Carbohydrate differentiation antigens: probable ligands for cell adhesion molecules.* Trends Biochem Sci, 1991. **16**(3): p. 84-6.

116. Fujita, T., *Evolution of the lectin-complement pathway and its role in innate immunity.* Nat Rev Immunol, 2002. **2**(5): p. 346-53.
117. Takahashi, K., et al., *Mannose-binding lectin and its associated proteases (MASPs) mediate coagulation and its deficiency is a risk factor in developing complications from infection, including disseminated intravascular coagulation.* Immunobiology, 2011. **216**(1-2): p. 96-102.
118. Wu, F., et al., *Complement component C3a plays a critical role in endothelial activation and leukocyte recruitment into the brain.* J Neuroinflammation, 2016. **13**: p. 23.
119. Shields, K.J., et al., *Complement proteins C3 and C4 bind to collagen and elastin in the vascular wall: a potential role in vascular stiffness and atherosclerosis.* Clin Transl Sci, 2011. **4**(3): p. 146-52.
120. Michailidou, I., et al., *Complement C3 on microglial clusters in multiple sclerosis occur in chronic but not acute disease: Implication for disease pathogenesis.* Glia, 2017. **65**(2): p. 264-277.
121. Farrokhi, M., et al., *Mannose-binding Lectin Mediated Complement Pathway in Autoimmune Neurological Disorders.* Iran J Allergy Asthma Immunol, 2016. **15**(3): p. 251-6.
122. de la Rosa, X., et al., *Mannose-binding lectin promotes local microvascular thrombosis after transient brain ischemia in mice.* Stroke, 2014. **45**(5): p. 1453-9.
123. Kwok, J.Y., et al., *Mannose binding lectin mediated complement pathway in multiple sclerosis.* J Neuroimmunol, 2011. **239**(1-2): p. 98-100.
124. Kawasaki, N., et al., *Highly fucosylated N-glycan ligands for mannan-binding protein expressed specifically on CD26 (DPPVI) isolated from a human colorectal carcinoma cell line, SW1116.* Glycobiology, 2009. **19**(4): p. 437-50.
125. Nonaka, M., et al., *Mannan-binding protein, a C-type serum lectin, recognizes primary colorectal carcinomas through tumor-associated Lewis glycans.* J Immunol, 2014. **192**(3): p. 1294-301.
126. Geijtenbeek, T.B., A. Engering, and Y. Van Kooyk, *DC-SIGN, a C-type lectin on dendritic cells that unveils many aspects of dendritic cell biology.* J Leukoc Biol, 2002. **71**(6): p. 921-31.
127. Bo, L., et al., *Distribution of immunoglobulin superfamily members ICAM-1, -2, -3, and the beta 2 integrin LFA-1 in multiple sclerosis lesions.* Journal of Neuropathology and Experimental Neurology, 1996. **55**(10): p. 1060-1072.
128. Arjmandi, A., K. Liu, and K. Dorovini-Zis, *Dendritic cell adhesion to cerebral endothelium: role of endothelial cell adhesion molecules and their ligands.* J Neuropathol Exp Neurol, 2009. **68**(3): p. 300-13.
129. Galustian, C., et al., *High and low affinity carbohydrate ligands revealed for murine SIGN-R1 by carbohydrate array and cell binding approaches, and differing specificities for SIGN-R3 and langerin.* Int Immunol, 2004. **16**(6): p. 853-66.
130. Garcia-Vallejo, J.J. and Y. van Kooyk, *The physiological role of DC-SIGN: a tale of mice and men.* Trends Immunol, 2013. **34**(10): p. 482-6.
131. Powlesland, A.S., et al., *Widely divergent biochemical properties of the complete set of mouse DC-SIGN-related proteins.* J Biol Chem, 2006. **281**(29): p. 20440-9.
132. Hohlfeld, R. and H. Wekerle, *Drug insight: using monoclonal antibodies to treat multiple sclerosis.* Nat Clin Pract Neurol, 2005. **1**(1): p. 34-44.
133. Compston, A., *McAlpine's multiple sclerosis*. 4th ed. 2005, Philadelphia: Churchill Livingstone Elsevier. x, 982 p.
134. Reich, D.S., C.F. Lucchinetti, and P.A. Calabresi, *Multiple Sclerosis.* N Engl J Med, 2018. **378**(2): p. 169-180.
135. Dendrou, C.A., L. Fugger, and M.A. Friese, *Immunopathology of multiple sclerosis.* Nat Rev Immunol, 2015. **15**(9): p. 545-58.

136. Gaitan, M.I., et al., *Evolution of the blood-brain barrier in newly forming multiple sclerosis lesions.* Ann Neurol, 2011. **70**(1): p. 22-9.
137. Serres, S., et al., *Systemic inflammatory response reactivates immune-mediated lesions in rat brain.* J Neurosci, 2009. **29**(15): p. 4820-8.
138. Singh, S., et al., *Microglial nodules in early multiple sclerosis white matter are associated with degenerating axons.* Acta Neuropathol, 2013. **125**(4): p. 595-608.
139. Archelos, J.J. and H.P. Hartung, *The role of adhesion molecules in multiple sclerosis: biology, pathogenesis and therapeutic implications.* Mol Med Today, 1997. **3**(7): p. 310-21.
140. Merrill, J.E. and E.N. Benveniste, *Cytokines in inflammatory brain lesions: helpful and harmful.* Trends Neurosci, 1996. **19**(8): p. 331-8.
141. Serres, S., et al., *VCAM-1-targeted magnetic resonance imaging reveals subclinical disease in a mouse model of multiple sclerosis.* FASEB J, 2011. **25**(12): p. 4415-22.
142. Martin, R., H.F. McFarland, and D.E. McFarlin, *Immunological aspects of demyelinating diseases.* Annu Rev Immunol, 1992. **10**: p. 153-87.
143. Lee, D.H. and R.A. Linker, *The role of myelin oligodendrocyte glycoprotein in autoimmune demyelination: a target for multiple sclerosis therapy?* Expert Opin Ther Targets, 2012. **16**(5): p. 451-62.
144. Sospedra, M. and R. Martin, *Immunology of multiple sclerosis.* Annu Rev Immunol, 2005. **23**: p. 683-747.
145. Chitnis, T., *The role of CD4 T cells in the pathogenesis of multiple sclerosis.* Int Rev Neurobiol, 2007. **79**: p. 43-72.
146. Salou, M., et al., *Involvement of CD8(+) T Cells in Multiple Sclerosis.* Front Immunol, 2015. **6**: p. 604.
147. Michel, L., et al., *B Cells in the Multiple Sclerosis Central Nervous System: Trafficking and Contribution to CNS-Compartmentalized Inflammation.* Front Immunol, 2015. **6**: p. 636.
148. Villoslada, P., *Biomarkers for multiple sclerosis.* Drug News Perspect, 2010. **23**(9): p. 585-95.
149. Katsavos, S. and M. Anagnostouli, *Biomarkers in Multiple Sclerosis: An Up-to-Date Overview.* Mult Scler Int, 2013. **2013**: p. 340508.
150. Cross, A.H. and E. Waubant, *MS and the B cell controversy.* Biochim Biophys Acta, 2011. **1812**(2): p. 231-8.
151. Postigo, A.A., et al., *B-Lymphocyte Binding to E-Selectin and P-Selectin Is Mediated through the De-Novo Expression of Carbohydrates on in-Vitro and in-Vivo Activated Human B-Cells.* Journal of Clinical Investigation, 1994. **94**(4): p. 1585-1596.
152. Battistini, L., et al., *CD8+ T cells from patients with acute multiple sclerosis display selective increase of adhesiveness in brain venules: a critical role for P-selectin glycoprotein ligand-1.* Blood, 2003. **101**(12): p. 4775-82.
153. Lee, B.P. and B.A. Imhof, *Lymphocyte transmigration in the brain: a new way of thinking.* Nat Immunol, 2008. **9**(2): p. 117-8.
154. Hertwig, L., et al., *Distinct functionality of neutrophils in multiple sclerosis and neuromyelitis optica.* Mult Scler, 2016. **22**(2): p. 160-73.
155. Martin, J., et al., *The dialogue between endothelial cells and monocytes/macrophages in vascular syndromes.* Curr Pharm Des, 2007. **13**(17): p. 1751-9.
156. Zhang, J., et al., *Regulation of endothelial cell adhesion molecule expression by mast cells, macrophages, and neutrophils.* PLoS One, 2011. **6**(1): p. e14525.
157. Mestas, J. and K. Ley, *Monocyte-endothelial cell interactions in the development of atherosclerosis.* Trends Cardiovasc Med, 2008. **18**(6): p. 228-32.
158. Chen, T.C., et al., *High glucose-treated macrophages augment E-selectin expression in endothelial cells.* J Biol Chem, 2011. **286**(29): p. 25564-73.
159. Waisman, A., et al., *Homeostasis of Microglia in the Adult Brain: Review of Novel Microglia Depletion Systems.* Trends Immunol, 2015. **36**(10): p. 625-36.

160. Li, Q. and B.A. Barres, *Microglia and macrophages in brain homeostasis and disease.* Nat Rev Immunol, 2017.
161. Paolicelli, R.C., et al., *Synaptic pruning by microglia is necessary for normal brain development.* Science, 2011. **333**(6048): p. 1456-8.
162. Vogel, D.Y., et al., *Macrophages in inflammatory multiple sclerosis lesions have an intermediate activation status.* J Neuroinflammation, 2013. **10**: p. 35.
163. Bogie, J.F., P. Stinissen, and J.J. Hendriks, *Macrophage subsets and microglia in multiple sclerosis.* Acta Neuropathol, 2014. **128**(2): p. 191-213.
164. Lou, N., et al., *Purinergic receptor P2RY12-dependent microglial closure of the injured blood-brain barrier.* Proc Natl Acad Sci U S A, 2016. **113**(4): p. 1074-9.
165. da Fonseca, A.C., et al., *The impact of microglial activation on blood-brain barrier in brain diseases.* Front Cell Neurosci, 2014. **8**: p. 362.
166. Christiansen, C.F., *Risk of vascular disease in patients with multiple sclerosis: a review.* Neurol Res, 2012. **34**(8): p. 746-53.
167. D'Haeseleer, M., et al., *Vascular aspects of multiple sclerosis.* Lancet Neurol, 2011. **10**(7): p. 657-66.
168. Corthals, A.P., *Multiple sclerosis is not a disease of the immune system.* Q Rev Biol, 2011. **86**(4): p. 287-321.
169. Anthony, D.C., et al., *The systemic response to brain injury and disease.* Brain Behav Immun, 2012. **26**(4): p. 534-40.
170. Gabay, C. and I. Kushner, *Acute-phase proteins and other systemic responses to inflammation.* N Engl J Med, 1999. **340**(6): p. 448-54.
171. Parker, G.A. and C.A. Picut, *Liver immunobiology.* Toxicol Pathol, 2005. **33**(1): p. 52-62.
172. Wilcockson, D.C., et al., *The systemic and local acute phase response following acute brain injury.* J Cereb Blood Flow Metab, 2002. **22**(3): p. 318-26.
173. Scolding, N.J., et al., *Vesicular removal by oligodendrocytes of membrane attack complexes formed by activated complement.* Nature, 1989. **339**(6226): p. 620-2.
174. Minagar, A., et al., *Elevated plasma endothelial microparticles in multiple sclerosis.* Neurology, 2001. **56**(10): p. 1319-24.
175. Hristov, M., et al., *Apoptotic bodies from endothelial cells enhance the number and initiate the differentiation of human endothelial progenitor cells in vitro.* Blood, 2004. **104**(9): p. 2761-6.
176. Couch, Y., et al., *Circulating endothelial cell-derived extracellular vesicles mediate the acute phase response and sickness behaviour associated with CNS inflammation.* Sci Rep, 2017. **7**(1): p. 9574.
177. Hazelton, I., et al., *Exacerbation of Acute Traumatic Brain Injury by Circulating Extracellular Vesicles.* J Neurotrauma, 2018.
178. Friand, V., G. David, and P. Zimmermann, *Syntenin and syndecan in the biogenesis of exosomes.* Biol Cell, 2015. **107**(10): p. 331-41.
179. Zaborowski, M.P., et al., *Extracellular Vesicles: Composition, Biological Relevance, and Methods of Study.* Bioscience, 2015. **65**(8): p. 783-797.
180. Minciacchi, V.R., M.R. Freeman, and D. Di Vizio, *Extracellular vesicles in cancer: exosomes, microvesicles and the emerging role of large oncosomes.* Semin Cell Dev Biol, 2015. **40**: p. 41-51.
181. Li, Q., G.K. Tofaris, and J.J. Davis, *Concentration-Normalized Electroanalytical Assaying of Exosomal Markers.* Anal Chem, 2017. **89**(5): p. 3184-3190.
182. Ortiz, A., *Not all extracellular vesicles were created equal: clinical implications.* Ann Transl Med, 2017. **5**(5): p. 111.
183. van Niel, G., G. D'Angelo, and G. Raposo, *Shedding light on the cell biology of extracellular vesicles.* Nat Rev Mol Cell Biol, 2018.
184. Kanninen, K.M., et al., *Exosomes as new diagnostic tools in CNS diseases.* Biochim Biophys Acta, 2016. **1862**(3): p. 403-10.

185. Ramalho, J., et al., *Gadolinium-Based Contrast Agent Accumulation and Toxicity: An Update.* AJNR Am J Neuroradiol, 2016. **37**(7): p. 1192-8.
186. Cipolla, L., M. Gregori, and P.W. So, *Glycans in magnetic resonance imaging: determinants of relaxivity to smart agents, and potential applications in biomedicine.* Curr Med Chem, 2011. **18**(7): p. 1002-18.
187. Anselmo, A.C. and S. Mitragotri, *Nanoparticles in the clinic.* Bioeng Transl Med, 2016. **1**(1): p. 10-29.
188. Filippi, M., et al., *Prediction of a multiple sclerosis diagnosis in patients with clinically isolated syndrome using the 2016 MAGNIMS and 2010 McDonald criteria: a retrospective study.* Lancet Neurol, 2018. **17**(2): p. 133-142.
189. Cross, A.H. and R.T. Naismith, *Refining the use of MRI to predict multiple sclerosis.* Lancet Neurol, 2018. **17**(2): p. 105-106.
190. Chavhan, G.B., et al., *Principles, techniques, and applications of T2*-based MR imaging and its special applications.* Radiographics, 2009. **29**(5): p. 1433-49.
191. Modo, M.M.J.J. and J.W.M. Bulte, *Magnetic resonance neuroimaging : methods and protocols*. Springer protocols. 2011, New York: Humana Press. xiv, 598 p.
192. Migliore, L., et al., *Nanomaterials and neurodegeneration.* Environ Mol Mutagen, 2015. **56**(2): p. 149-70.
193. Patil, R.M., et al., *Comprehensive cytotoxicity studies of superparamagnetic iron oxide nanoparticles.* Biochem Biophys Rep, 2018. **13**: p. 63-72.
194. Corot, C., et al., *Recent advances in iron oxide nanocrystal technology for medical imaging.* Adv Drug Deliv Rev, 2006. **58**(14): p. 1471-504.
195. Tourdias, T., et al., *Assessment of disease activity in multiple sclerosis phenotypes with combined gadolinium- and superparamagnetic iron oxide-enhanced MR imaging.* Radiology, 2012. **264**(1): p. 225-33.
196. Perez-Balderas, F., et al., *Covalent assembly of nanoparticles as a peptidase-degradable platform for molecular MRI.* Nat Commun, 2017. **8**: p. 14254.
197. Del Boccio, P., et al., *Integration of metabolomics and proteomics in multiple sclerosis: From biomarkers discovery to personalized medicine.* Proteomics Clin Appl, 2016. **10**(4): p. 470-84.
198. Anthony, D.C., et al., *Anti-CD20 inhibits T cell-mediated pathology and microgliosis in the rat brain.* Ann Clin Transl Neurol, 2014. **1**(9): p. 659-69.
199. Rivers, T.M., D.H. Sprunt, and G.P. Berry, *Observations on Attempts to Produce Acute Disseminated Encephalomyelitis in Monkeys.* J Exp Med, 1933. **58**(1): p. 39-53.
200. Freund, J., E.R. Stern, and T.M. Pisani, *Isoallergic encephalomyelitis and radiculitis in guinea pigs after one injection of brain and Mycobacteria in water-in-oil emulsion.* J Immunol, 1947. **57**(2): p. 179-94.
201. Kopeloff, L.M. and N. Kopeloff, *Neurologic manifestations in laboratory animals produced by organ (adjuvant) emulsions.* J Immunol, 1947. **57**(3): p. 229-37.
202. Tourdias, T., et al., *Adapted focal experimental autoimmune encephalomyelitis to allow MRI exploration of multiple sclerosis features.* Exp Neurol, 2011. **230**(2): p. 248-57.
203. Wang, D., et al., *Uncovering cryptic glycan markers in multiple sclerosis (MS) and experimental autoimmune encephalomyelitis (EAE).* Drug Dev Res, 2014. **75**(3): p. 172-88.
204. Schmitz, K., G. Geisslinger, and I. Tegeder, *Monoclonal Antibodies in Preclinical EAE Models of Multiple Sclerosis: A Systematic Review.* Int J Mol Sci, 2017. **18**(9).
205. Engelhardt, B., et al., *E- and P-selectin are not involved in the recruitment of inflammatory cells across the blood-brain barrier in experimental autoimmune encephalomyelitis.* Blood, 1997. **90**(11): p. 4459-72.
206. Doring, A., et al., *E- and P-selectin are not required for the development of experimental autoimmune encephalomyelitis in C57BL/6 and SJL mice.* J Immunol, 2007. **179**(12): p. 8470-9.

207. Matyszak, M.K. and V.H. Perry, *Demyelination in the central nervous system following a delayed-type hypersensitivity response to bacillus Calmette-Guerin.* Neuroscience, 1995. **64**(4): p. 967-77.
208. Games and C. Transatlantic Multiple Sclerosis Genetics, *A meta-analysis of whole genome linkage screens in multiple sclerosis.* J Neuroimmunol, 2003. **143**(1-2): p. 39-46.
209. Hollenbach, J.A. and J.R. Oksenberg, *The immunogenetics of multiple sclerosis: A comprehensive review.* J Autoimmun, 2015. **64**: p. 13-25.
210. International Multiple Sclerosis Genetics, C., et al., *Analysis of immune-related loci identifies 48 new susceptibility variants for multiple sclerosis.* Nat Genet, 2013. **45**(11): p. 1353-60.
211. Goodin, D.S., *The nature of genetic susceptibility to multiple sclerosis: constraining the possibilities.* BMC Neurol, 2016. **16**: p. 56.
212. Hendrickx, D.A.E., et al., *Gene Expression Profiling of Multiple Sclerosis Pathology Identifies Early Patterns of Demyelination Surrounding Chronic Active Lesions.* Front Immunol, 2017. **8**: p. 1810.
213. Jurynczyk, M., et al., *Metabolomics reveals distinct, antibody-independent, molecular signatures of MS, AQP4-antibody and MOG-antibody disease.* Acta Neuropathol Commun, 2017. **5**(1): p. 95.
214. Itoh, N., et al., *Cell-specific and region-specific transcriptomics in the multiple sclerosis model: Focus on astrocytes.* Proc Natl Acad Sci U S A, 2018. **115**(2): p. E302-E309.
215. H, E.H., H.N. Noristani, and F.E. Perrin, *Microglia Responses in Acute and Chronic Neurological Diseases: What Microglia-Specific Transcriptomic Studies Taught (and did Not Teach) Us.* Front Aging Neurosci, 2017. **9**: p. 227.
216. Sanchez-Pla, A., et al., *Transcriptomics: mRNA and alternative splicing.* J Neuroimmunol, 2012. **248**(1-2): p. 23-31.
217. Schwanhausser, B., et al., *Global quantification of mammalian gene expression control.* Nature, 2011. **473**(7347): p. 337-42.
218. Sharma, K., et al., *Cell type- and brain region-resolved mouse brain proteome.* Nat Neurosci, 2015. **18**(12): p. 1819-31.
219. Nielsen, P.A., et al., *Proteomic mapping of brain plasma membrane proteins.* Mol Cell Proteomics, 2005. **4**(4): p. 402-8.
220. Farias, A.S., et al., *Ten years of proteomics in multiple sclerosis.* Proteomics, 2014. **14**(4-5): p. 467-80.
221. Han, M.H., et al., *Proteomic analysis of active multiple sclerosis lesions reveals therapeutic targets.* Nature, 2008. **451**(7182): p. 1076-81.
222. Satoh, J.I., H. Tabunoki, and T. Yamamura, *Molecular network of the comprehensive multiple sclerosis brain-lesion proteome.* Mult Scler, 2009. **15**(5): p. 531-41.
223. Raphael, I., et al., *Microwave & magnetic (M2) proteomics reveals CNS-specific protein expression waves that precede clinical symptoms of experimental autoimmune encephalomyelitis.* Sci Rep, 2014. **4**: p. 6210.
224. Murugesan, N., et al., *Analysis of mouse brain microvascular endothelium using laser capture microdissection coupled with proteomics.* Methods Mol Biol, 2011. **686**: p. 297-311.
225. Olsen, J.V., et al., *Quantitative proteomic profiling of membrane proteins from the mouse brain cortex, hippocampus, and cerebellum using the HysTag reagent: mapping of neurotransmitter receptors and ion channels.* Brain Res, 2007. **1134**(1): p. 95-106.
226. Badhwar, A., et al., *The proteome of mouse cerebral arteries.* J Cereb Blood Flow Metab, 2014. **34**(6): p. 1033-46.
227. Chun, H.B., et al., *The proteome of mouse brain microvessel membranes and basal lamina.* J Cereb Blood Flow Metab, 2011. **31**(12): p. 2267-81.
228. Torbett, B.E., A. Baird, and B.P. Eliceiri, *Understanding the rules of the road: proteomic approaches to interrogate the blood brain barrier.* Front Neurosci, 2015. **9**: p. 70.

229. Hoshi, Y., et al., *Quantitative atlas of blood-brain barrier transporters, receptors, and tight junction proteins in rats and common marmoset.* J Pharm Sci, 2013. **102**(9): p. 3343-55.
230. Slany, A., et al., *Contribution of Human Fibroblasts and Endothelial Cells to the Hallmarks of Inflammation as Determined by Proteome Profiling.* Mol Cell Proteomics, 2016. **15**(6): p. 1982-97.
231. Petrotchenko, E.V. and C.H. Borchers, *Crosslinking combined with mass spectrometry for structural proteomics.* Mass Spectrom Rev, 2010. **29**(6): p. 862-76.
232. Sinz, A., *The advancement of chemical cross-linking and mass spectrometry for structural proteomics: from single proteins to protein interaction networks.* Expert Rev Proteomics, 2014. **11**(6): p. 733-43.
233. Sumranjit, J. and S.J. Chung, *Recent advances in target characterization and identification by photoaffinity probes.* Molecules, 2013. **18**(9): p. 10425-51.
234. Pham, N.D., R.B. Parker, and J.J. Kohler, *Photocrosslinking approaches to interactome mapping.* Curr Opin Chem Biol, 2013. **17**(1): p. 90-101.
235. Liu, F., et al., *Proteome-wide profiling of protein assemblies by cross-linking mass spectrometry.* Nat Methods, 2015. **12**(12): p. 1179-84.
236. Shields, C.J., et al., *Photochemistry of Aryl Azides - Detection and Characterization of a Dehydroazepine by Time-Resolved Infrared-Spectroscopy and Flash-Photolysis at Room-Temperature.* Journal of the American Chemical Society, 1987. **109**(15): p. 4723-4726.
237. Murale, D.P., et al., *Photo-affinity labeling (PAL) in chemical proteomics: a handy tool to investigate protein-protein interactions (PPIs).* Proteome Sci, 2016. **15**: p. 14.
238. Brunner, J., *New photolabeling and crosslinking methods.* Annu Rev Biochem, 1993. **62**: p. 483-514.
239. Kawamura, A. and D.M. Mihai, *Probing proteomes with benzophenone photoprobes.* Methods Mol Biol, 2012. **803**: p. 65-75.
240. Kleiner, P., et al., *A Whole Proteome Inventory of Background Photocrosslinker Binding.* Angew Chem Int Ed Engl, 2017. **56**(5): p. 1396-1401.
241. Brunner, J., H. Senn, and F.M. Richards, *3-Trifluoromethyl-3-phenyldiazirine. A new carbene generating group for photolabeling reagents.* J Biol Chem, 1980. **255**(8): p. 3313-8.
242. Chee, G.L., et al., *A diazirine-based photoaffinity etoposide probe for labeling topoisomerase II.* Bioorg Med Chem, 2010. **18**(2): p. 830-8.
243. Hashimoto, M. and Y. Hatanaka, *Recent progress in diazirine-based photoaffinity labeling.* European Journal of Organic Chemistry, 2008(15): p. 2513-2523.
244. Mackinnon, A.L. and J. Taunton, *Target Identification by Diazirine Photo-Cross-linking and Click Chemistry.* Curr Protoc Chem Biol, 2009. **1**: p. 55-73.
245. Sakurai, K., *Photoaffinity Probes for Identification of Carbohydrate-Binding Proteins.* Asian Journal of Organic Chemistry, 2015. **4**(2): p. 116-126.
246. Chang, T.C., et al., *Synthesis and evaluation of a photoactive probe with a multivalent carbohydrate for capturing carbohydrate-lectin interactions.* Bioconjug Chem, 2013. **24**(11): p. 1895-906.
247. Sakurai, K., et al., *Comparison of the reactivity of carbohydrate photoaffinity probes with different photoreactive groups.* Chembiochem, 2014. **15**(10): p. 1399-403.
248. Sakurai, K., Y. Hatai, and A. Okada, *Gold nanoparticle-based multivalent carbohydrate probes: selective photoaffinity labeling of carbohydrate-binding proteins.* Chem Sci, 2016. **7**(1): p. 702-706.
249. Geurink, P.P., et al., *Design of Peptide Hydroxamate-Based Photoreactive Activity-Based Probes of Zinc-Dependent Metalloproteases.* European Journal of Organic Chemistry, 2010. **2010**(11): p. 2100-2112.
250. Sperling, R.A. and W.J. Parak, *Surface modification, functionalization and bioconjugation of colloidal inorganic nanoparticles.* Philos Trans A Math Phys Eng Sci, 2010. **368**(1915): p. 1333-83.

251. Sapsford, K.E., et al., *Functionalizing nanoparticles with biological molecules: developing chemistries that facilitate nanotechnology.* Chem Rev, 2013. **113**(3): p. 1904-2074.
252. Stark, W.J., *Nanoparticles in biological systems.* Angew Chem Int Ed Engl, 2011. **50**(6): p. 1242-58.
253. Stephen, Z.R., F.M. Kievit, and M. Zhang, *Magnetite Nanoparticles for Medical MR Imaging.* Mater Today (Kidlington), 2011. **14**(7-8): p. 330-338.
254. Lee, N., et al., *Iron Oxide Based Nanoparticles for Multimodal Imaging and Magnetoresponsive Therapy.* Chem Rev, 2015.
255. Sun, Y., et al., *Fluorine-18 labeled rare-earth nanoparticles for positron emission tomography (PET) imaging of sentinel lymph node.* Biomaterials, 2011. **32**(11): p. 2999-3007.
256. Cole, L.E., et al., *Gold nanoparticles as contrast agents in x-ray imaging and computed tomography.* Nanomedicine (Lond), 2015. **10**(2): p. 321-41.
257. Xing, Y., et al., *Radiolabeled Nanoparticles for Multimodality Tumor Imaging.* Theranostics, 2014. **4**(3): p. 290-306.
258. Sakdinawat, A. and D. Attwood, *Nanoscale X-ray imaging.* Nature Photonics, 2010. **4**(12): p. 840-848.
259. Zhu, Y., et al., *Synchrotron-based X-ray microscopy for sub-100nm resolution cell imaging.* Curr Opin Chem Biol, 2017. **39**: p. 11-16.
260. Shapiro, D., et al., *Biological imaging by soft x-ray diffraction microscopy.* Proc Natl Acad Sci U S A, 2005. **102**(43): p. 15343-6.
261. Szoboszlai, N., et al., *Recent trends in total reflection X-ray fluorescence spectrometry for biological applications.* Anal Chim Acta, 2009. **633**(1): p. 1-18.
262. Serpell, C.J., et al., *Carbon nanotubes allow capture of krypton, barium and lead for multichannel biological X-ray fluorescence imaging.* Nat Commun, 2016. **7**: p. 13118.
263. Corezzi, S., et al., *Synchrotron-based X-ray fluorescence imaging of human cells labeled with CdSe quantum dots.* Anal Biochem, 2009. **388**(1): p. 33-9.
264. Meyer-Ilse, W., et al., *High resolution protein localization using soft X-ray microscopy.* J Microsc, 2001. **201**(Pt 3): p. 395-403.
265. Wang, H.J., et al., *Quantitative imaging of element spatial distribution in the brain section of a mouse model of Alzheimer's disease using synchrotron radiation X-ray fluorescence analysis.* Journal of Analytical Atomic Spectrometry, 2010. **25**(3): p. 328-333.
266. Popescu, B.F., et al., *Iron, copper, and zinc distribution of the cerebellum.* Cerebellum, 2009. **8**(2): p. 74-9.
267. Pushie, M.J., et al., *Elemental and chemically specific X-ray fluorescence imaging of biological systems.* Chem Rev, 2014. **114**(17): p. 8499-541.
268. Bourassa, M.W. and L.M. Miller, *Metal imaging in neurodegenerative diseases.* Metallomics, 2012. **4**(8): p. 721-38.
269. Chwiej, J., et al., *Classification of nerve cells from substantia nigra of patients with Parkinson's disease and amyotrophic lateral sclerosis with the use of X-ray fluorescence microscopy and multivariate methods.* Anal Chem, 2005. **77**(9): p. 2895-900.
270. Tomik, B., et al., *Implementation of X-ray fluorescence microscopy for investigation of elemental abnormalities in amyotrophic lateral sclerosis.* Neurochem Res, 2006. **31**(3): p. 321-31.
271. Popescu, B.F., et al., *Mapping metals in Parkinson's and normal brain using rapid-scanning x-ray fluorescence.* Phys Med Biol, 2009. **54**(3): p. 651-63.
272. Szczerbowska-Boruchowska, M., A. Krygowska-Wajs, and D. Adamek, *Elemental micro-imaging and quantification of human substantia nigra using synchrotron radiation based x-ray fluorescence--in relation to Parkinson's disease.* J Phys Condens Matter, 2012. **24**(24): p. 244104.
273. Kastyak, M.Z., et al., *Pigmented creatine deposits in Amyotrophic Lateral Sclerosis central nervous system tissues identified by synchrotron Fourier Transform Infrared*

microspectroscopy and X-ray fluorescence spectromicroscopy. Neuroscience, 2010. **166**(4): p. 1119-28.
274. Habib, C.A., et al., *Assessing abnormal iron content in the deep gray matter of patients with multiple sclerosis versus healthy controls.* AJNR Am J Neuroradiol, 2012. **33**(2): p. 252-8.
275. Braidy, N., et al., *Metal and complementary molecular bioimaging in Alzheimer's disease.* Front Aging Neurosci, 2014. **6**: p. 138.
276. Pushkar, Y., et al., *Aging results in copper accumulations in glial fibrillary acidic protein-positive cells in the subventricular zone.* Aging Cell, 2013. **12**(5): p. 823-32.
277. Pushie, M.J., et al., *Prion protein expression level alters regional copper, iron and zinc content in the mouse brain.* Metallomics, 2011. **3**(2): p. 206-14.
278. Popescu, B.F. and H. Nichol, *Mapping brain metals to evaluate therapies for neurodegenerative disease.* CNS Neurosci Ther, 2011. **17**(4): p. 256-68.
279. Korbas, M., et al., *Localizing organomercury uptake and accumulation in zebrafish larvae at the tissue and cellular level.* Proc Natl Acad Sci U S A, 2008. **105**(34): p. 12108-12.
280. Korbas, M., et al., *Methylmercury targets photoreceptor outer segments.* ACS Chem Biol, 2013. **8**(10): p. 2256-63.
281. Delfino, R., et al., *X-ray fluorescence elemental mapping and microscopy to follow hepatic disposition of a Gd-based magnetic resonance imaging contrast agent.* Clin Exp Pharmacol Physiol, 2011. **38**(12): p. 834-45.
282. Zhang, J.Z., et al., *Getting to the core of platinum drug bio-distributions: the penetration of anti-cancer platinum complexes into spheroid tumour models.* Metallomics, 2012. **4**(11): p. 1209-17.
283. Yuan, Y., et al., *Epidermal growth factor receptor targeted nuclear delivery and high-resolution whole cell X-ray imaging of Fe3O4@TiO2 nanoparticles in cancer cells.* ACS Nano, 2013. **7**(12): p. 10502-17.
284. Liu, T., et al., *Quantitative synchrotron X-ray fluorescence study of the penetration of transferrin-conjugated gold nanoparticles inside model tumour tissues.* Nanoscale, 2014. **6**(16): p. 9774-82.
285. Cagno, S., et al., *Combined Computed Nanotomography and Nanoscopic X-ray Fluorescence Imaging of Cobalt Nanoparticles in Caenorhabditis elegans.* Anal Chem, 2017. **89**(21): p. 11435-11442.
286. Jackson, B.P., et al., *Synchrotron X-ray 2D and 3D elemental imaging of CdSe/ZnS quantum dot nanoparticles in Daphnia magna.* Anal Bioanal Chem, 2009. **394**(3): p. 911-7.
287. Saha, K., et al., *Gold nanoparticles in chemical and biological sensing.* Chem Rev, 2012. **112**(5): p. 2739-79.
288. Caltagirone, C., et al., *Silica-based nanoparticles: a versatile tool for the development of efficient imaging agents.* Chem Soc Rev, 2014.
289. Park, J.H., et al., *Biodegradable luminescent porous silicon nanoparticles for in vivo applications.* Nat Mater, 2009. **8**(4): p. 331-6.
290. Basle, E., N. Joubert, and M. Pucheault, *Protein chemical modification on endogenous amino acids.* Chem Biol, 2010. **17**(3): p. 213-27.
291. Sletten, E.M. and C.R. Bertozzi, *Bioorthogonal chemistry: fishing for selectivity in a sea of functionality.* Angew Chem Int Ed Engl, 2009. **48**(38): p. 6974-98.
292. Spicer, C.D. and B.G. Davis, *Selective chemical protein modification.* Nat Commun, 2014. **5**: p. 4740.
293. Lee, Y.C., C.P. Stowell, and M.J. Krantz, *2-Imino-2-methoxyethyl 1-thioglycosides: new reagents for attaching sugars to proteins.* Biochemistry, 1976. **15**(18): p. 3956-63.
294. Stowell, C.P. and Y.C. Lee, *Preparation of neoglycoproteins using 2-imino-2-methoxyethyl 1-thioglycosides.* Methods Enzymol, 1982. **83**: p. 278-88.
295. Pearce, O.M., et al., *Glycoviruses: chemical glycosylation retargets adenoviral gene transfer.* Angew Chem Int Ed Engl, 2005. **44**(7): p. 1057-61.

296. Robinson, M.A., et al., *LEAPT: lectin-directed enzyme-activated prodrug therapy.* Proc Natl Acad Sci U S A, 2004. **101**(40): p. 14527-32.
297. De Munari, S., T. Schiffner, and B.G. Davis, *A Triply Divergent Reagent for Glycoprotein Synthesis.* Israel Journal of Chemistry, 2015. **55**(3-4): p. 387-391.
298. Munari, S.D., *Thesis*, in *Chemistry*. 2016, University of Oxford: Oxford.
299. Saliba, R.C., *Design and synthesis of nanoparticles functionalised with Lewis oligosaccharides for selective targeting of DC-SIGN* in *Chemistry*. 2013, University of Oxford: Oxford.
300. Chevolot, Y., et al., *Immobilisation on polystyrene of diazirine derivatives of mono- and disaccharides: biological activities of modified surfaces.* Bioorg Med Chem, 2001. **9**(11): p. 2943-53.
301. Udenfriend, S., et al., *Fluorescamine: a reagent for assay of amino acids, peptides, proteins, and primary amines in the picomole range.* Science, 1972. **178**(4063): p. 871-2.
302. Kasteren, S.I.v., *Probes for the in vivo visualisation of cerebral inflammation*, in *Department of Chemistry*. 2007, University of Oxford: Oxford.
303. Benson, J.R. and P.E. Hare, *O-phthalaldehyde: fluorogenic detection of primary amines in the picomole range. Comparison with fluorescamine and ninhydrin.* Proc Natl Acad Sci U S A, 1975. **72**(2): p. 619-22.
304. Cayot, P. and G. Tainturier, *The quantification of protein amino groups by the trinitrobenzenesulfonic acid method: a reexamination.* Anal Biochem, 1997. **249**(2): p. 184-200.
305. Gioeli, C. and J.B. Chattopadhyaya, *The Fluoren-9-Ylmethoxycarbonyl Group for the Protection of Hydroxy-Groups - Its Application in the Synthesis of an Octathymidylic Acid Fragment.* Journal of the Chemical Society-Chemical Communications, 1982(12): p. 672-674.
306. Wuts, P.G.M., T.W. Greene, and T.W. Greene, *Greene's protective groups in organic synthesis*. 4th ed. 2007, Hoboken, N.J.: Wiley-Interscience. xxviii, 1082 p.
307. Gambi, A., M. Winnewisser, and J.J. Christiansen, *The Infrared-Spectrum of Diazirine - H2cn2 - Rovibrational Analysis of the Nu-3-Fundamental.* Journal of Molecular Spectroscopy, 1983. **98**(2): p. 413-424.
308. Bonner, O.D. and J.D. Curry, *Infrared Spectra of Liquid H2o and D2o.* Infrared Physics, 1970. **10**(2): p. 91-+.
309. Chan, W.C. and P.D. White, *Fmoc solid phase peptide synthesis : a practical approach*. The practical approach series. 2000, New York: Oxford University Press. xxiv, 346 p.
310. Chronopoulou, L., et al., *Osmosis based method drives the self-assembly of polymeric chains into micro- and nanostructures.* Langmuir, 2009. **25**(19): p. 11940-6.
311. Rao, J.P. and K.E. Geckeler, *Polymer nanoparticles: Preparation techniques and size-control parameters.* Progress in Polymer Science, 2011. **36**(7): p. 887-913.
312. Poklar, N. and G. Vesnaver, *Thermal denaturation of proteins studied by UV spectroscopy.* Journal of Chemical Education, 2000. **77**(3): p. 380-382.
313. Bernhart, F.W., *Denaturation and molecular splitting of egg albumin by ultraviolet radiation energy.* J Biol Chem, 1939. **128**: p. 289-295.
314. Carson, M.J., et al., *CNS immune privilege: hiding in plain sight.* Immunol Rev, 2006. **213**: p. 48-65.
315. Obermeier, B., A. Verma, and R.M. Ransohoff, *The blood-brain barrier.* Handb Clin Neurol, 2016. **133**: p. 39-59.
316. Obermeier, B., R. Daneman, and R.M. Ransohoff, *Development, maintenance and disruption of the blood-brain barrier.* Nat Med, 2013. **19**(12): p. 1584-96.
317. Lundquist, J.J. and E.J. Toone, *The cluster glycoside effect.* Chem Rev, 2002. **102**(2): p. 555-78.
318. Sibson, N.R., et al., *MRI detection of early endothelial activation in brain inflammation.* Magn Reson Med, 2004. **51**(2): p. 248-52.

319. Arosio, D., et al., *Effective Targeting of DC-SIGN by alpha-Fucosylamide Functionalized Gold Nanoparticles.* Bioconjug Chem, 2014. **25**(12): p. 2244-51.
320. Brodie, N.I., et al., *Isotopically-coded short-range hetero-bifunctional photo-reactive crosslinkers for studying protein structure.* J Proteomics, 2015. **118**: p. 12-20.
321. Greenwood, J., et al., *SV40 large T immortalised cell lines of the rat blood-brain and blood-retinal barriers retain their phenotypic and immunological characteristics.* J Neuroimmunol, 1996. **71**(1-2): p. 51-63.
322. Feizi, T., *Oligosaccharides That Mediate Mammalian Cell-Cell Adhesion (Vol 3, Pg 701, 1993).* Current Opinion in Structural Biology, 1994. **4**(2): p. 296-296.
323. Leteux, C., et al., *The cysteine-rich domain of the macrophage mannose receptor is a multispecific lectin that recognizes chondroitin sulfates A and B and sulfated oligosaccharides of blood group Lewis(a) and Lewis(x) types in addition to the sulfated N-glycans of lutropin.* J Exp Med, 2000. **191**(7): p. 1117-26.
324. Feinberg, H., et al., *Structural basis for selective recognition of oligosaccharides by DC-SIGN and DC-SIGNR.* Science, 2001. **294**(5549): p. 2163-6.
325. van Liempt, E., et al., *Specificity of DC-SIGN for mannose- and fucose-containing glycans.* FEBS Lett, 2006. **580**(26): p. 6123-31.
326. Levin, J.D., H.P. Ting-Beall, and R.M. Hochmuth, *Correlating the kinetics of cytokine-induced E-selectin adhesion and expression on endothelial cells.* Biophys J, 2001. **80**(2): p. 656-67.
327. Alberts, B., *Molecular biology of the cell*. 4th ed. 2002, New York: Garland Science. xxxiv, 1548 p.
328. Bailly, Y., *Hemopoietic System*. 1990: Springer-Verlag Berlin Heidelberg.
329. Sakurai, K., T. Yasui, and S. Mizuno, *Comparative Analysis of the Reactivity of Diazirine-Based Photoaffinity Probes toward a Carbohydrate-Binding Protein.* Asian Journal of Organic Chemistry, 2015. **4**(8): p. 724-728.
330. Crick, F., *Central dogma of molecular biology.* Nature, 1970. **227**(5258): p. 561-3.
331. Wang, J., et al., *Integrated Analysis of Transcriptomic and Proteomic Datasets Reveals Information on Protein Expressivity and Factors Affecting Translational Efficiency.* Methods Mol Biol, 2016. **1375**: p. 123-36.
332. Matyszak, M.K., M.J. Townsend, and V.H. Perry, *Ultrastructural studies of an immune-mediated inflammatory response in the CNS parenchyma directed against a non-CNS antigen.* Neuroscience, 1997. **78**(2): p. 549-60.
333. Anthony, D., et al., *CXC chemokines generate age-related increases in neutrophil-mediated brain inflammation and blood-brain barrier breakdown.* Curr Biol, 1998. **8**(16): p. 923-6.
334. Campbell, S.J., et al., *Loss of the atypical inflammatory response in juvenile and aged rats.* Neuropathol Appl Neurobiol, 2007. **33**(1): p. 108-20.
335. Erta, M., A. Quintana, and J. Hidalgo, *Interleukin-6, a major cytokine in the central nervous system.* Int J Biol Sci, 2012. **8**(9): p. 1254-66.
336. Okuda, Y., et al., *IL-6-deficient mice are resistant to the induction of experimental autoimmune encephalomyelitis provoked by myelin oligodendrocyte glycoprotein.* Int Immunol, 1998. **10**(5): p. 703-8.
337. Samoilova, E.B., et al., *IL-6-deficient mice are resistant to experimental autoimmune encephalomyelitis: roles of IL-6 in the activation and differentiation of autoreactive T cells.* J Immunol, 1998. **161**(12): p. 6480-6.
338. Yoshimura, R., et al., *Higher plasma interleukin-6 (IL-6) level is associated with SSRI- or SNRI-refractory depression.* Prog Neuropsychopharmacol Biol Psychiatry, 2009. **33**(4): p. 722-6.
339. Stadelmann, C., et al., *BDNF and gp145trkB in multiple sclerosis brain lesions: neuroprotective interactions between immune and neuronal cells?* Brain, 2002. **125**(Pt 1): p. 75-85.

340. Qiao, L.Y., et al., *Inflammation and activity augment brain-derived neurotrophic factor peripheral release.* Neuroscience, 2016. **318**: p. 114-21.
341. Takeda, K., et al., *Brain-Derived Neurotrophic Factor Inhibits Intercellular Adhesion Molecule-1 Expression in Interleukin-1beta-Treated Endothelial Cells.* Cell Biochem Biophys, 2016.
342. Toft-Hansen, H., et al., *Metalloproteinases control brain inflammation induced by pertussis toxin in mice overexpressing the chemokine CCL2 in the central nervous system.* J Immunol, 2006. **177**(10): p. 7242-9.
343. Dimitrijevic, O.B., et al., *Effects of the chemokine CCL2 on blood-brain barrier permeability during ischemia-reperfusion injury.* J Cereb Blood Flow Metab, 2006. **26**(6): p. 797-810.
344. Anthony, D.C., et al., *Differential matrix metalloproteinase expression in cases of multiple sclerosis and stroke.* Neuropathol Appl Neurobiol, 1997. **23**(5): p. 406-15.
345. Campbell, S.J., et al., *Reduction of excitotoxicity and associated leukocyte recruitment by a broad-spectrum matrix metalloproteinase inhibitor.* J Neurochem, 2004. **89**(6): p. 1378-86.
346. Reichel, C.A., et al., *Ccl2 and Ccl3 mediate neutrophil recruitment via induction of protein synthesis and generation of lipid mediators.* Arterioscler Thromb Vasc Biol, 2009. **29**(11): p. 1787-93.
347. Reichel, C.A., et al., *C-C motif chemokine CCL3 and canonical neutrophil attractants promote neutrophil extravasation through common and distinct mechanisms.* Blood, 2012. **120**(4): p. 880-90.
348. Xue, M.L., et al., *A critical role for CCL2 and CCL3 chemokines in the regulation of polymorphonuclear neutrophils recruitment during corneal infection in mice.* Immunol Cell Biol, 2007. **85**(7): p. 525-31.
349. Mantovani, A., et al., *Neutrophils in the activation and regulation of innate and adaptive immunity.* Nat Rev Immunol, 2011. **11**(8): p. 519-31.
350. Thomson, A.W., *The cytokine handbook*. 3rd ed. 1998, San Diego: Academic Press. xxii, 1017 p.
351. Gerard, C. and B.J. Rollins, *Chemokines and disease.* Nat Immunol, 2001. **2**(2): p. 108-15.
352. Elovaara, I., et al., *Adhesion molecules in multiple sclerosis: relation to subtypes of disease and methylprednisolone therapy.* Arch Neurol, 2000. **57**(4): p. 546-51.
353. Galimberti, D., et al., *E-selectin A561C and G98T polymorphisms influence susceptibility and course of multiple sclerosis.* J Neuroimmunol, 2005. **165**(1-2): p. 201-5.
354. Serres, S., et al., *Comparison of MRI signatures in pattern I and II multiple sclerosis models.* NMR Biomed, 2009. **22**(10): p. 1014-24.
355. Ingram, G., et al., *Complement in multiple sclerosis: its role in disease and potential as a biomarker.* Clin Exp Immunol, 2009. **155**(2): p. 128-39.
356. Ansel, K.M., R.B. Harris, and J.G. Cyster, *CXCL13 is required for B1 cell homing, natural antibody production, and body cavity immunity.* Immunity, 2002. **16**(1): p. 67-76.
357. Wang, K.X. and D.T. Denhardt, *Osteopontin: role in immune regulation and stress responses.* Cytokine Growth Factor Rev, 2008. **19**(5-6): p. 333-45.
358. Enoksson, S.L., et al., *The inflammatory cytokine IL-18 induces self-reactive innate antibody responses regulated by natural killer T cells.* Proc Natl Acad Sci U S A, 2011. **108**(51): p. E1399-407.
359. Hendrickx, D.A.E., et al., *Staining of HLA-DR, Iba1 and CD68 in human microglia reveals partially overlapping expression depending on cellular morphology and pathology.* J Neuroimmunol, 2017. **309**: p. 12-22.
360. Hansen, T.K., et al., *Association between mannose-binding lectin and vascular complications in type 1 diabetes.* Diabetes, 2004. **53**(6): p. 1570-6.
361. Hamad, O.A., et al., *Contact activation of C3 enables tethering between activated platelets and polymorphonuclear leukocytes via CD11b/CD18.* Thromb Haemost, 2015. **114**(6): p. 1207-17.

362. Valentijn, K.M., et al., *Functional architecture of Weibel-Palade bodies.* Blood, 2011. **117**(19): p. 5033-43.
363. Yamamoto, H. and M.E. Gurney, *Human platelets contain brain-derived neurotrophic factor.* J Neurosci, 1990. **10**(11): p. 3469-78.
364. Nakahashi, T., et al., *Vascular endothelial cells synthesize and secrete brain-derived neurotrophic factor.* FEBS Lett, 2000. **470**(2): p. 113-7.
365. Serra-Millas, M., *Are the changes in the peripheral brain-derived neurotrophic factor levels due to platelet activation?* World J Psychiatry, 2016. **6**(1): p. 84-101.
366. Oulmouden, A., et al., *Molecular cloning and expression of a bovine alpha(1,3)-fucosyltransferase gene homologous to a putative ancestor gene of the human FUT3-FUT5-FUT6 cluster.* J Biol Chem, 1997. **272**(13): p. 8764-73.
367. Rungaldier, S., et al., *Stomatin interacts with GLUT1/SLC2A1, band 3/SLC4A1, and aquaporin-1 in human erythrocyte membrane domains.* Biochim Biophys Acta, 2013. **1828**(3): p. 956-66.
368. Zuo, S., U. Hellman, and P. Lundahl, *On the oligomeric state of the red blood cell glucose transporter GLUT1.* Biochim Biophys Acta, 2003. **1618**(1): p. 8-16.
369. Jeanne, M., et al., *COL4A2 mutations impair COL4A1 and COL4A2 secretion and cause hemorrhagic stroke.* Am J Hum Genet, 2012. **90**(1): p. 91-101.
370. Shellswell, G.B., et al., *Identification and differential distribution of collagen types in the central and peripheral nervous systems.* FEBS Lett, 1979. **106**(2): p. 305-8.
371. Maxwell, W.L., et al., *The distribution of types I, III, IV and V collagens in penetrant lesions of the central nervous system of the rat.* Histochem J, 1984. **16**(11): p. 1215-29.
372. Mohan, H., et al., *Extracellular matrix in multiple sclerosis lesions: Fibrillar collagens, biglycan and decorin are upregulated and associated with infiltrating immune cells.* Brain Pathol, 2010. **20**(5): p. 966-75.
373. Amara, A., et al., *Stromal cell-derived factor-1alpha associates with heparan sulfates through the first beta-strand of the chemokine.* J Biol Chem, 1999. **274**(34): p. 23916-25.
374. Veldkamp, C.T., et al., *The monomer-dimer equilibrium of stromal cell-derived factor-1 (CXCL 12) is altered by pH, phosphate, sulfate, and heparin.* Protein Sci, 2005. **14**(4): p. 1071-81.
375. Baronas-Lowell, D., J.L. Lauer-Fields, and G.B. Fields, *Induction of endothelial cell activation by a triple helical alpha2beta integrin ligand, derived from type I collagen alpha1(I)496-507.* J Biol Chem, 2004. **279**(2): p. 952-62.
376. Bayas, A., et al., *Human cerebral endothelial cells are a potential source for bioactive BDNF.* Cytokine, 2002. **19**(2): p. 55-8.
377. Chen, J. and J.A. Lopez, *Interactions of platelets with subendothelium and endothelium.* Microcirculation, 2005. **12**(3): p. 235-46.
378. Herr, A.B. and R.W. Farndale, *Structural insights into the interactions between platelet receptors and fibrillar collagen.* J Biol Chem, 2009. **284**(30): p. 19781-5.
379. Hidalgo, A., et al., *Heterotypic interactions enabled by polarized neutrophil microdomains mediate thromboinflammatory injury.* Nat Med, 2009. **15**(4): p. 384-91.
380. Nuyttens, B.P., et al., *Platelet adhesion to collagen.* Thromb Res, 2011. **127 Suppl 2**: p. S26-9.
381. Rowley, J.W., H. Schwertz, and A.S. Weyrich, *Platelet mRNA: the meaning behind the message.* Curr Opin Hematol, 2012. **19**(5): p. 385-91.
382. Sreeramkumar, V., et al., *Neutrophils scan for activated platelets to initiate inflammation.* Science, 2014. **346**(6214): p. 1234-8.
383. Damasceno, A., et al., *Serum BDNF levels are not reliable correlates of neurodegeneration in MS patients.* Mult Scler Relat Disord, 2015. **4**(1): p. 65-6.
384. Hohlfeld, R., et al., *The neuroprotective effect of inflammation: implications for the therapy of multiple sclerosis.* J Neuroimmunol, 2000. **107**(2): p. 161-6.

385. Ellerbroek, S.M., Y.I. Wu, and M.S. Stack, *Type I collagen stabilization of matrix metalloproteinase-2.* Arch Biochem Biophys, 2001. **390**(1): p. 51-6.
386. Rempe, R.G., A.M. Hartz, and B. Bauer, *Matrix metalloproteinases in the brain and blood-brain barrier: versatile breakers and makers.* J Cereb Blood Flow Metab, 2016.
387. Liz, M.A., et al., *Substrate specificity of transthyretin: identification of natural substrates in the nervous system.* Biochem J, 2009. **419**(2): p. 467-74.
388. Sevastou, I., et al., *Characterisation of Transcriptional Changes in the Spinal Cord of the Progressive Experimental Autoimmune Encephalomyelitis Biozzi ABH Mouse Model by RNA Sequencing.* PLoS One, 2016. **11**(6): p. e0157754.
389. Plante-Bordeneuve, V., et al., *Diagnostic pitfalls in sporadic transthyretin familial amyloid polyneuropathy (TTR-FAP).* Neurology, 2007. **69**(7): p. 693-8.
390. Li, X. and J.N. Buxbaum, *Transthyretin and the brain re-visited: is neuronal synthesis of transthyretin protective in Alzheimer's disease?* Mol Neurodegener, 2011. **6**: p. 79.
391. Larsen, P.D. and L.J. DeLallo, *Cerebrospinal fluid transthyretin in multiple sclerosis.* Neurology, 1987. **37**(7): p. 1262-3.
392. Pieragostino, D., et al., *Oxidative modifications of cerebral transthyretin are associated with multiple sclerosis.* Proteomics, 2013. **13**(6): p. 1002-9.
393. Borish, L., et al., *Transthyretin is an inhibitor of monocyte and endothelial cell interleukin-1 production.* Inflammation, 1992. **16**(5): p. 471-84.
394. Goncalves, N.P., P. Vieira, and M.J. Saraiva, *Interleukin-1 signaling pathway as a therapeutic target in transthyretin amyloidosis.* Amyloid, 2014. **21**(3): p. 175-84.
395. Masunaga, R., et al., *Alteration of platelet aggregation in patients with thyroid disorders.* Metabolism, 1997. **46**(10): p. 1128-31.
396. Karmakar, S., et al., *Differential proteomics study of platelets in asymptomatic constitutional macrothrombocytopenia: altered levels of cytoskeletal proteins.* Eur J Haematol, 2015. **94**(1): p. 43-50.
397. Sousa, M.M., et al., *Up-regulation of the extracellular matrix remodeling genes, biglycan, neutrophil gelatinase-associated lipocalin, and matrix metalloproteinase-9 in familial amyloid polyneuropathy.* FASEB J, 2005. **19**(1): p. 124-6.
398. Davis, P.J., et al., *Actions of Thyroid Hormone Analogues on Chemokines.* J Immunol Res, 2016. **2016**: p. 3147671.
399. Fleming, C.E., A.F. Nunes, and M.M. Sousa, *Transthyretin: more than meets the eye.* Prog Neurobiol, 2009. **89**(3): p. 266-76.
400. Sousa, M.M. and M.J. Saraiva, *Internalization of transthyretin. Evidence of a novel yet unidentified receptor-associated protein (RAP)-sensitive receptor.* J Biol Chem, 2001. **276**(17): p. 14420-5.
401. Tsuji, T., et al., *Induction of superoxide anion production from monocytes an neutrophils by activated platelets through the P-selectin-sialyl Lewis X interaction.* J Leukoc Biol, 1994. **56**(5): p. 583-7.
402. Al-Amran, F. and M. Shahkolahi, *Oxytocin ameliorates the immediate myocardial injury in rat heart transplant through downregulation of neutrophil-dependent myocardial apoptosis.* Transplant Proc, 2013. **45**(6): p. 2506-12.
403. Allegra, A., et al., *Increased serum levels of neutrophil gelatinase-associated lipocalin in patients with essential thrombocythemia and polycythemia vera.* Leuk Lymphoma, 2011. **52**(1): p. 101-7.
404. Chakraborty, S., et al., *The multifaceted roles of neutrophil gelatinase associated lipocalin (NGAL) in inflammation and cancer.* Biochim Biophys Acta, 2012. **1826**(1): p. 129-69.
405. Faurschou, M. and N. Borregaard, *Neutrophil granules and secretory vesicles in inflammation.* Microbes Infect, 2003. **5**(14): p. 1317-27.
406. Iseri, S.O., et al., *Oxytocin protects against sepsis-induced multiple organ damage: role of neutrophils.* J Surg Res, 2005. **126**(1): p. 73-81.

407. Iseri, S.O., et al., *Oxytocin ameliorates oxidative colonic inflammation by a neutrophil-dependent mechanism.* Peptides, 2005. **26**(3): p. 483-91.
408. Kjeldsen, L., et al., *Identification of neutrophil gelatinase-associated lipocalin as a novel matrix protein of specific granules in human neutrophils.* Blood, 1994. **83**(3): p. 799-807.
409. Li, T., et al., *Approaches Mediating Oxytocin Regulation of the Immune System.* Front Immunol, 2016. **7**: p. 693.
410. Kim, S.Y., et al., *Transthyretin as a new transporter of nanoparticles for receptor-mediated transcytosis in rat brain microvessels.* Colloids Surf B Biointerfaces, 2015. **136**: p. 989-96.
411. Flo, T.H., et al., *Lipocalin 2 mediates an innate immune response to bacterial infection by sequestrating iron.* Nature, 2004. **432**(7019): p. 917-21.
412. Jin, M., et al., *Lipocalin-2 deficiency attenuates neuroinflammation and brain injury after transient middle cerebral artery occlusion in mice.* J Cereb Blood Flow Metab, 2014. **34**(8): p. 1306-14.
413. Lee, S., et al., *Lipocalin-2 Is a chemokine inducer in the central nervous system: role of chemokine ligand 10 (CXCL10) in lipocalin-2-induced cell migration.* J Biol Chem, 2011. **286**(51): p. 43855-70.
414. Al Nimer, F., et al., *Lipocalin-2 is increased in progressive multiple sclerosis and inhibits remyelination.* Neurol Neuroimmunol Neuroinflamm, 2016. **3**(1): p. e191.
415. Marques, F., et al., *Lipocalin 2 is present in the EAE brain and is modulated by natalizumab.* Front Cell Neurosci, 2012. **6**: p. 33.
416. Berard, J.L., et al., *Lipocalin 2 is a novel immune mediator of experimental autoimmune encephalomyelitis pathogenesis and is modulated in multiple sclerosis.* Glia, 2012. **60**(7): p. 1145-59.
417. Huitinga, I., et al., *IL-1beta immunoreactive neurons in the human hypothalamus: reduced numbers in multiple sclerosis.* J Neuroimmunol, 2000. **107**(1): p. 8-20.
418. Blaner, W.S., *STRA6, a cell-surface receptor for retinol-binding protein: the plot thickens.* Cell Metab, 2007. **5**(3): p. 164-6.
419. Berry, D.C., et al., *Cross talk between signaling and vitamin A transport by the retinol-binding protein receptor STRA6.* Mol Cell Biol, 2012. **32**(15): p. 3164-75.
420. Fragoso, Y.D., P.N. Stoney, and P.J. McCaffery, *The evidence for a beneficial role of vitamin A in multiple sclerosis.* CNS Drugs, 2014. **28**(4): p. 291-9.
421. Mizee, M.R., et al., *Astrocyte-derived retinoic acid: a novel regulator of blood-brain barrier function in multiple sclerosis.* Acta Neuropathol, 2014. **128**(5): p. 691-703.
422. Mizee, M.R., et al., *Retinoic acid induces blood-brain barrier development.* J Neurosci, 2013. **33**(4): p. 1660-71.
423. Zarbock, A., R.K. Polanowska-Grabowska, and K. Ley, *Platelet-neutrophil-interactions: linking hemostasis and inflammation.* Blood Rev, 2007. **21**(2): p. 99-111.
424. Nemzek, J.A., et al., *Differences in normal values for murine white blood cell counts and other hematological parameters based on sampling site.* Inflamm Res, 2001. **50**(10): p. 523-7.
425. Eigenmann, M.J., et al., *Quantification of IgG monoclonal antibody clearance in tissues.* MAbs, 2017. **9**(6): p. 1007-1015.
426. Gregory, S.H., et al., *Complementary adhesion molecules promote neutrophil-Kupffer cell interaction and the elimination of bacteria taken up by the liver.* Journal of Immunology, 2002. **168**(1): p. 308-315.
427. Bajt, M.L., A. Farhood, and H. Jaeschke, *Effects of CXC chemokines on neutrophil activation and sequestration in hepatic vasculature.* Am J Physiol Gastrointest Liver Physiol, 2001. **281**(5): p. G1188-95.
428. Larsen, E., et al., *PADGEM-dependent adhesion of platelets to monocytes and neutrophils is mediated by a lineage-specific carbohydrate, LNF III (CD15).* Cell, 1990. **63**(3): p. 467-74.
429. Granger, D.N. and E. Senchenkova, in *Inflammation and the Microcirculation*. 2010: San Rafael (CA).

430. Leeuwenberg, J.F., et al., *E-selectin and intercellular adhesion molecule-1 are released by activated human endothelial cells in vitro.* Immunology, 1992. **77**(4): p. 543-9.
431. Bodary, P.F., et al., *Generation of soluble P- and E-selectins in vivo is dependent on expression of P-selectin glycoprotein ligand-1.* J Thromb Haemost, 2007. **5**(3): p. 599-603.
432. Abou-Saleh, H., et al., *Neutrophil P-selectin-glycoprotein-ligand-1 binding to platelet P-selectin enhances metalloproteinase 2 secretion and platelet-neutrophil aggregation.* Thromb Haemost, 2005. **94**(6): p. 1230-5.
433. Issekutz, A.C., et al., *Intravenous IgG (IVIG) and subcutaneous IgG (SCIG) preparations have comparable inhibitory effect on T cell activation, which is not dependent on IgG sialylation, monocytes or B cells.* Clin Immunol, 2015. **160**(2): p. 123-32.
434. Macmillan, H.F., et al., *Intravenous immunoglobulin G selectively inhibits IL-1alpha-induced neutrophil-endothelial cell adhesion.* Autoimmunity, 2010. **43**(8): p. 619-27.
435. Hitoshi, S., et al., *Molecular cloning and expression of two types of rabbit beta-galactoside alpha 1,2-fucosyltransferase.* J Biol Chem, 1995. **270**(15): p. 8844-50.
436. Bassaganas, S., et al., *Inflammatory cytokines regulate the expression of glycosyltransferases involved in the biosynthesis of tumor-associated sialylated glycans in pancreatic cancer cell lines.* Cytokine, 2015. **75**(1): p. 197-206.
437. Padro, M., et al., *Regulation of glycosyltransferases and Lewis antigens expression by IL-1beta and IL-6 in human gastric cancer cells.* Glycoconj J, 2011. **28**(2): p. 99-110.
438. Bochner, B.S., et al., *Differences between human eosinophils and neutrophils in the function and expression of sialic acid-containing counterligands for E-selectin.* J Immunol, 1994. **152**(2): p. 774-82.
439. Nimrichter, L., et al., *E-selectin receptors on human leukocytes.* Blood, 2008. **112**(9): p. 3744-52.
440. Magalhaes, A., et al., *Muc5ac gastric mucin glycosylation is shaped by FUT2 activity and functionally impacts Helicobacter pylori binding.* Sci Rep, 2016. **6**: p. 25575.
441. Hauser, R., *Le(a) and Le(b) tissue glycosphingolipids.* Transfusion, 1995. **35**(7): p. 577-81.
442. Fabian, E., et al., *Tissue distribution and toxicity of intravenously administered titanium dioxide nanoparticles in rats.* Arch Toxicol, 2008. **82**(3): p. 151-7.
443. Shi, H., et al., *Titanium dioxide nanoparticles: a review of current toxicological data.* Part Fibre Toxicol, 2013. **10**: p. 15.
444. Sufian, M.M., et al., *Safety issues associated with the use of nanoparticles in human body.* Photodiagnosis Photodyn Ther, 2017. **19**: p. 67-72.
445. Anstee, D.J., *The relationship between blood groups and disease.* Blood, 2010. **115**(23): p. 4635-43.
446. Tong, M., et al., *Reprograming of gut microbiome energy metabolism by the FUT2 Crohn's disease risk polymorphism.* ISME J, 2014. **8**(11): p. 2193-206.
447. Maroni, L., et al., *Fucosyltransferase 2: a genetic risk factor for primary sclerosing cholangitis and Crohn's disease--a comprehensive review.* Clin Rev Allergy Immunol, 2015. **48**(2-3): p. 182-91.
448. Hein, H.O., P. Suadicani, and F. Gyntelberg, *The Lewis blood group--a new genetic marker of obesity.* Int J Obes (Lond), 2005. **29**(5): p. 540-2.
449. Hein, H.O., et al., *The Lewis blood group--a new genetic marker of ischaemic heart disease.* J Intern Med, 1992. **232**(6): p. 481-7.
450. Alexy, T., et al., *Abnormal blood rheology and chronic low grade inflammation: possible risk factors for accelerated atherosclerosis and coronary artery disease in Lewis negative subjects.* Atherosclerosis, 2015. **239**(1): p. 248-51.
451. Smith-Brown, P., et al., *Mothers Secretor Status Affects Development of Childrens Microbiota Composition and Function: A Pilot Study.* PLoS One, 2016. **11**(9): p. e0161211.
452. Pickard, J.M. and A.V. Chervonsky, *Intestinal fucose as a mediator of host-microbe symbiosis.* J Immunol, 2015. **194**(12): p. 5588-93.

453. Maynard, C.L., et al., *Reciprocal interactions of the intestinal microbiota and immune system.* Nature, 2012. **489**(7415): p. 231-41.
454. Berer, K., et al., *Commensal microbiota and myelin autoantigen cooperate to trigger autoimmune demyelination.* Nature, 2011. **479**(7374): p. 538-41.
455. Wacklin, P., et al., *Secretor genotype (FUT2 gene) is strongly associated with the composition of Bifidobacteria in the human intestine.* PLoS One, 2011. **6**(5): p. e20113.
456. Warner, H.B., G.S. Merz, and R.I. Carp, *Blood group frequencies in multiple sclerosis populations in the United States.* Neurology, 1980. **30**(6): p. 671-3.
457. Papiha, S.S. and D.F. Roberts, *Serum alkaline phosphatase in patients with multiple sclerosis.* Clin Genet, 1975. **7**(1): p. 77-82.
458. Markovic, S., et al., *Genetic markers in the blood of multiple sclerosis patients.* Neurol Croat, 1991. **41**(1-2): p. 3-12.
459. Sodar, B.W., et al., *Low-density lipoprotein mimics blood plasma-derived exosomes and microvesicles during isolation and detection.* Sci Rep, 2016. **6**: p. 24316.
460. Stoner, S.A., et al., *High sensitivity flow cytometry of membrane vesicles.* Cytometry A, 2016. **89**(2): p. 196-206.
461. de Rond, L., et al., *Comparison of Generic Fluorescent Markers for Detection of Extracellular Vesicles by Flow Cytometry.* Clin Chem, 2018. **64**(4): p. 680-689.
462. Valkonen, S., et al., *Biological reference materials for extracellular vesicle studies.* Eur J Pharm Sci, 2017. **98**: p. 4-16.
463. Akbar, N., et al., *Endothelium-derived extracellular vesicles promote splenic monocyte mobilization in myocardial infarction.* JCI Insight, 2017. **2**(17).
464. Frame, T., et al., *Synthetic glycolipid modification of red blood cell membranes.* Transfusion, 2007. **47**(5): p. 876-82.
465. Wokovich, A., et al., *Particle size determination of sunscreens formulated with various forms of titanium dioxide.* Drug Dev Ind Pharm, 2009. **35**(10): p. 1180-9.
466. Nishihara, E., et al., *Expression of copper trafficking genes in the mouse brain.* Neuroreport, 1998. **9**(14): p. 3259-63.
467. Kuo, Y.M., et al., *Copper transport protein (Ctr1) levels in mice are tissue specific and dependent on copper status.* J Nutr, 2006. **136**(1): p. 21-6.
468. Percival, S.S., *Copper and immunity.* Am J Clin Nutr, 1998. **67**(5 Suppl): p. 1064S-1068S.
469. Matusch, A., et al., *Cerebral bioimaging of Cu, Fe, Zn, and Mn in the MPTP mouse model of Parkinson's disease using laser ablation inductively coupled plasma mass spectrometry (LA-ICP-MS).* J Am Soc Mass Spectrom, 2010. **21**(1): p. 161-71.
470. Davies, K.M., et al., *Copper pathology in vulnerable brain regions in Parkinson's disease.* Neurobiol Aging, 2014. **35**(4): p. 858-66.
471. Scheiber, I.F., J.F. Mercer, and R. Dringen, *Metabolism and functions of copper in brain.* Prog Neurobiol, 2014. **116**: p. 33-57.
472. Chantarasrivong, C., et al., *Synthesis and Functional Characterization of Novel Sialyl LewisX Mimic-Decorated Liposomes for E-selectin-Mediated Targeting to Inflamed Endothelial Cells.* Mol Pharm, 2017.
473. Belogurov, A.A., Jr., et al., *Liposome-encapsulated peptides protect against experimental allergic encephalitis.* FASEB J, 2013. **27**(1): p. 222-31.
474. Butin-Israeli, V., et al., *Deposition of microparticles by neutrophils onto inflamed epithelium: a new mechanism to disrupt epithelial intercellular adhesions and promote transepithelial migration.* FASEB J, 2016. **30**(12): p. 4007-4020.
475. Huang, H., et al., *Evolutionary conservation and selection of human disease gene orthologs in the rat and mouse genomes.* Genome Biol, 2004. **5**(7): p. R47.
476. Nguyen, K., et al., *Molecular cloning and characterization of the Caenorhabditis elegans alpha1,3-fucosyltransferase family.* Glycobiology, 2007. **17**(6): p. 586-99.

477. Weston, B.W., et al., *Expression of human alpha(1,3)fucosyltransferase antisense sequences inhibits selectin-mediated adhesion and liver metastasis of colon carcinoma cells.* Cancer Res, 1999. **59**(9): p. 2127-35.
478. Durrant, L.G., P. Noble, and I. Spendlove, *Immunology in the clinic review series; focus on cancer: glycolipids as targets for tumour immunotherapy.* Clin Exp Immunol, 2012. **167**(2): p. 206-15.
479. Khodabandehlou, K., et al., *Targeting cell adhesion molecules with nanoparticles using in vivo and flow-based in vitro models of atherosclerosis.* Exp Biol Med (Maywood), 2017: p. 1535370217693116.
480. Thorne, S.A., et al., *Modified low density lipoprotein and cytokines mediate monocyte adhesion to smooth muscle cells.* Atherosclerosis, 1996. **127**(2): p. 167-76.
481. Meeran, K. and S.R. Bloom, *Lewis Phenotypes, Insulin-Resistance, and Risk of Ischemic-Heart-Disease.* British Heart Journal, 1994. **71**(4): p. 305-306.
482. Kang, H.W., et al., *Magnetic resonance imaging of inducible E-selectin expression in human endothelial cell culture.* Bioconjug Chem, 2002. **13**(1): p. 122-7.
483. Nelson, A.L., E. Dhimolea, and J.M. Reichert, *Development trends for human monoclonal antibody therapeutics.* Nat Rev Drug Discov, 2010. **9**(10): p. 767-74.
484. Sapatnekar, S. and P.I. Figueroa, *Cold Antibodies in Cardiovascular Surgery: Is Preoperative Screening Necessary?* Am J Clin Pathol, 2016. **145**(6): p. 789-95.
485. Liu, H., et al., *Label-free CEST MRI Detection of Citicoline-Liposome Drug Delivery in Ischemic Stroke.* Theranostics, 2016. **6**(10): p. 1588-600.
486. Garnier, B., et al., *Annexin A5-functionalized liposomes for targeting phosphatidylserine-exposing membranes.* Bioconjug Chem, 2009. **20**(11): p. 2114-22.
487. Allen, T.M. and P.R. Cullis, *Liposomal drug delivery systems: from concept to clinical applications.* Adv Drug Deliv Rev, 2013. **65**(1): p. 36-48.
488. Pattni, B.S., V.V. Chupin, and V.P. Torchilin, *New Developments in Liposomal Drug Delivery.* Chem Rev, 2015. **115**(19): p. 10938-66.
489. Sercombe, L., et al., *Advances and Challenges of Liposome Assisted Drug Delivery.* Front Pharmacol, 2015. **6**: p. 286.
490. Bulbake, U., et al., *Liposomal Formulations in Clinical Use: An Updated Review.* Pharmaceutics, 2017. **9**(2).

* (http://book.bionumbers.org/how-big-is-the-average-protein/ 375 amino acids + 110 Da average molecular weight of an amino acid) Last viewed 14-03-2018.

** https://www.thermofisher.com/uk/en/home/references/protocols/proteins-expression-isolation-and-analysis/protein-isolation-protocol/m-270-amine.html Last viewed 14-03-2018.

*** http://www.liposomes.org/2009/01/number-of-lipid-molecules-per-liposome.html Last viewed 14-03-2018.